PHYSI

VOLUME 67

THE PHYSICAL REVIEW

A journal of experimental and theoretical physics established by E. L. Nichols in 1893

Published by the American Institute of Physics for the

AMERICAN PHYSICAL SOCIETY

Officers

President

J. H. Van Vleck
Harvard University
Cambridge, Massachusetts

Vice-President

Enrico Fermi
Institute for Nuclear Studies
University of Chicago
Chicago 37, Illinois

Secretary

K. K. Darrow
Bell Telephone Laboratories
Office:
Columbia University
New York 27, New York

Treasurer

G. B. Pegram
Columbia University
New York 27, New York

Local Secretary for the Pacific Coast

J. Kaplan
University of California at Los Angeles
Los Angeles, California

Managing Editor

S. A. Goudsmit
Brookhaven National Laboratory
Upton, Long Island
New York

BOARD OF EDITORS

Editor

S. A. Goudsmit

Assistant Editor

S. Pasternack

Associate Editors

Harvey Brooks	M. Goldhaber	W. P. Allis
R. F. Christy	R. Hofstadter	F. G. Brickwedde
C. L. Critchfield	A. W. Lawson	W. B. Fretter
M. Deutsch	A. Pais	Conyers Herring
T. H. Johnson	R. Serber	H. W. Lewbenz
Bruno Rossi	C. H. Townes	Arnold Nordsieck

Manuscripts for publication should be submitted to S. A. Goudsmit, Brookhaven National Laboratory, Upton, Long Island, New York. The authors' institutions are requested to pay a publication charge of $15 per page which, if honored, entitles them to 100 free reprints. Instructions will be sent with galley proofs.

Proof and all correspondence concerning papers in the process of publication should be addressed to the Publication Manager, American Institute of Physics, 57 East 55 Street, New York 22, New York.

Subscription Price

United States and Canada $30.00
Members $22.00

Back Numbers

Yearly back number rate when complete year is available:
Prior to 1949: $25.00
Thereafter: $33.00
Single copies: $3.00 each, prior to July, 1929;
$1.50 each, July, 1929–December, 1945;
$3.00 each, January, 1942–December, 1946;
$1.50 each, thereafter.
General index, 1893–1926: $4.00.

Subscriptions, renewals, and orders for back numbers should be addressed to the American Institute of Physics, 57 East 55 Street, New York 22, New York.

Changes of address in the case of members of the American Physical Society should be addressed to the Treasurer; in the case of other subscribers to the American Institute of Physics.

[1] For Series I inquire of Physics Department, Cornell University, Ithaca, New York.

The Physical Review is published semi-monthly at Prince and Lemon Streets, Lancaster, Pennsylvania.

Entered as second-class matter March 6, 1917, at the Post Office at Lancaster, Pennsylvania, under the Act of March 3, 1879.

Acceptance for mailing at special rate of postage provided for in paragraph (d-2), section 34.40, P. L. & R. of 1948, authorized January 27, 1950.

THE
PHYSICAL REVIEW

A journal of experimental and theoretical physics established by E. L. Nichols in 1893

SECOND SERIES, VOL. 87, NO. 6 SEPTEMBER 15, 1952

Intermediate Coupling as Encountered in Some of the p-Shell Nuclei

D. R. INGLIS
Argonne National Laboratory, Chicago, Illinois
(Received June 4, 1952)

The manner in which a transition into intermediate coupling, between the extremes of (jj) coupling and (LS) coupling, accounts for much of the failure of the (jj) coupling shell model in the light nuclei of the p-shell is illustrated by some typical examples. The set of secular equations for the configurations p^2 and p^{-2} applying to Li^8+He^6 and to $N^{14}+C^{14}$ is sufficiently simple to be worked out in detail. In the configuration p^3 which applies to $C^{13}+B^{12}$ the states are much more numerous and the equations are too complex to be solved in detail, but the solutions for the low states of interest may be treated by approximate methods, relying on some knowledge of the asymptotic behavior in the extremes. The general features of observed energy spectra for p^{-2} and for p^3 are both compatible with the intermediate coupling scheme with the same ratio $a/K \approx 5$ of the spin-orbit coupling parameter a to the "exchange integral" K, which separates multiplets. The criterion for whether the spectrum of the low states slightly resembles (LS) coupling, as it does in $C^{12}+B^{12}$, rather than (jj) coupling, as in $N^{14}+C^{14}$, is not just the value of a relative to K but the magnitude of a relative to the multiplet separations provided by K in (LS) coupling, which are exceptionally large among the low states of C^{13}.

THE impressive success of the (jj) coupling shell model in the heavy nuclei[1] and its almost as spectacular failure in the light nuclei of the p-shell from helium to oxygen has left the question whether these light nuclei might be interpreted in terms of intermediate coupling[2] between the (jj) and (LS) extremes, or whether some other phenomenon such as nascent alpha-clustering[3] or (other) excessive complication of configuration interaction must be called upon to explain the irregularities. Experimental knowledge of the spectra of these nuclei is now becoming so sufficiently extensive that it seems worth exploring the possibility of an interpretation in terms of intermediate coupling in some detail, especially to see if the general features of level density of the low states, elevation of the first state of higher isotopic, spin, etc., may be accounted for. As more identifications of nuclear spin and parity of the excited states become known, further tests of the validity of the intermediate coupling interpretation will be possible.

Nuclei of three atomic weights are here treated as examples of the sort of interpretation that may be encountered, $A=6$ and 14 because of the facility with which the complete analysis of the p-shell states may be carried out, and $A=12$ as an example of another type of spectrum with widely spaced low states and high excitation of the higher isotopic spin. A more complete survey of the trends in all of the nuclei in the p-shell is being prepared to be submitted for publication in the *Reviews of Modern Physics*.

CRITERION FOR INTERMEDIATE COUPLING

In the spectra of the p-shell nuclei, as far as they are known,[4] one notes some striking contrasts of appearance. For example, B^{10} has a rather high density of low states, as might seem compatible with the expectation of four low states from the low (jj) configuration $p_{\frac{3}{2}}^{-2}$ as an example of (jj) coupling; but only one of the four low states, rather than two as would thus be expected, seems to have isotopic spin $T=1$, indicating that there has been some cross-over, perhaps in a transition a little way into intermediate coupling but leaving the ground state with nuclear spin $I=3$ as expected in (jj)

[1] M. G. Mayer, Phys. Rev. **75**, 1969 (1949); **78**, 16 (1950); Haxel, Jensen, and Suess, Phys. Rev. **75**, 1766 (1949); Naturwiss. **36**, 155 (1949); D. Kurath, Phys. Rev. **80**, 98 (1950).
[2] H. H. Hummel and D. R. Inglis, Phys. Rev. **81**, 910 (1951).
[3] D. R. Inglis, Phys. Rev. **85**, 492 (1952).
[4] Hornyak, Lauritsen, Morrison, and Fowler, Revs. Modern Phys. **22**, 291 (1950); T. Lauritsen, *Annual Reviews of Nuclear Science* (Stanford, California, 1952), Vol. I. Professor T. Lauritsen has very kindly supplied preliminary compilations and charts for a forthcoming revision in advance of publication. Experimental references available in the published review are omitted here, with apologies to the observers.

coupling.[5] On the other hand, C^{12} has very widely spaced low states, the first excited state being at 4.4 Mev and the next probably at 9.6 Mev (though there is a possibility of one at 7.3 Mev.) In (jj) coupling one would expect the first excited state to be one of a group of four corresponding to the (jj) configuration $p_{\frac{1}{2}}^{-1}p_{\frac{1}{2}}$. In (LS) coupling[6] there are three low singlets which are widely spaced as a result of the high degree of symmetry attainable in an even-even nucleus, and the first $T=1$ state is high because of the necessity of breaking up the four-structure to make B^{12}. The observed excitation of this state is indeed about 15 Mev. Thus, in C^{12} it seems that if there is actually any sort of intermediate coupling it must represent a transition only a little way out from the (LS) coupling extreme.

Ordinarily the criterion for the expectation of one or the other coupling scheme is expressed in terms of the relative size of two integrals which appear as competing parameters: the spin-orbit coupling parameter a which appears in the expression for the single-nucleon spin-orbit coupling energy,

$$H'=a(\mathbf{l}\cdot\mathbf{s}), \tag{1}$$

and the "exchange integral" K containing the specific interaction,[6] assumed central, between the particles involved. In atoms K contains the repulsive Coulomb potential e^2/r_{ij}, and in nuclei the attractive specific nuclear force. (In the p-shell nuclei, the direct integral L contributes as well as K, but they are related; so the contributions of the specific nuclear interactions may be expressed in terms of K, and beyond the p-shell still more integrals are involved.) One says that one expects an approximation to (jj) coupling when $a\gg K$, to (LS) coupling when $K\gg a$. Since K is expected to vary roughly as nuclear density, or as R^{-3}, and a about as R^{-2} for a given angular momentum l, we may expect the ratio a/K to vary slowly and smoothly across the p-shell. If the value of a/K were the sole criterion, one might thus expect a similar degree of intermediate coupling in various nearby nuclei.

TABLE I. Quantities referring to the multiplet energies for the configurations p^2 and p^{-2} taken from Feenberg and Phillips. The exchange operators P, 1, PQ, and Q refer to space exchange, nonexchange, space-spin exchange, and spin exchange. b and c apply to p^2, b' and c' to p^{-2}.

	P	1	PQ	Q
$b={}^1P$	$-L+3K$	$L-3K$	$-L+3K$	$L-3K$
$c={}^3D$	$L-K$	$L-K$	$L-K$	$L-K$
$d={}^1D-{}^1P$	$2L-4K$	$2K$	$-2K$	$-2L+4K$
$e={}^1S-{}^3P$	$2L-K$	$5K$	$-5K$	$-2L+K$
$f={}^1P-{}^3D$	$-2L+4K$	$-2K$	$-2K$	$-2L+4K$
$g={}^3S-{}^3D$	$3K$	$3K$	$3K$	$3K$
$b'={}^1P$	$3L+51K$	$45L-75K$	$-17L+51K$	$17L-51K$
$c'={}^3D$	$5L+47K$	$45L-73K$	$-15L+47K$	$17L-49K$

[5] Dieter Kurath, Phys. Rev. (to be published). B. H. Flowers, Phys. Rev. **86**, 254 (1952)

[6] E. Feenberg and E. Wigner, Phys. Rev. **51**, 95 (1937); E. Feenberg and M. Phillips, Phys. Rev. **51**, 597 (1937).

In studying light nuclei we focus our attention on the low states because their separations are apt to be more meaningful and better known; when we do this a more significant criterion for the degree of intermediate coupling to be expected is the magnitude of a, not relative to K itself, but *relative to the intervals between the low states caused by* K, as are most apparent in (LS) coupling.[7] Thus, while a/K may have about the same value in C^{12} and B^{10} (it seems to be about -5 in both cases), it causes much less confusion of the pattern of (LS) coupling in C^{12} than it does in B^{10} because the multiplets are much more closely spaced (and are not all singlets) in the latter. This seems to be the main reason for the lack of consistency of appearance of either coupling scheme in the p-shell and contributes also to the problem of understanding of the four-structure of the binding energies.

INTERMEDIATE COUPLING FOR THE CONFIGURATIONS p^2 AND p^{-2}

Since the p-shell for nucleons holds twice as many nucleons in a nucleus as electrons in an atom, most of the p-shell nuclei have ground configurations containing too many states to be calculable in their entirety. The configurations p and p^{-1} of He^5 and N^{15} at the two ends of the shell are trivial as examples of intermediate coupling, but the next configurations p^2 and p^{-2} of Li^6 and N^{14} are just complicated enough to be interesting and simple enough to be easily treated. In keeping with the theory of holes, the configurations p^2 and p^{-2} differ from one another in the formal treatment only in the sign of the spin-orbit coupling parameter a, which is negative for a nucleon (having "inverted doublets," relative to an electron) and positive for a hole. Their energy states can thus be treated as solutions of the same secular equations.

The configuration p^2 contains the (jj) configurations $p_{\frac{1}{2}}^2$, $p_{\frac{1}{2}}p_{\frac{3}{2}}$, and $p_{\frac{3}{2}}^2$ in order of ascending energy. (In p^{-2} the order is reversed, with negative exponents.) The configuration p^2 belongs not merely to the nucleus Li^6 but to the polyad $A=6$ (which we may denote by Py^6), that is, to the collection of isobars He^6, Li^6, Be^6 (etc.), a system of nucleons of which isotopic spin T is a dynamical variable. By listing, in the usual tabular form while treating isotopic spin variables analogously to ordinary spin variables, the fact that there is only one state of two $p_{\frac{1}{2}}$ nucleons with $M_I=3$, $T_z=0$, and only one with $M_I=2$, $T_z=1$, etc., compatible with the exclusion principle, one sees that the (jj) configuration $p_{\frac{1}{2}}^2$ contains the four states having the quantum numbers $(I,T)=(3,0)$, $(2,1)$, $(1,0)$, and $(0,1)$, respectively. Similarly the first excited (jj) configuration $p_{\frac{1}{2}}p_{\frac{3}{2}}$ contains four states, $(2,0)$, $(1,0)$, $(2,1)$, and $(1,1)$, and the next (jj) configuration consists of the two states $(1,0)$ and $(0,1)$. Of the ten states there is only one each

[7] The criterion is stated in this unsymmetrical way because the contributions of a, being made by nucleons singly, are less subject to the vagaries of nuclear symmetry than are those of K.

of (3,0), (2,0), and (1,1), while there are two each of (2,1) and (0,1), and there are three states (1,0). In the intermediate-coupling transition a/K is varied from zero, where L, S, I, M, and T are good quantum numbers, to infinity, where j_1, j_2, I, M, and T are good quantum numbers, under the assumption of a charge-independent Hamiltonian. In the intermediate situation I, M, and T remain good quantum numbers, M being trivial except for detailed methods of evaluation because the energy does not depend on it, and it has not been included in the above counting of the states. Thus, states with the same (I,T) get mixed up in the scalar problem, and we have two quadratic secular equations and one cubic.

The secular equations for the energies may be written with almost equal ease either by constructing the complete matrix including the nondiagonal elements of H' in the (LS) representation as described completely in Condon and Shortley's book,[8] or by Goudsmit's method[9] of determining the coefficients of the secular equation from knowledge of the diagonal elements alone in both extremes, the relative convenience of the methods depending upon what information is at hand. For the quadratics we use the latter method. The information at hand includes the separation of the multiplets, as dependent on the assumed exchange nature of the nuclear interactions, which are obtained by simple subtraction from the tables of Feenberg and Phillips,[6] and are listed here for convenience in Table I. We shall arrange to obtain the energies directly in a form for plotting in Fig. 1, in which the (jj) asymptotes are arranged symmetrically with slopes $0, \pm\frac{2}{3}$, by putting $\epsilon = E + a/2 + constant$, E being the energy of a state and the constant being a convenient zero of energy for each secular equation. The two states (2,1) are in (LS) coupling a $^3P_2$ and a $^1D_2$ with the asymptotes $\epsilon \to a$ and $\epsilon \to d + a/2$, respectively, where in this case $\epsilon = E + a/2 - b$. In (jj) coupling these states belong to the (jj) configurations $p_{\frac{3}{2}}^2$ and $p_{\frac{3}{2}}p_{\frac{1}{2}}$, having asymptotic slopes given by $\epsilon \to (3/2)a$ and $\epsilon \to 0$, respectively. The quadratic having these asymptotic values is

$$\epsilon^2 - (d + 3a/2)\epsilon + ad = 0, \tag{2}$$

as is easily seen by noting that the coefficient of $-\epsilon$ is the sum of the roots, and the term without ϵ the product of the roots, remembering that the asymptotic expressions are only the leading terms of expansions. Similarly for the two states (0,1) one obtains the quadratic secular equation

$$\epsilon^2 - e\epsilon - ae/2 - (3a/2)^2 = 0, \tag{3}$$

where again $\epsilon = E + a/2 - b$.

[8] E. U. Condon and G. H. Shortley, *Theory of Atomic Spectra* (Cambridge University Press, London, 1935).
[9] S. A. Goudsmit, Phys. Rev. **35**, 1325 (1930).

TABLE II. (jj) asymptotes of $E + a/2$ for configuration p^2 (or p^{-2}).

	(I,T)		For $0.8P + 0.2Q$
$p_{\frac{3}{2}}^2$	(0,1)	$-3a/2 + b + a/3$	$-1.5a + 0.4K - 3.23K^2/a$
	(1,0)	$-3a/2 + c + 2f/9 + g/27$	$-1.5a + 3.33K - 4.52K^2/a$
$p_{\frac{3}{2}}p_{\frac{1}{2}}$	(1,1)	b	$-1.8K$
	(2,1)	$b + 2d/3$	$1.4K + 3.41K^2/a$
	(1,0)	$c + 2f/9 + 16g/27$	$5K - 1.07K^2/a$
	(2,0)	e	$5K$
$p_{\frac{1}{2}}^2$	(2,1)	$3a/2 + b + d/3$	$1.5a - 0.2K - 1.71K^2/a$
	(1,0)	$3a/2 + c + 5f/9 + 10g/27$	$1.5a + 1.67K + 15.19K^2/a$
	(0,1)	$3a/2 + b + 2e/3$	$1.5a + 2.6K + 3.23K^2/a$
	(3,0)	$3a/2 + c$	$1.5a + 5K$

For the three states (1,0) the matrix for $\epsilon = E + a/2 - c$ is

	$^3D_1$	$^1P_1$	$^3S_1$
$^3D_1$	$-a$	$-(5/6)^{\frac{1}{2}}a$	0
$^1P_1$	$-(5/6)^{\frac{1}{2}}a$	$f + a/2$	$(3/2)^{\frac{1}{2}}a$
$^3S_1$	0	$(2/3)^{\frac{1}{2}}a$	$g + a/2$.

Here the terms in a are taken from the matrix of H' (given in reference 8, page 268). By setting the corresponding secular determinant equal to zero one obtains the cubic secular equation

$$\epsilon^3 - (f+g)\epsilon^2 + [fg - (f+g)a/2 - (3a/2)^2]\epsilon + fga + (f/2 + 4g/3)a^2 = 0. \tag{4}$$

The (jj) asymptotes given by Eqs. (2), (3), and (4) plus the three linear energies are listed in Table II, along with one additional term in the expansion for the special exchange interaction assumed in plotting Fig. 1.

With our present ignorance of the exact nature of nuclear interactions (and with the likelihood of at least a small amount of configuration interaction) we cannot hope to reproduce the details of nuclear spectra. We can, however, try to match the general features of rough level spacing, but to do this we must assume an interaction at least good enough to account for the excitation of the singlet state of the deuteron and roughly for the saturation properties of nuclear forces. Beyond these requirements, we wish to keep it as simple as possible, and therefore select a linear combination of of space-exchange and spin-exchange (Majorana and Bartlett) interactions:

$$O_{ij} = 0.8P_{ij} + 0.2Q_{ij}. \tag{5}$$

The ratio of the direct integral L to the exchange integral K depends on the size of the nucleus relative to the range of the nuclear forces, and a reasonable value seems to be[2]

$$L/K = 6. \tag{6}$$

Though it may vary slightly, we assume this same value throughout the p-shell.

With these specializations, the solutions of the secular equations are plotted in Fig. 1. The short straight lines in the middle are the asymptotes of the energies in the form of the multiplets of pure (LS)

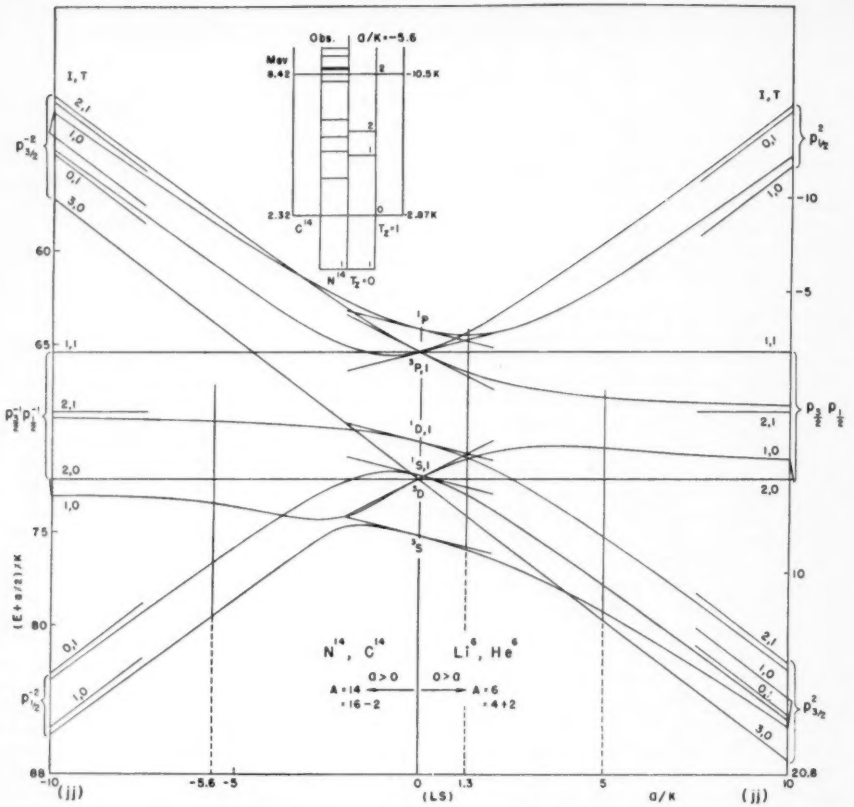

FIG. 1. Intermediate coupling transition of the energy levels of the configurations p^2 and p^{-2}. The exchange interaction specified by (5) and (6) has been assumed. K is negative, the interaction being attractive. The sign of the spin-orbit coupling parameter a refers to a nucleon on the right, to a "hole" on the left.

coupling. The straight lines near the right and left side are the (jj)-coupling asymptotes. It will be noted that the linear energy of the lone state with $(I,T)=(2,0)$ is the (jj) asymptote for one of the (1,0) states, and that in the (jj) configuration $p_{\frac{1}{2}}^2$ the state (1,0) remains rather far from its asymptote, in fact beyond the (0,1) state (compare Table II). This corresponds to an abnormally large matrix element between this and the nearer of the other two (1,0) states in the (jj) representation. The right half of the figure corresponds to positive a/K, or negative a since K is negative for attractive interactions; that is, to Py^6, the left side of the figure to Py^{14}. The (jj) configuration $p_{\frac{1}{2}}^2$ is the low one on the right side, the corresponding $p_{\frac{1}{2}}^{-2}$, with identical asymptotic spacings, is the high one on the left side, and only one state, (3,0), crosses over between the two.

In the comparison with experiment, the most valuable identifications of excited states for the nuclei here considered come through the identification of isotopic spin by comparison of the energy states of the pair of isobars. This is accomplished from the known disintegration energies[10] on the assumption that the Coulomb energy difference $N^{14}-C^{14}$ is the same as $N^{13}-C^{13}$, for example, which gives very good agreement (a good check on the charge-independence of the specific nuclear Hamiltonian), better than good enough for identification of the first $T=1$ state, after which exact equality for this state is assumed between the isobars. (For details of such comparisons, the reader is referred to reference 4, particularly the forthcoming revision.)

For Py^{14}, the value of a/K may be determined by

[10] Li, Whaling, Fowler, and Lauritsen, Phys. Rev. **83**, 512 (1951).

matching the energies of the ground state and the first two $T=1$ states (the only two known). This match between theory and experiment occurs at $a/K=-5.6$. The vertical line drawn at this value intersects the energy lines given by the secular equations at the levels indicated in the insert at the top of the figure, in the column $T_z=0$ for the $T=0$ states and in the columns $T_z=0$ and $T_z=1$ for the $T=1$ states. These should correspond to the p-shell states of N^{14} and C^{14}, respectively, and the observed states of these nuclei are shown in the other columns of the insert. This empirical match determines $K=-2.32$ Mev$/2.87=-0.81$ Mev, from which we obtain the spin-orbit coupling parameter $a=4.5$ Mev.

It is seen that only two $T=0$ states from the configuration p^{-2} are expected between about 3 and 7 Mev in N^{14}, whereas more states have been observed in this region.[11] The appearance of extraneous levels to be ascribed to excited configurations such as $p_{\frac{1}{2}}{}^{-3}d$ and $p_{\frac{1}{2}}{}^{-3}s$ beginning at about 4 or 5 Mev is not inconsistent with, for example, the levels in N^{15} beginning at 5.3 Mev which also appear to arise from excited configurations. It does, however, complicate the experimental verification of the present analysis of the ground configuration, and means that this is at best only part of the story. The ground-state nuclear spin $I=1$ of N^{14} is of course correctly given, being the same in both extremes. The nuclear spins of the first two states of C^{14} are predicted to be 0 and 2, respectively, as is familiar in other even-even nuclei. All these are essentially the results of (jj) coupling; there have been no cross-overs but the spacing of the levels has been markedly affected by the transition into intermediate coupling.

The puzzle of the long life[12] of C^{14} is not satisfactorily solved by this interpretation, since the beta-transition remains $I=0$ to $I=1$, with no parity change. The fact that one wave function arises from a quadratic secular equation and the other from a cubic means that there is ample opportunity for cancellation to occur in the matrix element, but an anomalous factor 10^{-2} to 10^{-3} is needed in the matrix element; and it is not really satisfactory to be forced to attribute so small a factor to fortuitous cancellation.

For $A=6$, the possibility of any successful comparison of the curves in Fig. 1 with experiment, as attempted in Fig. 2(a), depends on making a/K so small as to give the ground-state nuclear spin $I=1$, characteristic of (LS) coupling, rather than the value $I=3$, given by (jj) coupling[5] for both Li^6 and B^{10} and observed in B^{10}. Matching the lowest three clearly identifiable states as before, in this case the first two states with $T=0$ and the first state[13] with $T=1$, then gives the surprisingly low value $a/K=1.3$, rather near (LS) coupling. The only prediction that may be compared with presently available experimental results is then that the first excited state of He^6 should lie about 2.5 Mev above its ground state rather than 2 Mev as observed. This interpretation requires the implausible values of the parameters $K=-1.23$ Mev, $a=-1.6$ Mev. If we should compare with N^{14} alone, so small a value of a might be attributed to a larger size of the loosely-bound p-shell in Li^6, but this assumption would lead us to expect that K also should be smaller in Li^6 than in N^{14},

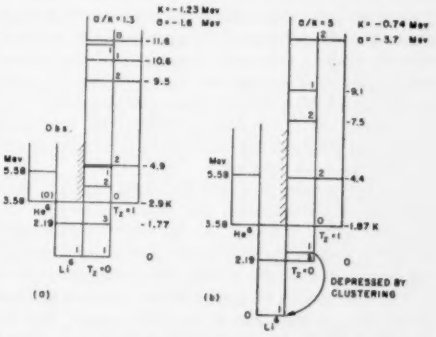

FIG. 2. Alternative interpretations of the energy spectrum of the polyad Py^6 consisting of Li^6, He^6, etc. In scheme (b) it is assumed that the ground state, which has the same (I,T) as the ground state of the alpha-model, is depressed by nascent alpha + deuteron clustering.

[11] The N^{14} states shown in the insert at 3.9, 5.1, 5.7, and 6.45 Mev are taken from the recent revision mentioned in reference 4, the result mainly of previous work with $N^{14}(p,p')$ and $C^{13}(d,n)$. Very recent work with the latter reaction [R. E. Benenson, Phys. Rev. **87**, 207 (1952), and private communication] suggests additional levels at 3.7, 4.8 (odd), 7.05, (7.5, odd), and 7.7 Mev, and perhaps others, and that the 5.7-Mev level is even, with $l_n=2$ as would be required for the (2,0) state with which it roughly agrees in energy. The configurations $p_{\frac{1}{2}}{}^{-3}d$ and $p_{\frac{1}{2}}{}^{-3}s$ give states 3^-, 2^-, 1^-, 0^-, 2^-, 1^- both for $T=0$ and $T=1$. (Still higher odd states arise from $p_{\frac{1}{2}}{}^{-1}p_{\frac{1}{2}}{}^{-2}d$, etc.) Since no breaking of four groups is involved in the transition $T=0$ to $T=1$ among these states, this additional excitation would be expected to have the same order of magnitude as the 2.32 Mev in $N^{14}\rightarrow C^{14}$ (or 3.56 and 1.74 Mev for the corresponding excitations in the polyads Py^6 and Py^{10}, which contrast strongly with 12.5 to 16.7 Mev in Py^8, Py^{12} and Py^{16}). The N^{14} state at 3.9 Mev could be the (1,0) state of p^{-2}, but if there is really a state with $T=0$ also at 3.7 Mev, either it or the one at 3.9 Mev arises from an excited configuration (with odd parity) and it may seem slightly surprising that it does not also give a $T=1$ state below 8.4 Mev. Between about 3 and 7 Mev in N^{14} the two even levels from p^{-2} are expected and several of the odd levels mentioned seem to appear. In addition to these, there might appear another even state O^+ near 6 Mev corresponding to the first excited state of O^{16}. It has been suggested by M. G. Mayer (private communication), as an alternative to the alpha-model explanation of D. M. Dennison, that the O^+ state at 6.05 Mev in O^{16} might be interpreted as $p_{\frac{1}{2}}{}^{-2}d_{\frac{5}{2}}{}^2$ arising from two-nucleon excitation and might lie low because of the large $d_{\frac{5}{2}}{}^2$ pairing energy (as does also the probable $P_{\frac{1}{2}}$ at 3.03 Mev in O^{17}). A O^+ state in N^{14} could similarly arise from $p^{-4}d^2_{\frac{5}{2}}$ and the other even states from this configuration would presumably lie considerably higher.

[12] E. Gerjuoy, Phys. Rev. **81**, 62 (1951); S. D. Warshaw, Phys. Rev. **80**, 111 (1950). Experimentally, however, the ground state of N^{13} is even relative to N^{13} assumed odd: Gibson and Thomas, quoted by S. T. Butler, Proc. Roy. Soc. (London) **208A**, 559 (1951); and both C^{14} and N^{14} ground states are even relative to C^{13} assumed odd, so one cannot assume opposite parity for them: reference 11 and D. A. Bromley and L. M. Goldman, Phys. Rev. **86**, 790 (1952).

[13] R. B. Day and R. L. Walker, Phys. Rev. **85**, 582 (1952).

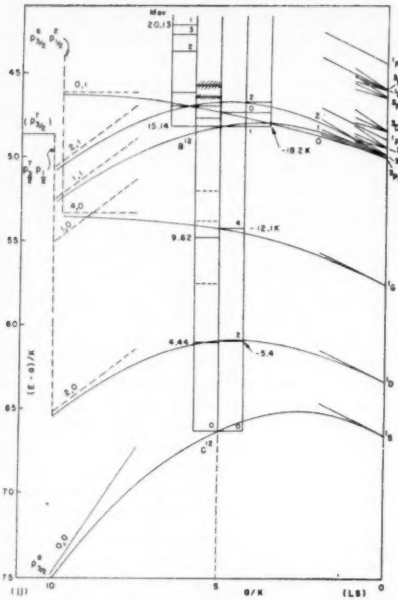

FIG. 3. Approximate intermediate coupling transition for the configuration p^8, and comparison with the observed levels in Py^{13}. The sign of a refers to a nucleon, not a "hole."

whereas it is in this interpretation about 50 percent larger. The comparison of the small value of a for Li^6 with the values dubiously derived from the virtual states of He^5+Li^5 is equivocal: it agrees with the value $(-3a/2)\approx 2.5$ Mev derived from reaction data,[14] but not with $(-3a/2)\approx 5$ Mev inferred from scattering data;[15] and the expected effect of the instability of He^5 on a has not been calculated.

As another more plausible but more complex interpretation of the situation one may assume that the values of a, K, and a/K do not vary so drastically across the p-shell, and thus that Li^6 is not so near (LS) coupling, but that the reason for the appearance of $I=1$ is that this is characteristic of the ground state of the alpha-model: that is, we may assume that the central model in intermediate coupling gives a good approximation to most states of most of the p-shell nuclei, but that under a certain condition there may be strong influence of alpha-clustering on the energy and other characteristics of a state. The (necessary but perhaps not sufficient) condition is plausibly that the internal binding energy of the constituent parts (alpha and deuteron) is large compared to their mutual binding. The internal binding of the deuteron in its ground state is 2.2 Mev, compared to 1.56-Mev mutual binding with the alpha. Correspondingly we assume that the $(I,T)=(1,0)$ state is considerably depressed by "resonating" with this alpha-model configuration, or, we might say, by nascent alpha-clustering. The excited state of the deuteron is unbound, that is, there is no internal binding, so clustering is not expected in the (0,1) state. With this assumption, arbitrarily taking the value $a/K=5$, for example, we have the comparison with experiment shown in Fig. 2(b), which appears to be satisfactory as far as it goes. On the basis of this sort of interpretation it may be predicted that the states (2,0) and (1,0) of Li^6 will be found considerably higher than (2,1) and a search for them should provide an interesting test.

INTERMEDIATE COUPLING FOR THE CONFIGURATION p^8

Some of the energy spectra encountered in the p-shell differ so drastically from one another that a very rough indication of the intermediate coupling schemes can contribute very significantly to an understanding of the general nature of their differences. As an example of a polyad with a spectrum very different from that of the polyad Py^{14}, we select Py^{12} with the ground configuration p^8. It has so many states that we cannot hope to give an exact treatment of the p-shell intermediate coupling scheme as we have done for p^2 and p^{-2}.

A practical procedure is suggested by the method[9] used in the above derivation of the quadratic secular equations. We list as many of the low states as we may need to consider in (LS) coupling, determine the lowest (jj) configuration to which each must correspond, plot as much information as we may have either exactly or approximately about the elevations and slopes of the (LS) and (jj) asymptotes, and then sketch in curves with the proper asymptotic behavior and with very gradual curvature, except where two curves of the same (I,T) come fairly close together and "repel" one another strongly.

The result of this procedure applied to p^8 is shown in Fig. 3. The spacings of the multiplets[6] on the (LS) coupling side are given for the special case (5). The multiplet splittings arise from an expression $A(\mathbf{L}\cdot\mathbf{S})$, where A is a constant times a, depending on details of the wave functions which have not been calculated in this many-nucleon configuration. As a guide by which to guess at reasonable values of A we may recall (a) that in the ground state of Li^7, $A=a/3$, corresponding intuitively to the fact that only one nucleon contributes to S while three participate equally in L so that $\cos(lL)=\frac{1}{3}$, and (b) that the hole theory leads to the expectation that all multiplet splittings reduce to zero as in surveying the elements of the p-shell we pass through B^{10} at the middle of the shell. For the nuclei lighter than B^{10}, A is in general a positive constant

[14] W. T. Leland and H. M. Agnew, Phys. Rev. **82**, 559 (1951); E. W. Titterton and T. A. Brinkley, Proc. Phys. Soc. (London) **64A**, 212 (1951).

[15] R. K. Adair, Phys. Rev. **83**, 873 (1951); C. L. Critchfield and D. C. Dodder, Phys. Rev. **76**, 602 (1949).

times a, whereas in the heavier half of the p-shell, the constant is generally negative, though there may in complicated cases be exceptions to this rule. For each of the multiplets with which we are concerned in Py^{12}, we accordingly assume that the constant relating A to a is negative and relatively small. We thus obtain the set of (LS) asymptotes shown on the right side of Fig. 3.

In Fig. 3, the ordinate is chosen as $(E-a)/K$, which gives a slope to the singlet asymptotes, in order to keep the figure compact and still leave one set of asymptotes [that for the (jj) configuration $p_{\frac{1}{2}}{}^6p_{\frac{1}{2}}{}^2$] horizontal. In ($LS$) coupling, the large spacing between the low singlets and the dense clustering thereafter are noteworthy for the contrast to Py^{14}. Aside from the ground state, the only bits of information used about the (jj) asymptotes are their slopes, and to indicate this they are drawn with broken lines. The spacings between them are calculable [on the basis of assumed interactions such as (5)] but have not been calculated. It is interesting to note that the slopes alone are helpful in inferring the general nature of the spectrum, and by doing so we see for which (jj) states and configurations it may be most significant to calculate the energies. In Fig. 3 the lines for the (jj) asymptotes for the excited states were drawn with fixed slope at such a height as to make possible gentle curves from the known (LS) asymptotes; and the comparison with experiment shown superposed in the middle of the figure was subsequently undertaken (only for the ground state is the height of the (jj) asymptote analytically known, being taken from reference 5). The value $a/K=-5$ is chosen for the comparison with experiment as a rough empirical compromise. Values smaller in absolute magnitude than this would bring the first two excited states of B^{12} closer to its ground state, larger values would raise the (2,0) and (4,0) states higher above the dependably observed 4.44-Mev and 9.62-Mev states of C^{12}, the energy scale having been determined by fitting the ground states of C^{12} and B^{12}. The decision to indicate the other possible, but less dependably observed, excited states of C^{12} with broken lines was not made as a result of this study, but was taken from charts independently prepared and kindly supplied in advance of publication by Professor T. Lauritsen.[4] This comparison does not suggest that those states do not exist, but that if they exist they have odd parity arising from excitation of one of the p-nucleons to the d (or s) shell; and there may well be a connection between the odd parity and the furtive ways both of these states and of those only recently observed[11] in N^{14}. The first odd state in N^{15} apparently lies at 5.3 Mev; it should be higher in C^{12} by roughly the single-nucleon doublet splitting, which makes the uncertain 7.3-Mev state seem a little low for the first odd state, but this rough sort of comparison is unreliable because energies expressible in K are also involved.[16]

[16] Compare the conclusions of L. J. Koester, Jr., Phys. Rev. **85**, 643 (1952) where in estimates of $(3a/2)$ insufficient allowance is made for energies expressible in K of the general nature of "pairing energies."

CONCLUSION

From the examples here given it begins to be clear that much of the complexity of the relations between energy spectra of the various light nuclei may be accounted for in terms of intermediate coupling. The variety of spacings of the low states provided by the symmetry properties in (LS) coupling accounts for the way in which some nuclei, though in intermediate coupling, resemble (LS) coupling more than others.

The four-structure of the stability curve has long seemed to be accounted for in a general way by these symmetry properties in (LS) coupling,[6] or alternatively by the alpha-model.[17] It has recently been shown that the four-structure does not show up so strongly in a similar treatment of (jj) coupling,[5] where the possibility of attaining high symmetry is suppressed by the demand for the quantum numbers j. If one takes into account not only the specific nuclear interactions but also the spin-orbit interaction (1), one obtains in (jj) coupling a sharp dip in the stability curve at C^{12} because of the negative-energy contribution $a/2$ per nucleon up to the closing of the $p_{\frac{1}{2}}$ sub-shell at $A=12$ and the positive-energy contribution a per nucleon beyond this point. It is apparent from Fig. 3 that in the intermediate coupling there indicated, both the symmetry of (LS) coupling and the spin-orbit contribution to the stability of (jj) coupling play important roles in contributing to the exceptional stability of C^{12}. Thus the interpretation of the p-shell nuclei in terms of intermediate coupling somewhat complicates the question of the four structure, but seems to leave a qualitative explanation at least of the dips in the binding-energy curve at $A=12$ and 16. In the neighborhood of $A=8$ it still appears likely that nascent alpha-clustering plays an important role, and there is no very good evidence for intermediate coupling in that region, as in the examples of Li^6 discussed above and Li^7 for which one possible type[18] of influence of the alpha-model was previously suggested.[3] However, it might instead be that the full complexity of the Feingold-Wigner mechanism of spin-orbit coupling[19] applies in Li, making its behavior anomalous, and is somehow averaged out to approximate (1) in slightly heavier nuclei.

[17] J. A. Wheeler, Phys. Rev. **52**, 1083 (1937); L. Hafstad and E. Teller, Phys. Rev. **54**, 681 (1938); E. Teller and J. A. Wheeler, Phys. Rev. **53**, 778 (1938).

[18] Another possibility for Li^7 is that the states arising in intermediate coupling from the ^2P are strongly intermixed with alpha-model states, which also include essentially a low and relatively stable ^2P, while the states arising from the ^2F remain unmodified by clustering (with 7/2 at 4.8 Mev and 5/2 at 7.4 Mev). The recently reported broad state at 6.4 Mev [S. Bashkin and H. T. Richards, Phys. Rev. **84**, 1124 (1951)] could then consist largely of the $^2\Sigma_g$ of the alpha-model.

[19] A. M. Feingold and E. P. Wigner, Phys. Rev. **79**, 221(A) (1950), and valued private communications.

Dynamic Characteristics of the Plasma in Discharges through Rare Gases*

H. N. Olsen† and W. S. Huxford
Northwestern University, Evanston, Illinois
(Received June 2, 1952)

The time variation of ion concentration in the plasma of flash discharges through neon and argon at low pressures has been determined from the Stark broadening of H_α and H_β lines. Hydrogen gas at about 1 percent of the total pressure was used for this purpose. A special method of oscilloscopic observation is employed. Analysis of the results explains differences in the time of appearance of various types of radiation in the discharge. A mechanism is proposed to account for the time variation of the intense continuum.

I. INTRODUCTION

THE properties of high current plasmas in sparks and in condensed flash discharges have been studied by several investigators. Rompe and Schulze[1] made measurements of mercury impulse discharges at higher pressures. The radiation emitted by condenser discharges through capillary tubes was observed by Hahn and Finkelnburg.[2] Several papers have recently been published on the plasmas formed in spark discharges.[3–5] The present investigation was undertaken to improve the oscilloscope method of observation and to obtain new information on the variation of ion concentration in flash discharges at reduced pressures.

A property common to all of these discharges is the emission of an intense rapidly changing continuum upon which spectral lines are superimposed. An understanding of the excitation processes involved requires accurate time resolution of the characteristics observed. A full analysis of the succession of events during the discharge period has not been achieved previously because of poor control of the flash and inadequate synchronization of recording apparatus.

In the present work, precisely timed non-oscillatory discharges have been produced in neon and argon. Hydrogen, added in small amounts to the filling gas to serve as a spectroscopic probe, was found not to change the nature of the flash. Ion concentrations in the plasma have been measured by means of Stark effect broadening of the hydrogen lines α and β.

Time variations in emission of continuum, spark lines and arc lines are compared with the changes observed in ion concentration. In this manner new information is secured as to the mechanisms involved in build-up and decay of the discharge.

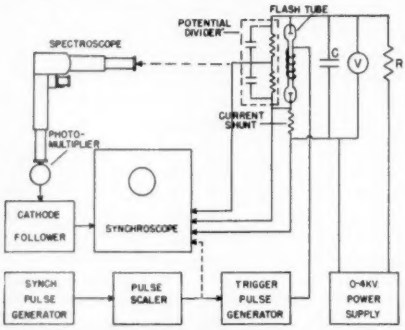

FIG. 1. Block diagram of flashing and detection apparatus.

II. APPARATUS

Apparatus used for synchronous operation of flash tubes and for detection of electrical and radiation characteristics is shown in the block diagram, Fig. 1. A detailed circuit diagram of the essential electrical components is given in Fig. 2.

The flash tubes used have small plane electrodes spaced 16 cm apart, enclosed in a quartz envelope with an internal diameter of 4 mm. Data were obtained using tubes filled with neon at 75 mm Hg, and argon at 34 mm Hg pressure. The internal electrodes were connected permanently to a condenser maintained at a potential less than the breakdown voltage ($\sim$4000 v) of the tube. Application of a rapidly changing potential to an external "trigger" electrode provides sufficient ionization for initiation of the discharge.

The square-wave output of a synchronous pulse generator is electronically differentiated to give sharp triggering pulses. A pulse scaler provides rates of 60, 30, 15, 7.5, 3.75, 1.88, and 0.94 pulses/sec, thus furnishing a range of flashing conditions. This allows the average power to be kept low enough to prevent overheating or excessive sputtering of electrode materials.

A small constant-deviation Hilger spectroscope equipped with an exit slit and photomultiplier housing was used to isolate narrow spectral regions for the purpose of measuring time variations of the intensity at points in the continuum and in individual spectral lines.

All data were recorded on the screen of a Navy radar synchroscope, Model *TS*-28/UPN. An RC compensated

* This work supported in part by Bureau of Ships, Navy Department.
† Now at Linde Air Products Company, Tonawanda, New York.
[1] R. Rompe and P. Schulze, Physik Z. **42**, 105 (1941).
[2] O. Th. Hahn and W. Finkelnburg, Z. Physik **122**, 37 (1944).
[3] J. D. Craggs and W. Hopwood, Proc. Phys. Soc. (London) **A59**, 755 (1947).
[4] Williams, Craggs, and Hopwood, Proc. Phys. Soc. (London) **A62**, 49 (1949).
[5] H. Edels and J. D. Craggs, Proc. Phys. Soc. (London) **A64**, 562 (1951).

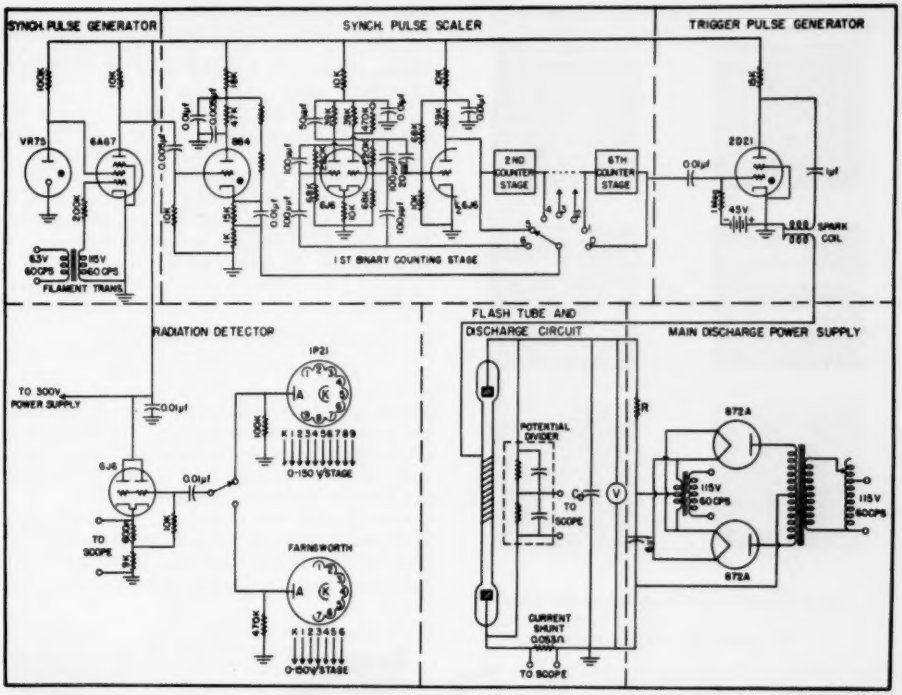

FIG. 2. Detailed circuit diagram.

voltage divider was used to record time variation of flash potential. Scope traces of current pulses were obtained with a low inductance resistance shunt. Examples of recorded traces of current, potential, and unresolved radiation are shown in Fig. 3. Here each trace represents 15 repeated flashes and illustrates the precision of synchronization in repetitive flashing.

Examples of typical recorded arc lines, spark lines and continua for discharges in argon and neon are given in Fig. 4. The Balmer lines shown were recorded from a neon discharge with hydrogen added at a partial pressure of less than 0.3 mm Hg.

III. OBSERVATION OF STARK EFFECT BROADENING

Methods used for observing time variations of individual lines proved suitable for recording the Balmer line intensity distributions over the spectral range covered by the broadened lines. A distribution, or profile, as it is subsequently referred to, corresponding to a certain instant of time in the discharge cycle was obtained by plotting as a function of wavelength the deflection of a point on the scope trace corresponding to that particular time.

Recorded H_α and H_β profiles for neon are shown in Figs. 5 and 6. Although a "clear channel" exists in the spectrum of this gas for H_β, several strong lines interfere with observation of H_α. Because of the relative sharpness of the neon lines it was possible to record the long wavelength wings of H_α profiles by extrapolation through the 6598A line. In the case of argon the H_β line is completely masked by strong ionic spark lines. Fortunately no argon lines interfere with observation of H_α and suitable profiles were obtained as shown in Fig. 7.

The characteristic shapes of both H_α and H_β are what one should expect from the theoretically predicted splitting of the Balmer lines in a uniform electric field. H_α should have a sharp peak due to a strong undisplaced central component. Theoretically, there are no undisplaced components in the split H_β line and this explains the observed central dip. This agreement with theory is evidence that the broadening is caused by fields of the ions present in the plasma.

The spectral response of the radiation detection system was determined by measuring the emission of a tungsten lamp having known radiation characteristics. Variation of this response over the regions covered by the broadened lines was found to be negligible.

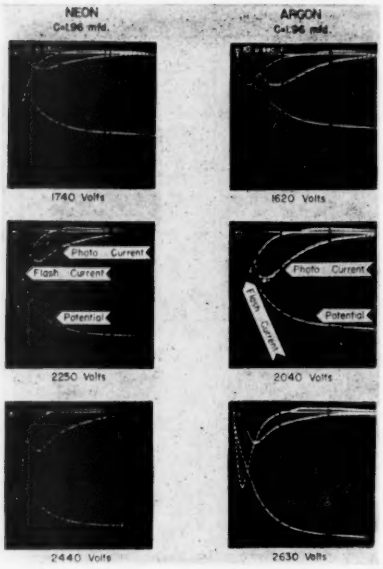

FIG. 3. Synchroscope traces of flash characteristics.

IV. ANALYSIS OF RESULTS

An emitting atom in a gas plasma experiences an inhomogeneous, statistically isotropic field which is caused by the mutual action of the surrounding positive ions. Due to the constant motion of these ions the field is continually changing in both magnitude and direction. A spectral line emitted by an atom in such a field is broadened into a band rather than split into discrete Stark components as would be the case in a uniform, unidirectional field. In order to specify the Stark broadening as a function of the field intensity one must know the probability for the existence of the field.

Holtsmark[6] has formulated a detailed theory of Stark effect broadening by inhomogeneous ionic fields which leads to the following probability functions:

$$W(\beta)d\beta=(4\beta^2/3\pi)d\beta[1-0.4628\beta^2+0.1227\beta^4 -0.02325\beta^6+\cdots], \quad 0<\beta<1.7; \quad (1)$$

$$W(\beta)d\beta=\frac{d\beta}{\pi\beta^{5/2}}2.350\left[1+\frac{5.106}{\beta^{3/2}}-\frac{7.4375}{\beta^3}+\cdots\right], \quad 1.7>\beta>\infty. \quad (2)$$

Here

$$\beta=F/F_n, \quad (3)$$

is the ratio of the actual to the "normal" field intensity, which is given by

$$F_n=2.61\epsilon n^{\frac{2}{3}}; \quad (4)$$

where ϵ is the charge of the ion and n the concentration measured in number of ions/cm^3.

Expressions (1) and (2) have been plotted as a function of β and compounded to give the continuous curve (3) in Fig. 8. Verweij[7] has calculated data for a plot of the probability function $W(\beta)$ for values of β ranging from 0 to 100 using Holtsmark's expression (1) for $0<\beta<3.25$. For values of $\beta>3.75$ he has re-evaluated the integral form from which Holtsmark obtained (2), arriving at the following expansion:

$$W(\beta)d\beta=\frac{2d\beta}{\pi\beta}\left[\frac{\frac{1}{2}\sqrt{2}\Gamma(7/2)}{\beta^{3/2}}+\frac{\Gamma(5)}{2!\beta^3}-\frac{\frac{1}{2}\sqrt{2}\Gamma(3/2)}{3!\beta^{9/2}}-\cdots\right]. \quad (5)$$

Verweij's data are also plotted in Fig. 8. The dashed portions represent sections where calculated values of $W(\beta)$ are not available. The probability curve plotted from Verweij's data is the more accurate and is used in the following application of the theory.

Verweij[7] and later Craggs and Hopwood[3] applied Holtsmark's theory by considering the broadening of each individual Stark component of the split line. In both treatments the resulting overlapping bands were

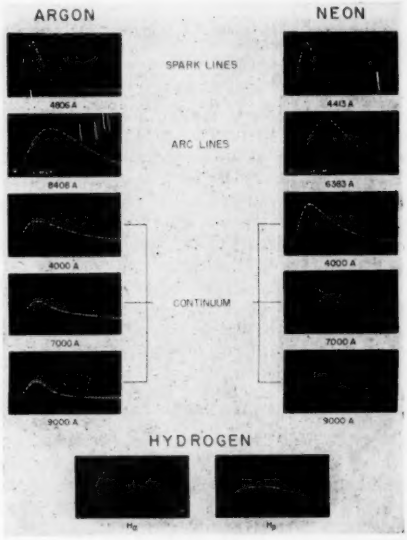

FIG. 4. Time-variations of individual spectral lines and continuous radiation. The hydrogen lines were observed from the neon discharge.

[6] J. Holtsmark, Ann. Physik **58**, 577 (1919).

[7] S. Verweij, Pub. Astr. Inst. Univ. Amstr. No. 5, (1936).

compounded to give a theoretical profile for the whole line. A similar procedure has been followed in the present work using Verweij's calculated values for $W(\beta)$.

At the instant a given line component is emitted a certain field intensity exists at the center of the atom. $W(\beta)$ denotes the probability that the value of this field is just β. If we denote the intensity distribution in the kth component by $J_k'(\beta, \delta\lambda)$, multiply this function by $W(\beta)$, and integrate over all β's, we obtain

$$J_k(\delta\lambda) = \int_0^\infty J_k'(\beta, \delta\lambda) W(\beta) d\beta. \tag{6}$$

The distribution function for the whole line is then given by

$$J(\delta\lambda) = \sum_k J_k(\delta\lambda) = \sum_k \int_0^\infty J_k'(\beta, \delta\lambda) W(\beta) d\beta. \tag{7}$$

In order to determine ion concentrations from observed profiles it is necessary to relate the theoretical distribution function in some way to the field F_n. If it is assumed that only the linear Stark effect is operative, for each component

$$\delta\lambda = C_k F. \tag{8}$$

This is a reasonably good assumption for the fields encountered here as has been shown by a consideration

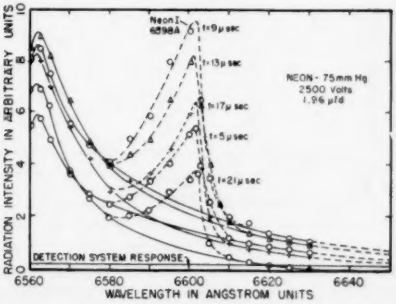

FIG. 5. Observed profiles of the H_α line in a neon discharge.

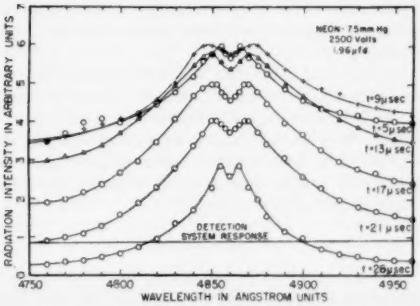

FIG. 6. Observed profiles of the H_β line in a neon discharge.

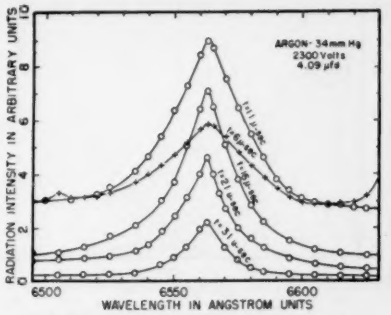

FIG. 7. Observed profiles of the H_α line in an argon discharge.

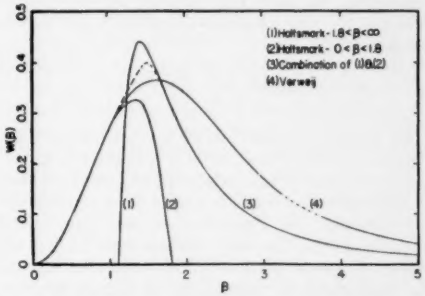

FIG. 8. Theoretical functions which give the probability of existence of the Stark field.

of data on the second-order effect obtained by Gebauer and von Traubenberg.[8] They have shown that at fields of 600,000 volts/cm the second-order effect is only 6 percent of the first order.

Combining (3) and (8) gives

$$\beta = (1/C_k)(\delta\lambda/F_n). \tag{9}$$

For abbreviation, $\delta\lambda/F_n$ is set equal to α. With this it is now possible to introduce F_n into the distribution function and obtain an expression for the distribution of intensity over α, with the result that

$$J_k(\alpha) = \int_0^\infty J_k'(\alpha) W(\beta) d(\alpha/C_k). \tag{10}$$

The function $J_k'(\alpha)$, in so far as the integration in (10) is concerned, can be nonzero in at most an interval $\Delta\beta$ equal to the inhomogeneity of the field over the dimensions of the emitting atom. With the fields present in the discharges studied it turns out that $W(\beta)$ is, for all practical purposes, constant over $\Delta\beta$. J_k' may then be considered to be a constant which is taken to be the theoretically calculated relative intensity I_k for the kth

[8] R. Gebauer and H. Rausch v. Traubenberg, Z. Physik **62**, 289 (1930).

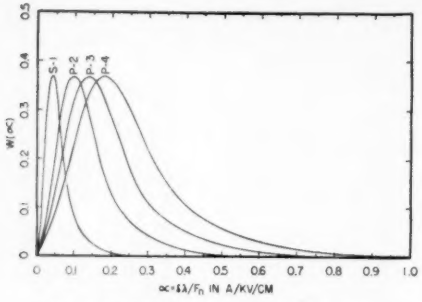

FIG. 9. Unscaled parametric curves for H_α line.

component. We have thus obtained the following expression for the intensity distribution of the kth component:

$$J_k(\alpha)=\frac{I_k}{C_k}\int_0^\infty W(\beta)d(\alpha). \tag{11}$$

By means of (9) the plot of $W(\beta)$, shown in Fig. 8, may be converted to a plot of $W(\beta)$ against α giving a family of curves with constants C_k as parameters. Each of these curves corresponds to one Stark component of the broadened line. Figure 9 shows such plots for components of H_α; the very weakest ones having been neglected. Values of C_k were taken from data published by Minkowski[9] on the splitting of Balmer lines at a field intensity of 104 kv/cm.

If $W(\beta)$ is interpreted as being the plot corresponding to the kth component, the integral in (11) is precisely the area under the parametric curve. I_k/C_k turns out, as it should, to be the constant factor by which this area must be multiplied if all areas are scaled to be proportional to the relative intensities. The curves of Fig. 9 have been properly scaled using values of I_k given by Minkowski and are replotted in Fig. 10. The final distribution curve $J(\delta\lambda/F_0)$ for the whole H_α line was obtained by compounding the component curves according to (7). Profiles for the first three Balmer lines are plotted in Fig. 11.

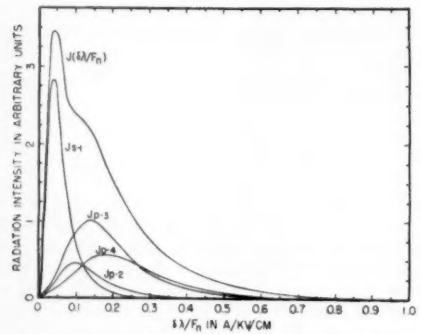

FIG. 10. Scaled component curves for the broadened H_α line.

[9] R. Minkowski, Handbuch der Physik (Verlag. Julius Springer, Berlin, 1929), Vol. 21, pp. 393–407.

It was noted that these profiles have shapes differing from those obtained by Craggs and Hopwood,[8] yet they agree with those given by Verweij.[7] In an attempt to determine the cause of this discrepancy it was found that, apparently, Craggs and Hopwood[8] had not actually scaled the areas to be proportional to the relative intensities. To reproduce their plot for H_β it was necessary to multiply the integral in (11) by I_k rather than I_k/C_k.

The curves of Fig. 11 can now be used to determine ion concentrations from the observed Balmer line profiles. To do so the theoretical curves are fitted to the observed profiles by adjusting the scaling factor F_0 on the wavelength axis. From known values of F_0, ion concentrations may be calculated by means of Eq. (4).

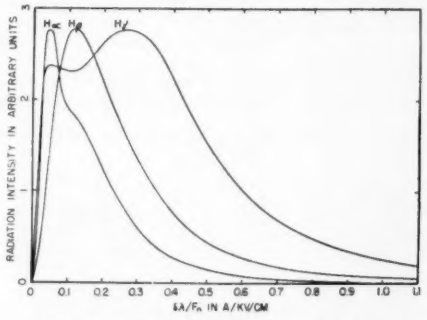

FIG. 11. Theoretical profiles for H_α, H_β, and H_γ.

Examples of such curve fittings are shown in Fig. 12. Since Holtsmark's theory does not account for the central undisplaced components, the theoretical profiles cannot be expected to fit those observed except along the wings of the lines. In the case of H_β where theoretically there is no undisplaced center component one would expect a somewhat better fit, and this is observed.

Normal field intensities and corresponding ion concentrations have been determined in the above manner for each of the observed profiles shown in Figs. 5–7. Results of these calculations are tabulated in Tables I and II. These ion concentrations are plotted along with the current and continuum traces in their proper phase relationships in Figs. 13 and 14.

V. DISCUSSION

The above results constitute new data on the variation of ion concentrations with time in flash discharges. The computed concentrations are considered to be well

within 10 percent of their correct values. This error is very small for concentration measurements where until recently only order-of-magnitude results have been obtained.

The concentrations in argon are lower than in neon at even higher flash energies, and this is not what might be expected judging from ionization potentials and collision cross sections for the two gases. However, these results agree with other observed properties of the discharges. For example, peak currents are higher in neon than argon under identical flashing conditions, although areas under the current traces are substantially the same. Breakdown potentials are observed to be lower for neon than argon in tubes of the same geometry and pressure. Penning[10] has shown, using very small currents, that in the range of E/p values encountered here, the fraction of energy lost in ionization is lower for argon than for neon.

In the present discharges the radiation peak is found to occur from 5 to 7 microseconds after the current

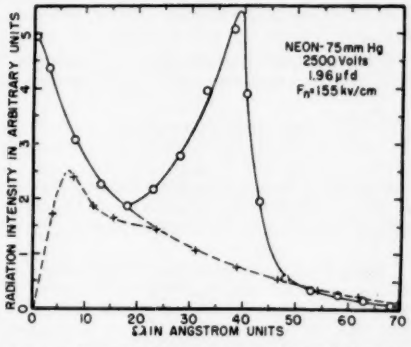

FIG. 12a. Theoretical (x) and observed (o) profiles for H_α.

peak. Similar delays have also been found in sparks by other investigators but to date have not been successfully explained. Results of the present study show that a delay in the build-up of the radiation is primarily due to a delay in formation of the plasma. In all cases the continuous radiation and ion concentration are found to build up together, reaching their peaks at the same time in the discharge phase.

During the plasma build-up time electrons are continually receiving energy from the applied field and ionization is occurring at a rapid rate. The high current which flows during this time indicates that ions and electrons are being removed from the plasma by the applied field. As a result the net ion concentration is increasing relatively slowly. Removal of charges neutralizes the capacitor charge and decreases the applied field. This in turn reduces the rate of removal and accounts for the sharp decrease in current.

[10] F. M. Penning, Physica **5**, 286 (1938).

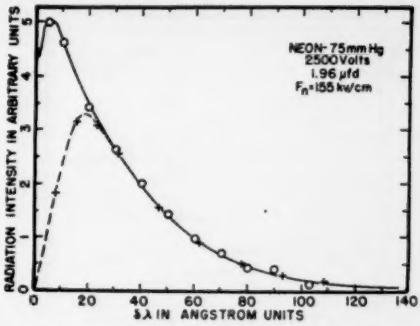

FIG. 12b. Theoretical (x) and observed (o) profiles for H_β.

Due to high energy electrons produced in the early stages of the plasma build-up and possibly to action of metastable atoms, ionization processes will continue for a while after the applied field is reduced to zero. Continued thermal ionization along with a reduction in the rate of removal of charges results in an increase in density of ions and electrons. A point in time is finally reached where the removal of charges by the field is negligible and the rate of ionization is just equal to the rate of removal of ions and electrons by recombination and diffusion to the walls. This point represents the peak of the concentration curve and should be expected to occur sometime after the peak current, as is observed.

Excitation of the Continuum

According to Unsöld's[11] theory of continuous radiation both bremsstrahlung and recombination continua are proportional to the product of ion and electron concentrations under conditions of temperature equilibrium. Therefore, a true gas plasma in thermal equilibrium should emit a continuous radiation which is proportional to the square of the ion concentration.

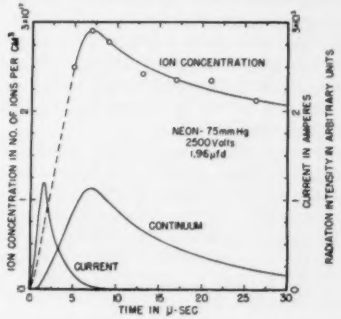

FIG. 13. Time-variation of ion concentration in neon discharge.

[11] A. Unsöld, Ann. Physik **33**, 607 (1938).

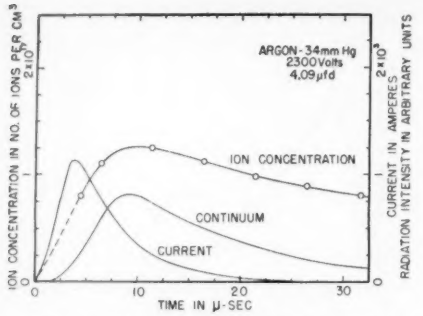

FIG. 14. Time-variation of ion concentration in argon discharge.

The data of Figs. 13 and 14 have been replotted in Fig. 15 to show the actual dependence of the continuum upon the ion concentration. Each point of these curves represents a certain instant of the flash. The points where the two branches of each curve meet represent the times of the peak of continuum and concentrations for both discharges.

In the build-up region of the plasma the slopes in both cases are in the neighborhood of 2. This may be interpreted as an indication that ion and electron concentrations build up together and that their relative temperatures do not change appreciably during this period of the flash.

However, in the region of the decaying plasma the situation is considerably different. Here the slopes more nearly approximate the value of 4. Such a relationship between continuum and concentration may be explained by any one or a combination of all of the following processes:

1. Preferential removal of electrons,
2. Decrease of electron temperature,
3. Decrease of ion temperature.

It is difficult to imagine processes by which many electrons disappear from the plasma without removal of positive ions. Removal by an applied field cannot be considered since there is little or no field across the tube during this phase of the discharge. Diffusion to the walls may account for a preferential loss of some electrons, but this process is limited by the amount of charge which may be built up there.

Electron and ion temperatures are certainly decreasing during the decay period when there is little or no energy input to the plasma. As electron velocities decrease one should expect a decrease in the intensity of radiation due to "free-free" transitions. On the other hand, as the average electron velocity decreases more electrons will fall into capture orbits resulting in an increase of recombination continuum.

A detailed analysis of the character of bremsstrahlung and recombination continua has been given by Unsöld.[11] According to his theory the continuous radiation intensity should be independent of wavelength. This holds for bremsstrahlung as well as for those overlapping bands of recombination continua which contribute in the longer wavelength regions.[12]

In the present work, emitted radiation has been observed only in the visible spectral region. Hence, according to Unsöld's theory, a study of the wavelength characteristics of this radiation would reveal little about the relative contributions of bremsstrahlung and recombination processes.

Some insight into the source of the continuous radiation, however, may be gained by a consideration of the change of electron temperature with time. Changes in electron energy distribution will affect quite differently the relative contributions of bremsstrahlung and of recombination continua. In the following it is assumed that the continuum observed at a given wavelength is entirely bremsstrahlung radiation. In this analysis the decaying portion of the continuum is assumed to be caused entirely by a decrease of electron temperature as the plasma cools. It is further assumed that a Maxwell-Boltzmann distribution of velocities exists at all times.

Under these conditions the continuous radiation intensity at a fixed frequency ν may be expressed as

$$S_\nu \sim n_i \int_{v_0}^{\infty} n_e(v) J(\nu, v) dv, \tag{12}$$

where v_0 is the lowest velocity an electron may have and still contribute to the radiation at the frequency ν. $J(\nu, v)$ is the intensity distribution function for con-

TABLE I. Ion concentration data for neon discharge.

Time μsec	F_n (kv/cm) H_α	H_β	Mean F_n	n (ions/cm³)
5	155	155	155	2.50×10^{17}
7[a]	···	165	165	2.93
9	160	160	160	2.77
13	148	143	146	2.42
17	145	140	143	2.35
21	145	140	143	2.35
26[a]	···	132	132	2.05

[a] Profiles for these results not presented in Fig. 6.

TABLE II. Ion concentration data for argon discharge.

Time μsec	F_n (kv/cm)	n (ions/cm³)
4[a]	72	0.84×10^{17}
6	85	1.07
11	90	1.25
16	87	1.12
21	80	0.98
26[a]	75	0.89
31	70	0.81

[a] Profiles for these results not presented in Fig. 7.

[12] The considerations do not apply to the individual isolated bands of recombination continua lying near the series limit in the range of short wavelengths.

tinuous bremsstrahlung radiation produced by a single electron retarded by a positive ion. Approximations of the quantum-mechanical form of this function are given by Maue.[13] In the range of frequencies and electron temperatures encountered in this work $J(\nu, v)$ may be approximated by $1/v^2$ in the integration of (12).

Introducing the Boltzmann speed distribution function into (12) and carrying out the integration with the above approximation for $J(\nu, v)$ gives

$$S_\nu = An^2T^{-\frac{1}{2}}[1-\varphi(\sqrt{a})], \tag{13}$$

where A is a proportionality constant, n the ion concentration (assumed equal to the electron concentration), T the electron temperature, $a=2.94\times10^4T^{-1}$ and $\phi(\sqrt{a})$ is the Gaussian error integral $\varphi(x)$ evaluated at $x=\sqrt{a}$.

With this expression the change of electron temperature required to account for the observed decay of continuous radiation with time may be determined taking into account the measured ion concentrations. In the case of argon (see Fig. 14) the electron temperature at the continuum peak calculated from Saha's equation is 10,600°K. It was calculated that a change of temperature from 10,600°K at the peak of the radiation to 8300°K at $t=30$ μsec will account for the fall-off of the observed continuum.

No doubt recombination is going on at all times during this decaying portion of the discharge. Because of the relatively few electrons having low velocities one should expect the contribution of recombination to be small in the intense portion of the flash. Evidence of this is given by the recombination arc lines which peak late in time phase (see Fig. 4).

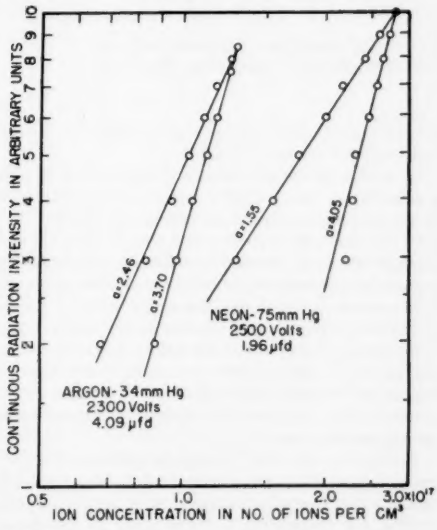

FIG. 15. Intensity of the continuum as a function of ion concentration for the rise and decay portions of the discharge.

[13] A. W. Maue, Ann. Physik **13**, 161 (1932).

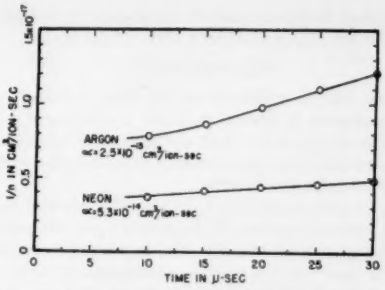

FIG. 16. Measured recombination coefficients for decaying plasmas of argon and neon discharges.

Recombination Coefficients

If recombination is to play an important role as a mechanism for the production of the continuum, the measured recombination coefficients should have reasonably large values. Craggs and Meek[14] have discussed mechanisms of afterglows in hydrogen and argon and suggest that the radiation can be due to recombination only if the coefficient $\alpha \geq 10^{-11}$ cm³/ion-sec.

In the present experiments recombination coefficients of the order of 10^{-13} have been determined for argon and neon according to the plots in Fig. 16. The observed constant values of these coefficients indicate that electron temperatures are changing rather slowly during this time of the decaying plasma. This is in good agreement with our previous theoretical interpretation of the continuous radiation process.

Kenty[15] has measured ion concentrations of the order of 10^{12} ions/cm³ in very low pressure argon arcs (0.4 amp, 0.8 mm Hg) using Langmuir probes. Approximately straight line plots of $1/n$ *vs* time gave $\alpha=2\times10^{-10}$ cm³/ion-sec. The comparatively small values of $\alpha(\sim10^{-13})$ observed in the present work seem to justify our assumption that recombination, although present, contributes comparatively little to the total radiation during the intense portion of the flash and in the spectral region studied.

The measured ion concentrations have enabled us to obtain accurate experimental values for recombination coefficients in intense arc plasmas where concentrations and electron temperatures are very high. Until now experimental values for high density plasmas have been determined from observations of the discharge afterglows assuming the radiation to be proportional to the square of ion concentration. Such an assumption would

[14] J. D. Craggs and J. M. Meek, Proc. Roy. Soc. (London) **A186**, 241 (1946).

[15] Carl Kenty, Phys. Rev. **32**, 624 (1928).

have lead to serious error in the present work where a square law relation has been shown to be invalid.

VI. CONCLUSIONS

The analysis presented in this study furnishes possible answers to several problems concerning the succession of events in a flash discharge and the probable mechanisms which are operative in exciting the various types of radiation observed.

It is quite obvious that the rate of increase of radiation intensity is primarily dependent upon the build-up of the plasma ion density. The maximum intensity of spark line emission occurs simultaneously with the occurrence of peak ion concentration, and this radiation is due to impact excitation. Arc line oscilloscope traces are broader and their maxima occurs later in time. Recombination of electrons and ions accounts for a large fraction of the arc line intensity although it amounts to only a few percent of the total radiation from the plasma. Arc lines are observed in the afterglow phase of the discharge long after the disappearance of spark lines.

The analysis shows that the intense continuum, accounting for most of the emitted radiation, is primarily due to retardation of electrons moving in orbits about ions ("free-free" transitions). The rate of decay of this bremsstrahlung radiation depends both on the rate of decrease of plasma ion density and the rate at which the mean energy of the electrons is diminishing.

During the portion of the flash period for which data is shown the electron "temperature" has not changed a great deal and the value of the recombination coefficient of electrons and ions remains essentially constant. Moreover, the small value of the coefficient obtained indicates that recombination processes contribute a relatively small amount to the continuous radiation in the visible spectral region.

It is believed that these results provide the correct explanations of delay of emission of radiation following the input of electrical power, and furnish the first semiquantitative picture of the excitation mechanisms involved in flash discharges at low gas pressures.

PHYSICAL REVIEW VOLUME 87, NUMBER 6 SEPTEMBER 15, 1952

The Decay Scheme of Ir^{192}

K. I. Roulston and R. W. Pringle
Physics Department, University of Manitoba, Winnipeg, Canada
(Received May 21, 1952)

Scintillation spectrometer time-correlation studies of the Ir^{192} disintegration have yielded new information about the Pt^{192} level scheme. Gamma-rays have been observed of considerably higher energy than any reported previously.

THE disintegration of Ir^{192} to Pt^{192} has been studied by a number of workers and a decay scheme has recently been proposed by Cork *et al.*,[1] based on accurate measurements of the energies of internal conversion electrons in a beta-spectrometer. Evidence for the existence of an alternative decay process (by K-capture) to Os^{192} was also produced.

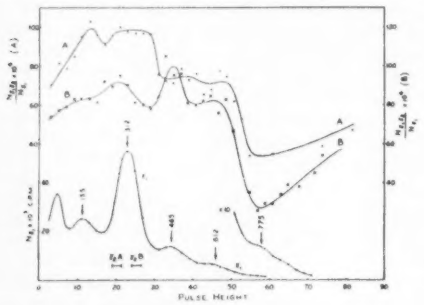

FIG. 1. Gamma-gamma coincidence curves for Ir^{192}.

In studies of the gamma-ray spectrum of Ir^{192} with a scintillation spectrometer, evidence for gamma-rays of energies higher than those previously reported (611 kev) was obtained. Two lines at approximately 775 and 870 kev have been detected with the spectrometer using a pulse-height analyzer. An oscillogram of the spectrum by a method similar to the grey wedge technique, using exponential intensity modulation of the cathode-ray tube beam, indicates further gamma-rays up to an energy of 1.2 Mev. There are really no distinctive features in the region 900 to 1200 kev but rather a continuum, which suggests the presence of several unresolved gamma-rays.

A check of the total energy involved in the Pt^{192} ground-state transition was made by placing a piece of the active material in contact with the scintillating crystal and comparing the end point of the pulse-height distribution curve with that of the distribution for the gamma-rays of Co^{60}. This gave a value of 1.58 $\pm$0.03 Mev in good agreement with previously ac-

[1] J. M. Cork *et al.*, Phys. Rev. **82**, 258 (1951).

cepted conclusions based on separate beta- and gamma-ray measurements.

Gamma-gamma coincidence studies, as previously proposed,[2] were carried out to obtain further information on the disintegration. The equipment consisted of two scintillation spectrometers of conventional design, the output pulses from the analyzers being passed to a British type 1036A coincidence unit. A resolving time of 0.3 microsecond was used. One analyzer was set to select pulses in a certain range of pulse heights and the spectrum was scanned by the other analyzer, both the coincidence and the single channel counting rates being measured concurrently.

In Figs. 1 and 2 are plotted the gamma-ray counting rate in channel 1, and the ratio of the coincidence counting rate to the gamma-ray counting rate for different selected ranges of pulse heights in channel 2, the ranges involved and the corresponding coincidence ratio curves being marked with letters *A*, *B*, *C*, *D*, and *E*.

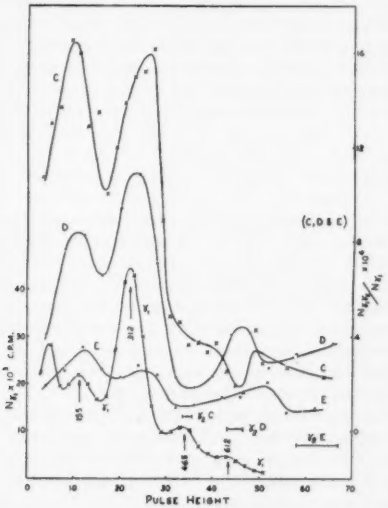

FIG. 2. Gamma-gamma coincidence curves for Ir^{192}.

In interpreting the results it must be borne in mind that, of the smaller pulses, some are due to high energy gamma-rays; this, combined with the effects of lower resolution for low energy gamma-rays, results in less distinctive features in the coincidence ratio curve for the small pulse-height region.

Examination of the curves confirms Cork's scheme, as far as it goes, but requires the addition of several

[2] Pringle, Roulston, and Taylor, Rev. Sci. Instr. **21**, 216 (1950).

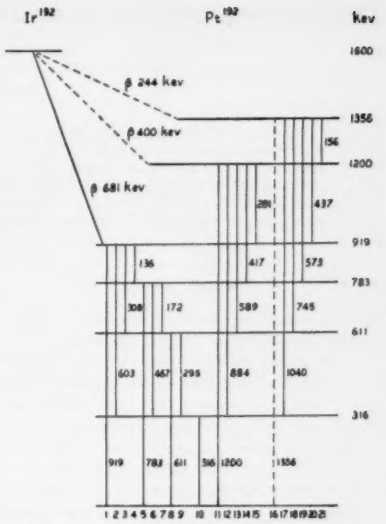

FIG. 3. Proposed level scheme for Pt^{192} following beta-emission from Ir^{192}.

higher energy gamma-rays. It should be noted that the 312-kev peak in the $N_{\gamma 1}$ curves consists of three unresolved components of energy 295, 308, and 316 kev.

Curve *A* requires the addition of two gamma-rays in the 700–800 kev region, e.g., lines 5 and 18 in Fig. 3. Curve *B* requires lines at energies approximately those of lines 5, 12, and 18, and possibly 17. Curve *C* can be explained by the existence of line 14 or line 20. Line 19 might also be necessary. Curve *E* requires lines 12 and 21.

Thus the gamma-gamma investigations require the addition of lines 5, 12, 18, 21, and possibly 17, 19, and 14 or 20 to those of Cork's scheme. Line 21 requires the addition of another energy level and one at 1356 kev is suggested. This would give an energy difference of 437 kev to the 919-kev level which could be identified with Cork's value of 438 kev for a gamma-ray. However, no evidence of a gamma-ray of energy 1356 kev has been obtained.

It might be noted that there is no direct support for the proposed level scheme from observations of the beta-spectrum itself. Most of the work done has indicated only a simple spectrum of end-point energy close to 681 kev. However, the partial beta-components of energy 400 and 244 kev are much less intense than the main component and will be difficult to detect in a conventional beta-ray spectrometer.

Our thanks are due the National Research Council of Canada for the support of this work.

The Differential Cross Section for the Scattering of 9.48-Mev Protons by Helium

T. M. PUTNAM*
Crocker Laboratory, Department of Physics, University of California, Berkeley, California
(Received May 5, 1952)

The angular distribution of protons scattered by helium has been measured at 9.48-Mev incident proton energy in the angular range of 10° to 172.5° in the laboratory system. Ilford C-2 photographic emulsions were used for detecting the scattered particles. The geometry of the multiplate scattering chamber and the accuracy of the construction was such that the results obtained have a relative accuracy within the counting statistics and an absolute accuracy to ±3 percent. The results are given in terms of the differential cross section per unit solid angle in the center-of-mass system and are compared to the results at other energies.

I. INTRODUCTION

THE scattering of protons from helium nuclei, as with the scattering of protons from other light nuclei, is of fundamental interest in the information which the angular distribution of the scattered products can give to aid in forming a theory of nuclear forces. Proton-helium angular distribution measurements have been made in the energy range of 1 to 3.5 Mev,[1] at 5.1 Mev,[2] and at 5.8 Mev.[3] Critchfield and Dodder have set the initial pattern for the phase shift analysis of the proton-helium case with their analysis of the low energy data.[4] Further work is being carried out on the data at 5.1 and 5.8 Mev.

In addition to the angular distribution of the scattered products, information has also been obtained concerning an excited state in Li^5. Several groups have investigated the possibility of resonance scattering in the proton-helium case. The Minnesota group (reference 1) has measured the angular distribution as a function of energy and has shown the existence of a broad resonance near 2 Mev. The earlier work in this field was limited somewhat by the maximum available proton energy and the resonance was not observed.

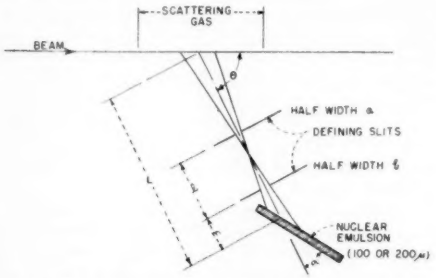

FIG. 1. Slit system geometry for scattering at angle of θ to the incident beam axis. Slit width = 0.045″; plate angle = 11°46′; slit separation = 2.875″.

The experiment to be described is the measurement, by means of photographic emulsions, of the angular distribution of the 9.5-Mev protons scattered by a "thin" helium gas target. The 20-Mev molecular hydrogen beam from the 60-in. cyclotron in Crocker Laboratory was used as the source of protons. The molecular hydrogen breaks up into two protons on passing through the thin foil at the entrance to the scattering chamber giving a beam of protons ofapproximately 9.5-Mev energy. The scattering measurements were limited to this single energy, hence no direct evidence could be obtained regarding an excited state in Li^5. However, since photographic emulsions were used to record the scattered particles, the existence of an excited state of He^4 in the energy range of approximately 1 to 8 Mev could be established by the presence of two ranges of scattered protons. Due to the limited energy resolution in the experiment, however, no evidence was obtained concerning such an excited state in the energy range used. The work by Allred[5] on the $He^3(dp)He^4$ case has also indicated a low cross section for an excited state below 20.9 Mev.

This experiment, then, extends the energy range of the measurements of proton-helium scattering to 9.48 Mev. The angular range has also been extended to 172.5° in the laboratory. Sufficient data has been obtained to indicate that the angular distribution curve at this energy does not possess any fine structure.

II. ASSOCIATED THEORY

The angular distribution of the products of a scattering process is customarily expressed in terms of the differential cross section per unit solid angle $d\sigma(\theta)/d\omega$. The differential element of the total yield of the process may be expressed as

$$dY = Nn[d\sigma(\theta)/d\omega]d\omega,$$

where N is the number of particles in the incident beam per unit area, n is the number of target nuclei per unit area, and $d\omega$ is the solid angle subtended by the detector at the angle θ.

The geometry of the scattering system is shown in Fig. 1. The beam can be assumed to be a line source of

* Present address, Los Alamos Scientific Laboratory, University of California, Los Alamos, New Mexico.
[1] Freier, Lampi, Sleator, and Williams, Phys. Rev. **75**, 1345 (1949).
[2] C. H. Braden, Phys. Rev. **84**, 762 (1951).
[3] W. E. Kreger (to be published).
[4] C. L. Critchfield and D. C. Dodder, Phys. Rev. **76**, 602 (1949).
[5] J. C. Allred, Phys. Rev. **84**, 695 (1951).

particles since it is collimated by circular apertures to a diameter of $\frac{3}{16}$ inch, and the distance to the detector is approximately 8 inches. (It can be shown analytically[6] that the difference, between the average solid angle subtended by the detector from the extreme edges of the beam and that subtended from the axis, is completely negligible.) The number of scattering centers n may then be expressed in terms of the product $n_0 dy$, where n_0 is the number of nuclei per unit volume and dy is the element of length along the beam axis from which particles are scattered into the detector. If Y is the total number of scattered particles on the photographic plate and N is the total number of incident particles, then

$$Y = n_0 N \frac{d\sigma(\theta)}{d\omega} \int\int dy d\omega.$$

If this number is recorded in a swath along the plate of width W and length dx, it may be expressed in terms of these quantities and the slit system geometry. The result, neglecting second-order terms, is[7]

$$Y = n_0 N \frac{d\sigma(\theta)}{d\omega} \frac{4abW}{lL \sin\theta}.$$

The expression for the differential cross section per unit solid angle is then

$$d\sigma(\theta)/d\omega = (Y/W)(lL \sin\theta / n_0 N a b),$$

where a and b now represent the full slit widths. It should be noted here that the only measurements necessary in evaluating the data are the determination of the number of incident protons, the number of target nuclei, and the yield of scattered particles per unit swath width on the nuclear plate detector. The angle of the detector to the scattered particle does not enter into the determination of the cross section. This is one of the prime advantages of the geometry used in the experiment.

III. APPARATUS

The scattering chamber used in this experiment was the Nuclear Multiplate Camera of J. C. Allred *et al.*,[8] which was developed at the Los Alamos Laboratories for studying the angular distribution of the products of nuclear reactions and nuclear scattering. Figure 2 shows the general experimental arrangement. The beam from the Berkeley 60-in. cyclotron was brought out through an iron snout[9] so that the camera could be located in a field-free region. Some magnetic shielding

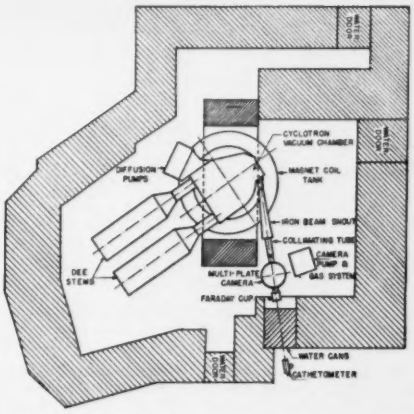

FIG. 2. Cyclotron and multiplate camera experimental arrangement.

was necessary, however, because of the proximity to the magnet yoke.

The details of the scattering chamber as well as its use in similar experiments have been given elsewhere.[8,10,11] The essential features as used in this experiment are the collimation of the beam to $\frac{3}{16}$-in. diameter, the multiple collimation of the scattered particles, eliminating an uncertainty in solid angle as discussed above, and the exposure of many plates (angles) at one time reducing the effect of variations in cyclotron output during the course of the experiment. Figure 3 shows the general collimation and plate arrangement. The nuclear emulsion plates are held in position between the outer slit ring and the wall of the scattering chamber such that the beam of scattered particles strikes the plate at a point about 3 cm from its inside edge. The arrangement allows the exact location of the plate to be determined and a repro-

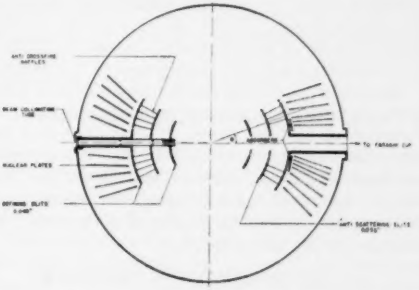

FIG. 3. Multiplate camera schematic showing beam collimation, defining slits, and nuclear plate arrangement.

[6] J. C. Allred (unpublished).
[7] The full expression for the yield with this geometry was first worked out by C. L. Critchfield at the University of Minnesota and contains terms involving the slit widths and the angle of the nuclear plate to the slit axis. However, the error introduced by neglecting these terms in less than 0.1 percent.
[8] Allred, Rosen, Tallmadge, and Williams, Rev. Sci. Instr. **22**, 191 (1951).
[9] T. M. Putnam (to be published).
[10] L. Rosen and J. C. Allred, Phys. Rev. **82**, 777 (1951).
[11] Rosen, Tallmadge, and Williams, Phys. Rev. **76**, 1283 (1949).

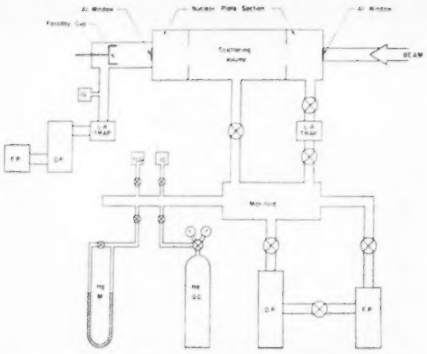

FIG. 4. Camera pump and gas system schematic. The chamber and Faraday cup pump systems are shown with the gas handling system. The symbols represent: DP, oil diffusion pump; FP, mechanical fore pump; IG, ion gauge; TCG, thermocouple gauge; HeGC, helium gas cylinder; HgM, mercury manometer; LA trap, liquid air trap.

ducible geometry is obtained. In addition, slots are provided in the outer ring assembly so that suitable foils may be inserted to slow down the scattered particles so that they will stop in the emulsion of the detector.

The angular spacing between the plates is 5° except at the forward angles. In this case three plates on one side and four on the other side of the beam axis have 2.5° spacing. With this arrangement, the angles on one side are shifted by 2.5° from the angles on the other, giving 2.5° coverage for all angles from 10° to 172.5°.

Additional features of the multiplate camera are: (1) The definining slit rings fit into recess in the camera lid and form a baffle which reduces the diffusion of water vapor from the emulsions into the scattering volume. (2) The accuracy with which the camera slit system and plate holders were machined makes it possible to obtain results which have a relative accuracy essentially within the counting statistics for each angle. The estimated error in the angle between two plates is of the order of 0.1 percent which is negligible compared to the statistical accuracy usually used (1.5–2 percent).

The camera pump and gas handling system is shown in Fig. 4. Separate oil diffusion pumps were used for the Faraday cup and the camera. It should be noted that the camera had two pump lines. The line with the liquid air trap, which was connected to the nuclear plate section, was used for evacuating the chamber and removing the condensable vapors while the second line was used for admitting the gas.

IV. NUCLEAR EMULSION TECHNIQUE

Ilford C-2 nuclear emulsion plates were used to detect the scattered particles. These were, in general, 100-micron plates, except at the forward angles where 200-micron plates were used. The principal advantages of the nuclear plate detector in a scattering experiment are (1) continuous sensitivity so that all products of the scattering process will be recorded during a run; (2) compact size enabling many angles to be measured in a single run; (3) almost complete discrimination against spurious and background particles. This is possible by the application of suitable criteria for valid tracks in the plate. The obvious disadvantages are that the data is not immediately available because of the time required for plate development and the rather extensive time required for analyzing each plate.

The analysis of the nuclear plates was made using Zeiss Jena Laboratory binocular microscopes with research microscope illuminators. Ribbon type filament lamps were used which give a uniform and intense source of light. Oil immersion objectives of 60× and compensated eyepieces of 10× were used and, with a body-tube magnification of 1.5×, a net magnification of 900× was obtained for all measurements. In order to facilitate the measurements of track lengths, a superstage driven by a precision screw was devised[12] and attached to the existing microscope stage. This superstage increased the speed and accuracy of the measurements by a factor of 3 to 5 and greatly reduced the time required to analyze a plate.

The swath width in which tracks were counted was defined by a reticule, consisting of a large ruled square subdivided into 100 sections, engraved on an optical glass disk. The disk was placed in one of the microscope eyepieces and the analyst used only that portion of the field of view within the square in selecting tracks that were to be counted.

The procedure used in analyzing a plate was as follows: From the geometry of the slit system, several initial criteria were established for all particles coming from the scattering volume: (1) Tracks must start on the surface of the emulsion. (2) They must proceed in such a direction as to have come from the scattering

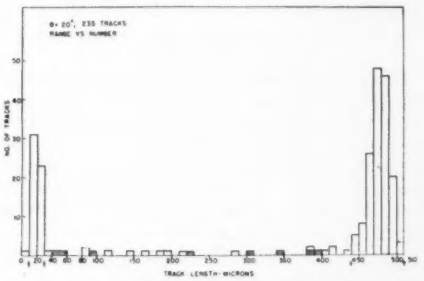

FIG. 5. Typical range *vs* number or range distribution histogram. Tracks in short peak were alpha-tracks from recoil helium nuclei. Long-range tracks were the scattered protons. Intermediate tracks were presumably slit and impurity scattered particles. Shaded areas represent tracks which fell outside the density distribution peak (see Fig. 6).

[12] T. M. Putnam and J. F. Miller (to be published).

volume. (3) They must enter the emulsion within given angular limits as determined by the slit geometry. With these criteria a preliminary measurement was made of the length of all tracks on several swaths across the plate and their position was noted in 2-mm intervals. This data when plotted as histograms gave the distribution of range and position of the tracks on the plate, as shown in Figs. 5 and 6. In Fig. 5 the short-range tracks are the recoil He nuclei which entered the plate. These tracks all fell within the density distribution. The shaded areas on the figure represent tracks which fell outside the density distribution. The other intermediate range tracks may be attributed primarily to slit-scattered particles, i.e., protons which have penetrated the slits sufficiently to lose some of their initial energy. These particles, by the nature of the defining system, have not come from the allowed scattering region or are not proceeding at the proper angle and, hence, are not counted.

From the slit geometry, it is also expected that the maximum number of tracks will occur at the intersection of the axis of the slit system with the plate and the number will fall to zero on each side of this. The position of the center of gravity of the track density histogram with respect to the edge of the plate will then enable the factor L to be determined quite accurately. In addition, from the density distribution one can be certain of including all of the tracks on the plate and, particularly at the forward angles where absorbers were used, one could determine whether or not all of the protons which pass through the slits entered the plate. This was found to be true, although the distribution was spread over a much larger portion of the plate than at larger angles where no absorbers were used.

To determine the range criterion for scattered protons, the range of the main peak of the range distribution histogram was compared with the expected proton range. This was determined from the approximate incident energy and the mechanics of the elastic scattering process, making suitable corrections for gas absorption and plate angle. By working in the opposite direction, i.e., using the measured ranges at each angle, the incident proton energy was determined. This method gave the actual value independent of any corrections for foil windows in the scattering chamber.

The track range distribution curve was also used to determine if any other process had taken place during the experiment that was observable on the plates. The limits of energy resolution are quite broad, however, because of the scattering and straggling of the tracks in the emulsion.

Thus, by applying suitable geometrical criteria together with limitations on acceptable range of valid tracks, the yield of scattered protons Y was determined. A sufficient number of complete swaths were scanned on each plate to give approximately 2500 tracks. The total swath width W was determined from the number of swaths and the known width of the reticule.

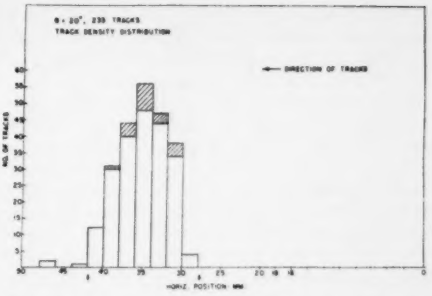

FIG. 6. Typical track density distribution histogram. Shaded areas represent tracks which fell outside the main range peaks (see Fig. 5).

V. EXPERIMENTAL PROCEDURE

The procedures used in this experiment were quite straightforward and followed the usual pattern for scattering experiments. Only a few of the more pertinent points need be mentioned. The most time-consuming part was the initial alignment of the camera. In order to fully utilize the extreme accuracy of its construction, the alignment along the beam axis was done very carefully using a cathetometer. The final data indicated that this was accomplished to better than one-quarter of one degree.

Preparation of Camera

Because of water vapor in the photographic emulsions, a rather extensive pumping time was required (four to six hours) to remove a sufficient amount of this vapor so that an appreciable error would not be introduced in the measurements. The liquid air trap in the line to the annular area containing the plates (shown in Fig. 4) was used during this period. A rate of rise of the system, with the pump and trap shut off, of 5 to 10 microns per minute was considered low enough for the experiment. The base pressure was usually in the neighborhood of 10^{-5} mm Hg at this point.

Gas Handling and Determination of n_0

The helium gas used in the experiment was taken from a tank of standard Grade A helium. No effort was made to purify the gas because of its rated purity and the almost complete discrimination against impurity-scattered particles which was possible in the counting. After the camera had been outgassed, the pump and liquid air trap were shut off from the system and the gas admitted to the desired pressure as determined by a mercury manometer.

The determination of the number of target nuclei per unit volume n_0 depended upon the accurate measure-

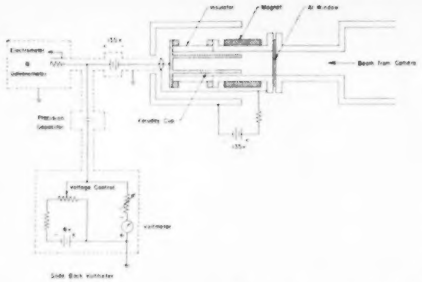

FIG. 7. Faraday cup and current integrating circuit schematic. Voltage across capacitor was maintained essentially at zero during a run by adjusting the slide-back voltmeter. Final balancing voltage was measured to determine the total charge accumulated.

ment of the pressure of the gas and its temperature. A precision cathetometer was used to measure the difference in height of the two arms of the mercury manometer. Measurements were made independently by two observers and averaged. The temperature of the gas was taken as the temperature recorded by a thermometer placed directly under the chamber. The mean of the temperature readings before and after a run was taken as the temperature of the gas during the run. Only slight differences were noted since the ambient temperature within the five-foot tanks surrounding the cyclotron remains fairly constant.

Integration of the Incident Beam and Determination of N

A separate Faraday cup unit was provided to integrate the beam passing through the chamber (Fig. 7). The cup itself was nine inches in length and $1\frac{3}{4}$ inches in inside diameter. The chamber and pump system was fastened to the scattering chamber but separated from it by a thin (0.001-inch) aluminum window. Two Alnico permanent magnets were located above and below the cup so as to create a field of the order of 1000 oersteds. The purpose of this was to trap secondary electrons produced in the cup by the positive ions. The Faraday cup was made negative with respect to ground to prevent the collection of the electrons knocked out of the window by the beam.

The primary sources of leakage which would produce errors in the value of N were assumed to be (1) ionization of the residual gas in the cup; (2) secondary electrons escaping from the cup; (3) conduction along the insulator surfaces.

Since the pressure in the Faraday cup was maintained in the range of 10^{-7} mm Hg, ionization of the residual gas should be a negligible factor and conduction along the inner surface of the insulator would be essentially eliminated. To check for the possibility of secondary electrons escaping from the cup, the cup was made positive with respect to the case. A positive charge placed on the integration condenser was neutralized indicating negative integration. No integration was observed with zero potential on the cup. In the first case, secondary electrons from the surrounding surfaces were possibly the cause, but it is more likely that it was due to leakage through the air as discussed below. The fact that no integration was observed when the cup was at zero potential indicates the effectiveness of the magnetic field in stopping secondary electrons from leaving the cup. In addition, the length of the cup and the large diameter gave added assurance that secondary electrons would not escape.

The only leakage point that needed correcting was the apparent conduction through the air and along the outside of the Faraday cup insulator. Since the experiment was performed inside the cyclotron water barrier, the radiation field (neutron and gamma ray) present when the beam was on was quite high. This apparently produced sufficient ionization of the air to cause conduction along the outside of the cup insulator. This leakage was essentially eliminated by the use of an electrostatic shield placed over the cup and put at a potential negative with respect to ground and of approximately the same value as that of the cup. This placed the cup and insulator essentially in a field-free region eliminating the leakage across the insulator. Checks of the over-all circuit indicated a total leakage current of the order of 3×10^{-12} ampere. Hence, no corrections were made to N (the number of incident protons) for leakage in the integrating circuit.

Figure 7 also shows the general circuit used for integrating the current. An accurately calibrated precision capacitor of 1.075-microfarad capacity was used to integrate the charge. The electrometer and galvanometer circuit was used to indicate the voltage on the capacitor. The voltage was maintained essentially at zero during a run by means of an associated slide-back voltmeter circuit. At the end of a run the voltage on the slide-back voltmeter, which was required to completely neutralize the accumulated charge on the condenser was measured with a Leeds and Northrup type K potentiometer and a General Radio type 654A decade voltage divider. A small drift in the electrometer was always present even with the capacitor discharged. A correction for this was applied by noting the zero drift at the end of each run.

The integrating capacitor was calibrated by means of comparison with a standard capacitor made commercially by the General Radio Company. This secondary standard was checked against the capacity of a Bureau of Standards calibrated condenser. The comparison was made with a General Radio capacitance bridge by two different observers. The value given was 1.075 ± 0.005 microfarads.

Exposure of the Plates

The exposure to be used for each run was determined from the results of a preliminary run. Examination of

the density of the tracks on the plates from this run indicated the general exposure needed for various angles to take account of the large variation in scattering cross section with angle. The exposures for the various runs are given in Table I.

A background run was also made to determine the presence of protons scattered from water vapor and other impurity gases other than those known to be present in the helium. This run was made following the same procedure as that used in handling the system for a regular exposure with the exception that no helium gas was admitted. The results of this run indicated that corrections were necessary only at the forward angles.

VI. CORRECTIONS

The techniques used in obtaining the data from the nuclear plates have already been discussed. Certain corrections were made to the raw data to correct for the effect of the absorbers used at the forward angles, for inherent background and for scattering from impurities in the gas.

The correction for absorbers at the forward angles was made for the loss of particles in a given swath width due to multiple scattering in the absorber. The amount of the correction was determined from data supplied by the Microscopy Laboratory at Los Alamos, which was obtained using the graphical method devised by Dickinson and Dodder.[13] This correction amounted to approximately six percent for the 0.008-inch aluminum absorbers used.

Background corrections were necessary due to the water vapor given off from the plates. These corrections were determined from an analysis of plates exposed in the background run. The number of tracks per centimeter swath width which would have been included in the normal counting at each angle was determined from the range analysis of the background plate at the same angle. This number was normalized for the rate of rise taken prior to each run as compared to that of the background run and for the integrated current used. The correction amounted to less than one percent at 10 degrees and above 20 degress was small enough (<0.03 percent) to be neglected.

The correction for impurity scattering due mainly to nitrogen in the helium gas was based on pure Coulomb scattering. By calculating the expected mean proton ranges of particles scattered from nitrogen and oxygen and comparing this with the accepted range for counting tracks on each plate, the angles over which a correction had to be applied were determined. It was found that below 37.5 degrees, particles scattered from nitrogen or oxygen would not be resolved from the main proton peak.

In order to determine the amounts of impurities in the helium gas used, an analysis was made of the gas by Dr. Amos Newton of the Radiation Laboratory using a Consolidated 180° Focusing Mass Spectrograph. The results of this analysis showed the primary contaminants to be hydrogen—0.02 percent, nitrogen—0.02 percent, and oxygen—0.01 percent. Using these figures and the cross sections for the Coulomb scattering of protons from nitrogen and oxygen, corrections were determined for impurity scattering. These amounted to approximately 0.5 percent at 10 degrees and were completely negligible at 20 degrees. No corrections were necessary for the hydrogen present due first to the smaller proton-proton scattering cross section in this energy range[14] and, secondly, to the fact that the ranges would be resolved above 15 degrees.

The alignment of the camera with the beam axis was determined from a graphical analysis of the data taken from the two sides of the beam. The above corrections were applied to the raw data and the results were compared. This analysis indicated that the beam was not exactly coaxial with the camera. A shift of laboratory angles of 0.2 degree was indicated and the final results were corrected for this shift.

Above 20 degrees there were no other corrections made to the data. One other source of background is open to question, however, This enters in the low energy "tail" of the range distribution peak. The incident proton beam was not monoenergetic and had a low energy tail from the nature of its production. This would similarly introduce a low energy tail on the range distribution. On the other hand, protons scattered by the slits would lose some energy and would contribute to this effect. In making the selection of the lower energy limit for acceptable tracks on the plate, this had to be considered. From an examination of the range distribution curves for each plate, it appears that the selection of ranges used would take care of this effect. Further corrections, if any, would be less than one percent and open to considerable error.

The effect of multiple scattering in the gas was also investigated. The loss of particles due to this effect was found to be completely negligible. The largest effect would have been at the backward angles where the scattered particle energy is of the order of 3 Mev. Calculations (based on reference 13) indicated that less than one percent of the particles would be deviated by only a few thousandths of a degree and, hence, the effect was completely negligible.

TABLE I. Experimental data for various runs.

Run	Gas pressure (cm Hg)	Gas temperature (°C)	Integrated current (micro-coulombs)
1	20.031	25.15	9.402
2	5.162	25.80	4.412
4	20.400	28.20	10.183
5	37.280	26.80	27.374
6	10.370	26.20	5.552

[13] W. C. Dickinson and D. C. Dodder, Los Alamos Report No. 1182 (1950).

[14] R. R. Wilson, Phys. Rev. 71, 384 (1947).

TABLE II. Measured cross sections as a function of angle in the center-of-mass system at 9.48-Mev incident particle energy. (Laboratory angles shifted 0.2 degree.)

θ	Ω	$[d\sigma(\Omega)/d\omega] \times 10^{24}$				
		1	2	4	5	6
9.8	12.2		1.1415			
10.2	12.8		0.9947			
12.3	15.3		0.6596			
12.7	15.9		0.6294			
14.8	18.4		0.5336			
15.2	19.0		0.5086			
17.3	21.5		0.4754			0.4662
20.2	25.2		0.4126			0.4018
22.3	27.7					0.3780
25.2	31.3					0.3580
27.3	33.9					0.3382
30.2	37.4			0.3116		0.3076
32.3	40.0			0.3016		0.3099
35.2	43.5			0.2804		
40.2	49.5			0.2392		
42.3	52.0			0.2322		
50.2	61.3			0.1719		
52.3	63.7			0.1668		
60.2	72.7	0.1195				
67.3	80.6				0.0822	
70.2	83.8				0.0715	
72.3	86.1				0.0653	
80.2	94.5				0.0431	
85.2	99.6				0.0322	
90.2	104.7				0.0278	
92.3	106.8				0.0251	
97.3	111.7				0.02302	
100.2	114.4				0.0220	
102.3	116.4				0.02302	
110.2	123.8				0.0273	
115.2	128.3				0.0333	
120.2	132.7				0.0392	
122.3	134.5				0.0423	
130.2	141.2				0.0527	
135.2	145.4				0.0562	
140.2	149.4				0.0669	
142.3	151.1			0.0686		
150.2	157.3			0.0802		
152.3	159.0			0.0809		
160.2	165.0			0.0854		
162.3	166.7			0.0867		
170.2	172.6			0.0922		
172.3	174.2			0.0967		

VII. RESULTS

The corrected results of the measurements of the angular distribution for the scattered protons are given in Table II and plotted in Fig. 8 in terms of the differential cross section per unit solid angle in the center-of-mass system. The data obtained from the two sides of the beam are distinguished by the solid circles and triangles. For the data at each angle approximately 2500 tracks were counted, giving a standard deviation of ± 2 percent. For the point at 60.2° in the laboratory system, however, only 547 tracks were obtained, giving ± 4.3 percent statistical accuracy. The plate peeled so badly before analysis could be completed that further counting would have been quite inaccurate; therefore the preliminary count was used.

In general, the internal consistency of the data for each run indicates an accuracy within the counting statistics. At the check points between runs, the differences are less than three percent which gives an indication of the reproducibility of the experimental conditions from run to run, as well as giving some confidence in the absolute accuracy of the data.

The factors whose errors enter into the over-all accuracy of the data are the current integration, measurement of the gas pressure and temperature, personnel factors in reading the plates, the calibration of the eyepiece reticule in the microscope, and the measurement of geometrical factors of the multiplate camera.

The accuracy of the current integration depended primarily on the calibration of the integrating condenser. The capacity of the standard capacitor used was given to ± 0.1 percent. From the spread of values obtained in making the calibration, the integrating capacity was given to ± 0.5 percent. A precision voltmeter was used to measure the voltage and the zero drift of the electrometer circuit during integration was included. As discussed earlier, numerous checks were made on the leakage of the Faraday cup and current integration system. One check was open to question, however. This is the leakage due to the ionization of the air around the cup. Checks were made prior to operation with a one-gram radium beryllium neutron source and with the radiation from the internal beam of the cyclotron. No check was made with the beam passing through the scattering chamber but blocked off from the Faraday cup. Since the electrostatic shield around the cup completely stopped any leakage in the tests that were made, it was felt at the time that this source of error had been eliminated and that no further tests were necessary. A probable error of ± 1 percent, however, appears to be a valid figure.

From the reproducibility of the measurements of the gas pressure and the necessary application of a correction for expansion of the mercury in the manometer, the probable error to be assigned to the gas pressure measurement is ± 0.2 percent. The temperature of the gas was measurable to ± 0.1 degree out of 25 to 30 degrees, giving a probable error of ± 0.5 percent.

The probable error in measurement of Y, the yield on each plate is somewhat difficult to assign. Frequent checks of the count on a single swath by two observers indicated, however, an over-all accuracy of better than one percent. Since these checks were made under possibly very favorable conditions, a more conservative figure for the probable error due to personnel factors would be ± 1.5 percent. For the calibration of the reticule from the spread in values obtained, a probable error ± 0.4 percent can be assigned.

The measurements of geometrical factors for the nuclear plate camera have an estimated probable error of less than one percent. These are: a, b -0.5 percent; -0.1 percent; L as measured on the plate -0.1 percent.

The resulting root-mean-square probable error for the measurements which enter into the cross section calculations is 2.1 percent. Considering the average statistical accuracy of 2 percent, a figure of ± 2.9 percent

for the absolute standard error can be assigned to all points in the angular range of 25 to 175 degrees (CM). The point at 72.7 degrees (CM), because of its statistical accuracy of 4.3 percent, can be assigned a probable error of ± 4.75 percent. At the more forward angles where large corrections are needed for the absorbers, an absolute standard error ± 5.0 percent can be assigned.

Figure 9 shows how the angular distribution of the scattered protons varies with the incident energy. It is interesting to note the similarity in shape of the distribution curves at 3.58, 5.8, and 9.48 Mev. The data at 5.1 Mev also agrees fairly well with that at 5.8 Mev except for the point near 150 degrees. This point is open to question because of the disagreement in shape with that of the other curves. The sudden change in shape of the distribution curve in the neighborhood of the resonance near 2 Mev (see reference 1) is also quite evident. Also included in the same figure is the differential cross section curve for pure Coulomb scattering as calculated for 9.48 Mev.

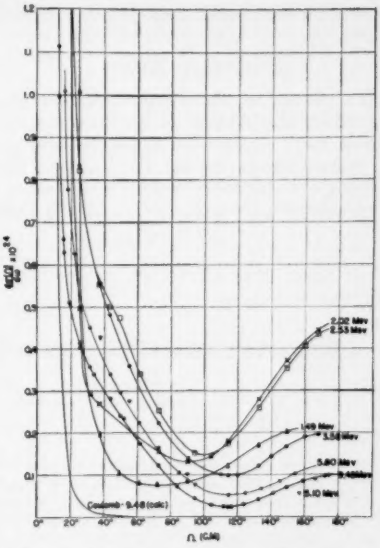

FIG. 9. Proton-helium scattering cross sections per unit solid angle in the center-of-mass system for various incident proton energies. For 5.1 Mev only the experimental points are shown.

VIII. DETERMINATION OF BEAM ENERGY

As indicated previously the beam energy can be determined directly from the scattered particle energy in this experiment, eliminating corrections for intervening windows. The method, of course, gives the average value of the energy during a given run.

For the determination of the beam energy, the mean value of the proton range at each angle was obtained from the range distribution analysis. This gave the mean-projected-range on the surface of the emulsion. Corrections were made for plate angle and emulsion shrinkage in determining the absolute mean range of the protons in the emulsion and allowances were made for the energy loss in the gas between the scattering center and the plate. The energy loss in the gas was determined by calculating the emulsion equivalent of the gas and assuming that the emulsion equivalent of one centimeter of air is equivalent to five microns of emulsion at N.T.P. The emulsion equivalent of the gas for each run was calculated from the relation

$$\frac{P_{\text{targ}}}{76}\times\frac{288}{T_{\text{targ}}}\times 5LS = \text{emulsion equivalent in microns},$$

where L = path length in the gas as determined from the center of gravity of the track density distribution on the plate. S is the stopping power of the gas with respect to that of air. This was determined over the energy interval in question from the range energy curves for protons in air and helium given by Aron, Hoffman, and Williams.[16] The value used was 0.155 for the stopping power of helium relative to air for the energy range of 3 to 9 Mev. The resulting values for the energy at each angle were averaged giving for the mean

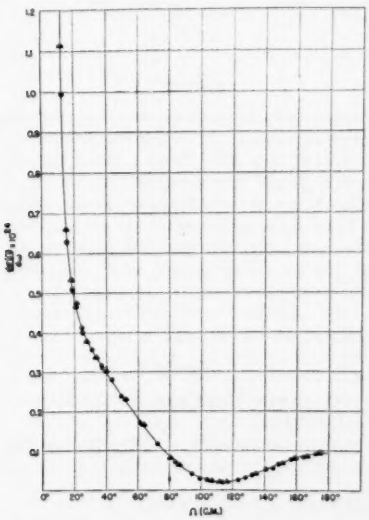

FIG. 8. The differential cross section as a function of angle in the center-of-mass system for the scattering of 9.48-Mev incident protons from helium. Points obtained from the two sides of the beam axis are indicated by closed circles and triangles.

[16] Aron, Hoffman, and Williams, unpublished University of California Radiation Laboratory Report No. 121 (Revised) (1949).

value of the energy from all the 47 plates 9.48 ± 0.15 Mev.

ACKNOWLEDGMENTS

It is a pleasure to acknowledge the encouragement and guidance of Professors E. M. McMillan, A. C. Helmholz, and J. G. Hamilton during the course of this work. Sincere thanks are also due Dr. Louis Rosen, for making this experiment possible by the use of the multiplate camera; Dr. J. C. Allred and Dr. R. O. Bondelid for their assistance in making the runs; Dr. Alice H. Armstrong for many helpful discussions.

The reading of the photographic plates was done in part at the Microscopy Laboratory at Los Alamos, chiefly by Mrs. J. Gammel and Mrs. M. Downs. Mrs. R. Gibbs and Mrs. T. M. Putnam assisted in the final counting of the tracks.

Thanks are also due the members of the Crocker Laboratory staff who contributed in many ways towards the completion of this work.

PHYSICAL REVIEW VOLUME 87, NUMBER 6 SEPTEMBER 15, 1952

Interaction between Electron and One-Dimensional Electromagnetic Field

NATHAN ROSEN
Department of Physics, University of North Carolina, Chapel Hill, North Carolina
(Received May 14, 1952)

For a single electron interacting with the quantized transverse electromagnetic field it is found that, in the one-dimensional case, the Schrödinger equation can be put into a form like that of a system of coupled harmonic oscillators. From the classical frequencies of the normal modes of oscillation of such a system the quantal energy can be determined. While the perturbation method gives a logarithmic divergence in the interaction energy, one finds by the present method that the energy diverges like the square root of a logarithm.

A QUESTION which does not appear to have received a satisfactory answer is whether the divergences arising in the interaction between a point electron and the quantized electromagnetic field are inherent in the problem or are due to the methods of calculation employed. The purpose of this paper is to attempt to throw some light on this question by considering a simplified case in which the electron and the field are constrained to one-dimensional motion. This may be regarded as a continuation of earlier work on one-dimensional fields.[1]

Let us consider first the more general case of a single electron, described by the Dirac equation, interacting with a quantized electromagnetic radiation field. Thus we do not make use of the hole theory of the vacuum. Nor do we concern ourselves here with the interaction with the longitudinal part of the field; this will be regarded as already included in the mass term of the Dirac equation. If we think of the system as satisfying a periodicity condition in a fundamental cube of side L, we can expand the field in a set of monochromatic plane polarized waves of proper frequencies with quantized amplitudes.[2] Let us label these modes of oscillation of the field by an integer λ. The Hamiltonian for the system can then be written

$$H=c\boldsymbol{\alpha}\cdot\mathbf{p}+mc^2\beta-e\boldsymbol{\alpha}\cdot\textstyle\sum_\lambda \mathbf{A}_\lambda+H_0, \tag{1}$$

where $\mathbf{p}$ is the electron momentum, H_0 is the Hamiltonian of the field,

$$H_0=\tfrac{1}{2}\textstyle\sum_\lambda(P_\lambda^2+\omega_\lambda^2Q_\lambda^2-\hbar\omega_\lambda), \tag{2}$$

and

$$\mathbf{A}_\lambda=c\pi^{\frac{1}{2}}L^{-\frac{1}{2}}\boldsymbol{\epsilon}_\lambda[Q_\lambda(e^{i\mathbf{k}_\lambda\cdot\mathbf{r}}+e^{-i\mathbf{k}_\lambda\cdot\mathbf{r}}) +(i/\omega_\lambda)P_\lambda(e^{i\mathbf{k}_\lambda\cdot\mathbf{r}}-e^{-i\mathbf{k}_\lambda\cdot\mathbf{r}})] \tag{3}$$

is the vector potential for the degree of freedom labeled by λ at the position of the electron specified by the vector $\mathbf{r}$. Here $\mathbf{k}_\lambda$ is $2\pi/L$ times a vector with integer components (positive and negative) depending on λ, $\omega_\lambda=c|\mathbf{k}_\lambda|$, and $\boldsymbol{\epsilon}_\lambda$ is the polarization vector, orthogonal to $\mathbf{k}_\lambda$. The amplitudes Q_λ and P_λ are pairs of conjugate variables satisfying the usual commutation relations for coordinates and momenta. In H_0 the zero-point energy has been subtracted.

We now consider the Schrödinger equation for a stationary state of energy E,

$$H\psi=E\psi, \tag{4}$$

where the operator H is given by (1) with $\mathbf{p}=-ih\nabla$, $P_\lambda=-i\hbar(\partial/\partial Q_\lambda)$.

To solve this equation let us write the wave function ψ as an expansion of the form

$$\psi=\textstyle\sum_{(n)} a_{n_1n_2}\cdots_{n_\lambda}\cdots U_{n_1n_2}\cdots_{n_\lambda}\cdots \times\exp[i(\mathbf{p}'/\hbar-n_1\mathbf{k}_1-n_2\mathbf{k}_2-\cdots)\cdot\mathbf{r}]. \tag{5}$$

Here

$$U_{n_1n_2}\cdots_{n_\lambda}\cdots=u_{n_1}(Q_1)u_{n_2}(Q_2)\cdots u_{n_\lambda}(Q_\lambda)\cdots, \tag{6}$$

[1] N. Rosen, Phys. Rev. **71**, 833 (1947), and **76**, 202 (1949); W. Sollfrey and G. Goertzel, Phys. Rev. **83**, 1038 (1951).

[2] See, e.g., W. Heitler, *The Quantum Theory of Radiation* (Oxford University Press, London, 1944), second edition.

where $u_n(Q)$ is a harmonic oscillator wave function with quantum number $n(=0, 1, 2, \cdots)$ describing the state of the unperturbed mode of oscillation,

$$\tfrac{1}{2}(P^2+\omega^2Q^2-\hbar\omega)u_n=n\hbar\omega u_n; \tag{7}$$

$\mathbf{p}'$ is a constant vector, the total momentum of the system; and $a_{n_1n_2}\cdots n_\lambda\cdots$ is a constant spinor expansion coefficient. The summation $\sum_{(n)}$ is carried out over all the states of all the degrees of freedom. Substituting the expression (5) into Eq. (4) and making use of the relations

$$\begin{aligned}[Q+(i/\omega)P]u_n&=(2n\hbar/\omega)^{\frac{1}{2}}u_{n-1},\\ [Q-(i/\omega)P]u_n&=(2(n+1)\hbar/\omega)^{\frac{1}{2}}u_{n+1},\end{aligned} \tag{8}$$

one finds that with some rearrangement of terms one gets an equation which leads to the following relation among the expansion coefficients:

$$\begin{aligned}[c\mathbf{p}'\cdot\boldsymbol{\alpha}+mc^2\beta+\hbar\textstyle\sum_\lambda n_\lambda(\omega_\lambda-c\mathbf{k}_\lambda\cdot\boldsymbol{\alpha})-E]a_{n_1n_2}\cdots n_\lambda\cdots\\ -K\textstyle\sum_\lambda\boldsymbol{\varepsilon}_\lambda\cdot\boldsymbol{\alpha}[(2(n_\lambda+1)\hbar/\omega_\lambda)^{\frac{1}{2}}a_{n_1n_2}\cdots(n_\lambda+1)\cdots\\ +(2n_\lambda\hbar/\omega_\lambda)^{\frac{1}{2}}a_{n_1n_2}\cdots(n_\lambda-1)\cdots]=0,\end{aligned} \tag{9}$$

where

$$K=ce\pi^{\frac{1}{2}}L^{-\frac{1}{2}}. \tag{10}$$

Now define a function φ, by

$$\varphi=\textstyle\sum_{(n)}a_{n_1n_2}\cdots n_\lambda\cdots U_{n_1n_2}\cdots n_\lambda\cdots, \tag{11}$$

and an operator

$$\begin{aligned}H'=c\mathbf{p}'\cdot\boldsymbol{\alpha}+mc^2\beta+\tfrac{1}{2}\textstyle\sum_\lambda(P_\lambda^2+\omega_\lambda^2Q_\lambda^2-\hbar\omega_\lambda)\\ \times[1-(c/\omega_\lambda)\mathbf{k}_\lambda\cdot\boldsymbol{\alpha}]-2K\textstyle\sum_\lambda Q_\lambda\boldsymbol{\varepsilon}_\lambda\cdot\boldsymbol{\alpha},\end{aligned} \tag{12}$$

and consider the equation

$$H'\varphi=E\varphi. \tag{13}$$

A simple calculation shows that this also leads to Eq. (9) as the relation among the expansion coefficients. Thus we see that the energy levels associated with the Hamiltonian H' are the same as those of H. (One can also discuss the transformation from H to H' as a unitary transformation from a representation in which the electron coordinates are diagonal to one in which the total momentum is diagonal.) The obvious advantage of Eq. (12) is that the electron coordinates have been eliminated.

Since the solution of Eq. (13) for the general case still presents difficulties, let us now go over the one-dimensional problem. Let the vector $\mathbf{p}'$ have only a Z component which will be denoted simply by p, and let the vectors $\mathbf{k}_\lambda$ also be along the Z axis, the polarization vectors $\boldsymbol{\varepsilon}_\lambda$ being in the X and Y directions. Equation (13) can then be written

$$[cp\alpha_z+mc^2\beta+H_0(1-\alpha_z)-2K(Q_x\alpha_x+Q_y\alpha_y)]\varphi=E\varphi, \tag{14}$$

where Q_x and Q_y are the two parts of $\sum Q_\lambda$ for $\boldsymbol{\varepsilon}_\lambda$ in the X and Y directions, respectively.

Multiplying both sides of the equation by $(1+\alpha_z)$ or $(1-\alpha_z)$ and using the properties of the Dirac matrices, one obtains relations which can be written

$$\begin{aligned}(E-cp)(1+\alpha_z)\varphi&=[mc^2\beta-2K(Q_x\alpha_x+Q_y\alpha_y)](1-\alpha_z)\varphi,\\ (E+cp-2H_0)(1-\alpha_z)\varphi&=[mc^2\beta-2K(Q_x\alpha_x+Q_y\alpha_y)](1+\alpha_z)\varphi.\end{aligned} \tag{15}$$

Eliminating $(1+\alpha_z)\varphi$ between these equations and writing $\chi=(1-\alpha_z)\varphi$, one obtains

$$(E-cp)(E+cp-2H_0)\chi=[m^2c^4+4K^2(Q_x^2+Q_y^2)]\chi. \tag{16}$$

If we write

$$E'=\tfrac{1}{2}[E+cp-m^2c^4/(E-cp)],\quad \sigma=4K^2/(E-cp), \tag{17}$$

this equation takes the form

$$[H_0+\tfrac{1}{2}\sigma(Q_x^2+Q_y^2)]\chi=E'\chi, \tag{18}$$

which looks like the Schrödinger equation for a system consisting of two sets of coupled oscillators (the coupling being given by the products $Q_\lambda Q_{\lambda'}$, present in Q_x^2 and Q_y^2).

Let us investigate the classical frequencies of the normal modes of oscillation of such a system. It will be enough for us to consider only the part of the system corresponding to polarization in the X direction, since the other part will have the same frequency distribution. For this case, if we let W be the energy, then classically

$$W=\tfrac{1}{2}\textstyle\sum_n(P_n^2+\omega_n^2Q_n^2)+\tfrac{1}{2}\sigma\sum_{m,n}Q_mQ_n, \tag{19}$$

with

$$\omega_n=\gamma|n|,\quad \gamma=2\pi c/L,\quad n=\pm1, \pm2, \cdots,$$

and the frequencies of the system are the roots ω of the secular equation[3]

$$\begin{vmatrix}\sigma+\gamma^2-\omega^2 & \sigma & \sigma & \cdots\\ \sigma & \sigma+\gamma^2-\omega^2 & \sigma & \cdots\\ \sigma & \sigma & \sigma+4\gamma^2-\omega^2 & \cdots\\ \cdots & \cdots & \cdots & \cdots\end{vmatrix}=0, \tag{20}$$

where the diagonal elements occur in equal pairs. Denoting the determinant by $F(\omega^2)$, one finds that it can be written

$$\begin{aligned}F(\omega^2)=[\prod_{n=1}^{\infty}\gamma^2n^2]^2(\gamma^2/\pi^2\omega^2)\sin^2(\pi\omega/\gamma)\\ \times\{1+\sigma/\omega^2-(\pi\sigma/\gamma\omega)\cot(\pi\omega/\gamma)\},\end{aligned} \tag{21}$$

so that the roots of (20) are given by the roots of the equations

$$\sin(\pi\omega/\gamma)=0\quad(\omega\neq0), \tag{22a}$$

$$(\omega^2+\sigma)\sin(\pi\omega/\gamma)=(\pi\sigma/\gamma)\cos(\pi\omega/\gamma). \tag{22b}$$

[3] E. T. Whittaker, *Analytical Dynamics* (Cambridge University Press, London, 1937, or Dover Publications, New York, 1944), fourth edition, p. 179.

It follows (because there are two waves traveling in opposite direction for each frequency) that half of the frequencies, those given by (22a), remain unchanged by the interaction. If we denote the roots of (22b) by ω_n' ($n=1, 2, 3, \cdots$), numbered in increasing order, then the quantal energy of the system in its lowest state is given by

$$E'=\hbar\sum_{n=1}^{\infty}(\omega_n'-\omega_n), \tag{23}$$

which has been doubled to take account of the two kinds of polarization.

The question now is whether the series in (23) converges. From (22b) one sees that for large values of ω,

$$\omega_n'-\omega_n\sim\sigma/n\gamma,$$

so that the series in (23) diverges logarithmically. Let us write

$$E'=(h\sigma/\gamma)w, \tag{24}$$

where $w\sim\Sigma(1/n)$. From (17) one then obtains the relation

$$E^2-c^2p^2-m^2c^4=(4h/\gamma)K^2w. \tag{25}$$

Although in the three-dimensional case K was taken as in Eq. (10), in the one-dimensional problem it is better to take

$$K=ce\pi^{\frac{1}{2}}L^{-\frac{1}{2}}S^{-\frac{1}{2}}, \tag{10a}$$

where we think of the electron and field as moving in a (long) cylinder of length L and cross-sectional area S. The right-hand member of (25) becomes $(2e^2hc/S)w$ and one gets, for the positive energy state,

$$E\sim e(2hc/S)^{\frac{1}{2}}w^{\frac{1}{2}}, \tag{26}$$

so that the energy diverges like the square root of a logarithm.

Thus we see that the interaction of the electron with the transverse field gives a divergence in the energy in the one-dimensional case. It is of some interest to note that, if one were using a perturbation calculation based on the assumption that the interaction between electron and field is weak, one would regard the right-hand member of (25) as small; and one would then get, taking $p=0$ for simplicity,

$$E\sim mc^2+(2hK^2/\gamma mc^2)w=mc^2+(e^2h/mcS)w, \tag{27}$$

which in view of the actual logarithmic divergence of w leads to a worse type of infinity than that of Eq. (26).

Although the three-dimensional case is much more complicated and involves features not present in the simple case discussed here, the result obtained in the latter suggests rather strongly that the transverse self-energy of the point electron in the three-dimensional case is inherently divergent.

In conclusion, I should like to express my indebtedness to Professor Wayne A. Bowers for helpful discussions.

PHYSICAL REVIEW VOLUME 87, NUMBER 6 SEPTEMBER 15, 1952

Capture of μ-Mesons in Heavy Elements*

J. W. KEUFFEL, F. B. HARRISON,† T. N. K. GODFREY, AND GEORGE T. REYNOLDS
Palmer Physical Laboratory, Princeton University, Princeton, New Jersey

(Received May 5, 1952)

Measurements have been made of the mean lifetimes of μ-mesons in several heavy elements. Time lags between the arrival of a cosmic-ray meson in the target and its subsequent absorption—as signaled by the neutrons and gamma-rays following capture—are measured using large liquid scintillation counters and a chronotron timing circuit. The timing uncertainty is about 2×10^{-9} sec, and the counting rates are such that a mean life can be determined to an accuracy of 10 percent in about a week's run at sea level. A short-lived component of the decay curves was found and identified as due to neutrons from proton-induced stars. Errors from this effect were avoided. Our latest results for the mean lives, in mμsec, are

Fe 163±27, Hg 58±4, Cu 116±9, Pb 76±4, Sb 99±11, Bi 68±5.

The results are in agreement with the Wheeler Z_{eff}^4 law up through Cu but disagree by a factor 3 for the heavier elements. They are in reasonable agreement with Kennedy's calculations (see following paper). The difference between the mean lives for Hg and Pb is also qualitatively predicted by Kennedy on the basis of a shell model of the nucleus. Our results, together with Kennedy's calculation for Pb, allow us to conclude that the μ-meson-nucleon coupling constant has the same value, within about 25 percent, as recent values of the coupling constants of beta-decay and of the spontaneous disintegration of the μ-meson.

I. INTRODUCTION

IT is now well established that the capture of negative μ-mesons by atomic nuclei is characterized by (1) a weak meson-nucleon coupling and (2) the transfer of most of the meson rest energy following nuclear capture to a light neutral particle.

That the μ-meson interacts weakly with neutrons and protons was convincingly demonstrated by the classic experiment of Conversi, Pancini, and Piccioni.[1]

* Assisted by the joint program of the AEC and ONR.

† Now at Los Alamos Scientific Laboratory, Los Alamos, New Mexico.

[1] Conversi, Pancini, and Piccioni, Phys. Rev. **71**, 209 (1947).

It was shown that negative μ-mesons stopping in condensed matter are not always captured, but that in light elements they decay. Calculations of Fermi and Teller[2] indicated that the time required for a slow meson to come to rest in condensed matter and to fall to the mesonic K-orbit of an atom was less than 10^{-10} sec, a time negligibly short compared with the 2.22-μsec mean life of the meson,[3] and hence entirely too short to explain the fact that negative mesons were not captured in light elements. Thus, the capture probability in light elements was only of the order of the spontaneous decay probability, and this weak interaction ruled out the μ-meson as a possible Yukawa particle.

If a meson in a K-orbit has a chance τ_0^{-1} per second of decaying and a chance Λ of being captured, it will have mean life τ given by $\tau^{-1}=\Lambda+\tau_0^{-1}$. The capture probability Λ may thus be found from a measurement of the mean life in a given element together with the known free decay mean life, τ_0. The mean life is independent of whether one observes decay electrons or any radiation accompanying capture. In a given element, a fraction τ/τ_0 of the mesons will decay. By comparing the yields of decay electrons for mesons stopped in various light elements. Sigurgeirsson and Yamakawa[4] estimated that capture and decay are equally probable in elements of $Z\sim 10$. The capture probabilities for O, NaF, Mg, Al, and S were measured by Ticho,[5] who selected negative mesons by means of a magnetic lens and observed their mean life in absorbers of the various elements. Similar results for Al were reported by Valley.[6] These experiments showed that the capture probability varies approximately as Z^4 and, again, that capture and decay compete on equal terms for $Z\sim 10$.

Besides adding to our knowledge of the strength of the meson-nucleon interaction, μ-meson capture studies may throw light on the question of just what happens to the rest mass of the meson when it disappears. Photographic emulsion work[7,8] and cloud-chamber studies[9,10] have demonstrated the absence of the stars of about 100 Mev which would certainly result if the entire rest energy appeared as nuclear excitation. The basic reaction involved in meson capture is therefore taken to be of the type

$$\mu^-+P\rightarrow N+\nu,$$

where the ν represents a neutrino or a neutral meson. On this picture, most of the rest energy of the μ^--meson is carried away by the light neutral entity. The latter is certainly not a photon, as demonstrated by Piccioni[11] and Chang.[10]

Although a large star will not be produced according to this capture mechanism, the nucleus is expected to receive an excitation of around 15 Mev, according to the calculations of Tiomno and Wheeler.[12] This will generally not suffice to eject a proton, particularly in the heavy nuclei where the Coulomb barrier is important, but one expects on the average one or two neutrons to be boiled off, and the remainder of the energy to appear as gamma-rays of a few Mev or less. We shall call these neutrons and gamma-rays together the meson *capture radiation*.

The above picture is borne out by the experiments of Sard *et al.*,[13] Groetzinger and McClure,[14] and Crouch and Sard,[15] who find that around two neutrons are emitted, on the average, when a μ-meson stops in Pb. These workers used a technique of moderating the neutrons in paraffin and detecting the slow neutrons. The existence of gamma-rays of low energy associated with the stopping of μ-mesons has been demonstrated by Chang,[10] Shanley,[16] and Harris[17] using a cloud chamber. Harris concluded that neither Bohr orbit transitions of the stopping meson nor nuclear transitions following capture were alone sufficient to explain the data.

In an experiment with photographic emulsions exposed below ground, George and Evans[8] found that 8.7 ± 1.7 percent of the μ-mesons captured in the emulsion produced low energy protons, that the average number of prongs per capture was 0.10 ± 0.02, and that the mean number of prongs and the prong distribution suggest that a nuclear excitation of about 15 Mev is produced.

In the experiment to be described, we use the gamma-rays and neutrons following the meson capture event to signal the disappearance of a meson whose time of arrival in the target was previously recorded. In this way we measure the mean life of negative mesons in various elements.

Wheeler[18] has given a theory which predicts that the capture probability is proportional to Z_{eff}^4, where Z_{eff} is an effective atomic number introduced to take account of the finite nuclear radius. This correction to Z is less than 10 percent up to $Z=10$, but becomes important for the heavier elements; in Pb, for example, $Z_{eff}=31.5$. We shall not discuss the theory, as it is reviewed in the following paper by J. M. Kennedy.

One could in principle calculate the constant of proportionality in the Z_{eff}^4 law in terms of the coupling constant g_A involved in the meson-nucleon interaction,

[2] E. Fermi and E. Teller, Phys. Rev. **72**, 399 (1947).
[3] W. E. Bell and E. P. Hincks, Phys. Rev. **84**, 1243 (1951).
[4] T. Sigurgeirsson and A. Yamakawa, Phys. Rev. **71**, 319 (1947).
[5] H. K. Ticho, Phys. Rev. **74**, 1337 (1948).
[6] G. E. Valley, quoted by B. Rossi, *Colston Papers* (Butterworths Scientific Publications, London, 1949), p. 55.
[7] Lattes, Muirhead, Occhialini, and Powell, Nature **159**, 694 (1947).
[8] E. P. George and J. Evans, Proc. Phys. Soc. (London) **64**, 193 (1951).
[9] T. H. Johnson and R. P. Shutt, Phys. Rev. **61**, 380 (1942).
[10] W. Y. Chang, Revs. Modern Phys. **21**, 166 (1949).
[11] O. Piccioni, Phys. Rev. **74**, 1754 (1948).
[12] J. Tiomno and J. A. Wheeler, Revs. Modern Phys. **21**, 153 (1949).
[13] Sard, Ittner, Conforto, and Crouch, Phys. Rev. **74**, 97 (1948).
[14] G. Groetzinger and G. A. McClure, Phys. Rev. **74**, 341 (1948).
[15] M. F. Crouch and R. D. Sard, Phys. Rev. **85**, 120 (1952).
[16] T. J. B. Shanley, Ph.D. thesis, Princeton (1951).
[17] G. G. Harris, Ph.D. thesis, Princeton (1951).
[18] J. A. Wheeler, Revs. Modern Phys. **21**, 133 (1949).

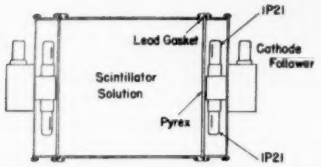

FIG. 1. Plan view of the liquid scintillation counter (S_1) used for the detection of the incident meson. The active volume of solution is 12 in.×11½ in.×1 in. deep.

and so obtain a value of g_A from the experimental values for the capture probabilities. An order of magnitude calculation of this sort was made by Tiomno and Wheeler,[18] who found that g_A was of the same order as the Fermi constant of β-decay and the constant g_μ of μ-meson decay.

Calculations on the absorption of μ-mesons using a shell model of the nucleus have recently been carried out by Kennedy and are reported in the following paper. From his results, one expects for the heavier elements a less rapid rise in the capture rates with Z than that predicted by the Z_{eff}^4 law. Also, abrupt changes are to be expected in the vicinity of Pb and possibly near the other closed-shell nuclei. Finally, a more accurate calculation of g_A in terms of the absorption rate for Pb is obtained.

A comparison of the theoretical predictions and our experimental values for the capture probabilities is made in a later section of this paper.

II. APPARATUS

A. The Scintillation Counters

The study of the μ-meson capture process has heretofore been limited to elements no heavier than sulfur by two experimental considerations. First, the mean lifetimes become of the same order of magnitude as the random lags of the Geiger counters which have until now been used. Second, the inefficiency of the Geiger counters for low energy gamma-rays and neutrons has made it necessary to measure the lifetimes by means of the decay electrons of those mesons which escape capture; since in the heavy elements the fraction of mesons escaping capture is small, the rates become prohibitively low.

The discovery of the liquid scintillation counter[19,20] and the subsequent development of a large-area version of this type of counter[21] made available an ideal detector for the meson capture experiments. The combination of large area, good efficiencies for the detection of both gamma-rays and neutrons in the Mev range, and fast pulses resulted in a successful technique for the measurement of mean life using sea-level mesons.

Two types of liquid scintillation counters were used. For the principles involved in their design, the reader is referred to the paper by Harrison.[21] A plan view of the first type—used for the detection of ionizing particles (the incident mesons) over a wide area—is shown in Fig. 1. The section containing the liquid was one inch deep, and 12 inches by 11½ inches in area. The scintillating material was a solution of terphenyl in toluene, 3.5 grams per liter. The windows were of one-eighth inch Pyrex, and a rough measurement showed that they absorb only a few percent of the light from the scintillations. The lead gaskets used to seal the windows have been very satisfactory; there have been no signs of leakage, and no windows were broken in assembly after the bearing surfaces were made properly flat. The tank was lined with a thin sheet of aluminum to reflect the light. The walls were made thin so as to reduce the amount of extraneous material to a minimum. There was a total of 1.75 g/cm² of copper and 0.25 g/cm² of aluminum above and below the liquid.

Four type 1P21 photomultipliers were used. They were selected for low noise background. The voltages on the dynodes of these tubes were adjusted so as to match the tubes for response to a given amount of light. The anodes of each pair of tubes were connected together and fed into a cathode follower, and the cathode followers were fed in parallel into the input of a fast amplifier. The efficiency of this type of counter for the detection of minimum ionizing particles averaged over the surface of the counter was about 65 percent when the counter was operated at a discriminator level such that the noise rate was 300 sec^{-1}.

The second type of scintillation counter (see Fig. 2) was designed for the detection of the meson capture radiation. Somewhat better light collection than in the first type of counter was achieved without very much reduction in sensitive volume by using type 5819 end-window photomultipliers mounted one at each end of a rectangular tube 3 inches square and one foot long. The efficiency of this counter for mesons was very nearly 100 percent, but the situation with regard to gamma-rays and neutrons is much more complicated. Both the chance that a photon or neutron will make a recoil particle, and the chance that the flash produced by the ionizing recoil will be detected, depend sensitively on the energy distribution of the capture radiation, and this is not known. As an order of magnitude, one may take perhaps 10 percent as the over-all efficiency for each type of radiation. A knowledge of the efficiency is fortunately not necessary in the present form of the experiment.

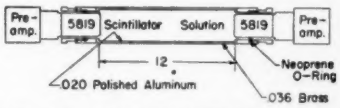

FIG. 2. Plan view of the liquid scintillation counter S_2 used for the detection of the capture radiation. The active volume of solution is 3 in.×3 in.×12 in.

[18] Reynolds, Harrison, and Salvini, Phys. Rev. **78**, 488 (1950).
[20] H. Kallmann, Phys. Rev. **78**, 621 (1950).
[21] F. B. Harrison, Nucleonics (to be published).

The four type 5819 photomultipliers used so far lasted for only $2\frac{1}{2}$ to $3\frac{1}{2}$ months of continuous operation. The over-all voltage applied to the tubes was about 800 volts and was held in each case to ± 2 volts. The sensitivity of each tube decreased gradually during the last month of its life and then faded out rapidly in a few days. The cathodes were at a negative high potential, and they were separated only by the glass envelope of the tube from the liquid scintillator which was at ground potential. The instability and short life of the 5819's may be peculiar to operation under the conditions described and not typical of normal 5819 behavior. The possibility that the close proximity of the grounded liquid to the cathode was the cause of the failure of the tubes is being investigated.

B. Counter Arrangement

The disposition of the counters and target is shown in Fig. 3. Whenever there was a "coarse" coincidence between the top tray "A" of Geiger counters, the scintillator S_1, and the scintillator S_2, but no count from the anticoincidence bank of Geiger counters "X," the timing circuit discussed below made a photographic record of the time interval between the pulses from S_1 and S_2. The system was designed to select negative cosmic-ray mesons which stop in the target, and there produce a non-ionizing radiation which crosses the top tray of the anticoincidence bank "X" and is detected in S_2. The mean life of negative mesons in the element used as target was then obtained from the distribution of the time delays of S_2 relative to S_1. The resolving time for the selection of events was longer than these delays, of course.

The present method of selecting stopped negative mesons, based on the requirement of a non-ionizing link, has the advantage over a selection system using a magnetic lens in that it accepts a very much larger cone of mesons incident upon the target. The question of how well the system discriminates against other types of events is discussed in Sec. IV.

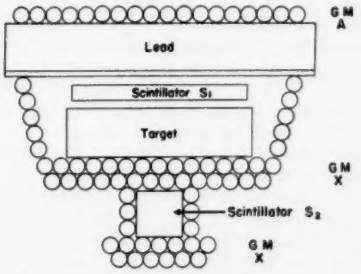

FIG. 3. Experimental disposition. All the G-M counters are 1 in. in diameter. The dimensions normal to the plane of the figure of the G-M counter bank "A," the Pb electron filter, the two scintillation counters, and the target are all 12 in. The 58 counters of the anticoincidence bank "X" have a 23-in. sensitive length.

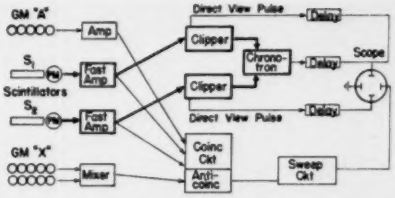

FIG. 4. Block diagram of the electronic apparatus. The coincidence circuit selects events where pulses from A, S_1, and S_2 coincide to within a few μsec, but there is no pulse from X. The precise time interval between S_1 and S_2 is measured by the chronotron. Pulses from the photomultipliers are amplified using Hewlett-Packard 460-A and 460-B distributed amplifiers, then shaped in the clippers and sent to the chronotron line. "Fast" portions of the circuit are shown in heavy black lines. The rise-time at the clipper input is about 5 mμsec. The scintillator pulses are also delayed and directly presented on the scope trace ("direct view" lines).

The targets have been approximately 10-cm thick and 30 cm$\times$30 cm in area. Since a gamma-ray has an absorption free path of only about 2 cm in a heavy element, even at the minimum of the absorption curve, such thick targets would not be worthwhile were it not for the neutrons of the capture radiation. These neutrons undergo principally elastic scattering which does not appreciably diminish the source strength. It will be shown later that most of our counts come from neutrons. The thick target is therefore definitely advantageous from the rate standpoint. For elements which are not available in large quantities, however, it is anticipated that dispositions involving smaller targets and larger, more efficient scintillators placed closer to the target will be employed.

C. Event Selector Circuits

The electronic equipment falls into two main divisions: the selector circuits and the timing circuit. Figure 4 shows a block diagram of the complete set-up. We shall first discuss the system that selects the stopped-meson events and actuates the camera.

Pulses from the counters go to a coincidence circuit of conventional design, whose output triggers the oscilloscope sweep circuit. A camera with the shutter continuously open views the scope screen; the oscilloscope beam is normally off, but is turned on by the sweep circuit, and a photograph is made of the trace associated with the desired coincidence. A univibrator-controlled motor then advances the 35-mm Linagraph Ortho film about 2.5 mm in readiness for the next event.

It is essential that the coincidence circuit response be independent of the delay of S_2 relative to S_1, over the range of time intervals dealt with. As will be seen later, this range was from -1.0 to $+1.5$ μsec. The pulse widths of the univibrators in each coincidence channel were carefully adjusted to give a range of at least -2.0 to $+3.5$ μsec, and the resolving time limits were experimentally checked using known delay lines.

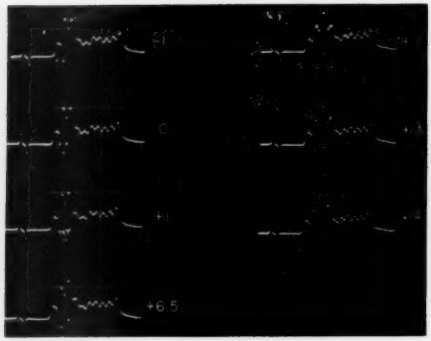

FIG. 5. Photographs of oscilloscope traces obtained using a pair of test pulses from a mercury-switch pulser. The sweep starts after 1.8 μsec. Then, left to right, we have the direct pulse from S_1, delayed 2.6 μsec; the direct S_2, delayed 3.0 μsec; and the chronotron superposition locus, with first detector pulse delayed 4.7 μsec. On the trace labeled "0" the test pulses met on the chronotron line midway between the second and third detectors, since the second and third detector pulses are up, and are just equal. The numbers opposite the other traces indicate the number of feet of Rg-7-U cable inserted between the pulse and the S_2 input of the chronotron; 1 ft = 1.225 mμsec. The zero setting of the chronotron can be shifted at will, of course, by inserting cable in one side.

The univibrator pulse width in the anticoincidence channel was made amply wide to overlap any possible coincidence combination. To allow for time lags in the firing of the anticoincidence counters, the pulse from S_1 was delayed 1.0 μsec before going into the coincidence circuit. Then if A, S_1, and S_2 were tripped simultaneously, a coincidence was not formed until the X bank had had a microsecond to signal an anticoincidence. The output of the X-bank mixer was also fed directly to the blanker input of the sweep circuit; in this way, part at least of the trace was blanked if any of the anticoincidence counters fired at any time during the trace. We rejected such traces, thus making our anticoincidence system independent of the time of firing of the X counters up to 10 μsec or more. The blanker also provided a constant check on the operation of the anticoincidence system generally.

The pulses from the two scintillation counter amplifiers were broadened before going into the coincidence circuit, in order to stabilize the triggering thresholds of the univibrators in each coincidence channel; these univibrators set the level at which scintillator pulses were accepted.

D. Timing Circuits

For each event that triggers the selector circuit, we wish to know the time interval between the pulse from S_1 (the arriving meson) and the pulse from S_2 (the radiation signaling the meson capture). The measurement is carried out with a chronotron-type timing circuit similar to the one described by Keuffel.[22] The pulses from each scintillation counter are amplified (see Fig. 4) and sent to a "clipper," whose function is to limit them in size and duration. A uniform pulse about 10 volts high and 25 mμsec wide at half-maximum emerges from each clipper; these pulses are applied, one to each end of a length of 100-ohm coaxial cable. The basic "chronotron" principle is to determine the time interval between the two pulses by observing the point at which they meet. Thus, for example, if the pulses are applied simultaneously to the ends of the line, they will evidently meet in the middle, while if one pulse is delayed with respect to the other, the meeting point will be shifted towards the side of the later pulse. The time interval between the two pulses is given by $2x/c$, where x is the displacement of the meeting point from the center and c is the velocity of propagation of the pulses.

The meeting point of the pulses is ascertained by means of 10 crystal diode detectors spaced along the cable at 16-mμsec intervals.[23] The output of each detector unit is a rounded pulse about 0.5 μsec wide, whose amplitude is proportional to the peak voltage at that point along the line. A plot of the detector outputs against the detector positions is called a *superposition locus*, and the maximum of this locus tells us the meeting point of the pulses. In order to record the superposition locus, each detector output pulse is passed through a delay line, amplified, and presented on the oscilloscope trace. By delaying the first detector pulse 4.7 μsec, the second 5.2 μsec, the third 5.7 μsec, and so on, the pulses are made to appear in order on the later part of the trace, leaving the first portion of the trace available for other purposes. Since the detector output pulses are rather slow, they may be delayed without much dispersion. The attenuation in each delay line is compensated by a potentiometer adjustment. The delay-line outputs are mixed before amplification, so that the relative gains depend primarily on the stability of the 1N34 crystals in the detectors and in the mixer.

Some photographs of oscilloscope traces are shown in Fig. 5. From the superposition locus it is possible to tell at a glance between which two detectors the pulses met and to which of these two detectors the meeting was closest. This gives us 18 chronotron channels; the ones at each end are not used, leaving 16 channels or a range of 256 mμsec for delay measurements.

The chronotron measures delays in the range 0 to 256 mμsec with a precision of about 2 mμsec. In addition, a coarse timing range which measures delays between −1.0 μsec and +1.5 μsec with a precision of perhaps 15 mμsec is provided by presenting the pulses from the two scintillators, suitably delayed, on the

[22] J. W. Keuffel, Rev. Sci. Instr. **20**, 197 (1949).

[23] The 16-mμsec detector spacing proved adequate for the mean lives measured so far, although a 6-mμsec interval between detectors was used for investigating the neutrons from proton-induced stars.

oscilloscope screen in the conventional manner. These "direct view" pulses may be seen at the beginning of the traces in Fig. 5.

At first sight it might seem that the chronotron is unnecessarily complicated compared to the direct presentation of the fast pulses on a scope sweep, but it has several important advantages. The provision of a fine and a coarse timing range on a single oscilloscope sweep is one such advantage. Another is that the chronotron permits the recording of the time delay to be postponed several μsec while the coincidence circuit —which involves slow Geiger counters—is making up its mind to accept or reject the event; fast pulses cannot be delayed without dispersion in presently available cables, but the slow chronotron detector pulses can be delayed. Also, the chronotron trace is easy to photograph, since the sweep speed is moderate (1.33 μsec/cm). Finally, the data can be read easily from the film. The delays are to be grouped in any case, and one can tell rapidly to which of the 16 channels a lag is to be assigned. The ease of reading is particularly important since a large percentage of the events selected and photographed show no appreciable lag (shower events, etc.), and these can be run through rapidly and reliably.

The chronotron may be regarded as a multichannel time discriminator, and as in every multichannel discriminator, the stability of the channel boundaries is a problem. We calibrated the instrument by feeding both fast amplifiers from a mercury-switch pulser whose output was shaped to simulate a scintillation pulse. Cable was inserted between the pulser and the S_2 amplifier input to shift the superposition locus. The time delay of the cable required to shift the locus to each channel boundary was measured using a crystal-calibrated oscillator. The channel boundaries (with 16 mμsec channels) were found to deviate randomly from their correct positions by about 2 mμsec. These deviations were due to several small effects, many of which we hope to eliminate in the future. In any case the boundary errors throw counts from one channel to an adjacent one but no counts are missed.

E. Over-all Timing Precision

In addition to the chronotron errors discussed above, errors are caused by fluctuations in the time lag between the passage of the particle through the counter and the arrival of a pulse at the chronotron. The random counter lags were studied as follows: Fast mesons passing through both scintillation counters were selected by requiring a coincidence AS_1S_2X, and the time lags between S_1 and S_2 were measured for each event. The distribution of these lags was roughly Gaussian in shape, with a standard deviation of 1.5 mμsec. Although it was not possible to check the shape of the curve accurately with the large chronotron channel width used (6 mμsec), the number of lags that fell outside of ± 6 mμsec was 0.1 percent or less.

During the timing uncertainty measurement, a 20-db attenuator was placed in the S_2 amplifier input to reduce the large meson pulses to a size comparable to the distribution of pulses produced by meson capture events. We also measured the relative lags between the pulses from the photomultipliers at each end of S_2 when gamma-rays were being counted; even with this stringent method the standard deviation was only about 2.5 mμsec.

It will be seen that time lag uncertainties as small as these introduce a negligible error in our results.

III. EXPERIMENTAL PROCEDURE

A. Scintillation Counter Settings

The initial adjustment in setting up the apparatus for a run was to set the level at which scintillation counter pulses were accepted. Using the mercury-switch pulser, we first determined the pulse required at the amplifier input to cut off the limiter tube in the clipper. The coincidence circuit sensitivity for that channel was then adjusted so that it would accept only pulses larger than this value. In this way we made sure that for any event accepted by the selector circuits, the scintillation pulse was big enough to actuate the chronotron properly. Next, the photomultiplier voltages were adjusted until the total noise rate accepted from each scintillation counter was about 300 sec^{-1}. The coincidence rates (S_1X) and (S_2X) were then measured, the latter with a standard 20-db attenuator in the S_2 amplifier input. These rates were taken as a measure of the over-all efficiency of each scintillator, since they represent the efficiency of the scintillators for counting a certain flux of ionizing cosmic rays. The purpose of the attenuator was to make the efficiency of S_2 more sensitive to the level of pulse heights accepted by the apparatus. Once the (S_1X) and (S_2X) rates had been measured, they were held constant to about 10 percent during a run, and as nearly as possible from one run to the next, by adjusting the photomultiplier voltages. As far as the mean life measurements are concerned, of course, rate stability is not necessary, but it is desirable as an over-all check on the apparatus. Rates were checked daily, and the only serious drift was in the sensitivity of the 5819 photomultipliers, as mentioned earlier.

B. Chronotron Adjustments

The potentiometers in each chronotron detector circuit were first adjusted so that, with a standard test pulse applied to each detector in turn, the corresponding pulses on the superposition locus were identical. Crystal characteristics vary from one crystal to another, but are quite stable with respect to time; it was necessary to equalize the detectors at a level corresponding to two clipper pulses meeting at or near the detector, but once so adjusted, their stability was excellent and a monthly readjustment more than adequate.

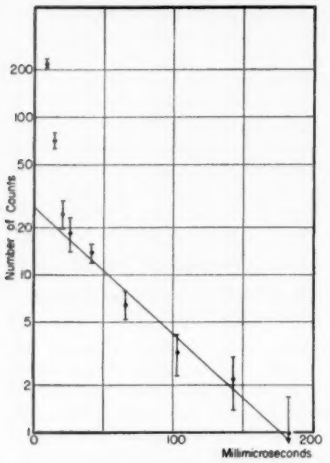

FIG. 6. Typical differential distribution of delayed counts in S_2, obtained with high time resolution (6 mμsec chronotron channel width). Each point represents the total number of counts in 72 hours of counting per 6 mμsec of delay. The short-lived component is due to proton-induced stars and the long component to μ-meson capture. Small backgrounds due to noise and positive meson decay have been subtracted. Disposition: Hg target, thickness 136 g/cm², no Pb filter above S_1.

The variations in photoelectron transit time from one photomultiplier to another are negligible for the 1P21 tubes. The 5819's, however, were individually matched (a matter of 2 or 3 ft of cable) and the chronotron "zeroed" as follows: Fast mesons passing through both scintillators were selected using the coincidence circuit, and the time delays between S_1 and S_2 were measured. The lengths of cable from the 5819's to the S_2 amplifier, and from the S_1 clipper to the chronotron, were then adjusted so that the center of the relative delay distribution lay at the boundary between the first two chronotron channels. During this adjustment a 20-db attenuator was inserted at the S_2 input, in order to make the pulse-height distribution from the mesons more nearly like the pulses from the capture radiation.

In order to minimize channel boundary errors, the zero of the chronotron was rotated regularly, during a run, over four different channel boundaries—two at one end of the chronotron and two at the other with the instrument switched end-for-end. After each switch, the zero was checked by observing straight-through mesons in the manner just described.

Accurate knowledge of the oscilloscope sweep speed is necessary for measuring lags longer than the range of the chronotron. We calibrated the sweep by photographing a 2-Mc/sec signal from a crystal-controlled oscillator.

Apart from the rate adjustments, chronotron zero rotation and trace calibrations, the apparatus ran automatically on a 24-hour basis. There were very few failures, and almost all failures showed up immediately on the oscilloscope pictures. The continuous check made possible by the oscilloscope photographs greatly increased our confidence in the data.

IV. ANALYSIS OF THE PICTURES

Approximately 10 percent of the pictures show lags that could be interpreted as μ-meson captures. This is to be expected since the selection of events by the coincidence circuit is purposely made very loose with respect to time delays between S_1 and S_2. The detailed classification of events according to time delays is carried out with the aid of the pictures. This procedure removes much of the "blindness" of cosmic-ray counting experiments. It enables us to identify effects due to components other than μ-mesons and to correct for them if need be. In this section the time delay analysis of the pictures is discussed in terms of the various cosmic-ray components, and the procedure outlined by which the mean lives are obtained.

A. Zero Lag Events: Soft Component

We call a picture showing a lag in either of the two chronotron channels adjacent to the zero of time a "zero lag." Some 70 percent of the pictures fall in this category, and they are due to a number of causes. The soft component may produce the right combination of electrons in A and S_1, plus a photon that crosses the anticoincidence counters and is detected in S_2. A fast meson may be recorded due to anticoincidence inefficiency. Or the gamma-radiation from the Bohr-orbit transitions of a stopped meson may be detected. A considerable number of zero lag pictures also come from the nuclear events discussed below. Since the random delay errors of the scintillation counters are very small, the zero lag events cause no trouble except to increase the number of pictures that must be scanned and rejected.

B. Very Short Lags and the Nuclear Component

At first sight one would not expect the nuclear component to produce delayed events. Decays from π-mesons locally produced by the nuclear component are ruled out by the requirement of a non-ionizing link and by the very short μ-meson range. In a preliminary series of experiments, however, the decay curves for Bi, Pb, Hg, and Fe were examined with the chronotron detector spacings set up to give 6 mμsec channels. The delay distributions exhibited in all four cases two components, one with a mean life at least 10 times shorter than the other. Figure 6 shows a typical curve. We have identified the short component with events where a proton of some hundreds of Mev triggers A and S_1, and makes a nuclear interaction either in the target or the Pb above it; an evaporation neutron of a few Mev then crosses the anticoincidence bank of counters and is

recorded, with a delay due to its time of flight, in S_2. If the nuclear interaction is in the Pb above S_1, there must, of course, be either an ionizing secondary or another neutron which triggers S_1; but in either case the event must not be so violent as to produce penetrating secondaries which would discharge the anticoincidence counters.

An estimate of the frequency of such nuclear events relative to the rate of μ-meson absorption events may be made from photographic emulsion data.[24] The rate of proton-induced stars of three or more prongs, multiplied by 2 (as a guess) to include events with 2, 1, or zero prongs, and divided by 12 to get from mountain altitudes to sea level, is about 4 kg^{-1} hr^{-1}. For the rate of stopped negative μ-mesons in our apparatus (effective solid angle ~ 1) we obtain from Rossi's differential range spectrum[25] the value 5 kg^{-1} hr^{-1}. The mean multiplicity of neutrons from proton-induced stars is not known, but for the roughly similar stars produced in Pb by negative π-mesons, Tongiorgi and Edwards[26] find a value ~ 7. The multiplicity from μ-capture found by Sard is ~ 2. Since the chance of detecting a given event in our apparatus is small, the observed rates should be proportional to the neutron multiplicities. We assume that a neutron from a star has about the same chance of being detected in S_2 as a μ-meson produced neutron, in spite of different energy distributions; this may not be too bad an assumption as most of the neutrons probably have an energy of a few Mev for both types of events, and the lower cross section of the high energy neutrons is compensated by the larger scintillations they produce. We should therefore expect to see roughly three times as many nuclear events as meson absorptions.

This ratio is to be compared with the ratio 4:1 between the total numbers of counts in each of the two components of Fig. 6. The data were taken with no Pb filter above S_1, so that the short component would come from stars produced in the target only. Both components were assumed to follow exponential decays in deducing the ratio of counts in each. Since it is impossible to distinguish the short component from the "zero lag" events in the first chronotron channel (0 to 6 mμsec), an extrapolation was necessary.

In view of the large uncertainties of the calculation, the close agreement of the short component rate with that predicted by the proton-induced star hypothesis must be considered fortuitous.

The exponential nature of the short delay component may be understood on the basis of a sort of diffusion of the neutrons. Their mean free path is about 5 cm, and before emerging they are likely to make a small number of elastic collisions with the heavy nuclei. The mean life of the exponential is 4 mμsec, which is about the time it takes a 3-Mev neutron to go 10 cm.

To test our hypothesis further as to the identity of the short component, we performed a series of auxiliary experiments. It was first established that the mean life of the long component varied with atomic number, while the short component exhibited no very strong Z dependence. Next, we varied the thickness of the Pb filter above S_1 from 0 to 8 in., and found that the intensity and mean life of the long component changed very little, as would be expected from the flat μ-meson range spectrum. On the other hand, as the thickness of Pb increased the over-all rate of lags in the 0–30 mμsec region decreased, but there was an increase in the number of lags in the 18–30 mμsec region. Since many protons will interact or stop in the filter, we should expect a decrease in the number of stars in the target, and hence fewer short lags, but an increase in lags corresponding to stars produced in the filter. Neutrons from the filter must diffuse a longer distance than neutrons from the target, and hence would appear in the later region.

In a further attempt to verify that protons were indeed responsible for the short component, a 34 g/cm^2 layer of carbon was placed above the apparatus. According to the results of Ballam,[27] the number of protons produced in a 44 g/cm^2 layer of carbon by neutrons is comparable to the number originally present in the cosmic-ray beam at sea level. A large auxiliary Geiger counter tray was placed above the carbon and connected to a neon bulb, which was photographed along with the trace. We found that for the short component, 25 percent of the incident rays were non-ionizing as they entered the carbon generating layer; whereas the primaries of the long component were all ionizing except for a small fraction attributable to the inefficiency of the Geiger tray.

As a result of the foregoing calculations and experiments, we conclude (1) that the long component is due to μ-mesons, (2) that most—and probably all—of the short component is due to proton-induced stars. We think it unlikely that some other process, as, for example, the neutrons accompanying extensive air showers, plays much of a role.

Whatever the origin of the short component, it can be eliminated from our experiment by starting to count μ-mesons only after a sufficiently long time, and by using as thin a Pb filter as possible. For the mean life measurements reported here, we started to count only after 32 mμsec, a comfortable margin. The short component caused a large error in our previously reported result for Sb,[28] although the earlier value for Cu was not much affected.

[24] Brown, Camerini, Fowler, Heitler, King, and Powell, Phil. Mag. **40**, 862 (1949).
[25] B. Rossi, Revs. Modern Phys. **20**, 537 (1948).
[26] V. Cocconi-Tongiorgi and D. A. Edwards, Bull. Am. Phys. Soc. **27**, No. 3, 44 (1952).
[27] J. Ballam (to be published).
[28] Harrison, Keuffel, and Reynolds, Phys. Rev. **83**, 680 (1951).

TABLE I. Typical counting rates.

Target		100 kg Pb
Running time		165 hours
Total pictures		5100
μ^- events (lags between 32 and 256 mμsec)		507
μ^+ background (spread out over 2 μsec)		500
Noise (lags between -1.0 and $+2.5$ μsec)		450
Zero lags (showers, nuclear component, etc.)		3650
Counts in first useful channel (32 to 48 mμsec):		
μ^-	115	
μ^+ background	3.8	
Noise background	1.2	
Ratio, μ^- to background	23	

C. Positive Mesons and Random Noise

The remaining 20 percent of the pictures show lags of the order of 1 or 2 μsec, and some of the lags are negative, that is, S_2 fired before S_1. The negative lags, and some of the positive lags, are due to a noise pulse from S_2, combining with either an accidental or a real coincidence between A and S_1; the real coincidences are the most numerous. The random noise background rate for positive lags is found from the rate of negative lag pictures.

When the noise background has been subtracted from the long positive lags, it is found that the remaining lags show a distribution that is consistent with the 2.22-μsec mean life of the positive μ-meson. These pictures are assumed to be due to positive mesons that stop in the target and decay; the decay positron has scant chance of emerging from the target, but is almost certain to radiate, and will in any case annihilate, producing a gamma-ray which may cross the anticoincidence bank and be detected in S_2. The positive meson background in the region of short delays is found by extrapolation, using the number of lags between 0.5 and 1.5 μsec and the 2.22-μsec mean life.

Despite the fact that the total number of background counts is comparable to the useful μ^- rate, the background is not serious as it is spread out over a delay range 10 to 20 times longer than typical negative meson mean lives for elements with $Z \geq 30$. The background is the factor limiting the application of the present form of the experiment to lighter elements.

D. Satellite Pulses from Photomultipliers

In the course of the experiment it was noticed that there was sometimes a second pulse from one of the scintillators, even when we selected events where only one particle, a fast meson, had passed through the tank. These pulses occurred in both tanks, and had time delays of the order of a microsecond. An investigation of the effect showed that the satellite pulses are a photomultiplier effect and do not come from the phosphor. The investigation has been previously reported.[29]

The presence of these delayed pulses made it necessary to count only the first pulse from either tank. So long as this is done—and it was always possible to do so—the satellite pulses introduce no error.

[29] Godfrey, Harrison, and Keuffel, Phys. Rev. **84**, 1248 (1951).

V. RESULTS

Counting rates for a typical 8-day run are presented in Table I. The μ^- rate agrees with the value to be expected from Rossi's meson range spectrum[25] if we take the efficiency of S_2 for neutrons as 30 percent. This value seems high, but there are uncertainties of perhaps a factor 2 in the calculation. Figure 7 shows a differential decay curve for one of two runs taken with Hg as the target. The noise and positive meson backgrounds, which amounted to approximately 1/20 the counting rate in the first chronotron channel, have been subtracted. This run represents about 450 counts, approximately half of our data for Hg. The mean lives are determined by the method of Peierls,[30] and the line shown on the graph was drawn using the slope and intercept obtained from the Peierls analysis of the data for that run.

Figure 8 shows a similar plot for Pb, in this case representing some 950 counts. A summary of individual runs and the weighted means for each of six elements is given in Table II.

The errors quoted are the statistical errors obtained by the Peierls method. In each case the relative standard error is given by $(\sigma/M)^{\frac{1}{2}}$, where σ is a constant that depends upon the counting-rate-to-background ratio, but is usually about 3, and M is the net number of counts observed. According to Peierls, it is worthwhile to count delays up to three or four mean lives; there is a broad optimum in the maximum value of delay to be taken, which depends on the background.

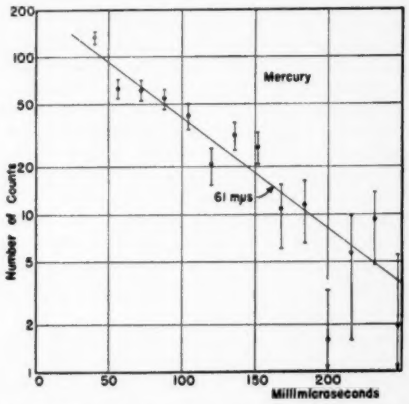

FIG. 7. Differential decay curve for one of two runs with Hg target. The total number of counts was 450. The slope and intercept of the line were drawn according to the Peierls analysis for this run. The flags shown are statistical. Chronotron channel boundary errors, which throw counts from one channel into an adjacent one but do not much affect the mean life, are also present.

[30] R. Peierls, Proc. Roy. Soc. (London) **A149**, 467 (1935).

The individual points of the differential decay curves show fluctuations about the lines larger than one should expect on the basis of the flags shown, which are the usual statistical ones. These additional fluctuations are attributed to chronotron channel boundary errors, which are expected to amount to 1 or 2 mμsec for each boundary, or perhaps 2 or 3 mμsec out of 16 mμsec for the width of a channel. We believe channel width errors of this magnitude suffice to account for the observed fluctuations. The channel boundary errors have a very much worse effect on the appearance of the differential decay curves than they do on the mean lives because counts thrown out of one channel are not lost, but appear in the adjacent channel, and the magnitudes of the boundary shifts are small compared to the mean lives measured. It is hard to estimate the effect quantitatively, but we believe the absolute error from this source can hardly exceed 5 percent in the worst case, that of Hg. The relative error from one element to the next should be negligible in comparison to the statistical errors.

The internal consistency of the data as shown by the agreement between the various runs in Table II is quite satisfactory, lending support to the correctness of the statistical analysis.

It has so far been assumed that the time lag between the capture of a meson and the chronotron pulse resulting therefrom is negligible. As pointed out by Rossi,[31] timing errors will not affect the shape of the decay curve provided (*a*) that the time lag error distribution is independent of the true delay, and (*b*) that one does not start counting until a time greater than the largest error expected. In the case of the random time-lag uncertainties of the scintillation counters, which are less than 2 mμsec, the conditions are certainly satisfied; we do not start counting until 32 mμsec. It is possible, however, that lags may occur between the capture of the meson and the scintillation in S_2 owing to two effects: time of flight of the neutrons and isomeric transitions of the gamma-rays.

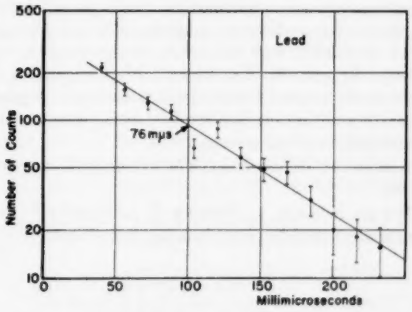

FIG. 8. Differential delay curve similar to Fig. 7 for Pb. A total of 950 counts are represented.

[31] B. Rossi and N. Nereson, Phys. Rev. **62**, 417 (1942).

TABLE II. Summary of mean lives.

Element	Z	Z_{eff}[a]	Mean life (mμsec) Individual runs	Weighted mean	Accuracy %
Fe	26	19.5	161±30 171±60	163±27	17
Cu	29	20.6	117±14 95±18 122±14[b]	116±9	7.5
Sb	51	27.2	105±12 92±12 (50±6)[b]	99±11	11
Hg	80	31.2	54±5 61±5	58±4	6.5
Pb	82	31.4	73±10 73±6 80±6	76±4	5
Bi	83	31.5	63±8 72±7	68±5	8

[a] From Wheeler (see reference 18).
[b] Previously published result (see reference 28). The early Sb value was strongly affected by nuclear events and is not included in the mean.

Before discussing these effects we shall describe an auxiliary measurement which shows that our counts are due almost entirely to neutrons. A comparison was made for Pb and for Cu between the meson capture rate with a 10-cm target and with a 2.5-cm target, other conditions remaining the same. We found that after solid angle corrections had been made, the thin target gave about one-fourth as many counts as the thick one for both elements. The result is consistent with the behavior of neutrons; the stopping mesons provide a diffuse, reasonably uniform source and the elastic scattering does not much affect the counting rate. On the other hand, practically all the gamma-rays, if any, would come from the 2.5 cm closest to S_2 because of absorption. From our measurements we believe that about one-eighth of the counts from the usual 10-cm target are due to gamma-rays.

Time lags from isomeric transitions following capture can therefore be ruled out. For not only are gamma-rays scarce, but in addition, most nuclei with a few Mev excitation are expected to find their way promptly to the ground state. It should also be remembered that even if the capturing nucleus has but a single isotope, the residual nuclei which radiate will consist of a number of isotopes corresponding to the parent nucleus less 0, 1, 2, or even 3 neutrons. No single isomeric level could predominate. Finally, most isomeric gamma-rays are of low energy and very strongly absorbed.

Time lags due to neutron time-of-flight are certainly present. Such lags, however, are independent of the delay between the arrival of the meson and its capture. Consequently, the shape of the decay curve will be unaffected provided we start counting at a time greater than the largest expected time-of-flight. Now the problem of neutron time-of-flight has already been discussed in connection with the neutrons from proton-induced stars; by accepting only counts delayed more than 32 mμsec we eliminate both of these effects. While the mean neutron energy will be somewhat less for

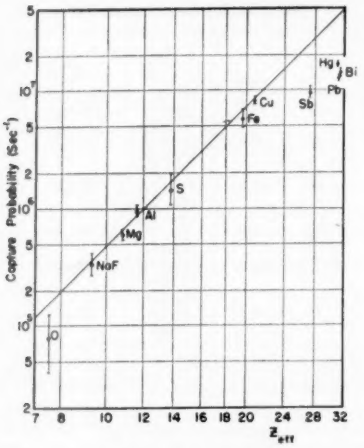

FIG. 9. Capture probabilities *vs* Z_{eff} of Wheeler Theory. Points shown in circles are the results of Ticho. Our results are shown as solid dots. A line with a slope corresponding to the Z_{eff}^4 law has been fitted to the elements up through Cu.

neutrons from meson capture than from stars, and hence the time lags greater, the diffusion mean life for the star-induced neutrons was only 4 mμsec. The 32-mμsec margin is obviously ample.

The effect of extraneous materials in the target region (Fe supports and Cu counter walls) on the measured mean lives is estimated to be less than 1 percent.

The capture probabilities computed from our results for the mean lives are plotted in Fig. 9 against the Z_{eff} of Wheeler. Previous results of Ticho[5] and Valley[6] for the light elements are also shown. The straight line is a fourth-power law fitted to the elements up through Cu.

It is seen that the Z_{eff}^4 law is in agreement with experiment over a considerable range, but that the capture probabilities for the heavier elements fall below the curve by approximately a factor three.

In the following paper Kennedy calculates the capture probabilities for Ca and for Pb, using a shell model of the nucleus. He finds for the ratio of these probabilities the value 6.1. Although we have not yet measured the capture rate for Ca ($Z_{eff}=16.1$), it probably does not lie far from the line drawn through the neighboring elements. Taking the value for Ca from the line, we find the ratio to be 4.3. If the capture probability for Ca falls below the line because of the closed-shell character of the Ca nucleus, the ratio will be larger. The agreement is thus satisfactory, considering the present incompleteness of the theory and the experimental uncertainties.

In Fig. 10 we show a linear plot of capture probability *vs* Z. The difference between the rate for Hg and for Pb is well outside the statistical error. Such a difference is to be expected due to the closed-shell properties of the Pb isotopes; the effect is qualitatively discussed by Kennedy, who estimates a dip of about 20 percent, as compared with the 30 percent we observe.

The point for Sb appears to be rather low, and it will be interesting to examine the group of elements in this vicinity. Indeed, while we can say that the capture probability curve is certainly not as regular as was expected according to the Wheeler picture, we have as yet only a sketchy notion of its general character.

A new apparatus is now under construction which will permit us to use much smaller targets. The measurements will then be extended to a larger number of elements.

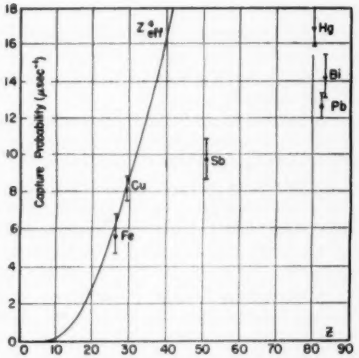

FIG. 10. Capture probabilities *vs* Z, showing especially the discrepancy between Hg and Pb.

Kennedy's calculation of the absorption rate for Pb together with our experimental result gives for the coupling constant between μ-mesons and nucleons the value 3.0×10^{-49} erg cm^3, with an uncertainty of perhaps 25 percent. The strength of this coupling is close to the present values of the beta-decay coupling constant and the constant involved in the spontaneous disintegration of the μ-meson.

A more detailed discussion will be found in Kennedy's paper.

We are indebted to Professor J. A. Wheeler for his continuing interest and stimulating discussions.

μ-Meson Capture and Nuclear Shell Structure*,†

JAMES M. KENNEDY
Palmer Physical Laboratory, Princeton University, Princeton, New Jersey
(Received May 5, 1952)

The rate of absorption of negative μ-mesons in lead and in calcium is calculated, using an interaction of the charge-exchange type described by Wheeler. A shell model of the nucleus is used in making explicit calculations of the various nuclear matrix elements. The ratio of the absorption rate in lead to that in calcium is found to be 6.1, in contrast to the value 14.3 predicted by the simpler Wheeler theory. Another result is that the absorption rate in mercury should be greater than that in lead by 20 percent in spite of its smaller atomic number. These results are in fair agreement with recent experimental measurements. The coupling constant for the charge-exchange reaction is $g \sim 3\times10^{-49}$ erg cm³, approximately the same as the coupling constants for β-decay and μ-decay.

I. INTRODUCTION

THE theory of the absorption of negative μ-mesons by nuclei has been developed by Wheeler[1] and Tiomno.[2] These authors have shown that the capture of the meson from its lowest Bohr orbit (into which it falls owing to electromagnetic forces) may be regarded as a charge-exchange reaction:

$$P+\mu^- \rightarrow N+\nu,$$

formally analogous to ordinary K capture. The particle denoted by ν is a light neutral particle with spin ½, which will be referred to as a neutrino in what follows, although it may in fact have a small finite rest mass. The dependence of the rate of absorption on the atomic number of the nucleus involved was then calculated by these authors on the basis of simple assumptions about the properties of the nucleus. Their calculations led to the formula

$$\Lambda = \text{constant} \times Z_{\text{eff}}^4$$

for the absorption probability. Z_{eff} is defined so as to take account of the effect of the finite size of the nucleus on the meson wave function, and reduces to the atomic number Z for light nuclei. This point is of considerable importance since the Bohr radius of the meson K orbit is comparable with the nuclear radius.

This theory has been fairly well confirmed by experiments in the lighter elements,[3] but recent measurements in the heavy elements near lead by Keuffel *et al.*[4] have shown large deviations, the calculated absorption rates being larger than the experimental values by factors of 2 or more. These discrepancies have prompted a reexamination of the theory to determine to what extent they are due to oversimplification of the nuclear model, or whether a fundamental revision in our understanding of the reaction is required. The more detailed calculations in the following sections also lead to a more accurate estimate of the strength of the nonelectromagnetic interaction between μ-mesons and nucleons.

II. OUTLINE OF THE THEORY

In order to show more clearly the way in which the various properties of the nucleus are taken into account, it is useful tc recapitulate briefly the assumptions used by Tiomno and Wheeler in deriving the Z_{eff}^4 absorption law. Fundamentally it was assumed that the reaction is induced by an interaction Hamiltonian of the form

$$H = gO_{HL}\tau_H\tau_L\delta(\mathbf{x}_H-\mathbf{x}_L)+\text{compl. conj.} \qquad (1)$$

Here g is a constant, having the physical dimensions erg cm³, which measures the strength of the interaction; O_{HL} is one of the five relativistically invariant combinations of Dirac operators well known from β-decay, or a linear combination of these; τ_H is an operator that changes a proton into a neutron; and τ_L is an operator that changes a meson into a neutrino. The corresponding result for the absorption probability involved the coupling constant g and the wave functions of the various particles taking part in the reaction.

The meson wave function was determined by the influence of electromagnetic forces alone, and as a result of the finite extension of the nucleus is intermediate in behavior to the function for a harmonic oscillator and that for a Coulomb potential. The neutrino was regarded as a free particle. Instead of dealing with the nucleon wave functions in detail, these authors used a Fermi gas model of the nucleus, with $A=2Z=2N$ nucleons confined to a sphere of suitable radius. These fill all states in momentum space up to a fixed level, 216 Mev/c, corresponding to a kinetic energy of 25 Mev. The meson absorption probability quoted above was then calculated by the application of conservation of energy and momentum to the geometry of momentum space.

As a guide to the magnitudes involved, it is convenient to note that a free proton at rest may take up about 5.5-Mev kinetic energy from the annihilation of

* A short account of this work was presented at the New York meeting of the American Physical Society, January 31–February 2, 1952.

† Supported by the joint program of the ONR and AEC.

[1] J. A. Wheeler, Revs. Modern Phys. **21**, 133 (1949).

[2] J. Tiomno and J. A. Wheeler, Revs. Modern Phys. **21**, 154 (1949).

[3] Harrison, Keuffel, and Reynolds, Phys. Rev. **83**, 680 (1951).

[4] Keuffel, Harrison, Godfrey, and Reynolds, Phys. Rev. **87**, 942 (1952).

the meson, while the remainder of the 107-Mev rest energy is carried off by the neutrino. A nucleon with 25-Mev kinetic energy cannot acquire more than about 22 Mev, while the neutrino takes off at least 85 Mev. It is this fact that accounts for the relatively low excitation of the nucleus in the reaction and makes it possible to handle the final states of the reaction with some assurance.

There are two respects in which the treatment just outlined is too crude. The first is the assumption that the numbers of protons and neutrons in the nucleus are equal. In heavy nuclei the excess neutrons occupy states in momentum space which would otheriwse be available as final states for the reaction. As a consequence, the total transition probability for heavy nuclei estimated on this theory is too large. A second remark is that the statistical distribution of states used in the Fermi gas model does not take account of the angular momentum of the particles. In effect, the theory assumes that arbitrary changes of spin are permitted. This is equivalent to the assumption that the wavelength of the neutrino is small compared to the nuclear radius. Since a typical neutrino, with energy 90 Mev or so, has a reduced wavelength $\hbar/p=2\times10^{-13}$ cm, it is clear that transitions involving changes of angular momentum $\Delta J>3$ are forbidden for all practical purposes, even for the heaviest nuclei. This also tends to decrease the transition probability in the heavier nuclei. The effect is less pronounced in the light nuclei, in spite of their smaller radius, since the angular momentum of the various states is small, and large changes would not be expected anyway.

In order to investigate these two effects quantitatively, the absorption probability has been recalculated using a shell model of the nucleus based on $j-j$ coupling to provide the wave functions of the nucleons. Regarding the total nuclear wave function as an antisymmetric combination of products of single particle wave functions, the total transition probability may be reduced to a sum of contributions from single particle transitions. This procedure has already been applied by Tiomno and Wheeler in calculating the absorption in oxygen; with the improved knowledge of nuclear shell structure available at present, it is now possible to handle other cases. Similar ideas have also been applied to β-decay by Nordheim, Mayer, and Moskowski.[5]

Owing to the large amount of calculation involved, and to the ambiguities in the single particle configuration assignments to many nuclei, the detailed calculations are performed only for two isolated cases, Ca^{40} and Pb^{208}. These nuclei are appropriate for the present work, as they lie far apart in the periodic table, and will therefore emphasize deviations from the Z^4 behavior. Also, both have closed shells of both protons and neutrons, so that it is possible to assign their configurations unambiguously and to make use of symmetry properties to reduce the amount of computation.

Most of the essentials of the calculation are carried out in Sec. III. After the results for calcium and lead are known, it is possible to make some qualitative observations about the capture probabilities in neighboring nuclei. This point is discussed along with some other conclusions in Sec. IV.

[5] L. Nordheim, Revs. Modern Phys. **23**, 315 (1951); Nordheim, Mayer, and Moskowski, Revs. Modern Phys. **23**, 322 (1951).

III. DETAILS OF CALCULATIONS

The total absorption probability is regarded as a sum of contributions from individual particle transitions, in which a proton in some nuclear state is transformed into a neutron which must be in a state previously unoccupied. The probability of such a transition may be found from time-dependent perturbation theory. Considering for the moment that the operator O_{HL} of Eq. (1) is either of the scalar or the vector type, reducing simply to 1 in the nonrelativistic approximation, the transition probability is

$$\Lambda=(2\pi/\hbar)g^2\left|\int\psi_N^*\psi_P\psi_\nu^*\psi_\mu d\tau\right|^2\rho_f, \qquad (2)$$

where g is again the coupling constant for the interaction, ρ_f is the density of final states of the reaction, the subscripts on the various wave functions have the obvious significance, and the integration is carried out over the volume of the nucleus. In the formulas which follow, the subscripts P, N, μ, ν, refer to the particles involved in the reaction, while small Roman subscripts, n, l, j, m, etc., refer to quantum numbers of various states.

The meson wave function ψ_μ is the lowest eigenfunction for the particle under the electromagnetic attraction of the nucleus. This is obtained by solving the Schrödinger equation for the meson in the field of a charge Z uniformly distributed over a sphere of radius a, where a is the radius of the nucleus in question. This state is of course an s-state.

The neutrino is taken to be a free particle normalized in a large sphere of radius b. Explicitly,

$$\psi_\nu=(2/b)^{\frac{1}{2}}k_\nu j_l(k_\nu r)Y_l^m(\Omega)\chi_s,$$

where k_ν is the wave number of the neutrino ($k_\nu=p/\hbar$), $j_l(x)$ is a spherical Bessel function, $Y_l^m(\Omega)$ is a normalized spherical harmonic, and χ_s is an eigenfunction of the z component of spin. It will be convenient in what follows to use α and β for the eigenfunctions corresponding to $m_s=\hbar/2$ and $-\hbar/2$, respectively. Since the reaction takes place between well-defined states of the nucleus, the density of final states may be found by examining the density of neutrino states alone. This is fixed by the condition $\psi_\nu(b)=0$, which leads directly to $\rho_f=b/\pi\hbar c$. It is apparent that b does not appear in the final expression for Λ.

According to the $j-j$ coupling model, the wave function for a nucleon is characterized by its orbital

angular momentum l, its total angular momentum j, and m, the z component of j. There is also a "principal quantum number," n, which in this case gives the number of nodes of the radial part of the wave function. The spin and angular dependence of the wave functions are well known from group theoretical considerations:

$$\psi(n,l,j=l+\tfrac{1}{2},m)=R_{nl}(r)\left[\left(\frac{l+m+\frac{1}{2}}{2l+1}\right)^{\frac{1}{2}}\alpha Y_l^{m-\frac{1}{2}}+\left(\frac{l-m+\frac{1}{2}}{2l+1}\right)^{\frac{1}{2}}\beta Y_l^{m+\frac{1}{2}}\right],$$

$$\psi(n,l,j=l-\tfrac{1}{2},m)=R_{nl}(r)\left[-\left(\frac{l-m+\frac{1}{2}}{2l+1}\right)^{\frac{1}{2}}\alpha Y_l^{m-\frac{1}{2}}+\left(\frac{l+m+\frac{1}{2}}{2l+1}\right)^{\frac{1}{2}}\beta Y_l^{m+\frac{1}{2}}\right].$$

When the various factors are inserted in Eq. (2) and account is taken of the orthogonality properties of the spin eigenfunctions, the expression on the right side splits into the product of two integrals. One of these depends only on the radial functions:

$$I=\left|\int_0^\infty R_P R_N \psi_\mu j_l(k_\nu r) r^2 dr\right|^2,$$

while the other is an integration over angles:

$$J=\left|\int Y_N^* Y_P Y_\nu^* d\Omega\right|^2,$$

or rather the sum of two such expressions. In order to evaluate the radial integral, a further assumption must be made about the radial dependence of the nucleon wave functions. In what follows it has been assumed that

$$R_{nl}=C_{nl}j_l(\xi_{nl}r/a),$$

where C_{nl} is a normalizing constant and ξ_{nl} is the nth zero of $j_l(x)$. This choice of functions would be correct if the nucleus were actually a deep square well; it is reasonable to assume that they have the same general behavior as the true eigenfunctions.

The angular integrals may be evaluated by a formula due to Gaunt.[6] In applications, there will be a sum of such contributions over all final neutrino states. Conservation of angular momentum and parity of the total wave function is automatically assured by the orthogonality properties of the spherical harmonics. For a transition from a proton state with orbital angular momentum l_P to a neutron state l_N, the neutrino may have orbital angular momentum from $l_\nu=l_P+l_N$ to $l_\nu=|l_P-l_N|$, provided that $l_P+l_N+l_\nu$ is an even integer.

[6] See, for example, E. Condon and G. Shortley, *Theory of Atomic Spectra* (Cambridge University Press, Cambridge, 1935), p. 176. Condon and Shortley also give tables of these integrals for small values of l.

TABLE I. Classification of nucleon states according to $j-j$ coupling.

Shell No.	Nucleon quantum numbers
I	$(1s)^2$
II	$(1p)^6$
III	$(1d)^{10}(2s)^2$
IV	$(1f)^{14}(2p)^6(1g_{9/2})^{10}$
V	$(1g_{7/2})^8(2d)^{10}(3s)^2(1h_{11/2})^{12}$
VI	$(1h_{9/2})^{10}(2f)^{14}(3p)^6(1i_{13/2})^{14}$
VII	$(1i_{13/2})^{14}(2g)^{18}(3d)^{10}(4s)^2(1k_{15/2})^{16}$

The remainder of the calculation consists of evaluating expressions of the type (2) for all possible single particle transitions. Determination of which transitions actually occur is made by applying energy and momentum conservation principles to the various initial and final states available in the nucleus in question. This requires some prescription for assigning energies to the nuclear particles. The following procedure was found to be the most useful:

(1) The order of filling the various shells was carried over from the $j-j$ coupling model of the nucleus.[7] For reference, this is shown in Table I. The quantum numbers (nl_j) refer to the principal quantum number defined previously, the orbital angular momentum, and the total angular momentum. If no value of j is given, both $j=l+\frac{1}{2}$ and $j=l-\frac{1}{2}$ are present in the same shell. The precise order of filling the levels within a shell is not of importance here, since the nuclei under consideration are both "doubly magic." In calcium the first three shells of both protons and neutrons are filled, while in lead the first five proton shells and the first six neutron shells are completed.

(2) The energies of the individual particles were tentatively determined by assuming that the nuclear potential was a square well with infinitely high walls.

(3) The mean energy of the particles was then computed, and the result adopted as the common energy of all particles in that shell. This more or less smooths out the complicated spin-orbit energies, pairing energies, etc.

(4) The energy scale was normalized so that the highest filled proton shell was 25 Mev above the bottom of the potential well. This, in effect, fixes the radius of the nucleus, and should give a value that corresponds to that known from other considerations. If there is a neutron excess, the energy of the highest occupied neutron shell must be equal to that for the protons. This was accomplished by lowering the neutron well an appropriate amount. This gives an approximate treatment of the effect of Coulomb forces.

This prescription takes account of the essential features of the nucleus without introducing details that do not have much effect on the present problem. It is to be noted that while the occupied neutron states have the same maximum energy as the proton states, their maximum momentum in the nucleus may be greater,

[7] M. G. Mayer, Phys. Rev. **78**, 16 (1950).

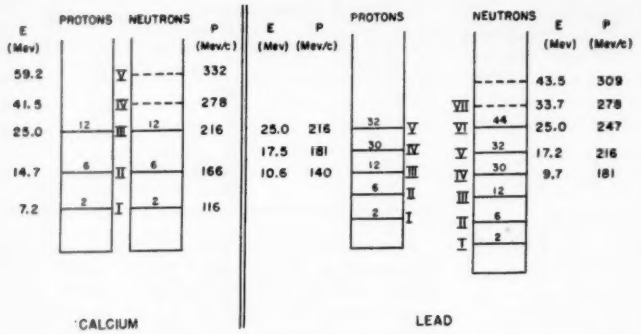

FIG. 1. Energy levels in calcium and lead. Roman numerals refer to the shells listed in Table I. Numbers on the lines give the numbers of nucleons in the shells. Momenta are determined from the kinetic energies in the potential well. Energies are fixed so that the proton states are filled up to 25 Mev above the bottom of the potential well.

since this depends on the depth of the potential well. This influences the number of transitions allowed by energy and momentum conservation.

The results of applying these rules to calcium and lead are shown in Fig. 1. Application of energy and momentum conservation to the various individual particle transitions implies that the sum,

$$\text{energy change}+(c\times\text{momentum change}),$$

between initial and final nucleon states must not exceed the total energy liberated by the annihilation of the meson. For calcium this total energy is essentially the full rest energy since the binding energy in the K orbit is fairly small; for lead the total energy available is about 97.5 Mev, taking account of the 9.5-Mev binding energy in the K orbit. Examination of Fig. 1 shows that the only admissable transitions are those from the highest filled proton shell to the lowest unoccupied neutron shell in each case. The remainder of the computation is straightforward. For calcium the relative importance of the various individual particle transitions is shown in Table II. In each entry of the table, the sum over the magnetic quantum numbers has been carried out. It is seen that for $l_\nu>2$, the contributions are insignificant. In this computation it was found sufficiently accurate to remove the meson wave function from the radial integrals, using the Wheeler definition of Z_{eff} to give an appropriate mean value. For lead, however, the correct wave function, as tabulated numerically by Wheeler, was used. A table similar to Table II was obtained. The total absorption probabilities were found by carrying out the appropriate sums over final states and averages over initial states in the spin space of the light particles.

IV. RESULTS AND DISCUSSION

The final results of the calculation are as follows:

$$\Lambda_{\text{Pb}}=1.56\times10^{10^4}\ \text{g}^2\ \text{sec}^{-1},$$
$$\Lambda_{\text{Ca}}=2.7\ \times10^{10^3}\ \text{g}^2\ \text{sec}^{-1}.$$

For comparison with experiment is the absorption rate in natural lead which is of interest. The rates in Pb^{206} and Pb^{207} are somewhat larger than that in Pb^{208}, as these isotopes have vacancies in the highest neutron shell. Since the spin of Pb^{207} is $\frac{1}{2}$, these vacancies may be assumed to occur in the $3p_{\frac{1}{2}}$ subshell of shell VI. The additional allowed transitions, which may be either from proton shell IV or V, may be examined in the same way as the others above, and their influence on the absorption rate determined. The calculated rate for absorption in natural lead works out to $\Lambda_{\text{Pb}}'=1.6\times10^{10^4}\ \text{g}^2\ \text{sec}^{-1}$. This gives for the ratio of the rates in lead and calcium

$$\Lambda_{\text{Pb}}'/\Lambda_{\text{Ca}}=6.1.$$

By comparison, the Z_{eff}^4 formula gives 14.3 for this ratio. Direct comparison with experiment cannot be given at present, as the absorption in calcium has not been measured. However, under the assumption that it lies on the Z_{eff}^4 curve, which holds quite well in this part of the periodic table, comparison with the mean life of a μ-meson in lead obtained by Keuffel *et al.*[4] gives a quasi-experimental value somewhat smaller than 5. In view of the number of assumptions involved in the theory, this agreement is fairly satisfactory. If it should turn out that the closed shell character of the calcium nucleus decreases its absorption rate below that of its neighbors in a manner similar to the observed behavior in the vicinity of the lead nucleus, the agreement between theory and experiment will be improved.

The fact that the observed absorption rate in mercury ($Z=80$) is greater than that in lead in spite of its smaller charge may be predicted qualitatively from this theory. Referring to Fig. 1, the mercury nucleus differs from the diagram for lead in two respects. First, there are two protons missing from the highest shell; this of course decreases the absorption probability. On the other hand, there are three to eight neutrons (depending on the isotope) absent from the highest neutron shell. This leaves a number of additional final states of fairly low energy available for transitions by the particles that remain. While uncertainties in the configura-

tions for some of the mercury isotopes makes a detailed analysis difficult, it can be estimated that the net result of the two effects is an increase of roughly 20 percent in the absorption rate in passing from lead to mercury. The experimental values show an increase of about 30 percent.

The measured mean life in lead may also be used to obtain a numerical value for the strength of the interaction:

$$g \sim 3 \times 10^{-49} \text{ erg cm}^3.$$

This is probably accurate to within about 25 percent, although a good estimate of the error is not easy to make. This value of g agrees with the value of the β-decay coupling constant calculated from Robson's[8] data on the decay of the neutron, and the μ-decay coupling constant estimated by MacCallum and Wightman[9] from the spectrum of Sagane *et al.*[10] and the theory of Wheeler and Tiomno.[11] These values are

$$g_\beta = (3.1 \pm 0.4) \times 10^{-49} \text{ erg cm}^3,$$
$$g_\mu = (3.2 \pm 0.4) \times 10^{-49} \text{ erg cm}^3.$$

The possibility of a universal interaction among spin $\frac{1}{2}$ particles has been discussed by various authors.[11–14] For the present it is sufficient to remark that the improved accuracy in the absorption coupling constant is still consistent with a common value for all three interactions.

In deriving the results quoted above, a scalar or vector interaction was used. The same calculation may be carried out using a tensor or pseudovector interaction, which reduces to $O_{HL} = \boldsymbol{\sigma}_H \cdot \boldsymbol{\sigma}_L$ in the nonrelativistic limit. With an interaction of this sort, the individual particle transitions which give the large contributions are somewhat different, but the total transition probability is roughly the same. More precisely, the value of the coupling constant must be increased by 5 percent in order to obtain agreement with the measured mean life in lead. With the present accuracy of the theory, this cannot be regarded as significant. Hence, it is not possible to distinguish between the various types of fundamental interactions.

There are several other points about the calculation of Sec. III which may be discussed in estimating the sources of inaccuracy in the results. The model of the nucleus has a number of obvious deficiencies—the assignment of the energies to the various shells and the choice of radial functions are examples. The former of these is probably not too serious, as the choice of which transitions are allowed is more or less independent of the particular assumptions made in this respect. The latter point, and with it the implicit assumption that the total wave function is simply an antisymmetrized product of the single particle functions, is a more serious drawback. However, it is reasonable to suppose that the ratios of absorption probabilities in different elements will be given fairly accurately even if the absolute values are somewhat in error. Another remark is that for simplicity the final neutron states have been regarded as bound to the nucleus, whereas in fact they are in the continuum. The effect of this assumption is that an integration over all final neutron energies is replaced by a sum over the resonances in the neutron emission cross section.

Within the accuracy to be expected of the theory, the agreement with observation seems to confirm the validity of the charge-exchange conception of the meson capture reaction. At the present it does not seem practical to make further refinements in the calculations, although a more detailed study may be desirable in the future when our knowledge of nuclear structure is more precise. Recent measurements by Crouch and Sard[15] of the number of neutrons emitted when a μ-meson is captured in lead indicate that the average yield is greater than is to be expected from the 15- to 20-Mev excitation given to the nucleus according to this model. This conflict must be resolved before the theory can be regarded as completely satisfactory. A related question, which has not been studied in detail, is to determine the extent to which the assumption of conservation of energy and momentum among the individual particles is valid; in the lighter nuclei it would seem possible that a significant amount of momentum might be used to give motion to the nucleus as a whole.

If some of these improvements can be incorporated into the calculations and combined with slightly

TABLE II. Single particle transitions in calcium. Apart from a constant factor, $|M|^2$ is the square of the radial integral multiplied by the sum of the squares of the angular integrals taken over all values of the magnetic quantum numbers.

Transition	l_p	$\|M\|^2$
$2s \rightarrow 1f$	3	0.01
$2s \rightarrow 2p$	1	0.48
$2s \rightarrow 1g_{9/2}$	4	($\ll$0.01)
$1d \rightarrow 1f$	1	2.71
$1d \rightarrow 1f$	3	0.02
$1d \rightarrow 1f$	5	($\ll$0.01)
$1d \rightarrow 2p$	1	0.18
$1d \rightarrow 2p$	3	($\ll$0.01)
$1d \rightarrow 1g_{9/2}$	2	0.19
$1d \rightarrow 1g_{9/2}$	4	($\ll$0.01)
$1d \rightarrow 1g_{9/2}$	6	($\ll$0.01)

[8] J. W. Robson, Phys. Rev. **83**, 349 (1951).
[9] C. J. MacCallum and A. S. Wightman (unpublished).
[10] Sagane, Gardner, and Hubbard, Phys. Rev. **82**, 537 (1951). More recent determinations of the μ-decay spectrum have thrown some doubt on the validity of these results, but the value of g_μ should not be much different from the one quoted. See A. Lagarrique and C. Peyrou, Compt. rend. **233**, 478 (1951).
[11] J. A Wheeler and J. Tiomno, Revs. Modern Phys. **21**, 144 (1949).
[12] M. Ruderman and R. Finkelstein, Phys. Rev. **76**, 1458 (1949).
[13] C. N. Yang and J. Tiomno, Phys. Rev. **79**, 498 (1950).
[14] L. Michel, Proc. Phys. Soc. (London), **A63**, 514 (1950).
[15] M. F. Crouch and R. D. Sard, Phys. Rev. **85**, 120 (1952).

greater precision in the experimental measurements, it is possible that useful data on nuclear configurations may be derived from μ-meson interactions. The local fluctuations in absorption probability such as those in the vicinity of lead reflect the properties of nuclear shell structure, and since the interaction is not confined to one or two particles near the top of the potential distribution, this reaction gives access to information which is not available from other types of nuclear reaction.

PHYSICAL REVIEW VOLUME 87, NUMBER 6 SEPTEMBER 15, 1952

Theory of Slip-Band Formation

JOHN C. FISHER, EDWARD W. HART, AND ROBERT H. PRY
Research Laboratory, General Electric Company, Schenectady, New York
(Received March 26, 1952)

The fine structure of slip bands on the surfaces of plastically deformed crystals, as described by Heidenreich and Shockley and by Brown, is explained in terms of the model of dislocation-loop generation proposed by Frank and Read. The back-stress at an active Frank-Read source, produced by an expanding avalanche of about 300 dislocation loops, is shown to be sufficient to stop dynamic loop generation at the source. Slip, therefore, occurs in avalanches separated in time.

Avalanches from other slip systems crossing a slip plane containing an active source lead to the observed stepped surface markings, with successive avalanches from the given source displaced relative to each other.

PLASTIC deformation of crystals often occurs by slip, which takes place on only a few of many crystallographically equivalent planes. The translation per active plane is considerable, however, and large amounts of plastic flow can result. Frank and Read,[1] by means of a simple model of dislocation-loop generation, have explained the inactivity of most prospective slip planes, but the concentration of slip into hundred- or thousand-loop avalanches on each active plane has not been accounted for.

We propose that slip avalanches result from the dynamic generation of loops at a Frank-Read source, and are terminated by their own stress fields. The observations of slip-band distribution and fine structure can be interpreted satisfactorily in this way.

OBSERVATION OF SLIP BANDS

A surface marking, or slip band, appears at the intersection of an active slip plane and the free surface of a crystal. Yamaguchi,[2] using a light microscope, has made an extensive study of the relationships between slip-band distribution and work hardening. Heidenreich and Shockley,[3] and Brown,[4,5] using electron microscopes, have examined the fine structure of slip bands. Based largely upon these observations of slip in aluminum, Brown[6] has summarized the current state of knowledge regarding the structure of slip bands and the relationship between slip bands and work hardening. Restated, his summary is as follows:

(1) Plastic deformation in aluminum proceeds by slip on a relatively small number of crystal planes.

(2) Each slip band is composed of one or more avalanches, as sketched in Fig. 1.

(3) The offset per avalanche is nearly independent of stress and temperature.

(4) The number of avalanches per band increases as the temperature or stress increases.

(5) A plot of stress *versus* number of slip bands is nearly independent of temperature.

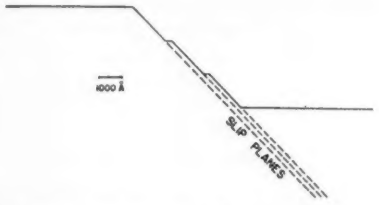

FIG. 1. Slip band fine-structure in aluminum, according to Brown (see reference 6). Cross section of a slip band containing three avalanches.

TWO QUESTIONS RAISED BY THE EXISTENCE OF AVALANCHES

An avalanche of about 10^3 dislocations appears to be the smallest unit of slip in an ordinary slip band. At low stresses and small strains most slip bands contain a single avalanche. The existence of such avalanches poses two questions.

The first is how so many dislocations are generated on a single slip plane. It has been answered convincingly

[1] F. C. Frank and W. T. Read, Phys. Rev. **79**, 722 (1950).

[2] K. Yamaguchi, Sci. Papers Inst. Phys. Chem. Research (Tokyo), **8**, 289 (1928).

[3] R. D. Heidenreich and W. Shockley, J. Appl. Phys. **18**, 1029 (1947).

[4] A. F. Brown, Nature **163**, 961 (1949).

[5] A. F. Brown, Compt. rend. I^{er} Congr. Internatl. Microscopie Electronique, Paris (1950).

[6] A. F. Brown, J. Inst. Metals **80**, 115 (1951–52).

by Frank and Read.[1] They point out that a dislocation segment, lying in a slip plane and pinned at both ends, is a source of an unlimited number of dislocation loops. Such segments are known as Frank-Read sources, and they react to stress as sketched in Fig. 2. At low stresses the dislocation segment bows in the slip direction and stops at an equilibrium curvature: further glide would increase the energy of the dislocation, by increasing its length, more than the decrease in energy due to glide in the stress field that is present. When a critical resolved shear stress is reached, for which the segment is approximately semicircular, continued growth of the loop is possible with a net decrease in energy, for the energy increase associated with increased length of dislocation is more than offset by a decrease due to glide.

The critical resolved shear stress is approximately

$$\tau^* = Gb/L, \tag{1}$$

where G is the shear modulus, b is the magnitude of the Burgers vector, and L is the length of the Frank-Read source. For a stress greater than τ^* an unlimited number of dislocation loops can be generated, as shown in the figure. After each loop is formed, the segment is regenerated and acts again to form another loop. In this way the grouping of dislocations into an avalanche of a thousand or so loops on a single slip plane can be understood.

The second question raised by the existence of avalanches of dislocations is: why does the generation of dislocation loops in an avalanche stop, and why at a rather definite number of loops?

INTERPRETATION OF CONSTANT OFFSET PER AVALANCHE

In a perfect single crystal and in the absence of any work hardening whatever, it is proposed that the generation of dislocation loops at a Frank-Read source would cease in time because of the back-stress produced by loops already generated, for each dislocation loop has a stress field that opposes the applied stress in the neighborhood of the source. When enough loops have been generated, the stress at the source will fall to a value so low that additional loops cannot form. Only after the original avalanche of loops has moved some distance away can another avalanche occur.

A first estimate of the minimum stress at a Frank-Read source, below which the source ceases to generate loops, might be τ^*, the critical stress for loop generation; but τ^* is the critical stress for loops that must grow from a standing start. After the first, all loops that form at a given source form with a running start. A regenerated segment has kinetic energy as it moves through its position of minimum length, and continues to have work done upon it as it moves toward the position of maximum energy. Under a stress τ^*, therefore, a dislocation loop will pass through the critical semicircular shape with a positive velocity. Even

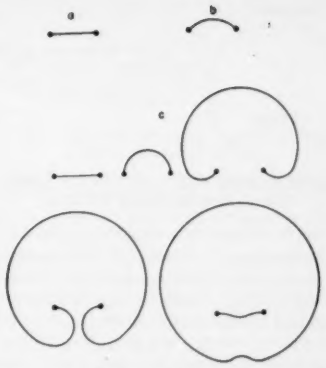

FIG. 2. Response of a Frank-Read source to stress. (a) Equilibrium under no stress. (b) Equilibrium under a subcritical stress. (c) Loop generation under a supercritical stress.

though the stress drops somewhat below τ^*, loops still can be generated.

In order to calculate the number of loops that should be present in an avalanche, it is necessary to estimate (a) the back-stress produced by a number of successive loops occurring in one burst, and (b) the minimum stress at which a Frank-Read source, once started, can continue to operate.

ESTIMATION OF BACK-STRESS CAUSED BY AN AVALANCHE

The stress at a distance r_i from a straight screw dislocation is

$$\tau_i = Gb/2\pi r_i. \tag{2}$$

As a first approximation, it is also the back-stress at the center of a single dislocation loop of radius r_i. The back-stress at the center of a number of concentric loops will be

$$\tau_b = \sum \tau_i = (Gb/2\pi)\sum 1/r_i. \tag{3}$$

If the length of the Frank-Read source is L, the spacing of loops will be approximately πL, so that

$$r_i = \pi L i, \tag{4}$$

and the back-stress is

$$\begin{aligned} \tau_b &= (Gb/2\pi)\sum 1/\pi L i \\ &= (Gb/2\pi^2 L)\ \ln i, \end{aligned} \tag{5}$$

where i is the number of loops. Since the applied stress is just the critical stress to start the first loop, as given by Eq. (1), the ratio of back-stress to applied stress is

$$\tau_b/\tau^* = \ln i/2\pi^2 \tag{6}$$

for an avalanche of i loops, independent of stress or temperature. For a hundred loops, $\tau_b/\tau^* = 0.23$, and for a thousand $\tau_b/\tau^* = 0.35$.

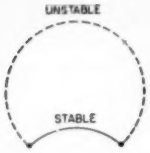

FIG. 3. Stable and unstable equilibrium positions for a Frank-Read source subjected to a subcritical stress.

MINIMUM STRESS FOR CONTINUED OPERATION OF A FRANK-READ SOURCE

In order to estimate the minimum stress at which a Frank-Read source can operate, it is necessary to know the extent to which energy is conserved during the motion of a dislocation. There are two limiting cases, one corresponding to high losses, where the dislocation can have no kinetic energy, and the other to low losses, where the sum of the potential and kinetic energies of the dislocation remains constant. We shall consider the second case, for the first leads to the generation of only a single loop per avalanche.

The potential energy of a free dislocation loop of radius r lying in a slip plane where the resolved shear stress is τ is

$$\Delta E = 2\pi r\gamma - \pi r^2 b\tau, \tag{7}$$

where $\gamma = Gb^2/2$ is the energy per unit length of dislocation. The first term is the self-energy of a dislocation at rest, the second the potential energy decrease associated with the motion of a dislocation with Burgers vector b through area πr^2 in a resolved shear stress field τ. The energy ΔE is a maximum when

$$r = r^* = \gamma/b\tau = Gb/2\tau, \tag{8}$$

for which $\partial\Delta E/\partial r = 0$ and the loop is in unstable equilibrium. A Frank-Read source of length L will have two equilibrium positions, one stable and one unstable, both with radius r^*, as long as $r^* > L/2$. In the unstable position the dislocation line is a longer than semicircular arc, and in the stable position a shorter than semicircular arc, as sketched in Fig. 3. When $r^* < L/2$ there are no equilibrium positions and the Frank-Read source must generate loops. The limiting condition, $r^* = L/2$, together with the approximation $\gamma = Gb^2/2$, leads to Eq. (1) for the critical stress to activate a Frank-Read source.

The Frank-Read source configuration just after the birth of a new loop and the regeneration of the dislocation segment is sketched in Fig. 4a for a stress $\tau < \tau^*$. The position of unstable equilibrium also is sketched. The minimum stress τ for which another loop can be generated is that for which the energy (kinetic plus potential) of the regenerated segment just equals the potential energy of the loop at the unstable equilibrium position, where an infinitesimal disturbance will cause it to grow with continuously decreasing potential energy.

Figure 5 shows the potential energy of a regenerated dislocation segment as a function of the area swept out. Calculated curves are given for several stresses. The top one, for $\tau = \tau^*$, is monotonically decreasing. The others, for $\tau < \tau^*$, have a minimum and a maximum corresponding to the two equilibrium positions. In the absence of energy dissipation, and neglecting the kinetic energy of the regenerated segment, dynamic loop generation can continue as long as the initial energy E_0 of the regenerated segment exceeds the energy E_1 of the unstable equilibrium position. The minimum stress for continued operation of a source is that for which $E_0 = E_1$. According to the figure this stress is about $0.5\tau^*$.

The minimum stress can be calculated more easily and probably more accurately by assuming that the regenerated segment has the shape shown in Fig. 4b or 4c, for it is relatively unlikely that energy is conserved near the sharp apex of the regenerated segment of Fig. 4a. The points E_0' in Fig. 5 correspond to regenerated segments sketched by hand as in Fig. 4b, and to a minimum stress of about $0.7\tau^*$ for dynamic loop generation. Assuming the configuration in Fig. 4c for numerical calculation, the potential energy of the regenerated segment is

$$E_0' = 2\theta r^*\gamma, \tag{9}$$

where θ is the angle shown in Fig. 4c and γ is the energy per unit length of dislocation. The corresponding potential energy of the loop in the unstable position is

$$E_1 = (2\pi - 2\theta)r^*\gamma - \pi r^{*2} b\tau. \tag{10}$$

The single term in E_0' and the first term in E_1 represent the energies of the corresponding dislocation segments. The second term in E_1 represents the energy change associated with the area swept out between the two configurations. The stress in question is that for which $E_0' = E_1$, or for which

$$\theta = (\pi/4)(2 - r^* b\tau/\gamma) = \pi/4. \tag{11}$$

When $\theta = \pi/4$, the minimum stress τ for continued loop generation is seen to be

$$\tau/\tau^* = \tau/(Gb/L) = L/2r^* = \sin\theta = 1/\sqrt{2}. \tag{12}$$

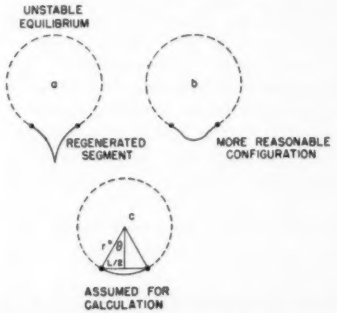

FIG. 4. Alternate configurations of regenerated dislocation segments.

According to Eq. (12), a stress as low as $1/\sqrt{2}=0.71$ of the critical stress required to start a Frank-Read source will suffice to continue it in operation, in the absence of energy dissipation. If the stress reduction from τ^* to $\tau^*/\sqrt{2}$ is caused by a back-stress $\tau_b/\tau^*=1-1/\sqrt{2}=0.29$ due to an avalanche of loops, Eq. (6) states that there are $i=320$ loops in the avalanche. In other words, according to the back-stress model, and with the approximations here employed, Frank-Read sources should generate loops in avalanches of about 300 loops each.

INTERPRETATION OF SLIP-BAND FINE STRUCTURE

Since the number of slip bands observed in a crystal depends only upon the stress, it is reasonable to assume that each band is produced by the action of a single Frank-Read source. Generation of the first avalanche at a source is easily understood. When the stress at the source reaches τ^*, loops are generated, and continue to be generated until the back-stress stops the avalanche. A second avalanche will not occur immediately in polycrystals, for the loops in the first avalanche are stopped or partially stopped at grain boundaries, and at least a portion of the back-stress remains. Even in single crystals there is enough crystal irregularity that not all loops leave the crystal, and some back-stress remains. Only if the external stress is increased substantially will a second avalanche be formed. In this way the formation of additional avalanches with rising stress can be understood.

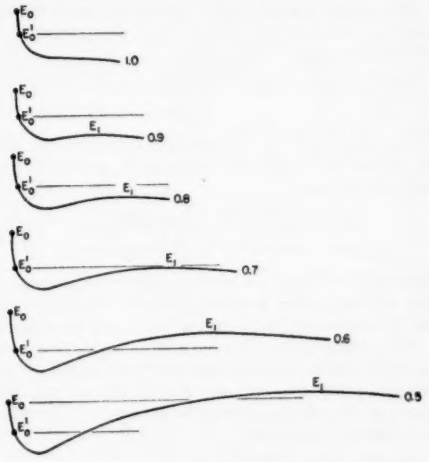

FIG. 5. Potential energy of a dislocation segment (vertical coordinate) *versus* area swept out (horizontal coordinate) for stresses in the range $0.5\tau^* \leq \tau \leq \tau^*$. Points E_0 correspond to Fig. 4a, points E_0' to Fig. 4b. Numbers beside each curve give values of τ/τ^*.

FIG. 6. Expected slip band fine-structure for large strains and cross slip.

At high temperatures recovery processes are known to reduce the back stress. A Frank-Read source that is subjected to a constant stress a little higher than τ^* will produce another avalanche every time recovery brings the back-stress down.

It remains to explain the displacement of successive avalanches by a small amount normal to the slip plane, thereby accounting for the observed fine structure of slip bands. A displacement of this type requires that a Frank-Read source move relative to the surface where slip bands are observed. Avalanches on other dihedrally inclined slip planes that pass between a Frank-Read source and its surface slip markings must produce such relative displacements, and whenever slip is occurring on more than one slip system it would be possible, in an inter-avalanche period, for one or more avalanches to pass between a Frank-Read source and its associated surface marking. These avalanches should all produce relative displacements of the same sign, so that the surface configuration in the neighborhood of a slip band could appear as in Fig. 6, where slips of several hundred atom diameters appear on parallel planes that are several times as widely separated.

Figure 6 is the inverse of Fig. 1 which gives the reported configuration in the neighborhood of a slip band as determined by electron microscopic observation of aluminum oxide replicas. In Fig. 1, slips of a thousand or so atom diameters occur on parallel planes whose relative offset is several times less than the slip per plane. Either configuration could be expected to occur, that in Fig. 1 at low strains where there is less than one intersecting avalanche per inter-avalanche period, and that in Fig. 6 at large strains where there are several.

CONCLUSION

The model of slip based upon (a) Frank-Read sources, and (b) a limitation of the offset per slip by back-stress, appears to explain satisfactorily the observed structure and distribution of slip bands.

Electron Excitation of Nuclei*

JOSEPH A. THIE,† CHARLES J. MULLIN, AND E. GUTH
University of Notre Dame, Notre Dame, Indiana

(Received March 17, 1952)

The cross section for an electric 2^l-pole transition produced by the electromagnetic field of fast electrons is derived in the Born approximation. Electric dipole-quadrupole interference is also obtained. Deuteron electrodisintegration is further developed, the theory now extending to 150-Mev energy transfers. Characteristic features of electron excitation experiments are mentioned, in particular the possibilities of obtaining information about nuclei and of observing the scattered electrons.

I. INTRODUCTION

NUCLEI bombarded with electrons can be excited by virtue of the interaction of the electron's electromagnetic field with the nucleons. Dipole cross sections have been calculated by Bethe and Peierls,[1] and Peters and Richman,[2] while Wick,[3] and Sneddon and Touscheck[4] also give electric quadrupole. Mullin and Guth[5] obtained the Coulomb correction to the Born approximation for nonrelativistic positive particles. Smith[6] was able to treat all electric poles at once by considering large electron momentum changes. Amaldi *et al.*[7] likewise were able to treat all pole transitions by assuming wave functions for light nuclei.

However, since transitions higher than electric quadrupole could be observed, especially at high energies, these are calculated here. Furthermore, even at moderate energies, dipole-quadrupole interference can be noticed. It is also felt that a discussion regarding the use of electrons in obtaining information about nuclei is worthwhile.

While electrons are treated relativistically, nucleons are taken to be nonrelativistic, terms of order v^2/c^2 being neglected. Nuclear recoil is of order v^2/c^2, as is the 2^{l+1}th pole cross section if the 2^lth is the first nonvanishing one. For the same reason the correction for the finite size of a nucleon can be neglected.[8] Thus the theory is valid for electron energies which are quite high and can suffer losses of the order of a couple hundred Mev, at which point one must begin to take into account finite size effects.

Electric transitions can be derived without reference to any nuclear force theory. Sachs and Austern[9] show that nuclear interaction effects need not be considered in calculations of electric transitions. Unfortunately, however, this is not the case for magnetic transitions.

The Born approximation used is generally valid for relativistic electrons. The nonrelativistic correction factor given by Mullin and Guth[5] can be used approximately here, remembering that their n is now negative. However, for high Z the lack of an accurate Coulomb correction can be serious.

It might be mentioned that μ-mesons can also electromagnetically excite nuclei. Thus the present theory can be applied with merely a change in mass.

II. EXCITATION CROSS SECTIONS

The matrix element for a transition from a nuclear state a and electron state i to a final state bf is $(bf|H'|ai)$, where

$$(f|H'|i)=\sum_n[-(\mathbf{A}_n\cdot\dot{\mathbf{r}}_n+\dot{\mathbf{r}}_n\cdot\mathbf{A}_n)q_n/2c+q_n\phi_n-\mu_n\boldsymbol{\sigma}_n\cdot(\nabla\times\mathbf{A}_n)] \quad (1)$$

is the interaction of the Møller[10] potentials, $\mathbf{A}_n$ and ϕ_n, at the nth nucleon with velocity $\dot{\mathbf{r}}_n$, charge q_n, and magnetic moment μ_n.

$$\mathbf{A}_n=4\pi e\mathbf{a}(K^2-\omega^2/c^2)^{-1}\exp(i\mathbf{K}\cdot\mathbf{r}_n),$$
$$\phi_n=-4\pi e a_0(K^2-\omega^2/c^2)^{-1}\exp(i\mathbf{K}\cdot\mathbf{r}_n). \quad (2)$$

Here $\hbar\mathbf{K}$ and $\hbar\omega$ are momentum and energy losses of the electron, while $\mathbf{a}$ and a_0 are the relativistic spin matrix elements of the Dirac $\boldsymbol{\alpha}$ and 1, respectively.

By expanding the exponential in a Taylor series, the matrix element can be separated into terms of decreasing orders of magnitude. The electric and magnetic parts of the velocity interaction are separated by using the following relations:

$$i\omega(b|(\mathbf{K}\cdot\mathbf{r}_n)^{l-1}\mathbf{a}\cdot\mathbf{r}_n|a)=\tfrac{1}{2}(b|\{\mathcal{P}_{l-1}\mathbf{K}\cdot\dot{\mathbf{r}}_n(\mathbf{K}\cdot\mathbf{r}_n)^{l-2}\}\mathbf{a}\cdot\mathbf{r}_n+(\mathbf{K}\cdot\mathbf{r}_n)^{l-1}\mathbf{a}\cdot\dot{\mathbf{r}}_n+\mathbf{a}\cdot\dot{\mathbf{r}}_n(\mathbf{K}\cdot\mathbf{r}_n)^{l-1}+\mathbf{a}\cdot\mathbf{r}_n\mathcal{P}_{l-1}\mathbf{K}\cdot\dot{\mathbf{r}}_n(\mathbf{K}\cdot\mathbf{r}_n)^{l-2}|a), \quad (3)$$

$$(\mathbf{K}\times\mathbf{a})\cdot(\mathbf{r}_n\times\dot{\mathbf{r}}_n)=(\mathbf{K}\cdot\mathbf{r}_n)\mathbf{a}\cdot\dot{\mathbf{r}}_n-(\mathbf{a}\cdot\mathbf{r}_n)\mathbf{K}\cdot\dot{\mathbf{r}}_n, \quad (4)$$

* Part of a thesis submitted in partial fulfillment of the requirements for the degree of Doctor of Philosophy. This work has been supported in part by the ONR. Some results have been reported at the New York Meeting, January, 1952, of the American Physical Society.

† AEC Predoctoral Fellow, now AEC Postdoctoral Fellow at Cornell University, Ithaca, New York.

[1] H. A. Bethe and R. Peierls, Proc. Roy. Soc. (London) **A148**, 146 (1935).

[2] B. Peters and C. Richman, Phys. Rev. **59**, 804 (1941).

[3] G. C. Wick, Ricerca sci. **11**, 49 (1940).

[4] I. N. Sneddon and B. F. Touscheck, Proc. Roy. Soc. (London) **A193**, 344 (1948). Our results agree with Wick.

[5] C. J. Mullin and E. Guth, Phys. Rev. **82**, 141 (1951).

[6] J. Smith, thesis, Cornell University (1951).

[7] Amaldi, Fidecaro, and Mariani, Nuovo cimento **7**, 757 (1950).

[8] This is of course permitted only for small momentum transfers. However, the contribution of large momentum transfers to the total cross section is generally quite small.

[9] R. G. Sachs and N. Austern, Phys. Rev. **81**, 705 (1951).

[10] C. Møller, Z. Physik **70**, 786 (1931); Ann. Phys. **14**, 531 (1932).

$$\mathcal{P}_{l-1}[\mathbf{K}\cdot\mathbf{r}_n]^{l-2}[(\mathbf{K}\cdot\mathbf{r}_n)\mathbf{a}\cdot\hat{\mathbf{t}}_n] + \mathcal{P}_{l-1}[\mathbf{K}\cdot\mathbf{r}_n]^{l-2}[(\mathbf{a}\cdot\hat{\mathbf{t}}_n)\mathbf{K}\cdot\mathbf{r}_n] = (l-1)[(\mathbf{K}\cdot\mathbf{r}_n)^{l-1}\mathbf{a}\cdot\hat{\mathbf{t}}_n+\mathbf{a}\cdot\hat{\mathbf{t}}_n(\mathbf{K}\cdot\mathbf{r}_n)^{l-1}], \quad (5)$$

where $\mathcal{P}_{l-1}$ indicates the sum of $l-1$ permutations of $l-1$ factors. Hence

$$(b|\,\mathbf{a}\cdot\mathbf{r}_n\exp(i\mathbf{K}\cdot\mathbf{r}_n)+[\exp(i\mathbf{K}\cdot\mathbf{r}_n)]\mathbf{a}\cdot\hat{\mathbf{t}}_n|\,a) = 2\sum_{l=1}^{\infty}(b|\,(i^l/l!)\omega(\mathbf{K}\cdot\mathbf{r}_n)^{l-1}\mathbf{a}\cdot\mathbf{r}_n|\,a) + 2\sum_{l=2}^{\infty}(b|\,(i^{l-1}/l!)\mathcal{P}_{l-1}[\mathbf{K}\cdot\mathbf{r}_n]^{l-2}[(\mathbf{K}\times\mathbf{a})\cdot(\mathbf{r}_n\times\hat{\mathbf{t}}_n)]|\,a). \quad (6)$$

The differential cross section is given by[11]

$$\frac{d\sigma}{d\Omega}=\frac{2\pi}{\hbar}\frac{E_i}{c^2\hbar k_i}\tfrac{1}{2}\sum_i^+\sum_f^+\frac{1}{2j+1}\sum_a\sum_b|(bf|H'|ai)|^2\times\frac{k_fE_f}{8\pi^3c^2\hbar^2}, \quad (7)$$

where $(\hbar\mathbf{k}_i, E_i/c)$ and $(\hbar\mathbf{k}_f, E_f/c)$ are initial and final electron 4-momenta, $2j+1$ is the initial nuclear degeneracy, and the spin sums are over positive energies only. Thus from (1), (2), (6), and (7) the electric 2^l-pole and magnetic 2^{l-1}-pole differential cross sections are respectively

$$\frac{d\sigma_l}{d\Omega}=\frac{e^4E_iE_fk_f}{2(mc^2Q)^2k_i(2j+1)}\sum_i^+\sum_f^+\sum_a\sum_b\left|\frac{i^l}{l!}(b|\,\mathbf{Q}^{(l)}|\,a)\cdot\left[\mathbf{K}^{l-1}\left(a_0\mathbf{K}+\frac{\omega}{c}\mathbf{a}\right)\right]\right|^2, \quad (8)$$

$$\frac{d\sigma_{l-1}^{(m)}}{d\Omega}=\frac{e^2\mu_0^2E_iE_fk_f}{2(mc^2Q)^2k_i(2j+1)}\sum_i^+\sum_f^+\sum_a\sum_b\times\left|\frac{2(l-1)i^{l-1}}{l!}(b|\,\mathbf{M}^{(l-1)}|\,a)\cdot[\mathbf{K}^{l-2}(\mathbf{K}\times\mathbf{a})]\right|^2, \quad (9)$$

where[12]

$$Q=\hbar^2K^2/2m-\hbar^2\omega^2/2mc^2,\quad \mathbf{Q}^{(l)}=\sum_n(q_n/e)(\mathbf{r}_n)^l,$$

$$\mathbf{M}^{(l-1)}=\frac{1}{\mu_0(l-1)}\sum_n\mathcal{P}_{l-1}\mathbf{r}_n^{l-2}\left(\frac{q_n}{2c}\mathbf{r}_n\times\hat{\mathbf{t}}_n+\frac{l}{2}\mu_n\boldsymbol{\sigma}_n\right),$$

$$\mu_0=e\hbar/2Mc.$$

However, only the electric cross section is unambiguous in view of the work of Sachs and Austern,[9] and in general one cannot be confident in Eq. (9).

Performing the spin sums by trace theorems, one obtains

$$\frac{d\sigma_l}{d\Omega}=\frac{e^4k_f\sum_a\sum_b}{2(l!mc^2Q)^2k_i(2j+1)}\{|(b|\,\mathbf{Q}^{(l)}|\,a)\cdot\mathbf{K}^l|^2(2E_iE_f-mc^2Q)+m\omega^2Q[(b|\,\mathbf{Q}^{(l)}|\,a)\cdot\mathbf{K}^{l-1}]^*\cdot[(b|\,\mathbf{Q}^{(l)}|\,a)\cdot\mathbf{K}^{l-1}]+2\hbar\omega E_i|(b|\,\mathbf{Q}^{(l)}|\,a)\cdot(\mathbf{K}^{l-1}\mathbf{k}_f)|^2-2\hbar\omega E_f|(b|\,\mathbf{Q}^{(l)}|\,a)\cdot(\mathbf{K}^{l-1}\mathbf{k}_i)|^2\}. \quad (10)$$

By means of the theorems of the Appendix, Eq. (10) is averaged over the random orientations of these transition moments:

$$\frac{d\sigma_l}{d\Omega}=\frac{8\pi l!^2e^4k_f(2K)^{2l-2}P_l^2}{(2l+1)!^2k_i(mc^2Q)^2}\Bigg\{(2E_iE_f-mc^2Q)K^2+\frac{2l+1}{l}m\omega^2Q+\frac{8\pi\hbar\omega}{l!^2(2l-1)}\sum_{m=1-l}^{l-1}(l^2-m^2)\times[k_f^2E_i|\,\mathcal{Y}_{l-1,m}(\alpha_f,\beta_f)|^2-k_i^2E_f|\,\mathcal{Y}_{l-1,m}(\alpha_i,\beta_i)|^2]\Bigg\}, \quad (11)$$

where α_i, β_i and α_f, β_f are the polar angles describing $\mathbf{k}_i$ and $\mathbf{k}_f$ with $\mathbf{K}$ as the polar axis, and where (23) defines P_l.

In view of the similarity between the above and the photoeffect it was possible to obtain the photoelectric cross section $\sigma_l^{(\gamma)}$ by using the above methods. The result is[13]

$$\sigma_l^{(\gamma)}=2^{2l+3}\pi^3(l+1)!(l-1)!(2l+1)!^{-2}\times\alpha\hbar\omega(\omega/c)^{2l-2}P_l^2, \quad (12)$$

α being the fine structure constant. Division of (11) by (12) gives $dN_l/d\Omega$, the number of virtual quanta per unit energy per unit solid angle for the electric 2^l-pole transition, a purely electrodynamical quantity. Integration over $d\Omega$ gives

$$\sigma_l=\int(dN_l/d\Omega)d\Omega\sigma_l^{(\gamma)}=N_l\sigma_l^{(\gamma)}, \quad (13)$$

$$N_1=\frac{\alpha}{\pi\hbar\omega}\left[-2\frac{k_f}{k_i}+\frac{E_i^2+E_f^2}{(\hbar k_i)^2}\ln\xi\right], \quad (14)$$

$$N_2=\frac{\alpha}{\pi\hbar\omega}\left[\frac{8k_f}{3k_i}\left(\frac{m^2c^4+E_iE_f}{(\hbar\omega)^2}\right)+\frac{E_i^2+E_f^2-2m^2c^4}{(\hbar k_i)^2}\ln\xi\right], \quad (15)$$

[11] Unless otherwise stated, formulas refer to excitation to a discrete level where b is normalized to unity. However, these are readily adapted to disintegrations by normalizing b to unit energy and replacing σ by $d\sigma/dE_f$ or by normalizing b to unit energy and unit solid angle Ω_n and replacing σ by $d^2\sigma/dE_fd\Omega_n$.

[12] The notation used here is such that vectors in corresponding positions from the left edges of the two generalized dyadics separated by a dot have their scalar product formed. For example, $(\mathbf{qrs})\cdot(\mathbf{uvw})=\mathbf{q}\cdot\mathbf{u}(\mathbf{r}\cdot\mathbf{v})\mathbf{s}\cdot\mathbf{w}$; $(\mathbf{u}\cdot\mathbf{r}^2)\cdot\mathbf{s}=\mathbf{u}\cdot\mathbf{r}(\mathbf{r}\cdot\mathbf{s})$; $(\mathbf{r}^n\cdot\mathbf{u}^{n-1})\cdot(\mathbf{s}^n\cdot\mathbf{v}^{n-1})=(\mathbf{r}\cdot\mathbf{u})^{n-1}\mathbf{r}\cdot\mathbf{s}(\mathbf{s}\cdot\mathbf{v})^{n-1}$. Also $\mathcal{P}_3(\mathbf{r}^2\mathbf{s})\cdot(\mathbf{u}^2\mathbf{v})=(\mathbf{r}\cdot\mathbf{u})^2\mathbf{s}\cdot\mathbf{v}+\mathbf{s}\cdot\mathbf{v}(\mathbf{r}\cdot\mathbf{u})^2+\mathbf{r}\cdot\mathbf{u}(\mathbf{s}\cdot\mathbf{v})\mathbf{r}\cdot\mathbf{u}$.

[13] Note that for excitations to discrete levels $\sigma^{(\gamma)}$ has dimensions area times energy here.

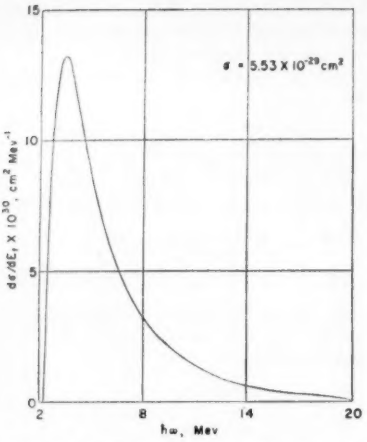

FIG. 1. Energy distribution of scattered electrons (or the outgoing nucleons) from the electric dipole disintegration of the deuteron by electrons with $E_i - mc^2 = 20$ Mev.

$$N_1 = \frac{\alpha}{\pi\hbar\omega}\int_{k_i}^{k_f}\left(2+\frac{4E_i^2E_f^2+4E_iE_fm^2c^4-8m^4c^8}{(\hbar\omega)^4}+\frac{9E_iE_f-m^2c^4}{(\hbar\omega)^2}\right)+\frac{E_i^2+E_f^2-4m^2c^4}{(c\hbar k_i)^2}\ln\xi\Bigg], \quad (16)$$

$$N_1^{(m)} = \frac{\alpha}{\pi\hbar\omega}\left[\frac{E_i^2+E_f^2-2m^2c^4}{(c\hbar k_i)^2}\ln\xi\right], \quad (17)$$

where

$$\xi = (E_iE_f + c^2\hbar^2k_ik_f - m^2c^4)/mc^2\hbar\omega.$$

The magnetic expression (17) is given, as it is quite likely that it can be used in a number of cases, although perhaps with limited validity.

For disintegrating nuclei a preferred nuclear moment orientation exists and the averaging of the Appendix may be omitted. By normalizing b to unit energy and unit solid angle Ω_n, one obtains (10) with $d\sigma_l/d\Omega$ replaced by $d^3\sigma_l/d\Omega dE_f d\Omega_n$. Interference between two adjacent multipole transitions is of order $(\hbar\omega/Mc^2)^{\frac{1}{2}}$ times the lower order transition. In particular the electric dipole-quadrupole interference is

$$\frac{d^3\sigma_{1\sim 2}}{d\Omega dE_f d\Omega_n} = \frac{e^4k_f}{2(mc^2Q)^2k_i(2j+1)}\sum_a\sum_b \times \mathrm{Re}\{[\mathbf{K}^2(2E_iE_f - mc^2Q)+\hbar^2\omega^2\mathbf{K}(\mathbf{k}_i\mathbf{k}_f+\mathbf{k}_f\mathbf{k}_i) - \mathbf{K}(E_f\mathbf{k}_i+E_i\mathbf{k}_f)\hbar\omega\mathbf{K}-\hbar\omega\mathbf{K}^2(E_f\mathbf{k}_i+E_i\mathbf{k}_f)] \cdot[(b|i\mathbf{Q}^{(2)}|a)^*(b|\mathbf{Q}^{(1)}|a)] + m\omega^2Q[(b|i\mathbf{K}\cdot\mathbf{Q}^{(2)}|a)^*]\cdot(b|\mathbf{Q}^{(1)}|a)\}. \quad (18)$$

III. DEUTERON DISINTEGRATION

To obtain explicit cross-section values it is necessary either to evaluate P_l, which entails a knowledge of nuclear wave functions, or to infer its value from photoexcitation experiments. In the case of the deuteron, P_1 has been calculated.[14] The range parameter in the theory was taken to be such that the theoretical electric dipole cross section agrees with photo experiments[15] at 3, 6, and 18 Mev.

Equations (13) and (14) give the energy spectrum of the scattered electrons or ejected nucleons for electric dipole disintegrations. Figure 1 shows this and is also quite typical of what to expect at other E_i's. The peak occurs just below $\sigma_1^{(\gamma)}$'s maximum. It might be mentioned that Fig. 1 resembles quite closely the photonucleon yield had from the bremsstrahlung spectrum of 20-Mev electrons.

Equations (10), (17), and (18) should represent the deuteron's electrodisintegration up to energy transfers of the order of 150 Mev.[16] Discrepancies between existing theory[14] and 80- to 150-Mev photodisintegration experiments[17] would also be observable in electrodisintegration.

IV. DISCUSSION

N_1, like the bremsstrahlung spectrum, can be taken as $C(E_i)/\hbar\omega$ for approximate calculations, where $C(E_i)$ is taken to be independent of $\hbar\omega$. Thus the method of Levinger and Bethe[18] can be utilized to obtain the cross section for excitation of all electric dipole levels (which of course requires a large E_i)

$$\sigma_1 \approx C(E_i)\int\frac{\sigma_1^{(\gamma)}}{\hbar\omega}d(\hbar\omega) \approx \frac{C(E_i)}{(\hbar\omega)_H}\int\sigma_1^{(\gamma)}d(\hbar\omega), \quad (19)$$

where both the harmonic mean absorption energy, $(\hbar\omega)_H$, and $\int\sigma_1^{(\gamma)}d(\hbar\omega)$ are discussed by these authors. For the deuteron with a Yukawa half-exchange potential one finds $\sigma_1 \approx 3.86C(E_i)$ mb, which is a fair approximation even at 20 Mev; using $C(E_i, (\hbar\omega)_H) = 0.0117$ gives $\sigma_1 \approx 0.0452$ mb as compared with 0.0553 mb in Fig. 1.

Two chief methods of observing electron excitation of nuclei are detecting the decay product (1) of the excited state itself and (2) of a state to which the ex-

[14] L. I. Schiff, Phys. Rev. **78**, 733 (1950); J. F. Marshall and E. Guth, Phys. Rev. **78**, 738 (1950).

[15] Russell, Sachs, Wattenberg, and Fields, Phys. Rev. **73**, 545 (1948); Wilson, Collie, and Halban, Nature **163**, 245 (1949); Snell, Barker, and Sternberg, Phys. Rev. **75**, 1290 (1949); Barnes, Stanford, and Wilkinson, Nature **165**, 69 (1950).

[16] The integrated forms of (10) and (18), i.e., $d^2\sigma_l/dE_f d\Omega_n$ and $d^2\sigma_{1\sim 2}/dE_f d\Omega_n$, also exist. See Thie, Mullin, and Guth (to be published).

[17] T. S. Benedict and W. M. Woodward, Phys. Rev. **85**, 924 (1952); W. S. Gilbert and J. W. Rose, Phys. Rev. **85**, 766 (1952).

[18] J. S. Levinger and H. A. Bethe, Phys. Rev. **78**, 115 (1950).

cited state decays. A third possible method might be the observation of the inelastically scattered electrons.

In order to observe the latter it is necessary first to filter out unwanted electron energies. Then for nuclei excited to a discrete level there results an inelastic peak superimposed on a background of electrons which have radiated a quantum. To observe this peak for typical low Z nuclei at moderate energies, the filter must have a band width of the order of 0.001 percent of the energy being observed. However, for disintegrating nuclei the electrons can readily be detected by coincidence counting them with the decay product. Additional information can be had in some cases by this procedure.

Regarding methods (1) and (2), two upper limits on the allowable target thickness are had from the decay product's range and from photoexcitations due to γ-rays produced in the target.[19] The ratio of photon to electron excitations in a target having nt nuclei per unit area is

$$\frac{nt}{2\cos\bar{\theta}}\frac{d\sigma^{(b)}/dE_f}{N},$$

where $\bar{\theta}$ is an average multiple scattering angle and $d\sigma^{(b)}/dE_f$ is the bremsstrahlung cross section per unit energy. In view of the similarity of the latter with N_1 for electric dipole transitions the above ratio is of order $0.0002(Z^2/A)t'/\cos\bar{\theta}$ with t' being in mg/cm.

Multiplying these expressions by 2 and evaluating them instead for the γ-ray production target gives one the relative photon and electron *thin* target yields for the nucleus under investigation, i.e., yields with and without the γ-ray target intercepting the beam (assuming all γ-rays are forward). This ratio of photoexcitations to electroexcitations will determine $(d\sigma^{(b)}/dE_f)/N$ which on comparison with theoretical ratios can give information about the type of transition. However, for high Z in view of the Coulomb correction needed in both numerator and denominator, perhaps some known transition must be used as a normalizer.

APPENDIX

To average $|(b|\mathbf{u}\cdot\mathbf{r}(\mathbf{v}\cdot\mathbf{r})^{l-1}|a)|^2$, where $\mathbf{u}$ and $\mathbf{v}$ are arbitrary vectors over the randomness in nuclear moment orientations and over the axial symmetry of $\mathbf{v}$ with respect to $\mathbf{u}$, one makes the decomposition[20]

$$ur\cos\theta(\mathbf{v}\cdot\mathbf{r})^{l-1}=4\pi uv^{l-1}r^l\sum_{n=0}^{l-1}a_{l-1,n}\sum_{m=-n}^{n}Y_{n,m}^*(\alpha,\beta)\times\left[\left(\frac{(n+m+1)(n-m+1)}{(2n+1)(2n+3)}\right)^{\frac{1}{2}}Y_{n+1,m}(\theta,\phi)+\left(\frac{(n+m)(n-m)}{(2n+1)(2n-1)}\right)^{\frac{1}{2}}Y_{n-1,m}(\theta,\phi)\right],\quad(20)$$

where $a_{l-1,n}$ is nonvanishing only for even $l-1-n$,

$$a_{l-1,n}=\frac{2^{l-1}(l-1)!\lceil(l-1+n)/2\rceil!}{\lceil(l-1-n)/2\rceil!(l+n)!},$$

and where $\mathbf{u}$ is the polar axis of the θ, ϕ describing $\mathbf{r}$, and α, β describing $\mathbf{v}$.

Only the $n=l-1$ term gives a contribution to the electric 2^l-pole transition as defined here. Consequently,

$$\begin{aligned}|(b|\mathbf{u}\cdot\mathbf{r}(\mathbf{v}\cdot\mathbf{r})^{l-1}|a)|^2&\frac{(2l-1)!^2}{16\pi^2u^2(2v)^{2l-2}(l-1)!^4}\\&=\left|\sum_{m=1-l}^{l-1}\left(\frac{(l+m)(l-m)}{(2l-1)(2l+1)}\right)^{\frac{1}{2}}Y_{l-1,m}^*(\alpha,\beta)\times(b|r^lY_{l,m}|a)\right|^2\\&=\frac{1}{2l+1}\left[\sum_{m=-l}^{l}|(b|r^lY_{l,m}|a)|^2\right]\times\left|\sum_{m=1-l}^{l-1}\left(\frac{(l+m)(l-m)}{(2l-1)(2l+1)}\right)^{\frac{1}{2}}Y_{l-1,m}^*(\alpha,\beta)\right|^2\\&=\frac{1}{2l+1}\left[\sum_{m=-l}^{l}|(b|r^lY_{l,m}|a)|^2\right]\times\sum_{m=1-l}^{l-1}\frac{(l+m)(l-m)}{(2l+1)(2l-1)}|Y_{l-1,m}(\alpha,\beta)|^2.\end{aligned}\quad(21)$$

Generalizing,

$$\sum_a\sum_b|(b|\mathbf{Q}^{(l)}|a)\cdot(\mathbf{v}^{l-1}\mathbf{u})|^2/(2j+1)=\frac{64\pi^2u^2(2v)^{2l-2}l!^4}{l^2(2l+1)!^2(2l-1)}P_l^2\sum_{m=1-l}^{l-1}(l^2-m^2)\times|Y_{l-1,m}(\alpha,\beta)|^2,\quad(22)$$

where

$$P_l^2=\sum_{m=-l}^{l}|(b|\sum_n(q_n/e)r_n{}^lY_{l,m}|a)|^2/(2j+1)\quad(23)$$

is the definition of the electric 2^l-pole transition moment. Similarly one can show that

$$\sum_a\sum_b[(b|\mathbf{Q}^{(l)}|a)^*\cdot\mathbf{v}^{l-1}]\cdot[(b|\mathbf{Q}^{(l)}|a)\cdot\mathbf{v}^{l-1}]/(2j+1)=\frac{16\pi(2v)^{2l-2}}{l(2l)!^2(2l+1)}P_l^2.\quad(24)$$

[19] Skaggs, Laughlin, Hanson, and Orlin, Phys. Rev. **73**, 420 (1948); J. S. Blair, Phys. Rev. **75**, 907 (1949). To the authors' knowledge perhaps the only experiment with a sufficiently thin target for pure electrodisintegration was the disintegration of Be[7] by M. Wiedenbeck, Phys. Rev. **69**, 236 (1945).

[20] The method is similar to that of C. J. Mullin and E. Guth, reference 5, and D. L. Falkoff, thesis, University of Michigan (1948).

Ion Concentrations and Recombination in Expanding Low Pressure Sparks*

RICHARD G. FOWLER, WILLIAM R. ATKINSON, AND LUTHER W. MARKS
University of Oklahoma, Norman, Oklahoma

(Received May 12, 1952)

Passage of a capacitor discharge through a low pressure gas between electrodes results in an abrupt expansion of the gas along any avenues open to it. In hydrogen, the expanding luminous gas shows strong Stark broadening. Applying this effect, ion concentrations have been measured ranging up to 30 percent of the initial particle concentration. Intensity measurements indicate that the quantized radiation is a result of electronic recombination. Time and space studies show that the ion concentration appears to reach a maximum at some remote position down the expansion avenue, but that all discharges reach a maximum at about the same time.

I. INTRODUCTION

IT has been noted previously[1] that the luminosity fronts which move down expansion tubes during and subsequent to the discharge of a condenser through a confined gas at low pressure are accompanied by intense continua and a broadening of the spectral lines emitted, especially in hydrogen. Other workers have observed similar broadening in related situations. Finkelnburg,[2] using spark discharges in hydrogen at pressures of one atmosphere and above, noted strong broadening of the Balmer lines and an intense continuum, which he stated to be of different origin from the molecular continuum, and which he called the pressure continuum. He assumed the broadening to be Stark broadening, and calculated ion concentrations from them based on Holtsmark's[3] theory. Craggs and Hopwood[4] have utilized similar effects in their study of the expansion of initial spark streamers into full fledged arc columns during the course of a spark discharge. They point out that the contours of the broadened lines are just what would be expected of Stark broadening, and cite reasons for believing that the luminosity produced during the spark must be largely contributed by electronic recombination. We have observed these peculiar line contours in our discharges and arrived at the same conclusion: that they constitute the strongest evidence for interpreting the broadening as Stark broadening.

II. APPARATUS

The discharges under study were produced in the stem of a T-shaped quartz tube when a 15 μfd capacitor charged to potentials in the range from 3000 to 5000 volts was discharged between electrodes at the ends of the cross arm. The spectroscopic studies on the discharge were carried out with a Hilger E-1 quartz spectrograph. In ion concentration studies the tube was imaged on the slit of the spectrograph, so that a point by point record of the tube's luminosity could be obtained. In radiation law studies, the tube was placed close to the slit of the spectrograph so that light from a limited area of the tube (about 1 cm^2) filled the collimator. Photometry of the spectral lines was carried out on a Knorr-Albers microphotometer.

Accurate plate calibration with a discharge of the brevity of this one posed a problem of some difficulty. Our solution was to compare a series of spectra taken with multiple discharges of the tube on the assumption that reciprocity law failure was small, and that any intermittency effect was eliminated by the intercomparison of the data. This assumption is countenanced in some degree by Mees[5] and by information supplied by the Eastman Company[6] on its materials. It was further borne out by the agreement between data taken at different levels of intensity.

Pure hydrogen was obtained by diffusion through palladium.

III. EXPERIMENTAL RESULTS

1. Ion Concentrations

Half-widths of the broadened Balmer lines H_α, H_β, H_γ, and H_δ were measured as a function of position along the expansion tube for several gas pressures and several capacitor potentials. Each value is the average of three to five measurements at as many levels of exposure. The over-all agreement between half-widths measured at different exposures was quite good, the deviation from the mean being 13 percent.

2. Integrated Intensities

At two selected positions along the discharge tube, total integrated exposures and half-widths were measured simultaneously using the H_β line. Two methods of obtaining the integrated exposures were used with equal success. First, after study of several representative line contours had shown them to be of nearly Gaussian profile, the product of the maximum exposure and half-width for each line was used as a measure of the

* Research supported by the ONR.

[1] Fowler, Goldstein, and Clotfelter, Phys. Rev. **82**, 879 (1951).

[2] W. Finkelnburg, Z. Physik **70**, 375 (1931).

[3] J. Holtsmark, Physik. Z. **20**, 162 (1919); J. Holtsmark, Physik. Z. **25**, 73 (1924).

[4] J. D. Craggs and W. Hopwood, Proc. Phys. Soc. (London) **59**, 755 (1947).

[5] C. E. K. Mees, *Theory of the Photographic Process* (The MacMillan Company, New York, 1942).

[6] Eastman Photographic Plates for Scientific and Technical Use, sixth edition.

integrated exposure. Second, a number of actual profiles were converted from blackening to exposure, point by point, and planimetered as a check on the first method. This second method would be the method of choice were it not for the enormous amount of computation needed.

3. Continuum Studies

There is an intense continuum associated with the Balmer series. A spectrum of the discharge is given in Fig. 1. The origin of this continuum has not been definitely established. Some authors have assigned it a molecular origin, while others[2] speak of it as a "pressure" continuum, although the implication that it is caused by pressure processes seems doubtful. Experiments were therefore conducted to establish additional facts about it.

An attempt was made to detect the existence of a similar continuum in the vicinity of the Paschen series. Inferior dispersion and the rapid fluctuation of sensitivity with wavelength for Eastman *Z* plates made it difficult to interpret the spectra obtained, but a continuum was definitely observed. Whether the distribution of intensities in this continuum was similar to that of the Balmer associated continuum is debatable. The impression given by subjective study of the plates and photometer tracings is that the Balmer associated continuum is more far-flung than the Paschen continuum, extending as it does from some point between the series members at around 5000A to a point well below 2000A.

To investigate the possible molecular origin of the continuum, water vapor was substituted for hydrogen gas in the discharge. Before each discharge the tube was carefully pumped out to remove any hydrogen which might have formed during the previous discharge. The spectrum of the Balmer associated continuum was identical in every detail with that obtained in pure hydrogen. A few additional lines caused by the oxygen atoms were present in the spectrum. The continuum cannot, therefore, be caused by molecular dissociation in H_2.

Contrast of the Balmer associated continuum with the molecular continuum obtained from a glow discharge shows a considerable difference in the distribution of intensities, and calls attention to two other features of distinction: the thousandfold disparity between the intensities of the two continua, and the multiline spectrum which accompanied the molecular continuum but not the Balmer associated continuum.

It seems certain that at least part of the Balmer associated continuum is caused by recombination processes. Unless, however, the random fields of the ions produce some sort of enhancement and Stark broadening of the continuous levels of the atom as well as of the discrete levels, it seems probable that there is some other process than recombination responsible for a large part of the continuum. Another fact which points to this conclusion is that continua are observed in about this same general region 5000–3000A with all of the other gases which have been used, argon, neon, helium, and nitrogen. Hahn and Finkelnburg,[7] and Olsen and Huxford[8] have suggested that a bremsstrahlung process may be needed to explain this.

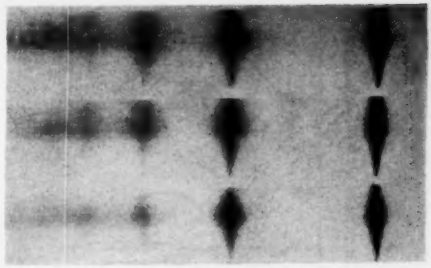

FIG. 1. Stigmatic spectrum of H_2 covering 14 cm of expansion chamber.

4. Level of Excitation

Spectrograms of the discharge in H_2 at pressures less than 1 mm show the tube wall is decomposed during the discharge. The spectra of these wall impurities have shown that excited systems having energies 167 ev above the ground state are present 5 cm down the expansion chamber. Silicon IV lines were graded in intensity, the lines being most intense at the head of the expansion chamber and becoming unobservable 5 cm down the expansion chamber. Silicon III lines had a slight intensity gradation and were visible 8 cm down the expansion chamber. Silicon II lines were visible throughout the entire 14-cm region investigated and had a maximum intensity 6 cm down the side tube. The lines of Silicon I were not present at all near the head of the expansion chamber, but were found throughout the lower 9 cm of the 14-cm region investigated. The ionized forms of oxygen showed analogous behavior.

Two alternative implications of the observed intensity distribution may be obtained. Assuming that the atoms are ionized and excited at the position where their spectra are observed, one would conclude that the energy available for ionizations decreased with distance down the expansion chamber. On the other hand, assuming that the atoms are all ionized in the main discharge tube and that they then travel to the point where their spectra are observed, one would conclude that a Si atom starts its journey as Si IV and captures electrons as it moves down the tube, becoming successively Si III, Si II, and finally Si I.

[7] O. Th. Hahn and W. Finkelnburg, Z. Physik **122**, 37 (1944).
[8] H. N. Olsen and W. T. Huxford, J. SMPTE **55**, 289 (1950).

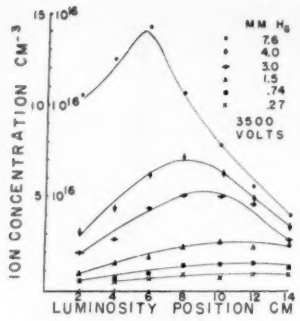

FIG. 2. Ion concentrations at constant voltage.

IV. INTERPRETATION

1. Ion Concentrations

The half-widths δ were interpreted as a measure of ion concentration n according to the relation of Holtsmark

$$\delta = 3.25 A e n^{\frac{1}{2}}.$$

Data computed in this fashion are given in Figs. 2 and 3. These data are weighted averages of the results from all four of the Balmer lines. In the application of Holtsmark's theory, estimation of the Stark coefficient A is a critical matter. Holtsmark defined it as the separation in cm^{-1} per unit field between the extreme Stark components of the line in question. He further assumed a uniform distribution of energy between the outermost components. As he was aware, and as Fig. 4 shows, this is not the case in actuality. Ion concentrations calculated on these assumptions do not show very close agreement between the results reported by different lines of the Balmer series. Considerable improvement can be made by replacing the separation between extreme Stark components by the separation between the widest pair which is strong enough to contribute significantly to the line intensity. In some cases, the extreme component is so weak that it has never as yet been detected experimentally.

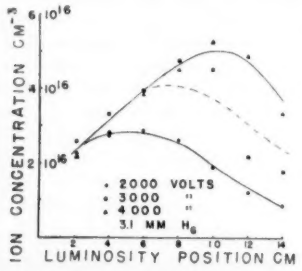

FIG. 3. Ion concentration at constant pressure.

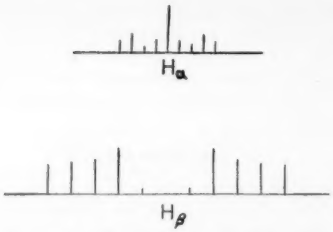

FIG. 4. Stark components of the Balmer lines.

While this change brings the two Holtsmark assumptions into better accord, there is still one feature of the component array which is completely neglected by the Holtsmark theory. The odd members of the Balmer series have a strong undeviated component which the even members lack. This results in a sharp peaking of the H_α and H_γ lines in comparison to the H_β and H_δ lines. A microphotometer tracing which shows this effect is given in Fig. 5. This characteristic serves as an identifying criterion for Stark broadening, but makes the calculations of ion concentration from the odd series members too low.

We have observed another effect which we believe also originates in the Stark effect, which will tend, on the other hand, to make the results from the even members too high. In the presence of extremely high fields, the H_β line is observed to be doubled. This is not ordinary self reversal because it is not shown by the other members of the series. It seems probable that it comes about because of the great vacancy in the center of the array of the even components. Holtsmark's distribution function for random fields has a maximum probability at a finite value of field intensity, and a zero probability of zero field. These two causes may combine to produce the splitting of H_β in strong random fields. The Holtsmark relation suggests another simple test for Stark broadening. The ratios of the half-widths of the various Balmer series members under any given condition are independent of ion concentration and strictly proportional to the ratios of the separations of the outer Stark components selected as discussed above.

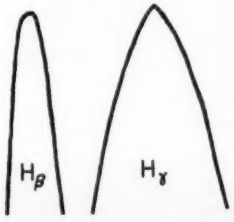

FIG. 5. Contours of H_β and H_γ.

These ratios are given in Table I. The agreement is best between lines of similar contour. The material of which the tube wall is composed has a considerable effect on the ion concentration observed. Higher concentrations are present in quartz tubes than in Pyrex. This fact is inferred from the extinction of the Balmer series at lower values of n in the latter case, although no measurements have been made as yet on line broadening. In Pyrex, the Balmer series terminates at H_9, in quartz at H_4. Rausch von Traubenberg[9] has shown that the complete washing out of the upper quantized states of an atom is a measure of the Stark fields in which the atom is placed. This approach can be used to obtain an independent estimate of the ion concentration, but has been neglected here in favor of the line broadening technique.

A special treatment of the ion concentration data reveals a regularity in the discharge which has not yet been explained. If the abscissas (positions along the expansion chamber) are divided by the initial velocity of the fronts to obtain a time, which we call a "synthetic" time, and the ordinates are divided by the product of gas pressure and capacitor potential, the data at all capacitances and gas pressures can be represented on a single graph within the experimental error. This graph is given in Fig. 6.

TABLE I. Internal consistency of half-widths.

Lines	Experimental average ratios	Theoretical ratios
H_7/H_8	1.3	1.8
H_3/H_8	2.7	2.8
H_8/H_7	2.2	1.6

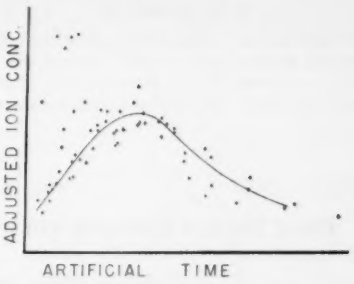

FIG. 6. Ion concentration *versus* time.

2. Radiation Law

An investigation was next made of the relation between ion concentration as determined above, and the total integrated intensity of the H_8 line. A logarithmic plot of these intensities against half-widths interpreted as concentrations is given in Fig. 7.

In actual fact, the quantity measured was not intensity, but exposure. Since the fronts at various pressures (and hence at different ion concentrations) pass the spectrograph's field of view in different time intervals because of their differing speeds, one would expect that a velocity correction should be made on these exposures to give a quantity more nearly proportional to the intensity. To make this correction the exposures should all be multiplied by the velocities of advance of the luminosities.

Another possible correction on the data is suggested by the mirrorgrams from which the front velocities were obtained. Each mirrorgram is a space-time diagram for the luminous gas, and duration of the luminosity at any point of the tube can be found directly from it. The duration of luminosity could be regarded as a measure of exposure time, and this correction might also be made.

Neither of these corrections has been made on the data of Fig. 7. To make such corrections results in a much greater scatter of the experimental points, and introduces systematic differences between the points obtained with different capacitors. (We interpret this result as an indication that many of the radiating systems are not advancing with the front velocity. At first it was thought that perhaps all the radiating systems were at rest with respect to the tube, but Doppler measurements have shown that part of them at least are in motion with velocities which closely approximate the front velocity.) Whether or not the velocity corrections are made, the slope of the curve in Fig. 7 is very nearly two. Uncorrected it is 1.9. Corrected for velocity it is 1.8. Correction for duration reduces the slope to 1.5, but we do not feel that our present method of estimating these durations is adequate to rest any confidence in. Since the uncorrected data are always superior in agreement to the corrected data, it seems that in the final analysis it is possible that these corrections should not be made.

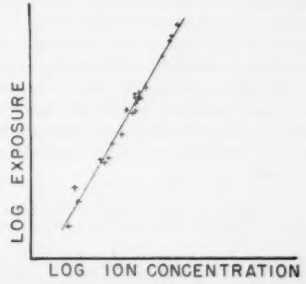

FIG. 7. Intensity *versus* ion concentration.

[9] H. Rausch von Traubenberg, Physik. Z. **31**, 958 (1930).

V. CONCLUSIONS

The expansion of a spark discharge is accompanied by moving luminosity in a highly ionized gas which appears to increase in ion concentration as the luminosity advances. The ion concentration can be estimated by analysis of the Stark broadening of the Balmer lines in hydrogen. The relation between radiated intensity and ion concentration for the moving luminosity is that which would be expected of random electronic recombination.

PHYSICAL REVIEW VOLUME 87, NUMBER 6 SEPTEMBER 15, 1952

Plural Electron Scattering and Its Influence on Electron Diffraction Patterns*

S. G. ELLIS
RCA Laboratories Division, Radio Corporation of America, Princeton, New Jersey
(Received May 12, 1952)

The peak ring intensity (I_R') and the background intensity (I_B') for the most intense rings in the electron diffraction patterns of aluminium and thallium chloride have been measured, as a function of film thickness and accelerating voltage.

It is shown that part of the discrepancy between the results and the theories of Bethe and Morse is due to plural electron scattering.

A semi-empirical theory that includes the effect of plural scattering has been developed to explain the variation of I_R' and I_B' with specimen thickness. The contrast in the patterns (I_R'/I_B') increases rapidly with accelerating voltage and falls rapidly with increase in film thickness. The maximum film thickness (T_{max}) that will yield an observable pattern increases less rapidly than the accelerating voltage, between 50 and 150 kv, in agreement with the results of Möllenstedt.

INTRODUCTION

THE electron diffraction pattern obtained from a thin polycrystalline film of material consists of a number of rings seen against a continuous background. It has long been known that if the film thickness is increased, or the electron speed reduced, the intensity of the rings is reduced as compared with the background. In other words, the contrast in the pattern is reduced. Thomson[1] has attributed this to the attenuation of the diffracted beams by incoherent scattering in the film.

It has been difficult to treat this problem theoretically because of the complex character of electron scattering in the range of voltages and film thicknesses used. When electrons with energies of the order 10^5 electron volts pass through films with thicknesses between a few hundred and a few thousand Angstrom units (hereafter shown as A), they are, in general, scattered more than once, but not so many times that a mean angle of scattering can be calculated readily from a statistical consideration of the individual scattering processes. The phenomena is called plural scattering to distinguish it from multiple scattering in which the number of collisions is large enough to justify the use of statistical procedures. A general review of electron scattering has been given by Zworkin *et al.*,[2] who provide references to the earlier work.

The complexity of plural electron scattering also makes it difficult to interpret the results of scattering experiments. If the angular distribution of electrons scattered incoherently by a thin film is measured, there is no simple way of deducing the nature of the individual scattering processes from the results. On the other hand, the study of electron diffraction patterns permits the measurement of coherent and incoherent scattering in the same film and, hence, yields added information on the scattering process. As acknowledged below, the experimental realization of the method has been greatly facilitated by developments in other branches of experimental physics.

The electrons that enter the rings of a diffraction pattern must have been scattered in one of the following ways: (1) by an elastic coherent scattering process in one crystal; (2) by two or more elastic coherent scatterings in the same crystal. Such electrons have not made any incoherent or inelastic encounters. The electrons that enter the background have been scattered as follows: (3) by a single inelastic or incoherent scattering process; (4) by several successive encounters of type (3); (5) by a coherent scattering process of type (1) followed or preceded by scatterings of type (3) or (4); or (6) by successive elastic coherent scatterings in different crystals. In the type of pattern reported by Cowley, Rees, and Spink[3] such scatterings give rise to recognizable spots in the pattern. In the type of pattern discussed here, where the number of diffracting crystals is large, such spots would form part of the background; with many crystals none of the individual

* Part of this paper was presented at the National Bureau of Standards Symposium on Electron Physics, Washington, D. C., November 5–7, 1951.

[1] G. P. Thomson, Proc. Roy. Soc. (London) **A125**, 352 (1929).

[2] Zworykin, Morton, Ramberg, Hillier, and Vance, *Electron Optics and the Electron Microscope* (John Wiley and Sons, Inc., New York, 1945).

[3] Cowley, Rees, and Spink, Proc. Phys. Soc. (London) **A64**, 609 (1951).

spots are resolved. In all but the thinnest films, scatterings of types (1), (4), and (5) seem to determine the contrast.

Thomson and Cochrane[4] in reviewing the studies of the background in electron diffraction patterns made prior to 1939 concluded that the results were anomalous, in that they did not agree with the theories of Bethe[5] and Morse,[6] based on single scattering.

The work reported here began with a study of the influence of specimen thickness and accelerating voltage on contrast in the electron diffraction patterns from uniform thin films. If, in Fig. 1, Q_R = charge entering a given ring of the pattern, and Q_B = charge entering the background of the ring in the same time, then $C = Q_R/Q_B$ may be defined as the contrast in the pattern for this particular ring. It is convenient in practice to define the peak contrast as $C' = Q_R'/Q_B'$, where Q_R' = peak charge density in the ring, and Q_B' = charge density of the background at the peak density of the ring since this is more readily measured.

The maximum thicknesses of aluminum that will give observable patterns have been measured by Möllenstedt[7] for voltages up to 600 kv. Möllenstedt judged the visibility of the rings from observations made on a fluorescent screen. He states that when one ring could be seen on the screen, several could be observed in a photograph of the same pattern. It was considered desirable to repeat Möllenstedt's measurements in the range of voltages 50 to 150 kv (these being more widely available) determining at least C', as defined above, for a range of specimen thicknesses t. This would remove any ambiguity due to the characteristics of the fluorescent screen or photographic plate.

In the course of this work it was realized that measurements of the relation between Q_R' and t, and Q_B' and t separately would throw some light on the plural scattering process. Such measurements were subsequently made.

DESIGN OF THE EXPERIMENT

The study reported below has been greatly facilitated by recent advances in other fields of physics. Electron microscope studies of thin evaporated films have given us a better understanding of their morphology and, hence, permit us to choose films more nearly ideal for electron diffraction studies than the thinned or sputtered films that were previously in common use. Secondly, the development of the multiple beam interference techniques by Tolansky and particularly the method described by Scott, McLauchlan, and Sennett[8] provides a simple and dependable method of measuring

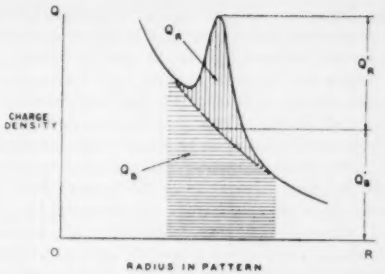

FIG. 1. An illustration of the method of defining the Q's.

the thickness of the films used in the experiments. Finally the more recent studies of the optics and faults of electron diffraction cameras by Hillier and Baker,[9] and Rymer and Butler[10] permit the experiments to be carried out so that the electron diffraction camera contributes negligible disturbances to the charge distribution in the diffraction pattern.

The ideal scattering film for the type of experiment contemplated here would be a system of randomly oriented crystals forming a thin parallel faced slab. The film should be stable in air and under electron bombardment. The material should yield a sharp, well-defined, electron diffraction pattern, and one would prefer to be able to carry out the study on both metallic and nonmetallic films. One material chosen was thallium chloride, since Boswell[11] has shown that it yields very sharp electron diffraction patterns. Electron microscope studies of the thinner films of thallium chloride indicated that the particles had a very flat sessile form. In consequence, one would expect the effect of the inner potential to be small in the pattern. Evaporated thallium chloride films are not stable under the current densities of bombardment that are sometimes employed in the electron microscope but proved to be fairly, though not completely, stable under the current densities of bombardment used in the electron diffraction camera.[12] The thicker films appeared to be continuous so far as could be told from electron microscope observations and from the appearance of shadow images formed in the electron diffraction camera.

Evaporated films of aluminium were also used since this would provide a comparison with the work of Möllenstedt.[7] The aluminium films proved to be sufficiently stable for this work, and while the thinner films appeared to be irregular in thickness, the thicker ones were uniform enough for the present study.

[4] G. P. Thomson and W. Cochrane, *Theory and Practice of Electron Diffraction* (Macmillan and Company, Ltd., London, 1939).
[5] G. Bethe, Ann. Physik **5**, 325 (1930).
[6] P. M. Morse, Physik. Z. **33**, 443 (1932).
[7] G. Möllenstedt, Nachr. Akad. Wiss. Gottingen, Math.-physik. Kl. **1**, 83 (1946).
[8] Scott, McLauchlan, and Sennett, J. Appl. Phys. **21**, 843 (1950).
[9] J. Hillier and R. F. Baker, J. Appl. Phys. **17**, 12 (1946).
[10] T. B. Rymer and C. C. Butler, Phil. Mag. **36**, 515 (1945).
[11] F. W. C. Boswell, Phys. Rev. **80**, 91 (1950).
[12] The idea that evaporated films may be unstable receives support from other observations: recrystallization under electron bombardment in the electron microscope; the fact that even for continuous thin metal films the specific resistivity may be greater than that of the bulk metal; and the variation of the optical properties of thin films with time.

The diffraction camera was an experimental high voltage electron microscope that had previously been used for the study of contrast in electron microscopy. The lenses and specimen holder were rearranged to provide a camera of the sort that has been described by Hillier and Baker.[9] There was no lens between the specimen and the photographic plate so that the electron distribution in the diffraction pattern was not influenced by the chromatic aberration of the focusing lens. The distance from the specimen to the photographic plate was 47 cm and using magnesium oxide as a standard specimen the accelerating potentials were found from a measurement of ring diameters to be 51.5 kv, 99.5 kv, and 150 kv. The focal length of the first lens was made short enough that the width of the central spot was negligible compared with the minimum ring width in the diffraction patterns of thallium chloride or magnesium oxide. Most of the optical path was surrounded by three concentric cylinders of soft iron to provide magnetic shielding. There was, nevertheless, a small magnetic deflection in the final pattern, but care was taken to obtain the photometer traces along directions perpendicular to the direction of the magnetic shift which was small enough to introduce no error into the final results.

As shown by Hillier and Baker, electron scattering from the walls of the instrument and from a diaphragm in the first lens can give a background in the pattern which is not small compared with that produced by the specimen. Diaphragms were used in both lenses, and another was placed below the specimen so that the contribution of electrons scattered from the walls of the instrument was negligible in the pattern except for a very small region near the central spot which was not used in the final measurements. The illuminated area of the specimen was 16-mesh openings of a copper screen which had been etched until the individual openings were approximately 70-micron squares.

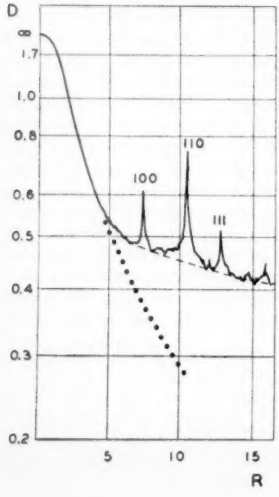

FIG. 2. Photodensitometer trace for one of the thicker thallium chloride films.

A focal series of exposures was taken with no specimen in the camera and with the photographic plate being rapidly traversed during the individual exposures. From these traces it was possible to estimate the residual value of the deflection due to stray magnetic field, the size of the central spot, and the exact current in the focusing lens at which the camera focused. These values were then used in the experiments described below.

EXPERIMENTAL PROCEDURE

The specimen materials, thallium chloride and aluminum, were evaporated onto collodion films supported on copper meshes which were themselves supported on clean glass microscope slides. Close to the meshes the microscope slides were covered by pieces of wire so that there would be a narrow strip on the slide not covered by the evaporated material. It was found that the spacial distribution of evaporated material was by no means uniform from the hair-pin filament used, but this did not influence the results since the thicknesses of the individual specimens were subsequently found by measuring the step height at the strip previously covered by the wire, using the variation of the Tolansky multiple beam interference technique described by Scott, McLauchlan, and Sennett. The collodion films used were found to have thicknesses between 80 and 120A.

When the specimens had been placed in the diffraction camera, the focusing lens was turned off and the resulting shadow image of the specimen was examined on a small fluorescent screen with the aid of a low power light microscope. Care was taken to see that there were no holes in the region of the specimen that was used in the production of the diffraction pattern. This is important since if there had been thinner regions or holes in the specimen or if parts of the evaporated film had turned over and were parallel to the beam, an abnormally high contribution to the ring intensity might have been obtained with the thickest specimens in which the ring intensity normally falls to low values.

In most of the experiments one photographic plate recorded an exposure series in which the exposures were increased by a factor of two, the same specimen and the same accelerating voltage being used in all exposures. In some experiments the accelerating voltage and exposure time were maintained constant, and different specimen thicknesses were used for subsequent exposures. The plates used were Kodak Medium Lantern Slide. They were developed for three minutes in DK-71, diluted one to two, at 68°F.

The variation of photographic density with radial distance was recorded for all plates, using a Leeds and Northrup recording microphotometer. If the density D_P at the peak of the thallium chloride 110 ring is

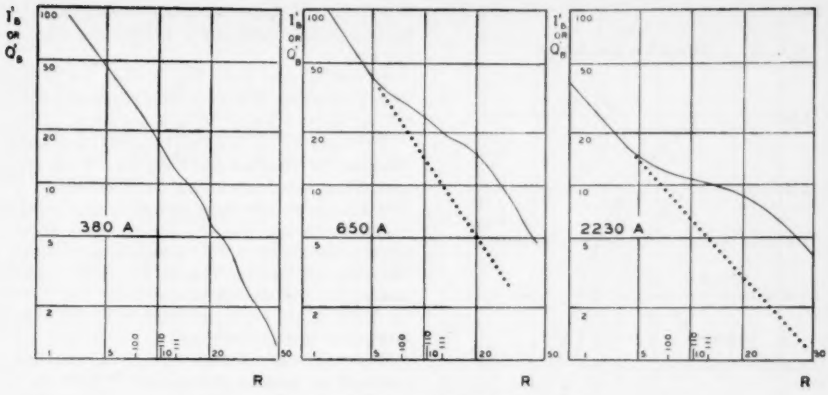

FIG. 3. Radial variation of background current density.

plotted against the log of the exposure (using the results from a single plate where the specimen and the accelerating voltage are identical in all exposures), one obtains a characteristic curve agreeing in shape with the curve published by Baker, Ramberg, and Hillier.[13] A curve of similar shape is obtained if one plots the densities from any other point in the pattern, or if one uses a different voltage, specimen, development time, or temperature. The only difference will be that the curves will be displaced along the log exposure scale. This feature of the characteristic curve has two important uses. All the results can be applied to establishing the shape of the characteristic curve. Any departure of the points of one exposure series from this characteristic curve indicates a change in the specimen during the production of the exposure series.

It was found in this way that the thallium chloride specimens became more crystalline under electron bombardment, eventually reaching a stable state. The results shown below are for the stabilized films.

In this work the characteristic of the photographic plate has been used to measure the ratio of charges. This can be done with acceptable accuracy if all the relevant measurements are made from one plate. It is less satisfactory to compare measurements of charge using plates which have been developed separately.

The trend of the final results will depend upon the division of the observed charges between the rings and the continuous background. The method employed therefore requires some justification, the more so since it may at first sight appear to be somewhat arbitrary. Figure 2 shows a typical photodensitometer trace for one of the thicker thallium chloride films. The background photographic density was estimated by drawing a smooth curve as shown by the dashed line. The corresponding charge densities Q_B' were deduced from the photographic characteristic and were plotted as a function of radial distance R in the photographic plate, Fig. 3. A comparison of the results for different film thicknesses is not justified since the graphs were obtained from different plates. The curves were smooth for thin films but for the thicker films showed an unexpected increase in background in the vicinity of the rings. This increase could be explained if it were supposed that diffraction in the part of the film nearer to the entrance side of the electrons caused fairly intense beams in the direction of the diffraction rings and that these beams were subsequently scattered through small angles to increase the background in the region of the rings when thick films were employed.

In the case of the thick films it will be noticed that $d(\log Q_B')/d(\log R)$ becomes the same outside the low order diffraction rings as at a smaller radius inside the rings. The dotted curve of Fig. 2 shows the values of photographic density corresponding to the dotted extrapolation of the $\log Q_B'$:$\log R$ curve of Fig. 3. The dashed curve of Fig. 2 is considered to be the proper estimate of the background since the shape of the lines for small film thickness will not justify using the dotted curve of Fig. 2 for the background. Secondly, in estimating the contrast it is the local background in the immediate vicinity of the diffraction rings that controls their visibility, and therefore, in any study of the variation of the visibility of these rings with specimen thickness and voltage it is the immediate background to the rings that must be measured.

RESULTS

In the range of film thicknesses (t) for which electron diffraction patterns can be obtained the distribution of background charge changes slowly with increase in film thickness. In a first approximation the charge density for the region inside the diffraction rings decreases with increasing film thickness, while the charge density in

[13] Baker, Ramberg, and Hillier, J. Appl. Phys. **13**, 450 (1942).

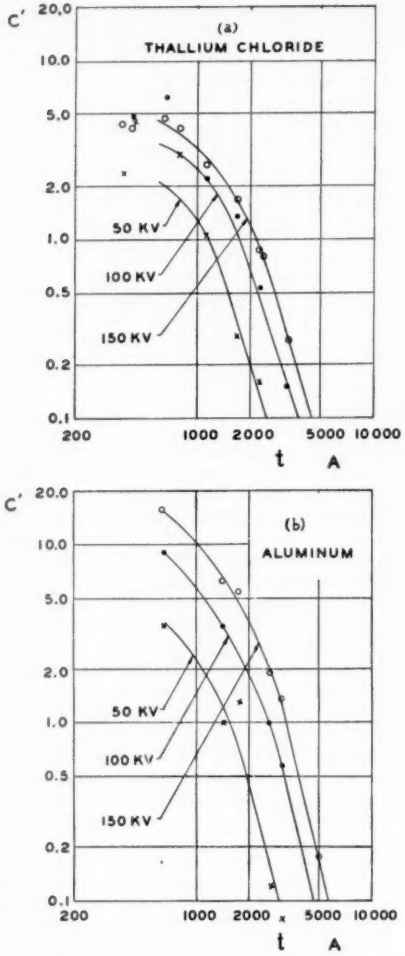

FIG. 4. Peak contrast as a function of film thickness (a) for thallium chloride (b) for aluminum.

the outer parts of the pattern increases with increasing film thickness. The charge density in the vicinity of the inner rings changes very little.

While the ring width at any one voltage is approximately independent of film thickness, the current into the ring decreases rapidly with increasing film thickness so that eventually the ring becomes invisible against the continuous background. Since the ring diameter is proportional to $V^{-\frac{1}{2}}$ (V is the accelerating potential applied to the electron gun) and the contribution of the inner potential to the ring width is proportional to V_i/V (V_i is the inner potential), increasing the voltage on the camera produces a smaller but also sharper pattern.

It will be seen from Fig. 3, that the background charge densities Q_B' are not simply related to the radius R. The slopes $d(\log Q_B')/d(\log R)$ are shown in Table I.

The quantity Q_B' is proportional to the function $f(r)$ discussed by Thomson and Cochrane.[14] From the above results one would judge that the films used by White[15] and Kirchner[16] were thick enough to give considerable plural scattering. For the thinner films above, $f(r)$ approaches the form r^{-2}, though even in these cases the films are not thin enough for single scattering to predominate. It cannot be concluded that the results of Table I are in disagreement with the theoretical work of Bethe[5] and Morse.[6]

With all specimens an increase in electron speed produces an increase in contrast (C'), and this is often very marked (Fig. 4). For example with a 2000A film of thallium chloride the contrast increases from 0.2 to 0.65 to 1.2 on increasing the voltage from 50 to 100 to 150 kv. If, on the other hand, T_{max} denotes the greatest film thickness that will yield an observable pattern (the value of t for which $C'=0.1$ was taken as T_{max} in this study), it is found that T_{max} increases only as $V^{\frac{1}{2}}$ for V less than 150 kv. This trend is in agreement with the results of Möllenstedt,[7] though his values for T_{max} correspond more nearly to those for $C'=0.8$. Möllenstedt, on the other hand, finds that at higher voltages T_{max} increases more nearly as V^2.

The variation of contrast with specimen thickness could not be reconciled with the theoretical treatment due to Thomson.[1] To clarify the situation, measurements of the current entering the ring (I_R) and the current entering the background (I_B), for a given current (I_0) entering the specimen, were made for different specimen thicknesses. If τ is the exposure time for a given pattern,

$$Q_R=I_R\tau, \quad Q_B=I_B\tau.$$

It is convenient to define I_R' and I_B' by

$$Q_R'=I_R'\tau, \quad Q_B'=I_B'\tau.$$

At any one voltage the line profile does not change with specimen thickness; therefore, the functional form

TABLE I. Variation of background charge distribution with specimen thickness.

Specimen	Thickness, A	Voltage, kv	$d(\log Q_B')/d(\log R)$	$\sin\theta/\lambda$
Thallium chloride	380	150	−1.7	0.9×10^8
	380	150	−1.4	0.07×10^8
	2230	150	−1.1	0.07×10^8
Aluminium	650	150	−1.6	0.2×10^8
	5157	150	−1.0	0.2×10^8

[14] Reference 4, p. 103, ff.
[15] P. White, Phil. Mag. **9**, 641 (1930).
[16] F. Kirchner, Ann. Phys. **13**, 38 (1932).

of the relation between I_R' and t is similar to that between I_R and t. Since the absolute value I_0 of the current incident on the specimen is unknown, the absolute values of I_R and I_B are of no interest. It then simplifies the measurements to make them in terms of Q_R' and Q_B', which are in turn proportional to I_R' and I_B'. The significance of the measurements will be more apparent if they are considered in the light of the theory outlined below.

THEORY

We shall calculate the total current entering one diffraction ring I_R and the total current entering the background at the ring I_B. Figure 5 shows the significance of the symbols used.

Consider a current I_0, proceeding in the Ox direction and entering a film of thickness t. The film is considered to be polycrystalline. Of this current, a residue I remains unscattered when it reaches the lamina AB of thickness dx.

Let it be supposed that (1) a fraction Ik_1dx is coherently scattered into the solid angle defined by 2θ and $2\theta+d\theta$; (2) a fraction Ik_2dx is incoherently scattered into the same solid angle; (3) a fraction Ik_3dx is scattered in directions other than the solid angle defined above.

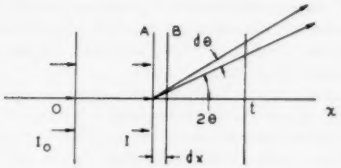

FIG. 5. Geometrical arrangement.

Let $K=k_1+k_2+k_3$. Then

$$I=I_0e^{-Kx}. \tag{1}$$

Of the current Ik_1dx a fraction $e^{-K(t-x)}$ remains unscattered between AB and the exit side of the film.

$$I_R=\int_0^t I_0k_1e^{-Kx}\cdot e^{-K(t-x)}dx$$

$$=I_0k_1e^{-Kt}t. \tag{2}$$

The ring intensity is therefore a maximum for

$$t=1/K, \tag{3}$$

and falls off rapidly with increasing film thickness.

In Fig. 6 $\log(I_R'/t)$ is plotted against t for aluminum at 150 kv.

It might be thought that, employing a similar argument, the background current is

$$I_B=I_0k_2e^{-Kt}t. \tag{4}$$

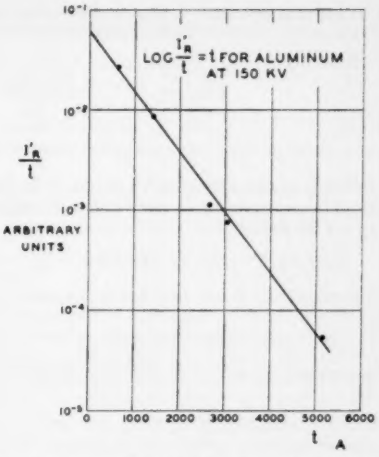

FIG. 6. Variation of ring intensity with specimen thickness.

This is shown in Fig. 7 by the dotted curve. It is evident that electrons are entering the lamina AB in other than the Ox direction and are being scattered into the background at the ring. The effective value of I is, therefore, larger than I_0e^{-Kx}. If one writes

$$I=I_0, \tag{5}$$

then

$$I_B=I_0(k_2/K)(1-e^{-Kt}). \tag{6}$$

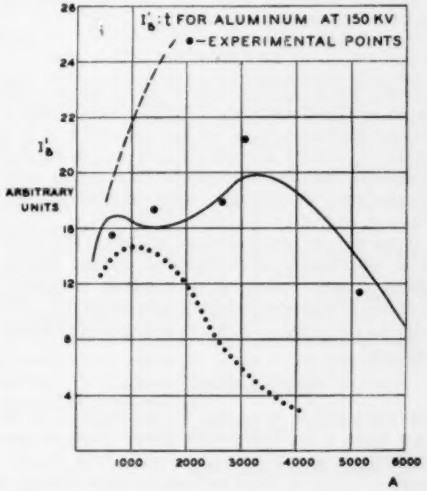

FIG. 7. Variation of background intensity with specimen thickness. The line ····· is a plot of $I_0k_2e^{-Kt}\cdot t$, and the line – – – – – – – a plot of $I_0(k_2/K)(1-e^{-Kt})$.

TABLE II. Scattering parameters for evaporated aluminum films.

Voltage, kv	50	150
K, cm^{-1}	2.22×10^{6}	1.37×10^{6}
α, cm^{-4}	4.46×10^{19}	6.45×10^{18}
k_1'/k_2'	2.9	8.4
K^{-1} (A)	450	730

This is shown by the dashed curve of Fig. 7. A closer analysis of the scattering in successive laminae suggests that I_B has the form

$$I_B = I_0 k_2 e^{-Kt} \cdot t(1+a_1 t+a_2 t^2+a_3 t^3+\cdots), \quad (7)$$

and that empirically it may be possible to approximate I_B by

$$I_B = I_0 k_2 e^{-Kt}(t+\alpha t^n). \quad (8)$$

The contrast for a uniform film of material would then be

$$C = I_R/I_B \quad (9)$$

$$= k_1/[k_2(1+\alpha t^{n-1})]. \quad (10)$$

From the slope of the logC':log$t$ curves at large t, one obtains $n=5$ for aluminium at 150 kv, taking the nearest integral value. In a graph of C':$C't^4$ the intercept on the C' axis is k_1'/k_2' and the slope is $-\alpha$. The dashes again refer to peak values. The graph of logI_R'/t:t gives K (Fig. 6).

The values of K, and α deduced in this way have been substituted in Eq. (8), and the value of I_0k_2 has been adjusted to give the best fit. The result is shown by the full line of Fig. 7.

Table II lists some values of the parameters that have been determined for aluminium.

CONCLUSIONS

These results clearly indicate the important role played by plural scattering in limiting the visibility of electron diffraction rings. In this connection it is of interest to observe the reduction of the background obtained by Boersch[17] through the use of a filter which removed from the scattered beam electrons that had lost more than a few electron-volts of energy.

It can also be seen that plural scattering affects the radial distribution of background current density, making it more uniform as the specimen thickness is increased. It follows that if one fails to obtain diffraction rings but the radial variation of background current is large, i.e.,

$$d(\log Q_B')/d(\log R) > -1.6,$$

then the specimen is lacking in crystallinity. On the other hand, if the background current shows a more uniform distribution a possible cause of failure to obtain diffraction rings may be excessive specimen thickness.

The simple theory given above further indicates that for very thin unsupported films the peak contrast should approach k_1'/k_2'. The experimental points in this region were scattered, perhaps owing to orientation and the presence of a supporting membrane. Mukherjee and Row[18] have suggested that there is an optimum thickness for an evaporated aluminium film which will give a pattern of maximum contrast. This seems probable since with very thin films the lines may be broadened owing to a decreased crystal size, and furthermore, a given amount of amorphous contaminant will produce a proportionately greater background with a thin film specimen. It is not believed that the results of Mukherjee and Row invalidate the theoretical considerations outlined above.

The scheme of analysis shown above permits the construction of a semi-empirical theory of electron scattering for substances that can be obtained in thin crystalline films. In some studies it is important to work as near as possible to the region of single scattering. This is the case when studying the characteristic energy losses of electrons in passing through solids. It can be seen that for single scattering to predominate, we require $t<K^{-1}$ for the particular electron speed being used.

While it appears likely that equations of the form of Eqs. (2), (8), and (10) will hold for other materials and other angles of scattering, it is not possible to make these equations more general in a quantitative sense. One reason for this is that the parameters k_1 and k_1' depend both on the degree of crystallinity of the diffracting material, and the extent to which it may show specific orientation with respect to the incident electron beam. A specimen with a completely random orientation of crystals is perhaps more rare in electron diffraction studies than is generally recognized.

A surprising feature of the results is the rather slow increase of T_{max} with V in the range of voltage used here. T_{max} is the greatest film thickness that will yield observable rings. This implies that the usefulness of an electron diffraction camera may increase less rapidly than the accelerating voltage, but the result, as stated, holds only for the study of uniform thin films. Equations (2) and (8) can be used for the calculation of the contrast when the specimen has other morphologies. This will be the subject of a subsequent paper.

I wish to acknowledge the help given by Dr. E. G. Ramberg and Dr. James Hillier of this laboratory in several discussions of the experimental results. Dr. Ramberg derived the expansion of Eq. (7).

[17] H. Boersch, Optik **5**, 436 (1949).

[18] N. R. Mukherjee and O. Row, J. Appl. Phys. **22**, 681 (1951).

Construction of a Potential from a Phase Shift

RES JOST AND WALTER KOHN*
Institute for Theoretical Physics, Copenhagen, Denmark,
and
Institute for Advanced Study, Princeton, New Jersey
(Received March 21, 1952)

Two methods of constructing a potential, in the form of a series, from a given S phase shift are described. The convergence of one of these is analyzed. Examples show that it can converge comfortably even for potentials which are so strong as to have a bound state. The ambiguity of the potential, connected with the existence of bound states, is discussed in an appendix.

1. INTRODUCTION

SINCE the early work of Faxén and Holtsmark[1] the analysis of scattering data into phase shifts has been a very useful tool for the interpretation of collision processes. In the case of the scattering of two nucleons extensive investigations have been carried out, aimed at interpreting the phase shifts by means of a potential acting between the colliding particles.[2] The question, to what extent a potential can in principle be determined from a knowledge of the phase shifts and binding energies, has therefore been of considerable interest.

The problem has been recently clarified in the papers of Bargmann[3,4] and Levinson.[5] Levinson was able to show that under very general conditions a short range potential is uniquely determined by the phase shift (for all energies) corresponding to a single angular momentum l, provided there exist no bound states with the same angular momentum. Thus the phase shift corresponding to an l so high as to exclude the possibility of a bound state does at least in principle determine the potential unambiguously.

On the other hand, Bargmann has given a number of examples which show that in the presence of bound states there can be a great variety of widely different potentials giving identical phase shifts and binding energies.

It became clear therefore that, for example, for a system with bound S states, the potential is in general not uniquely determined by the S phase shift and binding energies. However, even in the absence of bound states, the Levinson uniqueness proof gave no hint as to how the underlying potential could be constructed.

An attempt in this direction was made by Fröberg.[6] Since his results were somewhat inconclusive, we thought it worthwhile to make a fresh investigation of this problem.

The main part of this paper is devoted to a method of constructing the potential, which is described in Sec. 3. In Secs. 4 and 5 conditions are established under which our procedure leads to a solution. Section 6 contains two examples in which our method is found to converge comfortably, even for nuclear potentials. It was somewhat unexpected to find that it converges even in the presence of a bound state; however, in that case we obtain only one potential out of the whole family which presumably exists.

In Sec. 7 we describe an alternative procedure which has the advantage of omitting one of the steps in our other construction. The convergence is only illustrated by an example. This section may be read independently of the rest of the paper.

The authors are well aware of the limited usefulness of these procedures for an analysis of the two-nucleon system. The difficulties are manifold. Our method, in common with the more usual fitting procedures, requires an accurate knowledge of the S phase for all energies, which is difficult to extract from scattering data, particularly at high energies. In the case of the neutron-proton system there is the additional problem of separating the singlet and triplet scattering. It is well known that the low energy scattering data suffice only to determine two characteristic constants of the potential, but not its exact shape.[7] Finally, it is quite problematical whether the two nucleon system can at all be adequately described by a potential, particularly at high energies.

Possible generalizations to describe higher angular momenta, tensor forces, and Coulomb and relativistic scattering are briefly discussed at the end of the paper.

In Appendix 2 we give a generalization of the Levinson uniqueness theorem which shows which additional parameters are necessary to determine the potential uniquely. The number of these parameters is equal to the number of bound states.

2. PRELIMINARIES

In this section we introduce the concepts which we shall use in constructing the potential from the phase shift.

* Postdoctoral N.R.C. Fellow, 1950–51.
[1] H. Faxén and J. Holtsmark, Z. Physik **45**, 307 (1927).
[2] See, for example, N. F. Mott and H. S. W. Massey, *The Theory of Atomic Collisions* (Clarendon Press, Oxford, 1949) second edition; R. S. Christian and E. W. Hart, Phys. Rev. **77**, 441 (1950); R. S. Christian and H. P. Noyes, Phys. Rev. **79**, 85 (1950).
[3] V. Bargmann, Phys. Rev. **75**, 301 (1949).
[4] V. Bargmann, Revs. Modern Phys. **21**, 488 (1949).
[5] N. Levinson, Kgl. Danske Videnskab Selsab, Mat.-fys. Medd. **25**, No. 9 (1949).
[6] C. E. Fröberg, Arkiv Mat. Astron. Fys. **34A**, No. 28 (1948); **36A**, No. 11 (1949); Arkiv Fys. **3**, No. 1 (1951).
[7] J. M. Blatt and J. D. Jackson, Phys. Rev. **76**, 18 (1949); H. A. Bethe, Phys. Rev. **76**, 38 (1949).

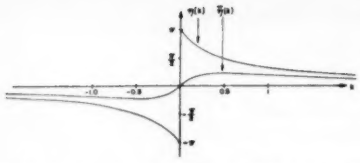

FIG. 1. The phase shift $\eta(k)$ and the modified phase shift $\bar{\eta}(k)$, corresponding to the Eckert potential for the $n-p$ ^3S state.

Restricting ourselves to S states, we start with the Schrödinger equation

$$\varphi''+k^2\varphi=V\varphi, \tag{2.1}$$

where $V(r)$ satisfies the condition

$$\int_0^\infty |V(r)|r dr<\infty. \tag{2.2}$$

Let $f(\pm k, r)$[5] be the two linearly independent solutions of (2.1) which behave at infinity like

$$\lim_{r\to\infty} e^{\pm ikr}f(\pm k, r)=1. \tag{2.3}$$

The S matrix element and the scattering phase are then related to $f(k, 0)$ by the equations

$$S(k)=e^{2i\eta(k)}=f(k, 0)/f(-k, 0), \quad k\gtrless 0. \tag{2.4}$$

Since

$$f(-k, 0)=f^*(k, 0), \tag{2.5}$$

we can write

$$\eta(k)=\mathrm{Im}[\log f(k, 0)]. \tag{2.6}$$

We now extend (2.4) and (2.6) also to negative k values. Owing to (2.5), one then has the relation $\eta(k)+\eta(-k)=2n\pi$, where we may set $n=0$. This gives

$$\eta(-k)=-\eta(k). \tag{2.7}$$

For the further development it is convenient to make the following definitions:

$$\left.\begin{aligned} z&=2ik,\\ g(z, r)=g(2ik, r)&=e^{ikr}f(k, r),\\ g(z)&=g(z, 0).\end{aligned}\right\} \tag{2.8}$$

Then (2.6) reads

$$\eta(k)=\mathrm{Im}[\log g(2ik)]. \tag{2.9}$$

The differential equation (2.1) with the initial values (2.3) can be combined in the integral equation[4]

$$g(z, r)=1+\int_r^\infty \frac{1}{z}[1-e^{-z(r'-r)}]V(r')g(z, r')dr'. \tag{2.10}$$

As shown in reference 4 this equation can be solved by iteration for $\mathrm{Re}[z]\geqq 0$, whenever (2.2) is satisfied. The resulting series converges uniformly in z and r. It follows that $g(z, r)$ and especially $g(z)$ is regular in $\mathrm{Re}[z]>0$ and continuous in $\mathrm{Re}[z]\geq 0$. The zeros, ξ_i of $g(z)$ in $\mathrm{Re}[z]>0$, lie on the real axis (corresponding to negative imaginary values of k) and are simple; they determine the energies of the bound states:[6]

$$E_i=-\tfrac{1}{4}\xi_i^2. \tag{2.11}$$

With the help of (2.2) one verifies easily that

$$\lim_{z\to\infty} g(z)=1 \tag{2.12}$$

uniformly for $\mathrm{Re}[z]\geqq 0$. Hence, by (2.9), we can set

$$\eta(\infty)=0. \tag{2.13}$$

If, furthermore,

$$\int_0^\infty r^2|V(r)|dr<\infty,$$

one can show[5] that

$$\left.\begin{aligned} \eta(+0)&=m\pi \quad \text{if} \quad g(0)\neq 0,\\ \eta(0)&=(m+\tfrac{1}{2})\pi \quad \text{if} \quad g(0)=0,\end{aligned}\right\} \tag{2.14}$$

where m is the number of bound states.

In the absence of bound states $\log g(z)$ is regular for $\mathrm{Re}[z]>0$; if further $g(0)\neq 0$, it is continuous for $\mathrm{Re}[z]\geq 0$ and its imaginary part on the imaginary z axis is given by the phase shift according to (2.9). We can therefore express $\log g(z)$ in $\mathrm{Re}[z]\geq 0$ in terms of the phase shift $\eta(k)$ by Poisson's integral

$$\log g(z)=-\frac{2i}{\pi}\int_{-\infty}^{\infty}\frac{\eta(k')}{2ik'-z}dk', \tag{2.15}$$

where we have made use of (2.12).

When the potential does have bound states, both $\eta(k)$ and the energies of the bound states are required for the construction of $g(z)$. This function now has zeros at the ξ_i and hence $\log g(z)$ has logarithmic branch points there. However, the function $\mathfrak{g}(z)$, defined by

$$\mathfrak{g}(z)=g(z)\prod_i^m\frac{(z+\xi_i)}{(z-\xi_i)}, \tag{2.16}$$

does not vanish for $\mathrm{Re}[z]>0$ and furthermore has the same asymptotic properties as $g(z)$. It can therefore be expressed in terms of its phase $\bar{\eta}(k)$ on the imaginary z axis:

$$\log \mathfrak{g}(z)=-\frac{2i}{\pi}\int_{-\infty}^{\infty}\frac{\bar{\eta}(k)}{2ik-z}dk, \tag{2.17}$$

where by the definition of $\mathfrak{g}(z)$,

$$\bar{\eta}(k)=\eta(k)-2\sum_{i=1}^m\tan^{-1}\frac{\xi_i}{2k} \tag{2.18}$$

(see Fig. 1).

[5] R. Jost, Helv. Phys. Acta **20**, 256 (1947).

Once $\mathfrak{g}(z)$ is calculated, $g(z)$ can be obtained from it by Eq. (2.16).

It is now convenient to replace $g(z)$ by an auxiliary potential $V_1(r)$. For this purpose we iterate Eq. (2.10) which gives

$$g(z)-1=\sum_{l=1}^{\infty}\int_0^{\infty}dr_1\int_{r_1}^{\infty}dr_2\cdots\int_{r_{l-1}}^{\infty}dr_l\frac{1}{z^l}\times(1-e^{-zr_1})(1-e^{-z(r_2-r_1)})\cdots(1-e^{-z(r_l-r_{l-1})})\cdot V(r_1)V(r_2)\cdots V(r_l). \quad (2.19)$$

For small $V(r)$ this equation reduces to

$$g(z)-1\cong\frac{1}{z}\int_0^{\infty}dr(1-e^{-zr})V(r), \quad (2.20)$$

which suggests the introduction of the auxiliary potential $V_1(r)$ defined by

$$g(z)-1=\frac{1}{z}\int_0^{\infty}dr(1-e^{-zr})V_1(r), \quad (2.21)$$

or, from (2.19), by

$$\int_0^{\infty}(1-e^{-rz})[V_1(r)-V(r)]dr=\sum_{l=2}^{\infty}\int_0^{\infty}dr_1\cdots\int_{r_{l-1}}^{\infty}dr_l\frac{1}{z^{l-1}}(1-e^{-zr_1})\times(1-e^{-z(r_2-r_1)})\cdots(1-e^{-z(r_l-r_{l-1})})\cdot V(r_1)V(r_2)\cdots V(r_l). \quad (2.22)$$

Under the assumption

$$|rV(r)|<M, \quad (2.23)$$

the right-hand side of (2.22) tends to zero as z approaches infinity. This suggests that the solution $V_1(r)$ of (2.22) satisfies the condition

$$\int_0^{\infty}[V_1(r)-V(r)]dr=0, \quad (2.24)$$

which will be verified after the solution is obtained (see Appendix 1). Equation (2.22) now takes the form

$$\int_0^{\infty}e^{-sr}[V(r)-V_1(r)]=\sum_{l=2}^{\infty}\int_0^{\infty}dr_1\cdots\int_{r_{l-1}}^{\infty}dr_l\frac{1}{z^{l-1}}\times(1-e^{-zr_1})\cdots(1-e^{-z(r_l-r_{l-1})})\cdot V(r_1)V(r_2)\cdots V(r_l). \quad (2.25)$$

Next we formally carry out the Laplace-inversion[9] and obtain

$$V_1(r)=V(r)-\sum_{l=2}^{\infty}\int_0^{\infty}dr_1\int_{r_1}^{\infty}dr_2\cdots\int_{l-1}^{\infty}dr_l\times K(r,r_1r_2\cdots r_l)V(r_1)V(r_2)\cdots V(r_l), \quad (2.26)$$

where

$$\begin{aligned}K(r,r_1\cdots r_l)&=L^{-1}\left\{(1-e^{-zr_1})\frac{1}{z}(1-e^{-z(r_2-r_1)})\cdots\frac{1}{z}(1-e^{z(r_l-r_{l-1})});r\right\}\\&=\int_0^{r_1}dt_1\int_0^{r_2-r_1}dt_2\cdots\int_0^{r_l-r_{l-1}}dt\times L^{-1}\{z\cdot e^{-z(t_1+t_2+\cdots+t_l)};r\}\\&=\int_0^{r_1}dt_1\int_0^{r_2-r_1}dt_2\cdots\int_0^{r_l-r_{l-1}}dt_l\times\delta^l(r-t_1-t_2-\cdots-t_l)\end{aligned} \quad (2.27)$$

or

$$K(r,r_1r_2\cdots r_l)=\frac{\partial}{\partial r}\int_0^{r_1}dt_1\int_0^{r_2-r_1}dt_2\cdots\int_0^{r_l-r_{l-1}}dt_l\times\delta(r-t_1-t_2-\cdots-t_l); \quad (2.28)$$

$\delta(x)$ denotes Dirac's δ-function.

The proof that the series (2.26) for V_1 converges and satisfies Eqs. (2.25), (2.24), and therefore (2.22) is given in Appendix 1.

The results of this paragraph can be summarized as follows:

If a potential satisfies the conditions

$$\int_0^{\infty}r|V(r)|dr<\infty, \quad (2.29)$$

$$\int_0^{\infty}r^2|V(r)|dr<\infty, \quad (2.30)$$

$$r|V(r)|<M<\infty, \quad (2.31)$$

then

(a) $\eta(k)$ is an odd function which is continuous and differentiable except possibly at $k=0$ [see Eq. (2.14)] and which tends to zero as $k\to\pm\infty$.

[9] G. Doetsch, *Theorie und Anwendung der Laplace Transformation* (Dover Publications, New York, 1943).

(b) $g(z)$ is regular for $\mathrm{Re}[z]>0$ and is expressible in terms of $\eta(k)$ and the energy values of the bound states by Eqs. (2.16)–(2.18); for $z\to\infty$, $g(z)\to 1$.

(c) There exists a potential $V_1(r)$, satisfying (2.21), which obeys the inequalities

$$\int_0^\infty r|V_1(r)|dr<\infty, \tag{2.32}$$

$$r|V_1(r)|<M_1. \tag{2.33}$$

3. CONSTRUCTION OF THE POTENTIAL FROM THE PHASE

We now turn to the construction of a potential which will reproduce a given phase shift $\eta(k)$ and given energy levels.

In the presence of bound states it is by no means certain that, for given phase and binding energies, this inversion problem has a unique solution. In fact, Bargmann[4] has constructed continuous families of potentials with identical phase shifts and bound states. A complete solution of the inversion problem would consist of a construction of all potentials corresponding to a given phase and binding energies. The method of the present paper, however, yields at best a single potential out of this manifold.

On the other hand, when $\eta(0)=0$, so that no bound states exist, these complications do not arise if one admits only potentials satisfying the conditions (2.29) and (2.30), and the inversion problem has at most a single solution. This result has been proved by Levinson.[5]

Our procedure will be to construct successively the functions $g(z)$, $V_1(r)$, and $V(r)$ from Eqs. (2.16)–(2.18), (2.21), and (2.26).

We first construct from the given phase and energy levels the function $g(z)$ by means of (2.16)–(2.18). We then postulate that there exists a solution $V_1(r)$ of Eq. (2.21). In particular, if the expression

$$rV_1(r)=\lim_{R\to\infty}\frac{1}{2\pi i}\int_{x_0-iR}^{x_0+iR}e^{rz}\frac{d}{dz}z(g(z)-1)dz,\ x_0>0 \tag{3.1}$$

vanishes for $r<0$, is of bounded variation, and is absolutely integrable, it represents the solution.[9] We assume further that

$$r|V_1(r)|<M_1<\infty, \tag{3.2}$$

$$\int_0^\infty r|V_1(r)|dr=I_1<\infty. \tag{3.3}$$

It will be recalled from (c) in Sec. 2, that these conditions are in fact satisfied whenever the phase and energy levels are due to a potential $V(r)$ satisfying (2.29) and (2.31).

Finally, we formally solve the integral equation (2.26) for $V(r)$ by successive approximation. To do this, we introduce an auxiliary parameter λ, by which we multiply $V_1(r)$ and expand $V(r)$ in a power series in λ:

$$V(r)=\lambda V_1(r)+\sum_{m=2}^\infty \lambda^m V_m(r). \tag{3.4}$$

Introducing (3.4) into the integral equation gives

$$\lambda V_1(r)=V(r)-\sum_{l=2}^\infty\int_0^\infty dr_1\int_{r_1}^\infty dr_2\cdots\int_{r_{l-1}}^\infty dr_l \times K(r,r_1\cdots r_l)V(r_1)V(r_2)\cdots V(r_l) \tag{3.5}$$

and equating to zero the coefficient of λ^m, $m\geqq 2$ leads to the recursion relation

$$V_m(r)=\sum_{l=2}^m\sum_{r_1+r_2+\cdots+r_l=m}\int_0^\infty dr_1\int_{r_1}^\infty dr_2\cdots\int_{r_{l-1}}^\infty dr_l \times K(r,r_1r_2\cdots r_l)V_{r_1}(r_1)V_{r_2}(r_2)\cdots V_{r_l}(r_l). \tag{3.6}$$

When this is solved, we set $\lambda=1$ and obtain formally

$$V(r)=\sum_{m=1}^\infty V_m(r). \tag{3.7}$$

We will show in the next section, that the series (3.7) converges (almost everywhere), provided that

$$\int_0^\infty r|V_1(r)|dr\leqq 2\ln 2-1=0.38630. \tag{3.8}$$

We cannot prove that the $V(r)$ defined by (3.7) will satisfy the integral equation (2.26). However, we will show in Sec. 5 that under the condition

$$\sum_{m=1}^\infty\int_0^\infty |V_m(r)|rdr=K<\infty. \tag{3.9}$$

$V(r)$ exists (almost everywhere) and satisfies (2.22) and therefore (2.19). From this it follows that $V(r)$ reproduces the original phase $\eta(k)$. Since the condition (3.8) implies (3.9), we are sure that (3.7) represents a solution of the inversion problem.

The estimate (3.8) is probably rather crude and potentials for which it is satisfied cannot have bound states. The examples discussed in Sec. 6 converge considerably beyond this estimate, in fact well into the region of bound states.

4. THE CONVERGENCE PROOF

In this section we will prove that (3.8) implies the convergence of the series in (3.7) and we will derive properties of the $V(r)$ thus defined. To do this we need first some properties of the kernels $K(r, r_1\cdots r_l)$, defined in (2.28), to which we devote a subsection.

The Kernels $K(r, r_1 \cdots r_l)$[10]

These are conveniently discussed with the help of the non-negative quantities

$$M(r, u_1 \cdots u_l) = \int_0^{u_1} dt_1 \int_0^{u_2} dt_2 \cdots \int_0^{u_l} dt_l \times \delta(r - t_1 - t_2 - \cdots - t_l). \quad u_k \geqq 0. \tag{4.1}$$

We obviously have

$$\int_0^\infty e^{-sr} M(r, u_1 \cdots u_l) dr = \prod_{k=1}^{l} \frac{1}{s}(1 - e^{-su_k}). \tag{4.2}$$

By multiplying out the product on the right-hand side in (4.2) and Laplace-inverting term-by-term, we get

$$M(r, u_1 \cdots u_l) = \frac{1}{(l-1)!}\{[r]^l - \sum_k [r - u_k]^l + \sum_{k<s} [r - u_k - u_s]^l \cdots + (-1)^l [r - u_1 - u_2 - \cdots - u_l]^l\}, \tag{4.3}$$

where

$$[x] = \begin{cases} x & \text{for } x \geqq 0 \\ 0 & \text{for } x < 0. \end{cases} \tag{4.4}$$

It follows from (4.1) that

$$\left.\begin{aligned} &M(r, u_1 \cdots u_l) = 0 \\ \text{for} \quad &r < 0 \quad \text{and} \quad r > \sum_{k=1}^{l} u_k. \end{aligned}\right\} \tag{4.5}$$

Furthermore, it is easy to see from (4.1) that $M(r, u_1 \cdots u_l)$ as a function of r is symmetrical around the point

$$r_0 = \tfrac{1}{2} \sum_{k=1}^{u} u_k$$

and monotonically increasing for $r < r_0$ and correspondingly decreasing for $r > r_0$.

Finally, by integrating (4.1) first over t_l we get the estimate $M(r, u_1 \cdots u_l) \leqq u_1 u_2 \cdots u_{l-1}$, and since u_l may be taken as the largest u_k, it follows that

$$M(r, u_1 \cdots u_l) \leqq (u_1 u_2 \cdots u_l)^{(l-1)/l}. \tag{4.6}$$

By the definition (2.28) of the kernels we have

$$\left.\begin{aligned} &K(r, r_1 \cdots r_l) = \frac{\partial}{\partial r} M(r, u_1 \cdots u_l), \\ &u_1 = r_1 \quad u_2 = r_2 - r_1 \cdots u_l = r_l - r_{l-1}; \end{aligned}\right\} \tag{4.7}$$

but from (4.1)

$$\frac{\partial M(r, u_1 \cdots u_l)}{\partial r} = M(r, u_1 \cdots u_{l-1}) - M(r - u_l, u_1 \cdots u_{l-1}), \tag{4.8}$$

and since $r_i \geqq u_i$, (4.6) gives the estimate

$$|K(r, r_1 r_2 \cdots r_l)| \leqq (r_1 r_2 \cdots r_{l-1})^{(l-2)/(l-1)} \leqq (r_1 r_2 \cdots r_l)^{(l-2)/l}. \tag{4.9}$$

We also require an estimate for

$$\int_0^\infty r |K(r, r_1 \cdots r_l)| dr \leqq \int_0^\infty r M(r, u_1 \cdots u_{l-1}) dr + \int_0^\infty r M(r - u_l, u_1 \cdots u_{l-1}) dr; \tag{4.10}$$

but

$$\int_0^\infty r M(r - \alpha, u_1 \cdots u_{l-1}) dr = -\frac{d}{dz} \int_0^\infty e^{-sr} M(r - \alpha, u_1 \cdots u_{l-1}) dr \Big|_{s=0} = -\frac{d}{dz} e^{-\alpha z} \prod_{k=1}^{l-1} \frac{1}{z}(1 - e^{-zu_k}) \Big|_{z=0} \tag{4.11}$$

and therefore

$$\int_0^\infty r |K(r, r_1 \cdots r_l)| dr \leqq -\frac{d}{dz}(1 + e^{-zu_l}) \prod_{k=1}^{l-1} \frac{1}{z}(1 - e^{-zu_k}) \Big|_{z=0} \leqq u_1 u_2 u_3 \cdots u_{l-1} (\sum_{k=1}^{l} u_k) \tag{4.12}$$

or with (4.7)

$$\int_0^\infty r |K(r, r_1 \cdots r_l)| dr \leqq r_1 r_2 \cdots r_l. \tag{4.13}$$

The explicit form of $K(r, r_1 r_2)$ is shown in Fig. 2.

The Convergence of the Series

First we notice that the conditions (3.2) and (3.3) are sufficient to ensure the existence and integrability of $rV_m(r)$ [compare (4.9) and Fig. 2]. From (3.6) we get the estimate

$$I_m = \int_0^\infty r |V_m(r)| dr \leqq \sum_{l=2}^{m} \sum_{\Sigma r_k = m} \int_0^\infty dr_1 \int_{r_1}^\infty dr_2 \cdots \int_{r_{l-1}}^\infty dr_l \times \int_0^\infty r |K(r, r_1 \cdots r_l)| dr |V_{r_1}(r_1)| \cdots |V_{r_l}(r_l)|, \tag{4.14}$$

[10] These kernels are discussed by E. Rufener, *Mitteilungen der Vereinigung Schweizer Versicherungsmathematiker* (to be published).

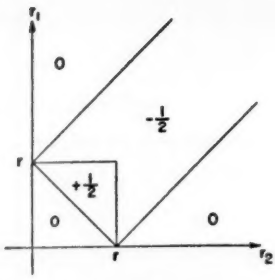

FIG. 2. The kernel $K(r, r_1 r_2)$ used in the construction of the second and higher approximations [see Eq. (3.6)].

and with (4.13),

$$I_m \leqq \sum_{l=2}^{m} \sum_{\Sigma \nu_k = m} \int_0^\infty dr_1 \int_{r_1}^\infty dr_2 \cdots \int_{r_{l-1}}^\infty dr_l \prod_{k=1}^{l} r_k |V_{\nu_k}(r_k)|. \quad (4.15)$$

For symmetry reasons this can be rewritten as

$$I_m \leqq \sum_{l=2}^{m} \frac{1}{l!} \sum_{\Sigma \nu_k = m} \prod_{k=1}^{l} \left[\int_0^\infty r |V_{\nu_k}(r)| dr \right] \quad (4.16)$$

and finally

$$I_m \leqq \sum_{l=2}^{\infty} \frac{1}{l!} \sum_{\Sigma \nu_k = m} I_{\nu_1} I_{\nu_2} \cdots I_{\nu_l} (m = 2, 3 \cdots). \quad (4.17)$$

If we now define J_m by

$$\left.\begin{aligned} J_1 &= I_1, \\ J_m &= \sum_{l=2}^{\infty} \frac{1}{l!} \sum_{\Sigma \nu_k = m} J_{\nu_1} J_{\nu_2} \cdots J_{\nu_l} (m = 2, 3 \cdots), \end{aligned}\right\} \quad (4.18)$$

then we have

$$I_m \leqq J_m \quad (m = 1, 2, 3 \cdots). \quad (4.19)$$

To solve the recursion (4.18) we introduce the generating function

$$W(x) = \sum_{m=1}^{\infty} J_m x^m; \quad (4.20)$$

then substituting from (4.18) gives

$$W(x) - I_1 x = e^{W(x)} - 1 - W(x) \quad (4.21)$$

or

$$x = I_1^{-1} [2W(x) + 1 - e^{W(x)}]. \quad (4.22)$$

The singularity, which determines the convergence radius of (4.20), is located at the smallest root of the equation

$$dx/dW = 0 = [2 - e^{W(x)}]/I_1, \quad (4.23)$$

or

$$W(x_0) = \log 2 = 0.69315 \quad (4.24)$$

and

$$x_0 = [2 \log 2 - 1]/I_1 = 0.38630/I_1. \quad (4.25)$$

The series (4.20) will therefore converge at $x = 1$, provided that

$$I_1 \leqq 0.38630; \quad (4.26)$$

note that in this case

$$W(1) \leqq 0.69315. \quad (4.27)$$

Summarizing, we have the result: If (4.26) is satisfied, then

$$\sum_{m=1}^{\infty} \int_0^\infty r |V_m(r)| dr \leqq 0.69315. \quad (4.28)$$

Applying now a theorem from the theory of real functions,[11] we can conclude that

$$\sum_{m=1}^{\infty} r V_m(r) = r V(r) \quad (4.29)$$

converges almost everywhere to an integrable function (in the sense of Lebesgue) and that

$$\int_0^\infty r V(r) dr = \sum_{m=1}^{\infty} \int_0^\infty r V_m(r) dr; \quad (4.30)$$

therefore,

$$\int_0^\infty r V(r) dr \leqq \sum_{m=1}^{\infty} I_m \leqq 0.69315 < 1, \quad (4.31)$$

and according to a well-known theorem it follows that if (4.26) holds, the potential $V(r)$ does not produce bound states.[12]

We have now constructed a $V(r)$ and shown that it leads to a finite

$$\int_0^\infty r |V(r)| dr.$$

We can, however, not be sure that it satisfies the Eq. (2.26) from which it was constructed, since our estimates for the kernels $K(r, r_1 \cdots r_l)$ do not guarantee the proper convergence of the integrals. However, to prove that a potential reproduces a given phase shift (and given bound states, when such exist), it is sufficient to show that it satisfies (2.22). This will be done in the next section.

5. PROOF THAT $V(r)$ REPRODUCES THE PHASE

The result, which we want to prove in the paragraph, is a little more general than would be necessary to prove that the $V(r)$ constructed in Sec. 4 reproduces the phase $\eta(k)$. It is the following:

If the $V_m(r)$ constructed by (3.6) have the property

[11] C. Carathéodory, *Vorlesungen ueber reelle Funktionen* (B. G. Teubner, Leipzig, 1918), p. 605, Satz 3.

[12] A potential can have a bound state only if $\int_0^\infty r |V(r)| dr \geqq 1$; see, for example, R. Jost and A. Pais, Phys. Rev. **82**, 840 (1951).

that

$$\sum_{m=1}^{\infty} I_m = K < \infty, \tag{5.1}$$

where

$$I_m = \int_0^\infty r|V_m(r)|\,dr, \tag{5.2}$$

then

$$r\cdot\sum_{m=1}^{\infty} V_m(r) = r\cdot V(r) \tag{5.3}$$

converges almost everywhere to an integrable function; $V(r)$ satisfies Eq. (2.22) and therefore reproduces the phase $\eta(k)$ and the bound states.

The existence of $V(r)$ as well as the inequality

$$\int_0^\infty |V(r)|r\,dr \leqq K \tag{5.4}$$

follows from (5.1) by an argument similar to that of the last section.

To show that $V(r)$ satisfies Eq. (2.22) we are now going to transform the left-hand side of that equation until it is equal to the right-hand side, but before we do this, we need the convergence of a series, which is related to the sequence of the I_m's.

We consider the analytical function

$$f(x) = \sum_{m=1}^{\infty} I_m x^m \tag{5.5}$$

which is, according to (5.1), regular for $|x|<1$ and continuous for $|x|\leqq 1$. The same therefore holds for

$$F(x) = e^{f(x)} = 1 + \sum_{m=1}^{\infty} a_m x^m, \tag{5.6}$$

where

$$a_m = \sum_{l=1}^{m} \frac{1}{l!} \sum_{\Sigma\nu_k = m} I_{\nu_1} I_{\nu_2} \cdots I_{\nu_l} \geqq 0. \tag{5.7}$$

In particular, $F(1)$ exists so that

$$F(1) = 1 + \sum_{m=1}^{\infty} a_m < \infty, \tag{5.8}$$

and therefore the series $\sum_{m=1}^{\infty} a_m$ converges.[13]

Let ϵ be an arbitrarily small positive number; then we can determine an N in such a way that

$$\sum_{l=N+1}^{\infty} \frac{K^l}{l!} < \frac{\epsilon}{3}, \tag{a}$$

$$\sum_{m=N+1}^{\infty} I_m < \frac{\epsilon}{3}, \tag{b}$$

$$\sum_{m=N+1}^{\infty} a_m < \frac{\epsilon}{3}. \tag{c}$$

[13] K. Knopp, *Theorie und Anwendung der unendlichen Reihen* (Julius Springer, Berlin, 1931), third edition, p. 519.

We transform the left-hand side of (2.22) $[\mathrm{Re}[z]\geq 0]$ in the following way:

$$\Lambda(z) = -\frac{1}{z}\int_0^\infty dr(1-e^{-sr})[V_1(r)-V(r)]$$

$$= -\frac{1}{z}\int_0^\infty dr(1-e^{-sr})\sum_{m=2}^{N} V_m(r) + R_1(z), \tag{5.9}$$

where

$$R_1(z) = -\frac{1}{z}\int_0^\infty dr(1-e^{-sr})\sum_{m=N+1}^{\infty} V_m(r). \tag{5.10}$$

Introducing the recursions (3.6) for V_m in the first term of (5.9), we get

$$\sum_{m=2}^{N} V_m(r)$$

$$= \sum_{m=2}^{N}\sum_{l=2}^{m}\sum_{\Sigma\nu_k = m}\int_0^\infty dr_1\int_{r_1}^\infty dr_2$$

$$\cdots\int_{r_{l-1}}^\infty dr_l K(r, r_1\cdots r_l)$$

$$\times V_{\nu_1}(r_1)V_{\nu_2}(r_2)\cdots V_{\nu_l}(r_l)$$

$$= \sum_{l=2}\sum_{\Sigma\nu_k\leqq N}\int_0^\infty dr_1\int_0^\infty dr_2$$

$$\cdots\int_{r_{l-1}}^\infty dr_l K(r, r_1\cdots r_l)$$

$$\times V_{\nu_1}(r_1)V_{\nu_2}(r_2)\cdots V_{\nu_l}(r_l). \tag{5.11}$$

Substituting this in (5.9), interchanging the order of integration,[14] and using the definition of $K(r, r_1\cdots r_l)$, (2.27), gives

$$\Lambda(z) = \sum_{l=2}^{N}\int_0^\infty dr_1\int_{r_1}^\infty dr_2$$

$$\cdots\int_{r_{l-1}}^\infty dr_l\frac{1}{z^l}(1-e^{-sr_1})(1-e^{-s(r_2-r_1)})$$

$$\cdots(1-e^{-s(r_l-r_{l-1})})\sum_{\Sigma\nu_k\leqq N} V_{\nu_1}(r_1)V_{\nu_2}(r_2)$$

$$\cdots V_{\nu_l}(r_l) + R_1(z)$$

$$= \sum_{l=2}^{N}\int_0^\infty dr_1\int_{r_1}^\infty dr_2$$

$$\cdots\int_{r_{l-1}}^\infty dr_l\frac{1}{z^l}(1-e^{-sr_1})(1-e^{-s(r_2-r_1)})$$

$$\cdots(1-e^{-s(r_l-r_{l-1})})V(r_1)V(r_2)$$

$$\cdots V(r_l) + R_2(z) + R_1(z), \tag{5.12}$$

[14] Since all our integrals and sums are absolutely convergent, the order of integrations and summations can be freely interchanged.

where

$$R_2(z)=\sum_{l=2}^{N}\int_0^\infty dr_1\int_{r_1}^\infty dr_2 \cdots \int_{r_{l-1}}^\infty dr_l \frac{1}{z^l}(1-e^{-zr_1}) \cdots (1-e^{-z(r_l-r_{l-1})}) \sum_{\Sigma r_k>N} V_{\nu_1}(r_1)V_{\nu_2}(r_2) \cdots V_{\nu_l}(r_l). \quad (5.13)$$

Finally,

$$\Lambda(z)=\sum_{l=2}^{\infty}\int_0^\infty dr_1\int_{r_1}^\infty dr_2 \cdots \int_{r_{l-1}}^\infty dr_l \frac{1}{z_l}(1-e^{-zr_1})(1-e^{-z(r_2-r_1)}) \cdots (1-e^{-z(r_l-r_{l-1})})V(r_1)V(r_2) \cdots V(r_l)+R_3(z)+R_2(z)+R_1(z), \quad (5.14)$$

where

$$R_3(z)=\sum_{l=N+1}^{\infty}\int_0^\infty dr_1\int_{r_1}^\infty dr_2 \cdots \int_{r_{l-1}}^\infty dr_l \frac{1}{z^l}(1-e^{-zr_1}) \cdots (1-e^{-z(r_l-r_{l-1})})V(r_1)\cdots V(r_l). \quad (5.15)$$

What remains is to estimate $R_1(z)$, $R_2(z)$, $R_3(z)$. With the help of

$$\left|\frac{1}{z}(1-e^{-z\alpha})\right|=\left|\int_0^\alpha e^{-z\alpha'}d\alpha'\right|\leqq\alpha, \quad \mathrm{Re}[z]\geqq 0, \quad (5.16)$$

one justifies easily

$$|R_1(z)|\leqq\int_0^\infty r\sum_{m=N+1}^{\infty}|V_m(r)|=\sum_{m=N+1}^{\infty}I_m<\frac{\epsilon}{3} \quad (5.17)$$

$$|R_2(z)|\leqq\sum_{l=2}^{N}\int_0^\infty dr_1\int_{r_1}^\infty dr_2 \cdots \int_{r_{l-1}}^\infty dr_l \sum_{\Sigma r_k>N} r_1|V_{\nu_1}(r_1)|r_2|V_{\nu_2}(r_2)| \cdots r^l|V_{\nu_l}(r_l)|\leqq\sum_{m=N+1}^{\infty}\sum_{l=2}^{m}\frac{1}{l!}\sum_{\Sigma r_k=m}I_{\nu_1}I_{\nu_2} \cdots I_{\nu_l}<\sum_{m=N+1}^{\infty}a_m<\frac{\epsilon}{3} \quad (5.18)$$

$$|R_3(z)|\leqq\sum_{l=N+1}^{\infty}\int_0^\infty dr_1\int_{r_1}^\infty dr_2 \cdots \int_{r_{l-1}}^\infty dr_l\, r_1|V(r_1)|r_2|V(r_2)| \cdots r_l|V(r_l)|\leqq\sum_{l=N+1}^{\infty}\frac{1}{l!}K^l<\frac{\epsilon}{3}, \quad (5.19)$$

where (a), (b), (c) have been used as well as (5.1), (5.7). Therefore,

$$|R_1(z)+R_2(z)+R_3(z)|<\epsilon. \quad (5.20)$$

From (5.9), (5.14), and (5.20) it follows that (2.22) is satisfied. This concludes the verification.

6. TWO EXAMPLES

$k\cot\eta(k)=-\alpha+\frac{1}{2}r_0k^2$

We shall now work out in detail a simple example which shows how the method can in principle be used for a determination of the potential. We consider a particle obeying the Schrödinger equation (2.1) whose phase shift is given by

$$k\cot\eta(k)=-\alpha+\tfrac{1}{2}r_0k^2. \quad (6.1)$$

This expression is taken from the theory of the effective range[7] and luckily is particularly easy to treat by our method.

We first discuss the case $\alpha<0$, $r_0>0$, which corresponds, for example, to singlet neutron-proton scattering. In this case one can see from (6.1) that $\eta(+0)=0$ so that the system has no bound state [compare (2.14)].

By means of the relation $\tan^{-1}x=(i/2)\log[(1-ix)/(1+ix)]$, we write $\eta(k')$ explicitly as

$$\eta(k')=\tan^{-1}[(k'/-\alpha+\tfrac{1}{2}r_0k^2)] =i/2\log[(z'+a)(z'-b)/(z'-a)(z'+b)], \quad (6.2)$$

where

$$z'=2ik', \quad (6.3)$$

$$a=(2/r_0)[1+(1-2\alpha r_0)^{\frac{1}{2}}], \quad b=(2/r_0)[-1+(1-2\alpha r_0)^{\frac{1}{2}}]. \quad (6.4)$$

We now calculate $g(z)$ by means of Eq. (2.15):

$$\log g(z)=-\frac{2i}{\pi}\int_{-\infty}^{\infty}\frac{\eta(k')}{2ik'-z}dk' =\frac{1}{2\pi i}\int_{-i\infty}^{i\infty}\frac{dz'}{z'-z}\left[\log\frac{z'+a}{z'+b}+\log\frac{z'-b}{z'-a}\right] =-\log[(z+a)/(z+b)]; \quad (6.5)$$

since $a>b>0$, we have integrated the first and second terms by closing contours in the right and left half-planes, respectively. Hence we obtain the simple ex-

pression

$$g(z)=(z+b)/(z+a)$$
$$=1+\lambda 2a/(z+a), \tag{6.6}$$

where

$$\lambda=-(a-b)/2a. \tag{6.7}$$

Expanding the potential $V(r)$ in powers of λ,

$$V(r)=\sum_1^\infty \lambda^m V_m(r), \tag{6.8}$$

we find first, by Eq. (3.1),

$$\lambda r V_1(r)=\frac{1}{2\pi i}\int_{-i\infty}^{i\infty} e^{rz}\frac{d}{dz}z[g(z)-1]dz$$
$$=\frac{2a^2\lambda}{2\pi i}\int_{-i\infty}^{i\infty} e^{rz}\frac{1}{(z+a)^2}dz$$
$$=2a^2\lambda r e^{-ar}, \tag{6.9}$$

or

$$V_1(r)=2a^2e^{-ar}. \tag{6.10}$$

In the present case the calculation of the higher approximations is best carried out by Laplace transforming Eq. (3.6), using the first expression of Eq. (2.27) for the kernels:

$$\int_0^\infty e^{-zr}V_m(r)dr$$
$$=\sum_{l=2}^{m}\sum_{r_1+r_2+\cdots r_l=m}\int_0^\infty dr_1\int_{r_1}^\infty dr_2$$
$$\cdots\int_{r_{l-1}}^\infty dr_l(1-e^{-zr_1})\frac{1}{z}(1-e^{-z(r_2-r_1)})$$
$$\cdots\frac{1}{z}(1-e^{-z(r_l-r_{l-1})})V_{r_1}(r_1)V_{r_2}(r_2)$$
$$\cdots V_{r_l}(r_l). \tag{6.11}$$

Thus with (6.10) we find

$$\int_0^\infty e^{-zr}V_2(r)dr=2a^2\left(-\frac{1}{z+a}+\frac{2}{z+2a}\right) \tag{6.12}$$

so that

$$V_2(r)=2a^2(-e^{-ar}+2e^{-2ar}). \tag{6.13}$$

Similarly,

$$V_3(r)=2a^2(e^{-ar}-4e^{-2ar}+3e^{-3ar}), \tag{6.14}$$

etc. The total potential, therefore, is

$$V(r)=2a^2\{e^{-ar}(\lambda-\lambda^2+\lambda^3-\cdots)$$
$$+e^{-2ar}(2\lambda^2-4\lambda^3+\cdots)$$
$$+e^{-3ar}(3\lambda^3-\cdots)$$
$$+\cdots\}. \tag{6.15}$$

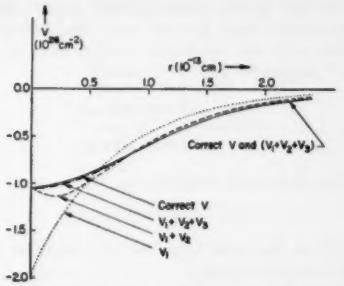

FIG. 3. Three successive approximations to the Eckert potential V, corresponding to $n-p$ singlet scattering.

The first three approximations with numerical constants corresponding to $n-p$ singlet scattering ($\alpha=-0.0422\times10^{+13}$ cm^{-1}, $r_0=2.6\times10^{-13}$ cm, $a=1.45\times10^{13}$ cm^{-1}, $\lambda=-0.469$) are plotted in Fig. 3. In the same figure the exact solution corresponding to the $g(z)$ of Eq. (6.6) is plotted, *viz.*:

$$V(r)=2\lambda(1+\lambda)a^2e^{-ar}/[1+\lambda(1-e^{-ar})]^2. \tag{6.16}$$

We see from (6.16) that the radius of convergence is $|\lambda|=1$, more than twice the value appropriate for $n-p$ singlet scattering. The convergence of our procedure is therefore unexpectedly good, when compared with our criterion (3.8), which assures convergence only up to $|\lambda|=0.193$.

As a second case we consider again (6.1), this time with $\alpha>0, r_0>0$ and $2\alpha r_0<1$. This means that $\eta(+0)=\pi$ so that the system has one bound state whose energy, $E_0=-\frac{1}{4}\xi_0^2(\xi_0>0)$, is necessary for the construction of $g(z)$.

We first write down the auxiliary phase

$$\tilde{\eta}(k')=\eta(k')-2\tan^{-1}(\xi_0/2k')$$
$$=-\frac{i}{2}\log\frac{(z'-b)(z'+a)(z'-\xi_0)^2}{(z'-a)(z'+b)(z'+\xi_0)^2}, \tag{6.17}$$

where a and b are given by (6.14) and $a>0$, $b<0$ (see Fig. 1).

The function $\tilde{g}(z)$ is given, according to (2.17), by

$$\log\tilde{g}(z)=-\frac{2i}{\pi}\int_{-\infty}^{\infty}\frac{\tilde{\eta}(k')}{2ik'-z}dk'$$
$$=\frac{1}{2\pi i}\int_{-i\infty}^{i\infty}\frac{dz'}{z'-z}\log\frac{(z'-b)(z'+a)}{(z'+\xi_0)^2}$$
$$=\log\frac{(z+\xi_0)^2}{(z-b)(z+a)}, \tag{6.18}$$

and therefore $g(z)$ is, by Eq. (2.16),

$$g(z)=\tilde{g}(z)(z-\xi_0)/(z+\xi_0)$$
$$=(z^2-\xi_0^2)/[(z-b)(z+a)]. \tag{6.19}$$

In the case of the neutron-proton system one finds experimentally that $\xi_0=-b$; i.e., the bound state coincides with the absolutely smaller zero of the S matrix[15] defined by Eq. (6.1), namely,

$$S(k)=\frac{(2ik+b)(2ik-a)}{(2ik-b)(2ik+a)}. \tag{6.20}$$

Equation (6.19) now simplifies to

$$g(z)=(z+b)/(z+a), \tag{6.21}$$

which is of the same form as (6.6); however, in the present case b is negative.

The construction of V is exactly the same as before, leading again to (6.15) and (6.16). The numerical values for $n-p$ triplet scattering are: $\alpha=0.186\times10^{13}$ cm^{-1}, $r_0=1.56\times10^{-13}$ cm, $a=2.114\times10^{13}$ cm^{-1}, $\lambda=-0.606$. Therefore the convergence of our method is only slightly worse than for singlet-scattering where λ was -0.469.

It should be recalled, however, that in general, when there are bound states, there is no guarantee that the potential constructed by our method is the only solution. In the present case this ambiguity is illustrated by the family of alternative potentials which has been constructed by Bargmann.[4] Figure 4 shows the potential $V(r)$, Eq. (6.16), to which our method leads, as well as two equivalent potentials $V_2(r)$ and $V_4(r)$, selected from Bargmann's Eqs. (4.10) and (4.12) by setting $\theta=0.1$ and 0, respectively.

The Exponential Potential

In order to see whether the good convergence in the last example was accidental we have also calculated a second example.

We have taken an exponential potential,

$$V(r)=\mu e^{-r} \tag{6.22}$$

(where r is measured in convenient units), and calculated the $g(z)$ which corresponds to its phase shift and bound states. In this case it is not necessary to calculate first $\eta(k)$ and the ξ_i explicitly, since the $g(z)$ for this potential is well known:[16]

$$g(\mu,z)=1+\sum_{n=1}^{\infty}\frac{\mu^n}{n!}\frac{1}{(1+z)(2+z)\cdots(n+z)}$$
$$=1+\sum_{s=1}^{\infty}\frac{(-1)^{s-1}}{(s-1)!}\frac{1}{(s+z)}\mu^s\sum_{m=0}^{\infty}\frac{\mu^m}{m!(m+s)!}. \tag{6.23}$$

$V_1(r)$ is now calculated from (2.21)

$$g(\mu,z)-1=\frac{1}{z}\int_0^{\infty}dr(1-e^{-zr})V_1(r)$$
$$=\int_0^{\infty}dre^{-zr}\left(\int_r^{\infty}V_1(r')dr'\right), \tag{6.24}$$

which gives after Laplace inversion and differentiation

$$V_1(r)=\sum_{s=1}^{\infty}\frac{(-1)^{s-1}se^{-sr}}{(s-1)!}\mu^s\sum_{m=0}^{\infty}\frac{\mu^m}{m!(m+s)!}. \tag{6.25}$$

For the $n-p$ triplet system, we take our unit of length as $r_0=0.75\times10^{-13}$ cm and $\mu=2.13$. Then one finds

$$V_1(r)=-[0.538e^{-r}+2.061e^{-2r}+1.374e^{-3r}$$
$$+0.369e^{-4r}+0.052e^{-5r}+0.004e^{-6r}+\cdots]. \tag{6.26}$$

To calculate V_2 and V_3 one uses the easily established formulas

$$\int_0^{\infty}dr_1\int_{r_1}^{\infty}dr_2K(r,r_1,r_2)e^{-\alpha r_1}e^{-\beta r_2}$$
$$=-\frac{1}{\alpha(\alpha+\beta)}e^{-\beta r}+\frac{1}{\alpha\beta}e^{-(\alpha+\beta)r} \tag{6.27}$$

$$\int_0^{\infty}dr_1\int_{r_1}^{\infty}dr_2\int_{r_2}^{\infty}K(r,r_1r_2r_3)e^{-\alpha r_1}e^{-\beta r_2}e^{-\gamma r_3}$$
$$=\left(\frac{1}{\alpha(\beta+\gamma)(\alpha+\beta)}-\frac{1}{\alpha\beta(\alpha+\beta+\gamma)}\right)e^{-\gamma r}$$
$$+\frac{1}{\alpha\beta(\alpha+\beta+\gamma)}e^{-(\beta+\gamma)r}$$
$$-\frac{1}{\alpha(\beta+\gamma)(\alpha+\beta)}e^{-(\alpha+\beta+\gamma)r}. \tag{6.28}$$

To simplify the calculation of V_3 we have used the approximate expression

$$V_1(r)\approx-(0.6e^{-r}+3.8e^{-2.4s}),$$

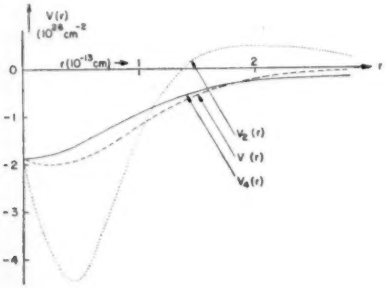

FIG. 4. Three phase equivalent potentials corresponding to the $n-p$ triplet state. All the curves go through the same point at $r=0$.

[15] For the few potentials examined so far the S matrix vanishes at points in the k plane corresponding to bound states.

[16] For example, reference 12, p. 845.

which is accurate to within a few percent. The potentials obtained in the first three approximations, which can be calculated with relatively little effort, are shown in Fig. 5, together with the exponential potential. The curves apparently converge satisfactorily towards the exponential potential.[17] It might be remarked here that for the same potential, successive Born approximation diverge up to about 20 Mev.

7. THE TANGENT METHOD

Instead of basing our construction of the potential on the integral Eq. (2.10) whose solutions behave like $f(k, r)\sim e^{-ikr}$ for large r, one can also consider integral equations corresponding to other boundary conditions. One of the most natural possibilities is

$$\varphi(0)=0, \tag{7.1}$$

$$r\to\infty:\ \varphi(r)\to\sin kr+\tan\eta\cos kr. \tag{7.2}$$

The integral equation which is equivalent to the Schrödinger equation (2.1) and these boundary conditions is

$$\varphi(r)=\sin kr+\int_0^\infty g(r, r')V(r')\varphi(r')dr',^{18} \tag{7.3}$$

where

$$g(r, r')=-\frac{1}{2k}\left(\sin k(r+r')-\sin k|r-r'|\right)$$

$$=-\frac{1}{2}\int_{|r-r'|}^{r+r'}\cos ktdt. \tag{7.4}$$

For $r\to\infty$, (7.3) gives

$$\varphi(r)=\sin kr+\left(-\frac{1}{k}\int_0^\infty \sin kr'V(r')\varphi(r')dr'\right)\cos kr \tag{7.5}$$

so that

$$-k\tan\eta=\int_0^\infty \sin krV(r)\varphi(r)dr. \tag{7.6}$$

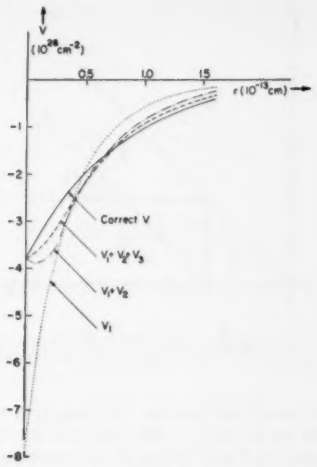

FIG. 5. Three successive approximations to the exponential potential $V(r)$ corresponding to the $n-p$ triplet state.

We now solve (7.3) by iteration and substitute the resulting series into (7.6):

$$-k\tan\eta(k)=\int_0^\infty \sin^2krV(r)dr+\sum_{n=1}^\infty\int_0^\infty dr\int_0^\infty dr_1$$

$$\cdots\int_0^\infty dr_n\sin krV(r)g(r, r_1)V(r_1)$$

$$\cdots g(r_{n-1}, r_n)V(r_n)\sin kr_n. \tag{7.7}$$

To solve this equation for $V(r)$, in terms of $\tan\eta(k)$, we write formally

$$-k\tan\eta(k)=\mu F(k), \tag{7.8}$$

$$V(r)=\sum_1^\infty \mu^m V_m(r), \tag{7.9}$$

substitute into (7.7), and equate to zero the coefficients of μ, μ^2, $\cdots$. Finally we set $\mu=1$. This gives the following set of equations:

$$-k\tan\eta(k)=\int_0^\infty \sin^2krV_1(r)dr, \tag{7.10}$$

$$0=\int_0^\infty \sin^2krV_m(r)dr+\sum_{l=2}^\infty\sum_{\Sigma\nu_k=m}\int_0^\infty dr_1$$

$$\cdots\int_0^\infty dr_l\sin kr_1V_{\nu_1}(r_1)g(r_1, r_2)V_{\nu_2}(r_2)$$

$$\cdots g(r_{l-1}, r_l)V_{\nu_l}(r_l)\sin kr_l,\quad m=2, 3, \cdots. \tag{7.11}$$

[17] A simple function—theoretic argument shows that if our procedure converges it must converge to the exponential potential.

[18] Fröberg's method (see reference 6) is equivalent to starting with the integral equation

$$\varphi(r)=\sin(kr+\eta)+\int_r^\infty k(r, r')V(r')\varphi(r')dr',$$

where $k(r, r')=(1/k)\sin k(r'-r)$. The solution of this equation, which has the asymptotic form $\varphi(r)\to\sin(kr+\eta)$, is obtained by iteration and substituted into the equation

$$0=\sin\eta(k)+\int_0^\infty k(0, r')V(r')\varphi(r')dr',$$

which comes from the boundary condition $\varphi(0)=0$. Finally, one writes $\sin\eta(k)=\lambda F(k)$, expands both $V(r)$ and $\sin(kr+\eta)$ in powers of λ, and equates to zero the coefficients of λ^m. The resulting equations can be solved for the successive terms in the expansion of $V(r)$.

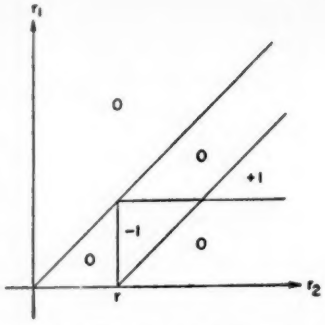

FIG. 6. The kernel $\bar{K}$ $(r, r_1 r_2)$ used in the tangent method for the construction of the second and higher approximations [see Eq. (7.15)].

Given $\tan\eta(k)$ we can now successively solve these equations for $V_1, V_2, \cdots$. We first differentiate (7.10) with respect to k and Fourier invert, obtaining as first approximation

$$rV_1(r)=-\frac{4}{\pi}\int_0^\infty \frac{d}{dk}(k\tan\eta(k))\sin 2kr dr. \quad (7.12)$$

To solve for $V_m(r)$, $m\geq 2$, we begin by writing the first term in (7.11) as

$$\frac{1}{2}\int_0^\infty (1-\cos 2kr)V_m(r)dr \quad (7.13)$$

and assume, subject to later verification, that

$$\int_0^\infty V_m(r)dr=0, \quad m\geq 2. \quad (7.14)$$

Now we Fourier invert (7.11) and obtain

$$V_m(r)=\sum_{l=2}^{\infty}\sum_{\Sigma r_k=m}\int_0^\infty dr_1\int_0^\infty dr_2$$

$$\cdots\int_0^\infty dr_l \bar{K}(r, r_1\cdots r_l)V_{r_1}(r_1)\cdots V_{r_l}(r_l), \quad (7.15)$$

where

$$\bar{K}(r, r_1\cdots r_l)$$

$$=\frac{4}{\pi}\int_{-\infty}^{\infty} dk\cos 2kr \sin kr_1 g(r_1, r_2)$$

$$\cdots g(r_{l-1}, r_l)\sin kr_l. \quad (7.16)$$

One verifies (7.14) immediately from the fact that

$$\int_0^\infty \bar{K}dr=0.$$

In practical applications it may be most convenient to substitute (7.16) into (7.15) and do the integrations over the r_i before that over k. However, in Fig. 6 we also show $\bar{K}(r, r_1 r_2)$ as function of r, r_1, and r_2.

We do not consider it worthwhile to present here a proof for the convergence of this procedure for small enough $\eta(k)$. Such a proof can be given along the lines of Sec. IV. One can notice immediately, however, that the method does not apply to potentials with bound states since in that case $(d/dk)[k\tan\eta(k)]$ has a quadratic singularity where $\eta(k)=(\pi/2)$, and hence $V_1(r)$, Eq. (7.12), does not exist.

To illustrate how this method works, we consider again the phase shift given by (6.1), which we now write as

$$-k\tan\eta=-\mu\gamma k^2/(\beta^2+k^2), \quad (7.17)$$

where

$$\gamma=2/r_0, \quad \beta^2=-2\alpha/r_0, \quad (7.18)$$

and μ is eventually taken as 1. We restrict ourselves to the case where β is real and, for definiteness, positive to avoid a singularity in $\tan\eta$. From (7.12) and (7.15) we find

$$V_1(r)=-4\gamma\beta e^{-2\beta r}, \quad (7.19)$$

$$V_2(r)=-4\gamma^2 e^{-2\beta r}+4\gamma^2\beta r e^{-2\beta r}+4\gamma^2 e^{-4\beta r}. \quad (7.20)$$

To determine the conditions under which the series (7.9) for $V(r)$ converges when $\mu=1$, we use the fact that the potential corresponding to (7.17) is exactly known and, since there are no bound states, even unique. With our present notation we have [compare (6.16), (6.7), (6.4), and (6.1)]

$$V(r)=2\lambda(1+\lambda)a^2e^{-ar}/[1+\lambda(1-e^{-ar})]^2, \quad (7.21)$$

where

$$a=\mu\gamma+(\mu^2\gamma^2+4\beta^2)^{\frac{1}{2}}, \quad (7.22)$$

$$\lambda=\mu^2(\gamma/2\beta)^2-\mu(\gamma/2\beta)[\mu^2(\gamma/2\beta)^2+1]^{\frac{1}{2}}. \quad (7.23)$$

Thus we see that the expansion (7.9) for $V(r)$ converges for $\mu=1$ only if

$$|\gamma/2\beta|<1. \quad (7.24)$$

Comparison with (7.17) shows that for this particular potential one has convergence only if

$$|\eta(k)|<\pi/4 \quad (7.25)$$

for all k.

It is interesting to compare the convergence of this procedure with that of the method discussed earlier. At the limits of convergence of the present expansion of $V(r)$ we find

$$\begin{aligned}\mu/2\beta&=\ \ 1: \quad \lambda=1-\sqrt{2}=-0.414,\\ \mu/2\beta&=-1: \quad \lambda=1+\sqrt{2}=\ \ 2.414,\end{aligned} \quad (7.26)$$

so that in the case of the attractive potential $(\mu/2\beta=1)$

our other procedure has a larger radius of convergence, while for the repulsive potential the present method is better.

8. CONCLUDING REMARKS

In conclusion we should like to survey briefly some possible generalizations of our procedure.

The simplest of these is the generalization to higher angular momenta. It is easy to give the formal expressions corresponding to our kernels $K(r, r_1 r_2 \cdots r_l)$. As a result of the centrifugal barrier, the potential becomes effectively weaker for higher l, and therefore the convergence of our method for a given potential is likely to become better. Also, for sufficiently high l, the uniqueness problem, connected with the existence of bound states does not occur. On the other hand, the phases for $l>0$ are not so well known experimentally, and the kernels considerably more complicated than for S states.

The inclusion of tensor forces in the framework of our procedure does not seem to be unfeasible, but is undoubtedly quite complicated.

The extension to the case of a repulsive Coulomb field seems to be promising. Jauho[19] has already generalized Levinson's results to this case, and there can be little doubt that the present method can also be adapted to it. For the proton-proton system one has the advantages of more accurate measurements and no bound state complications. These would seem to make a study of this case worth while.

Finally an investigation of the relativistic equation may be interesting for application to the scattering of high energy electrons by nuclei.

This paper was begun at the Institute for Theoretical Physics in Copenhagen and concluded at the Institute for Advanced Study in Princeton. We should like to express our great appreciation to Professors Niels Bohr and Robert Oppenheimer for making our collaboration on this problem possible. We are also very grateful to Professor V. Bargmann for many helpful discussions.

APPENDIX 1. CONVERGENCE PROOF FOR THE SERIES 2.26

We have to show that under the assumptions

$$|rV(r)|<M<\infty, \tag{A1.1}$$

$$\int_0^\infty r|V(r)|dr=I<\infty, \tag{A1.2}$$

the function $V_1(r)$ defined by (2.26) exists and has the properties

$$|rV_1(r)|<M_1<\infty, \tag{A1.3}$$

$$\int_0^\infty r|V_1(r)|dr=I_1<\infty. \tag{A1.4}$$

With the notation

$$F_l(r)=-\int_0^\infty dr_1\int_{r_1}^\infty dr_2 \cdots \int_{r_{l-1}}^\infty dr_l K(r, r_1\cdots r_l)V(r_1)\cdots V(r_l), \tag{A1.5}$$

the series in (2.26) reads

$$V_1(r)=V(r)+\sum_{l=2}^\infty F_l(r). \tag{A1.6}$$

We will first prove (A1.3). From (A1.1) and (A1.2) we find

$$A\equiv\int_0^\infty g(r)|V(r)|dr<\infty, \tag{A1.7}$$

where

$$g(r)=\begin{cases}\sqrt{r} & \text{for } 0\leq r<1\\ r & \text{for } 1\leq r\end{cases}. \tag{A1.8}$$

Analyzing first $rF_2(r)$, we get from Fig. 2

$$\begin{aligned}|rF_2(r)|&\leqq r\int_0^r dr_1\int_r^{r+r_1}dr_2|V(r_1)||V(r_2)|\\ &\quad+r\int_r^\infty dr_1\int_{r+r_1}^\infty dr_2|V(r_1)||V(r_2)|\\ &\leqq\int_0^r dr_1\int_r^{r+r_1}dr_2r_2|V(r_1)||V(r_2)|\\ &\quad+\int_r^\infty dr_1g(r_1)\int_r^\infty dr_2g(r_2)|V(r_1)||V(r_2)|,\end{aligned} \tag{A1.9}$$

and finally with (A1.1), (A1.2), and (A1.7)

$$|rF_2(r)|\leqq MI+A^2<\infty. \tag{A1.10}$$

For the estimate of $rF_l(r)$, $l\geqq 3$, we use the first estimate in (4.9) together with the property of the kernels $K(r, r_1\cdots r_l)$ to vanish for $r>r_l$ [compare (4.5)]. This gives for $rF_l(r)$

$$\begin{aligned}|rF_l(r)|\leqq&\int_0^\infty dr_1\int_{r_1}^\infty dr_2\\ &\cdots\int_{r_{l-1}}^\infty dr_1g(r_1)g(r_2)\cdots g(r_l)V(r_1)V(r_2)\\ &\cdots V(r_l)\leqq A^l/l!.\end{aligned} \tag{A1.11}$$

Introducing (A1.10), (A1.11), and (A1.1) into (A1.6) gives

$$|rV_1(r)|<M+MI+A^2+\sum_{l=2}^\infty\frac{1}{l!}A^l=M_1<\infty, \tag{A1.12}$$

which proves (A1.3).

[19] P. Jauho, Ann. Acad. Sci. Fennicae, Ser. A, **80** (1951).

The proof of (A1.4) goes exactly along the lines of the convergence proof in Sec. 4. Using (4.13) one verifies easily

$$\int_0^\infty r|V_1(r)|dr \leqq I+\sum_{l=2}^{\infty}\frac{I^l}{l!}=I_1<\infty. \quad \text{(A1.13)}$$

Furthermore, we note that as a consequence of (2.30) we also have

$$\int_0^\infty r^2|V_1(r)|dr<\infty, \quad \text{(A1.14)}$$

an equation which, however, we did not use in the text. Therefore we omit the simple proof.

Finally, it follows easily from (A1.1) and (A1.2) that all the $F_l(r)$ are integrable, and from (2.27) we get

$$\int_0^\infty F_l(r)dr=0, \quad \text{(A1.15)}$$

which together with (A1.6) gives

$$\int_0^\infty [V(r)-V_1(r)]dr=0. \quad \text{(A1.16)}$$

APPENDIX 2. A GENERALIZATION OF LEVINSON'S THEOREM[5]

Levinson has proved that for a given S phase shift and in the absence of bound states there exists at most one potential satisfying the conditions

$$\int_0^\infty r|V(r)|dr<\infty, \quad \text{(A2.1)}$$

$$\int_0^\infty r^2|V(r)|dr<\infty. \quad \text{(A2.2)}$$

We shall now give a generalization of this theorem under the same conditions (A2.1) and (A2.2). In the notation we follow the paper of Jauho.[19] For simplicity we first discuss the case of a single bound state.

We assume that for the given phase shift and binding energy there exist two potentials $V(r)$ and $\bar{V}(r)$ and corresponding wave functions $\varphi(k,r)$ and $\bar{\varphi}(k,r)$ satisfying the equations

$$\varphi''+k^2\varphi=V\varphi, \quad \text{(A2.3)}$$

$$\bar{\varphi}''+k^2\bar{\varphi}=\bar{V}\bar{\varphi}, \quad \text{(A2.4)}$$

and the boundary conditions

$$\varphi(k,0)=0, \quad \varphi'(k,0)=1, \quad \text{(A2.5)}$$

$$\bar{\varphi}(k,0)=0, \quad \bar{\varphi}'(k,0)=1. \quad \text{(A2.6)}$$

These functions are related to the functions $f(k,r)$ and $\bar{f}(k,r)$ of (2.3) by the equations

$$\varphi(k,r)=(1/2ik)\{f(k)f(-k,r)-f(-k)f(k,r)\}, \quad \text{(A2.7)}$$

$$\bar{\varphi}(k,r)=(1/2ik)\{f(k)\bar{f}(-k,r)-f(-k)\bar{f}(k,r)\}; \quad \text{(A2.8)}$$

here we have abbreviated $f(k,0)$ by $f(k)$ and $\bar{f}(k,0)$ by $\bar{f}(k)$ and used the fact that by our assumptions

$$f(k)=\bar{f}(k). \quad \text{(A2.9)}$$

$\varphi(k,r)$ and $\bar{\varphi}(k,r)$ are regular functions for all complex values of k.[8] For large $|k|$ they behave as

$$\varphi(k,r)\sim\sin kr/k, \quad \text{(A2.10)}$$

$$\bar{\varphi}(k,r)\sim\sin kr/k. \quad \text{(A2.11)}$$

Similarly we have, for large $|k|$ and $\mathrm{Im}[k]\leqq 0$,

$$f(k,r)\sim e^{-ikr}, \quad \text{(A2.12)}$$

$$\bar{f}(k,r)\sim e^{-ikr}, \quad \text{(A2.13)}$$

and therefore

$$f(k)\sim 1. \quad \text{(A2.14)}$$

Following reference 19 we discuss the expressions

$$\Phi_1(k,r)=\frac{k}{f(k)}\varphi(k,r)\int_r^\infty \bar{f}(k,\rho)F(\rho)d\rho \quad \text{(A2.15)}$$

and

$$\Phi_2(k,r)=\frac{k}{f(k)}\bar{f}(k,r)\int_0^r \varphi(k,\rho)F(\rho)d\rho, \quad \text{(A2.16)}$$

where $F(r)$ is a continuous and continuously differentiable function, which is different from zero only in a finite r interval.

Integrating $\Phi_1(k,r)$ over a contour C consisting of a large semicircle in the lower half-plane and the real axis, we get a contribution only from the zero of $f(k)$ at $k=-i\kappa$:[20]

$$\int_C \Phi_1(k,r)dk=-2\pi i\frac{(-i\kappa)}{\dot{f}(-i\kappa)}\varphi(-i\kappa,r)\times\int_r^\infty \bar{f}(-i\kappa,\rho)F(\rho)d\rho, \quad \text{(A2.17)}$$

where

$$\dot{f}(k)\equiv(df/dk). \quad \text{(A2.18)}$$

We now introduce the following abbreviations for the bound state wave function:

$$\varphi(-i\kappa,r)\equiv\varphi_0(r), \quad \text{(A2.19)}$$

$$\bar{\varphi}(-i\kappa,r)\equiv\bar{\varphi}_0(r), \quad \text{(A2.20)}$$

and the notation

$$C=[2i\kappa f'(-i\kappa,0)/\dot{f}(-i\kappa)], \quad \text{(A2.21)}$$

$$\bar{C}=[2i\kappa\bar{f}'(-i\kappa,0)/\dot{f}(-i\kappa)]. \quad \text{(A2.22)}$$

C and $\bar{C}$ are real and positive (see reference 8 p. 265). Finally, we clearly have the relations

$$\varphi_0(r)=[f(-i\kappa,r)/f'(-i\kappa,0)], \quad \text{(A2.23)}$$

$$\bar{\varphi}_0(r)=[\bar{f}(-i\kappa,r)/\bar{f}'(-i\kappa,0)]. \quad \text{(A2.24)}$$

[20] In terms of the notation of Sec. 2, $\kappa=\xi/2$.

We can now rewrite (A2.17) as

$$\int_{-K}^{+K}\Phi_1(k,r)dk-\pi i\bar{C}\varphi_0(r)\int_r^\infty\bar{\varphi}_0(\rho)F(\rho)d\rho$$
$$=-\int_{S.C.}\Phi_1(k,r)dk, \quad \text{(A2.25)}$$

where the first integral goes over the real axis and the last over the large semicircle. Levinson has shown that one can substitute in the last integral the asymptotic expressions (A2.10–14), which gives

$$-\int_{S.C.}\Phi_1(k,r)dk$$
$$=-\int_{S.C.}dk\,\sin kr\int_r^\infty e^{-ik\rho}F(\rho)d\rho+R(K), \quad \text{(A2.26)}$$

where

$$\lim_{K\to\infty}R(K)=0. \quad \text{(A2.27)}$$

An integration by parts leads to

$$\int_r^\infty e^{-ik\rho}F(\rho)d\rho=\frac{1}{ik}e^{-ikr}[F(r)+R_1(K)], \quad \text{(A2.28)}$$

where again

$$\lim_{K\to\infty}R_1(K)=0. \quad \text{(A2.29)}$$

Substituting (A2.28) into (A2.26) gives

$$-\int_{S.C.}\Phi_1(k,r)dk$$
$$=\tfrac{1}{2}F(r)\int_{S.C.}\frac{dk}{k}(1-e^{-2ikr})+R_2(K)$$
$$=-\tfrac{1}{2}i\pi F(r)+R_2(K), \quad \text{(A2.30)}$$

where

$$\lim_{K\to\infty}R_{2,3}(K)=0. \quad \text{(A2.31)}$$

Finally, substituting (A2.30) into (A2.25) gives

$$F(r)=2\bar{C}\varphi_0(r)\int_r^\infty\bar{\varphi}_0(\rho)F(\rho)d\rho$$
$$+\frac{2i}{\pi}\int_{-\infty}^{+\infty}\frac{kdk}{f(k)}\varphi(k,r)\int_r^\infty\bar{f}(k,\rho)F(\rho)d\rho. \quad \text{(A2.32)}$$

A similar procedure applied to (A2.16) yields

$$F(r)=2\bar{C}\bar{\varphi}_0(r)\int_0^r\varphi_0(\rho)F(\rho)d\rho$$
$$+\frac{2i}{\pi}\int_{-\infty}^{+\infty}\frac{kdk}{f(k)}\bar{f}(k,r)\int_0^r\varphi(k,\rho)F(\rho)d\rho. \quad \text{(A2.33)}$$

We now add to (A2.32) its complex conjugate which, with (A2.8), leads to

$$F(r)=2\bar{C}\varphi_0\int_r^\infty\bar{\varphi}_0(\rho)F(\rho)d\rho$$
$$+\frac{2}{\pi}\int_{-\infty}^{+\infty}\frac{k^2dk}{|f(k)|^2}\varphi(k,r)\int_r^\infty\bar{\varphi}(k,\rho)F(\rho)d\rho; \quad \text{(A2.34)}$$

similarly we obtain from (A2.33)

$$F(r)=2\bar{C}\bar{\varphi}_0(r)\int_0^r\varphi_0(\rho)F(\rho)d\rho$$
$$+\frac{2}{\pi}\int_{-\infty}^{+\infty}\frac{k^2dk}{|f(k)|^2}\bar{\varphi}(k,r)\int_0^r\varphi(k,\rho)F(\rho)d\rho. \quad \text{(A2.35)}$$

Interchanging the role of φ and $\bar{\varphi}$, C and $\bar{C}$, we find from the last equation

$$F(r)=2C\varphi_0(r)\int_0^r\bar{\varphi}_0(\rho)F(\rho)d\rho$$
$$+\frac{2}{\pi}\int_{-\infty}^{+\infty}\frac{k^2dk}{|f(k)|^2}\varphi(k,r)\int_0^r\bar{\varphi}(k,\rho)F(\rho)d\rho. \quad \text{(A2.36)}$$

If now $C=\bar{C}$, i.e., $f'(-i\kappa,0)=\bar{f}'(-i\kappa,0)$, addition of (A2.34) and (A2.36) yields

$$F(r)=C\varphi_0(r)\int_0^\infty\bar{\varphi}_0(\rho)F(\rho)d\rho$$
$$+\frac{2}{\pi}\int_{-\infty}^{+\infty}\frac{k^2dk}{|f(k)|^2}\varphi(k,r)\int_0^\infty\bar{\varphi}(k,\rho)F(\rho)d\rho. \quad \text{(A2.37)}$$

Since without the bar this is the usual completeness relation, one can now easily prove that, in fact, $\bar{\varphi}(k,r)=\varphi(k,r)$ and $\bar{\varphi}_0(r)=\varphi_0(r)$ and hence $\bar{V}(r)=V(r)$. This demonstration follows reference 5, p. 14 or reference 19, p. 39.

Thus to a given $\eta(k)$, κ, and C there corresponds, at most, one potential satisfying the conditions (A2.1) (A2.2). On the other hand, two potentials with the same $\eta(k)$ and κ but different C are, of course, necessarily different since their bound state wave functions are different. In the cases of the phase equivalent potentials of Bargmann (reference 4) the positive parameter C assumes all values between zero and infinity so that there cannot be any additional phase equivalent potentials with the same binding energies satisfying (A2.1) and (A2.2).[21]

Clearly in the general case of m bound states the potential is uniquely characterized by $\eta(k)$, κ_i and the m positive parameters C_i.

Note added in proof:—Since this paper was submitted, explicit expressions have been found for a family of potentials with the same phase shift and binding energies as those of a given potential. This family can be shown to be complete since the parameters C_i

[21] In case (b) reference 4, p. 491, one finds $f'(-i\kappa,0)=\sigma/(\beta-1)$, $1<\beta<\infty$; in case (c), $f'(-i\kappa,0)=\sigma/(1+\alpha)$, $-1<\alpha<\infty$. In both cases $\sigma>0$.

of Appendix 2 take on all values $0<C_i<\infty$ [paper submitted to The Physical Review; see also B. Holmberg, Nuovo cimento **9**, 597 (1952)].

Further, an important paper by I. M. Gel'fand and B. M. Levitan [Doklady Akad. Nauk. S.S.S.R. n Ser. **77**, 557 (1951)] has come to our attention. By adapting their methods to the present case the problem of finding the potential corresponding to given $f(k)$ and constants C_i is reduced to the solution of linear integral equations. One introduces an auxiliary potential $V^{(1)}(\gamma)$ with corresponding solutions $\varphi^{(1)}(k,\gamma)$ and bound states at $E_i^{(1)}$. It's "spectral function" $\rho^{(1)}(E)$ is defined by

$$\frac{d\rho^{(1)}(E)}{dE}=\Sigma C_i^{(1)}\delta(E-E_i^{(1)}), \quad E<0,$$

$$\frac{d\rho^{(1)}(E)}{dE}=\frac{1}{\pi}\frac{\sqrt{E}}{|\rho^{(1)}(\sqrt{E})|^2}, \qquad E\geq 0.$$

To find the potential $V(r)$ corresponding to a given $\rho(E)$ one evaluates

$$G(r,s)=\int d[\rho(E)-\rho^{(1)}(E)]\varphi^{(1)}(\sqrt{E},r)\varphi^{(1)}(\sqrt{E},S)$$

and solves the integral equations

$$K(r,s)+G(r,s)+\int_0^r K(r,t)G(s,t)dt=0$$

for positive r. Then

$$V(r)=V_1(r)+2\frac{dK(r,r)}{dr}.$$

It is a simple consequence of this theory that for a given phase shift, the position of the bound states is completely arbitrary.

A paper on applications of the Gel'fand Levitan theory to scattering problems is in preparation.

PHYSICAL REVIEW VOLUME 87, NUMBER 6 SEPTEMBER 15, 1952

Excitation Cross Section for Helium Atoms*

SAUL ALTSHULER
Department of Physics, Iowa State College, Ames, Iowa
(Received February 28, 1952)

The excitation scattering of electrons from helium atoms is investigated in order to examine quantitatively the errors introduced by the fact that the description of the helium target is only approximately known. The cross section is calculated in Born approximation using formally equivalent matrix elements which weight the wave functions differently in space. Similar shapes for angular distribution and total cross section *vs* energy curves are obtained although absolute values differ.

SINCE exact wave functions for complex atoms are not available, there is an uncertainty introduced in scattering calculations which is distinct from those inherent in the Born approximation. The approximate wave functions, such as those of Slater, usually are well determined with respect to the energy of the state and are less well determined in regions other than those which contribute the most to the energy. For scattering problems such errors may be quite serious. A similar situation occurs in the calculation of optical transition probabilities, and investigations have been reported.[1] This difficulty has never been quantitatively examined for collision problems.

To make this study, we follow the suggestion, advanced by Bates, Fundaminsky, and Massey,[2] of employing two formally equivalent expressions for the differential cross section, both of which are within the Born approximation. These expressions are not necessarily the same in actual calculation since they weight the various regions of coordinate space differently.

The cross section for a momentum change dK for excitation of an atom from state p to state q is given in Born approximation[3] by

$$I(K)dK=\frac{8\pi dK}{k_p^2K^3}\left|\sum_i^n\int e^{-iKr_i}\psi_p\psi_q^*d\tau_1d\tau_2\cdots d\tau_n\right|^2, \quad (1)$$

where the summation is made over the atomic electrons, and where $\mathbf{K}=\mathbf{k}_q-\mathbf{k}_p$, k_p=wave number of the incident electron, k_q=wave number of the scattered electron, $k_q^2=k_p^2-2\Delta E$, and $\Delta E=E_q-E_p$, the internal energy change of the target; in all of these symbols Hartree units have been used.

The summation over the atomic electrons is made readily if product type wave functions are used. For the ground state of helium

$$\psi_p=\psi_0(N|r_1)\psi_0(N|r_2), \qquad (N=1.687)$$

while for an excited state—other than an S state—the Eckhart approximation[2] to the wave function is used, i.e.,

$$\psi_q=2^{-\frac{1}{2}}\{\psi_0(2|r_1)\psi_{nlm}(1|r_2)+\psi_0(2|r_2)\psi_{nlm}(1|r_1)\},$$

where $\psi_{nlm}(N|r)$ is the wave function of a single electron in the nlm state moving in a field of charge N.

* The research reported in this paper has been sponsored by the Geophysical Research Division of the Air Force Cambridge Research Center.

[1] D. R. Bates and A. Damgaard, Trans. Roy. Soc. (London) **A242**, 101 (1949); S. Chandrasekhar, Astrophys. J. **102**, 223 (1945).

[2] Bates, Fundaminsky, and Massey, Trans. Roy. Soc. (London) **A243**, 93 (1950).

[3] N. F. Mott and H. S. W. Massey, *Theory of Atomic Collisions* (Clarendon Press, Oxford, England, 1949), second edition, pp. 226 ff.

With these assumptions,

$$\sum_i^n \int e^{-iKz}\psi_p\psi_q^* d\tau_1 \cdots d\tau_n$$

$$= \sqrt{2}\int e^{-iKz}\psi_0(N|r)\psi_{nlm}^*(1|r)d\mathbf{r}.$$

Choosing the final states with their polar axis along the momentum transfer vector $\mathbf{K}$ establishes the selection rule $\Delta m=0$ for the process. Therefore, the differential cross section becomes

$$I(K)dK=\frac{16\pi dK}{k_p^2K^3}\left|\int e^{-iKz}\psi_0(N|r)\psi_{nl}(1|r)d\mathbf{r}\right|^2. \quad (2)$$

By making use of the equations satisfied by exact helium atom wave functions, ψ_q and ψ_p, the product $\psi_q^*\psi_p$ appearing in (1) is replaced by

$$\psi_q^*\psi_p=\frac{\psi_q^*(\nabla_1^2+\nabla_2^2)\psi_p-\psi_p(\nabla_1^2+\nabla_2^2)\psi_q^*}{2(E_q-E_p)},$$

and by a straightforward analysis, using the Eckhart wave functions, an alternative expression for the differential cross section can be shown to be

$$I(K)dK=\frac{4\pi dK}{(\Delta E)^2Kk_p^2}\left|\int e^{-iKz}\left\{\psi_{nl}^*(1|r)\frac{\partial}{\partial z}\psi_0(N|r)\right.\right.$$

$$\left.\left.-\psi_0(N|r)\frac{\partial}{\partial z}\psi_{nl}^*(1|r)\right\}d\mathbf{r}\right|. \quad (3)$$

Equation (2) and Eq. (3) have been applied to two cases, namely, the transition 1^1S to 2^1P and 1^1S to 3^1P. All results using Eq. (2) will be designated as method I; those using Eq. (3) will be designated as method II. Method I is the one conventionally used and many applications appear in reference 2.[4]

For the transition 1^1S to 2^1P, the differential cross section per unit solid angle, $I(\theta)$, in units of πa_0^2, after transforming from momentum to angular variables, is

$$2\pi I(\theta)=1.176\times10^4\frac{k_q}{k_p}\frac{1}{K^2(p^2+K^2)^6} \text{ by method I,} \quad (4)$$

$$2\pi I(\theta)=2.532\times10^2\frac{k_q}{k_p}\frac{[8.069-0.687K^2]^2}{K^2(p^2+K^2)^6}$$

by method II, (5)

where $p^2=4.783$. For this transition $\Delta E=0.779$ in Hartree units.

[4] Application of method I in the present investigation reveals a slight discrepancy between cross sections reported here and those reported by Mott and Massey in reference 2 for the 1^1S to 2^1P transition.

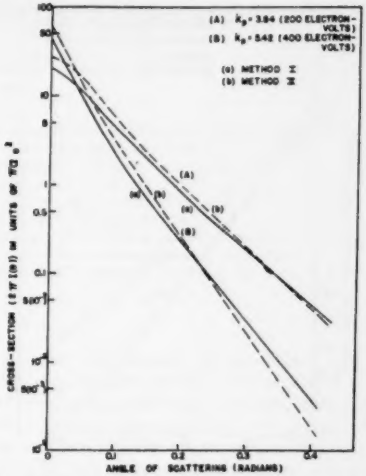

FIG. 1. Angular distributions for excitation scattering of electrons by helium atoms (^1S to 2^1P transition).

The corresponding total cross sections,

$$\int_0^\pi 2\pi I(\theta)\sin\theta d\theta,$$

are

$$Q_{\rm I}(k_p)=\frac{1.176\times10^2}{k_p^2}\left[\frac{1}{X^5}\left\{2.091+0.5464X\right.\right.$$

$$+0.1523X^2+4.777\times10^{-2}X^3+1.997\times10^{-2}X^4$$

$$\left.\left.+4.176\times10^{-3}X^5\ln\frac{K^2}{X}\right\}\right]_{k_p-k_q}^{k_p+k_q} \text{ by method I,} \quad (6)$$

$$Q_{\rm II}(k_p)=1.402Q_{\rm I}+\frac{2.987}{k_p^2}\left[\frac{5K^2-89.18}{X^5}\right]_{k_p-k_q}^{k_p+k_q}$$

by method II, (7)

where $X=p^2+K^2$.

For the transition 1^1S to 3^1P, where $\Delta E=0.8474$, the final results are

$$2\pi I(\theta)=1.507\frac{k_q}{k_p}\frac{[52.55K^2+1.168\cdot10^2]^2}{K^2(p^2+K^2)^8}$$

by method I, (8)

$$2\pi I(\theta)=0.5245\frac{k_q}{k_p}\frac{[-8.28K^4+87.62K^2+228.8]^2}{K^2(p^2+K^2)^8}$$

by method II, (9)

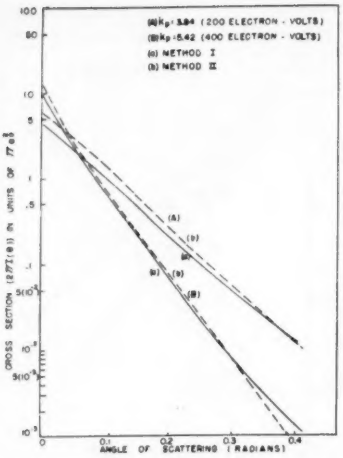
(a) k_p = 3.84 (200 ELECTRON - VOLTS)
(b) k_p = 5.42 (400 ELECTRON - VOLTS)
(a) METHOD I
(b) METHOD II
CROSS SECTION ($2\pi I(\theta)$) IN UNITS OF πa_0^2
ANGLE OF SCATTERING (RADIANS)

FIG. 2. Angular distributions for excitation scattering of electrons by helium atoms (^1S to 3^1P transition).

where $p^2=4.093$;

$$Q_{\mathrm{I}}(k_p)=\frac{1.507}{k_p{}^2}\left[\frac{1}{X^7}\left\{-1.012\times10^3-2.301\times10^2K^2\right.\right.$$

$$67.93X+19.92X^2+6.084X^3+1.982X^4+0.7265X^5$$

$$\left.\left.+0.3550X^6+8.675\cdot10^{-2}X^7\ln\frac{K^2}{X}\right\}\right]_{k_p-k_q}^{k_p+k_q}$$

by method I, (10)

$$Q_{\mathrm{II}}(k_p)=1.335Q_{\mathrm{I}}-\frac{0.5245}{k_p{}^2}\left[\frac{1}{X^7}\left\{8.570K^6-1.241\times10^2K^4\right.\right.$$

$$\left.\left.-1.303\times10^3K^2-2.175\times10^3\right\}\right]_{k_p-k_q}^{k_p+k_q}$$

by method II, (11)

where $X=p^2+K^2$, as before.

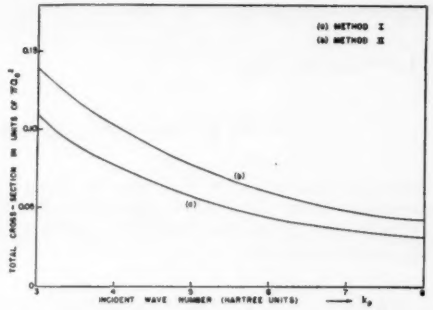

FIG. 3. Total excitation cross section for electron impact with helium atoms as a function of incident energy (^1S to 2^1P transition).

The angular distributions for the two transitions appear in Figs. 1 and 2, while the total cross sections are presented in Figs. 3 and 4. Particular significance is

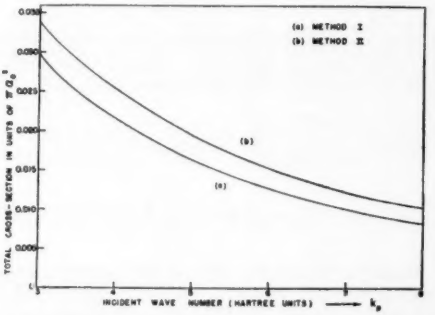

FIG. 4. Total excitation cross section for electron impact with helium atoms as a function of incident energy (^1S to 3^1P transition).

attached to the results since, except for magnitudes of the cross sections, the general behavior is quite similar for the two methods. Therefore, the results of either may be successfully normalized to measured cross sections.

Transmission of X-rays through Calcite near the Bragg Angle*†

GEORGE L. ROGOSA AND GUENTER SCHWARZ
Department of Physics, Florida State University, Tallahassee, Florida
(Received May 21, 1952)

Transmitted and diffracted intensities of monochromatic x-ray radiation through single crystals of calcite have been recorded. Wavelengths between 0.631A and 2.29A and crystal thicknesses from 0.1 mm to 3.06 mm were used. A double-crystal spectrometer served as monochromator. Intensities were measured with a Geiger counter. The measurements permit an angular correlation between the transmitted and diffracted curves to within one second of arc. The results show an anomalous absorption near the Bragg angle. Characteristically different results are obtained depending on the crystal thickness and the wavelength. For "thin" crystals the transmitted intensity decreases at the Bragg angle. For "thick" crystals the transmitted intensity increases at the Bragg angle. At each particular wavelength there exists a region of "intermediate" crystal thicknesses for which the transmitted intensity passes through a maximum and minimum as the crystal is rotated through the Bragg angle.

I. INTRODUCTION

THE diffraction of x-rays by large single crystals has received much attention in regard to both theory and experiment. There still exist, however, problems in this field with relatively little experimental data and until very recently incomplete theoretical treatment. Such a problem is that of the transmission of x-rays through a crystal in the direction of the incident beam at a position where a Laue diffraction occurs. Investigations of this transmitted and reflected radiation have been made in only a few cases and without the precision of x-ray spectroscopic techniques available today.

Bragg and others[1] have observed that when a rock-salt crystal is oriented so that Mo $K\alpha$ radiation undergoes a Laue reflection, the transmitted intensity is less at this Bragg angle than that which is transmitted when the crystal is off the Bragg angle. This decrease in intensity is due to primary extinction.[2] Campbell[3] has recently shown that the transmitted intensity may undergo large increases when the crystal is set at a Bragg angle. The work of Campbell was done with single-crystal monochromatization using Cu $K\alpha$ and Cu $K\beta$ radiation and Geiger counter intensity recording. Borrmann,[4] using a divergent beam technique and photographic recording, has investigated this effect with quartz and calcite crystals.

We have investigated the transmission of monochromatic x-rays between 0.63A and 2.29A through single crystals of calcite of thicknesses 0.1 to 3 mm and have recorded the changes in transmitted and reflected intensities near the Bragg angle with a much higher precision than previously reported. New results have been obtained showing that at the Bragg angle, the transmitted intensity may increase, decrease, or fluctuate with both an increase and decrease, depending on the wavelength of the radiation and the thickness of the crystal.

II. EXPERIMENTAL

The experimental arrangement is shown in Fig. 1. A standard full-wave rectified high voltage supply was used in this work. The input voltage was stabilized with a Sorenson model 2000-S electronic voltage regulator. The high voltage applied to the x-ray tube was electronically regulated with a modified Pepinsky type circuit.[5] The x-ray tube current was stabilized using a circuit similar to the one described by Le Mieux and Beeman.[6] Commercial Machlett A-2 x-ray tubes with Cr, Cu, Mo, and W targets were used. Tests showed that after an initial warm-up period, the intensity of x-ray radiation was constant over long periods.

A double-crystal spectrometer was used to monochromatize the x-rays. The first crystal was mounted on a slide perpendicular to a line connecting the focal spot and the axis of rotation for the second crystal and

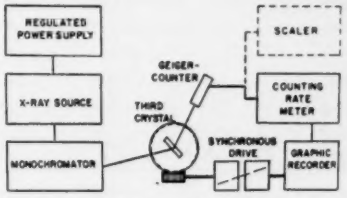

FIG. 1. Block diagram of apparatus used.

* A preliminary report of this work was presented at the spring meeting of the American Physical Society in Washington, D. C., 1952. See also Guenter Schwarz and George L. Rogosa, Phys. Rev. **86**, 421 (1952).

† This work was supported in part by a grant from the Research Corporation.

[1] Bragg, Bosanquet, and James, Phil. Mag. **42**, 1 (1921).

[2] See, e.g., A. H. Compton and S. K. Allison, *X-Rays in Theory and Experiment* (D. Van Nostrand and Company, Inc., New York, 1935).

[3] H. N. Campbell, Acta Cryst. **4**, 180 (1951); J. Appl. Phys. **22**, 1139 (1951).

[4] G. Borrmann, Physik. Z. **43**, 157 (1941); G. Borrmann, Z. Physik **127**, 297 (1950).

[5] R. Pepinsky and Paul Jarmotz, Rev. Sci. Instr. **19**, 247 (1948); Guenter Schwarz and Earl H. Byerly, Rev. Sci. Instr. **19**, 273 (1948).

[6] A. F. Le Mieux and W. W. Beeman, Rev. Sci. Instr. **17**, 130 (1946).

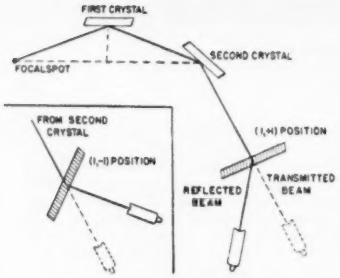

FIG. 2. Arrangement of crystals.

halfway between them. The second crystal was mounted on a table which could be rotated in steps of a second of arc by means of an arrangement of levers and a precision micrometer head. This table was supported by a set of high precision Timken roller bearings.[7] The micrometer screw was calibrated by measuring the separation of the Cu $K\alpha$ lines, using different parts of the screw. The calibration was linear over the range of the screw which covered an angular region of 83′ of arc. The accuracy of resetting was checked by measuring $(1, -1)$ curves. It was possible to reset the crystal to within a second of arc.

The perfection of the cleaved calcite crystals on the spectrometer was checked by measuring the width of $(1, -1)$ curves and line widths in the $(1, +1)$ position. The half-width of the $(1, -1)$ curve at Cu $K\alpha$ was 10.3″ which is very close to the theoretical value of 9.8″. The half-width of the Cu $K\alpha_1$ line was 44″.

The monochromatic beam coming from the second crystal passed over the axis of a Gaertner spectrometer[8] on which the crystal to be investigated was mounted. The crystal table of this spectrometer could be rotated by a synchronous motor drive at angular speeds of

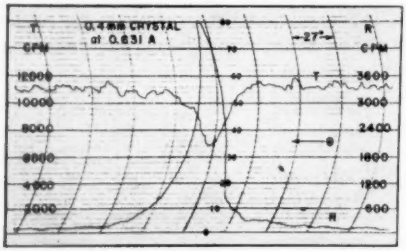

FIG. 3. Transmitted and reflected intensities through a 0.4-mm calcite crystal showing extinction at the Bragg angle.

[7] We would like to express our appreciation to Mr. R. G. Harmon of the Timken Roller Bearing Company for providing us with a set of precision roller bearings.

[8] This spectrometer is on loan from the University of Chicago through the courtesy of Professor S. K. Allison.

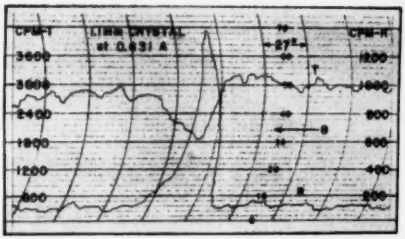

FIG. 4. Transmitted and reflected intensities through a 1.1-mm calcite crystal showing the transition to asymmetrical transmission.

7.5 or 27 seconds of arc per minute of time. Manual setting of this table could be done to within 1″. The angular position of the table could be read accurately by means of two microscopes. The circle had been recently re-engraved by the Gaertner Company.

X-ray intensities were measured with a high pressure argon filled counter in conjunction with a General Radio counting rate meter. The output was plotted by means of an Esterline Angus Recording Milliammeter. In some cases intensities were measured by counting for a fixed time, using a Berkeley model 2000 scaler and rotating the crystal manually in small steps.

Figure 2 shows a diagram of the arrangement of the calcite crystals. The crystal under study was mounted with a face parallel to and on the axis of the Gaertner spectrometer. In order to align the internal planes the Bragg reflection from the planes parallel to this face was first detected by the Geiger counter. A rotation of 105° 3.5′ or 74° 56.5′ depending on how the crystal was positioned would then bring a similar set of internal planes into position to give a Laue reflection. This technique enabled one to quickly find the diffraction positions of the crystal. The internal planes were carefully adjusted to give the narrowest rocking curve. We used two different diffracting positions for each crystal. These two positions can be conveniently designated as $(1, +1)$ or $(1, -1)$ using the standard double crystal spectrometer nomenclature and referring the crystal under investigation to the second crystal of the mono-

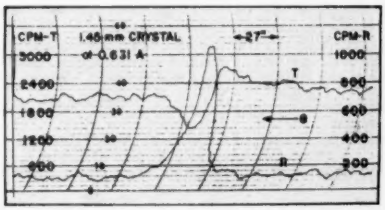

FIG. 5. Transmitted and reflected intensities through a 1.45-mm calcite crystal showing asymmetrical transmission.

chromator. The monochromator itself was used in the $(1, +1)$ position for the work reported here except in the case of the Cr $K\alpha$ radiation.

The calcite crystals, through which the transmitted radiation was measured, were cleaved from large single crystals. With care it was possible to cleave suitable crystals as thin as 1 mm. The size of these crystals was approximately 10 mm by 20 mm. For thicknesses between 0.3 mm and 1 mm, cleaved crystals were ground with emery of mesh 275 and then etched in HCl.[9] In addition, thinner crystals were obtained by prolonged etching reaching 0.1 mm. Work was also done with crystals cut such that the reflecting planes were perpendicular to the surface. Crystal thicknesses were constant to less than 0.01 mm over the area used in the experiments. All calcite used came from optically clear pieces.

III. EXPERIMENTAL RESULTS

Experiments were performed at wavelengths corresponding to characteristic line radiation from the various targets. The lines used were Mo $K\beta_1$, Mo $K\alpha_1$, W $L\gamma_1$, Cu $K\alpha_1$, and Cr $K\alpha$ giving a spread of wavelength from 0.63A to 2.29A. The results indicated that

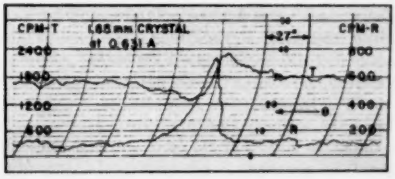

FIG. 6. Transmitted and reflected intensities through a 1.65-mm calcite crystal showing asymmetrical transmission.

there was no need to perform experiments at other intermediate wavelengths.

Figures 3 to 8 show the results obtained at a wavelength of 0.631A for calcite of thicknesses 0.4 mm to 2.56 mm. These curves show the significant features observed in this work. All of them were recorded with an x-ray tube voltage of 28 kv and current of 20 ma. No second-order radiation was passed by the spectrometer. T represents the intensity of the transmitted beam, and R represents the Laue reflected intensity. These curves were all taken in the $(1, -1)$ position as illustrated in Fig. 2. θ represents the angle between the incident beam and the reflecting crystal planes and increases to the left in the curves. Some care has to be exercised in making quantitative calculations from these curves. With a counting rate meter, in regions where the intensity changes fast compared to the response time of the instrument, corrections have to be applied. In particular, peak intensities will be recorded too low. The transmitted and reflected curves were

[9] K. V. Manning, Rev. Sci. Instr. **5**, 316 (1934).

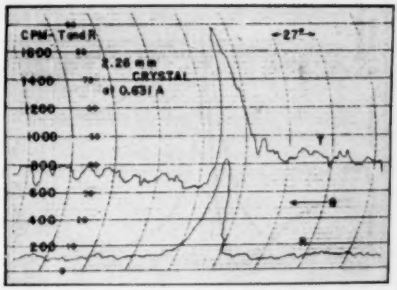

FIG. 7. Transmitted and reflected intensities through a 2.26-mm calcite crystal showing anomalous transparency.

taken successively. Their abscissas are matched to within 1″.

The crystal thicknesses given in the figures represent the perpendicular distance between crystal faces. The crystal planes make an angle close to 15° with this perpendicular. In calculating absorption coefficients, the actual path of the radiation through the crystal has to be known.

Figure 3 shows an example of the "thin" crystal case. In this and all following curves the Bragg angle θ_B is defined by the peak of the reflection curve. There is a decrease in the transmitted intensity at the Bragg angle. In Fig. 4 an asymmetry appears showing a decreased absorption near θ_B on the side of $\theta<\theta_B$. The absorption on both sides of the Bragg angle is still different for angular separations of several minutes. This asymmetry becomes much more pronounced with increasing crystal thickness as seen in Figs. 5 and 6. The transmission curve in both cases shows the decreased absorption near θ_B for $\theta<\theta_B$ followed by an increased absorption for $\theta>\theta_B$. Even at an angular distance of several minutes off the Bragg angle the absorption itself is not the same on both sides. The transmission curve is characterized by an inflection point near the Bragg angle, and because of the increase and decrease we shall refer to this as "asymmetrical transmission." The crystals used in the curves of Figs. 7 and 8 approach the "thick" crystal case, and the curves show the

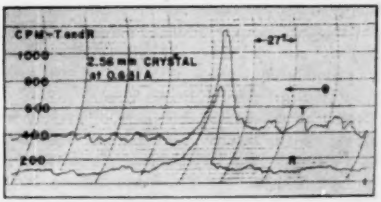

FIG. 8. Transmitted and reflected intensities through a 2.56-mm calcite crystal showing anomalous transparency.

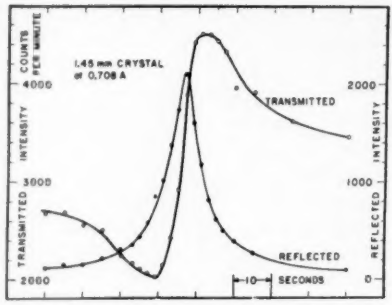

FIG. 9. Detailed plot of asymmetrical transmission case.

anomalous transparency at the Bragg angle. The absorption off the Bragg angle still remains different on both sides.

With Mo $K\alpha_1$ radiation of 0.708A, crystals from 0.4 mm to 3.06 mm were investigated. The 0.4-mm crystal showed a pronounced dip in the transmitted intensity, while the 3.06-mm crystal showed a pronounced increase. At 0.75 mm the effect was mainly a decrease, while at 2.56 mm it was still an increase. Between these two values the results gave asymmetrical transmission. Figure 9 shows the curves of the transmitted and reflected intensities for a crystal of 1.45 mm thickness. Here intensities were recorded by using the scaler and rotating the crystal manually in steps of 2″ near the Bragg angle. The transmitted and reflected intensity was measured by switching the Geiger counter to fixed positions as shown in Fig. 2 for each angular crystal setting.

At 1.096A, W $L\gamma_1$ radiation, a 0.9-mm crystal showed the "thick" crystal type increase in the transmitted intensity. The 0.1-mm crystal, which was the thinnest available in this work, showed a dip. Intermediate thicknesses produced asymmetrical transmission.

At Cu $K\alpha_1$ the thinnest crystal available at the time was 0.4 mm, and this gave a pronounced increase of transmission. All thicker crystals also gave anomalous transparency with no significantly new features. The sawcut crystals with the internal reflecting planes perpendicular to the faces were used at this wavelength and gave results similar to cleaved crystals.

Calcite is highly absorbing at 2.29A, Cr $K\alpha$, and crystal thicknesses were limited to less than 1 mm because of the x-ray intensity available. A 0.4-mm crystal gave a pronounced increase in the transmitted intensity when rotated through the Bragg angle.

In order to determine the effect of surface imperfections upon the results, a comparison was made between a cleaved crystal and a ground crystal of about the same thickness. No significant differences in the shapes of the transmitted curves were observed. Transmission and reflection curves were always taken in both $(1,-1)$ and $(1,+1)$ positions. In general, the effects were somewhat more pronounced in the $(1,-1)$ position.

IV. DISCUSSION

The theory of these phenomena has received the attention of Von Laue[10] and very recently Ramachandran,[11] Zachariasen,[12] Hirsch,[13] and Ewald.[14] Von Laue[10] has considered a possible explanation. Since his numerical calculations are for rocksalt and Cu $K\alpha$ radiation, they cannot be directly compared with our data. However, his predicted shapes of the transmitted curves are similar to those that we have recorded. Ramachandran[11] has used the theory of Von Laue to calculate the diffracted and transmitted intensities through "thick" crystals of calcite in order to compare with the results of Borrmann and Campbell. Ramachandran significantly points out that the peaks of the reflected and transmitted beams are not coincident but that a shift occurs which decreases for increasing crystal thickness. Our experimental results confirm this theoretical prediction.

Zachariasen[12] has derived an expression for the absorption coefficient at the Bragg angle for the "thick" crystal case, and he finds good agreement with data of Borrmann and Campbell. Zachariasen concludes that anomalous transparency only results when $\mu_0 \cdot t_0 > 1$, μ_0 being the ordinary absorption coefficient and t_0 being the thickness of the crystal plate. Zachariasen's results follow from equations in his dynamical theory of x-ray diffraction.[15]

Hirsch[13] has treated this problem starting with the dynamical theory as given by Zachariasen. He has calculated the intensity curves for both the transmitted and reflected beams for the "thin," "intermediate," and "thick" crystal cases. We find good agreement with the shapes of his calculated curves. Quantitative details are being further investigated.

We wish to express our appreciation to Professor P. P. Ewald for very helpful discussions. Thanks are due Mr. Lewis V. Eckhart who built the monochromator and made many valuable contributions to its design and to Mr. L. C. Brown for help in making the measurements.

[10] M. Von Laue, Acta Cryst. **2**, 106 (1949).
[11] G. N. Ramachandran, J. Appl. Phys. **23**, 500 (1952); G. N. Ramachandran and Gopinath Kartha, Proc. Indian Acad. Sci. **35**, 145 (1952).
[12] W. H. Zachariasen, Proc. Natl. Acad. Sci. **38**, 378 (1952).
[13] P. B. Hirsch, Acta. Cryst. **5**, 176 (1952), and private communication.
[14] P. P. Ewald, private communication.
[15] A private communication from Zachariasen has pointed out that his theory predicts asymmetrical transmission for intermediate crystal thicknesses.

Mean Free Path of the High Energy N Component of Cosmic Radiation*

ROBERT R. BROWN
Department of Physics, University of California, Berkeley, California
(Received April 28, 1952)

The mean free path of charged particles that produce penetrating showers has been measured in carbon, sulfur, and iron. Preliminary measurements with carbon were carried out at 130-m elevation and the mean free path obtained was 89±12 g/cm². Measurements at 2765-m elevation gave mean free paths in carbon, sulfur, and iron of 65±5, 76±7, and 115±12 g/cm², respectively. The carbon data were used to get an estimate of the mean free path in nuclear matter of high energy nucleons.

I. INTRODUCTION

IN recent years a number of experiments have been performed to determine the mean free paths of the particles that produce penetrating showers.[1-7] The results of the experiments in which lead was used as an absorber are in good agreement and indicate that mean free paths in heavy elements are determined by nuclear geometric cross sections. For light elements, such as carbon, the results do not agree very well but do indicate that mean free paths are determined by cross sections significantly smaller than geometric cross sections. The present paper will report measurements of the mean free paths in carbon, sulfur, and iron. These measurements were begun in the spring of 1951 near sea level at Berkeley, California, and continued the following summer at an elevation of 2765 m at Lake Sabrina, California.

II. APPARATUS

The arrangement of counters and absorbers used in this experiment is shown in Fig. 1. Tray A contained 14 1½-inch by 15½-inch counters while trays B, C, and D each contained 3 1-inch by 15½-inch counters. Pulses from the various counters in a tray were mixed by means of crystal diodes, and the combined output was fed through a coaxial cable to the appropriate element in the electronic apparatus.

Trays E and F each contained 20 ½-inch by 15½-inch counters. Each counter in trays E and F had a separate input unit associated with it, and the pulses from a counter were fed directly to the input unit through a coaxial cable.

Trays A, B, C, and D served as master trays, i.e., a fourfold coincidence $ABCD$ started the cycle of operation of the apparatus, while trays E and F served as hodoscope trays and operated a neon bulb system.

The nature and amount of absorber S_1 was varied, whereas absorbers P and S_2 remained the same throughout the experiment. Absorber P served as a production layer for penetrating showers and consisted of 38 g/cm² of graphite, while absorber S_2 was used to establish the penetrating nature of the particles produced in P and consisted of 170 g/cm² of lead.

Pulses from the counters in trays A, B, C, and D were fed into separate pulse forming circuits, and the output of these circuits was put in coincidence by means of crystal diodes. Whenever a fourfold coincidence $ABCD$ occurred, additional timing circuits were set in operation, and a pulse was sent out to each of the input units associated with the counters of the hodoscope trays. If the pulse from the timing unit was in coincidence with a pulse from a hodoscope counter, the neon bulb associated with that counter was extinguished for approximately 1 second The neon bulbs were displayed in two rows, corresponding to the two hodoscope trays, and were photographed while extinguished by a camera actuated by the timing circuit. A very loose selection of events was obtained with this arrangement, the minimum requirements being that one charged particle pass through tray A and three charged particles pass through trays B, C, and D. By examining the hodoscope pictures, a more stringent selection was made.

The photographs of the hodoscope neon bulb system were examined and classified as to the number of particles which entered and left the graphite layer P. Those photographs which showed one upper neon bulb and one lower neon bulb extinguished corresponded to showers produced in absorber S_2 by particles which traversed absorbers S_1 and P, whereas those photographs which showed one upper neon bulb and three or more lower neon bulbs extinguished corresponded to penetrating showers produced in absorber P by particles which traversed absorber S_1.

The events selected for consideration in the present experiment were those in which a shower was produced in the graphite layer P. This procedure was adopted in order to reduce the background events due to the collision and radiation processes of mu-mesons.

The nature and amount of absorber S_1 was varied, and by measuring the rate of penetrating showers produced in the graphite as a function of thickness of absorber, the mean free paths in carbon, sulfur, and iron were determined.

* Assisted by the joint program of the ONR and AEC.
[1] J. Tinlot and B. Gregory, Phys. Rev. **75**, 519 (1949).
[2] G. Cocconi, Phys. Rev. **75**, 1074 (1949).
[3] W. D. Walker, Phys. Rev. **77**, 686 (1950).
[4] K. Sitte, Phys. Rev. **78**, 714 (1950).
[5] R. H. Rediker and H. S. Bridge, Phys. Rev. **79**, 206 (1950).
[6] Walker, Walker, and Griesen, Phys. Rev. **80**, 546 (1950).
[7] E. P. George and A. C. Jason, Proc. Roy. Soc. (London) **A63**, 1081 (1950).

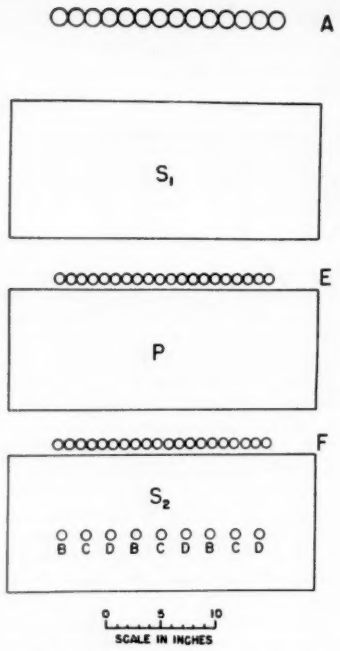

FIG. 1. Arrangement of absorbers and counters.

III. DATA AND RESULTS

The results of the measurements at Berkeley (130-m elev., 1020 g/cm²) and at Lake Sabrina (2765-m elev., 738 g/cm²) are given in Tables I and II. The data in Table I represent showers produced in the graphite layer P, whereas those of Table II represent showers produced in absorber S_2. The probable errors indicated in these tables are based on the total number of counts. The data given in Table I are plotted on a logarithmic scale in Figs. 2 and 3, and the mean free paths have been calculated by passing straight lines through the experimental points by the method of least squares. The results of these calculations are as follows:

At 130-m elevation,

In C, $\lambda_C = 89 \pm 12$ g/cm².

At 2765-m elevation,

In C, $\lambda_C = 65 \pm 5$ g/cm²,
In S, $\lambda_S = 76 \pm 7$ g/cm²,
In Fe, $\lambda_{Fe} = 115 \pm 12$ g/cm².

The increase in counting rate, with 0 g/cm² absorber, between Berkeley and Lake Sabrina corresponds to an absorption mean free path in air of 132 ± 17 g/cm². It should be pointed out that there remains some uncertainty in the mean free path of sulfur. The sulfur absorbers were cast in large cakes and the thickness was not the same throughout. When the experiment was completed, the sulfur cakes were broken up and the mean thickness estimated in each case.

The probable errors of the mean free paths are those determined by the internal consistency of the data, i.e., the amount of data available. In every case the probable error determined by the external consistency of the data, i.e., the fit of the data with an exponential, was smaller than that determined by the internal consistency.

In the course of the experiment the number of counters struck by shower particles emerging from the graphite production layer were recorded, and size-frequency distributions were made for each thickness of absorber. At Lake Sabrina, it was found that the size-frequency distributions of the penetrating showers were essentially the same for each absorber thickness. This indicates in a qualitative way that the nature of the showers produced in P did not change appreciably as the nature and amount of absorber S_1 was varied. The size-frequency distributions obtained at Berkeley were roughly the same but cannot be compared with those obtained at Lake Sabrina because of poor statistics.

While events corresponding to showers produced in the lead absorber S_2 were also recorded, the data ob-

TABLE I. Rate of showers in absorber P as a function of thickness of absorber S_1.

Absorber S_1 (g/cm²)	P showers (hr⁻¹) $ABCD+E^1+F\geq^2$
Lake Sabrina	
0 C	1.030±0.055
38 C	0.530±0.029
72 C	0.341±0.018
37 S	0.612±0.032
64 S	0.449±0.026
40 Fe	0.700±0.036
80 Fe	0.516±0.026
Berkeley	
0 C	0.122±0.009
38 C	0.084±0.006
72 C	0.054±0.005

TABLE II. Rate of showers in absorber S_2 as a function of thickness of absorber S_1.

Absorber S_1 (g/cm²)	S_2 showers (hr⁻¹) $ABCD+E^1+F^1$
Lake Sabrina	
0 C	1.216±0.059
38 C	0.702±0.036
72 C	0.531±0.022
37 S	0.720±0.035
64 S	0.644±0.031
40 Fe	0.994±0.044
80 Fe	0.713±0.031
Berkeley	
9 C	0.195±0.011
38 C	0.118±0.007
72 C	0.090±0.005

tained was used only for comparison with previous work and not for the calculation of mean free paths. In view of the findings of Cocconi,[8] the showers produced in absorber S_2 can be interpreted as a mixture of penetrating showers due to high energy nucleons and electronic showers due to the collision and radiation processes of mu-mesons. The extent to which the background events due to mu-mesons has been reduced by considering showers produced in the graphite production layer P is not clear from the present experiment. At Lake Sabrina, the rate of showers in S_2 falls off somewhat slower than the rate of showers in P with increasing absorber thickness, while at Berkeley, both types of events decrease at about the same rate. From the variation of the counting rates it appears that there was some background present, but only at the lower altitude, where the mu-meson component is relatively more abundant, does the background seriously influence the mean free path measurements. The measurements made at the higher altitude can be used as upper limits for the mean free paths.

IV. DISCUSSION

If nuclei were completely opaque to high energy nucleons, the mean free path would be determined by the nuclear geometric cross section and given by

$$\lambda_0 = A/N_0\pi R^2,$$

where A is the mass number, N_0 is Avogadro's number, and R is the nuclear radius. Assuming

$$R = (0.5 + 1.37A^{\frac{1}{3}}) \times 10^{-13} \text{ cm},^{9}$$

the mean free paths for carbon, sulfur, and iron are 48, 72, and 89 g/cm², respectively.

If instead nuclei were transparent to high energy nucleons, the mean free paths would be longer than those derived from nuclear geometric cross sections. The optical model of the nucleus of Fernbach, Serber, and Taylor[10] gives the mean free path as

$$\lambda = \lambda_0\{1 - [1 - (1+2KR)e^{-2KR}]/2K^2R^2\}^{-1},$$

where K is the reciprocal of the mean free path in nuclear matter and R is the nuclear radius. With the aid of the above model, the carbon data obtained at Lake Sabrina may be used to get an estimate of the mean free path in nuclear matter of high energy nucleons. Using 65 ± 5 g/cm² for the mean free path in carbon, one obtains a mean free path in nuclear matter of $(3.2 \pm 0.6) \times 10^{-13}$ cm. With this value of $1/K$, the calculated mean free paths in sulfur and iron are 88 ± 5 and 105 ± 6 g/cm² in fair agreement with the measured values.

The mean free path in carbon measured at Lake Sabrina is shorter than previously reported results[2,5-7]

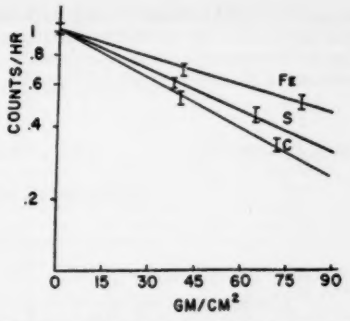

FIG. 2. Frequency of showers produced in asborber P, as a function of thickness of absorber S_1. (2765-m altitude.)

and might be accounted for by an increase in the cross section with energy. Recent work by Walker *et al.*[11] has shown that the multiplicity of penetrating particles produced in lead is greater than that in carbon, indicating that the production involves both multiple and plural processes. Owing to the small size of the carbon nucleus, multiple production is probably the dominant factor in carbon, whereas both processes can take place in a large nucleus such as lead. On this basis, showers of a given multiplicity will be derived from more energetic incident particles in the case of carbon than in the case of lead. With the bias of the detector toward large showers, it would seem that the apparatus selected a more energetic part of the incident spectrum than previous experiments.

The author is indebted to Professor W. B. Fretter for

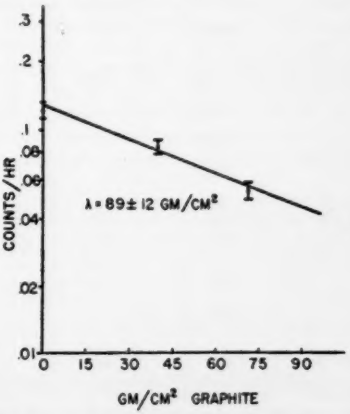

FIG. 3. Frequency of showers produced in absorber P, as a function of thickness of absorber S_1. (130-m altitude.)

[8] G. Cocconi, Phys. Rev. **76**, 984 (1949).
[9] Cook, McMillan, Peterson, and Sewell, Phys. Rev. **75**, 7 (1949).
[10] Fernbach, Serber, and Taylor, Phys. Rev. **75**, 1352 (1949).
[11] Walker, Duller, and Sorrells, Phys. Rev. **85**, 773 (1952).

his generous advice and assistance during the course of this work and to Dr. W. D. Walker for discussions regarding the interpretation of the experimental results. The assistance of Merritt L. MacKnight and Bruce J. Harris in constructing the apparatus is also gratefully acknowledged. Appreciation should also be expressed for the loan of the sulfur used in the experiment by the San Francisco Sulfur Company.

PHYSICAL REVIEW VOLUME 87, NUMBER 6 SEPTEMBER 15, 1952

Forbidden Line of N II in the Aurora*

W. PETRIE†
University of Saskatchewan, Saskatoon, Saskatchewan, Canada
(Received April 11, 1952)

A feature of the auroral spectrum is the presence of moderately intense O II and N II permitted lines and the apparent absence of lower energy level forbidden lines of the same ions. A weak feature at 5755A has been detected in high dispension auroral spectrograms, and this is interpreted as due to the forbidden N II transition $^1D-^1S$. The likely cause of the weakness of O II and N II forbidden lines is discussed.

RECENTLY, a report has been prepared[1] on a high dispersion study of the auroral spectrum. In this report it was noted that the forbidden O I and N I lines are stronger than the permitted lines of the same atoms, whereas in the case of O II and N II permitted lines are present, but the forbidden lines are either very weak or absent.

More recently, stronger spectrograms have been secured in the regions of the forbidden lines, and definite statements may be made regarding their presence or absence. Relevant data on the forbidden lines in the wavelength region examined are given in Table I. The fourth column lists the Einstein A value of each multiplet.[2]

TABLE I. Data regarding O II and N II forbidden lines.

Transition	Wavelength (A°)	Excitation potential (ev)	A (sec^{-1})
O II $^4S-^2D$	3726	3.31	6×10^{-5}
	3729		
O II $^2D-^2P$	7318.6	5.00	8.3
	7319.4		
	7329.9		
	7330.7		
N II $^3P-^1D$	6527	1.89	3×10^{-2}
	6527		
	6548		
	6584		
N II $^1D-^1S$	5755	4.04	1.7

All the denser plates in the 5500A region show a sharp feature at 5755A near the first head of the (12, 8), first positive nitrogen band. This feature is not part of the band and is likely to be the $^1D-^1S$ N II line. The $^3P-^1D$ lines are absent, which is not surprising considering the A value. Since N II and O II ions are few in number compared to the neutral atoms, it appears that the ions are formed in excited levels as a result of simultaneous ionization and excitation from the neutral atoms. If the excitation is from the ground ^4S level of N I, only triplet levels of N II can be formed, whereas the λ5755 N II line arises from a ^1S level. However, it is apparent from the intensity of the forbidden N I lines at λ5200 that there is a considerable population in the ^2D levels of N I, which levels have lifetimes of the order of eight hours. Hence a number of ionizations will take place from these levels, in which case the ^1S level of N II may be directly populated. Furthermore, we know from the presence of other N II lines in the spectrum which permitted levels are populated, and an examination of the energy level diagram indicates that a cascade process will populate the ^1S level.

A dense spectrogram has been secured of the 7300A region on a 103-U Eastman plate, and the O II lines in this region are missing. Hence, considering the A values of the O II multiplets, it is unlikely that the weak auroral feature at λ3727 is the result of the O II ion. Simultaneous ionization and excitation from the ground ^3P levels of O I can form O II in both the ^2D and ^2P levels, and a selective excitation is unlikely.

The weakness of the forbidden O II and N II lines is likely due to the fact that a single process (i.e., ionization and excitation from the low levels of O I and N I) populates the levels involved, whereas the strong forbidden lines of the neutral atoms are excited by several processes.

* This work has been supported by contract with the Geophysics Research Division, Air Force Cambridge Research Center.

† Now at Radio Physics Laboratory, Defence Research Board, Ottawa, Canada.

[1] To be published in the Astrophysical Journal.

[2] I. S. Bowen, Revs. Modern Phys. **8**, 55 (1936).

Cloud-Chamber Studies of the Production of Light "Positive Particles" near Negative Beta-Ray Emitters*

GERHART GROETZINGER† AND FRED L. RIBE‡
Institute for Nuclear Studies, University of Chicago, Chicago, Illinois
(Received May 4, 1951)

A series of experiments was performed with a cloud chamber to investigate the nature of the particles producing the positive tracks near negative beta-ray emitters reported in various investigations. Special emphasis was laid on the questions of whether the tracks are (1) due to electrons reentering the source and (2) due to electrons emerging from the source multiply scattered to show an apparent positive curvature. While the second possibility can account for only a negligible fraction of the tracks, it is found that, depending upon the source arrangement and the manner of investigating cloud-chamber photographs, a considerable fraction of observed "positive" tracks may be due to electrons which reenter or appear to reenter the source. With stereoscopic analysis and an appropriate source arrangement, the fraction of spurious positive tracks may be reduced to a few percent. With these precautions we find for P^{32} a ratio of positive particles to electrons of 3×10^{-4}. This ratio is increased by covering the source with carbon or lead. It is shown that the estimate of two electron masses previously obtained for the mass of these particles by comparing their multiple scattering with that of electrons was not influenced by the difference in the momentum distributions of the two species of particles used in the determination.

I. INTRODUCTION

DURING the past twenty years, a number of investigators[1–14] have observed tracks in magnetic cloud chambers which they have attributed to positive particles produced in the vicinity of electron emitters which, on account of the requirements of conservation of energy, cannot alternatively decay by the emission of positrons. The positive particles in question have further been observed in much greater numbers[4,6,15,16] than would be expected theoretically[17] if they were positrons resulting from internal or external pair formation by the beta-particles or by the gamma-rays emitted by some of the sources. Furthermore, the apparent absence of annihilation radiation[18] makes it appear extremely unlikely that positrons are responsible for these tracks.

There has, however, been considerable doubt expressed that the tracks in question are due to positively charged particles at all. First, several investigators[19] have suggested that these tracks were due not to positive particles but rather to electrons traveling toward the source or to electron tracks having reversed curvatures as the result of multiple scattering. Second, the earlier attempts to detect positive particles produced by such emitters with magnetic spectrometers were generally unsuccessful.[8,20–24]

A number of recent experiments, however, have provided considerable evidence that such particles exist. Groetzinger and Kahn[25] for instance, hypothesized that the positive particles were not found with magnetic spectrometers because of the fact that the required path length in conventional instruments of this sort was too long (in view of the possibility that these particles may be unstable). Consequently, they constructed a (nonevacuated) spectrometer of reduced dimensions (4.5-cm path length) using a photographic

* This research was supported in part by the joint program of the ONR and AEC. An account of this investigation and of two earlier ones (references 25 and 27) together with a comprehensive survey of the literature on these particles is given in the unpublished 1949–1950 Progress Report of the Research Program with the Chicago Cyclotron (Navy contract) p. 56, by Groetzinger, Ribe, and Kahn.

† Now at the Lewis Laboratory, NACA, Cleveland, Ohio.
‡ Now at the Los Alamos Scientific Laboratory, Los Alamos, New Mexico.

[1] Chadwick, Blackett, and Occhialini, Proc. Roy. Soc. (London) **144**, 235 (1934).
[2] D. Skobelzyn and E. Stepanowa, Nature **133**, 565 (1934).
[3] D. Skobelzyn and E. Stepanowa, Nature **133**, 646 (1934).
[4] D. Skobelzyn and E. Stepanowa, J. Phys. **6**, 1 (1935).
[5] A. M. da Silva, Ann. phys. **11**, 504 (1939).
[6] G. J. Sizoo and F. Berendregt, Physica **6**, 1085 (1939).
[7] F. Barendregt and G. J. Sizoo, Physica **7**, 490 (1940).
[8] Bradt, Hein, and Scherrer, Helv. Phys. Acta **16**, 491 (1943).
[9] H. G. Heine, Helv. Phys. Acta **17**, 273 (1944).
[10] J. Ambroson, Z. Physik **91**, 43 (1935).
[11] Barendregt, Griffioen, and Sizoo, Physica **7**, 860 (1940).
[12] L. Smith and G. Groetzinger, Phys. Rev. **70**, 96 (1946).
[13] T. H. Pi and C. V. Chao, Phys. Rev. **72**, 639 (1947).
[14] J. S. Barlow and F. T. Rogers, Phys. Rev. **74**, 700 (1948).
[15] A. M. da Silva, Compt. rend. **202**, 2071 (1936).
[16] D. Skobelzyn and E. Stepanowa, Nature **137**, 212 (1936).
[17] H. J. Bhabha, Proc. Roy. Soc. (London) **152**, 559 (1935); N. Arley and C. Møller, Kgl. Danske Videnskab. Selskab **15**, 9 (1938); J. C. Jaeger and H. R. Hulme, Proc. Roy. Soc. (London) **148**, 708 (1935); W. Heitler, *The Quantum Theory of Radiation* (Oxford University Press, London, 1936), p. 196.
[18] Chien-Shiung Wu, Phys. Rev. **59**, 481 (1941); E. H. Stahel and Guillissen, J. phys. radium **1**, 12 (1940); K. Siegbahn and H. Slätis, Arkiv. Mat. Astr.-fys. **34A**, Paper 6 (1947–48); N. Feather and J. V. Dunworth, Proc. Cambridge Phil. Soc. **34**, 435 (1938); H. Bradt, Helv. Phys. Acta **17**, 59 (1944); Cleland, Konneker, and Hughes, Phys. Rev. **79**, 229 (1950).
[19] Erdman, Kokotaila, and Scott, Phys. Rev. **76**, 1262 (1949); C. B. A. McCusker, Nature **161**, 564 (1948); J. H. Spaa and G. J. Sizoo, Physica **15**, 316 (1949); Spaa, Steneker, and Sizoo, Physica **16**, 55 (1950).
[20] H. R. Crane and J. Halpern, Phys. Rev. **55**, 838 (1948).
[21] S. Benedetti, J. phys. et radium **7**, 205 (1936).
[22] K. Shinohara, Sci. Papers Inst. Phys. Chem. Research (Tokyo) **31**, 174 (1937).
[23] K. T. Bainbridge (account of Harwell Conference), Nature **160**, 492 (1947).
[24] H. R. Holt, private communication reported in paper by C. B. A. McCusker, Nature **161**, 564 (1948).
[25] G. Groetzinger and D. Kahn, Phys. Rev. **80**, 108 (1950).

plate as a detector and succeeded for the first time in finding the positive particles with a magnetic spectrometer. More recently, Yuasa[26] performed a similar experiment with a small evacuated spectrometer with a G-M counter as a detector and also obtained positive results. In addition, other measurements have made it possible to assign a definite mass to these particles. Smith and Groetzinger[12] studied the tracks of positive particles which had passed through a foil in the cloud chamber and deduced from the energy loss a mass between one-and-one-half and two electron masses. Groetzinger and Ribe[27] arrived at a value of about two electron masses by studying the multiple scattering of the particles in the cloud chamber according to the method developed by Groetzinger, Berger, and Ribe.[28] Champion and Ahmed[29] and Yuasa[26] have recently classified a large number of cloud-chamber tracks produced in the vicinity of negative β-emitters, and come to the conclusion that certain of these are fairly definitely associated with positive particles. Weinzierl[30] has reviewed the work on this subject and concluded that positive particles of this sort (distinct from positrons) probably exist.

The present paper is a report of some experiments we have performed regarding the occurrence of tracks which could be attributed to such particles in the magnetic cloud chamber. In particular, we were interested in eliminating the possibility that these tracks might have been produced by electrons which were either traveling toward the source or else were scattered in such a fashion as to achieve the same curvature as a positive particle. In the course of this work we also studied the effect of covering the source on the rate of production of the positive particles. Finally, we undertook to determine whether our estimate of the mass of these particles, made on the basis of the determination of the multiple scattering,[27] might have been in error as the result of the difference in the momentum distribution of these particles and electrons used for the purpose of comparison.

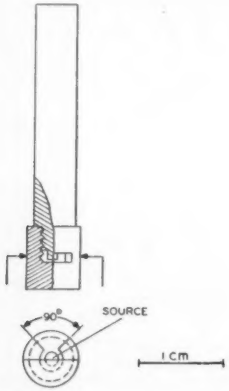

FIG. 1. Source arrangement No. 1.

II. CLOUD-CHAMBER EXPERIMENTS WITHOUT A COLLIMATING ARRANGEMENT

Our cloud chamber had a diameter of 24 cm and a height of 7.5 cm, of which about 3 cm was illuminated. Pictures were taken at a rate of one per minute showing a direct view inclined 3° to the axis of the chamber and a mirror view inclined 23° in the opposite direction. The magnetic field, which varied somewhat for different exposures, was produced by a set of Helmholtz coils and had a strength of from 325 to 355 gauss. The gas was a mixture of three parts helium and two parts argon at one atmosphere total pressure. The source was P^{32} (no nuclear gamma-radiation) obtained from the Isotope Branch of the Atomic Energy Commission as "separated radio isotope" in the chemical form $H_3P^*O_4$, which was evaporated in all our arrangements on an aluminum backing. In source arrangement No. 1, shown in Fig. 1, the radioactive phosphorus was deposited on the small cylindrical tip of the rod which was screwed into a cylindrical sleeve closed at the bottom. This served to suspend the source from the top glass plate at a height corresponding to the middle of the illuminated section and at a position 6 cm from the center of the chamber. The sleeve had a thickness of 1.9 mm and a horizontal slot 1.5 mm in height so that electrons emerging through the slot with a spread of approximately 120° in a horizontal plane, as well as those which had traversed the aluminum thickness of the sleeve in other directions, could be observed.

We will define here as a positive track, a track ending[31] in the source or the material covering the source or ending in the orifice of the collimating channel described in Sec. IV, which has a curvature in the magnetic field in the direction an (unscattered) positively charged particle moving away from the source would have. Such tracks were observed ending in the front (position of the slit) as well as the back of the source.

Only positive tracks of lengths in excess of 4 cm were considered. However, in the study of the effects of multiple scattering described in Sec. V, only tracks of length in excess of 7 cm were used. Similar restrictions concerning the length were imposed on electron tracks emerging from the source or its cover, whose number was determined in order to compare it with the number of positive tracks obtained under the same conditions. Furthermore, tracks with an ionization several times larger than the minimum ionization, which usually

[26] T. Yuasa, Compt. rend. **234**, 619 (1952).
[27] G. Groetzinger and F. L. Ribe, Phys. Rev. **79**, 904 (1950).
[28] Groetzinger, Berger, and Ribe, Phys. Rev. **77**, 584 (1950).
[29] F. C. Champion and A. A. Ahmed, Nature **168**, 780 (1951).
[30] P. M. Weinzierl, Acta Phys. Austriaca **5**, 18 (1951).

[31] The meaning of the "end of a track" here and in the following does not imply any statement concerning the direction of motion of the particle producing the track. The method used to determine accurately the position of the end of a track is described below.

showed appreciable large angle single scattering, were eliminated from the considerations.

In order to classify a track as a "positive track" it is obviously essential to ascertain as accurately as possible that it really ends in the regions specified above. Tracks with a "positive curvature" satisfying the criteria of length and ionization density and ending in both views in the source we shall call candidates. In case it was doubtful whether a track lined up with the source in both views, it was not included among the candidates. This was the case when the end of a track near the source was covered by electron tracks or when the chamber was insensitive in the neighborhood of the source. The possible number of candidates lost by excluding these dubious cases amounted to about 50 percent. In the count of the electron tracks, on the other hand, no tracks were excluded due to the above-mentioned circumstances. The total number of positive candidates ending in front and back of source arrangement No. 1 in 8800 pictures was 46. By counting the electron tracks emerging from the source in about five to ten out of every hundred pictures, a total number of electron tracks of 96,700 was derived. Since there is no doubt that the electrons emerge from the source, no further (stereoscopic) investigation of these tracks was made.

The criterion that a track ends in both views in the source (as is the case with the positive candidates) is, however, in the case of source arrangement No. 1 not yet sufficiently selective with respect to the height of the track near the aluminum sleeve of the source arrangement. Some of the tracks of particles traversing the chamber at random could satisfy this condition and still not line up vertically with the source. Therefore, all candidate tracks were investigated stereoscopically, using the camera with which the pictures were taken to project both views on a ground glass screen, which could be adjusted in order to bring the two images of the track near the source into coincidence. The position of the screen could be read from three attached scales. In order to determine the errors involved in this measurement of the track height, the tracks of 37 electrons emerging from the source were also examined stereoscopically. Figure 2 gives the results of this investigation, in which the measured height of the end of the electron tracks near the source with respect to the center of the slit in the source cover is indicated on the left side of the diagram. The spread in height is partly due to the extent in height of the radioactive P^{32}, partly due to the fact that the height is measured not at the position of the P^{32} but at the circumference of the aluminum sleeve surrounding it, and partly due to errors in the stereoscopic measuring. Figure 2 contains on the right side a similar plot for the 46 positive candidates. The peak, which is obtained near the center of the source has a shape similar to the electron peak and can only be explained as being due to emitted particles. Above the source the distribution is hardly

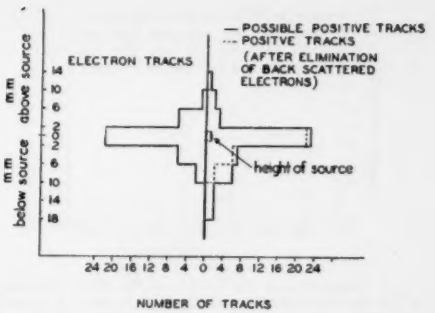

FIG. 2. Plot of the stereoscopically obtained height distribution of the electrons and positive particles obtained with source arrangement No. 1.

more spread out than that of the electrons. Below the source, however, the distribution extends beyond that of the electrons. This fact is so pronounced that it must be attributed to electrons re-entering the source rather than to a statistical fluctuation. The fact that back-scattered electrons are more numerous below the source than above it can be explained as follows: Positive candidates which are due to electrons scattered on the sidewalls of the chamber are eliminated by the fact that in most cases this process is directly observable. The spurious positive tracks are, therefore, more likely to be caused by electrons scattered on the top or bottom of the chamber which are outside the illuminated region and subtend furthermore a considerably larger solid angle with respect to the source. In our chamber the bottom consisted of velvet mounted on a thin (stationary) mesh above the piston, so that compared to those reflected by the glass top, particles scattered from the bottom are rather rare. The chance that an electron reflected at the top of the chamber has a track length exceeding four centimeters in the illuminated section will increase with the depth at which it hits or passes below the source. Of course, the number of backscattered electrons appearing in the distribution on the right side of Fig. 2 does not increase with the distance below the source due to the condition that the tracks have to end in the source in both views in order to be included among the candidates.

The dotted curve in Fig. 2 represents a distribution of the positive tracks corrected (somewhat arbitrarily) for the backscattered electrons, in such a way that it becomes similar to the distribution of the electrons emitted by the source. The stereoscopic investigation excludes in this way 11 candidates. It should be mentioned here that for all practical purposes elimination of tracks recorded as six millimeters above or below the center of the source leaves only about two reflected spurious positive particles out of a total of 33. The momentum spectrum of the positive particles shown in Fig. 3 is based on the cases contained in this interval.

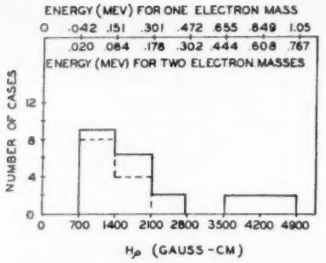
ENERGY (MEV) FOR ONE ELECTRON MASS
0 .042 .151 .301 .472 .655 .849 1.05
.020 .084 .178 .302 .444 .608 .767
ENERGY (MEV) FOR TWO ELECTRON MASSES
NUMBER OF CASES
0 4 8 12
0 700 1400 2100 2800 3500 4200 4900
Hρ (GAUSS-CM)

FIG. 3. Distribution of $H\rho$ for the positive tracks emerging from the uncovered portion (solid line) and from the covered portion (dashed line) of the P^{32} source in arrangement No. 1.

On the basis of the experiments described so far it can be seen that the error introduced by electrons re-entering the source arrangement No. 1 can be made approximately 6 percent. We should like to mention here that this arrangement is much more susceptible to the re-entering of electrons than the source arrangements No. 2 and No. 3 to be described below. According to the results described in Sec. V, it is extremely unlikely that the positive particles are due to electrons emerging from the source, deflected by multiple scattering in a direction corresponding to positively charged particles. We may talk, therefore, in the remainder of the paper, at least for the sake of expediency, about positive particles.

An investigation of the number of positive particles N^+ and the number of electrons N^- emerging from the slit in front (120° sector of the circumference) of the source arrangement and from the back (240° sector), which correspond to an uncovered source and one covered by 0.47 g/cm² of aluminum, shows a ratio of $N^+/N^- = 2.9\times10^{-4}$ and 7.4×10^{-4}, respectively. It follows from a comparison of the two ratios that the aluminum cover increases the number of positive particles relative to the number of electrons. Since some of the positive particles and some of the electrons observed in front of the source might actually emerge from the aluminum sleeve rather than from the slit, it might well be that the ratio of the numbers of positive particles and electrons for a really bare source is even smaller.

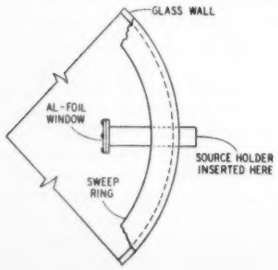

FIG. 4. Source arrangement No. 2.

III. CLOUD-CHAMBER EXPERIMENTS WITH THE SOURCE COVERED WITH CARBON OR LEAD

In order to study the influence of various materials covering the source on the number of the positive particles emerging from them, a different arrangement (source arrangement No. 2) was used. A brass tube of 1.3-cm outer diameter was extended along a radius 4.0 cm into the cloud chamber through a hole in its side wall. This tube was closed at the end inside the chamber by a 5-mil aluminum foil of 0.7-cm diameter. The source and the various covers were put into the tube through its outer (open) end in such a way that the source and the surface of the cover next to the source were in all cases in the same position. The source covers were constructed so that leakage of electrons around the cover was prevented. Pictures were taken without a cover (except for the window of thin aluminum foil) and with carbon and lead covers of various thicknesses. Arrangement No. 2 is shown in Fig. 4. The number of positive particles occurring with the various covers was again determined by the procedure outlined before. Table I contains the results of this investigation. The first two columns list the material covering the radioactive P^{32} and its thickness in g/cm²; the third and fourth, the number of the observed positive particles N^+ and electrons N^-; the fifth, the ratio N^- to the number of electrons N_0^- which would have been emitted into the same solid angle without the source cover; the sixth, the ratio N^+/N^-; and the seventh column, the ratio N^+/N_0^-, which represents a measure of the number of positive particles per disintegration. Owing to the fact that only one positive particle was obtained with arrangement No. 2 without a cover, the "bare source" results obtained with arrangement No. 1 are included in the table. As mentioned before, the number of positive particles per electron might be somewhat too high in this case, owing to the effects of the edges of the slit. Since with the large cover thicknesses fairly strong sources had to be used, it was not possible to take cloud-chamber pictures with these sources uncovered, which is necessary to obtain N_0^-. Therefore,

TABLE I. Influence of a source cover on the relative number of the positive particles, N^+; the number of electrons, N^-; and the number of electrons which would be emitted with the same solid angle with no cover, N_0^-.

Source cover Material	Thickness	N^+	N^-	N^-/N_0^- ×100	N^+/N^- ×10⁴	N^+/N_0^- ×10⁴
No cover		1	7300	100	1.2	1.2
No cover		22[a]	81,000	100	2.9	2.9
C	0.27 g/cm²	10	4400	4.8	23	1.1
C	0.46	8	9800	0.65	8.2	0.05
Pb	0.066	8	8300	36	9.6	3.4
Pb	0.34	5	12,000	0.42	4.3	0.02

[a] Obtained with arrangement No. 1.

in order to take pictures without a cover, the source was weakened by removing part of the deposit by an amount which was determined by the use of a G-M counter. In computing the various ratios the decay of the source was taken into account. The statistical accuracy of all the ratios depends almost entirely on the number N^+, since the numbers N^- and N_0^- are always based on the counting of a much higher number of tracks.

From these results we feel justified only in drawing the following qualitative conclusions: The effect of material covering the source is to increase the ratio of N^+/N^-, while N^+/N_0^-, after a possible initial increase, decreases. It follows from a consideration of the energy loss of the electrons that the positive tracks observed for the larger absorber thicknesses in the table cannot be due to electrons with energies in excess of 1 Mev.

IV. CLOUD-CHAMBER EXPERIMENTS WITH A COLLIMATING ARRANGEMENT

Figure 5 shows a part of the cloud chamber with a 3.3-cm long collimating tube which had a radius of curvature of 3 cm and thus discriminated to some extent against particles of either positive or negative charge traversing it, depending upon the direction of the magnetic field of approximately 350 gauss in the chamber and in the collimator. The source was placed on an aluminum backing at the end of the tube which was made of lead tubing of 0.15-cm wall thickness lined with 0.15 cm of aluminum so that a channel with a circular cross section of 0.4-cm diameter resulted. No window was used, so that the same mixture of helium and argon was present in the collimator as in the chamber. The discriminating power of the arrangement (which we shall call source arrangement No. 3) is rather poor. The distribution of the number of electrons as a function of $H\rho$ is shown in Fig. 6 for the case that the magnetic field supports their passing through the channel (curve A) and for the case that the field supports the passage of positively charged particles (curve B). These distributions are based on 62 and 63 particles, respectively. A count of several hundred tracks for each field direction shows that the number of electrons changes by a factor of 2.2 if the field is reversed. Curves A and B are drawn so as to take this factor into account. Figure 6 contains furthermore the P^{32} spectrum as obtained in a recent investigation by Agnew[32] with a beta-ray spectrometer (curve C). The spectrum is drawn to such a scale that the number of electrons per momentum interval at approximately 1100 gauss-cm coincides with that of the electrons emerging from the channel with the magnetic field supporting their passage, this momentum being the one the channel favors. It must be kept in mind that spectra obtained in a cloud chamber and in a spectrometer will differ slightly, owing to the effect of the backing of the source,

[32] H. M. Agnew, Phys. Rev. **77**, 655 (1950).

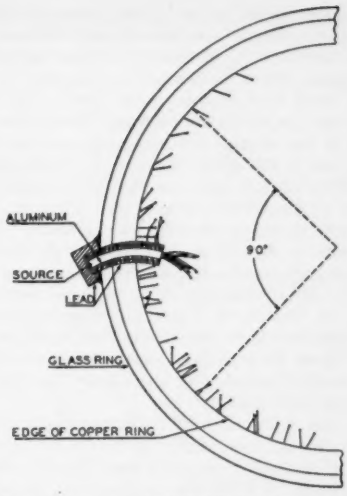

FIG. 5. Source arrangement No. 3 with the ends of tracks either due to positively charged particles emerging from or electrons entering into the orifice or the side wall of the collimator and the 3 cm high illuminated section of the side wall of the cloud chamber.

and that in the cloud chamber even without the collimator the obtained spectra will be somewhat influenced by such geometrical conditions as the required minimum track length, etc.

Figure 5 shows short portions of tracks at points where they end either in the orifice or in the wall of the collimator; these tracks—if we disregard the possibility of multiple scattering producing a curvature in a direction opposed to that which would occur under the influence of the magnetic field alone—being either due to positive particles emerging or electrons entering at these points. Similar tracks ending in the illuminated

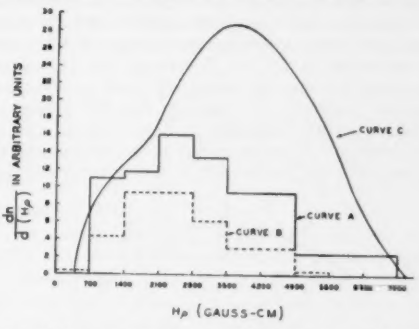

FIG. 6. Momentum distribution of the electrons emerging from source arrangement No. 3 with the magnetic field supporting (curve A) and opposing (curve B) the passage of negatively charged particles. Curve C represents the P^{32} electron spectrum.

part of the sidewall of the chamber are only photographed to points 1.2 cm from the wall, the outer rim of the chamber being obscured by a brass ring on top. The figure contains the position and direction of these tracks where they become visible. None of all these tracks are due to electrons coming directly from the orifice of the channel without being reflected. Nine tracks end in the orifice, three in the outside wall of the collimator, and 26 in the illuminated part of the quarter of the sidewall next to the collimator. Six of the tracks ending in the orifice can be traced back to the source at the end of the channel while the other three, if they are due to positively charged particles, must be either scattered or be produced inside the collimator. The tracks of electrons emerging from the collimator, even in the case that the field has a direction which favors their passage, show a larger fraction of particles not traceable to the source and therefore scattered in the channel.

The area of the orifice is 0.12 cm^2 and the illuminated part of the quarter of the side wall next to the collimator is 48 cm^2 so that per unit area more than 100 times as many tracks of either electrons entering or positive particles emerging, end in the orifice than in the illuminated part of the glass wall next to the collimator. The possibility that an appreciable number of the tracks ending in the orifice are due to reflected electrons is therefore excluded; and, moreover, the direction of these tracks at the orifice is indicative of emerging positively charged particles.

Assuming that both objections against the cloud-chamber evidence of the existence of these positive particles are disproved,[23] one can obtain a ratio of the number of positive particles emerging from the collimator to the number of electrons emerging from it (with the field supporting the passage of positively charged particles). This ratio is 5×10^{-4}. By the use of the distribution functions (curves A and C) in Fig. 6 the ratio of the positive particles emerging from the collimator to the electrons of a spectral distribution as it occurs in the P^{32} spectrum emitted into the same solid angle as the positives can be estimated. This ratio is approximately 1×10^{-4}. In spite of the experimental uncertainties (e.g., the ratios are based on only nine positive particles), it is unlikely that the number of positive particles emerging from the channel can be accounted for by positrons due to the bremsstrahlung produced by the P^{32} electrons or due to pair production by the P^{32} electrons for which, experimentally, an upper limit of 1.3×10^{-5} per disintegration electron from P^{32} has been found.[8,22] The difference between the ratio determined here and that found with the bare source might be partly due to the fact that the additional length (of the channel) which the positives have to traverse, decreases their number. This would be consistent with the failure to detect these particles with beta-ray spectrometers, where they have to traverse longer distances.

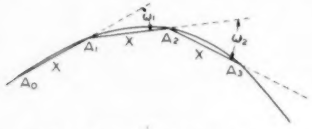

FIG. 7. Method of analysis of a cloud-chamber track.

[23] The objection against multiple scattering being responsible for the positive tracks is treated more fully in Sec. V.

In this connection it should be mentioned that out of the 34 positive tracks observed with source arrangement No. 1, three seemed definitely to end abruptly in the illuminated section of the cloud chamber. In none of these cases was a higher ionization density observed at the end of the track.

V. ERRORS DUE TO MULTIPLE SCATTERING OF THE PARTICLES PRODUCING THE POSITIVE TRACKS

(a) General Considerations

We will be concerned with two sorts of errors introduced into the cloud-chamber study of the tracks attributed to positive particles as a result of multiple scattering. In the first place, we want to estimate the probability that these tracks are due to electrons which have been scattered in such a fashion as to have a curvature appropriate to positive particles. In the second place, we want to see whether the experimental scattering law and hence the mass found by Groetzinger and Ribe[27] for the particles associated with these tracks might be in error because of difficulties in determining the momenta of the particles arising from multiple scattering itself.

Our approach to this problem will be based on the analysis of multiple scattering in the magnetic cloud chamber carried out by Groetzinger, Berger, and Ribe[28] (in a publication referred to as GBR in the following). The tracks as projected onto a plane perpendicular to the magnetic field are divided into sections in the manner indicated in Fig. 7. A_0, A_1, $\cdots$, A_n, and A_{n+1} are dividing points separated by chords of an equal length x, here taken as one centimeter, which are very close to the length of a section of the track. The n angles between the $(n+1)$ successive chords are designated as ω_1, ω_2, $\cdots\omega_n$, while the deflections of the track between successive points are designated as ϕ_0, ϕ_1, $\cdots$, ϕ_n. It follows from the theory of multiple scattering that the angles ω_i and the angles ϕ_i obey a normal distribution about a magnetic mean deflection $\mu=x/\rho$ with a variance of ψ^2 and σ^2, respectively, where ρ is connected with the momentum p of the particle and the magnetic field H in the chamber by the relation

$$eH\rho=pc. \tag{1}$$

It can be shown that

$$\psi^2=(2/3)\sigma^2. \tag{2}$$

In case μ and ψ^2 are unknown, the best estimates for

TABLE II. Probabilities P and $\bar{P}$ (as defined in the text) which are a measure of the likelihood that positive tracks are due to electrons emerging from the source deflected in a positive sense by multiple scattering.

	Electrons					Positive track with $\bar{\omega}=10.4°$ (1967 gauss-cm)		Positive track with $\bar{\omega}=6.0°$ (4280 gauss-cm)	
k	E kev	μ_k	ψ_{exp} in degrees	ψ_{th}	α_k in %	P_{exp}	P_{th}	P_{exp}	P_{th}
1	40	−29.8	18.0	21.8	1.2[a] 2.3	3.3×10^{-7}	2.0×10^{-5}	6×10^{-6}	1.2×10^{-4}
2	50	−26.4	15.3	18.2	6.8	4.6×10^{-8}	3.1×10^{-6}	1.3×10^{-6}	3.5×10^{-5}
3	200	−12.5	5.2	6.19	65.0	$<10^{-22}$	1.1×10^{-11}	1.5×10^{-15}	8.0×10^{-12}
4	1000	− 4.32	2.68	···	24.7	$<10^{-22}$	···	3.6×10^{-15}	···
5	1730	− 2.81	···	···		···	···	···	···
	40 to 1730				98.8	$\bar{P}_{exp}$ $<1.1\times10^{-9}$	$\bar{P}_{th}$ $<6.7\times10^{-7}$	$\bar{P}_{exp}$ $<2.3\times10^{-7}$	$\bar{P}_{th}$ $<5.1\times10^{-6}$

[a] Fraction of electrons with energies below 40 kev.

these quantities obtainable from the measurement of the ω_i's of a single track are, respectively,

$$\bar{\omega}=\frac{1}{n}\sum_{i=1}^{n}\omega_i \tag{3a}$$

and

$$(\omega^2)_{av}=[1/(n-1)]\sum_{i=1}^{n}(\omega_i-\bar{\omega})^2. \tag{3b}$$

(b) Occurrence of "Positive Tracks" as the Result of Multiple Scattering of Electrons

The probability that a track with a mean deflection equal to or greater than a given value of $\bar{\omega}$ is due to a particle of a particular type which has a momentum corresponding to an average deflection μ can be estimated as follows. If tracks containing individual deflections through large angles are excluded, as was done here, then the distribution of the individual ω_i's for particles of a given type and momentum follows a Gaussian distribution with variance ψ^2. Consequently, the quantity $n\bar{\omega}$ for different tracks will have a normal distribution about the mean $n\mu$ with $\frac{1}{2}$ variance $n\psi^2$. The quantity ψ^2 as a function of the momentum can be obtained from theoretical considerations or preferably from an experimental determination of the scattering of a large number of particles of the same kind with the conditions under which the track was obtained and using the same method of analysis. Thus, since μ, $\bar{\omega}$, and ψ^2 are known the probability in question can be calculated.

We are interested in determining the probability that the tracks attributed to positive particles actually be due to electrons. To carry out this computation for a given track, it is first necessary to determine the probability $P(\mu, \bar{\omega})$ that a track of an electron of a momentum corresponding to an average deflection μ have a deflection equal to or larger than $\bar{\omega}$, using as explained above either an experimental or theoretical value of ψ^2. In determining P, it must be remembered that $\bar{\omega}$ and μ have different signs for the "positive" tracks considered here. We make the convention that the $\bar{\omega}$'s are positive so that the μ's are negative. (This means that μ increases with increasing energy.) Then if the proportion of electrons emitted by P^{32} with momenta corresponding to values of μ between μ and $\mu+d\mu$ is $f(\mu)d\mu$, the total probability $\bar{P}(\bar{\omega})$ of the occurrence of such a track is

$$\bar{P}(\bar{\omega})=\int_{\mu_{min}}^{\mu_{max}} f(\mu)P(\mu, \bar{\omega})d\mu. \tag{4}$$

μ_{max} is the value of μ associated with an electron of maximum energy (1700 kev for P^{32}), and μ_{min} is the value of μ associated with the least energy (here about 40 kev) which an electron can have without producing a track of such high ionization as to be excluded from consideration. In our calculations the integral in Eq. (4) was approximated by the sum

$$\bar{P}(\bar{\omega})=\sum_{k=1}^{m}\alpha_k P(\mu_k, \bar{\omega}), \tag{5}$$

where α_k is the fraction of electrons with values of μ between μ_k and μ_{k+1}. The limits are chosen so that μ_1 and μ_{m+1} are equal to μ_{min} and μ_{max}, respectively. This way of choosing the intervals assures that the approximate value of $\bar{P}$ obtained is at least as high as the exact value since $P(\mu, \bar{\omega})$ decreases with increasing μ. The values μ we employed correspond to energies of 40, 50, 200, 1000, and 1700 kev.

The value of $\bar{P}$ was calculated for a pair of representative "positive" tracks each containing six sections ($n=5$). Table II gives the values of the quantities entering Eq. (5) for these tracks. The values of α_k shown are the approximate fractions of electrons in the beta-ray spectrum of P^{32} in energy intervals bounded by the energies $E=0$, 40, 50, 200, 1000 kev and the upper limit near 1700 kev, which were obtained from the investigation by Agnew[22] (curve C of Fig. 6). In order to calculate $P(\mu_k, \bar{\omega})$ it is necessary to know the root-mean-square angle of scattering ψ for a one-centimeter chord in the gas used. As remarked before, this quantity may be obtained either by a theoretical estimate or by a direct experimental determination of

the scattering of electrons. The quantity ψ_{exp} given in Table II was deduced from an experimental scattering law obtained for electron tracks with six sections in the specified mixture of argon and helium by the method outlined in GBR. The value given for 1000 kev is a direct experimental result, while those for 40, 50, and 100 kev are difficult to determine directly (see GBR) and were, therefore, extrapolated from the value of ψ found for 400 kev by assuming an energy dependence for ψ^2 of the form:

$$\psi^2 \propto \frac{1}{p^2v^2} \log \frac{0.1}{(mc/p)(Z^{\frac{1}{3}}/181)}. \tag{6}$$

Expression (6) is based on the theory of Williams[34] with limiting angles (contained in the logarithmic part) due to Bethe,[35] which showed, according to GBR, good agreement with the results of their experimental determination of the multiple scattering law for electrons of momenta between 2000 and 7000 gauss-cm in one atmosphere of argon. The quantity $Z^{\frac{1}{3}}$ occurring in expression (6) was obtained by averaging $Z^{\frac{1}{3}}$ for the proportions of helium and argon used in this investigation. The corresponding value of $P(\mu_k, \tilde{\omega})$ for a given value of μ_k is given in Table II as P_{exp} and of $\bar{P}(\tilde{\omega})$ as $\bar{P}_{exp}$. The theoretical values ψ_{th} of ψ given in Table II were obtained by using Eq. (6) with the factor of proportionality as given by Williams. The corresponding values of $P(\mu_k, \tilde{\omega})$ and $\bar{P}(\tilde{\omega})$ are given in the table as P_{th} and $\bar{P}_{th}$.

The values of $\bar{P}_{th}$ found in this fashion are much greater than those found for $\bar{P}_{exp}$, but each of these is much less than 10^{-4} which is roughly the actual proportion of positive tracks among those with a length in excess of 6 cm. Furthermore, basing one's arguments only on tracks of a larger number of sections, which leaves the ratio between the positive tracks and the electron tracks practically unchanged, reduces all the probabilities by a large factor.

The argument against the possibility that the positive tracks are due to electrons scattered in the "wrong" direction can be further strengthened by considering the distribution of the $\tilde{\omega}$'s of the positive tracks observed in the course of an investigation. Whatever the energy distribution of the electrons assumed to be responsible for the positive tracks may be, the number of these tracks should be essentially a rapidly increasing function of the mean radius of curvature $\rho = x/\tilde{\omega}$ or the apparent momentum. This is obviously not the case; the momentum spectra reported in various investigations contain only a very small fraction of particles of "positive" momenta exceeding 3800 gauss-cm and none in excess of 6400 gauss-cm.

[34] E. J. Williams, Proc. Roy. Soc. (London) **169**, 531 (1939); Phys. Rev. **58**, 292 (1940).
[35] H. A. Bethe, Phys. Rev. **70**, 821 (1946).

(c) Effect of the Difference in the Momentum Distribution of Electrons and the Positive Particles on the Determination of their Mass Ratio by Investigating the Multiple Scattering

In order to compare the mass of the positive particles with that of electrons, Groetzinger and Ribe[27] undertook to obtain ψ as a function of μ for both species of particles by measuring the tracks of such particles in a magnetic cloud chamber. Each pair of values (ψ, μ) representing a point of the curve was obtained by equating ψ to $[(\omega^2)_{Av}]^{\frac{1}{2}}$ and μ to $\tilde{\omega}$ for the track in question. As remarked above, $\tilde{\omega}$ is certainly the best estimate for μ for a given track in the case of a set of tracks all due to particles of the same momentum. This is also true in case the particles are distributed over a whole range of μ's provided that the number of particles per unit range of μ, $dN/d\mu$ is a constant independent of μ. Here the chance that the track be due to a particle with $\mu < \tilde{\omega}$ is equal to the chance that it be due to a particle with $\mu > \tilde{\omega}$ so that $\tilde{\omega}$ remains the best estimate for μ. If, however, $dN/d\mu$ increases (decreases) with μ in the neighborhood of the obtained $\tilde{\omega}$, it is more likely that $\tilde{\omega}$ is due to a particle with a $\mu > \tilde{\omega} (\mu < \tilde{\omega})$. In the case that one is not interested in the best estimate of the μ of an individual particle but rather in establishing a scattering law for a group of particles, this fact is of no importance as long as the scattering does not depend strongly on μ or $H\rho$, as is the case for the higher momenta considered by us. For a comparison of the scattering of two groups of particles even at momenta where the scattering changes rapidly with μ, it is sufficient that the momentum spectra of the two groups are rather similar.

In order to make an estimate of this error in the determination of the momentum $H\rho$, we consider the case of a disintegration electron of P^{32} of an energy of 200 kev ($H\rho \sim 1650$ gauss-cm) in a magnetic field of 350 gauss in our mixture of helium and argon whose track has a length to give 8 individual deflections between chords of one centimeter length. (This is somewhat less than the average number of angles of the tracks whose scattering has been studied.) With the total mean deflection between the first and the last chord being 8μ and a variance of $8\psi^2$, the probable error r in μ is

$$r = 0.674\psi/(8)^{\frac{1}{2}}. \tag{7}$$

Taking, for a conservative estimate of the error, for ψ the ψth for the energy of 200 kev from Table II which is somewhat too high, the limits of the momentum interval bounded by the probable error in μ are 1473 and 1880 gauss-cm. With a and b being the value of the distribution function $dN/d\mu$ at these points, a rough measure of the (systematic) error ϵ in the estimate of μ will be

$$\epsilon = r(b-a)/(a+b). \tag{8}$$

Taking the values a and b from curve C in Fig. 6, considering that here the distribution $dN/d\mu$ is required rather than $dN/d(H\rho)$ which is shown in the figure, gives the result that in the case of P^{32} electrons of a length to give 8 angles between successive chords of one centimeter for the conditions prevailing in our chamber an $\bar{\omega}$ corresponding to an apparent momentum of 1587 gauss-cm will most likely be due to an electron of a μ corresponding to a momentum of 1650 gauss-cm. It follows from the curve in Fig. 1, reference 27, that this error of approximately 60 gauss-cm in $H\rho$ near the lower end of the curve will not essentially change the experimental scattering law for electrons above 1500 gauss-cm which is represented by this curve.

In the case of the positive particles, $dN/d\mu$ varies only slightly at momenta around 2000 gauss-cm so that the best estimate of μ is hardly affected by this error, while at higher momenta this error has little effect since the scattering is insensitive to a change in momentum.

In order to approach this source of error experimentally, 26 tracks of electrons of momenta between 1500 and 3700 gauss-cm emerging from the collimating arrangement shown in Fig. 5, with the field in a direction favoring particles of positive charge, have been analyzed As can be seen from a comparison of curves B and C. of Fig. 6, these particles have a different spectral distribution than the ones obtained without the collimator. Their distribution is, furthermore, more similar to that of the positives, since above an $H\rho=1600$ gauss-cm, the number of electrons per momentum interval is decreasing with increasing momentum while without the collimator this number is increasing up to momenta of approximately 3600 gauss-cm. The scattering of the electrons emerging from the channel showed very good agreement with that of the electrons obtained without the collimator, which proves again that the error introduced by the spectral distribution is not appreciable in our case.

VII. DISCUSSION AND SUMMARY OF THE RESULTS

The results described above indicate that positively charged particles originate from radioactive P^{32}, a substance which is energetically incapable of decaying by positron emission. Cloud-chamber evidence concerning these positive particles has in the past been criticized on the grounds that the tracks attributed to positively charged particles emerging from the source are in reality due to electrons entering the source, or due to electrons emerging from the source but with a positive curvature caused by strong multiple scattering. With special source arrangements and a stereoscopic method of analysis of the cloud-chamber tracks we have been able to reduce the number of spurious positive tracks due to electrons reentering the source to a few percent of the total observed positive tracks. The use of the collimator arrangement described in Sec. IV reduces this error even to approximately one percent. The fact that the reentering electrons can account for only a small fraction of the resulting observed tracks follows also from the amount of multiple scattering that these tracks show, which is different from that of electrons of the same momentum (mean curvature). Detailed analysis of multiple scattering showed that the appearance of scattering-produced positive curvatures has a negligible probability.

The ratio of positive tracks to electron tracks reported in this investigation is in general smaller than that reported in previous investigations for P^{32}. While we found this ratio for a bare source to be approximately 3×10^{-4}, Barlow and Rogers[14] report a value of 1.5×10^{-3}. Pi and Chao[13], on the other hand, find for a bare source a ratio which is of the order of magnitude of the experimental error caused by reflected electrons but with a cover of a light substance (aluminum or glass) of 0.1 g/cm^2 a ratio of 5×10^{-4} (after correcting for this error). In the investigation of Smith and Groetzinger[12] using a collimator which favored the appearance of positively charged particles in the chamber, a ratio of somewhat less than 1×10^{-3} was found which was, however, based on positive tracks with a length in excess of 4 cm and electron tracks in excess of 10 cm. The two older papers concerned with P^{32} sources[10,11] report ratios of the order of 1×10^{-3}, the authors being, however, at the time not aware of the error which could be introduced by reentering electrons.

By covering the P^{32} source with lead or carbon the ratio of the numbers of observed positive particles and electrons was increased. The number of positive particles, however, decreased with increasing absorber thickness (except for a possible increase for small absorber thicknesses). Although our experimental material concerning this point is rather limited, it suggests—together with the evidence concerning the ionization-loss, which was certainly not smaller than for electrons of comparable momentum—that a primary radiation with a range in matter greater than that of the positive particles may be responsible for their production. It also follows that P^{32} electrons with energies (at the point of production of the positive particles) in excess of one Mev are excluded as possible primaries.

We are greatly indebted to Lewis B. Leder and Watts S. Humphrey for their continued help in operating the cloud chamber and analyzing the data and to Martin J. Berger and David Kahn for their help in performance of calculations and for valuable discussions.

The Exchange Scattering of an Electron by an Atom and Inverse Auger Effect

TA-YOU WU
National Research Council, Ottawa, Canada
(Received June 4, 1952)

The theory of exchange scattering of an electron by an atom given by Mott and Massey is discussed. A new formulation of an approximate treatment of the problem is suggested that leads to a system of differential integral equations similar to the Fock equations for the discrete state of atoms. This method leads to Oppenheimer's result as a first approximation. The resonance scattering arising from the inverse process of auto-ionization (Auger effect) is treated in a phenomenological manner.

I. INTRODUCTION

THE theory of scattering of an electron by an atom including the effect of exchange is first given by Oppenheimer.[1] Another treatment of the problem is given by Mott and Massey[2] which leads to a different result from that of Oppenheimer. Recently this difference in the matrix element for the scattering of an electron by a 2- or more electron atom has been the subject to discussion by a few authors.[3,4] In a recent note[5] the so-called "prior-post discrepancy" arising from this difference has been discussed. The purpose of the present note is to examine the theory of exchange scattering as given by Mott and Massey and to propose a formulation of another approximate theory which gives the total scattering, direct and exchange, in a way analogous to the Fock theory for discrete states and leads to Oppenheimer's result in a first approximation.

II. THEORY OF MOTT AND MASSEY

To simplify the discussion in the following without losing sight of the main features of the problem, we shall consider the scattering by a hydrogen atom of an electron with energy less than that necessary to ionize the atom. The Hamiltonian of the system of two electrons is

$$H(1,2)=-\nabla_1^2-\nabla_2^2-Z/r_1-Z/r_2+1/r_{12}. \quad (1)$$

In Oppenheimer's theory, out of the last three terms in (1), a perturbation $V(1,2)$ is so defined that the matrix elements in the first Born approximation corresponding to the transition between an initial state with the atom in state 0 and a free electron with momentum k_0, and a final state with the atom in the state n and a free electron with momentum k_n are given by

$$f_n\propto\int\int e^{-i\mathbf{k}_n\cdot\mathbf{r}_2}\psi_n^*(1)\left[-\frac{Z}{r_2}+\frac{1}{r_{12}}\right]\psi_0(1)e^{i\mathbf{k}_0\cdot\mathbf{r}_2}d\mathbf{r}_1d\mathbf{r}_2, \quad (2)$$

$$g_n\propto\int\int e^{-i\mathbf{k}_n\cdot\mathbf{r}_2}\psi_n^*(1)\left[-\frac{Z}{r_1}+\frac{1}{r_{12}}\right]\psi_0(2)e^{i\mathbf{k}_0\cdot\mathbf{r}_1}d\mathbf{r}_1d\mathbf{r}_2, \quad (3)$$

for the direct and exchange scattering, respectively.

Before discussing the theory of Mott and Massey for the effect of exchange, let us first treat the problem of two distinguishable electrons and denote by the index 1 the atomic and by the index 2 the incoming electron. A solution of the Schrödinger equation,

$$H(1,2)\psi(1,2)=E\psi(1,2), \quad (4)$$

is sought in the form

$$\psi(1,2)=\sum_n\psi_n(1)F_n(2), \quad (5)$$

where the ψ_n's are the complete set of the solutions of the hydrogenic wave equation

$$[\nabla_1^2+Z/r_1+\epsilon_n]\psi_n(1)=0, \quad (6)$$

the summation sign in (5) indicating summation over both the discrete and the continuous part of the spectrum. The F_n's satisfy the system of equations

$$[\nabla_2^2+(E-\epsilon_m)]F_m(2)=-\int\psi_m^*(1)\left[\frac{Z}{r_2}-\frac{1}{r_{12}}\right]\psi(1,2)d\mathbf{r}_1, \quad (7)$$

or

$$[\Delta_2^2+(E-\epsilon_m)]F_m(2)=-\sum_n V_{mn}(2)F_n(2),$$

where

$$V_{mn}(2)=\int\psi_m^*(1)\left[\frac{Z}{r_2}-\frac{1}{r_{12}}\right]\psi_n(1)d\mathbf{r}_1. \quad (7a)$$

To obtain the scattered waves, one seeks solutions $F_m(2)$ that have the following asymptotic forms for large r_2:

$$F_0(2)\rightarrow e^{i\mathbf{k}_0\cdot\mathbf{r}_2}+\frac{e^{ik_0r_2}}{r_2}f_0(\vartheta,\varphi),$$

$$F_m(2)\rightarrow\frac{e^{ik_mr_2}}{r_2}f_m(\vartheta,\varphi), \quad E-\epsilon_m>0, \quad (8)$$

$F_\mu(2)$ finite at the origin and vanishing exponentially at large r_2, for $E-\epsilon_\mu<0$.

The solution (5) with (8) means that for all states m (discrete in the case considered) of the atom that can be excited by the incoming electron, the incoming electron will emerge and will be described by a spherical

[1] J. R. Oppenheimer, Phys. Rev. **32**, 361 (1928); G. Wentzel, *Handbuch der Physik* (J. Springer, Berlin, 1933), Vol. 24, No. 1.
[2] W. F. Mott and H. M. Massey, *Theory of Atomic Collisions* (Clarendon Press, Oxford, 1949), 2nd edition, pp. 140. 215, 258.
[3] Bates, Fundaminsky, Leech, and Massey, Trans. Roy. Soc. (London) **A243**, 117 (1950).
[4] D. Layzer, Phys. Rev. **84**, 1221 (1951).
[5] Corinaldesi, Trainor, and Wu, Nuovo cimento **9**, 436 (1952).

wave at large distances. For states (discrete and continuous in this case) for which $E-\epsilon_\mu<0$, the incoming electron 2 is described by $F_\mu(2)$, i.e., it becomes captured by the atom. We shall assume that the asymptotic conditions (8) completely and uniquely determine the F's over the whole range of r_2, and hence also completely and uniquely determine the function $\psi(1, 2)$ in (5) over the whole r_1 and r_2 space.

To obtain the effect of electron exchange in which electron 1 goes out and electron 2 is left in the atom, Mott and Massey re-expand the function $\psi(1, 2)$ in the alternative form

$$\psi(1, 2)=\sum_n \varphi_n(2)G_n(1), \tag{9}$$

where the φ_n's are the complete set of hydrogenic wave functions (we shall denote these by φ's instead of by ψ's for convenience in the argument in the following), and the G_n's are solutions of the system of equations

$$[\nabla_1^2+(E-\epsilon_m)]G_m(1) = -\int \varphi_m^*(2)\left[\frac{Z}{r_1}-\frac{1}{r_{12}}\right]\psi(1, 2)d\mathbf{r}_2, \tag{10}$$

or by a system (10a) similar to (7a) but with G's replacing the F's and with the indexes 1, 2 interchanged. The solutions G's are to have the asymptotic forms

$$G_m(1)\rightarrow\frac{e^{ik_m r_1}}{r_1}g_m(\vartheta, \varphi), \qquad E-\epsilon_m>0,$$
$$G_\mu(1)\rightarrow\text{finite at the origin and vanishing exponentially at large } r_1 \text{ for } E-\epsilon_\mu<0. \tag{11}$$

To describe the scattering with the symmetry in the two electrons taken into account, one employs the symmetrized function

$$\Psi(1, 2)=\psi(1, 2)\pm\psi(2, 1) =\sum_n[\psi_n(1)F_n(2)\pm\psi_n(2)F_n(1)]. \tag{12}$$

The function $\psi(2, 1)=\sum\psi_n(2)F_n(1)$ represents electron 2 originally in the atom and 1 incident on and scattered by the atom. On re-expanding this $\psi(2, 1)$ in the alternative way (9),

$$\psi(2, 1)=\sum_n\varphi_n(1)G_n(2), \tag{13}$$

Mott and Massey identify the φ_n's and ψ_n's to be the same set (i.e., covering the same spectrum) and obtain

$$\Psi(1, 2)=\sum_n\psi_n(1)[F_n(2)\pm G_n(2)]. \tag{14}$$

Hence, the scattered amplitude is given by the asymptotic amplitude of $F_n(2)\pm G_n(2)$, and from (8) and (11), by

$$f_m\pm g_m, \quad E-\epsilon_m>0. \tag{15}$$

On putting in (7) and (10),

$$\psi(1, 2)=\psi_0(1)e^{ik_0\cdot r_2},$$

one obtains, to the first approximation,

$$f_m\propto\int\int e^{-ik_m\cdot r_2}\psi_m^*(1) \times\left[-\frac{Z}{r_2}+\frac{1}{r_{12}}\right]\psi_0(1)e^{ik_0\cdot r_2}d\mathbf{r}_1d\mathbf{r}_2, \tag{16}$$

$$g_m\propto\int\int e^{-ik_m\cdot r_2}\psi_m^*(1) \times\left[-\frac{Z}{r_2}+\frac{1}{r_{12}}\right]\psi_0(2)e^{ik_0\cdot r_1}d\mathbf{r}_1d\mathbf{r}_2. \tag{17}$$

Before discussing this treatment of Mott and Massey, we shall first note that although the expression (17) for the exchange scattered amplitude has Z/r_2 instead of Z/r_1 as in (3), the two expressions (3) and (17) can be shown to be equal to each other.

We shall now show that the above treatment contains a difficulty connected with the two sets of boundary conditions (8) and (11) for the same function (9),

$$\psi(1, 2)=\sum\psi_n(1)F_n(2)=\sum\varphi_n(2)G_n(1). \tag{9}$$

From (9), one obtains

$$F_n(2)=\sum_m\int\psi_n^*(1)G_m(1)d\mathbf{r}_1\cdot\varphi_m(2)\equiv\sum_m a_{nm}\varphi_m(2),$$
$$G_m(1)=\sum_n\int\varphi_m^*(2)F_n(2)d\mathbf{r}_2\cdot\psi_n(1)\equiv\sum_n b_{mn}\psi_n(1). \tag{18}$$

From (18), we first note that if the same complete spectrum (regular at the origin and incoming and outgoing waves) is employed for the ψ's in (5) and the φ's in (9), there are in general also incoming waves in $G_m(1)$ coming from the incoming waves in the spectrum of $\psi_n(1)$.

Since the $F_n(2)$'s given by Eq. (7) are determined by the asymptotic conditions (8), Eq. (18) will completely determine the G_n's as defined by the expansion (9). The question is whether the G_n's given by the solution of Eq. (1) with the asymptotic condition (11) are compatible with the G_n's given by (18). Let us denote by $G_n'(2)$ these solutions of (10) subject to (11). These can be written

$$G_m'(2)=-\frac{1}{4\pi}\int\int\frac{e^{ik_m|r_2-r_j|}}{|\mathbf{r}_2-\mathbf{r}_j|}\psi_m^*(j)\left[\frac{Z}{r_j}-\frac{1}{r_{ij}}\right] \times\psi(j, i)d\mathbf{r}_id\mathbf{r}_j, \quad E-\epsilon_m>0,$$
$$G_\mu'(2) \text{ finite at the origin and vanishing exponentially at large } r_2, \text{ for } E-\epsilon_\mu<0. \tag{19}$$

Let us expand $G_n'(2)$ in terms of the complete set of ψ_n's of (6),

$$G_n'(2)=\sum_m b_{nm}'\psi_m(2)+\sum_\mu b_{n\mu}'\psi_\mu(2), \tag{20}$$

where, for example,

$$b_{n\mu}' = \int \psi_\mu^*(2) G_n'(2) d\mathbf{r}_2$$

$$= -\frac{1}{4\pi} \int\int\int \psi_\mu^*(l) \frac{e^{ik_n|\mathbf{r}_l - \mathbf{r}_j|}}{|\mathbf{r}_l - \mathbf{r}_j|} \psi_n^*(i) \left[\frac{Z}{r_j} - \frac{1}{r_{ij}}\right] \times \psi(j, i) d\mathbf{r}_i d\mathbf{r}_j d\mathbf{r}_l. \quad (21)$$

On the other hand, from (18), the coefficient $b_{n\mu}$ of G_n is given by

$$b_{n\mu} = \int \varphi_n^*(1) F_\mu(1) d\mathbf{r}_1,$$

where F_μ is given by (8). Comparison between this and (21) shows that in general

$$b_{n\mu}' \neq b_{n\mu}. \quad (22)$$

Hence, G_n' as given by (10) and (11) are in general not the same as the G_n defined by the alternative expansion (9).

The theory of Mott and Massey has also been given in another form[2,3] which seems not to involve the two sets of asymptotic conditions (8) and (1) separately. The function (14) can be written as

$$\Psi'(1, 2) = \sum \Phi_n(2) \psi_n(1), \quad (23)$$

and the Φ's are given by a system of equations similar to (7), with $\psi(1, 2)$ in the integrand replaced by $\Psi'(1, 2)$, and are subject to the asymptotic conditions

$$\Phi_0(2) \to e^{i\mathbf{k}_0 \cdot \mathbf{r}_2} + \frac{e^{ik_0 r_2}}{r_2} \eta_0(\vartheta, \varphi),$$

$$\Phi_n(2) \to \frac{e^{ik_n r_2}}{r_2} \eta_n(\vartheta, \varphi), \quad E - \epsilon_n > 0, \quad (24)$$

$\Phi_\mu(2)$ exponentially decreasing at large r_2, $E - \epsilon_\mu < 0$. The solution $\Psi'(1, 2)$ so obtained, however, does not ensure the symmetry requirement

$$\Psi'(1, 2) = \pm \Psi'(2, 1),$$

or

$$\Phi_n(1) = \sum_m \int \psi_n^*(2) \Phi_m(2) d\mathbf{r}_2 \cdot \psi_m(1). \quad (25)$$

Apart from this question of satisfying simultaneously both the symmetry requirement (12) or (25) and the two sets of asymptotic conditions (8) and (11), another related point may be raised in this theory. The function (12) or (14), being obtained from (5) and (13) without exchange, corresponds to a Hartree approximation; while an exact theory should correspond to a Fock approximation, i.e., the functions F_n's in (12) should be given by an infinite system of differential-integral equations obtained by putting (12) into (4).

Thus the theory of exchange scattering of Mott and Massey, and the approximation (17) in particular, must be accepted only as a definite approximation, which is, however, different from that made in the usual Born approximation without exchange.

III. A PROPOSED TREATMENT OF EXCHANGE SCATTERING

In view of the difficulty discussed in the preceding section in the treatment of Mott and Massey, a new treatment of the problem is suggested which is somewhat analogous to the theory of Fock for the discrete states of an atom.

Let us consider, for definiteness, the scattering by a hydrogen atom of an electron of energy k_0^2 sufficient to excite the discrete states 0, 1, $\cdots$, m but not sufficient to ionize the atom. The physical condition of the problem is therefore the scattering of one of the electrons with an energy $k_n^2 = E - \epsilon_n = k_0^2 - (\epsilon_n - \epsilon_0)$, leaving behind the other electron in the state n of the atom. E is the total energy of the system; ϵ_0, ϵ_n are the energies of the initial and the excited state of the atom. To describe this condition of the problem, we shall construct a symmetrized wave function for the system

$$\Psi(1, 2) = \sum_{n=0}^{m} [\psi_n(1) \phi_n(2) \pm \psi_n(2) \phi_n(1)], \quad (26)$$

where the ψ's are the wave functions of those discrete states of the hydrogen atom that can be excited with the energy available, and the ϕ's are the wave functions of the incident and scattered electron. On putting (26) into the Schrödinger Eq. (4), one obtains the system $m+1$ differential-integral equations

$$[\nabla_1^2 + k_n^2] \phi_n(1)$$

$$= -\frac{Z}{r_1} \phi_n(1) + \sum_{l=0}^{m} \int \psi_n^*(2) \psi_l(2) \frac{1}{r_{12}} d\mathbf{r}_2 \cdot \phi_l(1)$$

$$\pm \sum_l \int \psi_n^*(2) \left[-\nabla_2^2 - \frac{Z}{r_2} - k_l^2 + \frac{1}{r_{12}}\right] \phi_l(2) d\mathbf{r}_2 \cdot \psi_l(1)$$

$$= -\sum_{l=0}^{m} V_{nl}(1) \phi_l(1) \pm \sum_{l=0}^{m} \int \psi_n^*(2) \left[\epsilon_n - k_l^2 + \frac{1}{r_{12}}\right] \times \phi_l(2) d\mathbf{r}_2 \cdot \psi_l(1), \quad (27)$$

where $V_{nl}(1)$ is given by an expression similar to (7a), and where $\epsilon_n - k_l^2 = \epsilon_l - k_n^2$ on account of the energy conservation $E = k_n^2 + \epsilon_n = k_l^2 + \epsilon_l$.

We seek solutions that have the following asymptotic behavior:

$$\phi_0(1) \to e^{i\mathbf{k}_0 \cdot \mathbf{r}_1} + \frac{e^{ik_0 r_1}}{r_1} \eta_0(\vartheta, \varphi),$$

$$\phi_n(1) \to \frac{e^{ik_n r_1}}{r_1} \eta_n(\vartheta, \varphi), \quad n = 1, \cdots m. \quad (28)$$

The amplitudes η_0, η_n for the elastic and inelastic scattering, being obtained from Eqs. (27) that include the

effect of the use of symmetrized wave functions, already contain the direct and the exchange scattering. As the system (27) is a finite number of equations, the solutions ϕ_n can in principle be obtained at least by successive approximation.

The approximation involved in this method is contained in the form (26) for the wave function. It is seen that the function (26) together with (28) satisfies the physical conditions required of the solution. In limiting the hydrogenic wave functions ψ's to only those states $\epsilon_n<\epsilon_m$ where $\epsilon_m\leqslant k_0^2+\epsilon_0$, the function (1) errs in the regions of the configuration space where both r_1 and r_2 are small. But it is exactly here that the usual Born and Oppenheimer approximations are also bad, since in these approximations the whole wave function $\psi(1, 2)$ in the integrand of Eqs. (7), (10) is replaced by only one term. By finding solutions ϕ's of the system of Eq. (27), the coupling among the various scattered wave ϕ's is better accounted for than in the Born approximation in which the coupling is neglected. The chief interest of this method is perhaps the less ambiguous way in which the exchange effect is included in the scattered waves ϕ's. The total scattering including the effect of symmetry is given by the system of differential integral Eqs. (27), quite analogous to the Fock equations for the discrete states of an atom.

It is of interest to note that if, to a first approximation, one puts on the right-hand side in Eqs. (27)

$$\phi_0(r)=e^{ik_0\cdot r},\qquad \phi_l(r)=0,\quad l\neq 0, \tag{29}$$

the system of simultaneous equations becomes a system of independent inhomogeneous equations and one obtains, to this approximation,

$$\phi_0(1)\rightarrow e^{ik_0\cdot r_1}+\frac{e^{ik_0r_1}}{r_1}(f_0\pm g_0),$$

$$\phi_n(1)\rightarrow\frac{e^{ik_nr_1}}{r_1}(f_n\pm g_n), \tag{30}$$

where the f_n's are given (2) and g_n by (3). Thus, Oppenheimer's result follows as a first approximation to the method here.

IV. INVERSE AUGER TRANSITION AND RESONANCE SCATTERING

Let us consider the case when the total energy of the system $E=k_0^2+\epsilon_0$ is just equal to the energy E_a of one of the quasi-stationary, doubly excited states (such as $2s3s$, $3s^2$, etc.) which are subject to the radiationless auto-ionization similar to the Auger transitions in x-rays. In this case there is the possibility of the incoming electron being captured and re-emitted. An exact treatment of the auto-ionization process is difficult; but its inverse process can be treated in an approximate way as follows. When k_0^2 is such that $k_0^2+\epsilon_0=E_a$, we shall, instead of the wave function (27), assume the wave function[6]

$$\Psi(1, 2)=\sum_{n=0}^{m}[\psi_n(1)\phi_n(2)\pm\psi_n(2)\phi_n(1)]+\psi_a(1)\phi_a(2)\pm\psi_a(2)\phi_a(1), \tag{31}$$

where $\psi_a(1)$ is again a discrete hydrogen wave function. On putting (31) into Eq. (4), one obtains the following system of $m+2$ differential-integral equations:

$$[\nabla_1^2+k_n^2]\phi_n(1)=-\sum_{l=0}^{m,a}V_{nl}(1)\phi_l(1)\pm\sum_{l=0}^{m,a}\int\psi_n^*(2)\left[\epsilon_n-k_l^2+\frac{1}{r_{12}}\right]\phi_l(2)d\tau_2\cdot\psi_l(1),\qquad n=0, 1, \cdots m, a, \tag{32}$$

where $k_a^2=E-\epsilon_a$ is negative. The solutions sought are to have the following asymptotic forms:

$$\phi_0(1)\rightarrow e^{ik_0\cdot r_1}+\frac{e^{ik_0r_1}}{r_1}\xi_0(\vartheta, \varphi),$$

$$\phi_n(1)\rightarrow\frac{e^{ik_nr_1}}{r_1}\xi_n(\vartheta, \varphi),\quad n=1, 2, \cdots m, \tag{33}$$

$\phi_a(1)$ decreasing exponentially at large r_1.

The difference of the amplitudes ξ's in (31) from the η's in (29) represent the resonance scattering arising from the possibility of the inverse process of the Auger transition. When the differential cross sections are studied at various energies k_0^2, there would be an anomaly when $k_0^2+\epsilon_0=E_a$, the energy of one of the doubly excited states, corresponding to the differential cross sections passing from $|\eta(\vartheta, \varphi)|^2$ to $|\xi(\vartheta, \varphi)|^2$ and back to $|\eta(\vartheta, \varphi)|^2$.

Experimentally, one may study this resonance effect by measuring the scattering at a fixed angle (preferably a large angle) for a continuous range of electron energy. The question as to what the theoretical energies E_a are cannot be answered in this "phenomenological" treatment given above. But in the sense of successive approximations, one may perhaps locate the positions of the doubly excited states by a separate calculation based on the variational principle, for example.

The writer has had many discussions of the problem with Dr. E. Corinaldesi, Dr. L. Trainor, and Dr. E. Bauer, and is particularly indebted to Dr. S. T. Ma and Dr. T. D. Lee for clarifying discussions.

Note added in proof:—In a recent paper [Proc. Roy. Soc. (London) **A212**, 512 (1952)] G. A. Erskine and H. W. S. Massey calculate the excitation cross section for the $2S$ state of hydrogen in an approximation quite similar to that of Sec. III above, except that in the function (26) only two states, namely, the initial and the final, are included.

[6] This approximate treatment is not free from ambiguity in that, for the doubly excited state such as $2s3s$, it is not clear whether one should put ϕ_a equal to ψ_{2s} or to ψ_{3s}. One may, of course, include two terms in (31), namely,

$$\psi_{2s}(1)\phi_a(2)\pm\psi_a(2)\phi_a(1)+\psi_{3s}(1)\phi_b(2)\pm\psi_{3s}(2)\phi_b(1).$$

Radiative Capture of Thermal Neutrons by Cd^{113}

R. W. PRINGLE, H. W. TAYLOR, AND K. I. ROULSTON
Physics Department, University of Manitoba, Winnipeg, Canada
(Received May 16, 1952)

Study of the radiative capture of thermal neutrons by Cd^{113} with a scintillation spectrometer gave 9.20 Mev as the neutron binding energy of Cd^{114}, and nuclear levels at 0.57, 1.33, 2.63, 3.49, 4.03, and 4.43 Mev. The relationship between the resolution of the spectrometer and gamma-ray energy is shown.

STUDY of neutron capture gamma-radiation affords a convenient method for the investigation of the energy level structure of the product nucleus. From data obtained with a conventional magnetic pair spectrometer, Kinsey[1] has recently proposed level schemes for several isotopes. Preliminary work with a scintillation spectrometer[2] indicated the value of this approach to the problem, and it is our object to present certain new results concerning, in particular, the gamma-rays arising from the reaction

$$Cd^{113}+n^1 \rightarrow Cd^{114}+\gamma.$$

Because of the high capture cross section of Cd^{113} for thermal neutrons, this reaction is particularly well suited to the method in question.

The pulses from the scintillation spectrometer (E.M.I. 5311 photomultiplier, $\frac{3}{4}$-in. cube NaI-Tl crystal) were analyzed with a 5-channel kicksorter (Harwell Type 1074 A). The cadmium target was in the form of metallic foil shaped to fit snugly over the crystal. Slow neutrons which were absorbed by the cadmium gave rise to capture gamma-radiation, some of which was detected by the crystal. Neutrons from a 400-mC RaD–Be source were thermalized in a paraffin block, and a 3-in. lead plug was used to absorb gamma-rays coming from the source.

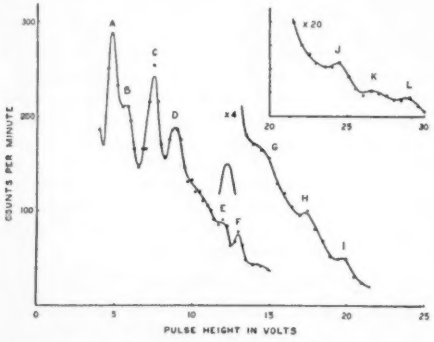

FIG. 1. Scintillation pulse-height distribution for the gamma-rays produced in the reaction $Cd^{113}(n,\gamma)Cd^{114}$. The distribution has been corrected for background radiation.

The spectrum of pair lines associated with the neutron capture gamma-radiation from cadmium, corrected for background, is shown in Fig. 1. With the exception of A, we interpret all the main features of the distribution as being due to the creation of electron pairs in the crystal by high energy gamma-rays. The crystal is sufficiently small for the escape of most of the annihilation radiation to take place, so that the lowest energy pair line ($E_\gamma - 1.02$ Mev) predominates in each case. The nature of feature A will be discussed shortly. Just above E and F the location of the well-known Po–Be pair line is indicated.[3] This line was used to calibrate the pulse-height axis assuming proportionality of the device for high energy gamma-rays. No evidence for any lack of linearity in the spectrometer was found during the course of this work. Feature L, the pair line of a 9.20-Mev gamma-ray, is associated with the ground-state transition and gives a measure of the binding energy of the last neutron in the Cd^{114} nucleus. The gamma-ray energies of the features of Fig. 1 have been listed in Table I together with some results due to Kinsey,[4] and it can be seen that the two sets of results are reasonably consistent. Energy sums can be selected for those gamma-rays which appear to be in cascade:

$$\begin{aligned} K+0.57^5&=9.12 \text{ Mev},\\ J+A&=9.25 \text{ Mev},\\ I+B&=9.22 \text{ Mev},\\ H+D&=9.34 \text{ Mev},\\ E+F&=9.14 \text{ Mev},\\ F+C+A&=9.18 \text{ Mev}. \end{aligned} \qquad \text{Mean}=9.21 \text{ Mev}.$$

Clearly these sums are in good agreement with the energy of the ground-state transition as determined from feature L.

It was realized that determination of the relative intensities of the gamma-rays was complicated by the presence of several Compton distributions, and by the variation of detection efficiency of the spectrometer with energy. A decay scheme, shown in Fig. 2, was drawn up which was consistent with the energies quoted

[1] See Kinsey, Bartholomew, and Walker, Phys. Rev. **85**, 1012 (1952), for references to earlier work by this group.
[2] R. W. Pringle and G. Isford, Phys. Rev. **83**, 467 (1951).
[3] Pringle, Roulston, and Standil, Phys. Rev. **78**, 627 (1950).
[4] Private communication from Dr. Bartholomew.
[5] Mei, Mitchell and Zaffarano, Phys. Rev. **76**, 1883 (1949); C. T. Hibdon and C. O. Muehlhause, Phys. Rev. **87**, 222 (1952).

TABLE I. Gamma-ray energies associated with the $Cd^{113}(n,\gamma)Cd^{114}$ reaction.

Feature	γ-ray energy (Mev) Kinsey	Present determination
A	...	1.33
B	...	2.61
C	...	3.14
D	...	3.49
E	4.58	4.43
F	4.82	4.71
G	5.26	5.17
H	5.96	5.85
I	6.60	6.61
J	7.81	7.92
K	8.50	8.55
L	9.33	9.20

above, the shape of the pulse-height distribution, and the known variation with energy of the relative cross sections for the photoelectric and pair production processes in iodine.

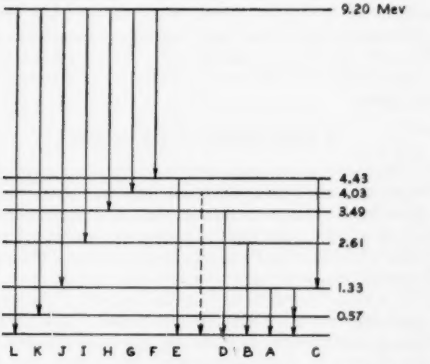

FIG. 2. Level scheme for Cd^{114} proposed on the basis of the Fig. 1 results.

Two levels in Cd^{114}, one at 0.57 Mev and the other at 1.27 Mev, seem to be well established[5] from a study of the *K*-capture process in In^{114}. Feature *A* was assumed to be a photoelectric, rather than a pair, line corresponding, within experimental error, to the ground state transition from the 1.27-Mev level. The gamma-ray arising from a transition between the level at 4.03 Mev and the ground state was not observed although the shape of the pulse-height distribution between *D*

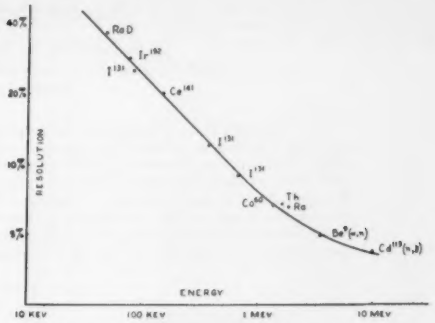

FIG. 3. Resolution—energy relationship for the scintillation spectrometer.

and *E* suggests the possible existence of such. A transition between the 1.33 and 0.57 Mev levels (Mei *et al.*, reference 5) suggests that a feed to the former other than *J* should be present in the scheme. It was observed that *C* could serve as a feed to the 1.33-Mev level and thus resolve the difficulty.

In view of a few additional gamma-rays which were found by Kinsey *et al.*, it is clear that the level scheme proposed here is incomplete, for it must contain only those levels associated with the most intense gamma-rays of the capture gamma-ray spectrum.

The radiative capture of slow neutrons by aluminum and chromium has also been studied by this method. Gamma-rays from excited states in aluminum were found at 7.20 and 7.70 Mev, the latter in good agreement with work done by Kinsey,[6] and in chromium at 8.17 and 9.35 Mev. Intensity and resolution difficulties prevented the precise measurement of a number of gamma-ray energies below those quoted above.

In this neutron capture gamma-ray analysis a large energy range is covered and it is important to know how certain properties of the spectrometer vary as functions of energy. Figure 3 serves to indicate the resolution-energy relationship which has been attained. The resolution is defined as the full width of a line at half height. It will be noted that a resolution of 4 percent is obtained at an energy of 10 Mev.

Our thanks are due the National Research Council of Canada for the support of this work and for the award of a bursary to one of us (H.W.T.).

[6] Kinsey, Bartholomew, and Walker, Phys. Rev. **83**, 519 (1951).

Isotope Shifts in Erbium*

LAWRENCE WILETS† AND LEE C. BRADLEY, III
Palmer Physical Laboratory, Princeton University, Princeton, New Jersey
(Received May 28, 1952)

An investigation of the erbium isotope shifts has been conducted in the region between 4000 and 7000A using the dispersion of a Fabry-Perot interferometer crossed with a Steinheil three-prism glass spectrograph. Structures were measured in 68 lines, and components due to the even isotopes Er^{166}, Er^{168}, and Er^{170} have been identified. The ratio of the isotope shifts $(\nu_{168}-\nu_{170})/(\nu_{166}-\nu_{168})$ is close to unity in nearly all lines measured, and it is concluded that the undisturbed value of the ratio probably does not differ from unity by more than 4 percent. Electron configurations have been proposed to describe the observed shifts, and in particular those lines, in which the component due to Er^{170} is shifted to larger wave numbers than the components due to the other even isotopes, probably arise from the two-electron transitions $4f^{11}6s6p$ to $4f^{11}5d^2$.

I. INTRODUCTION

THERE are two general effects which give rise to isotope shifts: the (finite) nuclear mass and the extension of the nuclear charge over a finite volume. The nuclear mass effect, which has been divided into the normal (reduced) mass and specific mass effects for convenience, dominates the isotope shifts among the light elements but decreases in magnitude with increasing atomic weight and is apparently very small among the heavy elements. The nuclear effects dominate among the heavy elements; these arise primarily from the nuclear volume,[1-3] nuclear polarization,[4] and the nonelectrical neutron-electron interaction.[5] The neutron-electron interaction is very small; the nuclear polarization has not been calculated quantitatively but could account for the even-odd staggering of the isotope shift patterns; the nuclear volume effect probably is the most important. The observed isotope shifts among the heavy elements are in qualitative agreement with the predictions of the theory of the volume effect, but the theory predicts shifts which are twice as large as the observed ones[6] if one assumes a charge distribution either uniform throughout the nucleus or uniform over the surface and a change in nuclear radius which follows the law $r_0=1.5\times10^{-13}A^{\frac{1}{3}}$. The discrepancy may be due to the incomplete redistribution of protons when neutrons are added to a nucleus.[6]

Studies of isotope shifts have a twofold interest. First, because the observed shifts are proportional to the change in an effective nuclear (or more properly, nuclear charge) radius, they yield valuable information about the changes in nuclear radius with the addition of neutrons for a fixed Z. The second interest in the isotope shifts lies in the possibility of identification of electron configuration. This is particularly true among the rare earth elements, which have defied spectral analysis with the exception of a few of the elements which lie at the beginning, at the end, or at the very middle of the group. Even when terms have been identified, it has often been difficult or impossible to identify the electron configuration. The present work was undertaken with both of these points of interest in mind.

II. EXPERIMENTAL APPARATUS

The source of spectral lines was a modification of the liquid-air cooled hollow cathode discharge of the type described by Arroe and Mack.[7] An initial charge of 30 mg of erbium oxide (Er_2O_3) gave very intense erbium lines, which persisted strongly after more than 35 hours running time at currents of about 100 ma.

A quartz Fabry-Perot interferometer supplied the resolving power of the optical system. The etalon plates were 42 mm in diameter and were silvered by evaporation in vacuum. Auxiliary dispersion was supplied by a Steinheil three-prism glass spectrograph.

III. EXPERIMENTAL RESULTS

A. Observed Structures

With the four spacers available, interferograms of erbium lines were taken in the region of the spectrum from 4000 to 7000A. More than 100 lines showed structure, and measurements were made on 68. The structure in each case consists of three components, decreasing in intensity either toward the large or toward the small wave numbers. The components are designated A, B, and C, where A is the most intense and C is the least intense of the three components. The separations, which are given in Table I, are designated as positive if the order of the components with respect to increasing frequency is $C-B-A$, and negative if the order is $A-B-C$. The reason for this choice will be discussed later.

* This article is based upon a thesis by Mr. Wilets presented to the Faculty of Princeton University in candidacy for the degree of Doctor of Philosophy. A preliminary report appeared in Phys. Rev. **84**, 1055 (1951).

† AEC Predoctoral Fellow; now at the James V. Forrestal Research Center, Princeton University, Princeton, New Jersey.

[1] G. Racah, Nature **129**, 723 (1932).

[2] J. E. Rosenthal and G. Breit, Phys. Rev. **41**, 459 (1932).

[3] G. Breit, Phys. Rev. **42**, 348 (1932).

[4] Breit, Arfken, and Clendenin, Phys. Rev. **78**, 390 (1950); Breit, Arfken, and Clendenin, Phys. Rev. **77**, 569 (1950).

[5] L. Wilets and L. C. Bradley, III, Phys. Rev. **78**, 390 (1950).

[6] M. F. Crawford and A. L. Schawlow, Phys. Rev. **76**, 1310 (1949).

[7] O. H. Arroe and J. E. Mack, J. Opt. Soc. Am. **40**, 386 (1950).

The limits of accuracy for each measurement given in the table are based upon the internal consistency of the measurements and not upon possible systematic disturbances, which are discussed below.

Figure 1 shows a histogram of the average values of the separations CB and BA for all lines. Although there is a considerable spread for both positive and negative separations, the positive values are grouped around 0.045 and 0.046 cm^{-1} and the negative values are grouped around 0.047 and 0.048 cm^{-1}.

An exploration with a quartz 2-prism spectrograph below 4000A uncovered very few lines with structure, although the spectrum was quite dense and included some of the strongest lines of the spectrum.

B. Interpretation of the Isotope Shifts

Natural erbium ($Z=68$) contains six isotopes with the following relative abundances:

Atomic weight	Relative abundance, %
162	0.136
164	1.56
166	33.4
167	22.9
168	27.1
170	14.9

The identification of the components A, B, and C with the erbium isotopes 166, 168, and 170 on the basis of intensity and relative abundance is unambiguous. In most lines, the intensities agree quite well with the values to be expected from the relative abundances of the isotopes. In some cases, however, the intensities do vary considerably from the expected values, and this is probably due to the disturbing influence of Er^{167}.

In several lines a fourth component was observed beyond A. Its position could be measured fairly well in λ5826. On the basis of position and relative intensity, the component could be attributed to Er^{164}, but it is also possible that it is due to a component of the hfs of the odd isotope.

No components in the structure could be definitely attributed to Er^{167} in any case observed. It is evident from the appearance of the lines that the structure of the odd isotope is not localized between Er^{166} and Er^{168}. Er^{167} is reported[8] to have a spin of 7/2.

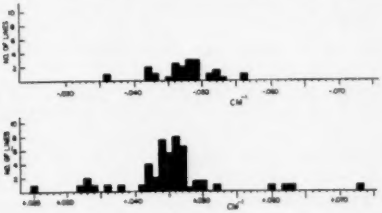

FIG. 1. Distribution of the mean values of the isotope shifts, $\frac{1}{2}(P_{166}-P_{170})$.

[8] B. Bleany and H. E. Scovil, Proc. Phys. Soc. (London) **A64**, 204 (1951).

TABLE I. Isotope shifts in the spectrum of Er. The values quoted are averages of the measurements made with various sizes of interferometer spacers. *i* indicates that the intensities differ from the expected values.

λ(A)	Mean shift $P_{166}-P_{170}$ (10^{-2} cm^{-1})	Mean shift $P_{166}-P_{168}$ (10^{-2} cm^{-1})	Ratio
6583.46	−48.6±1.0	−46.7±1.0	1.04
6541.53	42.7±1.2	44.2±1.2	0.97
6326.11	42.0±1.2	42.4±1.2	0.99
6308.79	−47.7±1.2	−48.5±1.2	0.98
6299.41	46.6±2.0	41.3±1.6	1.13
6286.86	65.8±3.0	58.9±3.0	
6262.56	43.8±1.2	44.6±1.2	0.98
6076.44	42.3±2.0	42.6±1.6	0.98
6022.56	41.9±2.5	41.9±2.5	1.00
6014.83	50.0±2.0	49.0±2.0	1.02
6006.80	45 ±5		
5855.32	34.6±1.4	33.9±1.2	1.02
5853.6 (?)	31.7±2.5	32.3±2.5	0.98
5826.79	32.6±1.0	33.4±1.0	0.98
5800.77	36.4±1.2	35.8±1.0	1.02
5782.81	42 ±7		
5769.92	24.2±2.5	26.4±2.5	0.92
5762.79	*i* 33.2±1.2	*i* 33.1±1.0	1.00
5739.18	48 ±5	45 ±5	
5726.99	−47.0±1.5	−46.4±1.5	1.01
5719.53	44 ±5	44 ±5	
5675.82	48 ±5	41 ±5	
5664.95	42.1±1.5	43.6±1.5	0.97
5640.34	42.7±2.5	44.7±1.5	0.96
5622.02	48.1±3.5	43.4±2.5	
5503.78	43 ±4	40.9±2.5	
5485.93	44 ±5	48 ±5	
5468.32	47.4±2.0	46.1±1.2	1.03
5456.60	45.7±1.0	46.3±1.0	0.99
5350.44	46.9±2.5	40.2±1.5	1.17
5348.04	44.5±1.5	43.9±1.5	1.01
5285.65	−45 ±5	−45.5±4	
5277.70	50.0±1.3	48.5±1.2	1.02
5246.11	*i* 46.6±1.2	*i* 42.3±1.2	1.10
5211.16	50 ±5		
5172.75	39.3±1.0	37.2±1.0	1.06
5164.77	45.3±1.4	43.9±1.4	1.03
5160.35	46.1±2.5	46.9±1.4	0.98
5131.52	44.4±1.2	46.7±1.2	0.95
5124.56	−48.2±1.2	−49.0±1.2	0.98
5080.51	−49 ±5	−46.8±2.5	
5058.62	*i* −56.5±2.0	*i* −55.6±2.0	1.02
5035.94	48.1±1.2	45.4±1.2	1.06
5028.32	44.6±1.2	47.4±1.5	0.94
5007.25	−43.1±2.5	−43.4±1.5	0.99
5004.1 (?)	46 ±5	49 ±5	
4966.99	−46.1±3.0	−38.3±3.0	1.20
4944.36	46.8±1.4	47.2±1.4	0.99
4928.86	62.7±1.2	57.2±1.2	1.09
4888.86	76.6±1.3	69.6±1.3	1.10
4861.10	53 ±5		
4857.43	47.4±1.2	45.0±1.2	1.05
4848.83	46.6±1.2	43.0±1.3	1.08
4820.75	−52.3±1.5	−51.0±1.5	1.02
4816.63	62.1±2.5	63.1±1.5	0.98
4739.2 (?)	−49 ±5		
4729.04	46.6±1.0	46.6±1.0	1.00
4722.77	−50.6±1.0	−51.3±1.0	0.99
4673.16	−49.5±1.0	−46.9±1.0	1.06
4606.62	−45.6±1.0	−45.6±1.0	1.00
4552.13	45.8±1.0	47.6±1.0	0.96
4531.11	47.5±1.0	44.6±1.0	1.07
4496.38	44.7±1.0	45.9±1.0	0.97
4426.77	−47.2±1.0	−50.0±1.0	0.94
4424.57	−43.8±1.0	−40.4±1.0	1.08
4409.35	−45.1±1.0	−46.2±1.0	0.98
4331.35	−53.0±1.0	−52.0±1.0	1.02
4286.52	−37.3±2.0	−34.3±2.0	1.09

The case[9] of ytterbium supplies an example of what may be expected in erbium. The hyperfine structure of the two odd isotopes Yb^{171} ($I=1/2$) and Yb^{173} ($I=5/2$) is much larger than the isotope shifts of the three even isotopes, even though the magnetic moments of the odd ytterbium isotopes are relatively small (0.45 and -0.65 nuclear magnetons).

Large hyperfine structure splittings may be expected from the odd erbium isotope also, but because of the large spin and because of the large J-values which may be expected in the strong lines of the erbium spectrum, a great number of hfs components are probable. Although the abundance of the odd isotope is comparable with that of the most abundant even isotopes, distribution of the intensity among the numerous hfs components can logically account for the absence of observable structure due to it. If a line should be found which connects levels of low J-values, the hfs of Er^{167} should be observable.

Even though components of the odd isotope are not visible, they may be expected to influence measurements on the even isotopes, and this will be discussed later.

Recently there has appeared a report by Murakawa and Suwa[10] on measurements of isotope shifts in a number of Er lines. The results are qualitatively in agreement with our own, but disagreements exist which lie outside the assigned limits of error. We have measured four of the five lines on which Murakawa and Suwa have reported; the fifth line, λ4086.7, was not observed although we did observe (but did not measure) the strong line λ4087.6 which has a structure similar to that reported for λ4086.7. They quote an average ratio of the isotope shifts which corresponds in our convention to a ratio of 1.09 ± 0.05 (their ratio is the inverse of ours); such a large value seems unlikely on the basis of our measurements. Only in the case of λ5172.8 do we obtain a ratio in close agreement with their value for the same line. Since in every case reported their measurement of the shift (168–166) is distinctively smaller than ours, the possibility is suggested that the centers of gravity of these two components have shifted towards one another in their plates because of insufficient resolution, possibly influenced by the components of Er^{167}. That this may indeed be the case is further suggested by the fact that their source was water-cooled, whereas ours was cooled with liquid nitrogen. Our measurements on Er^{164} are not considered sufficiently accurate for any meaningful comparison.

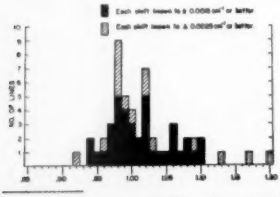

FIG. 2. Distribution of the ratios of the isotope shifts, $(\nu_{168}-\nu_{170})/(\nu_{168}-\nu_{166})$.

According to the volume picture of isotope shifts, the shifts should be proportional to the change in effective nuclear radius. It is not possible to calculate the change in effective nuclear radius in these investigations since no analysis of the spectrum is available. However, it is possible to investigate whether or not the change in radius is uniform for the three even isotopes, since the ratio of the isotope shifts $(\nu_{168}-\nu_{170})/(\nu_{168}-\nu_{166})$, should be proportional to the changes in a nuclear radius for the corresponding isotopes.

The ratios of the isotope shifts are given in the table wherever both splittings are known to ±0.0025 cm^{-1} or better. The average of these ratios is 1.015. If the average is restricted to those lines whose splittings are known to ±0.0015 cm^{-1} or better, the ratio is 1.010.

A histogram of the ratios is shown in Fig. 2. Although the ratios in the individual lines are in most cases equal to unity within experimental error, the spread of values must be attributed more to the disturbing effects of the odd isotope than to the inaccuracy of the measurements. In many cases the deviation from unity, above or below, is outside of experimental error.

It is quite possible that the disturbing effects of the odd isotope do not cancel out when the results from many lines are averaged; rather, there may be a systematic shifting of the ratios. It is perhaps significant that one of the largest ratios observed, 1.10, comes from the line (λ4888) which shows the largest isotope shift. When the shifts are large, as they are in this particular line, the disturbing effects of the odd isotope would be expected to have less influence on the ratio than in the case of smaller splittings, simply because for the same disturbing effect upon an individual components, the relative disturbance of the shift is less.

Except for the one case mentioned above, there appears to be no evidence to indicate that the ratio of the even isotope shifts differs from unity by more than 0.04 in either direction.

C. Assignment of Electron Configuration

Very little in the way of analysis has been accomplished in the rare earth spectra. Although some classifications have been made at both ends and in the very middle of the group, the accomplishments elsewhere have been fragmentary or nonexistent.

Zeeman and hyperfine structure patterns are very useful in spectral analysis, particularly in the identification of terms and J-values. Isotope shift data can be equally useful in the assignment of electron configurations, which frequently defy identification even after the terms are known.

Roughly speaking, the rare earths are formed by the filling in of $4f$ electrons inside the valence electrons. Lanthanum ($Z=57$) begins the group with a structure of $5d6s^2$ outside the closed xenon shell of 54 electrons.

[9] Schüler, Raig, and Korsching, Z. Physik **111**, 165 (1938); H. Schüler and H. Korsching, Z. Physik **111**, 386 (1938).
[10] K. Murakawa and S. Suwa, Phys. Rev. **85**, 683 (1952).

At lutecium the f-shell is filled and the final structure is $4f^{14}5d6s^2$. The single ion is obtained by the removal of one of the valence electrons.

The unfilled f-shell gives rise to a tremendous number of terms[11] for the valence electrons to build on. The spectra are further complicated by the competition of the $4f$, $5d$, and $6s$ electrons which are nearly equal in energy and which give rise to many electron configurations of comparable energy. The number of strong lines which can arise is tremendous: thirteen of the rare earths (Pm omitted) account for more than one-fourth of the atomic lines in the *MIT Wavelength Tables*,[12] while cerium alone accounts for more than 5 percent with 5755 lines out of the more than 100,000 listed.

Configuration interactions are quite common in rare earth spectra, and arise because of the competition of the f, d, and s electrons. The angular momenta of the individual electrons are not constants of the motion and the quantum numbers of a particular electron are not "good" quantum numbers. Generally the admixture of different configurations is not necessary in order to obtain a good approximation to the state of the atom, but where the electron energies corresponding to different l-values are nearly equal, the mixing of configurations of the same parity may become quite strong. In Gd II, for example, Russell[13] could not distinguish between the P terms arising from the $4f^7 6s6p$ configuration and those arising from $4f^7 5d6p$.

A relatively small admixture of a second configuration may impart much of its own characteristics to the primary configuration. A common result is the appearance of double electron transitions. For example, a pd configuration admixed with some ps could make a transition to s^2. Such double transitions are relatively common in rare earth spectra and will be seen to play an important role in the interpretation of the origin of the erbium isotope shifts.

In those rare earths where analyses have been made it is often not certain what the lowest levels are, for there often exist a set of low even and a set of low odd levels for which no intercombinations have been discovered, probably because they lie too far into the infrared. The low configurations of one group are $4f^n5d^2$, $4f^n5d6s$, $4f^n6s^2$, and for the other group, $4f^{n+1}5d$ and $4f^{n+1}6s$. The intermediate configurations which can combine with these are found by replacing either a $5d$ or a $6s$ electron with a $6p$.

It is most probable that the shifts observed arise from the second spectrum of erbium (Er II), although it is possible that some of the smaller shifts in the red may be due to the first spectrum. There are several reasons for believing this to be true: First, hollow cathodes usually excite the ion of rare earth spectra, particularly when He is the carrier gas. Secondly, the intensities of the lines which show structure were found to agree more closely with spark spectra data[14] than with arc, in the regions where both were available. This was confirmed by an arc spectrogram, which showed that the lines in question were enhanced near the poles of the arc. Finally, the isotope shifts are of the same magnitude as shifts due to the second spectrum of other elements in the region.

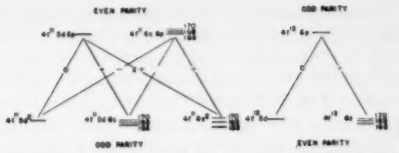

FIG. 3. Proposed electron configurations and transitions in Er II.

The diagram in Fig. 3 shows the more probable configurations of the erbium spectrum, and what combinations may be expected among them. Each configuration contains many terms and even more levels. In this schematic representation, the levels of all isotopes are adjusted to coincide for these configurations where there is no s valence electron. The isotope shifts are roughly the same for all levels with one $6s$ electron and roughly twice this amount for two $6s$ electrons. Account has not been taken of the $6p_{\frac{1}{2}}$ electrons, which should contribute shifts about 5 percent as great as the $6s$ electrons. When a p electron is designated in a term, it may be a $p_{\frac{1}{2}}$, a $p_{\frac{3}{2}}$ or a linear combination of the two. In general, the p electrons may be said to contribute a shift 0 to 5 percent of the normal $6s$ shift. The lightest isotope (Er^{166}) is always lowest, and, of course, combinations can only occur between levels of the same isotope.

The p to s transitions give rise to the normal isotope shifts, with the component due to the heaviest isotope (Er^{170}) appearing displaced to the small wave numbers; shifts of this type were designated as positive in the table. According to the scheme proposed in Fig. 3 there are three different transitions which could give rise to such positive shifts, and also one double transition which could give a positive shift about twice the magnitude.

The negative shifts observed undoubtedly arise from the double electron transition $4f^{11}6s6p$ to $4f^{11}5d^2$, since no other probable transitions among low terms of Er II can account for them. The large number of rather strong lines with negative shifts indicates that configuration mixing is taking place quite strongly. Perhaps the mixing of configurations which have isotope shifts with those which do not accounts for part of the spread in values of the isotope shifts (Fig. 1). On the other hand, the spread of values is small enough to justify the assignment of a single configuration to most levels.

[11] See, for example, L. Pauling and S. A. Goudsmit, *Structure of Line Spectra* (McGraw-Hill Book Company, Inc., New York, 1930), p. 156.

[12] G. R. Harrison, *MIT Wavelength Tables* (J. Wiley and Son, New York, 1939).

[13] H. N. Russell, J. Opt. Soc. Am. **40**, 550 (1950).

[14] A. Gatterer and J. Junkes, *Spektren der Seltenen Erden* (Specola Vaticona, Vatican City, 1945).

The configuration $4f^{11}6s^2$ should show isotope splittings roughly twice that of configurations with only a single 6*s* valence electron. The splittings are somewhat less than twice the normal value because of the mutual screening of the *s*-electrons. The screening effects cannot be estimated very well in this case because of the lack of an analysis, but in the case Tl II, Crawford and Schawlow[6] estimated that the shift in the $6s^2$ configuration should be about 7 percent less than twice the shift of a single 6*s* electron. It is possible that the line λ4888 arises from the double electron transition $4f^{11}5d6p$ to $4f^{11}6s^2$, although the mean value of the shift (72.9 cm^{-1}) is somewhat less than 93 percent of twice the value of the normal positive shifts (45.5 cm^{-1}). The transition $4f^{11}6s6p$ to $4f^{11}6s^2$ should show shifts which are about 14 percent less than the other positive shifts ($4f^{11}5d6p$ to $4f^{11}5d6s$ and $4f^{12}6p$ to $4f^{12}6s$). The shifts around either 0.033 cm^{-1} or 0.042 cm^{-1} (see Fig. 1) may arise from this transition.

In summary, the negative shifts almost certainly arise from the double electron transition $4f^{11}6s6p$ to $4f^{11}5d^2$. Most of the positive shifts probably arise from the transitions $4f^{11}5d6p$ to $4f^{11}5d6s$ and $4f^{12}6p$ to $4f^{12}6s$. The shifts arising from the transition $4f^{11}6s6p$ to $4f^{11}6s^2$ are probably smaller than the normal positive shifts. The double electron transition $4f^{11}5d6p$ to $4f^{11}6s^2$ should give a shift nearly twice the normal positive shift, and one line of this transition may have been observed.

It is interesting to note in which regions most of these various shifts occur. The normal positive shifts are distributed quite uniformly throughout the region from 6600 to 4500A, but the negative shifts appear more abundantly between 5125 and 4250A. Between 6600 and 4300A, the number of strong lines which show structure exceeds those which do not, but below 4000A there are very few lines which show structure at all, although some of the most intense lines in the erbium spectrum are to be found in this region.

PHYSICAL REVIEW VOLUME 87, NUMBER 6 SEPTEMBER 15, 1952

Neutrons from the Disintegration of Phosphorus by Deuterons*

S. C. SNOWDON
Bartol Research Foundation of the Franklin Institute, Swarthmore, Pennsylvania
(Received July 23, 1951)

The neutron spectrum at 0° and 90° from the $P^{31}(d,n)S^{32}$ reaction has been investigated using nuclear emulsions. The energies of the excited states in S^{32} are 0.5, 1.5, 2.2, 2.7, 3.3, 3.8, 4.1, 4.5, 4.9, 5.2, and 5.5-Mev, each with an uncertainty of about ±0.1-Mev.

INTRODUCTION

TWO previous measurements of the energies of the excited states in S^{32} have been reported. Dicke and Marshall[1] measured the inelastic scattering of protons by sulfur giving excited states in S^{32} at 2.25 Mev and 4.34 Mev. Grace, Beghian, Preston, and Halban[2] using absorption techniques found a 2.35-Mev gamma-ray when fast neutrons were inelastically scattered from S^{32}. In this work the energy levels in S^{32} have been found using the $P^{31}(d,n)S^{32}$ reaction and the photographic plate technique.

EXPERIMENTAL PROCEDURE

A thick target of 99+ percent pure red phosphorus[3] was bombarded by 1.60-Mev deuterons from the Bartol electrostatic generator. The resultant neutron spectrum was found by observing the proton recoils in 100μ Eastman NTA nuclear emulsions mounted 3 cm from the target at angles of 0° and 90° to the direction of the beam. The proton recoils were observed only in a narrow band in the front half of the plate such that an acceptance angle of ±12° could be used. A total of 1700 tracks were measured on the 0° plates and 1100 tracks on the 90° plates. In order to improve the statistical accuracy, 3.19 times as many fields of view were observed above 3.0 Mev on the 90° plates as were observed in the same range when tracks of all energies were counted; on the 0° plates, the factor was 1.79 for the same energy range. The data, corrected for the variation of neutron-proton scattering cross section,[4] geometry,[5] and the above mentioned statistical weights, are shown in Fig. 1 and Fig. 2. The vertical line through each of the observed points has a total length equal to twice the estimated standard deviation of the measurement.

The only likely impurity in the phosphorus was boron since the red phosphorus was prepared from distilled

* Assisted by the joint program of the ONR and AEC.
[1] R. H. Dicke and J. Marshall, Jr., Phys. Rev. **63**, 86 (1943).
[2] Grace, Beghian, Preston, and Halban, Phys. Rev. **82**, 969 (1951).
[3] Courtesy of J. H. Walthall, Tennessee Valley Authority, Wilson Dam, Alabama. No chemical analysis supplied; however, a statement as to the method of purification was supplied.
[4] R. K. Adair, Revs. Modern Phys. **22**, 249 (1950).
[5] H. T. Richards, Phys. Rev. **59**, 796 (1941).
[6] Crawford and Schawlow, Phys. Rev. **76**, 1310 (1949).

white phosphorus in a boro-silicate glass apparatus.[5] A normal boron (d,n) neutron spectrum previously had been run in this laboratory using $E_D = 1.30$-Mev and had shown a rather high intensity of tracks at 10-Mev.[6] The relative intensity of the remaining groups was no more than five times as intense as this group. Therefore, from the fact that no tracks corresponding to the 10-Mev group appeared on the present plates, it may be concluded that the boron reaction contributes a negligible distortion to the observed spectrum. Since the lowest energy peak in the spectrum occurs at about the position of $C^{12}(d,n)N^{13}$ neutrons the phosphorus spectrum will be distorted by the presence of the carbon surface contaminant. A distortion due to D−D neutrons is not likely with our bombarding currents (0.5–1.0 μa).

In order to reduce the carbon contaminant three fresh targets were used during the 0.05-coulomb bombardment. No background run was made to check other possible contaminants. However, a similar experiment[7] in which Si^{28} was bombarded by deuterons for a similar length of time showed that no appreciable number of neutrons in the energy range 2.0 Mev to 9.0 Mev was present. The analysis of the $P^{31}(d,n)S^{32}$ spectrum was made assuming that carbon was the only possible contaminant.

ANALYSIS OF DATA

As may be seen from Figs. 1 and 2, the statistical accuracy of each of the 0° and 90° determinations of the proton recoil spectrum is rather poor. In order to extract the maximum amount of information from the data as a whole, two things need to be done. First, a method of plotting all of the data as a unit must be found. Secondly, one must know the theoretical line shape of the recoil spectrum of a single neutron group. Strictly speaking, one cannot combine the 0° and 90° data on to a single energy scale using any transformation, since the shape of the proton recoil range distribution, corresponding to a monoergic neutron, changes as the neutron energy is varied. However, since P^{31} is relatively heavy, an artifice may be employed to effect the transformation approximately. It can be shown that, for the $P^{31}(d,n)S^{32}$ reaction, the errors involved in treating any particular range as an actually existing energy of a neutron through the range energy relation for photographic emulsions leads to discrepancies in the center-of-mass distribution that are well within the uncertainties allowed by the statistical accuracy involved. The result then is that, if the range scales of the 0° and 90° data are transformed to energy scales by the range-energy relation,[8] the corresponding proton and hence neutron energies may each be transformed to the center-of-mass energy scale of the

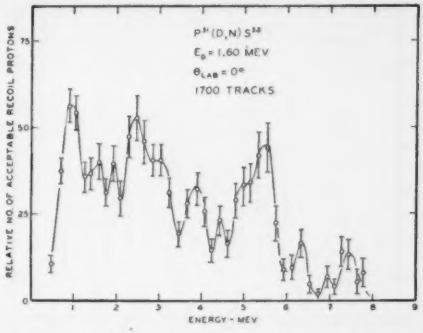

FIG. 1. Relative number of acceptable recoil protons per 200-kev interval *versus* the recoil proton or neutron energy at 0°. Standard deviation of the measurements are indicated at each point.

$P^{31}(d,n)S^{32}$ reaction. When this is done the two sets of data may be added together to improve the statistical accuracy. No meaning can be attached to the resulting intensities other than that of the sum of the 0° and 90° data of the laboratory coordinate system.

The line shape of the recoil proton spectrum that corresponds to a single neutron group may now be found by employing several assumptions. It is assumed first that the Gamow penetrability factor[9] gives the shape of the yield of each neutron group. This assumption should be justified for our low bombarding energy (1.6 Mev). Secondly, it is assumed that the range straggling parameter for monoenergetic protons is given for our detecting geometry by the root mean square of the deviation of all track lengths in the group as given by Richards *et al.*[8] Since the range-energy relation in

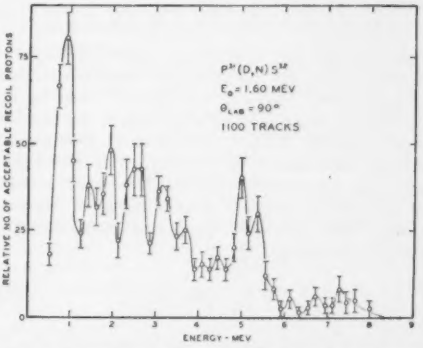

FIG. 2. Relative number of acceptable recoil protons per 200-kev interval *versus* the recoil proton or neutron energy at 90°. Standard deviation of the measurements are indicated at each point.

[5] C. P. Swann (private communication).
[7] Mandeville, Swann, Chatterjee, and Van Patter, Phys. Rev. **85**, 193 (1952).
[8] Richards, Johnson, Ajzenberg, and Laubenstein, Phys. Rev. **83**, 994 (1951).
[9] J. Mattauch and S. Fluegge, *Nuclear Physics Tables* (Interscience Publishers, Inc., New York, 1946), p. 65.

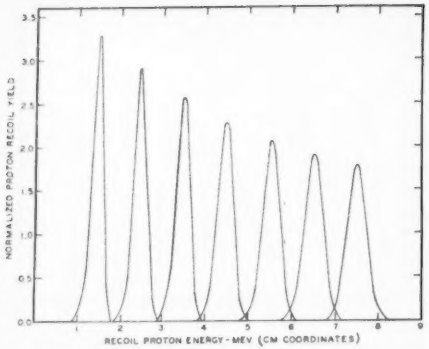

FIG. 3. Plot of typical resolution functions, $R(x, a_k)$, showing the combined effect of the thick target and the range straggling of the recoil protons in the nuclear emulsion on the resolution of the various energy neutron groups.

Richard's paper was found using (p,n) and (d,n) reactions, the corresponding width of the proton recoil groups should be a good measure of that part of the width of our groups that is caused by the detection of a monoenergetic neutron in a photographic emulsion.

Since our targets may be considered as infinitely thick, the observed line shape of a single neutron group may be found by folding a Gaussian distribution having the above-mentioned straggling parameter into a Gamow yield function each suitably displaced in energy to give the result in the center-of-mass energy scale. Typical line shapes for different neutron groups each normalized to unit area are shown in Fig. 3. This function is designated by $R(x, a_k)$, where x is the energy in the center-of-mass coordinates. The parameter a_k is related to the kth Q value by the equation

$$a_k = M_R Q_k/(M_T+M_B)+M_T M_R E_B/(M_T+M_B)^2, \quad (1)$$

where M_B, M_T, and M_R are the masses of the bombarding, target, and residual nuclei, respectively. E_B is the bombarding voltage and Q_k is the Q value for the kth neutron group. The tabular form of the function used is given in Table I. The observed proton recoil spectrum then should be a superposition of the preceding line shapes each adjusted in intensity to account for the relative amounts of each group of neutrons present. Thus, the observed proton recoil spectrum should be written as

$$y = \sum_{k=1}^{\nu} A_k R(x, a_k). \quad (2)$$

The theory of least squares[10] may be used to fit Eq. (2) to the observed points and thereby unfold the data to give the relative intensity A_k and the energy a_k of the kth neutron group. The method also gives the uncertainties in the adjusted parameters A_k and a_k. However, it is not possible on *a priori* grounds to choose the correct number of groups ν. A number may be selected for ν and the statistical χ^2 test may be employed to judge the over-all suitability of the resulting fit.

[10] W. E. Deming, *Statistical Adjustment of Data* (John Wiley and Sons, Inc., New York, 1943).

EXPERIMENTAL RESULTS

The 0° and 90° laboratory coordinate data of Figs. 1 and 2 were plotted after applying a correction for the angular straggling (2.28 percent). As explained in the previous section, the relative yields in 0.20-Mev intervals were found in the center-of-mass energy scale. Figure 4 represents the sum of these two sets of transformed data except that the doubtful carbon contamination peak has been subtracted out. Reasonable choices for A_k, a_k, and ν were next assumed, and the resulting value of the weighted sum of the squares of the deviations, S_0, was found. By inspection the values of A_k and a_k were adjusted and a new value of S_k was computed. This process was continued until S_0 could not be reduced further. This smallest value of S_0 was taken as χ^2, since the weight of each observation was set equal to the reciprocal of the square of its standard deviation. The trial and error method by which the parameters were found leads one to a fair estimate of the uncertainties involved. In general, A_k is uncertain by about 15 percent and the uncertainty in a_k is about ±0.1-Mev.

TABLE I. Resolution function $R(x, a_k)$. Note that a_k is connected to Q_k by Eq. (1); however, since the chief effect of Q_k is included in $x-a_k$, the changing shape of the function with a_k of Q_k is indicated only in gross intervals of $\Delta Q_k = 1$-Mev. Units of x, a_k, and Q are Mev.

$x-a_k$ \ Q	0.0	1.0	2.0	3.0	4.0	5.0	6.0
−0.80	0.002	0.005	0.010	0.017	0.026	0.036	0.048
−0.75	0.007	0.012	0.020	0.031	0.045	0.061	0.077
−0.70	0.022	0.030	0.043	0.059	0.076	0.097	0.121
−0.65	0.050	0.061	0.077	0.098	0.123	0.154	0.184
−0.60	0.094	0.105	0.128	0.158	0.193	0.231	0.269
−0.55	0.154	0.172	0.205	0.248	0.291	0.337	0.383
−0.50	0.242	0.269	0.316	0.374	0.427	0.479	0.528
−0.45	0.373	0.415	0.474	0.542	0.607	0.668	0.721
−0.40	0.566	0.630	0.696	0.763	0.834	0.884	0.912
−0.35	0.843	0.918	0.987	1.050	1.103	1.128	1.134
−0.30	1.222	1.300	1.353	1.384	1.397	1.386	1.358
−0.25	1.705	1.765	1.770	1.745	1.685	1.608	1.558
−0.20	2.268	2.243	2.180	2.071	1.924	1.789	1.708
−0.15	2.862	2.687	2.488	2.277	2.067	1.912	1.789
−0.10	3.302	2.912	2.579	2.279	2.042	1.877	1.782
−0.05	3.170	2.650	2.378	2.142	1.938	1.778	1.684
0.00	2.211	2.055	1.917	1.788	1.677	1.582	1.510
0.05	1.015	1.249	1.330	1.345	1.338	1.318	1.283
0.10	0.292	0.612	0.786	0.894	0.981	1.019	1.028
0.15	0.051	0.234	0.392	0.533	0.660	0.747	0.779
0.20	0.004	0.090	0.165	0.271	0.406	0.507	0.556
0.25		0.014	0.057	0.131	0.229	0.330	0.374
0.30		0.003	0.017	0.052	0.117	0.190	0.237
0.35		0.001	0.005	0.022	0.054	0.095	0.141
0.40			0.001	0.008	0.023	0.047	0.079
0.45				0.001	0.008	0.021	0.041
0.50					0.003		

Figure 4 and Table II give the important results of this paper. The resulting curve through the points was drawn by using Eq. (2) with the constants A_k and a_k given in Table II. Let the groups be labeled 1, 2, 3, etc., beginning with the ground-state group. If the first 12 groups are tested for goodness of fit by the χ^2 test,[11] the probability P that the observed value of $\chi^2=15.1$ will be exceeded for $9(=33-2\times12)$ degrees of freedom is 0.06. If the 13th group of neutrons is included, $\chi^2=59.8$ and, for $12(=38-2\times13)$ degrees of freedom, the value of P is less than 0.01. In interpreting these values of P it is customary to say that if P lies between 0.9 and 0.1 the assumed distribution very probably corresponds to the observed one, while if P is less than 0.02 or more than 0.98 the assumed distribution is unlikely and is to be questioned seriously. Hence, we may say that there is reasonable assurance that the first 12 groups are present, but that in order to include the 13th group, an additional group would be needed between the 12th and 13th group to account for the observed high point. We have adopted the procedure of including only those groups that seem to persist in Fig. 1, Fig. 2, and Fig. 4. In order for a group to persist, however, it is not necessary that its detailed structure be in evidence. If a group seemed too wide to be admitted as a single group in all the figures, it was analyzed into two or more groups in the center-of-mass system. The sensitivity of the χ^2 test is also made evident when the one point that does not fall reasonably close to the assumed distribution causes the goodness of fit test to question seriously the assumed distribution.

Table II gives the results of the inelastic scattering determination of the levels in S^{32} by Dicke and Marshall[1]

TABLE II. Neutron groups from the $P^{31}(d,n)S^{32}$ reaction and the energy levels in S^{32}. To identify the groups, k runs from 1 to 12 beginning with $k=1$ for the ground-state group. A_k is the relative intensity of the kth group, a_k is the energy of the kth group in the center-of-mass system of coordinates, and Q_k, is the corresponding Q value. E_k is the excitation energy of S^{32}. Uncertainty in E_k is ±0.1 percent.

		Present work			Ref. 1	Ref. 2
k	A_k	a_k (Mev)	Q_k (Mev)	E_k (Mev)	E_k (Mev)	E_k (Mev)
1	5.3	7.5	6.2	0.0		
2	8.3	7.0	5.7	0.5		
3	7.9	6.0	4.7	1.5		
4	29.0	5.3	4.0	2.2	2.25 (pp')	2.35 (nn', γ)
5	26.1	4.8	3.5	2.7		
6	17.4	4.3	2.9	3.3		
7	15.6	3.8	2.4	3.8		
8	15.6	3.5	2.1	4.1		
9	23.7	3.1	1.7	4.5	4.34 (pp')	
10	24.1	2.7	1.3	4.9		
11	21.6	2.4	1.0	5.2		
12	24.1	2.1	0.7	5.5		

[11] R. A. Fisher, *Statistical Methods for Research Workers* (Oliver and Boyd, Edinburgh, 1932).

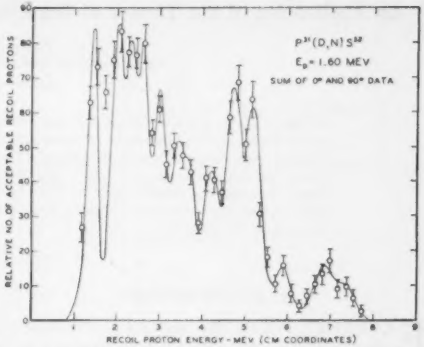
P³¹(D,N)S³²
E_D = 1.60 MEV
SUM OF 0° AND 90° DATA
RELATIVE NO OF ACCEPTABLE RECOIL PROTONS
RECOIL PROTON ENERGY - MEV (CM COORDINATES)

FIG. 4. Plot of the sum of the 0° and 90° laboratory coordinate data transformed to the center-of-mass energy scale. The probable error (0.675× standard deviation) of the observed points are shown with each observed point.

and by Grace, Beghian, Preston, and Halban.[2] The agreement of the excited states determined by the various methods is within the uncertainties of the experiments. Finally the ground-state Q value was found to be 6.2 Mev. Using the latest determination of the masses of P^{31} and S^{32} reported by Motz[12] this Q value should be 6.63 ± 0.07 Mev. It should be noted that if the ground-state group was missed, then the γ-ray observed by Grace *et al.*[2] cannot be to the ground state if it is to be associated with the strong group ($k=4$). The preferred interpretation is that the γ-ray is associated with the ($k=4$) group and that the relative accuracy of the determination of the groups is much better than the absolute accuracy. Because of the difficulty in maintaining strictly the $\pm12°$ acceptance angle criterion, there is a rather large uncertainty in correcting for the group shifts. In particular it was felt that the uncertainty in correcting for the group shifts due to the angles of emission of the neutrons around 0° and the angular straggling of the recoil protons in the nuclear emulsions could easily cause the energy scale to be four or five percent low. Hence it is felt that the excited states in S^{32} have the uncertainties given in the analysis but that the ground-state Q values of 6.2 Mev are subject to a larger absolute error.

In conclusion the author wishes to acknowledge his indebtedness to Mr. T. A. Haddad, who helped with the plate reading, to Mrs. E. A. Seaman for the computational assistance, to Dr. L. Eisenbud for several discussions concerning the chi-test, and finally to Dr. W. F. G. Swann, Director of the Bartol Research Foundation for his continued interest in this problem, especially in its curve fitting aspect.

[12] H. T. Motz, Phys. Rev. **81**, 1061 (1951).

An Application of the Theory of the Effective Range to Meson-Nucleon Scattering*

KEITH A. BRUECKNER
Physics Department, Indiana University, Bloomington, Indiana
(Received June 9, 1952)

A theory of the effective range for P-state scattering is developed and the extent of its validity is investigated. It is found that a parameter of the theory can meaningfully be identified as an effective range and that the energy dependence of the effective range is very weak. The resulting formula for the energy dependence of the phase shift is shown to be exactly equivalent, if the relativistic energy is used, to a simple form of the Wigner-Eisenbud one-level formula for P-states in which the level shift is neglected. An application to meson-nucleon scattering is made which illustrates the use of the method and which suggests a high lying resonance in the scattering.

I. INTRODUCTION

EXPERIMENTS on the scattering of mesons by protons[1] have shown that a large fraction of the scattering is due to contributions from the partial waves of unit angular momentum. It has been pointed out that this result is a partial verification of the predictions of pseudoscalar meson theory with pseudovector coupling which predicts predominant P-state interactions.[2,3] In addition an attempt has been made by the author[3] to account for the details of the scattering by an analysis using the generalized single-level formulas of Wigner and Eisenbud[4] and assigning the level parameters on the basis of weak and strong coupling pseudoscalar meson theory with symmetric pseudovector coupling. The weak coupling theory gave the ratios of the level widths to the resonance energies and the strong coupling theory gave the resonance energies.

The applicability of the Wigner-Eisenbud formulas to scattering phenomena of this character, however, is possibly of doubtful validity because of the large level width (about 100 Mev) required to describe the data.[5] An examination of the Wigner-Eisenbud result [obtained from their Eq. (57)], which gives

$$\tan\delta_\lambda=\tfrac{1}{2}\Gamma_\lambda/(E_\lambda+\Delta_\lambda-E), \tag{1}$$

shows that the approximate formula,

$$\tan\delta_\lambda\approx\tfrac{1}{2}\Gamma_\lambda/(E_\lambda-E), \tag{2}$$

can be used other than in the vicinity of resonance only if the level shift is small relative to E_λ. In the notation of Wigner and Eisenbud, for P-states, we have

$$\Gamma_\lambda=(k^3a^2\gamma_\lambda^2)/(1+k^2a^2),\quad \Delta_\lambda=-\tfrac{1}{2}\Gamma_\lambda/(ka), \tag{3}$$

where k is the momentum, a the radius of the internal region, and γ_λ^2 is a constant. Implicit in these formulas is also the smallness of the quantity ka. The condition for the validity of the approximate formula of Eq. (2) is therefore that

$$(k^2a\gamma_\lambda^2)/(1+k^2a^2)\ll 2E_\lambda, \tag{4}$$

over the range for which Eq. (2) is expected to hold. For example, at a meson energy of 200 Mev in the laboratory system corresponding to $k^2=3\mu^2$ in the barycentric system, with $E_\lambda\approx\mu$, and with $a^2=1/(2\mu^2)$ as assumed in reference 3, the condition is that

$$\gamma_\lambda^2\ll 2.18. \tag{5}$$

The assignment of γ_λ^2 made in analyzing the scattering data can be obtained by comparing Eq. (13) of reference 3 with Eq. (3) and that was $\gamma_\lambda^2=1.40$, so that the condition of Eq. (5) is only partially satisfied. Because of the possible lack of validity of formulas such as Eq. (2), it is of interest to show that these phenomena may be described from an entirely different viewpoint[6] making use of the theory of the effective range as developed by Bethe,[6] Chew and Goldberger,[7] and others,[8] which gives essentially identical results. Chew and Goldberger give a formula of general validity for arbitrary angular momentum states which can be specialized to our case of scattering in P-states; the result can, however, be derived directly in a simple manner which follows Bethe's treatment closely.

II. THEORY

We consider the Klein-Gordon equation for a meson moving in a potential V[9]

$$[\Delta-\mu^2+(E-V)^2]\psi=0. \tag{6}$$

In this equation, we let $\psi=\Sigma_l P_l(\cos\theta)u_l(r)/r$, $k^2=E^2-\mu^2$, and find

$$(d^2/dr^2-l(l+1)/r^2+k^2-2EV+V^2)u_l=0. \tag{7}$$

* Assisted by the joint program of the ONR and AEC.

[1] Anderson, Fermi, Long, Martin, and Nagle, Phys. Rev. **85**, 934 (1952); Anderson, Fermi, Long, and Nagle, Phys. Rev. **85**, 936 (1952); Fermi, Anderson, and Nagle (to be published).

[2] Nagle, Anderson, Fermi, Long, and Martin, Phys. Rev. **86**, 603 (1952).

[3] K. A. Brueckner, Phys. Rev. **86**, 106 (1952).

[4] E. P. Wigner and L. Eisenbud, Phys. Rev. **72**, 29 (1947).

[5] The usefulness of this method was pointed out to the author by Dr. Richard Christian in connection with the analysis of reactions involving light nuclei.

[6] H. A. Bethe, Phys. Rev. **76**, 38 (1949).

[7] G. F. Chew and M. L. Goldberger, Phys. Rev. **75**, 1637 (1949).

[8] J. M. Blatt and J. D. Jackson, Phys. Rev. **76**, 18 (1949); F. C. Barker and R. E. Peierls, Phys. Rev. **75**, 312 (1949).

[9] The representation of the meson-nucleon interaction by a static potential can at best be an approximate description. The potential does not, however, appear in our final formulas so that the results are to some extent independent of this assumption.

If we define a new potential function,

$$2\mu v = 2EV - V^2, \tag{8}$$

then Eq. (7) reduces to the ordinary Schrödinger equation except that the relativistic momentum appears. The potential v then is according to Eq. (8) energy dependent; however, in the applications which interest us, the potential V is considerably larger than the energy E and in addition the energy E varies only from about 170 Mev to 280 Mev for meson scattering with kinetic energies in the laboratory system varying from 50 to 200 Mev. We shall therefore consider v to be constant and shall expect small energy dependent corrections to the effective range from the variations in v.

Now specializing to the case $l=1$, we introduce the functions u_1 and ψ_1 corresponding to the momentum k_1, which satisfy Eq. (7) except that ψ_1 is the solution with $V=0$, u_1 will have the form outside the range of the potential

$$u_1 = \text{constant} \times \left[\cos(k_1 r + \delta_1) - \frac{\sin(k_1 r + \delta_1)}{k_1 r}\right], \tag{9}$$

which is also the general form of ψ_1 for all r. We fix the normalization by requiring that ψ_1 be equal to unity at ϵ much less than the range of the potential (we cannot take $\epsilon = 0$ because of the singularity of ψ_1)[10] and that $u_1 = \psi_1$ outside the range of the potential. Following Bethe's procedure, we now form the expression

$$\int_\epsilon^\infty \left\{\frac{d}{dr}\left(u_1\frac{du_2}{dr} - u_2\frac{du_1}{dr}\right) - \frac{d}{dr}\left(\psi_1\frac{d\psi_2}{dr} - \psi_2\frac{d\psi_1}{dr}\right)\right\} dr$$

$$= (k_1^2 - k_2^2)\int_\epsilon^\infty (u_1 u_2 - \psi_1\psi_2)dr. \tag{10}$$

Making use of the equality of u_1 and ψ_1 at large distances, the vanishing of u at ϵ (to order $k\epsilon$), and the normalization of ψ, we find

$$\left(\frac{d\psi_1}{dr} - \frac{d\psi_2}{dr}\right)_{r=\epsilon} = (k_2^2 - k_1^2)\int_\epsilon^\infty (u_1 u_2 - \psi_1\psi_2)dr. \tag{11}$$

The expression for ψ which satisfies the normalization at $r=\epsilon$ is

$$\psi(r) = \left[\cos(kr+\delta) - \frac{\sin(kr+\delta)}{kr}\right] \times \left[\cos(k\epsilon+\delta) - \frac{\sin(k\epsilon+\delta)}{k\epsilon}\right]^{-1}. \tag{12}$$

Expanding this for small r gives

$$d\psi(\epsilon)/dr = -1/\epsilon + k^2\epsilon + k^3\epsilon^2\cot\delta + \mathcal{O}(k^4\epsilon^3). \tag{13}$$

Combining this result with Eq. (11) leads to the useful expression

$$k_1^3\cot\delta_1 - k_2^3\cot\delta_2 = \frac{(k_2^2 - k_1^2)}{\epsilon^3}\left[\int_\epsilon^\infty (u_1u_2 - \psi_1\psi_2)dr + \epsilon\right], \tag{14}$$

in which the singular terms in $1/\epsilon$ have canceled. We now define the quantity

$$\frac{1}{\epsilon^3}\left[\int_\epsilon^\infty (u_1u_2 - \psi_1\psi_2)dr + \epsilon\right] = [\rho(k_1, k_2)]^{-1}, \tag{15}$$

and write Eq. (14) in the form

$$k_1^3\cot\delta_1 - k_2^3\cot\delta_2 = (k_2^2 - k_1^2)/\rho(k_1, k_2). \tag{16}$$

Equation (16) is the analog for P-states of Bethe's Eq. (12) for S-states.[6]

This result can be expressed in two particularly useful ways. Consider first the limit as $k_1 \to 0$, $k_2 = k$. We define

$$\lim_{k\to 0} k^3\cot\delta = a^{-3}, \tag{17}$$

where a is the "scattering length,"[11] and make use of the effective range approximation,

$$\rho(0, k) = r_0, \tag{18}$$

to introduce the "effective range" r_0. Equation (15) then takes the form

$$k^3\cot\delta = a^{-3} - k^2/r_0. \tag{19}$$

The approximate energy independence of $\rho(0, k) = r_0$ follows, as Bethe has shown, from the form of the integral of Eq. (14). The integrand is finite only within the range of the forces and, for a strong interaction, will be insensitive to variations in the energy. We also can obtain another useful form for Eq. (16) in the vicinity of the vanishing point of $\cot\delta$ which we assume to be at a momentum value k_0. Then we have

$$k^3\cot\delta = (k_0^2 - k^2)/\rho(k, k_0) \cong (k_0^2 - k^2)/r_0. \tag{20}$$

Equation (19) can be written in a form which clearly shows its relation to the Wigner-Eisenbud expression of Eq. (1). This is

$$\tan\delta = \frac{1}{2}\frac{(-2k^3r_0/2\mu)}{(r_0/2\mu a^3 - \text{“}E\text{”})}, \tag{21}$$

where we have introduced "E"$=k^2/2\mu$ which reduces to the kinetic energy in the nonrelativistic limit. If we identify $2k^3r_0/2\mu = -\Gamma_\lambda$, $r_0/2\mu a^3 = E_\lambda$, then Eq. (21) is identical with Eq. (2), except that E has been replaced by "E". The form of this result shows that the energy dependence and "resonance" behavior of the phase shifts given by the effective range theory are almost

[10] In all expressions which we derive, we shall implicitly understand that the limit as $\epsilon \to 0$ is to be taken.

[11] The parameter a is of course not a scattering length in the sense of the corresponding constant which appears in the description of S-state scattering.

identical with the predictions of the Breit-Wigner resonance theory.

We shall next consider the validity of the approximations involved in the use of the simple effective range formula of Eq. (18). We write

$$\frac{1}{\rho(k,0)}=\frac{1}{\epsilon^2}\left[\int_\epsilon^\infty (u_0^2-\psi_0^2)dr+\epsilon\right]$$
$$+\frac{1}{\epsilon^2}\int_\epsilon^\infty [u_0(u_k-u_0)-\psi_0(\psi_k-\psi_0)]dr$$
$$\equiv\frac{1}{\rho(0,0)}+\frac{1}{\epsilon^2}\int_\epsilon^\infty [u_0(u_k-u_0)-\psi_0(\psi_k-\psi_0)]dr. \quad (22)$$

The first term in this equation we have identified as the reciprocal of the effective range r_0; the second gives the energy dependent correction to the effective range. To show the connection between r_0 and the range R of the potential, we first write the expression of Eq. (12) for ψ correct to terms quadratic in k

$$\psi_k(r)=\epsilon\left[\frac{1}{r}+\frac{r^2}{3a^3}\right]+k^2\frac{\epsilon r}{3}\left[\frac{3}{2}-\frac{r}{r_0}-\frac{r^3}{10a^3}\right]$$
$$\equiv\epsilon(\alpha_0+k^2\alpha_1). \quad (23)$$

A correctly normalized expression for u, if $v(r)$ is a solution of Eq. (7), is

$$u(r)=v(r)\psi(R)/v(R), \quad (24)$$

where R is the range of the potential at which point u and ψ are defined to be equal. Using these results, we have

$$\frac{1}{r_0}=\int_\epsilon^\infty\left\{\left[\frac{v_0(r)}{v_0(R)}\alpha_0(R)\right]^2-\alpha_0^2(r)\right\}dr+\frac{1}{\epsilon}. \quad (25)$$

The singular terms in $\alpha_0^2(r)$ can be canceled if we write

$$\frac{1}{\epsilon}=\int_\epsilon^R r^{-2}dr+\frac{1}{R}.$$

We then have

$$\frac{1}{r_0}=\frac{1}{R}+\int_0^R\left\{\left[\frac{v_0(r)}{v_0(R)}\alpha_0(R)\right]^2-\frac{2}{3}\frac{r}{a^3}-\left(\frac{r^2}{3a^3}\right)^2\right\}dr. \quad (26)$$

The contribution from the integral will in general not be a large correction if a^3 is not small compared with the range R, since the integrand vanishes at $r=0$ and is equal to $1/R^2$ at $r=R$. We therefore see that r_0 is of the magnitude of R and can meaningfully be identified as an effective range.

To obtain the energy dependent correction term, we make use of the expansion for ψ and in addition write

$$u(k)=u_0+k^2v_1. \quad (27)$$

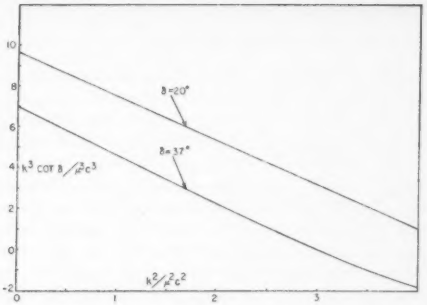

FIG. 1. Effective range plot for scattering from an attractive square well potential of range $\frac{1}{2}\hbar/\mu c$. The potential strengths have been adjusted to give a phase shift of 20° and of 37° at $k=1.30\mu c$. The effective range is approximately $0.44\hbar/\mu c$ for both well depths.

We then have

$$\frac{1}{\rho(k,0)}-\frac{1}{r_0}=k^2\int_0^\infty\left(\frac{u_0v_1}{\epsilon^2}-\alpha_0\alpha_1\right)dr. \quad (28)$$

To estimate the size of this correction, we notice that

$$\alpha_0\alpha_1=\tfrac{1}{3}(1+r^3/3a^3)(\tfrac{3}{2}-r/r_0-r^3/10a^3) \quad (29)$$

vanishes at approximately $r=(3/2)r_0$ if R^3/a^3 is not large. We also note that u_0v_1/ϵ^2 vanishes at $r=0$, and is equal to $\alpha_0\alpha_1$ at the range of the forces, so that the integrand vanishes at $r=R$. We therefore clearly set an upper limit on the integral if we evaluate

$$\int_0^R(-\alpha_0\alpha_1)dr\approx-\tfrac{1}{3}r_0. \quad (30)$$

If we now write

$$\rho(k,0)=r_0+Pk^2r_0^3, \quad (31)$$

where the numerical factor P gives the size of the energy-dependent correction, this argument leads us to include that P is somewhat less than $\frac{1}{3}$. This result shows that we can expect a high degree of validity for the approximation of treating $\rho(k,0)$ as a constant, as long as kr_0 is of the order of one or less, contrary to what we might expect on the basis of a purely dimensional argument. The results obtained by Bethe[6] and by Blatt and Jackson[8] in the analysis of nucleon scattering show that a similar situation holds for S-state interactions.

To show for a simple case the extent of the validity of the formula of Eq. (19), we have explicitly calculated the P-state scattering from an attractive square well potential of range one-half the meson compton wavelength. The results are given in Fig. 1, plotting $(k^3/\mu^3c^3)\cot\delta$ against k^2/μ^2c^2, where the well depth has been adjusted to give phase shifts of 20° and 37° at $k=1.3\mu c$. The "scattering length" a in these cases is approximately $a=0.48\hbar/\mu c$ and $0.95\hbar/\mu c$, respectively; the effective range is very nearly the same for both and

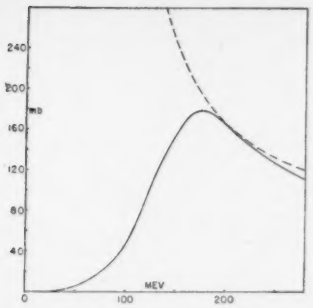

FIG. 2. $P_{\frac{1}{2}}$ scattering from the deeper square well potentials of Fig. 1. The laboratory energy is indicated. The dashed line gives the maximum possible $P_{\frac{1}{2}}$ scattering corresponding to a phase shift of 90°.

is $r_0=0.44\hbar/\mu c$. It is possible to obtain explicitly the first correction term to the effective range from these results. For the case of the deeper well, $\rho(k, 0)$ is approximately

$$\rho(k, 0)=r_0+0.18k^2r_0^3, \tag{32}$$

showing the smallness of the coefficient P of Eq. (22) in agreement with the conclusions reached above. Since in this case the effective range is about one-half the meson Compton wavelength, the correction to r_0 is negligible over the range of energies considered. It is apparent from these results that the approximation of treating $\rho(k, 0)$ as a constant gives an excellent description of the scattering, although at the higher energies, the ratio r_0/λ increases to nearly one: It is also interesting that the scattering from the deeper potential, with $\delta=37°$ at $k=1.3\mu c$, passes through a "resonance" at $k^2=3.08\mu^2c^2$, corresponding to a laboratory energy of 202 Mev.[12] This is shown in Fig. 2 which gives the scattering from this potential or what is equivalent, with the phase shift given by the effective range formula of Eq. (19) with the parameters a and r_0 deduced from the effective range plot in Fig. (1). The scattering reaches a maximum below the resonance and falls off at higher energies, as the phase shift passes 90°, slightly more rapidly than $8\pi\lambda^2$, the maximum $P_{\frac{1}{2}}$ cross section.

TABLE I. Evaluation of $k^3\cot\delta$ for meson scattering. Columns 1 and 2 give the laboratory energy and total cross section, column 3, the meson momentum in the barycentric system, columns 4 and 5 the values of $k^3\cot\delta$ uncorrected for and corrected for S-state scattering. The experimental points are from the work of Fermi *et al.* (see reference 1) except for the 52-Mev point which is due to R. P. Shutt and co-workers (private communication).

E(Mev)	σ(mb)	k^2/μ^2c^2	$k^3/(\mu^3c^3)\cot\delta$	$k^3/(\mu^3c^3)\cot\delta$
52	20±4	0.60	2.95±0.30	4.16±0.42
82	50±13	1.00	2.99±0.37	3.36±0.42
110	74±5	1.41	3.67±0.12	3.55±0.12
118	91±6	1.54	3.10±0.10	3.29±0.11
135	121±19	1.78	2.71±0.23	2.93±0.24
135	152±14	1.78	2.17±0.10	2.35±0.11

[12] It is interesting that the P-state scattering from any strongly attractive short-ranged potential will show this resonance behavior if the "scattering length" a is positive, since the phase shift passes through 90° at $k^2=r_0/a^3$.

III. APPLICATION TO MESON SCATTERING

To illustrate the method further, we apply it to an analysis of the scattering of positive pions in hydrogen. The cross sections are summarized in Table I together with the corresponding values of the meson momentum in the barycentric system. The phase shift δ can be calculated if it is assumed that the scattering is entirely due to the $P_{\frac{1}{2}}$ state,[13] since in this case the total cross section is given by

$$\sigma=8\pi\lambda^2\sin^2\delta.$$

The values of $k^3\cot\delta$ calculated on this basis are given in column 4 of Table I. Fermi[1] finds evidence for some even-odd wave interference at high energies with a magnitude for the even-wave contributions of 10 to 20 mb estimated on the assumption that it is entirely due to S-waves. The values of $k^3\cot\delta$ obtained when the total cross section has been corrected for a even-state contribution of 10 millibarns are given in column 5 of Table I. These results are also given in Fig. 3, plotting $k^3\cot\delta$ against k^2 which, according to Eq. (18), should give a straight line with vertical intercept at $k^2=0$ of $1/a^3$ and intercept at $k^3\cot\delta=0$ of r_0/a^3. These results, although rather rough, indicate a "scattering length" a of about $9.67\hbar/\mu c$ and an effective range with a sign such that the phase shift will pass through 90° at energies considerably above 135 Mev. This is not at present in disagreement with the hypothesis of a resonance for the $J=\frac{3}{2}$ state in the vicinity of 200 Mev.

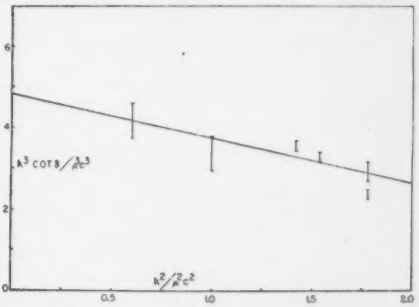

FIG. 3. Effective range plot for meson-nucleon scattering. The experimental points are from column 5 of Table I. The straight line is for a "scattering length" of $0.590\hbar/\mu c$ and effective range of $0.91\hbar/\mu c$. The extrapolated phase shift passes through 90° at $k=3.10\mu c$.

[13] Measurements by Fermi *et al.* and by Shutt *et al.* of the angular distribution of positive pions scattered in hydrogen strongly suggest that the $P_{\frac{1}{2}}$ scattering accounts for almost all of the total cross section. The author is indebted to E. Fermi and his collaborators and to R. P. Shunt and his collaborators for preprints of their papers in advance of publication.

These remarks can of course be made much more definite when further information on the scattering is available.

IV. CONCLUSIONS

It is found that in so far as a potential can be meaningfully used to describe a strong P-state interaction, an effective range theory is applicable. Therefore, as in S-state scattering, only two parameters can be determined, the "scattering length" which determines the low energy scattering, and the effective range which is a measure of the range of the potential. This theory is applicable over a considerable range of energies because of the smallness of the energy dependent corrections to the effective range. The theory is equivalent to a simple form of the Wigner-Eisenbud generalized single-level (neglecting the level shift and taking $ka \ll 1$) except that the relativistic energy must be used. As a consequence, the scattering will show the usual resonance features associated with the Breit-Wigner theory, and in fact, such resonance behavior seems typical of a sufficiently strong P-state interaction.

Application of the theory to meson scattering shows that over the range of energies for which experimental data is available, the effective range plot seems valid. If extrapolated to high energies, it suggests a resonance at an energy considerably higher than the highest energy at which experiments have been made of 135 Mev.

PHYSICAL REVIEW VOLUME 87, NUMBER 6 SEPTEMBER 15, 1952

Average Energy of Secondary Electrons in Anthracene Due to Gamma-Irradiation*

G. D. Prestwich,† T. H. Colvin,† and G. J. Hine‡
Department of Physics and Radioactivity Center of the Laboratory for Nuclear Science and Engineering, Massachusetts Institute of Technology, Cambridge, Massachusetts

(Received May 16, 1952)

The average energy of the electrons produced in anthracene scintillators by γ-rays in the energy range from 0.28 to 2.76 Mev is determined experimentally. The values obtained are in good agreement with theory. Above 1 Mev γ-ray energy, crystal size is shown to be of importance due to leakage of high energy electrons from the crystal surfaces.

FOR electrons incident on an anthracene crystal, it has been shown that the scintillation pulses are proportional to the electron energy in the range from 0.1 to about 3 Mev.[1,2] The same behavior can be assumed for secondary electrons produced inside the crystal by incident γ-rays, provided all the electron energy is expended within the scintillator. If the energy spectrum of the secondary electrons produced in anthracene is the same as that from the absorption of the same γ-rays in air, the crystal is said to be "air-equivalent." Since the average energy is a measure of the electron energy spectral distribution, we have determined theoretically and experimentally the average energy of the secondary electrons produced in anthracene by sources of various γ-ray energy.

For γ-rays of energy E_γ (in Mev) incident on any matter, it can be shown[3] that the average energy of the secondary electrons produced by the three γ-ray absorption processes is given by

$$E_{h\nu}=\frac{\sigma_a E_\gamma+\tau(E_\gamma-W)+\kappa(E_\gamma-1.02)}{\sigma+\tau+\kappa},$$

where τ and κ are the linear photoelectric and pair-production absorption coefficients, $\sigma=(\sigma_a+\sigma_s)$ is the total linear Compton absorption coefficient in the usual Klein-Nishina notation, and W is the electronic binding energy. The values of $E_{h\nu}$ thus computed for various monochromatic γ-ray energies are shown in Fig. 1 for air, anthracene, and sodium iodide as absorbing media. From Fig. 1 it can be seen that anthracene is "air-equivalent" in the energy range considered, while the inorganic NaI(Tl) scintillator deviates widely below 1 Mev, due to photoelectric absorption by the high-Z elements therein.

Experimentally, $E_{h\nu}$ was determined in anthracene for the γ-rays from Hg^{203}, Cs^{134}, Co^{60}, Na^{24}, and a radium needle with 0.5-mm platinum filtration. Two different anthracene crystals were used: (a) a round crystal 0.6 cm thick and 3 cm in diameter, and (b) a rectangular crystal 2 cm thick and 1×2 cm in cross section. The efficiency of light collection was increased by covering top and side faces of the crystals with a ¼-mil aluminum foil. The crystals were joined to the RCA 5819 photomultiplier tube by a Lucite light pipe, with mineral oil

* This work has been supported in part by the joint program of the ONR and AEC, and also in part by the Bureau of Ordnance, U. S. Navy.

† Now on sea duty, U. S. Navy. Performed these investigations while a U. S. Naval Post-Graduate student at Massachusetts Institute of Technology, Cambridge, Massachusetts.

‡ From Biophysics Section, National Cancer Institute, Bethesda, Maryland.

[1] J. I. Hopkins, Phys. Rev. **77**, 406 (1950).

[2] J. I. Hopkins, Rev. Sci. Instr. **22**, 29 (1951).

[3] G. D. Prestwich and T. H. Colvin, unpublished S.M. thesis, Massachusetts Institute of Technology (1952).

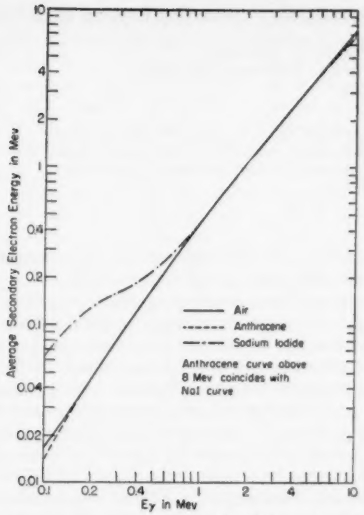

FIG. 1. Average energy (computed values) of secondary electrons produced by monoenergetic γ-rays in air, anthracene and sodium iodide.

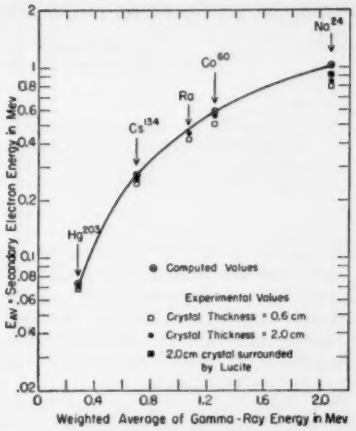

FIG. 2. Average energy of secondary electrons produced by γ-rays from various radionuclides in anthracene. Solid curve represents the computed values derived from Fig. 1. Experimental values are displayed for two crystals of thickness 0.6 and 2.0 cm.

films at the interfaces. Different lengths of light pipe from 0.5 cm to 3 cm did not affect the determination of $E_{h\nu}$. Differential pulse-height spectra were obtained for each radionuclide using a differential discriminator and counting rate meter. Energy calibration was accomplished by measurement of the Cs^{137} conversion electron line. From these data, graphical methods produced experimentally determined values of $E_{h\nu}$, which are given as separate points in Fig. 2 for the above γ-ray sources. The solid curve of Fig. 2 is the theoretical variation of $E_{h\nu}$ obtained from Fig. 1 by weighting each γ-ray component from the particular radionuclide by its abundance. The ordinate is also corrected for the effects of crystal thickness in attenuating unequally the different energy components from a non-monoenergetic γ-ray source.

By comparing the curve with the experimental points it follows that:

(a) While anthracene is theoretically exactly "air-equivalent" from 0.2 Mev to 8 Mev, the experimental data show a fall-off in $E_{h\nu}$ for γ-ray energies greater than 1 Mev. This fact can be explained as follows. For the 280-kev γ-rays of Hg^{203} with a maximum secondary electron energy of 146 kev, and a corresponding range in anthracene of 0.15 cm, very few electrons leak out from either of the two crystals employed. For the more energetic γ-rays a greater number of secondary electrons have ranges in anthracene equal to or greater than the distance from their point of origin to a crystal surface. (For example, the range of a 2.5-Mev electron in anthracene is about 1 cm.) Therefore, the fall-off of $E_{h\nu}$ can be attributed to "leakage" of energetic electrons from the crystal. This is experimentally verified by the increase in $E_{h\nu}$ for the Na^{24} secondary electrons when the crystal was surrounded by Lucite (Fig. 2) in order to scatter some of the leaking electrons back into the crystal.

(b) Plural scattering would increase $E_{h\nu}$ since the first and succeeding collisions are nearly simultaneous and produce a scintillation pulse corresponding to the total secondary electron energy produced in all collisions. The probability for plural scattering is greatest for low-energy γ-rays and long crystal path. Therefore, it would be expected that the maximum effect on $E_{h\nu}$ due to plural scattering would be encountered for the Hg^{203} data with the 2-cm crystal (Fig. 2). Since even this point falls below the theoretical curve, and as described above, leakage is negligible for this source, it may be concluded that plural scattering is negligible for all γ-ray energies in crystals of this size.

(c) In Fig. 2 the experimental values of $E_{h\nu}$ for the radium needle have been fitted in with the other data. This results in an average γ-ray energy of 1.06 Mev for this type of radium source. This value is in substantial agreement with a previously determined value.[4]

[4] G. J. Hine, Phys. Rev. **82**, 755 (1951).

A Study of the Spectrum of the Neutrons of Low Energy from the Fission of U^{235}†

T. W. Bonner,* R. A. Ferrell,‡ and M. C. Rinehart
University of California, Los Alamos Scientific Laboratory, Los Alamos, New Mexico

(Received April 14, 1952)

A cloud chamber has been used to determine, in the energy range 0.05 to 0.7 Mev, the distribution of prompt neutrons produced by the fissions of U^{235} in a thermal neutron beam. The ratio of proton recoils in the energy range 0.05 to 0.6 Mev to the recoils in the energy range 0.6 Mev to infinity was also determined. The data fit a distribution function $N(E)=\sinh(2E)^{\frac{1}{2}}e^{-E}$.

THE neutron spectra of the fission of U^{235} and Pu^{239} have been extensively studied by various techniques.[1–6] The photographic plate technique and the ionization chamber method were the first to be widely used to study the spectra. Both of these methods have limitations with regard to minimum energy of neutrons which may be detected.

In 1945, Richards[6] carried out experiments from which he hoped to obtain information on the neutrons below 1.5 Mev. He used a cloud chamber filled with hydrogen gas and alcohol vapor, and obtained data down to 250 kev. These rather preliminary experiments were interrupted by the end of the war. However, his data indicated a very strange neutron distribution—very few neutrons at 250 kev, in fact only about $\frac{1}{10}$ as many as at 1 Mev. This result is quite contrary to an evaporation model[4,7,8] where at very low energies the number of neutrons should increase as $E^{\frac{1}{2}}$.

In view of these puzzling results, it was considered desirable to look at the energy distribution of neutrons from about 50 kev to 600 kev, using cloud-chamber techniques. In order to get longer proton tracks for a given energy in the cloud chamber, hydrogen gas was used at a pressure of $\frac{1}{3}$ of an atmosphere; and water vapor was used in place of alcohol, reducing the stopping power of the vapor by a factor of about three. With this mixture, a stopping power of 0.10 was obtained and a recoil proton with an energy of 50 kev has a track length of 7 mm. Under the experimental conditions, tracks of this length were believed to be the shortest tracks that could be reliably measured, both with regard to length and direction, although shorter tracks were easily observable on the photographs.

The experimental set-up is shown in Figs. 1 and 2. The source of neutrons was the thermal column of the Water Boiler. The neutrons were collimated by cadmium so that a beam of thermal neutrons with a 4-in. by 4-in. cross section was obtained at the front of the thermal column. Since the neutrons had a cadmium ratio of 400 under the conditions of the experiment, there were only 0.25 percent with energies over a few volts. This beam of thermal neutrons had a flux of 5×10^5 neutrons per cm^2 per sec at a distance of 6 ft from the face of the pile, where the U^{235} foil was placed. The foil was 3 cm by 10 cm by 0.010 inches thick, making the source strength of fission neutrons approximately equal to $5\times10^5\times30\times2.5=3.7\times10^7$ neutrons per sec. The cloud chamber was placed well outside the beam of neutrons, at a distance of 35 cm from the U^{235} sample. The cloud chamber, about 12 in. in diameter and about 9 in. deep, was especially designed to

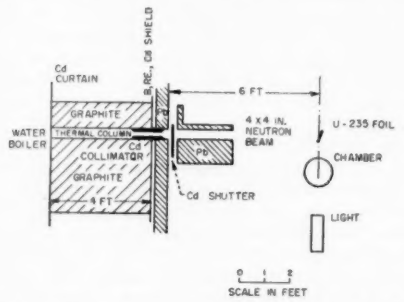

FIG. 1. The relative position of the beam of thermal neutrons, the Cd shutter, the U^{235} foil and the cloud chamber are shown in this diagram.

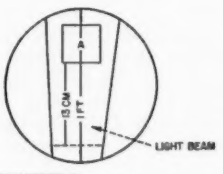

FIG. 2. Enlarged top view of the cloud chamber showing the region A where the recoils must originate in order to be counted.

† This work done under the auspices of the AEC during the summer of 1948.

* Now at Rice Institute, Houston, Texas.

‡ Now at Princeton University, Princeton, New Jersey.

[1] W. H. Zinn and L. Szilard, Phys. Rev. **56**, 619 (1939).

[2] Rotblat, Pickavance, Rowlands, Hall, and Chadwick, unpublished report BR-47 (1942).

[3] W. E. Bennett and H. T. Richards, unpublished report CF-325 (1943).

[4] Bloch, Staub, Hammermesh, Nicodemus, and de Vault, unpublished Los Alamos Declassified Report No. 934 (1943).

[5] H. T. Richards and I. H. Perlman, unpublished Los Alamos Declassified Report No. 909 (1944).

[6] H. T. Richards, unpublished Los Alamos Report No. 556 (1946).

[7] N. Feather, unpublished report BR-335 (1942); R. Peierls, unpublished report MS-65 (1942).

[8] G. N. Plass, unpublished report CF-1261 (1944).

have as small an amount of scattering material in it as possible. To this end, the cloud chamber was placed 49½ inches above the floor and the chamber walls were made of $\frac{3}{16}$-inch Pyrex glass. The walls and roof of the room were negligible scatterers because of their large distance from the chamber. A fast-acting, mechanical cadmium shutter was placed at the opening of the thermal column to allow synchronization of the flux of neutrons on the U^{235} sample with the expansion of the cloud chamber. Excessive general fogging of the cloud chamber was caused by the large number of hard gamma-rays coming from the cadmium plates of the shutter. A thick collimator of lead was effective in reducing the intensity of gamma-radiation in the chamber to a level sufficiently low that it did not cause troublesome fogging in the cloud chamber. A somewhat better method of eliminating gamma-radiation would be to use a shutter made of enriched boron of mass 10, which gives off fewer gamma-rays than cadmium. Even more important, these gamma-rays only have a quantum energy of 479 kev and can easily be absorbed by a small amount of lead. A shutter of this type was not used because of the prohibitive fabrication time.

TABLE I. The data on the energy distribution of the recoil-protons and the neutrons.

Energy interval in kev	Track length in cm	No. of tracks	σ in barns	Track-length correction	Relative No. (N) of neutrons per 100-kev interval
50–99	0.7–1.4	24	14.5	1.04	34.2±5.0
100–199	1.5–2.8	43	11.6	1.09	40.3±4.1
200–299	2.9–4.5	41	9.3	1.15	50.6±5.3
300–399	4.6–6.4	34	7.6	1.23	55.3±6.5
400–499	6.5–8.5	29	6.6	1.33	58.6±7.2
500–699	8.6–13.5	51	5.6	1.50	68.0±6.5

Under the experimental conditions outlined above, from 5 to 15 recoil protons were obtained each time the cloud-chamber expanded. As a check to make sure that fast neutrons from the pile were not causing recoil-protons in the cloud chamber, expansions of the cloud-chamber were observed without opening the cadmium shutter. Under these conditions less than 1 percent as many tracks were observed.

RESULTS

2800 pairs of stereoscopic pictures were taken with the apparatus and approximately 25,000 recoil protons were observed. In order to obtain the energy distribution of the neutrons, only recoil protons which made angles of less than 15° with the direction of the incident neutron were measured, ensuring that essentially all the energy of the neutron was transferred to the proton. In order to minimize the geometrical correction for the probability of observing tracks of different lengths, only tracks were measured which began in region A of the cloud chamber as indicated in Fig. 2. Thus tracks with lengths up to 13 cm have almost as great a probability of ending in the illuminated section of the cloud chamber as tracks of much shorter length. The tracks which were measured fell into two categories—those that ended in the gas, and those that continued into the wall of the chamber. A total of 437 tracks were measured which began in region A and made angles less than 15° with the direction of the primary neutrons. Of these tracks, 237 ended in the gas and 200 continued into the walls of the chamber.

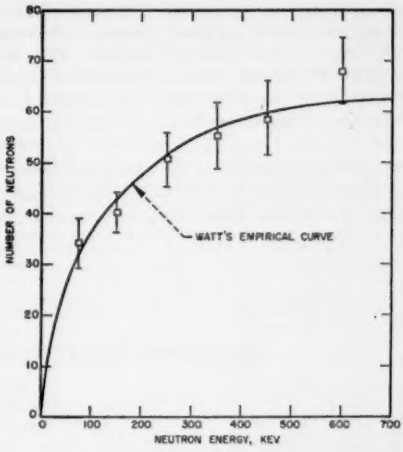

FIG. 3. The experimental distribution in energy of the neutrons compared with the empirical formula.

The data on these recoil-protons are given in Table I, in the form of the relative number of recoil-protons in a given energy interval. To convert from the number of recoil protons to the number of primary neutrons one must take into account the varying cross section for neutron-proton scattering, which is indicated by σ in Table I. As a final correction one must multiply by the geometrical correction factor for the probability of measuring tracks of different lengths. This factor varied from 1.04 for tracks with a length of 1.1 cm to 1.56 for tracks with a length 12.2 cm. The relative number of neutrons $N(E)$ with different energies is obtained from these calculations.

The relative number of neutrons $N(E)$ is plotted in Fig. 3 as a function of the energy of the neutrons. The experimental curve indicates that at 100 kev there are approximately one-half as many neutrons as at 600 kev. The solid curve shown in Fig. 3 is given by the relation $N(E)=\sinh(2E)^{\frac{1}{2}}e^{-E}$, which is a semi-empirical relation obtained by Watt[9] to describe the energy distribution from 0.6 Mev to 15 Mev. This relation fits our experimental data quite well over the 75-kev to 600-kev range.

Our experimental data give more information than

[9] B. E. Watt [Phys. Rev. 87, 1037 (1952)].

the shape of the curve from 0.05 to 0.6 Mev. Data on the relative number of recoil protons with energy greater than 0.6 Mev were also obtained, allowing a comparison of our data with any theoretical neutron distribution as regards the relative number of recoil-protons above and below 0.6 Mev. From our experimental data, we found the value of the ratio of the number of recoil protons in the range 50–600 kev to that in the range 600–∞ to be 0.54 ± 0.05, compared to a value of 0.50 from Watt's formula.[9] The calculated values were obtained by numerical integration of the curves and from the known variation of the cross section of neutron-proton scattering. This ratio fixes the scale factor used in comparing our results below 0.6 Mev with the formula. The agreement with the empirical relation is quite good, and this experiment, together with those by Watt[9] and by Hill,[10] indicates that this relation fits the entire neutron spectrum from 75 kev up to 15 Mev.

[10] D. L. Hill, Phys. Rev. **87**, 1034 (1952).

PHYSICAL REVIEW VOLUME 87, NUMBER 6 SEPTEMBER 15, 1952

The Neutron Energy Spectrum from U^{235} Thermal Fission*

DAVID L. HILL†
Argonne National Laboratory, Chicago, Illinois
(Received April 14, 1952)

A Ranger measurement of the distribution-in-range of knock-on protons from thin paraffin layers indicates the distribution-in-energy from 0.4 Mev to 7 Mev of the neutrons emitted from uranium bombarded by neutrons from the thermal column of the Argonne Heavy Water Reactor. The spectrum shows a broad maximum near 0.75 Mev and follows closely an exponential drop from 2 Mev to 7 Mev with a relaxation energy of 1.55 Mev. The observed neutron intensity does not go to zero below 16 Mev.

SEVERAL observations[1] have indicated the general course above 1 Mev of the energy spectrum for neutrons released in the thermal-neutron-induced fission of U^{235}. Like most heavy particle distributions-in-energy obtained prior to 1946, however, these measurements suffer from poor statistical determination. It therefore seemed fitting, in the summer of 1946, to apply the Ranger[2,3] to the study of this problem. Approximately one week was required to obtain the data summarized in Fig. 2, based upon the range measurements of 44,000 protons ejected from paraffin layers under various conditions detailed below.

The operation of the Ranger as a neutron detector may be schematized in terms of two parallel coaxial disks, S and D, of identical diameter and thickness. The source plate, which we label S, is a layer of paraffin mounted on an aluminum plate. The effective detector, which we label D, is the interface between three coincidence counters and one anticoincidence counter. A remote control mechanism selects the range of protons stopping in D by adjusting the absorptive path between S and D. The instrument retains constant sensitivity for protons within the range of observation; for the present measurement these limiting ranges correspond to proton energies of 0.27 Mev and 17 Mev.

The Ranger was operated for the study of this energy spectrum in substantially the same manner as it was applied to the measurement[2,4] of the energy spectrum of the radium-alpha-beryllium source, CO_2 at a pressure of 40 mm Hg being used as the ionizing medium for the protons, and the test polonium alpha-source being used in the same way to insure accurate gain settings for counting the protons. The considerations there given on background, counting efficiency, energy resolution, and the expressions for the counting rates are equally applicable here when adjustment is made for the different dimensions involved.

The source of the neutrons studied was a flat circular plate of uranium metal or oxide placed in the 20-cm $\times$20-cm beam of neutrons from the thermal column of the Argonne Heavy Water Reactor. The sketch of Fig. 1 shows a top view of the irradiation arrangement. This position of equipment minimizes the number of neutrons entering the front face of the chamber after being scattered from the massive pile face. Those neutrons which pass through the chamber making an angle of more than 90° with the inner normal to the front face of the chamber can have no effect upon the counting rates. There remains a small perturbation from those neutrons scattered from the concrete floor 85 cm below the level of the thermal neutron beam and from those neutrons doubly scattered in the chamber,

* The work described in this article was done under the auspices of the Atomic Energy Project, and the information contained herein will also be included in the *National Nuclear Energy Series* (Manhattan Project Technical Section).
† Now at Vanderbilt University, Nashville, Tennessee.
[1] For citations of early work see reference 6. See also N. Nereson, Phys. Rev. **85**, 600 (1952).
[2] Unpublished Atomic Energy Commission Declassified Report No. 1945-(Rev.), available from the Office of Technical Services, Department of Commerce, Washington, 25, D. C. This document gives a detailed account of the Ranger and of this measurement, as well as all other Ranger work in 1946.
[3] D. L. Hill, Rev. Sci. Instr. (to be published).
[4] D. L. Hill, Rev. Sci. Instr. (to be published).

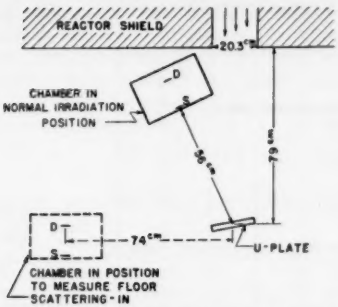

FIG. 1. Relative positions of detecting chamber, thermal neutron beam, and fast neutron source.

but these contributions to the counting rate were measured as indicated in Fig. 1, found to be less than 4 percent even after introduction of the factor 2.3 to account for the different solid angles used by the scattered neutrons for the two chamber positions, and therefore were subtracted from the observed counting rates without significantly disturbing their precision.

To avoid errors from pile power fluctuations (which seldom exceeded 5 percent) a monitoring fission counter was used in a position where its counting rate was about 50,000 per minute. This counter was turned on and off in coincidence with the Ranger counts so that accurate normalization of all Ranger counts to constant neutron source strength was possible.

For exploring different parts of the neutron spectrum, two different fast neutron sources and four different resolutions were used in six different studies, as indicated in Table I. First used as fission neutron source was a plate of natural uranium 0.5 cm thick and 15 cm in diameter; later used was a disk of pressed uranium oxide enriched in U^{235} and of similar dimensions to the first source so that it provided 8.6 times as many fast neutrons per unit of thermal neutron flux.

In the first study S was mounted on the chamber[2,3] wall, 13.0 cm from D; in the other studies it was mounted on a sliding card just in front of the first counter, and a collimator made by drilling closely spaced 0.16-cm diameter holes in a 0.3 cm thick plate was mounted between the first and second coincidence counters. For the position of S in Study No. 1 the mean energy of the protons observed is 0.95 times the energy of the neutrons producing them; for the position of S and the collimator used in the other studies this factor becomes 0.92.

TABLE I. Summary of experimental conditions. S denotes the thickness of the paraffin layer,[a] D the thickness of the effective detector, A_0 the minimum absorption path, A_m the maximum absorptive path; the last two columns give the total number of points and hours per study.

Study	Neutron source	S c.a.e.	D c.a.e.	A_0 c.a.e.	A_m c.a.e.	Points	Hours
1	natural U	4	4.16	0.92	37.28	10	13
2	natural U	1	1.03	0.35	13.41	14	19
3	natural U	4	4.16	0.35	76.57	20	17
4	natural U	16	16.0	0.35	270.5	20	14
5	enriched U	1	1.03	0.35	15.31	16	20
6	enriched U	¼	0.36	0.35	3.06	12	13

[a] See reference 5.

TABLE II. Calculation of U^{235} fission neutron energy distribution. Given in successive columns are the mean absorptive path, A_{mean}, for the observed protons; the range resolution, δA; the energy E corresponding to A_{mean}; the observed counting rate $C(A)_{mean}$ after normalization to uniform fast neutron source strength and uniform proton source and detector thickness; the neutron-proton scattering cross section $\sigma(E)$; the slope $(dR/dE)_E$ of the proton range-energy relation; the product of $C(A)$ by $(\sigma^{-1}dR/dE)_E$ to give numbers which are proportional to the distribution-in-energy $N(E)$ of the observed protons and hence to $N(1.08E)$ for the fission neutrons; and, finally, the fractional statistical uncertainty for each value of $N(E)$.

A_{mean} c.a.e.	δA c.a.e.	E Mev	$C(A)$ counts/min	$\sigma(E)$ barns	$(dR/dE)_E$ c.a.e./Mev	$KN(E)$ $(\text{Mev})^{-1}$	$\Delta N/N$
0.65	0.30	0.400	20.3	7.20	2.01	5.7	0.04
0.92	0.30	0.525	17.6	6.16	2.30	6.6	0.06
1.18	0.30	0.635	16.3	5.65	2.53	7.3	0.05
1.45	0.30	0.725	10.3	5.32	2.81	5.4	0.07
1.59	0.30	0.790	11.6	5.11	3.00	6.8	0.07
1.86	0.30	0.865	10.7	4.91	3.19	7.0	0.07
2.12	0.30	0.945	8.2	4.67	3.32	5.8	0.10
2.29	1.02	1.000	8.4	4.59	3.40	6.2	0.02
2.39	0.30	1.030	8.1	4.47	3.45	6.3	0.10
2.65	0.30	1.095	7.2	4.30	3.71	6.2	0.11
2.92	0.30	1.160	5.1	4.15	4.01	4.9	0.15
3.10	0.30	1.215	6.8	4.07	4.14	6.9	0.12
3.35	1.02	1.26	5.7	4.00	4.2	6.0	0.02
4.33	1.02	1.49	4.4	3.6	4.6	5.6	0.02
5.40	1.02	1.70	3.7	3.4	5.2	5.7	0.03
6.39	1.02	1.88	3.11	3.20	5.7	5.53	0.02
7.33	1.02	2.04	2.34	3.05	6.0	4.61	0.03
8.30	1.02	2.20	1.87	2.92	6.3	4.03	0.03
8.3	4.1	2.20	1.87	2.92	6.3	4.03	0.02
9.38	1.02	2.36	1.66	2.81	6.9	4.07	0.03
10.30	1.02	2.50	1.24	2.71	7.1	3.24	0.04
11.40	1.02	2.64	1.13	2.62	7.3	3.15	0.04
12.34	1.02	2.77	0.83	2.53	7.5	2.46	0.06
12.5	4.1	2.80	0.94	2.51	7.6	2.85	0.03
16.7	4.1	3.32	0.56	2.26	9.0	2.23	0.05
20.8	4.1	3.76	0.35	2.09	9.8	1.52	0.08
24.6	4.1	4.15	0.23	1.95	10.2	1.20	0.12
28.7	4.1	4.55	0.14	1.83	10.9	0.83	0.13
32.4	16.0	4.87	0.134	1.75	11.8	0.90	0.07
32.6	4.1	4.91	0.14	1.74	11.8	0.94	0.19
36.7	4.1	5.23	0.09	1.65	12.2	0.74	0.30
41.1	4.1	5.57	0.07	1.57	13.1	0.58	0.25
44.2	4.1	5.80	0.10	1.53	13.3	0.86	0.27
46.4	16.0	5.98	0.069	1.49	13.6	0.63	0.10
48.4	4.1	6.11	0.05	1.47	13.8	0.47	0.3
48.4	16.0	6.11	0.022	1.47	13.8	0.21	0.15
52.5	4.1	6.43	0.03	1.41	14.4	0.31	0.7
52.7	16.0	6.44	0.016	1.41	14.4	0.16	0.21

In each of these studies neutron counts were taken for every total absorptive value between A_0 and A_m which (approximately) satisfied the relation $A=A_0+nS$, where n is an integer. Optimum coverage of the distribution-in-range of the recoil protons is then obtained, for with S equal to D, the response function is a triangle stretching from $A-S$ to $A+S$, with its maximum at A.

Background counts were taken by sliding the card bearing the paraffin layer out of sight of the counters

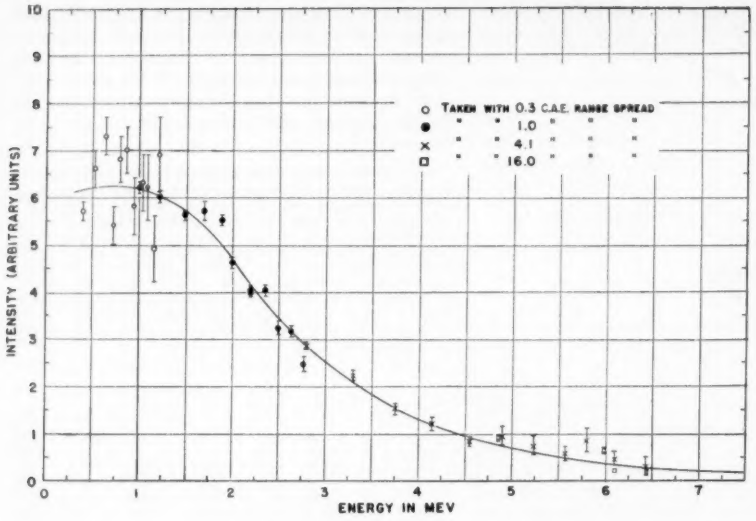

FIG. 2. The collected observations on the U^{235} fission neutron energy spectrum, for four different range resolutions of the instrument.

and dropping a 140 c.a.e.[5] aluminum absorber in front of the first counter, to match the thickness of the aluminum plate bearing the paraffin layer. The background counts averaged about 10 percent of the total counting rates.

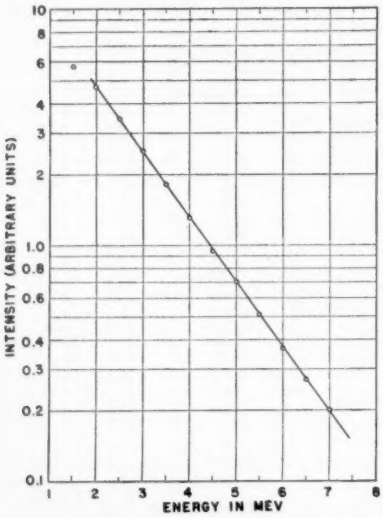

FIG. 3. The mean course of the spectrum of Fig. 2 is seen to follow closely an exponential drop between 2 Mev and 7 Mev.

After this small background correction was made, the data from these different studies were then normalized[2,4] to a common source strength and to a common S and D thickness, the natural uranium plate being chosen as the standard source, with 1 c.a.e. being chosen as the standard thickness. Division by the neutron-proton scattering cross section and multiplication by the slope of the range energy relation, dR/dE, then gives numbers, $KN(E)$, proportional to the distribution-in-energy, as listed in Table II and plotted in Fig. 2, along with their statistical uncertainties. No correction is here made for the fact mentioned above that the energy of the observed protons is 0.92 times the mean energy of the neutrons producing them. In reading this plot one should recall that the Ranger response function goes to zero at ordinates approximate to those of the two adjacent points of the same species. The solid line to indicate the mean course of the spectrum has been drawn in accord with the statistical weight of the plotted points. When this line is transformed to a logarithmic plot, as in Fig. 3, we note that from 2 Mev to 7 Mev the course of the spectrum is well described by the exponential function, $\exp(-E/1.55)$, where E is given in Mev.

The data taken were not sufficient to determine the shape of the spectrum above 7 Mev. Above 16 Mev the neutron intensity was so low as to be unobservable with the present arrangement.

When this measurement was made time was not available for the more extended study needed for the

[5] To avoid confusion of different length measures we introduce a special unit, the c.a.e. (centimeters of air equivalent). One c.a.e. is an absorptive unit equivalent, for range diminution of an alpha-particle or proton, to one centimeter of air at 15°C and 760 mm Hg pressure.

low and high energy ends of the spectrum. These sections have, however, been measured by other techniques by Bonner *et al.*[6] and by Watt.[7] Watt also gives[7] an empirical formula which fits satisfactorily the spectrum obtained as a composite of these three independent measurements.

In developing the instrumental techniques applied to this measurement I have been generously supported and assisted by others of the Argonne National Laboratory, as indicated in the report on the Ranger[3,5] design.

[6] Bonner, Ferrell, and Rinehart, Phys. Rev. **87**, 1032 (1952).
[7] B. E. Watt, Phys. Rev. **87**, 1037 (1952).

PHYSICAL REVIEW VOLUME 87, NUMBER 6 SEPTEMBER 15, 1952

Energy Spectrum of Neutrons from Thermal Fission of U^{235}

B. E. WATT
Los Alamos Scientific Laboratory, University of California, Los Alamos, New Mexico
(Received April 14, 1952)

A proton recoil counter has been used to determine the neutron spectrum, in the energy range 3.3–17 Mev, of a beam produced by irradiating 95 percent U^{235} (metal) in the central experimental hole of the Los Alamos Homogeneous Reactor. Most of the fissions were induced by slow neutrons. The data are combined with those obtained by D. Hill and by T. W. Bonner, R. A. Ferrell and M. C. Rinehart; the composite spectrum so obtained extends from 0.075 to 17 Mev. Fits with two general formulas are discussed.

INTRODUCTION

THE present experiment was designed specifically to obtain the high energy portion of the fission neutron spectrum, as previous investigators had measured the spectrum up to about 6 Mev.

It was known that the intensity of the very high energy neutrons would be low, so the apparatus was designed to operate stably for long periods and to have a low background count in the presence of the intense (but well collimated) beam of neutrons and gamma-rays available from a U^{235} sample placed in the central experimental hole ("glory hole") of the Los Alamos Homogeneous Reactor.[1] A more detailed report of the present experiment is available as Los Alamos Declassified Report No. 935.

APPARATUS

The neutron beam was produced by inserting samples of U^{235} (95 percent U^{235}, 5 percent U^{238}) in the "glory hole" of the water boiler, where they were exposed to a thermal neutron flux of 3×10^{11} per square centimeter per second. Two such sources were used: (1) a 28.5-g disk of U^{235} 0.168 in. thick mounted on a graphite rod, and (2) 54.1 g of U^{235} as an assembly of 31 disks 0.010 in. thick equally spaced along an 18-in. aluminum tube. Figure 1 shows the placement of the latter of these sources as well as the method of collimating the neutron beam.

It was necessary to consider the effect of neutron scattering in the walls of the collimating tube on the neutron energy spectrum of the emergent beam. A very crude calculation considering only single isotropic scattering indicated that less than one percent of this beam had been scattered in the walls. Since the most objectionable feature of such scattering is distortion of the spectrum through degradation, and since an energy loss of 3 Mev would put neutrons observed in this experiment into a group about ten times as strong as the parent group, it is believed that wall scattering is negligible in this experiment.

The distribution in energy of the fast neutrons was measured by means of the spectrometer shown in Fig. 2. Recoil protons ejected from any one of four polyethylene foils were detected by observing coincidences between counts of three proportional counters. In order to reduce the counting rates in the three counters and thereby the background produced by accidental coincidences, the counters were located outside the neutron beam as shown in Figs. 1 and 2. To increase the stability of the counter characteristics, no moving parts were placed in the counters. The distribution in energy of the neutrons was deduced from the distribution in range of the recoiling protons. Any desired combination of seven aluminum absorbers could be introduced between the polyethylene foils and the counters. An integral proton range distribution was obtained by counting all the

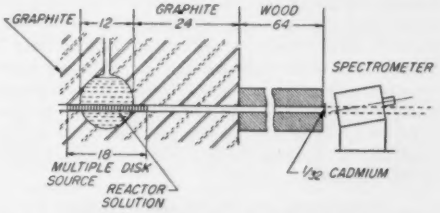

FIG. 1. Diagram of the experimental set-up to show the arrangement of materials surrounding the beam. Numbers give dimensions in inches.

[1] Rev. Sci. Instr. **22**, 489 (1951).

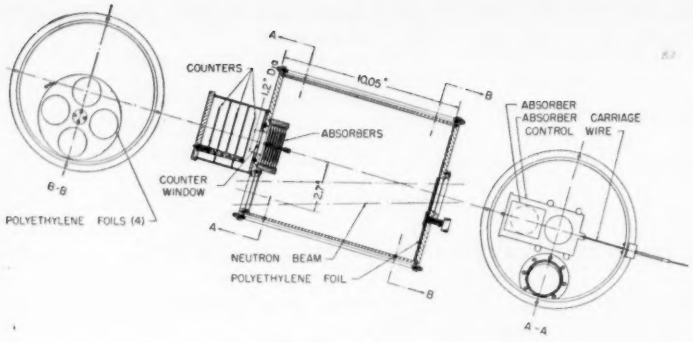

FIG. 2. Cross sections of the proton recoil spectrometer used to investigate the high energy portion of the fission neutron spectrum.

protons with energy greater than the minimum required to penetrate the particular combination of absorbers and produce a coincidence count. The differential proton range distribution and hence the neutron energy distribution was obtained by taking differences between the coincidence counts obtained with different absorbers.

The thickness of the aluminum absorbers ranged from 6.4 to 216 mg/cm² and that of the polyethylene foils from 2.06 to 71.9 mg/cm². Particular combinations of absorbers and polyethylene foils were chosen to give the desired minimum proton energy and energy resolution.

In order to avoid coincidence counts produced by electrons, it is necessary to bias the counters against particles of low specific ionization. Since the specific ionization of protons decreases with increasing proton energy, this bias will determine a maximum proton energy which will result in a coincidence count. When the absorber thickness is changed, different parts of the range of protons of a given energy will lie in the counter, and thus the maximum proton energy for which a coincidence count will occur depends on the absorber thickness. Since the differential proton range distribution is obtained under the assumption that all protons which have sufficient range to penetrate through all three counters will produce a coincidence, care must be taken to avoid the loss of an appreciable number of protons of low specific ionization. In the present experiment the proton energy distribution decreased rapidly enough with energy so that this loss was inappreciable. In all cases the operating characteristics of the spectrometer were chosen so that there was at least a separation of 6 Mev between the minimum and maximum proton energies capable of producing a coincidence count. For the observed spectrum less than one percent of the protons would be lost because of their low specific ionization. By varying the bias on the counters, a check of this number was made.

CALCULATIONS OF PROTON ENERGY

The minimum possible path within the counters necessary to produce a triple coincidence was 5.1 cm, the maximum possible path was 7.6 cm, and the mean value was 6.3 cm. In computing the range equivalent of the counters, the value 6.3 cm was used; the maximum error was 1 cm. At the operating pressure of 22 in. of mercury and with the 7.91 mg/cm² Duralumin counter window, the minimum proton range capable of producing a triple coincidence was 15 ± 1 mg/cm², corresponding to an energy of 2.45 ± 0.1 Mev. At the higher energies, the maximum error is less (0.05 Mev at 5 Mev). From the characteristics of the counter, it is believed that the probable error is less than 0.05 Mev at the lowest energy, and correspondingly lower at the higher energies.

From the atomic stopping powers it was computed that 1 mg/cm² of $(CH_2)_x$ was equivalent to 1.40 mg/cm² of aluminum. From the thicknesses of the polyethylene foils and aluminum absorbers and the equivalent thickness of the counters and their window, the average minimum range of a proton giving a triple coincidence was computed. The range was then converted to proton energy by the range-energy relation computed by Smith.[2] The energy difference between particular combinations of absorbers was also computed from the same data, but could be used only when the polyethylene foil and the absorber combination were not simultaneously changed.

CALCULATION OF THE NEUTRON DISTRIBUTION FROM THE OBSERVED COUNTING RATES

It is convenient to define the following quantities: C_p = proton counting rate = number of protons/min penetrating the counters; E_p = minimum average proton energy in Mev required for a count (lower bound of the integral proton count); E_n = neutron energy in Mev; P = "Water Boiler" power level, kilowatts (proportional to source strength); σ_s = total proton scattering cross section, barns; the scattering taken to be isotropic in c.m. system; $(t\rho)$ = polyethylene foil thickness, mg/cm²; and $N(E_n)$ = neutron distribution function, neutrons/cm²-sec-Mev.

[2] J. H. Smith, Phys. Rev. **71**, 32 (1947).

The neutron-proton scattering cross sections used were obtained from the theoretical curves of Bohm and Richman,[3] and Goldstein.[4] The curve developed by Bohm and Richman fits the data of Bailey *et al.*[5] quite well in the energy range 0.4 to 6 Mev. The curve developed by Goldstein fits the data of Sherr,[6] and Sleator[7] in the energy range 9 to 23 Mev. However, "reasonable extrapolations" into the gap cannot be made to join. A smooth curve was constructed by drawing a rather arbitrary join meeting Bohm and Richman's curve at 4 Mev and Goldstein's curve at about 14 Mev. Acceptable joins could be made which differed by 10 percent, so systematic errors of the order of 5 percent at 8 Mev are to be expected.

The relation between the neutron flux and the proton counting rate, and the relation between the neutron and proton energies, were derived from the geometry of the spectrometer.

The resulting formulas were

$$\langle N(E_n)\rangle_{Av}=3.04\times10^6\Delta(C_p/Pt\rho)/\sigma_s\Delta E_p, \quad (1)$$

$$0.93E_n=E_p, \quad (2)$$

where $\langle N(E_n)\rangle_{Av}$ is the average of $N(E_n)$ over the energy interval corresponding to the recoil proton energy interval ΔE_p. As a compromise between statistical accuracy and resolving power, the values of ΔE_p were chosen to be about 1 Mev.

RESULTS

The first spectrum observed was that of a beam produced by the 28.5-g disk of U^{235} 0.168 in. thick mounted on a graphite rod and placed in the center of the water boiler. The spectrum obtained could be fitted with the empirical equation:

$$N(E_n)=4.05\times10^6Pe^{-E_n/1.16}, \quad 3\leqslant E_n\leqslant 12 \text{ Mev}. \quad (3)$$

It became evident that the data could not yield the desired fission spectrum because (1) the intensity was too low to reach 15 Mev and (2) the number of neutrons produced in the reactor's solution and subsequently scattered into the beam by the walls of the collimating tube and the graphite rod backing constituted about a third of the total beam.

TABLE I. The "open hole" neutron distribution produced by the reactor without the U^{235} sample in position.

E_n Neutron energy in Mev	$N(E)\times10^{-4}$ Neutrons/Mev-kw-sec
3.06	6.1 ±0.3
3.87	2.93±0.1
4.73	1.50±0.17
5.68	1.02±0.05
6.86	0.48±0.03
7.86	0.13±0.04
8.80	0.11±0.02
9.90	0.05±0.015

TABLE II. The spectrum of the neutron beam produced by the U^{235} disk source. The values of E_p and ΔE_p are the lower bound and widths of the proton energy intervals used. The fission spectrum was obtained by subtracting the intensities given by Eq. (4).

E_p Mev	ΔE_p Mev	E_n Mev	σ_s barns	$N(E_n)\times10^{-4}$ neutrons Mev-kw-sec	$N(E_n)\times10^{-4}$ fission spectrum neutrons/ Mev-kw-sec
2.58	1.07	3.30	2.18	119.5 ±1.5	114.3 ±1.5
3.65	1.08	4.46	1.75	56.3 ±0.8	54.0 ±0.8
4.73	1.21	5.68	1.48	24.0 ±0.3	23.0 ±0.3
5.91	1.00	6.86	1.29	9.7 ±0.2	9.26 ±0.2
6.91	0.85	7.86	1.15	4.4 ±0.2	4.18 ±0.2
7.78	1.22	8.97	1.03	2.2 ±0.1	2.1 ±0.1
9.00	0.71	10.04	0.93	0.8 ±0.05	0.75 ±0.05
9.71	1.21	11.04	0.85	0.42 ±0.02	0.40 ±0.02
10.91	0.85	12.16	0.78	0.20 ±0.02	0.18 ±0.02
11.75	1.06	13.17	0.72	0.10 ±0.02	0.094±0.02
12.83	0.98	14.29	0.67	0.03 ±0.01	0.027±0.01
13.49	0.98	15.00	0.64	0.016±0.003	0.014±0.003
14.46	1.01	16.05	0.59	0.016±0.003	0.015±0.003
15.48	1.15	17.22	0.54	0.001±0.003	0.001±0.003

A new source was designed to reduce the amount of material capable of scattering neutrons from the reactor into the beam and to raise the beam intensity as much as possible. The design chosen comprised 31 disks of U^{235}, each 0.010 in. thick and equally spaced along an 18-in. aluminum tube. The neutrons produced in the disk farthest from the spectrometer passed through 0.3 in. of uranium, so the distortion produced by inelastic scattering and absorption in the source was negligible.

The spectrum of the beam produced when the "glory hole" was empty was measured and the result is listed in Table I. The data can be fitted reasonably well with the equation

$$N(E_n)=5.5\times10^5Pe^{-E_n/1.2}, \quad 3\leqslant E_n\leqslant 10 \text{ Mev}. \quad (4)$$

The spectrum produced by the fissions in the disks alone was obtained by subtracting the values given by Eq. (4) from the values obtained for the beam from the multiple disk source; Eq. (4) was assumed to hold throughout the energy range 3–17 Mev. Since the shape of the open hole spectrum is essentially the same as the spectrum of the beam from the multiple disk source, and constitutes only 4 percent of the total beam, it is believed that errors introduced by the subtraction are negligible. The final results are presented in Table II.

DISCUSSION

It is interesting to compare the observed spectrum with the predictions of the theoretical picture of the fission process. For this purpose, it is useful to combine the data of D. Hill and the data of T. W. Bonner *et al.* (given in the preceding papers) with the present data. In the following discussion the subscript n has been dropped from the neutron energy, E_n.

The first formula tried for fit was that developed by

[3] D. Bohm and C. Richman, Phys. Rev. **71**, 570 (1947).
[4] Louis Goldstein, unpublished Los Alamos Report No. 702 (1948).
[5] Bailey, Bennett, Bergstralh, Nuckolls, Richards, and Williams, Phys. Rev. **70**, 583 (1946).
[6] R. Sherr, Phys. Rev **68**, 240 (1945).
[7] W. Sleator, Jr., Phys. Rev. **72**, 207 (1947).

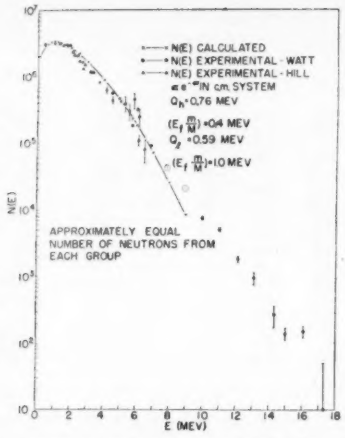
N(E) CALCULATED
N(E) EXPERIMENTAL - WATT
N(E) EXPERIMENTAL - HILL
$\propto e^{-E/Q}$ IN c.m. SYSTEM
Q_h = 0.76 MEV
$(E_f \frac{m}{M})_l$ = 0.4 MEV
Q_l = 0.59 MEV
$(E_f \frac{m}{M})_h$ = 1.0 MEV
APPROXIMATELY EQUAL NUMBER OF NEUTRONS FROM EACH GROUP
N(E)
E (MEV)

FIG. 3. Energy spectrum of fission neutrons. The calculated curve is based on Feather's assumptions. The subscripts l and h refer to the light and heavy fission fragments, respectively, and $\alpha = E'/Q$. It can be seen that above about 7 Mev the calculated curve deviates markedly from the experimental points.

Feather.[8] His three basic assumptions were (1) isotropic emission in the center-of-mass system of fragment and neutron; (2) neutron distribution in the c.m. system proportional to $E'e^{-E'/Q}$, where Q is an energy corresponding to the "temperature" of the fragment and E' is the neutron energy in the c.m. system; (3) fragment velocity at the time of neutron emission corresponding to the full kinetic energy.

The second assumption is based on the expected distribution of particles from a liquid drop model of the fragment. The third is based on the expectation that the neutron leaves the fragment in a time of the order 10^{-15} sec after the fragments separate; from the range energy relation deduced for such fragments, it is calculated that the fragment loses a negligible fraction of its original energy in that time, though several collisions may have occurred.

Attempts to find values for the two constants (Q and the product $E_f m/M$, where E_f is the kinetic energy of the fragment at the time of neutron emission and m and M are the masses of the neutron and fragment, respectively) appearing in the equation assuming one average fragment were unsuccessful. The curve computed by adding the spectra of two fragments, one having the average energy and mass of the light group and the other the average energy and mass of the heavy group, is shown in comparison with the composite curve in Fig. 3. The fit was regarded as unsatisfactory. Since rather laborious calculations are necessary to determine the spectrum given by Feather's formula, no attempt was made to add the spectra of a large number of fragments.

It is interesting to note that a simple formula giving quite acceptable fits is obtained by assuming a Maxwellian distribution ($E^{\frac{1}{2}}e^{-E/Q}$) in place of assumption (2) above. The resulting formula is

$$N(E) = \text{const} \times e^{-E/Q} \sinh[2Q^{-1}(EE_f m/M)^{\frac{1}{2}}]. \quad (5)$$

Several early reports on the fission spectrum mention this formula but none give the originator. It seems likely that it was derived by several investigators and spread by private communications. Assuming only one fragment, acceptable fits are obtainable with several sets of the constants Q and $(E_f m/M)$ which are to some extent interrelated. Partly because of the simplicity of the resulting equation, the values $Q = 1.00$ Mev and $E_f m/M = 0.5$ Mev were chosen as best representing the data. The formula is then

$$N(E) = 4.75 \times 10^6 \sinh(2E)^{\frac{1}{2}} e^{-E}. \quad (6)$$

Equation (6) and the present data together with those of Hill are plotted in Fig. 4. The results of Bonner *et al.* which cover the energy range 0.075 Mev to 0.6 Mev are not plotted in Fig. 4. However, their data are also represented by Eq. (6) which thus provide a good approximation to the fission neutron energy spectrum from 0.075 Mev to 17 Mev.

In order to see if Eq. (5) could be made to give an acceptable fit when the spectra from several groups were added, two such terms were used in which the products $(E_f m/M)$ were set equal to the averages for the heavy and light groups; as a second condition, the number of neutrons from each group were set equal, and as a third,

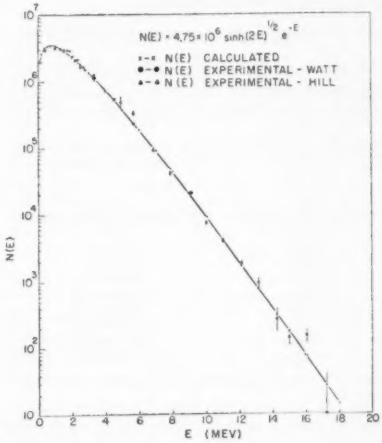

FIG. 4. Energy spectrum of fission neutrons. The calculated curve is based on the assumption of a Maxwellian distribution in the center-of-mass system for the neutrons emitted by a fission fragment.

[8] Norman Feather, unpublished report BM-148.

the values of constants (Q) were set equal. The absolute value of Q is then the only remaining arbitrary constant (except the normalization constant needed to fit any particular set of data) and was determined from the slope of the data in the region around 9 Mev. The resulting equation is

$$N(E)=1.088\times10^6\sinh(1.92E^{\frac{1}{2}})e^{-E/0.875}+2.937\times10^6\sinh(1.28E^{\frac{1}{2}})e^{-E/0.875}. \quad (7)$$

Both Eqs. (6) and (7) show curvature on a logarithmic plot, while the data fall more nearly on a straight line. The deviation of the data is of the same order of magnitude as the systematic error expected from the arbitrary join in the curves used for the (n,p) scattering cross section, and so cannot be taken as real. To explore the implications of a real deviation like that observed and to find an equation giving a fit passing more nearly through all points, the conditions of equal number from each group and equal Q for each group were abandoned.

The curvature of all the calculated spectra can be removed by assuming different Q's for the neutron emitting fragments, and several cases were calculated. Equations were found which passed within the standard deviation of each point, but the increased complexity seems hardly justified with the present data and the simplified assumptions leading to Eq. (6). However, the improvement of the fit seems to indicate that Feather's formula can be made to fit the data by assuming many fragments having different velocities, masses, and excitations.

Several of the equations developed were computed by Mr. Dura W. Sweeney whose help is gratefully acknowledged. I am also indebted to many other members of this laboratory for helpful discussions and criticisms.

PHYSICAL REVIEW VOLUME 87, NUMBER 6 SEPTEMBER 15, 1952

Conservation of Isotopic Spin in Nuclear Reactions*

ROBERT K. ADAIR
University of Wisconsin, Madison, Wisconsin
(Received June 2, 1952)

The effects of the charge independence of nuclear forces on nuclear reaction experiments is discussed. It is pointed out that charge independence establishes relationships between cross sections for some reactions and results in forbidding certain other reactions.

IT is well known[1,2] that if the forces between two nucleons are independent of their charge states and depend only on their space and spin coordinates, the wave function of a system of nucleons will be invariant under certain charge transformations. This symmetry is usually described in terms of a constant of motion, the isotopic spin. Important consequences of this invariance of nuclear structure with respect to rotation in isotopic spin space have been discussed by Wigner[3,4] and others.

There is no very conclusive evidence to establish the charge independence of nuclear forces. While the similarity of energy levels of mirror nuclei strongly suggests the equivalence of neutron-neutron forces and proton-proton forces,[5] there is not yet much information on the equality of the neutron-proton interaction and the forces between like nucleons. In particular, no definite conclusions have been derived from nucleon-nucleon scattering. Although the low energy scattering experiments are not in contradiction to a description in terms of charge independent forces,[6] it is not clear that this is true of higher energy measurements.[7]

It appears to have been largely overlooked in recent work that information on the charge independence of nuclear forces may be obtained from observations on nuclear reactions. Charge independence has observable consequences in such reactions; in particular, it results in forbidding certain transitions which are allowed solely from considerations of spin and parity.

For the purpose of this discussion the third component T_3 of the isotopic spin T of a nucleus is defined, as usual, as the number of neutrons minus the number of protons in the nucleus divided by two. Systems having the same isotopic spin but different T_3 components form a set of multiplicity $2T+1$, which differ in energy only through Coulomb forces. On the assumption that it is a good quantum number, the value of T for any nucleus is easily determined by an examination of the binding energies of nuclei.[8,9] Generally the binding energy of light nuclei depends strongly upon T. Since there is close competition between low states with different values of T only in the

* Work supported by the AEC and the Wisconsin Alumni Research Foundation.
[1] E. Wigner, Phys. Rev. **51**, 106 (1937).
[2] N. Kemmer, Proc. Cambridge Phil. Soc. **34**, 354 (1938).
[3] E. Feenberg and E. Wigner, Phys. Rev. **51**, 95 (1937).
[4] E. Wigner, Phys. Rev. **56**, 519 (1939).
[5] See, e.g., V. R. Johnson, Phys. Rev. **86**, 302 (1952).
[6] J. Schwinger, Phys. Rev. **78**, 135 (1950).
[7] R. S. Christian and H. P. Noyes, Phys. Rev. **79**, 85 (1950).
[8] E. Feenberg and M. Phillips, Phys. Rev. **51**, 597 (1937).
[9] Hornyak, Lauritsen, Morrison, and Fowler, Revs. Modern Phys. **22**, 291 (1950).

$4n-2$ group of nuclei, most of the interesting applications of charge symmetry selection rules take place in reactions involving these systems. A typical example of such a system is the C^{14}, N^{14}, O^{14} triad. The isotopic spin function representing the ground state of N^{14} can be written as $\varphi'_0{}^0$, of C^{14}, $\varphi_1{}^1$, and of O^{14}, $\varphi_1{}^{-1}$, where the superscript represents the value of the T_3 component and the subscript the value of T. The $\varphi_1{}^0$ state will be an excited state of N^{14} displaced in energy from the O^{14} and C^{14} ground states by Coulomb forces and the neutron-proton mass difference. This appears to be the 2.3-Mev level of N^{14}.

The transformation properties of isotopic spin are the same as for angular momentum. Since the assumption of charge independence is equivalent to requiring the conservation of total isotopic spin and conservation of charge insures the conservation of the T_3 component, isotopic spin selection rules are identical with those of angular momentum. An example of a reaction forbidden because of isotopic spin selection rules is the $O^{16}(d, \alpha)$ reaction to the 2.3-Mev state of N^{14}. Since the isotopic spin of O^{16}, the deuteron, and the alpha-particle are all zero, while the N^{14} level has an isotopic spin of one, the transition will not be allowed. Although this reaction has been investigated by several groups[10–12] under a variety of experimental conditions it has not been observed.

There are a number of other reactions which should be forbidden by analogous considerations. The $C^{12}(d, \alpha)$ reaction to the 1.7-Mev state of B^{10} should not be observed, as this level appears to be the $\varphi_1{}^0$ state of the Be^{10}, B^{10}, C^{10} triad of total isotopic angular momentum one. The $C^{12}(d, \alpha)$ reaction has not been investigated at energies which would excite the 1.7-Mev level. For similar reasons the $Ne^{20}(d, \alpha)$ reaction to states in F^{18} which have corresponding levels in O^{18} should be forbidden, as these transitions would also violate the conservation of isotopic spin. Middleton and Tai investigated[13] the $Ne^{20}(d, \alpha)$ reaction and found a prominent group of alpha-particles which leave the F^{18} nucleus in a 1.05-Mev excited state. This is near the energy where one would expect the isotopic spin-one level corresponding to the ground state of O^{18}. According to the shell model F^{18} consists of a closed P-shell plus a neutron and a proton. There is close competition between $S_{\frac{1}{2}}$ and $D_{\frac{1}{2}}$ states in this region. Since the beta-decay of F^{18} to O^{18} is allowed, the ground state of F^{18} probably belongs to the spin one, isotopic spin zero, triplet $(S_{\frac{1}{2}})^2$ configuration. The spin zero, singlet $(S_{\frac{1}{2}})^2$ configuration with isotopic spin one, corresponding to the ground state of O^{18}, would be somewhat higher and might be close to the lowest $(D_{\frac{1}{2}})^2$ level, probably with spin five and isotopic spin zero. It therefore seems possible that this reaction does not violate charge independence but that the 1.05-Mev state reached by this reaction is an isotopic spin-zero level very close in energy to the isotopic spin one level corresponding to the ground state of O^{18}.

The inelastic scattering of deuterons and alpha-particles by Li^6, B^{10}, and N^{14} will be affected by charge independence selection rules. Since the ground states of these nuclei, and the deuteron or alpha-particle, all have an isotopic spin of zero, the low-lying isotopic spin-one levels of these nuclei should not be excited appreciably in the reactions.

It must be emphasized that, since the transition probability depends upon the square of the matrix element, reaction experiments are not a sensitive test of charge independence. A reaction cross section leading to a state consisting of a mixture of 10 percent of a wave function to which the transition were allowed and 90 percent of a wave function to which the transition were forbidden would result in a cross section only of the order of one percent of a completely allowed reaction. Conversely, the selection rules should hold reasonably well even if nuclear forces are only approximately charge independent. It is therefore necessary to place rather small upper limits on the cross sections for forbidden reactions in order to restrict very severely the dependence of nuclear forces on the nuclear charge. Coulomb forces will couple states of different isotopic spin but their influence on the wave functions of light nuclei is probably small. However, one cannot then expect to detect differences in the specifically nuclear forces of the magnitude of the Coulomb forces.†

It is sometimes easier experimentally to place a small limit on level widths rather than on reaction cross sections. If elastic scattering is the most probable process taking place, the scattering cross section at resonance is reasonably large and practically independent of the magnitude of the reaction matrix element. The width of the level is proportional to the square of the matrix element. There exist levels[14] in B^{10} between 4.5 and 6.5 Mev above the ground state which can break up through heavy particle emission only to the isotopic spin-zero combinations of Li^6 plus an alpha-particle, or Be^8 plus a deuteron. If the specifically nuclear forces are charge independent, such transitions from isotopic spin one states will only occur through the difference in neutron and proton wave functions caused by Coulomb forces. This effect should

[10] A. Ashmore and J. F. Raffle, Proc. Phys. Soc. (London) **A64**, 754 (1950).

[11] Burrows, Powell, and Rotblat, Proc. Roy. Soc. (London) **A209**, 478 (1951).

[12] Craig, Donahue, and Jones (to be published); Van de Graff, Sperduto, Buechner, and Enge, Phys. Rev. **86**, 966 (1952).

[13] R. Middleton and C. T. Tai, Proc. Phys. Soc. (London) **A64**, 801 (1951).

† *Note added in proof:*—I wish to thank Dr. N. M. Kroll for pointing out to me that selection rules will obtain in self-conjugate nuclei from the less severe condition of charge symmetry of nuclear forces. [See also in this connection Lynne E. H. Trainor, Phys. Rev. **85**, 962 (1952).] The evidence for charge independence in reactions involving these systems then depends upon the conjoint existence of selection rules affecting isotopic spin-one states, and the existence and energy equivalence of isobaric members of the charge triplet.

[14] Fay Ajzenberg, Phys. Rev. **82**, 43 (1951).

be small, and isotopic spin-one states should have very small widths. It might be possible to observe such states and measure their widths by scattering alpha-particles from Li^6.

Isotopic spin-one states of Li^6 could be investigated in a similar manner by scattering deuterons from helium. The lowest isotopic spin-one level is available energetically but, as Fowler[15] has pointed out, probably has spin zero and even parity and cannot therefore decay into a deuteron and an alpha-particle. There should, however, exist a level of Li^6 of even parity, isotopic spin one, probably of total angular momentum two, about 6 Mev above the ground state, corresponding to the first excited state of He^6. This state is forbidden by charge conservation from breaking down to a deuteron and an alpha-particle and should, therefore, have a very small width. It is possible energetically for this state to break up into He^5 plus a proton. If this width is much larger than the scattering width the resonance will be damped out and not easily observed by bombarding alpha-particles with deuterons.

The effects of charge independence selection rules should be discernible in other interactions involving states in a compound nucleus. The resonant scattering of protons[16] from Be^9 at 1.087-Mev bombarding energy has been interpreted[17] in terms of the formation of a compound state of spin zero and odd parity in the compound nucleus B^{10}. Although lower levels decay by both alpha-particle and deuteron emission this state does not appear to do so, though these transitions are not unfavored by angular momentum considerations. This behavior might be explained by presuming the isotopic spin of the state to be one, as in that case transitions to the isotopic spin-zero combinations of Li^8 and an alpha-particle or Be^8 and a deuteron would be forbidden.

If the forces between nucleons are independent of their charge, relationships will be established between transition probabilities to states of different charge belonging to the same isotopic spin multiplet. An example of this is the $Be^9(d, p)$ and $Be^9(d, n)$ reactions to the ground state of Be^{10} and the 1.7-Mev state of B^{10}, respectively. These states are the $\varphi_1{}^1$ and $\varphi_1{}^0$ components of a charge multiplet. Writing the initial charge wave function, representing the system consisting of Be^9 plus the deuteron, as $I_{\frac{1}{2}}{}^{\frac{1}{2}}$, and the nuclear isotopic spin functions as $\tau_{\frac{1}{2}}{}^{\frac{1}{2}}$ for the neutron and $\tau_{\frac{1}{2}}{}^{-\frac{1}{2}}$ for the proton, we can expand I in terms of φ and τ:

$$I_{\frac{1}{2}}{}^{\frac{1}{2}}=(\sqrt{2}\varphi_1{}^1\tau_{\frac{1}{2}}{}^{-\frac{1}{2}}-\varphi_1{}^0\tau_{\frac{1}{2}}{}^{\frac{1}{2}})/\sqrt{3}.$$

The ratio of the transition probabilities to Be^{10} and B^{10} will then be $(I_{\frac{1}{2}}{}^{\frac{1}{2}}|\varphi_1{}^1\tau_{\frac{1}{2}}{}^{-\frac{1}{2}})^2/(I_{\frac{1}{2}}{}^{\frac{1}{2}}|\varphi_1{}^0\tau_{\frac{1}{2}}{}^{\frac{1}{2}})^2$, which is equal to two, multiplied by the relative volumes of phase space available to the final systems. Uncertainties in the magnitude of Coulomb effects are sufficiently large so that this type of reaction probably cannot be used as a sensitive check on charge independence. However, the cross section relations may be useful in determining which excited states in systems like N^{14}, B^{10}, and F^{18}, correspond to the levels of isotopic spin one found in their isobaric neighbors.

I wish to thank Professor J. M. Luttinger, who suggested the possible importance of charge independence in nuclear reactions, for his interest in this discussion.

[15] Quoted by R. B. Day and R. L. Walker, Phys. Rev. **85**, 582 (1952).

[16] Thomas, Rubin, Fowler, and Lauritsen, Phys. Rev. **75**, 1612 (1949).

[17] R. Cohen, Ph.D. Thesis, Cal. Inst. Tech. (1949).

Electron-Lattice Interaction and Superconductivity

K. S. SINGWI
Department of Physics, University of Illinois, Urbana, Illinois
(Received May 29, 1952)

An electron moving faster than sound would emit phonons in the form of a narrow wake behind it, analogous to the Čerenkov radiation. Two electrons would, therefore, interact strongly when one lies in the wake of the other. Based on this idea a model for the superconducting state is suggested. The electron-lattice interaction, obtained by using the Bloch-Nordsieck transformation, is examined in the coordinate space, and the "wake" character of the interaction is shown. In the appendix, using a canonical transformation, the interaction between two electrons is calculated.

I. INTRODUCTION

FRÖHLICH[1] and Bardeen[2] have, independently, developed a theory of superconductivity based on the interaction of electrons with lattice vibrations. That the basic idea of their theory is correct is proved by the experimental discovery of the isotope effect.[3]

Using the second-order perturbation theory, Fröhlich has calculated the self-energy of the electrons in the Fermi-distribution, arising as a result of the virtual emission and absorption of phonons. Because of the Pauli principle this interaction energy depends on the distribution of the electrons in the momentum space; and if the interaction is strong enough, it gives rise to a new distribution corresponding to a lower energy, in which a shell of electrons is lifted out of the Fermi distribution. Such a shell distribution of the electrons in the momentum space has been identified by Fröhlich with the superconducting state. Fröhlich derives a condition for the metal to be superconducting, and unfortunately, this also happens to be the condition for which the perturbation theory breaks down. It is, therefore, not unlikely that a more rigorous calculation of the interaction energy, which seems to be difficult at the present time, may not give the shell structure at all. Also, the energy difference between the superconducting and the normal states as calculated on the basis of Fröhlich's theory comes out to be large by a factor of one hundred. This is perhaps due to the fact that in his theory most of the contribution to the interaction energy comes from short wavelength phonons. The low energies involved in the transition may suggest that long wavelengths are more important. The primary aim of the present note is to propose an alternative model for the superconducting state. A similar model has also been proposed recently by Bohm and Staver.[4] The model is valid only when the wavelength of the phonons involved is large. However, it suffers from certain disadvantages. The experiments on thin films[5] and on colloidal mercury[6] indicate that there is very little change in transition temperature with dimensions even when the film thickness or particle size is as small as 5×10^{-6} cm, thereby indicating that it is the short wavelength phonons which are important in the electron-lattice interaction.

II. DISCUSSION OF THE MODEL

The electrons actually involved in the superconducting transition are those which lie near the top of the Fermi distribution and have velocity which in metals is nearly 10^2 times the velocity of sound in that medium. Such an electron would emit sound radiation (virtual phonons since we are considering the state of the system at $T=0$) in the form of a wake analogous to what is known as the Čerenkov[7] radiation. The angular width of the wake would be of the order of $v_{\text{sound}}/v_{\text{electron}}\approx10^{-2}$ radian. Any two electrons would, therefore, interact most strongly when one lies in the wake of the other. And, since the wake is extremely narrow, one electron would almost follow in line with the other. The interaction energy of two electrons as a result of the virtual emission and absorption of phonons is of the order of 10^{-4} ev and corresponds to the energy with which the two electrons are bound in the wake. This picture, therefore, leads to the formation of localized groups of co-moving electrons. These clusters are stable in the sense that it would require energy to dissolve them. Let us now examine qualitatively how far the concept of a wake helps to understand the basic property of a superconducting state.

It is now recognized that the basic property of a superconducting state is the Meissner effect, which is contained in the phenomenological equations of London.[8] The London equations can be derived from nonrelativistic quantum mechanics if one makes the assumption that the wave functions of the electrons are not altered in a magnetic field. In the normal state the wave functions of the electrons in the presence of a magnetic field coil up and are, therefore, strongly modified. However, the electrons in the superconducting state are certainly not to be considered free in the

[1] H. Fröhlich, Phys. Rev. **79**, 845 (1950).
[2] J. Bardeen, Phys. Rev. **79**, 167 (1950).
[3] E. Maxwell, Phys. Rev. **78**, 477 (1950). Reynolds, Serin, Wright, and Nesbitt, Phys. Rev. **78**, 487 (1950).
[4] D. Bohm and T. Staver, Phys. Rev. **84**, 836 (1951).
[5] E. T. S. Appleyard and A. D. Misener, Nature **142**, 474 (1938); Appleyard, Bristow, and Misener, Proc. Roy. Soc. (London) **A172**, 540 (1939).
[6] D. Schoenberg, Proc. Roy. Soc. (London) **A175**, 49 (1940).
[7] P. A. Čerenkov, Phys. Rev. **52**, 378 (1937).
[8] F. London and H. London, Physica **2**, 341 (1935).

sense of the ordinary conducting electrons. We have remarked in the foregoing paragraph that electrons in the superconducting state are bound up in the wake with an energy of the order of 10^{-4} ev, and if the strength of the resultant magnetic field is less than a certain critical value, it would not be able to throw the electron out of the wake. The electron would, therefore, continue to follow the path which it had in the absence of the field, and the wave functions would remain unaltered. Or one might say in the terminology of London that the wave functions behave as if they were rigid. A quantitative justification of these ideas is desirable.

In view of what has been said above it would be interesting to investigate the nature of the electron-lattice interaction in the coordinate space in the long wavelength limit of the lattice waves. The "wake" character of this interaction, using the Bloch-Nordsieck transformation, is shown explicitly in Sec. III. Also, using a canonical transformation, we have calculated, in the appendix, what may be called the Møller interaction of two electrons as a result of the virtual emission and absorption of phonons. Though formally this method is equivalent to the usual perturbation theory method used by Fröhlich, it has the advantage of giving a better understanding of the basic ideas of Fröhlich's theory. In addition, this method enables one to calculate the contribution of the nondiagonal elements of the interaction matrix. Fröhlich considers only the contribution of the diagonal terms.

III. "WAKE" CHARACTER OF THE INTERACTION

Using Bloch-Nordsieck transformation Bardeen[9] has obtained an expression for the interaction energy between electrons and lattice vibrations. The Bloch-Nordsieck transformation is valid for lattice waves of wavelength large compared to that of the electrons near the top of the Fermi distribution, and does not involve the approximation of a small coupling constant. The expression for the interaction energy as given by Bardeen[9] [see Eqs. (6-13) and (6-14) of reference 9] is

$$U(r)=-\sum_q \frac{|m_q|^2\cos\mathbf{q}\cdot(\mathbf{r}_1-\mathbf{r}_2)}{\omega_q^2-(\mathbf{v}\cdot\mathbf{q})^2}$$

$$+\frac{1}{2}\frac{(3(\mathbf{v}\cdot\mathbf{q})^2-\omega_q^2)\{m_q^2e^{i\mathbf{q}\cdot(\mathbf{r}_1+\mathbf{r}_2)}+m_q^{*2}e^{-i\mathbf{q}\cdot(\mathbf{r}_1+\mathbf{r}_2)}}{(\omega_q^2-(\mathbf{v}\cdot\mathbf{q})^2)^2}, \quad (1)$$

where

$$|m_q|^2=(2\omega_q/\hbar)|M_q|^2. \quad (2)$$

M_q is the matrix element corresponding the the transition $\mathbf{k}'=\mathbf{k}\pm\mathbf{q}$ and is given by Eq. (10A) of the appendix. ω_q is the angular frequency of lattice waves corresponding to the wave number $\mathbf{q}$ and $\mathbf{v}$ denotes the velocity of the electrons near the top of the Fermi distribution. $\mathbf{r}_1$ and $\mathbf{r}_2$ denote, respectively, the position vectors of electrons 1 and 2. Since we are concerned only with the interaction between two electrons, we have omitted the summation, which occurs in Bardeen's expression, over all electrons.

The quantity inside the curly brackets in the second term on the right-hand side of Eq. (1) can be put in the form

$$|m_q|^2\{e^{i\mathbf{q}\cdot(\mathbf{r}_1+\mathbf{r}_2)}e^{i\varphi_q}+e^{-i\mathbf{q}\cdot(\mathbf{r}_1+\mathbf{r}_2)}e^{-i\varphi_q}\},$$

where φ_q is the phase of the wave with wave vector $\mathbf{q}$. When one averages over-all possible phases of different q's, the second term in (1) would give zero contribution. Hence, it is only the first term which contributes to the interaction energy. Also, this term when transformed into momentum space gives the E_2 term of the Fröhlich theory [see Eq. (2-15) of reference 1] for the case of two electrons provided q^2 is neglected compared to k^2, where k is the wave number of the electron.

Using (2) in (1) and remembering that $\omega_q^2=S^2q^2$, we have

$$U(r)=-A\sum_q \frac{S^2q^2\cos\mathbf{q}\cdot\mathbf{r}}{S^2q^2-(\mathbf{v}\cdot\mathbf{q})^2}, \quad (3)$$

since the second term gives zero contribution. In (3)

$$A=(8C^2/9nVMS^2), \quad (4)$$

$\mathbf{r}_1-\mathbf{r}_2=\mathbf{r}$, and S denotes the velocity of sound. Equation (3) can be written as

$$U(r)=\Re A\nabla_r^2\sum_q \frac{S^2e^{i\mathbf{q}\cdot\mathbf{r}}}{S^2q^2-(\mathbf{v}\cdot\mathbf{q})^2}, \quad (5)$$

where $\Re$ means that we have to take the real part of the expression and the suffix r denotes that the derivative is with respect to r. Choosing the direction of $\mathbf{v}$ along the z axis and performing the following change of variables

$$q_x'=Sq_x, \quad q_y'=Sq_y, \quad q_z'=(S^2-v^2)^{\frac{1}{2}}q_z$$

and

$$x'=x/S, \quad y'=y/S, \quad z'=z/(S^2-v^2)^{\frac{1}{2}}, \quad (6)$$

and replacing the sum in (5) by an integration we have

$$U(r)=\Re A\frac{V}{(2\pi)^3}\cdot\frac{1}{(S^2-v^2)^{\frac{1}{2}}}\nabla_r^2\int\frac{e^{i\mathbf{q}'\cdot\mathbf{r}'}}{q'^2}d\mathbf{q}'$$

$$=\Re A\frac{V}{(S^2-v^2)^{\frac{1}{2}}}\nabla_r^2\left(\frac{1}{4\pi|\mathbf{r}'|}\right),$$

where V is the volume of the assembly.

Going back to the old coordinates we have

$$U(r)=\Re\frac{AV}{4\pi}\frac{\beta}{i}\nabla^2\left(\frac{1}{x^2+y^2-\beta^2z^2}\right), \quad (7)$$

where

$$\beta^2=(v^2/S^2-1)^{-1}. \quad (8)$$

[9] J. Bardeen, Revs. Modern Phys. 23, 268 (1951).

From (7) it is clear that the interaction $U(r)$ is real only within the cone (defined by $x^2+y^2-\beta^2z^2=0$) whose semivertical angle with the z axis, which is also the direction of $\mathbf{v}$, is $\theta\approx S/v\approx 10^{-3}$ radian. The interaction is attractive and is singular on the sound-cone. The singularity arises because the upper limit of q in the integration was taken as $+\infty$ for the sake of mathematical simplicity. As a matter of fact this upper limit for the theory to be valid would be much less than $q=q_{\max}$, corresponding to the Debye limit. Nevertheless, the "wake" character of the interaction would essentially remain the same as expressed by (7).

In order that the foregoing considerations be valid the distance between two electrons should not be less than one wavelength of the phonons, i.e., $r\geq 1/q$. Assuming that the theory is valid for wave numbers $\leq(1/100)q_{\max}$, we get for $r_{\min}$ the value 10^{-6} cm, since $q_{\max}=10^8$ cm^{-1}. Let us now make a rough estimate of the magnitude of $U(r)$ for $r=r_{\min}$. From (7),

$$U(r_{\min})\approx -\frac{AV}{4\pi}\frac{1}{r_{\min}^3}=-\frac{8C^2}{9nMS^2}\frac{1}{4\pi r_{\min}^2},$$

using (4), or

$$U(r_{\min})=-F\left(\frac{8\xi_0}{3n}\right)\cdot\frac{1}{4\pi r_{\min}^2}, \tag{9}$$

where F has been put equal to $(C^2/3\xi_0MS^2)$ and is a dimensionless constant of the order of unity [see Eq. (2.9) of reference 1] and ξ_0 is the Fermi energy which has the magnitude 10 ev. Substituting the numerical values of $n=10^{22}$, $r_{\min}=10^{-6}$ cm and $\xi_0=10$ ev in (9) we have

$$U_{\max}\approx 10^{-4}\text{ ev}. \tag{10}$$

Thus we see that an electron moving faster than sound would emit radiation in the form of a narrow wake; and that there would be no interaction between two electrons if one lies outside the wake of the other. An electron lying on the surface of the wake of another electron is sucked inside the wake with a force given by the gradient of (7). The maximum interaction between two electrons in this model is roughly 10^{-4} ev. Such a model would lead to clusters of co-moving electrons. However, the clusters would have all possible directions giving zero net current. Our model may provide a basis for superconductivity in the sense that the wave functions of the electrons in this model, as discussed qualitatively in Sec. II, do not change in a magnetic field and may thus lead to the quantum mechanical derivation of the phenomenological equations of London. This point needs a further quantitative investigation.

The author takes this opportunity to express his thanks to Professors R. Peierls and J. Bardeen for many stimulating discussions.

APPENDIX

In this section, using a canonical transformation, we shall calculate the Møller interaction of two electrons as a result of the virtual emission and absorption of phonons. The Hamiltonian of our system consisting of two electrons and lattice vibrations can be expressed in the form

$$\mathbf{H}=H_0+H+e^2/|\mathbf{r}_{12}|, \tag{1A}$$

where

$$\left.\begin{aligned} H_0&=H_{01}+H_{02}+H_p,\\ H&=H_1+H_2 \end{aligned}\right\}. \tag{2A}$$

and

H_0 denotes the unperturbed Hamiltonian of the electron-phonon system. The interaction Hamiltonian H consists of two terms H_1 and H_2, corresponding, respectively, to the interaction of electrons 1 and 2 with the phonon field. $e^2/|\mathbf{r}_{12}|$ represents the Coulomb interaction of two electrons, which we shall neglect in the subsequent discussion. We transform $\mathbf{H}$ with the help of a transformation matrix S, which is expanded according to the perturbation method so that terms containing powers of S higher than the second are neglected. Then

$$\begin{aligned}\mathbf{H}'&=e^{iS}\mathbf{H}e^{-iS}\\ &=\mathbf{H}-i[\mathbf{H},S]-\tfrac{1}{2}[[\mathbf{H},S],S]+\cdots\\ &=H_0+H_1+H_2-i[H_{01}+H_p,S_1]-i[H_{02}+H_p,S_2]\\ &\quad -i[H_1,S]-i[H_2,S]-\tfrac{1}{2}[[H_{01},S],S]\\ &\quad -\tfrac{1}{2}[[H_{02},S],S]-\tfrac{1}{2}[[H_p,S],S]+\cdots,\end{aligned} \tag{3A}$$

since $[H_{02},S_1]=[H_{01},S_2]=0$, and S has been put equal to S_1+S_2.

Let S_1 and S_2 be defined by

$$\left.\begin{aligned} H_1&=i[H_{01}+H_p,S_1]\\ H_2&=i[H_{02}+H_p,S_2] \end{aligned}\right\}. \tag{4A}$$

and

Equation (3) then becomes

$$\begin{aligned}\mathbf{H}'=H_0-i/2\{&[H_1,S_1]+[H_2,S_2]\\ &+[H_1,S_2]+[H_2,S_1]\}+\cdots.\end{aligned} \tag{5A}$$

Now since H_{01} and H_p are diagonal, and using (4A),

$$\begin{aligned}\langle m|H_1|n\rangle&=i\langle m|H_{01}+H_p|l\rangle\langle l|S_1|n\rangle\\ &\quad -i\langle m|S_1|l\rangle\langle l|H_{01}+H_p|n\rangle\\ &=i\langle m|S_1|n\rangle\{E_{1m}-E_{1n}+\hbar(\omega_m-\omega_n)\}.\end{aligned}$$

Therefore,

$$\langle m|S_1|n\rangle=\frac{-i\langle m|H_1|n\rangle}{E_{1m}-E_{1n}+\hbar(\omega_m-\omega_n)}, \tag{6A}$$

and a similar expression is possible for $\langle m|S_2|n\rangle$.

The matrix elements of the commutators $[H_1,S_2]$ and $[H_2,S_1]$ correspond to the emission of a phonon by one electron and the absorption of the same phonon by the other electron. On the other hand, the matrix

elements of the commutators $[H_1, S_1]$ and $[H_2, S_2]$ correspond to the emission and absorption of a phonon by the same electron. Now

$$\langle \mathbf{k}_1', \mathbf{k}_2'[H_1, S_2]\mathbf{k}_1, \mathbf{k}_2\rangle = i\frac{\langle \mathbf{k}_1', \mathbf{k}_2'|H_1|\mathbf{k}_1, \mathbf{k}_2'\rangle\langle \mathbf{k}_1, \mathbf{k}_2'|H_2|\mathbf{k}_1, \mathbf{k}_2\rangle}{E_{k_2}-E_{k_2'}-\hbar\omega_q} - i\frac{\langle \mathbf{k}_1', \mathbf{k}_2'|H_2|\mathbf{k}_1', \mathbf{k}_2\rangle\langle \mathbf{k}_1', \mathbf{k}_2|H_1|\mathbf{k}_1, \mathbf{k}_2\rangle}{E_{k_2}-E_{k_2'}+\hbar\omega_q}, \quad (7A)$$

where use has been made of Eq. (6A). In Eq. (7A) $\mathbf{k}_1$ and $\mathbf{k}_2$ are, respectively, the wave-vectors of electrons 1 and 2 in the initial state, and $\mathbf{k}_1'$ and $\mathbf{k}_2'$ are the corresponding wave-vectors in the final state. $\mathbf{q}$ denotes the wave-vector of the phonon. The conservation of momentum demands that

$$\mathbf{k}_2=\mathbf{k}_2'+\mathbf{q}, \qquad \mathbf{k}_1=\mathbf{k}_1'+\mathbf{q}. \quad (8A)$$

The diagonal elements of the matrix (7A) are those for which $\mathbf{k}_1'=\mathbf{k}_2$ and $\mathbf{k}_2'=\mathbf{k}_1$, i.e., those for which the two electrons have interchanged their roles after transition.

The evaluation of the matrix element (7A) has been given by Bethe and Sommerfeld.[10] We shall only give the final result for the diagonal term.

$$\langle \mathbf{k}_2, \mathbf{k}_1[H_1, S_2]\mathbf{k}_1, \mathbf{k}_2\rangle = -i\sum_q \frac{|M_q|^2\hbar\omega_q}{(E_{k_1}-E_{k_2})^2-(\hbar\omega_q)^2}, \quad (9A)$$

where

$$|M_q|^2=\left(\frac{4C^2\hbar\omega_q}{9nVMS^2}\right)\begin{pmatrix} n_\omega \\ 1+n_\omega \end{pmatrix}. \quad (10A)$$

[10] A. Sommerfeld and H. Bethe, Handbuch der Physik **24/2**, 517 (1933).

C is the interaction constant and has the dimensions of energy, V is the volume, M is the atomic mass, n is the number of atoms per unit volume, and S is the velocity of sound. n_ω denotes the number of phonons of angular frequency ω and is zero at the absolute zero of temperature. The other matrix element $\langle \mathbf{k}_2, \mathbf{k}_1[H_2, S_1]\mathbf{k}_1, \mathbf{k}_2\rangle$ has the same value as given by (9A). Substituting in (5A) we get for the exchange interaction energy of two electrons the expression

$$U \equiv \mathbf{H}'-H_0 = -2\sum_q \frac{|M_q|^2\hbar\omega_q}{(E_{k_1}-E_{k_2})^2-(\hbar\omega_q)^2}, \quad (11A)$$

where we have left out the self-energy terms $[H_1, S_1]$ and $[H_2, S_2]$.

Expression (11A) corresponds to the E_2 term of Fröhlich [see Eq. (2.15) of reference (1)]. It is this interaction which is interesting from the point of view of superconductivity and arises as a result of the Pauli principle. The E_1 term of Fröhlich corresponds to our $[H_1, S_1]$ and $[H_2, S_2]$. It has been suggested by Bohm and Staver[5] that the chief difference between their theory and that of Fröhlich and Bardeen is that whereas the former attribute the cause of superconductivity to the interaction of two neighboring electrons through the phonon field, the latter attribute it to the interaction of an electron with itself through the phonon field. This criticism by Bohm and Staver is, however, unjustified because there is an effective interaction between electrons through the Pauli principle. The interesting term in the Fröhlich theory is the E_2 term which is identical with the exchange interaction of two electrons corresponding to our expression (11A). The E_1 term in the self-energy expression is discarded by Fröhlich as being unimportant.

Hyperfine Structure in the Spectra of Iridium and Osmium

KIYOSHI MURAKAWA AND SHIGEKI SUWA
Institute of Science and Technology, Komaba-machi, Meguro-ku, Tokyo, Japan
(Received May 6, 1952)

The hyperfine structure in the spectra of Ir I and Os I was studied and the following results were obtained. (I) Both Ir^{191} and Ir^{193} have nuclear spins $\frac{3}{2}$, and the ratio of their magnetic moments is $\mu^{193}/\mu^{191}=1.04\pm0.04$, with $\mu^{193}=+0.17\pm0.03$ nm. Their quadrupole moments are given by $Q^{193}=(+1.0\pm0.5)\times10^{-24}$ cm² and $Q^{191}/Q^{193}=1.2\pm0.4$. Lines due to the transition $d^7s^2-d^7sp$ were observed to have an isotope displacement effect of the order of 0.063–0.071 cm^{-1}. (II) Os^{189} has a nuclear spin $\frac{3}{2}$, a nuclear magnetic moment $+0.70\pm0.09$ nm, and a quadrupole moment $(+2.0\pm0.8)\times10^{-24}$ cm².

I. IRIDIUM

THE hyperfine structure of the spectra of Ir I and Os I was studied using a water-cooled hollow-cathode discharge tube and a Fabry-Pérot etalon.

The line Ir I λ4198 $(9_{3/2}-d^7sp\ ^6D_{1/2})$[1] was observed to have the structure: 0 (3), 0.261 (5) cm^{-1}, where numbers in parentheses represent fairly accurate relative intensities. Since the term $9_{3/2}$ was observed to have a very small splitting, this structure is mainly due to the initial term. Iridium is known to consist of two odd isotopes Ir^{193} and Ir^{191} with relative abundances 61.5 and 38.5 percent, respectively.[2] From the above-mentioned structure of λ4198 it can be concluded that both Ir^{193} and Ir^{191} have spins $\frac{3}{2}$, and their magnetic moments are approximately equal.[3] This conclusion is supported by the structures of λ3800 and λ3513 shown in Fig. 1. Sibaiya[4] had previously published the structures of the same lines, but the present results might be considered better owing to an improved technique.

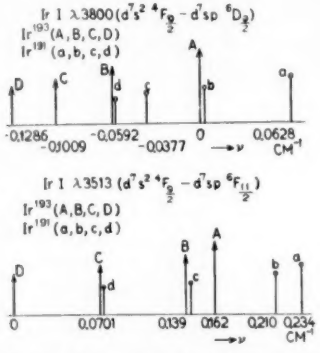

FIG. 1. Hyperfine structures of Ir I λ3800 and λ3513.

Denoting the interval factor and the quadrupole constant of the initial term and the final term of λ3800$(d^7s^2\ ^4F_{9/2}-d^7sp\ ^6D_{9/2})$ by A, B and A', B', respectively, we get from the observed structure of λ3800:

$$A-A'=0.00871,\quad B-B''=0.00004\ cm^{-1}\ \text{for}\ Ir^{193}.$$

$$A-A'=0.00836,\quad B-B'=0.00006\ cm^{-1}\ \text{for}\ Ir^{191}.$$

Taking the ratio of the values for $A-A'$, we get

$$\mu^{193}/\mu^{191}=1.04\pm0.04.$$

Taking the ratio of the values for $B-B'$, we get

$$Q^{191}/Q^{193}=1.5\pm0.8\ \text{from λ3800.}$$

However, the structure of λ3513 shows that the value of Q^{191}/Q^{193} is nearly equal to 1.0, so that the final value is

$$Q^{191}/Q^{193}=1.2\pm0.4.$$

We now calculate μ^{193} from the structure of λ3513· $(d^7s^2\ ^4F_{9/2}-d^7sp\ ^6F_{11/2})$. Denoting the interval factor and the quadrupole constant of the initial term and the final term by A, B and A', B', respectively, we get

$$6A-5A'=0.0475\ cm^{-1}\ \text{for}\ Ir^{193}.$$

Assuming a jj-coupling for the initial term and using the Fermi-Segrè-Goudsmit formulas with the correction introduced by Crawford and Schawlow,[5] we get

$$\mu(Ir^{193})=0.17\pm0.03\ \text{nm.}$$

This shows that $a(6s)=0.0797\ cm^{-1}$, $a(6p_{1/2})=0.0076\ cm^{-1}$ and $a(5d^7\ ^4F_{9/2})\approx0.0016\ cm^{-1}$ for Ir^{193}.

From the structure of λ3513, we get

$$55B-36B'=-0.0031\ cm^{-1}\ \text{for}\ Ir^{193}.$$

The numbers 55 and 36 are the values of $J(2J-1)$ for the initial and the final term of λ3513, respectively. Using the usual procedure, we get

$$Q(Ir^{193})=(+1.0\pm0.5)\times10^{-24}\ cm^2.$$

Figure 1 shows that Ir^{193} is displaced towards lower frequency side against Ir^{191} by 0.063 cm^{-1} and 0.071 cm^{-1} in the lines λ3800 and λ3513, respectively.

[1] W. Albertson, Phys. Rev. **54**, 183 (1938).
[2] M. B. Sampson and W. Bleakney, Phys. Rev. **50**, 732 (1936).
[3] The fact that the spin of Ir^{191} must be $>\frac{1}{2}$ was contained in a private communication by one of the authors (K.M.) quoted by J. E. Mack, Revs. Modern Phys. **22**, 64 (1950). Subsequently, Brix, Kopfermann, and Siemens, Naturwiss. **37**, 397 (1950), concluded that this spin is most probably $\frac{3}{2}$ and that the magnetic moments of Ir^{193} and Ir^{191} are approximately equal.
[4] L. Sibaiya, Phys. Rev. **56**, 768 (1939).
[5] M. F. Crawford and A. L. Schawlow, Phys. Rev. **76**, 1310 (1949).

II. OSMIUM

Kawada[6] found an isotope effect in some lines of Os I, and Suwa[7] measured the isotope effect more accurately in a larger number of lines. These authors deduced $\frac{1}{2}$ as the most probable value of the nuclear spin of Os^{189}. However, a critical review shows that a spin of $\frac{3}{2}$ with a large quadrupole moment for Os^{189} is not yet excluded. The present investigation was undertaken to test this assumption, using a much improved technique.

The structure of $\lambda 4260(d^6s^2\ {}^5D_4 - d^6sp\ {}^7D_5)$[8] is shown in Fig. 2. The isotope Os^{189} possesses a flag pattern consisting of four components, from which we conclude that the spin of Os^{189} is $\frac{3}{2}$. It was found that the structure of other osmium lines supports this conclusion.

Denoting the interval factor and the quadrupole constant of the initial term and the final term of $\lambda 4260$ by A, B and A', B', respectively, we get

$$11A - 9A' = 0.359 \text{ cm}^{-1}, \quad 45B - 28B' = -0.0087 \text{ cm}^{-1},$$

for Os^{189}. The former relation gives (as in the case of iridium)

$$\mu(Os^{189}) = 0.70 \pm 0.09 \text{ nm},$$

with $a(6s) = 0.305$ cm^{-1}, $a(6p_{1/2}) = 0.019$ cm^{-1}, and $a(5d^6\ {}^5D_4) \approx 0.0096$ cm^{-1}; and the latter relation gives

$$Q(Os^{189}) = (+2.0 \pm 0.8) \times 10^{-24} \text{ cm}^2.$$

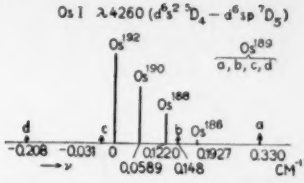

FIG. 2. Hyperfine structure of Os I λ4260.

[6] T. Kawada, Proc. Phys.-Math. Soc. Japan **20**, 653 (1938).
[7] S. Suwa, Phys. Rev. **83**, 1258 (1951).
[8] W. Albertson, Phys. Rev. **45**, 304 (1934).

PHYSICAL REVIEW VOLUME 87, NUMBER 6 SEPTEMBER 15, 1952

Distributions-in-Energy for Alpha-Particles and Protons from U^{235} Fission*

DAVID L. HILL†
Argonne National Laboratory, Chicago, Illinois
(Received April 28, 1952)

The Ranger has been applied to obtain the distributions-in-range for the alpha-particles and protons emitted from a thin film of U^{235} irradiated by thermal neutrons. For the alpha-particles the corresponding distribution-in-energy was obtained from 5.2 Mev to 50 Mev, showing appreciable intensity above 35 Mev and being well approximated in the high intensity region by a Gaussian curve centered at 15.2 Mev and with a 4.3 Mev rms half-width. The total intensity observed in this energy region corresponds to one alpha-particle in 220 fissions.

The proton intensity was found to be low above 2.1 Mev but to rise sharply as the energy was diminished to the limit of observation at 1.4 Mev, indicating about one proton with an energy in excess of 1.4 Mev emitted per 5000 fissions.

IN April, 1944, L. W. Alvarez observed light charged particles of about 21-cm range to be emitted from U^{235} bombarded by thermal neutrons. He used coincidence counting between two thin-walled ionization chambers irradiated in the thermal column of the Argonne Graphite Reactor. Since that time a number of observers[1] have studied this phenomenon, establishing that the bulk of the particles are helium nuclei emitted in a rare mode of U^{235} fission. Similar emission has been observed also in the fission of U^{233} and Pu^{239}.

The efforts of the author to establish the distribution-in-energy of these particles led to the development of the Ranger,[2] whose application to the study of neutron spectra has been described.[3] A number of measurements on the long-range particles from U^{235} and Pu^{239} made in the course of this development have been described.[3] The present note serves to record in the open literature the final measurements, made in February, 1946, on the long-range particles from U^{235}.

Figure 1 shows the arrangement by which a U^{235} foil one mg/cm^2 thick was irradiated in a beam of neutrons from the thermal column of the Argonne Heavy Water

* The work described in this article was done under the auspices of the Atomic Energy Project, and the information contained herein will also be included in the *National Nuclear Energy Series* (Manhattan Project Technical Section).
† Now at Vanderbilt University, Nashville, Tennessee.
[1] K. W. Allen and J. T. Dewan, Phys. Rev. **80**, 181 (1950); L. L. Green and D. L. Livesy, Trans. Roy. Soc. (London) **A241**, 323 (1949); Tsien, Ho, Chastel, and Vigneron, J. phys. radium **8**, 165, 200 (1947). See these papers for further references to the extensive literature on this subject.
[2] D. L. Hill, Rev. Sci. Instr. (to be published); see also unpublished Atomic Energy Commission Declassified Report No. 1945 (Rev.), which gives a detailed account of the Ranger and of the work done with it up to the summer of 1946.
[3] D. L. Hill, Rev. Sci. Instr. (to be published); D. L. Hill, Phys. Rev. **87**, 1034 (1952).

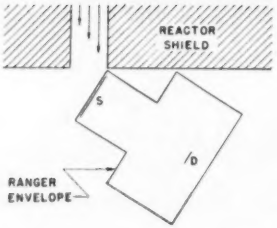

FIG. 1. Irradiation arrangement. A neutron beam 10 cm wide and 20 cm high emerges from the thermal column of the Argonne Heavy Water Reactor to strike the foil S, a layer of U^{235} deposited to a thickness of 1 mg/cm² on an aluminum plate 0.05 cm thick and 13.0 cm in diameter. The effective detector of the Ranger is a disk D of variable thickness which is parallel and coaxial to S, 31 cm displaced from S, and 3.8 cm in diameter.

Reactor. For the dimensions shown, the mean energy of the particles observed in the effective detector D of the Ranger differed by less than 2 percent from the energy which would be deduced from the absorbers used if the beam were prefectly collimated.

As has been explained,[2,3] a test polonium alpha-source enabled the gain of the gated electronic channels of the Ranger to be so adjusted that only particles of a given nuclear species were observed. We consider first the observations when the instrument was set to observe alpha-particles. The thickness of D was set at 1.05 c.a.e. (1.05-cm air equivalent);[4] the thickness of the source plate S, made by the familiar method[2] of electrodeposition from a rotating anode, was 0.3 c.a.e. Hence the range resolution of the instrument was as indicated by the 1.3 c.a.e. trapezoid drawn in at the top of Fig. 2, where the counting rate $C(A)$ as a function of total absorptive path is plotted.

For the gas filling of CO_2 at 40 mm Hg pressure, the minimum absorption path between S and D for the arrangement of Fig. 1 was 2.20 c.a.e. To eliminate interference from the naturally emitted alpha-particles from uranium the first point was taken for a mean absorptive path of 4.7 c.ae.; this and all other absorber thicknesses used were attained by the use of aluminum foils with the remote control arrangement[2] of the Ranger. Slight polonium contamination of the chamber gave a background counting rate of 0.2 per minute, which was eliminated by interposing 4 c.a.e. of absorption between the first and second coincidence counters as soon as the absorptive value of the points exceeded 6.2 c.a.e. All additional absorption as needed for the higher points was added between S and the first counter.

The background counting rate for all points above 6.2 c.a.e. was less than 0.01 per minute, as determined by interposing a 140 c.a.e. absorber between the first and second counters. This exceptionally low background, attainable with the Ranger, enables us to explore with precision the distribution-in-range, to higher values of A than are accessible by other techniques. For increased counting rates in this exploration above 40 c.a.e., the thickness of D was increased to 4 c.a.e. We found the distribution to fall off monotonically, reaching a counting rate of 0.2 per minute at 80 c.a.e. and falling to less than 0.01 per minute at 150 c.a.e.

At the low range end of the distribution, the linear extrapolation into the origin is suggested by the course of the curve, although some emission mechanism may conceivably give rise to more numerous alpha-particles of range less than 4 c.a.e.

The solid line, indicating the mean course of the distribution-in-range, has been transformed to give the distribution-in-energy in Fig. 3. We consider this mean course of the energy distribution to be accurate to better than 10 percent, as the individual points of the measured distribution-in-range were taken to a statistical accuracy of 5 percent to 10 percent.

The dashed line of Fig. 3 is the Gaussian curve

$$I(E)=K\times\exp[-(E-15.15)^2/(6.05)^2], \quad E \text{ in Mev},$$

drawn in to illustrate its close resemblance to the observed energy spectrum in the high intensity region.

The cross section for production of the helion energy spectrum described by the solid line of Fig. 3 is found to be 2.5 barns, with an estimated uncertainty of 15 percent. The 540-barn cross section for thermal-neutron-induced fission of U^{235} indicates about one alpha-particle emission for 220 fissions.

The results here presented appear to have been obtained with finer resolution, lower background, and better statistical determination—particularly at the low intensity ends of the spectrum—than those elsewhere reported. Subject to this qualification, the conclusions we may reach on the alpha-particle spectrum

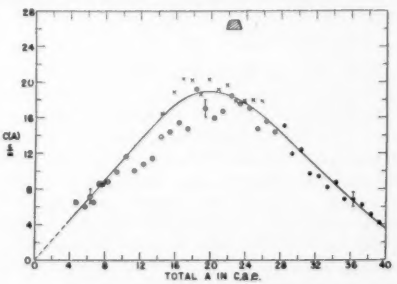

FIG. 2. Distribution-in-range for alpha-particles emitted in U^{235} fission. The observed counting rate for a D thickness of 1.05 c.a.e. and an S thickness of 0.3 c.a.e. is plotted against the mean absorptive path traversed by the counted particles. The width over which each range count extends is indicated by the trapezoid at the top of the figure. Three independent sets of data have been superposed, as indicated by the different point symbols, and the solid line drawn to indicate the apparent course of the spectrum. Probable statistical errors in the counts are indicated by the obelisks on three typical points.

[4] One c.a.e. (centimeter of air equivalent) is defined to be an absorptive unit equivalent, for range diminution of an alpha-particle or proton, to one centimeter of air at 15°C and 760 mm Hg pressure.

are in substantial agreement with those of other observers.[1]

This intensity for alpha-particle emission is somewhat larger than the value—about one in 300 fissions—commonly reported.[1] The shape of the spectrum which we obtained has been substantially corroborated by the work of Allen and Dewan, subject to the qualification that their counting techniques did not permit them to explore the range distribution below 10 c.a.e. or above 50 c.a.e.

PROTONS FROM U^{235} FISSION

With the apparatus arranged as described above, the existence of protons emitted from U^{235} fission could be investigated just as easily as the existence of alpha's. It was merely necessary to set the amplifier gains and the discriminator levels at the proper values to count protons only. It was then observed, however, that at a CO_2 pressure of 40 mm Hg, for which the fission fragments could reach the counting region but were stopped by an absorber in A_1,[2] the general ionization level was too high for proton counting. The effect presumably followed from the heavy ionization produced by the bremsstrahlung emitted by the fission fragments plunging into the aluminum absorber adjacent to the counters. Making the absorber in A_1 thicker had little effect, but when it was noted that the gamma-interference was much higher in the first counter than in the second, and practically negligible in the third, the gas filling pressure was increased to 60 mm Hg, and the interference from the presumed bremsstrahlung diminished sharply so that proton counting was easily possible. By the time the pressure was increased to 80 mm Hg, so that all of the fission fragments were stopped in the gas at least 8 cm from the first counter, the background of typical "gamma-hash" visible in the oscilloscope screen had diminished to a negligible level in all counters.

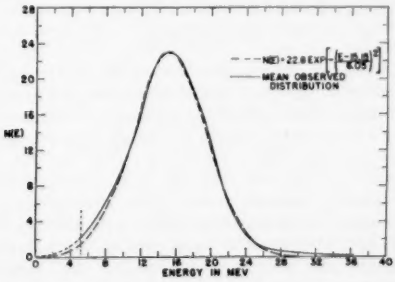

FIG. 3. Distribution-in-energy for alpha-particles emitted in U^{235} fission. The mean energy distribution, as represented by the solid curve, is seen to be a nearly symmetrical curve, with a high energy tail reaching to 36 Mev or more. The lower limit of observation is indicated by the vertical bar at 5.2 Mev. The Gaussian curve dashed in gives a fit within statistical uncertainties from 8 Mev to 26 Mev. The uncertainty of the solid line is estimated as 10 percent or less.

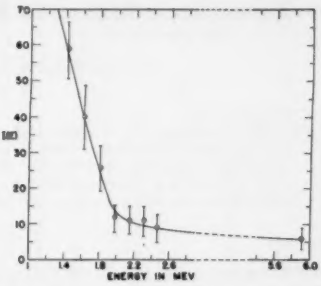

FIG. 4. Distribution-in-energy for protons from U^{235} fission. The points plotted were taken with a D thickness of 1.05 c.a.e. and multiplied by the slope of the range-energy relation. The solid line has been drawn in to indicate the apparent course of the resultant energy spectrum. If no protons are present below the limit of observation at 1.4 Mev, the intensity here plotted corresponds to about one proton per 5000 fissions.

The counting rates for protons were then found to be very low for all points except the first four or five when D was 1 c.a.e., and for the first two when D was 4 c.a.e. The range distribution so observed was converted to an energy distribution and is reproduced in Fig. 4, with indication of the statistical uncertainties; the intensity is plotted in arbitrary units. Care was taken here as in the measurements of neutron spectra[3] to have no hydrogeneous material in a position such that a neutron could knock a proton into the counting region. Thus, although the energies of the protons observed could be produced by transfer from the fission neutrons of the U^{235} foil, comparison with the background counting rates for the fission neutron measurements[3] indicated that the counting rates here observed are at least ten times too large to be susceptible to such an explanation.

The integral under the curve of Fig. 4 indicates that the cross section for the production of protons of energies between 1.4 Mev and 2.1 Mev, the region over which a significant intensity was observed, is 0.1 barn. Thus the yield of protons per fission approaches the order of magnitude of cyclotron yields, so the protons could perhaps be considered to arise from reactions produced by the fission fragments, including the fission neutrons. We have not obtained the intensity of the protons for energies less than 1.4 Mev, but if we choose to extrapolate the curve of Fig. 4 along the direction indicated until the ordinate of zero energy is reached, the area under the curve becomes ten times larger, and the corresponding protons become too numerous to be readily explained away as secondary fission products; such an extrapolation of the present data must, however, remain in doubt.

In developing the instrumental techniques applied to these measurements I have been generously supported and assisted by other members of the Argonne National Laboratory, as indicated in the report[2] on the Ranger.

Nuclear Cross Sections for Negative Pions of Energy 113 and 137 Mev*

RONALD L. MARTIN†
Institute for Nuclear Studies, University of Chicago, Chicago, Illinois
(Received May 26, 1952)

The measurements of the nuclear cross sections for negative pions at 85 Mev, recently made by Chedester, Isaacs, Sachs, and Steinberger, have been extended to 113 and 137 Mev. The total absorption plus inelastic scattering cross sections were obtained from a transmission measurement in poor geometry. The cross sections are all close to the geometrical value, $\pi A^{2/3}(\hbar/\mu c)^2$, within the accuracy (15 percent) of this technique. With the possible exception of carbon there is no evident energy dependence in the range 85 to 137 Mev.

AMONG mesons, the pi-mesons are distinguished by their strong nuclear interaction. With the availability from the large synchrocyclotrons of fairly intensive π^- meson (pion) beams well collimated and well defined in energy, it has become possible to make accurate measurements of the nuclear cross sections of pions as a function of energy. Using one of the pion beams of the Nevis cyclotron, Chedester, Isaacs, Sachs, and Steinberger[1] have obtained the absorption cross sections of various nuclei at 85 Mev by transmission measurements in poor geometry using scintillation counter techniques. Except for hydrogen, the cross sections which they obtained were close to the "geometrical value" $\pi A^{2/3}(\hbar/\mu c)^2$. A is the mass number and $\hbar/\mu c = 1.4\times10^{-13}$ cm is the range of nuclear interaction. Studies of negative pions in the energy range 30 to 110 Mev in photographic emulsions by Bernardini, Booth, and Lederman[2] showed that while the cross section for absorption and inelastic scattering for the nuclei in these emulsions is close to the geometrical value, there is some indication of a decrease in cross section with decreasing pion energy.

This paper reports an extension of the measurements of Chedester, Isaacs, Sachs, and Steinberger by essentially the same technique, using negative pions of energies 113 and 137 Mev. A preliminary report has already been made to this journal.[3]

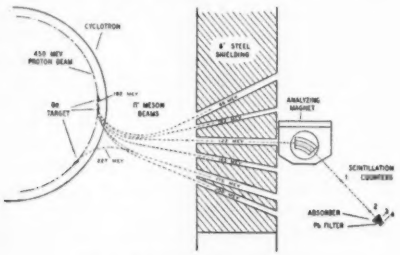

FIG. 1. Experimental arrangement.

THE PION BEAMS

Pions are produced by the bombardment of either beryllium or copper targets with the internal 450-Mev proton beam of the Chicago synchrocyclotron. Negative pions emitted in the forward direction are deflected outward by the magnetic field of the cyclotron and emerge from the vacuum chamber through a thin aluminum window. The cyclotron field separates the pions according to their energy by deflecting those of lower energy more; those of higher energy less. A certain amount of focusing takes place in the fringing field of the cyclotron such that a sizeable fraction of the mesons of given momentum leave the cyclotron in a fairly parallel beam. Channels were cut in the six-foot steel shield which separates the cyclotron from the experimental room so that a number of these beams having different energies are able to enter the experimental room.

The location of these channels was obtained from an empirical study of the meson trajectories using the current carrying wire method.[4] This method depends on the fact that if a given tension T is applied to a thin wire with current I in a transverse magnetic field $H_z(xy)$, the wire will contort itself into precisely the same horizontal trajectory as will be followed by a particle of charge e and momentum

$$P=(e/c)(T/I). \quad (1)$$

One end of the wire was fixed at the position of the target in the median plane of the cyclotron. The other end was brought into the experimental room, passed over a pulley, and attached to a weight so as to apply a known tension. The current in the wire was then adjusted until the wire remained in stable equilibrium. In this way channels were laid out corresponding to pion energies, calculated using (1), of 66, 102, 122, 145, 175, and 200 Mev. The target position to which these energies refer is 76-in. radius and 3.8° NE azimuth. The channels were all 2 in. high, some were 4 in. wide and others 6 in. wide. The general arrangement is shown in Fig. 1.

Since much stray radiation, mostly fast neutrons, come through the channel from the cyclotron, it was found expedient to use a magnet to deflect the pions

* Research sponsored by the ONR and AEC.
† AEC Predoctoral Fellow.
[1] Chedester, Isaacs, Sachs, and Steinberger, Phys. Rev. **82**, 958 (1951).
[2] Bernardini, Booth, and Lederman, Phys. Rev. **83**, 1075 (1951).
[3] Martin, Anderson, and Yodh, Phys. Rev. **85**, 486 (1952).
[4] J. J. Thomson, Phil. Mag., Series 6, **13**, 561 (1907).

through an angle of about 45° so as to obtain a purified beam of the desired particles. Muons and electrons having the same sign and momentum as the pions remain in the deflected beam. For the 122- and 145-Mev beams used in the present experiment these were found to amount to 7±4 percent of the pion intensity. The deflecting magnet has a focal length of 21 in. in the horizontal direction and so provides some focusing.

Positive pions up to 145 Mev have been obtained by reversing the direction of both the cyclotron and the deflecting magnet fields. Positive pions emitted in the direction backward from the proton beam (now reversed) follow the same trajectories and pass through the same channels as did their negative counterparts of the same energy. The number of positive pions obtained in this way is much smaller than the number of negatives, backward emission being far less favorable for the pions. In the experiments described herein only the 122-Mev and 145-Mev negative pion beams have been utilized.

EXPERIMENTAL ARRANGEMENT

The pions were detected by means of scintillation counters. Four such counters were arranged in the line of the pion beam. The first pair were 1 inch square by 1 cm thick terphenyl crystals spaced either 30.5 in. or 40 in. apart. The second pair were liquid scintillators having an effective diameter of 3 in. placed together and removed either 9.15 in. or 19.9 in. from the second crystal. The latter distances refer to a point 1 cm inside the last scintillator.

Coincidence circuits were arranged to record the quadruple coincidence produced when an ionizing particle penetrated all four scintillators, and also the double coincidence when the particle traversed the first pair. Thus, the ratio (Q/D) of quadruples to doubles is the fraction of particles which penetrate the last pair of scintillators after having passed through the first pair. An absorber placed in front of the second pair of scintillators removes pions from the beam with the result that the ratio quadruples to doubles is reduced. Comparison of this ratio with and without absorber is expressed as a cross section by means of the formula

$$Q/D \text{ with absorber}/Q/D \text{ without absorber} = \exp(-N\sigma), \quad (2)$$

where N is the number of atoms per cm² in the absorber and σ is the cross section in cm². Some amount of correction of the ratios Q/D was necessary to account for the effects of chance coincidences.

The last pair of scintillators were made purposefully large, and the absorbers left as close to them as possible so that the cross section measured in this way would not include much of the effects of Coulomb scattering and small angle diffraction scattering. A $\frac{1}{16}$ in. thick lead absorber was placed between the last two scintillators to render them insensitive to those protons of energy less than 100 Mev which might be emitted from the stars produced by the absorption of pions. The scintillators were rather insensitive to neutrons and gamma-rays which might come from such stars. The cross sections obtained in this way are primarily total cross sections for the absorption and inelastic scattering of pions.

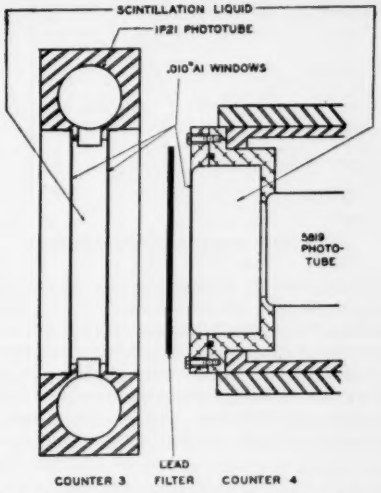

FIG. 2. Detail of counters No. 3 and No. 4. In use the two counters were fitted tightly together.

SCINTILLATION COUNTERS

The first two scintillators were 1 in.×1 in.×1 cm thick crystals of *p*-terphenyl of good optical quality. These were mounted using a thin layer of silicone grease to provide good optical contact between one edge of the crystal and the flat photo cathode of the EMI 5311 photomultiplier. The crystal was wrapped in thin aluminum foil to improve the optical efficiency. Photomultiplier and crystal were mounted together inside a $\frac{3}{8}$ in. thick steel cylinder which served as a magnetic shield. Openings $1\frac{1}{2}$ in.×$1\frac{1}{2}$ in. were cut in the shield opposite the crystal faces to allow for the uninterrupted passage of pions through the crystal. These openings were made light tight by a wrapping of black Scotch electric tape.

Scintillator No. 3 was of the liquid transmission type 4 in. in diameter and $\frac{3}{8}$ in. thick. The cell was machined out of a single block of low carbon steel and provided with 0.010-in. aluminum windows sealed in place with Araldite 101 cold setting adhesive. The scintillator liquid was viewed edge-on by two diametrically opposite 1P21 photomultiplier tubes set in cavities bored in the sides of the steel cell. The glass envelopes of these tubes was sealed to the steel with Araldite 101 adhesive so that the liquid scintillator was in direct optical contact with the glass window of the phototube. The liquid

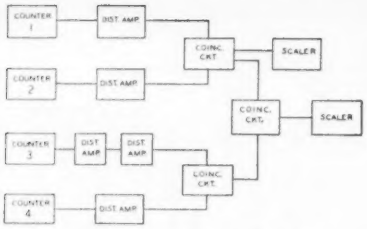

FIG. 3. Block diagram of counting arrangement.

scintillator was the 3 grams per liter mixture of terphenyl in phenylcyclohexane recommended by Kallman and Furst.[5] A sketch of the design is given in Fig. 2.

Scintillator No. 4 was an end-on type using the same type of liquid as scintillator No. 3. The scintillation cell was machined from aluminum and was 3 in. in diameter and $1\frac{1}{4}$ in. deep. This cell was viewed by a 5819 photomultiplier mounted on its central axis. The photocathode was sealed to the cell with Araldite No. 101 adhesive so that it made direct optical contact with the scintillation liquid. The design of this scintillator is also shown in Fig. 2.

The outputs of the photomultiplier tubes were fed directly into RG7U (95-ohm) cable which carried the pulses some 150 feet to the cyclotron control room. There they were amplified using 100-ohm distributed amplifiers[6] having a 3×10^{-9} second rise time and thence fed into the coincidence circuits. A gain of 100 was needed for scintillator No. 3; for the others a gain of 10 sufficed. A block diagram of the counting arrangement is shown in Fig. 3. The coincidence circuits were fashioned after that described by Garwin.[7] The resolving time of these circuits was about 5×10^{-8} second. It was necessary to lengthen the pulses from the photomultipliers to about this time in order to obtain satisfactory operation. Diode pulse lengtheners were used to accomplish this. One coincidence circuit operated from pulses of the first pair of scintillators and a second coincidence circuit operated from the pulses of the second pair. The quadruple coincidences were obtained by recording from a third and slower circuit the coincidence of the output pulses from the two primary coincidence circuits. Hewlett Packard fast decade scalers with a resolving time of 0.1μ sec made it possible to count as rapidly as 100,000 counts per minute without appreciable loss.

The pulses obtained from the scintillators were not uniform in height due to variation of optical efficiency over the sensitive area. However it was possible to count mesons with nearly 100 percent efficiency by using a sufficiently high voltage on the photomultipliers. Curves of coincidence counting rate in the meson beam as a function of photomultiplier high voltage were taken and showed satisfactory plateaus. A typical plateau curve is given in Fig. 4.

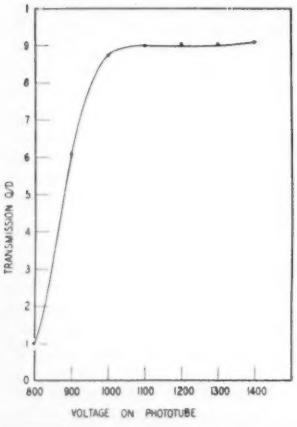

FIG. 4. Plateau curve of counter No. 4.

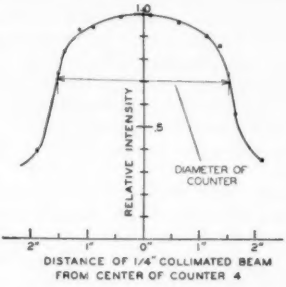

FIG. 5. Sensitivity of counter No. 4.

A study of the effective area of the second pair of scintillators was also made. For this a $\frac{1}{4}$-in. hole was bored in a 4 in. thick lead brick set in the meson beam. The counting rate of counters No. 3 and No. 4 was measured with various parts of their area exposed to this narrow pencil of mesons. The counting efficiency was found to be fairly uniform over most of the 3-in. diameter area of counter No. 4 as shown in Fig. 5.

TARGET

Beryllium was used as the meson-producing target of the cyclotron in the experiments with the 122-Mev beam, and copper in the experiments with the 145-Mev beam. The target is provided with a thermocouple arranged to monitor rather accurately the meson output of the machine. The target is connected through a calibrated heat leak to a large cylindrical drum, capable of

[5] H. Kallman and M. Furst, Nucleonics **8**, 32 (1951).
[6] Anderson, Martin, and Slattery, Rev. Sci. Instr. (to be published).
[7] R. L. Garwin, Rev. Sci. Instr. **21**, 569 (1950).

maintaining itself at a fairly constant temperature by radiation. The thermocouple junctions are connected across the heat leak so that the emf developed is a function of the heat flow through the leak. This emf is recorded on a Brown potentiometer and read as watts of power developed by the proton beam in the target. The proton beam loses energy to the target principally by ionization loss and to some extent by nuclear reaction, but in any case the energy loss is proportional to the path length of protons in the target and hence to the meson output. The thermocouple data are not an essential part of the measurements described here, but they have been useful as an over-all check on the operation of the equipment. Throughout these experiments the doubles count per target watt minute was computed. The constancy of this number for given geometry was taken as an indication that the equipment was operating reproducibly and reliably.

DEFLECTION MAGNET

A 45° sector magnet with a gap 2 in. high and 4 in. wide was used to deflect the mesons and separate them from undesirable radiation which comes through the channel in the shield. The current in the magnet was adjusted to give a maximum in the doubles rate of counters No. 1 and No. 2. Typical curves of this counting rate as a function of magnet current are given in Fig. 6. The width of these curves is due partly to the energy spread of the beams (±4 Mev) and partly from the finite extension of the channel openings and the scintillation detectors. The curves for the 122-Mev and the 145-Mev beams are not strictly comparable. The former were taken with a 40-in. spacing between the counters, the latter with 30.5-in. spacing. The intensity of the 122-Mev π^- beam was found to be some 7 times greater than that of the 145-Mev beam. This is due to the more abundant emission of the lower energy mesons and to the focusing properties of the cyclotron fringing field, which seems to be most efficient for the 122-Mev beam.

Some idea of the background level in the experimental room is given by the fact that with the magnet current turned off the singles rate of counter No. 1 was reduced to 5 percent of its value with the magnet current properly adjusted for the 122-Mev beam. The number of collimated particles capable of producing a double coincidence in counters No. 1 and No. 2 was negligible with the magnet turned off.

ENERGY AND COMPOSITION OF THE BEAMS

Wire measurements were made to establish the momentum of the particles accepted by the deflection magnet. These were made with the wire (No. 32 copper) fixed at the center of the channel on the cyclotron side and passing through the center of the channel, the slot in the deflecting magnet, and along the centerline of the scintillation counters, where it was fastened to a trip balance specially adapted to measure the horizontal

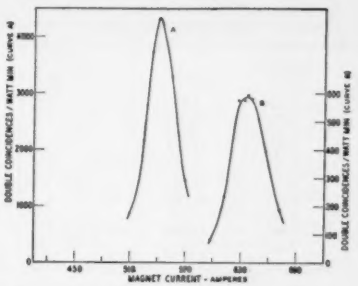

FIG. 6. Intensity vs deflecting magnet current.

tension in the wire directly in grams. The current in the wire was determined from a measurement, with a precision potentiometer, of the voltage it developed across a standard 0.1-ohm shunt. In the 122-Mev channel with the magnet current at the value which gave maximum beam intensity the following readings were obtained:

Tension (grams)	Current (amperes)	Momentum (units of μc)
106.2	1.4002	1.583
122.2	1.6145	1.578

This corresponds to an energy of 122.7 Mev for pions of mass $\mu = 276$ electron masses.

The range was measured by making transmission measurements with various thicknesses of aluminum. The transmissions obtained in this way are plotted on a logarithmic scale in Fig. 7. There are two sharp drops. The first occurs at the end of the pion range, the second at the end of the range of the muons which contaminate the beams. Without corrections the mean ranges in the 122-Mev beam are 42.2 g/cm² and 60.5 g/cm² of

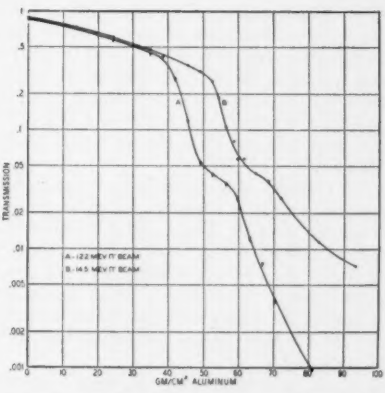

FIG. 7. Range curves in aluminum of 122-Mev and 145-Mev π^- beams.

TABLE I. Absorber data.

Absorber	Thickness (cm)	g/cm²	N (10^{22} atoms/cm²)	X_a[a] (cm)
C_1	3.33	5.202	2.609	4.43
C_2	6.50	10.231	5.131	6.01
Al_1	2.50	6.978	1.558	4.01
Al_2	5.00	13.965	3.119	5.26
Cu_1	1.00	8.931	0.846	3.24
Cu_2	2.00	17.764	1.683	3.76
Cd_1	1.27	10.963	0.587	3.40
Sn_1	1.27	9.281	0.471	3.40
Pb_1	1.20	13.608	0.3955	3.36
Pb_2	2.40	27.333	0.7945	3.96

[a] X_a is the distance from the center of the absorber to a point 1 cm inside the last scintillator.

aluminum. Other materials in the beam contribute 6.4 g/cm² aluminum equivalent as follows:

Material	Al equivalent g/cm²
Counters No. 1 and No. 2	3.0
Liquid of counter No. 3	2.0
Aluminum windows	0.2
1 cm of liquid of counter No. 4	1.2
Total aluminum equivalent	6.4 g/cm²

The energies were computed using the tables of proton ranges given by Smith,[8] taking as mass ratios, 6.65 for the proton to pion and 8.76 for the proton to muon. From the above data the energy of the primary pions in the 122-Mev channel was found to be 128 Mev; of the primary muons 150 Mev.

In the 145-Mev channel the wire measurements gave for the momentum the value $1.78\mu c$. The corresponding pion energy is 147 Mev. The range measurement gave 150 Mev for the pions and 167 Mev for the muons.

The pion energy obtained from the range measurement is slightly higher than that expected on the basis of the wire measurement in both channels. Some of this discrepancy is due to the way in which the range is measured. Negative pions that come to rest at the end of their range produce stars, the particles of which are able to penetrate an additional amount of absorber and produce a pulse in the final scintillators. In addition, the energy of the pions in a given channel depends on the position of the target and on the value of the cyclotron magnetic field and these are not always precisely reproduced.

For the purposes of the cross-section measurements the pertinent energy is the mean energy of the pions traversing the absorber. This was slightly different for the different absorbers used. Taking into account the energy loss in the first two scintillators the energy of the pions entering the absorbers, which was adopted on the basis of the studies described above, was 120±4 Mev for the 122-Mev channel and 143±4 Mev for the 145-Mev channel.

The muons have very nearly the same momentum as the pions and come partly from the vicinity of the target, from which they follow the same trajectory as the pions, and partly from the decay in flight of the pions in the beam. Their number may be estimated from the range curve and amounts to about 7 percent in both beams. The residual particles giving rise to the tail of the range curves were either neutrons from pion-produced stars or electrons. In the 122-Mev beam the electron content was less than 1 percent of the beam intensity while in the 145-Mev beam the electron content was somewhat larger because the cyclotron target for this beam was copper. In both cases the electron content was included in the estimate of the muon contamination so that the total beam contamination was 7±4 percent in both beams.

BACKGROUND

In the experiment, the principal source of background was the chance coincidence count due to the high beam intensity and the finite resolution of the coincidence circuits. The effect is aggravated by the pulsed operation of the cyclotron. The duty cycle of the cyclotron is about 1 percent so that the instantaneous counting rate is 100 times the average counting rate. The chance coincidence rate is proportional to the square of the beam intensity and to the ratio of the resolving time τ of the coincidence circuit and the duty cycle D of the cyclotron. The ratio τ/D was determined by exposing the counters to two different pion beams at the same time so that all coincidences were chance coincidences. The values found were 2.5×10^{-6} second for the doubles coincidence circuit of counters No. 1 and No. 2, and 1.0×10^{-4} second for the quadruples coincidence circuit.

TABLE II. Data of the 122-Mev π^- beam.

Abs.	Mean energy / Energy band Mev	Doubles count	Quad. count	Q/D	Q/D[a]	σ 10^{-27} cm² (experimental)
No abs.		153030	136695	0.8933 ±0.0011	0.8861	
C_1	114 / 105–124	160033	131821	0.8237 ±0.0015	0.8028	404 ±37
No abs.		147300	132558	0.8999 ±0.0031	0.8930	
Al_1	114 / 105–124	184786	152575	0.8257 ±0.0036	0.8118	655 ±54
No abs.		133520	120905	0.9055 ±0.0013	0.8988	
Cu_1	112 / 101–124	129788	109101	0.8407 ±0.0012	0.8281	1037 ±67
No abs.		136172	122842	0.9021 ±0.0022	0.8952	
Cd_1	112 / 100–124	130001	108241	0.8326 ±0.0014	0.8174	1659 ±127
No abs.		144637	130008	0.8989 ±0.0011	0.8913	
Sn_1	114 / 104–124	150263	126728	0.8434 ±0.0021	0.8279	1680 ±144
No abs.		144533	129974	0.8993 ±0.0016	0.8916	
Pb_1	111 / 98–124	144122	118861	0.8247 ±0.0017	0.8078	2668 ±208

[a] Corrected for background.

[8] J. H. Smith, Phys. Rev. **71**, 32 (1947).

The energy delivered to the target was used as an indication of the cyclotron operating level. At various times the singles counting rates S_1 and S_2 of counters No. 1 and No. 2 were recorded and also the doubles rate D_{34} of counters No. 3 and No. 4. With these data it was possible to distinguish the random from the true count. The backgrounds (bg) were computed using the formulas

$$\frac{D_{12}(\text{bg})}{\text{min}}=\frac{2.5\times10^{-6}}{60}\left(\frac{S_1}{\text{watt min}}-\frac{D_{12}}{\text{watt min}}\right)\times\left(\frac{S_2}{\text{watt min}}-\frac{D_{12}}{\text{watt min}}\right)\times\text{watts}^2, \tag{3}$$

$$\frac{Q(\text{bg})}{\text{min}}=\frac{1.0\times10^{-4}}{60}\left(\frac{D_{12}}{\text{watt min}}-\frac{Q}{\text{watt min}}\right)\times\left(\frac{D_{34}}{\text{watt min}}-\frac{Q}{\text{watt min}}\right)\times\text{watts}^2. \tag{4}$$

In the 145-Mev beam the backgrounds were about 0.3 percent of both the doubles and the quadruples count with the cyclotron operating at a 5-watt level. In the more intense 122-Mev beam the backgrounds were about 1 percent of the doubles count and 3 percent of the quadruples count with the cyclotron operating at a 12-watt level. The net effect of the background on the cross section was about 1.5 percent in the 145-Mev beam and 12 percent in the 122-Mev beam.

MEASUREMENTS

The transmission measurements were made in "poor" geometry with the absorber as close to counter No. 3 as possible. A list of the absorbers used, together with pertinent data about them is given in Table I. The thickness of the absorber was severely limited by the requirement that the effect of multiple Coulomb scattering should be kept small. Estimates of the magnitude of this effect were made using a simplified theory of the multiple scattering.[9] These effects were negligible for the 5.2-g/cm² graphite absorber and range to 7.5 percent in the worst case, 13.6-g/cm² of lead in the 122-Mev beam. These corrections would become very much greater if the absorbers were placed further from the last pair of counters. Such a geometry also precludes the measurement of pions scattered in the forward direction by nuclear interaction. The solid angle subtended by the fourth counter at the center of the absorber was of the order of 3.8 steradians. Thus, the cross sections which are obtained experimentally do not include processes in which ionizing particles are produced within this solid angle and which have sufficient penetrating power to traverse the last pair of scintillators. For the most part, these are the elastically diffracted pions. Estimates made by applying the theory of diffraction scattering show that all except 6 percent of the elastically scattered pions in the most favorable case (lead), and all except 20 percent in the worst case (carbon) enter the final pair of counters. Thus, these experiments measure primarily the total cross section for the nuclear absorption of the pions.

[9] B. Rossi and K. Greisen, Revs. Modern Phys. **13**, 240 (1941).

TABLE III. Data of the 145-Mev π^- beam.

Abs.	Mean energy / Energy band Mev	Doubles count	Quad. count	Q/D	Q/D[a]	σ 10^{-27} cm² (experimental)
No abs.		7704	7081	0.9191 ±0.0051	0.9155	
C_1	138 / 128–147	23632	19565	0.8279 ±0.0038	0.8276	414 ±27
No abs.		13641	11541	0.8461 ±0.0031	0.8461	
C_2	133 / 118–147	12284	8249	0.6715 ±0.0064	0.6694	480 ±27
No abs.		15943	14555	0.9129 ±0.0023	0.9139	
Al_1	138 / 126–147	25352	21119	0.8330 ±0.0024	0.8328	639 ±35
No abs.		11479	10412	0.9070 ±0.0038	0.9078	
Al_2	130 / 114–147	15258	11391	0.7466 ±0.0034	0.7478	666 ±35
No abs.		15281	13848	0.9062 ±0.0023	0.9072	
Cu_1	136 / 125–147	17926	14986	0.8360 ±0.0027	0.8360	1035 ±62
No abs.		12074	10997	0.9108 ±0.0026	0.9118	
Cu_2	129 / 110–147	16392	12490	0.7620 ±0.0031	0.7611	1150 ±53
No abs.		14293	13060	0.9137 ±0.0024	0.9147	
Cd_1	135 / 123–147	24214	20231	0.8355 ±0.0025	0.8355	1651 ±94
No abs.		13638	12416	0.9104 ±0.0025	0.9113	
Sn_1	136 / 126–147	20815	17693	0.8500 ±0.0030	0.8501	1581 ±115
No abs.		12381	11270	0.9103 ±0.0026	0.9112	
Pb_1	135 / 122–147	21022	17566	0.8356 ±0.0026	0.8356	2343 ±141
No abs.		7946	7237	0.9108 ±0.0032	0.9115	
Pb_2	126 / 105–147	13550	10178	0.7511 ±0.0037	0.7503	2622 ±124

[a] Corrected for background.

The experimental data of the measurements with the 122-Mev beam are collected in Table II. Table III gives the data obtained with the 145-Mev beam. In these tables columns 3 and 4 give the total counts of double and quadruple coincidences, respectively. With the 122-Mev beam these counts were obtained in four runs of one minute each with the cyclotron operating at a 12-watt level, while with the 145-Mev beam the counts were obtained in a number of separate runs of 2 minutes each, with the cyclotron operating at a 5-watt level. The ratio Q/D is given in column 5. The stated uncertainty is the larger of either the statistical value or that calculated from the internal consistency. Col-

TABLE IV. Experimental cross sections for negative pions.

Absorber	Experimental cross sections (10^{-27} cm^2) 85 Mev[a]	113 Mev	137 Mev	Geometrical cross section (10^{-27} cm^2) $\pi A^{2/3}(\hbar/\mu c)^2$
C	344± 13	404± 37	414± 27	322
Al	623± 25	655± 54	639± 35	553
Cu	990± 50	1040± 70	1035± 60	977
Cd	1590± 70	1660±130	1650± 90	1430
Sn		1680±140	1580±120	1480
Pb	2400±110	2670±210	2340±140	2150

[a] Data of Chedester, Isaacs, Sachs, and Steinberger, Phys. Rev. **82**, 958 (1951).

umn 6 gives the ratio Q/D after the background corrections have been made. The cross sections computed from these ratios by using (2) were increased by 7±4 percent to account for the muon-electron contamination of the beams, on the assumption that the nuclear interaction of the muons and electrons is negligible, and the resulting experimental cross sections are listed in column 7. The probable error has been increased because of an uncertainty in the background correction, due to the possible variation of the duty cycle of the cyclotron.

Without absorber about 90 percent of the pions which were recorded by the first pair of counters were also recorded by the second pair. Nuclear absorption in the second and third counters and in the lead filter account for 7 percent of the pions. About 1 percent of the pions were lost due to multiple scattering in the second crystal. The remaining 2 percent of the pions were missed due to inefficiency in the last pair of counters.

The experimental cross sections obtained in both beams with the thin absorbers are collected in Table IV. These values have not been corrected for diffraction and Coulomb scattering effects. In this form they are comparable to the values obtained by Steinberger *et al.*,[5] at 85 Mev, which are listed in column 2. For comparison, the geometrical value, $\pi A^{2/3}(\hbar/\mu c)^2$, is listed in column 5. The general result is that all the cross sections have the geometrical value within the accuracy (15 percent) of this experiment. With the possible exception of carbon, the cross sections are independent of energy between 85 and 137 Mev.

The cross sections obtained with the thick absorbers were somewhat larger because of the increase in the contribution of multiple and diffraction scattering effects. For this reason the thick absorber values were not included in Table IV.

TABLE V. Radiation lengths.[a]

Absorber	Radiation length g/cm^2
C	52
Al	26.3
Cu	13.3
Cd	8.9
Sn	8.7
Pb	5.9

[a] From D. J. X. Montgomery, *Cosmic Ray Physics* (Princeton University Press, Princeton, New Jersey, 1949), p. 63.

SCATTERING EFFECTS

The general result, that the nuclear cross sections are close to the geometrical values, suggests that reasonable estimates of the effect of the diffraction scattering might be had from a calculation based on an opaque sphere model.

With this model the result of a partial wave analysis is that, for each partial wave, the total cross section for diffraction scattering is equal to the total cross section for absorption. Using the experimental value for the absorption cross section, σ_a, the differential cross section for the diffraction scattering which includes all partial waves up to $l=l_0$ is

$$\frac{d\sigma_d}{d\Omega}=\frac{\sigma_a}{4\pi(l_0+1)^2}\left|\sum_{l=0}^{l_0}(2l+1)P_l(\cos\theta)\right|^2. \quad (5)$$

For a nucleus of radius $R=A^{1/3}(\hbar/\mu c)$ and a pion of wave number k, the diffraction is calculated by linear interpolation between those adjacent integral values of l_0 most nearly equal to the product kR.

The differential cross section obtained in this way is in reasonable agreement with the results of experiments by Byfield, Kessler, and Lederman[10] and by Isaacs, Sachs, and Steinberger[11] on the elastic scattering of negative pions of energy 62 and 90 Mev by carbon.

The diffraction scattering is predominantly forward and has the effect of spreading the pion beam laterally. The Coulomb scattering also contributes to the lateral spread of the beam. Although the two types of scattering have a different origin and a different angular distribution, it was considered sufficient for the present purpose to treat both effects together in a simple, if approximate, way. This was done by assuming that the pion beam at the last counter had a Gaussian distribution with total mean square radial displacement $\sum_i\langle r_i^2\rangle_{Av}$ given by the sum of the mean square displacements due to (a) original spread of the beam; (b) spread due to Coulomb scattering; and (c) spread due to diffraction scattering. The fraction of pions not recorded by the last counter is then

$$f=\exp(-R^2/\textstyle\sum_i\langle r_i^2\rangle_{Av}), \quad (6)$$

where R is the effective radius (3.81 cm) of the last counter.

The original spread of the beam is determined by the size of the first two crystals (2.54×2.54 cm^2) and the distance x_1 and x_2 of the crystals No. 1 and No. 2 to the last counter. In the present case,

$$\langle r_0^2\rangle_{Av}=1.08(x_1^2+x_2^2)/(x_1-x_2)^2. \quad (7)$$

[10] Byfield, Kessler, and Lederman, Phys. Rev. **85**, 718 (1952).
[11] Isaacs, Sachs, and Steinberger, Phys. Rev. **85**, 718 (1952).

The spread of the beam due to multiple Coulomb scattering may be calculated from a knowledge of the radiation length in the absorber[9] using the formula

$$\langle r_a^2\rangle_{Av}=(0.0226/\eta^2\beta^2)(\delta n/D_n)x_n^2, \tag{8}$$

where x_n is the distance from the center of the nth scatterer to a point 1 cm inside the last counter and $\delta n/D_n$ is the ratio of the thickness to radiation length of the nth scatterer, η is the momentum of the pions in units of μc, and $\beta=v/c$. The radiation lengths for the absorbers used are listed in Table V.

In the case of the second crystal the spread of the beam due to Coulomb scattering is given by

$$\langle r_c^2\rangle_{Av}=(0.000565/\eta^2\beta^2)x_c^2. \tag{9}$$

For the spread due to diffraction scattering, the fraction of those pions diffracted at angles less than θ_0 was computed for each absorber using the formula

$$g=\frac{2\pi}{\sigma_a}\int_0^{\theta_0}\frac{d\sigma_d}{d\Omega}\sin\theta d\theta. \tag{10}$$

For this fraction the mean square radial displacement at the last counter due to the diffraction in the last absorber alone is given by

$$\langle r_d^2\rangle_{Av}=x_a^2\frac{2\pi}{g\sigma_a}\int_0^{\theta_0}\tan^2\theta\frac{d\sigma_d}{d\Omega}\sin\theta d\theta. \tag{11}$$

TABLE VI. Comparison of thick and thin absorber cross sections in the 145-Mev beam.

Absorber	Absorption and inelastic scattering cross sections (10^{-27} cm^2)
C_1	362± 40
C_2	401± 54
Al_1	582± 50
Al_2	583± 58
Cu_1	978± 76
Cu_2	1080± 72
Pb_1	2262±157
Pb_2	2462±152

Then write

$$\langle r_1^2\rangle_{Av}=\langle r_0^2\rangle_{Av}+\langle r_c^2\rangle_{Av} \tag{12}$$

$$\langle r_2^2\rangle_{Av}=\langle r_1^2\rangle_{Av}+\langle r_a^2\rangle_{Av} \tag{13}$$

$$\langle r_3^2\rangle_{Av}=\langle r_2^2\rangle_{Av}+\langle r_d^2\rangle_{Av}. \tag{14}$$

The fractional acceptance of the last counter with no absorber is proportional to $1-\exp(-R^2/\langle r_1^2\rangle_{Av})$.

In calculating the fractional acceptance with absorber it was assumed that the absorption cross section and the total diffraction cross section have the same value σ. The fraction of pions transmitted by the absorber without being absorbed is $\exp(-\sigma N)$. Of this the fraction $1-\exp(-\sigma N)$ are diffracted and $\exp(-\sigma N)$ are transmitted without being diffracted. The latter have a mean square displacement $\langle r_2^2\rangle_{Av}$ so that the fraction $1-\exp(-R^2/\langle r_2^2\rangle_{Av})$ will be recorded. Of the diffracted pions only $g\,[1-\exp(-R^2/\langle r_3^2\rangle_{Av})]$ will be recorded.

The cross section corrected for spread of the beam effects is obtained by writing instead of (2),

$$\frac{Q/D \text{ with absorber}}{Q/D \text{ without absorber}}=\frac{e^{-\sigma N}\{e^{-\sigma N}[1-\exp(-R^2/\langle r_2^2\rangle_{Av})]+g(1-e^{-\sigma N})[1-\exp(-R^2/\langle r_3^2\rangle_{Av})]\}}{1-\exp(-R^2/\langle r_1^2\rangle_{Av})}. \tag{15}$$

From the data of Bernardini, Booth, and Lederman[2,12] it was estimated that 4±2 percent of the pions were scattered inelastically in the forward direction such that they would give a quadruple coincidence. The cross sections computed using (15) were increased by 11±5 percent to account for the muon-electron contamination of the beams and the inelastically scattered pions which gave quadruple coincidences. The resulting total cross sections for absorption plus inelastic scattering are listed in Table VII.

If the beam were better defined geometrically the effect of the multiple Coulomb scattering would be negligible. In the present experiments it leads to corrections to the cross sections which range from 0 percent (carbon) to 7.5 percent (lead) in the 122-Mev beam and from 0 percent (carbon) to 2.5 percent (26.3 g/cm^2 lead) in the 145-Mev beam. The corrections to the cross sections due to diffraction scattering range from 8 percent (lead) to 20 percent (carbon) in the 122-Mev beam and from 6 percent (13.6 g/cm^2 lead) to 21 percent (5.1 g/cm^2 carbon) in the 145-Mev beam.

In Table VI the cross sections obtained using (15) are listed for the measurements with the 145-Mev beam in which two thicknesses of absorber were used. The cross sections obtained with the thick absorbers are somewhat higher than those obtained with the thin absorbers. This indicates that the spread of the beam

TABLE VII. Absorption plus inelastic scattering cross sections.

Absorber	Absorption + inelastic scattering cross sections (10^{-27} cm^2) 113 Mev	137 Mev	Geometrical cross sections (10^{-27} cm^2) $\pi A^{2/3}(\hbar/\mu c)^2$
C	340± 50	360± 40	322
Al	570± 70	580± 50	553
Cu	940± 90	980± 80	977
Cd	1480±150	1570±110	1430
Sn	1500±160	1510±130	1480
Pb	2350±250	2260±160	2150

[12] Bernardini, Booth, and Lederman, Phys. Rev. **83**, 1277 (1951).

effects have been underestimated. For this reason an uncertainty amounting to 50 percent of the diffraction correction was included in computing the errors listed in Table VII, which lists the cross sections obtained from the thin absorber measurements alone.

The general result is that the nuclear cross sections for absorption plus inelastic scattering of negative pions in the energy range 85 to 137 Mev are close to the geometrical values.

I wish to thank Professor Herbert L. Anderson for his guidance and encouragement throughout this research and Mr. Gaurang B. Yodh for his assistance in conducting the experiment and assembling the equipment.

PHYSICAL REVIEW VOLUME 87, NUMBER 6 SEPTEMBER 15, 1952

Effect of Minority Carriers on the Breakdown of Point Contact Rectifiers

ERNST BILLIG
Research Laboratory, Associated Electrical Industries, Ltd., Aldermaston Court, Aldermaston, Berkshire, England
(Received May 13, 1952)

On the application of short high voltage pulses to point contact rectifiers in the inverse direction thermal instability is observed. Intrinsic conduction due to the thermal generation of electron-hole pairs and the subsequent passage of minority carriers (which are not affected by the potential barrier) is suggested as the cause of electrical breakdown.

IT is well known that the standard barrier layer theory of rectification[1,2] fails to account for the phenomenon of electrical breakdown. Various mechanisms have been suggested to explain the large increase in leakage current observed when the voltage approaches a critical value. As the electrical field in the barrier layer is increased on application of a higher voltage, the following phenomena occur:

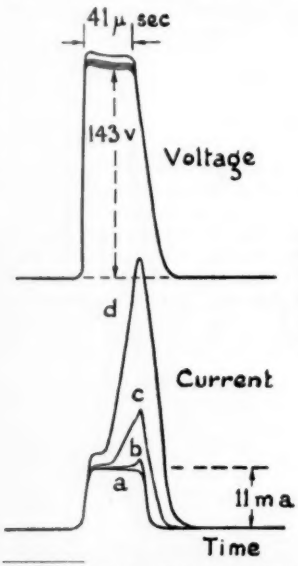

FIG. 1. Thermal instability demonstrated by the application to a Ge point contact diode of constant voltage pulses, with the pulse height increasing from curve *a* to *d*.

1. The image force[3] reduces the effective barrier height greatly easing the passage of carriers from the metal over the barrier into the semiconductor.

2. The barrier becomes sufficiently thin for carriers to tunnel[4] across it. Neither of these mechanisms by itself nor in combination is sufficient to account quantitatively for the experimental observations.

3. The power dissipated in the point contact may raise it locally to a temperature (~150°C in Ge, ~500°C in Si) sufficient for the onset of intrinsic conductivity.[5]

Thermal instability of the barrier layer has recently been shown[6] to account quantitatively for the observed breakdown values in large area (Se) rectifiers. Clear evidence for such instability in point contact rectifiers is given by the cathode-ray oscillogram traced in Fig. 1. Constant voltage pulses[7] of about 40 μsec duration,[8] produced by a low impedance generator, were applied at the rate of 300 per second to a commercial Ge point contact diode (B.T.H. Type CG1) in the inverse direction. Apart from the initial charging peak (not recorded), the current remained constant (curve a). When a certain critical voltage (U_0 = 143 volts) was applied, the current was observed to start rising rather suddenly towards the end of the pulse (curve b). As the voltage was raised only very slightly, the onset of the current

[1] W. Schottky, Z. Physik **118**, 539 (1942).
[2] N. F. Mott, Proc. Roy. Soc. (London) **A171**, 27 (1939).
[3] H. A. Bethe, unpublished MIT Radiation Laboratory Report No. 43–12 (1942).
[4] E. Courant, unpublished Cornell University report (1943).
[5] S. Benzer, J. Appl. Phys. **20**, 804 (1949).
[6] E. Billig, Proc. Roy. Soc. (London) **A207**, 156 (1951).
[7] This was first demonstrated by the author during a lecture on "The Physics of Transistors" given before the Institute of Physics in London on 18th March, 1952. I am indebted to Mr. M. S. Ridout for taking these oscillograms for me.
[8] Considerably shorter pulses (<1 μsec) have been used by Bennett and Hunter (Phys. Rev. **81**, 152 (1951)). The much higher voltage that contact rectifiers can withstand for such short times is in perfect agreement with the postulate of thermal instability (see reference 6).

rise occurred earlier and the current continued rising at a faster rate (curves c, d). With the voltage exceeding U_0 by only a few volts the current became excessive, being limited mainly by the external resistance. The critical voltage agreed closely with the "turn-over" value obtained on application of a continuous 50-cycle voltage.[9]

No proper explanation seems to have been given so far for the large increase in leakage current observed as the voltage is raised and the contact point reaches high temperature. In the usual rectifier model[1,2] current carriers are taken to flow from the metal into the semiconductor on application of inverse voltage; but the number of carriers available in the metal is not increased by high temperature. The explanation seems to be that by the mechanisms 1 and 2 described above—image force and tunnel effect—the current rises beyond the saturation value postulated in the simple theory. The ensuing power loss raises the local temperature at the contact point until intrinsic conduction sets in. Electrons are thus raised into the conduction band at a fast rate, leaving the same number of holes behind in the valency band. These electron-hole pairs are generated within the barrier or in its neighborhood sufficiently close by to drift towards it within their lifetime (10^{-6} to 10^{-4} second). Although the barrier is practically insuperable for the predominant carriers (electrons in *n*-type germanium), there is, of course, no barrier to stop the minority carriers (holes). This part of the leakage current is thus expected to rise exponentially with temperature and to become dominant as the intrinsic temperature is approached. The possibility of electrons and holes simultaneously carrying the current has already been discussed,[10] but the origin of the minority carriers, namely, intrinsic generation, seems to have escaped explanation so far.

[9] The current pulse as displayed on the cathode-ray screen remained steady for curves a and b. When the mean power exceeded about 25 mw, the current pulse crept up visibly. The power loss then apparently exceeded the heat dissipation, with the rectifier temperature increasing from one pulse to the next.

[10] J. Bardeen and W. H. Brattain, Phys. Rev. **75**, 1208 (1949).

PHYSICAL REVIEW VOLUME 87, NUMBER 6 SEPTEMBER 15, 1952

Equivalence Theorems for Pseudoscalar Coupling*

J. M. Berger,† L. L. Foldy, and R. K. Osborn‡
Case Institute of Technology, Cleveland, Ohio
(Received May 14, 1952)

By a unitary transformation a rigorous equivalence theorem is established for the pseudoscalar coupling of pseudoscalar mesons (neutral and charged) to a second-quantized nucleon field. By the transformation the linear pseudoscalar coupling is eliminated in favor of a nonlinear pseudovector coupling term together with other terms. Among these is a term corresponding to a variation of the effective rest mass of the nucleons with position through its dependence on the meson potentials. The question of the connection of the nonlinear pseudovector coupling with heuristic proposals that such a coupling may account for the saturation of nuclear forces and the independence of single nucleon motions in nuclei is briefly discussed. The new representation of the Hamiltonian may have particular value in constructing a strong coupling theory of pseudoscalar coupled meson fields. Some theorems on a class of unitary transformations of which the present transformation is an example are stated and proved in an appendix.

INTRODUCTION

In a recent communication[1] by one of the present authors it was demonstrated that by performing a particular unitary transformation on the Hamiltonian describing the interaction of a nucleon with a neutral pseudoscalar meson field through pseudoscalar coupling a new representation of the Hamiltonian was obtained which gave prominence to some features of this theory which are obscured in the usual representation. The present paper is the first of a series whose purpose is to generalize these results and to investigate, and perhaps exploit, their significance in our understanding of nucleonic properties and nuclear forces.

The unitary transformation referred to above can be regarded as generating a rigorous equivalence theorem, correct to all orders in the coupling constant, connecting the simple pseudoscalar coupling in the original representation with pseudovector coupling in the new representation. The latter is particularly interesting because the pseudovector coupling term has a nonlinear character of a type which one would anticipate would lead to saturating of the nucleon-meson coupling in the presence of large meson potentials. The attractive possibility is therefore suggested that within the framework of the ordinary pseudoscalar meson theory with simple pseudoscalar coupling may lie just the elements of nonlinear behavior responsible for the saturation of nuclear forces and for the relative independence of one-particle motions in nuclei (as evidenced by nuclear shell structure) which have been proposed on a heuristic

* Supported by the AEC.
† AEC Predoctoral Fellow.
‡ Now at Oak Ridge National Laboratory, Oak Ridge, Tennessee.
[1] L. L. Foldy, Phys. Rev. **84**, 168 (1951).

basis by several workers.[2] The new representation also has the advantage of exhibiting the Hamiltonian in a form in which nonrelativistic strong-coupling methods can be applied to its investigation; in the conventional representation, the pseudoscalar theory with pseudoscalar coupling has evaded such treatment. However, further discussion of these points will be left for succeeding papers in this series and the present paper will be concerned only with the establishment of rigorous equivalence theorems. We may then justify our attention to the present results simply on the basis that in view of recent experimental evidence favoring the pi-meson as having pseudoscalar character,[3] any new results concerning the properties of pseudoscalar fields may prove to have value in the future.

Previous derivations of equivalence theorems[4] have been concerned with obtaining a pseudoscalar coupling which is equivalent to a given pseudovector coupling. In the present treatment the emphasis is reversed, pseudoscalar couplings being reduced (to within certain other coupling terms) to an equivalent pseudovector coupling. The virtue of this procedure is that it makes easier the transition to an appropriate nonrelativistic Hamiltonian for the study of nonrelativistic problems. In the present paper the results of the earlier communication referred to above, which dealt with the case of a single nucleon interacting with a neutral pseudoscalar field, have been generalized by dealing with nucleons in the second-quantized representation and by considering four types of meson fields: two types of neutral fields, the charged field, and the symmetrical field. The work has also been carried out only in the Schrödinger representation though there appears to exist no difficulty in generalizing the results to the interaction representation. The execution of the transformations is effected in the following section. Use is made there of several theorems on unitary transformations which may have wider application than in the establishment of the present results. Statements and proofs of these theorems are given in an appendix.

RIGOROUS EQUIVALENCE THEOREMS

In this section we shall actually carry out the type of canonical transformation referred to in the introduction in order to derive rigorous equivalence theorems for pseudoscalar coupling. We do not attempt to derive the theorem in its most general form but content ourselves with four special cases: (1) the charge-symmetrical neutral theory in which the coupling constants of the neutron and proton to the neutral meson field have the same sign, (2) the charge-antisymmetrical neutral theory in which the coupling constants have opposite sign, (3) the charged theory, and (4) the symmetrical theory. The last is, of course, a combination of (2) and (3) with equal coupling constants for neutral and charged mesons. Complete generality has not been attempted in that an arbitrary mixture of all meson fields has not been considered, nor has the inclusion of pseudovector coupling in the original Hamiltonian. The interaction of the particles with electromagnetic fields has also been omitted. The methods employed can all be generalized to take care of these omissions, but it was not felt worthwhile to consider a more general case without some specific application of it in view. In order to avoid duplication of effort and to save space we shall introduce a notation which allows all of these cases to be treated together.

Our notation is as follows: We employ φ_0 to represent the potential of the charge-symmetrical neutral meson field, φ_1 and φ_2 to represent the potentials of the charged meson field, and φ_3 to represent the potential of the charge-antisymmetrical neutral meson field; π_0, π_1, π_2, and π_3 represent respective canonically conjugate momenta.[5] We employ τ_1, τ_2, and τ_3 to represent the components of the isotopic spin vector of the nucleon field, and where convenient we also use τ_0 to represent the unit isotopic spin matrix. To unify the treatment of the four different cases we introduce the quantities

$$\Phi=\tau_i\varphi_i, \quad \Pi=\tau_i\pi_i, \quad \phi=(\varphi_i\varphi_i)^{\frac{1}{2}}.$$

Here and in what follows a repeated Latin subscript is to be summed over the following values:

0 (only) in the charge-symmetrical neutral theory;
3 (only) in the charge-antisymmetrical neutral theory;
1, 2 in the charged theory;
1, 2, and 3 in the symmetrical theory.

The following relation then holds in all cases:

$$\Phi^2=\phi^2.$$

We may now write the Hamiltonian in all cases in the form

$$\mathcal{H}=\mathcal{H}_n+\mathcal{H}_\mu+\mathcal{H}_i,$$

where

$$\mathcal{H}_n=\int\psi^*(\beta M+\boldsymbol{\alpha}\cdot\mathbf{p})\psi d\mathbf{x}$$

$$\mathcal{H}_\mu=\tfrac{1}{2}\int[\pi_i\pi_i+\nabla\varphi_i\cdot\nabla\varphi_i+\mu^2\varphi_i\varphi_i]d\mathbf{x}$$

$$\mathcal{H}_i=if\int\psi^*\beta\gamma^5\Phi\psi d\mathbf{x}.$$

Here ψ^* and ψ represent the wave functions of the

[2] L. I. Schiff, Phys. Rev. **80**, 137 (1950); **83**, 239 (1951); **84**, 1, 10 (1951). See also: W. Heisenberg, Z. Naturforsch. **5a**, 251 (1950); R. Finkelstein and M. Ruderman, Phys. Rev. **81**, 655 (1951); F. Bloch, Phys. Rev. **83**, 1062 (1951).

[3] See, for example, R. E. Marshak, Revs. Modern Phys. **23**, 137 (1951).

[4] E. C. Nelson, Phys. Rev. **60**, 830 (1941); F. J. Dyson, Phys. Rev. **73**, 929 (1948); K. M. Case, Phys. Rev. **76**, 1 (1949).

[5] The connection between φ_1, φ_2, π_1, π_2 and the usual variables φ, φ^*, π, π^* employed to represent the charged meson field is given by the following equations:

$$\varphi_1=(\varphi^*+\varphi)/\sqrt{2}, \quad \varphi_2=i(\varphi^*-\varphi)/\sqrt{2},$$
$$\pi_1=(\pi+\pi^*)/\sqrt{2}, \quad \pi_2=i(\pi-\pi^*)/\sqrt{2}.$$

proton-neutron field in the usual eight-component representation, M represents the nucleon mass, μ the meson mass, g is the coupling constant (in rationalized units), $\mathbf{p}$ is the operator $-i\nabla$, and units are employed in which $\hbar$ and c are unity. Quantities which are functions of position such as $\psi^*(\mathbf{x})$ and $\pi(\mathbf{x})$ will be primed when they are to be evaluated at a primed coordinate, *viz.*, $\psi^{*\prime}=\psi^*(\mathbf{x}')$, $\pi'=\pi(\mathbf{x}')$, etc.

We now wish to perform a unitary transformation on the Hamiltonian:

$$H=e^{iS}\mathcal{H}e^{-iS},$$

with the provision that the generator of the transformation S be so determined that the pseudoscalar coupling term is eliminated from the Hamiltonian in favor of a pseudovector coupling term. We assume that S can be written in the form

$$S=\int\psi^*s\psi d\mathbf{x},\quad s=\gamma^5(\Phi/\phi)w,$$

where $w'=w[\phi(x')]$ is a function of ϕ' only.

The actual execution of the unitary transformation is facilitated by the use of several general theorems on unitary transformations of this type whose statement and proof are given in the Appendix. By the use of Theorem III of the Appendix we may write

$$\begin{aligned}
e^{iS}&\int\psi^*(\beta M+if\beta\gamma^5\Phi)\psi d\mathbf{x}e^{-iS}\\
&=\int\psi^*e^{is}(\beta M+if\beta\gamma^5\Phi)e^{-is}\psi d\mathbf{x}\\
&=\int\psi^*\left(\cos w+i\gamma^5\frac{\Phi}{\phi}\sin w\right)(\beta M+if\beta\gamma^5\Phi)\\
&\qquad\times\left(\cos w-i\gamma^5\frac{\Phi}{\phi}\sin w\right)\psi d\mathbf{x}\\
&=\int\psi^*\left[\beta M\left(\cos 2w+\frac{f\phi}{M}\sin 2w\right)\right.\\
&\qquad\left.+if\beta\gamma^5\Phi\left(\cos 2w-\frac{M}{f\phi}\sin 2w\right)\right]\psi d\mathbf{x},
\end{aligned}$$

and the employment of the same theorem gives us

$$\begin{aligned}
e^{iS}&\int\psi^*\boldsymbol{\alpha}\cdot\mathbf{p}\psi d\mathbf{x}e^{-iS}=\int\psi^*e^{is}\boldsymbol{\alpha}\cdot\mathbf{p}e^{-is}\psi d\mathbf{x}\\
&=\int\psi^*\left(\cos w+i\gamma^5\frac{\Phi}{\phi}\sin w\right)\boldsymbol{\alpha}\cdot\mathbf{p}\\
&\qquad\times\left(\cos w-i\gamma^5\frac{\Phi}{\phi}\sin w\right)\psi d\mathbf{x}\\
&=\int\psi^*\left[\boldsymbol{\alpha}\cdot\mathbf{p}-\frac{\Phi}{\phi}\frac{dw}{d\phi}\boldsymbol{\sigma}\cdot\nabla\phi-\frac{1}{2}\sin 2w\boldsymbol{\sigma}\cdot\nabla\left(\frac{\Phi}{\phi}\right)\right.\\
&\qquad\left.-i\sin^2 w\frac{\Phi}{\phi}\boldsymbol{\alpha}\cdot\nabla\left(\frac{\Phi}{\phi}\right)\right]\psi d\mathbf{x}\\
&=\int\psi^*\left[\boldsymbol{\alpha}\cdot\mathbf{p}-\frac{dw}{d\phi}\boldsymbol{\sigma}\cdot\nabla\Phi-\left\{\frac{1}{2}\sin 2w-\phi\frac{dw}{d\phi}\right\}\boldsymbol{\sigma}\cdot\nabla\left(\frac{\Phi}{\phi}\right)\right.\\
&\qquad\left.-\frac{i}{2}\sin^2 w\left\{\frac{\Phi(\boldsymbol{\alpha}\cdot\nabla\Phi)-(\boldsymbol{\alpha}\cdot\nabla\Phi)\Phi}{\phi^2}\right\}\right]\psi d\mathbf{x}.
\end{aligned}$$

We also have

$$\begin{aligned}
e^{iS}&\tfrac{1}{2}\int[\nabla\varphi_i\cdot\nabla\varphi_i+\mu^2\varphi_i\varphi_i]d\mathbf{x}e^{-iS}\\
&=\tfrac{1}{2}\int[\nabla\varphi_i\cdot\nabla\varphi_i+\mu^2\varphi_i\varphi_i]d\mathbf{x},
\end{aligned}$$

so that the only remaining term to be evaluated is $e^{iS}\frac{1}{2}\int\pi_i\pi_i d\mathbf{x}e^{-iS}$. To evaluate this term we write it as

$$\tfrac{1}{2}\int e^{iS}\pi_i e^{-iS}e^{iS}\pi_i e^{-iS}d\mathbf{x},$$

and then make use of Theorem I of the Appendix to write

$$\begin{aligned}
e^{iS}\pi_i e^{-iS}&=\pi_i+i\int\psi^{*\prime}[s',\pi_i]\psi' d\mathbf{x}'\\
&=\pi_i-\psi^*\gamma^5\frac{d\Phi}{d\varphi_i}\frac{dw}{d\phi}\\
&\qquad-\psi^*\pi^5\left[\frac{1}{2}\sin 2w-\phi\frac{dw}{d\phi}\right]\frac{d}{d\varphi_i}\left(\frac{\Phi}{\phi}\right)\psi\\
&\qquad-\frac{i}{2}\psi^*\frac{\sin^2 w}{\phi^2}\left[\Phi\frac{d\Phi}{d\varphi_i}-\frac{d\Phi}{d\varphi_i}\Phi\right]\psi.
\end{aligned}$$

On examining these results we note that the pseudoscalar coupling term can be eliminated by the choice

$$w(\phi)=\tfrac{1}{2}\tan^{-1}(f\phi/M).$$

Combining all of the above results, carrying out some simplifications, and introducing the abbreviation

$$M^*=M(1+f^2\phi^2/M^2)^{\frac{1}{2}},$$

the transformed Hamiltonian can be written as

$$H=e^{iS}\mathcal{H}e^{-iS}=\mathcal{H}_n+\mathcal{H}_\mu+H_1+H_2+H_3+H_4+H_5,$$

where $\mathcal{H}_n$ and $\mathcal{H}_\mu$ have the same meanings as above and

$$H_1=\int\psi^*(M^*-M)\psi d\mathbf{x},$$

$$H_2=-\frac{f}{4}\int\psi^*\left[\frac{M}{(M^*)^2}(\boldsymbol{\sigma}\cdot\nabla\Phi+\gamma^5\Pi)\right.$$
$$\left.+(\boldsymbol{\sigma}\cdot\nabla\Phi+\gamma^5\Pi)\frac{M}{(M^*)^2}\right]\psi d\mathbf{x},$$

$$H_3=-\frac{f}{4}\int\psi^*\left[\frac{M^*-M}{\phi^2(M^*)^2}(\phi^2\tau_i-\Phi\varphi_i)(\boldsymbol{\sigma}\cdot\nabla\varphi_i+\gamma^5\pi_i)\right.$$
$$\left.+(\boldsymbol{\sigma}\cdot\nabla\varphi_i+\gamma^5\pi_i)(\phi^2\tau_i-\Phi\varphi_i)\frac{M^*-M}{\phi^2(M^*)^2}\right]\psi d\mathbf{x},$$

$$H_4=-\frac{i}{8}\int\psi^*\left[\frac{M^*-M}{\phi^2M^*}(\Phi\tau_i-\tau_i\Phi)(\boldsymbol{\alpha}\cdot\nabla\varphi_i+\pi_i)\right.$$
$$\left.+(\boldsymbol{\alpha}\cdot\nabla\varphi_i+\pi_i)(\Phi\tau_i-\tau_i\Phi)\frac{M^*-M}{\phi^2M^*}\right]\psi d\mathbf{x},$$

$$H_5=\frac{1}{8}\int\left\{\psi^*\left[\gamma^5\frac{fM\tau_i}{(M^*)^2}+\frac{f\gamma^5(M^*-M)}{\phi^2(M^*)^2}(\phi^2\tau_i-\Phi\varphi_i)\right.\right.$$
$$\left.\left.+\frac{iM^*-M}{2\phi^2M^*}(\Phi\tau_i-\tau_i\Phi)\right]\psi\right\}^2 d\mathbf{x}.$$

We now discuss briefly the nature of the various interaction terms. H_1 represents a nonlinear spin-independent coupling of the meson field to the nucleons; its (meson) vacuum expectation value can be directly interpreted as a contribution to the renormalization of the nucleon mass. H_2 represents a simple pseudovector coupling term but with a nonlinear coefficient of a type which one would expect to lead to saturation effects in strong meson potentials. H_3 is a somewhat more complicated nonlinear pseudovector coupling term which vanishes in the two neutral meson theories. It is probably associated with the correlations existing between the emission of successive charged mesons resulting from the change in the isotopic spin coordinate of the nucleons. H_4 which also vanishes in the two neutral meson theories, represents a nonlinear vector coupling of the meson field to the nucleons of a rather unfamiliar character. H_5 represents a "contact" or "direct" interaction term; the second and third terms in the bracket in H_5 vanish for the two neutral meson theories.

It will be noted that when $\mathfrak{IC}_n$ and H_1 are combined they form a Hamiltonian corresponding to nucleons whose effective rest mass M^* is a function of position through its dependence on the meson potential: $M^*=(M^2+f^2\phi^2)^{\frac{1}{2}}$. In a succeeding paper some indications will be pointed out that this position dependence of the mass leads to such strong repulsion between nucleons at separations of the order of the meson Compton wavelength or smaller as possibly to preclude the existence of any bound states between two nucleons.

A final point which is worth mentioning is that the present calculations (as well as the earlier calculation of Dyson[4]) demonstrate that the distinction between a meson-nucleon coupling which is linear in the meson potential and one which is nonlinear is largely artificial in that a linear coupling in one representation of the Hamiltonian may be strongly nonlinear in another representation.

APPENDIX. SOME THEOREMS ON UNITARY TRANSFORMATIONS

Notation:

Let $\psi_\alpha^*(\mathbf{x})$ and $\psi_\alpha(\mathbf{x})$ with α running through the values 1, 2, $\cdots$, n be a set of operators which are functions of position and which obey the Jordan-Pauli anticommutation relations:

$$[\psi_\alpha^*(\mathbf{x}),\psi_\beta(\mathbf{x}')]_+=\delta_{\alpha\beta}\delta(\mathbf{x}-\mathbf{x}'),$$
$$[\psi_\alpha^*(\mathbf{x}),\psi_\beta^*(\mathbf{x}')]_+=[\psi_\alpha(\mathbf{x}),\psi_\beta(\mathbf{x}')]_+=0.$$

The quantities $s_{\alpha\beta}(\mathbf{x})$ represent the matrix elements of an $n\times n$ Hermitian matrix $s(\mathbf{x})$. The matrix elements of the matrix s are assumed to commute with one another and with ψ^* and ψ. The quantity S is defined by

$$S=\int\psi_\alpha^*(\mathbf{x})s_{\alpha\beta}(\mathbf{x})\psi_\beta(\mathbf{x})d\mathbf{x},$$

where repeated indices are summed from 1 to n in accordance with the usual summation convention. The $\alpha\beta$ element of a function $f(s)$ of the matrix s will be written $\{f(s)\}_{\alpha\beta}$. For example,

$$\{e^{is}\}_{\alpha\beta}=\delta_{\alpha\beta}+is_{\alpha\beta}-s_{\alpha\gamma}s_{\gamma\beta}/2!-is_{\alpha\gamma}s_{\gamma\delta}s_{\delta\beta}/3!+\cdots.$$

The quantity $Q_{\alpha\beta}(\mathbf{x},\partial/\partial\mathbf{x})$ is the $\alpha\beta$ element of an $n\times n$ matrix which is not necessarily Hermitian. The matrix elements of Q are assumed to commute with $\psi^*(\mathbf{x}')$ and $\psi(\mathbf{x}')$, but because of the presence of the differentiation operators, they do not commute with $\psi^*(\mathbf{x})$ and $\psi(\mathbf{x})$; they do not necessarily commute with the matrix elements of s.

Where no confusion can arise, subscripts will be dropped from matrix products, *viz.*,

$$\psi_\alpha^*(\mathbf{x}')\{e^{is(\mathbf{x}')}\}_{\alpha\beta}Q_{\beta\gamma}(\mathbf{x})\{e^{-is(\mathbf{x})}\}_{\gamma\delta}\psi_\delta(\mathbf{x}')$$
$$\equiv\psi^*(\mathbf{x}')e^{is(\mathbf{x}')}Q(\mathbf{x})e^{-is(\mathbf{x})}\psi(\mathbf{x}').$$

Position coordinates of which operators are functions will be suppressed by writing ψ_α^* for $\psi_\alpha^*(\mathbf{x})$ and $Q_{\alpha\beta}'$ for $Q_{\alpha\beta}(\mathbf{x}')$, for example.

The following readily established theorem will be used extensively in the proofs given below:

$$[\psi^*A\psi,\psi^{*\prime}B'\psi']=[\psi_\alpha^*A_{\alpha\beta}\psi_\beta,\psi_\gamma^{*\prime}B_{\gamma\delta}'\psi_\delta']$$
$$=\psi_\gamma^{*\prime}\psi_\alpha^*[A_{\alpha\beta}B_{\gamma\delta}'-B_{\gamma\delta}'A_{\alpha\beta}]\psi_\beta\psi_\delta'$$
$$+\psi_\alpha^*[A_{\alpha\beta}B_{\beta\gamma}'-B_{\alpha\delta}'A_{\beta\gamma}]\psi_\gamma\delta(\mathbf{x}-\mathbf{x}')$$
$$=\psi_\gamma^{*\prime}\psi_\alpha^*[A_{\alpha\beta},B_{\gamma\delta}']\psi_\beta\psi_\delta'$$
$$+\psi_\alpha^*[A,B']_{\alpha\gamma}\psi_\gamma\delta(\mathbf{x}-\mathbf{x}'). \quad \text{(A-1)}$$

Here A and B' are two $n\times n$ matrices.

Theorem I:

$$e^{iS}\psi_\alpha e^{-iS}=\{e^{-is}\}_{\alpha\beta}\psi_\beta=\{e^{is}\psi\}_\alpha,$$

or

$$e^{iS}\psi e^{-iS}=e^{-is}\psi.$$

Proof: Define

$$\psi_\alpha{}^\xi=e^{i\xi S}\psi_\alpha e^{-i\xi S}.$$

Then

$$\psi_\alpha{}^{\xi+d\xi}=\psi_\alpha{}^\xi+(\partial\psi_\alpha{}^\xi/\partial\xi)d\xi=e^{id\xi S}\psi_\alpha{}^\xi e^{-id\xi S}$$
$$=\psi_\alpha{}^\xi+id\xi[S,\psi_\alpha{}^\xi],$$

so

$$\partial\psi_\alpha{}^\xi/\partial\xi=i[S,\psi_\alpha{}^\xi]. \tag{A-2}$$

We will now show that

$$\psi_\alpha{}^\xi=\{e^{-i\xi s}\}_{\alpha\beta}\psi_\beta \tag{A-3}$$

is a solution of Eq. (A-2).

We have on differentiating (A-3)

$$\partial\psi_\alpha{}^\xi/\partial\xi=-i\{e^{-i\xi s}\}_{\alpha\beta}s_{\beta\gamma}\psi_\gamma,$$

and on evaluating the commutator

$$[S,\psi_\alpha{}^\xi]=\int[\psi_\mu{}^{*\prime}s_{\mu\nu}{}'\psi_\nu{}'\{e^{-i\xi s}\}_{\alpha\beta}\psi_\beta$$
$$-\{e^{-i\xi s}\}_{\alpha\beta}\psi_\beta\psi_\mu{}^{*\prime}s_{\mu\nu}{}'\psi_\nu{}']d\mathbf{x}'$$

$$=-\int\{e^{-i\xi s}\}_{\alpha\beta}\delta_{\beta\mu}\delta(\mathbf{x}-\mathbf{x}')s_{\mu\nu}{}'\psi_\nu{}'d\mathbf{x}'$$

$$=-\{e^{-i\xi s}\}_{\alpha\beta}s_{\beta\gamma}\psi_\gamma.$$

Hence we see that the equation is satisfied. Since $\psi_\alpha{}^0=\psi_\alpha$, we obtain on setting $\xi=1$:

$$(\psi_\alpha{}^\xi)_{\xi=1}=e^{iS}\psi_\alpha e^{-iS}=\{e^{-is}\}_{\alpha\beta}\psi_\beta.$$

Corollary:

$$e^{iS}\psi^*e^{-iS}=\psi^*e^{is}.$$

Theorem II:

If

$$[s_{\alpha\beta}{}'',[s_{\gamma\delta}{}',Q_{\mu\nu}]]=0,$$

then

$$e^{iS}Q_{\mu\nu}e^{-iS}=Q_{\mu\nu}+\int\psi_\alpha{}^{*\prime}[\{e^{is'}\}_{\alpha\beta}Q_{\mu\nu}\{e^{-is'}\}_{\beta\gamma}$$
$$-Q_{\mu\nu}\delta_{\alpha\gamma}]\psi_\gamma{}'d\mathbf{x}'$$

$$=Q_{\mu\nu}+i\int\psi_\alpha{}^{*\prime}[s_{\alpha\beta}{}',Q_{\mu\nu}]\psi_\beta{}'d\mathbf{x}'.$$

Proof: Define

$$Q_{\mu\nu}{}^\xi=e^{i\xi S}Q_{\mu\nu}e^{-i\xi S},$$

whence, as in the proof of Theorem I, one finds

$$\partial Q_{\mu\nu}{}^\xi/\partial\xi=i[S,Q_{\mu\nu}{}^\xi].$$

Then making use of the hypothesis together with (A-1) one can readily show that

$$Q_{\mu\nu}{}^\xi=Q_{\mu\nu}+i\xi\int\psi_\alpha{}^{*\prime}[s_{\alpha\beta}{}',Q_{\mu\nu}]\psi_\beta{}'d\mathbf{x}'$$

is a solution of the above equation and by the same reasoning as in Theorem I, one establishes the present theorem. Note that $Q_{\mu\nu}$ is not included in the matrix product occurring under the integral sign. This theorem also holds if $Q_{\mu\nu}$ is not a matrix element of an $n\times n$ matrix but still satisfies the hypothesis. Corollary: If the matrix element $Q_{\mu\nu}$ commutes with all matrix elements of s, then

$$e^{iS}Q_{\mu\nu}e^{-iS}=Q_{\mu\nu}.$$

Theorem III:

If all matrix elements of Q commute with all matrix elements of s then

$$e^{iS}\int\psi_\mu{}^*Q_{\mu\nu}\psi_\nu d\mathbf{x}e^{-iS}\equiv e^{iS}\int\psi^*Q\psi d\mathbf{x}e^{-iS}$$
$$=\int\psi^*e^{is}Qe^{-is}\psi d\mathbf{x}.$$

Proof: We have

$$e^{iS}\int\psi_\mu{}^*Q_{\mu\nu}\psi_\nu d\mathbf{x}e^{-iS}$$
$$=\int e^{iS}\psi_\mu{}^*e^{-iS}e^{iS}Q_{\mu\nu}e^{-iS}e^{iS}\psi_\nu e^{-iS}d\mathbf{x},$$

and using Theorem I and the corollary to Theorem II, we obtain

$$e^{iS}\int\psi^*Q\psi d\mathbf{x}e^{-iS}=\int\psi_\mu{}^*\{e^{is}\}_{\mu\alpha}Q_{\alpha\beta}\{e^{-is}\}_{\beta\nu}\psi_\nu d\mathbf{x}$$
$$\equiv\int\psi^*e^{is}Qe^{-is}\psi d\mathbf{x}.$$

This theorem could also be established by the methods employed in the proof of Theorems I and II.

Diffusion of Barium in Barium Oxide*

R. W. REDINGTON†
Cornell University, Ithaca, New York
(Received May 7, 1952)

The self-diffusion of barium in single crystals of barium oxide has been measured as a function of temperature in the range from 550°K to 1520°K. Two diffusion processes were found. Measurement of the ionic mobility (with a tracer technique) showed that one of these processes was charge-transporting (~2 electronic charges) and the other was not. At temperatures below 1350°K the diffusion was "structure sensitive" and could be affected by previous heat treatment. The temperature dependence for the non-charge-transporting diffusion was 11±2.2 ev above 1350°K and 0.44±0.03 ev below 1350°K. The corresponding figures for the charge-transporting diffusion were 12±2.3 ev and 0.3±0.05 ev. The surface diffusion constant for barium on barium oxide was also measured and had a temperature dependence of 0.16±0.03 ev.

I. INTRODUCTION

THE purpose of this experiment was to measure the internal diffusion constant of barium in barium oxide and the surface diffusion constant as a function of temperature and to determine the charge transported by the diffusing barium. The effects of previous heat treatment on the internal diffusion were also investigated. The study was undertaken for two reasons: (1) quantitative information on the diffusion of barium as a function of temperature is desirable for the interpretation of thermionic experiments with BaO and for studies of its semiconducting properties; (2) diffusion studies on divalent ionic crystals should add to the understanding of ionic crystals, which at present is built largely on experiments on alkali halides.

II. APPARATUS AND PROCEDURE

A radioactive tracer technique was used.[1] The tracer Ba was evaporated onto the surface of a crystal as BaO. After the crystal had been heated for some time the distribution of radioactive Ba in the crystal for the internal diffusion measurements was determined by sectioning the crystal with a microtome and measuring the activity of the sections; for the surface diffusion measurements a movable slit system was used to scan the distribution on the surface. The diffusion constants were calculated from these measured distributions.

The barium 140 used as the tracer was supplied by the Oak Ridge National Laboratories as BaCl in a weak acid solution. After the addition of about 0.1 mg carrier barium per millicurie of barium 140, the barium was precipitated as $BaSO_4$ and deposited in a small platinum evaporator cup in a centrifuge. This $BaSO_4$ was decomposed to the oxide by heating it to about 1100°K in the evaporator. The platinum cup was heated by a tungsten filament, and a platinum heat shield between the crystal sample and the platinum cup exposed the crystal to only the interior of the cup. The temperature of a crystal under normal evaporating conditions was measured with a platinum—platinum 10 percent rhodium thermocouple imbedded in a test crystal. This temperature was only 130°C above room temperature. The usual evaporating time was about one hour and the diffusion during this time, as estimated from the extrapolation of the temperature dependence data to this temperature, was negligible in every case except one (a quenched crystal measurement). For that one case, a correction was made using the diffusion constant from the extrapolation. The pressure during the evaporation was less than 10^{-5} mm of Hg.

The average dimensions of the crystal samples used were about 3×3×1 mm. The crystals for the internal diffusion measurements were mounted in a matrix of barium oxide. These crystal mounts were compressed from powdered barium oxide in a die with about 10^4 pounds/sq in. pressure. They were $\frac{3}{8}$ in. in diameter and about $\frac{1}{2}$ in. long, with a square face of the crystal exposed in one of the end faces. These mounts were sintered for about an hour at 1000°C. After this sintering operation and immediately before they were placed in the evaporator, the exposed crystal surface was ground and polished to present a fresh surface. This type of mount furnished a support during the heating of the crystal with a minimum of contamination and was much more convenient to mount in the microtome than the small crystals.

A sketch of the interior of the vacuum oven used to heat the crystals is shown in Fig. 1. It is shown with a crystal for an internal diffusion run in a crystal mount of sintered barium oxide. This oven was constructed on a male ground glass joint with a 4-lead press which could be sealed into the vacuum system. A second nickel heat shield was supported inside the vacuum system, and the portion of the oven shown in the figure fitted into this heat shield. The inner quartz tube was attached to the press and this tube supported the oven. The oven winding was a tungsten helix, and the current was supplied by a voltage regulating transformer. This temperature regulation was satisfactory as the largest

* This work has received support from a Frederick Gardner Cottrell Grant by the Research Corporation and from the ONR.
† Now at the General Electric Research Laboratory, Schenectady, New York.
[1] The general method and procedure were similar to that used in many previous investigations of diffusion, e.g., Mapother, Crooks, and Maurer, J. Chem. Phys. 18, 1231 (1950).

variation in temperature during a run was about 0.5 percent. The temperature was measured with a 0.007-in. platinum—platinum 10 percent rhodium thermocouple which had been calibrated against a 0.020-in. Leeds and Northrup platinum—platinum 13 percent rhodium thermocouple. The cold junctions were connected to a pair of copper leads waxed through two holes in the water-cooled press. This oven was modified by the addition of two platinum-rhodium electrodes for the ionic mobility measurements, and the modified oven was also used for the surface diffusion measurements.

For the internal diffusion and ionic mobility measurements, the surface of the crystal mount in which the crystal was exposed was removed by filing, and about $\frac{1}{2}$ mm of the four exposed edges of the crystal was removed in this operation. This procedure should eliminate edge effects because $\frac{1}{2}$ mm was large compared to the distances through which measurable diffusion took place.

A microtome was constructed to section the crystal using a standard microtome knife reground to a 45° edge. The crystal holder and advance screw were mounted on the end of a horizontal crank which made sliding contact with a steel way near the knife edge. This steel way and the vertical bearing of the crank determined the cutting plane. The crystals were mounted in a holder which fitted into a chuck on the crystal advance screw. This mounting was done in a jig which indexed against the surface of the crystal to be cut. The worst misalignment observed between the crystal surface and the cutting plane was about 0.005 radian. The variations in the thickness of the sections because of the tendency of the crystal to cleave rather than slice and because of the lack of rigidity of the blade were much more serious than the variations caused by alignment or by variations in the pitch of the advance screw. The material removed in a slice came off as a powder, part of which stuck to the knife blade and part of which fell onto a sample tray placed below the knife. The portion which stuck to the blade was collected with a damp "camel's hair" brush. The material was flushed from the brush with water onto the sample tray. The samples were evaporated to dryness, forming thin sources which could be conveniently counted.

The Geiger counter had a 2.3 mg/cm^2 mica end window, slightly larger than 1 in. in diameter and was shielded with $1\frac{1}{2}$ in. of lead. The sample trays, which were inverted aluminum culture dishes, fitted over a boss on a brass tray which could be placed in a rack with a choice of distances from the counter. This arrangement insured reproducible geometry for the counting operations. Because Ba^{140} has a radioactive daughter product, lanthanum 140, which is also a β, γ-emitter, it was necessary to measure the decay in activity of most of the samples to determine the amount of Ba^{140} that was present. This determination was quite easy as the 40-hour half-life of the La^{140} is appreciably shorter than the 12.8-day half-life of Ba^{140}.

For the surface diffusion measurements, a movable slit system with a $\frac{1}{4}$-mm resolving power was constructed on a tray which fitted into the counter rack. Underneath the slit, a small dry box with a cellophane window was constructed to hold the surface diffusion samples. A dry box was necessary as barium oxide reacts with the water vapor in the air. The slit itself was constructed in $\frac{1}{4}$-in. aluminum and could be moved above the crystal by a micrometer screw.

The crystals used were grown by Dash[2] from the vapor phase on magnesium oxide pseudoseeds. At the time of the low temperature diffusion constant measurements, there were no single crystals available that were large enough to be cleaved into several samples, and most of the data in that temperature range were taken on samples cleaved from a polycrystalline plate. Three measurements in this temperature range were made on samples cleaved from a single crystal. As the measurements on this single crystal and the polycrystalline plate were consistent, the points are not separately identified on the figures. The polycrystalline plate consisted of similarly oriented crystals, about 1 mm across. In the data on these polycrystalline samples, about 3 percent of the radioactive material was found deeper in the crystal than expected from the rest of the distribution. As this did not appear in the single-crystal samples, it was presumed to be caused by grain boundary diffusion and was treated as background. The rest of the data were taken on samples from single crystals which showed only a few small flaws when viewed under 24× magnification. All of the data on the effects of heat treatments were taken on samples cleaved from the same crystal, and all the low temperature ionic mobility measurements were taken on samples cleaved from a similar crystal.

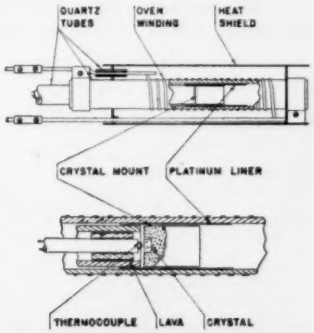

FIG. 1. Sketch of the vacuum oven. The upper figure shows the general arrangement of the oven and the lower figure shows an enlarged view of the immediate surroundings of the crystal.

[2] Sproull, Dash, Tyler, and Moore, Rev. Sci. Instr. 22, 410 (1951).

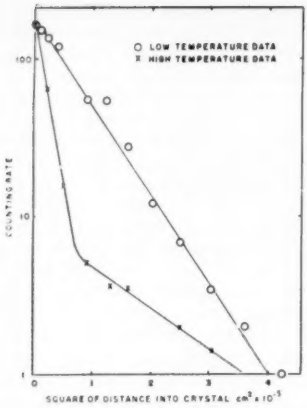

FIG. 2. The counting rate for a section plotted on a log scale against the square of the distance into the crystal at which the section was cut for a distribution obtained below 1350°K and for one obtained above 1350°K.

III. INTERNAL DIFFUSION

The distribution predicted by a solution of the diffusion equation for a one-dimensional, semi-infinite solid with all the tracer material originally at the origin is

$$C=[Q/(\pi Dt)^{\frac{1}{2}}]\exp(-x^2/4Dt),$$

where C is the concentration, Q is the total amount of tracer material, D is the diffusion constant, x is the distance, and t is the time. The counting rate for a section is proportional to the concentration at approximately the center of the section, and thus a plot of the logarithm of the counting rate against the square of the distance should give a straight line with a slope of $-(4Dt)^{-1}$.

The internal diffusion results can be divided into two temperature ranges, a high temperature range from 1350° to 1500°K and a low temperature range from 600° to 1350°K. Not only was the temperature dependence quite different in these two temperature ranges, but the distribution of radioactive Ba was also different. Samples of the two types of distribution are shown in Fig. 2. The low temperature distributions were as predicted, but the high temperature distributions were quite different. The high temperature distribution can be described by two terms of the above type. The quenched crystal results and the ionic mobility measurements show that two diffusion mechanisms were present, and the high temperature data were analyzed in terms of two diffusion constants. The larger diffusion constant (which describes the distribution deep in the crystal) was determined from the smaller slope in the high temperature curve in Fig. 2. The counting rates corresponding to this larger diffusion constant were subtracted from the counting rates near the surface, and the remainders were replotted on a log$C$ *vs* x^2 graph. The smaller diffusion constant which described the distribution near the surface was calculated from the slopes of this plot. On the curves this smaller diffusion constant is referred to as "diffusion near surface."

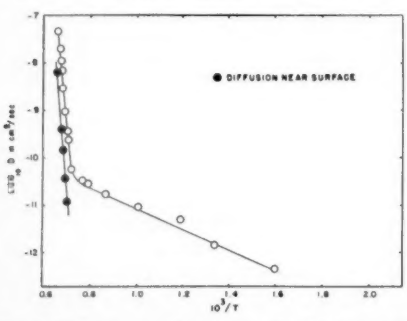

FIG. 3. The temperature dependence of the diffusion constants, log$D$ *versus* $10^3/T$. The open circles represent the non-charge-transporting diffusion and the filled circles the charge-transporting diffusion, which was determined from the distribution near the surface.

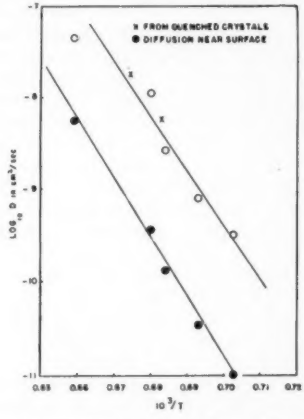

FIG. 4. The temperature dependence of the diffusion constants in the high temperature range. These are the same data as shown in Fig. 3, but plotted on an expanded scale.

The temperature dependence of the diffusion in these BaO crystals is shown in Figs. 3 and 4. Within the experimental error, the diffusion constants can be described by straight lines on these plots of log$D$ *vs* $10^3/T$. Thus the diffusion constants can be described by terms of the form

$$D=D_0\exp(-E/KT).$$

The values of D_0 and E for the various diffusion constants and temperature ranges are presented in Table I.

To investigate the "structure sensitive" low temperature range a series of measurements on the effects of

various heat treatments were made. The results are shown in Fig. 5. Most of the measurements were made at the same temperature, about 1150°K. These data were taken on samples cleaved from a different crystal than those used for the results in Fig. 3. The results of the internal diffusion measurements shown in Fig. 3 are replotted for comparison. An example of the difference in diffusion from crystal to crystal is shown by the measurement on the sample ("untreated crystal" on Fig. 5) which received the same treatment (i.e., mounting and polishing) as the previous crystals. This large variation was presumed to be caused by different impurity concentration. The quenched crystals showed the type of distribution found in the high temperature region with two diffusion constants. These are represented by the open and filled symbols on Fig. 5. The annealed crystal was heated to 1460°K and cooled at a slightly slower rate than that used in growing the crystals. This crystal showed the typical low temperature distribution. Two crystals were quenched simultaneously

TABLE I. Values of D_0 and E for various diffusion constants and temperature ranges. $D=D_0\exp(-E/KT)$.

Temperature range	Diffusion	E ev	D_0 cm²/sec
High	"Deep in crystal"	11 ±2.2	$10^{29\pm7}$
High	"Near the surface" (charged)	12 ±2.3	$10^{31\pm8}$
Low	"Deep in crystal"	0.44±0.03	$10^{-9\pm1}$
Low—crystals quenched from 1460 deg K	"Deep in crystal"	0.5±0.05	$3\times10^{-6\pm1}$
	"Near the surface" (charged)	0.3±0.05	$3\times10^{-10\pm1}$
	Surface diffusion	0.16±0.03	$10^{-6\pm1}$

* Note: These values depend on the crystal used, and for the quenched crystals on the quenching temperature.

from 1460°K. One of these was measured at 1150°K and the other at a lower temperature to give an indication of the temperature dependence. From these data a "deep in the crystal" diffusion constant at 1460°K was calculated using the temperature dependence observed in the unquenched crystals, with the assumption that the defects were "frozen in" at the quenching temperature. A similar calculation was made for the crystal quenched from 1475°K. These two extrapolated points are the X's in Fig. 4. Because they agree with the measured values, they show that the "freezing in" temperature is very nearly the temperature from which they were quenched and that the number of defects in the quenched crystals is approximately the equilibrium number at the quenching temperature.

IV. IONIC MOBILITY

A series of measurements was made using quenched crystals and Ba electrodes[3] at 550°K. Three samples

[3] The initial measurements were made using platinum-rhodium electrodes. With unquenched crystals in the low temperature range, no difference was detected between diffusion with and against the field. A measurement in the high temperature range showed that the slower or "near the surface" diffusion transported approximately 2 electronic charges. Because the operating conditions were unstable at high temperatures, the measurements were continued on quenched crystals in the low temperature range. Measurements on these quenched crystals with the platinum-rhodium electrodes gave inconsistent results (probably caused by polarization of the crystal) of a few tenths of an electronic charge transported by the "near the surface" diffusion and no charge transported by the faster diffusion.

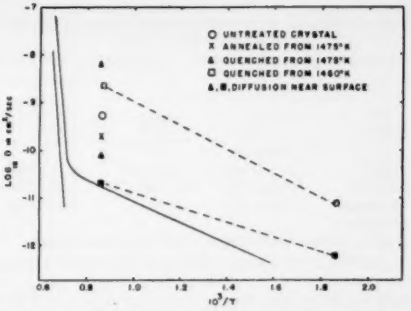

FIG. 5. The effects of heat treatment on the diffusion constants. The curves are replotted from Fig. 3, and the points are the diffusion constants in crystals receiving the treatment indicated in the key. The open symbols represent non-charge-transporting diffusion, and the filled symbols represent charge-transporting diffusion.

were cleaved from a crystal which had been quenched, and then ground and polished until it had two surfaces which were parallel within 0.001 radian. One was used with no field applied across the crystal. The other two were used with fields of 1100 v/cm and 3300 v/cm. The

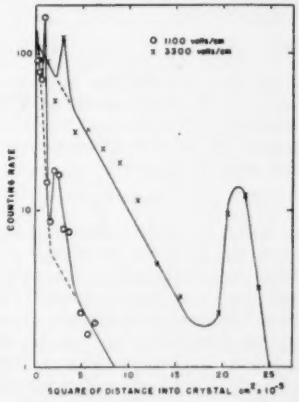

FIG. 6. The counting rate for a section plotted on a log scale against the square of the distance into the crystal at which the section was cut, for diffusion in the presence of the indicated dc electric fields, which were applied across the crystals in the plus x direction. The dotted portion of the curve at 1100 volts/cm was obtained from measurements with no applied field.

TABLE II. Data for three runs to measure ion mobility in the presence of an electric field.

Field volts/cm	D cm²/sec ($\times 10^{11}$)	$E\mu t$ cm ($\times 10^{8}$)	Mobility, μ cm/sec / volts/cm ($\times 10^{10}$)
—	1.80±0.25	—	—
1100±20	1.83±0.50	4.75±0.25	5.76±0.40
3300±60	1.23±0.50	14.75±0.25	5.93±0.22
Weighted averages	1.71±0.25		5.89±0.22

Average charge transported = 1.7±0.3 electronic charges.

results on these last two crystals are shown in Fig. 6. The dotted portions of the 1100 v/cm curve were calculated from the measurements with zero field. The first "peak" on each of the curves is caused by La^{140}, the radioactive daughter product of Ba^{140}; this was learned from the decay of the counting rate of these samples. The second "peak" in each case is Ba. The data for a field of 1100 v/cm shows a high counting rate near the origin as if the electric field were not applied to part of the crystal, probably because of poor electrode contact over part of the surface.

The predicted distribution for charge transporting diffusion in the presence of an electric field for $E\mu t \gg (4Dt)^{\frac{1}{2}}$ is approximately

$$C=[Q/(4\pi Dt)^{\frac{1}{2}}]\cdot[x/(x+E\mu t)]\exp[-(x-E\mu t)^2/4Dt],$$

where E is the field, μ is the ionic mobility, and the other symbols have the same meaning as before. Thus the location of the peak is $E\mu t$, and the half-width of the peak gives a measure of the diffusion constant. This equation was obtained by solving

$$\partial C/\partial t = D(\partial^2 C/\partial x^2) - E\mu(\partial C/\partial x)$$

by Laplace transforms with a delta-function at the origin at $t=0$ and with the concentration zero for negative x and approaching zero at x approaching ∞. The equation can be verified to order $(4Dt)^{\frac{1}{2}}/E\mu t$ by differentiation. The form of the equation can be shown qualitatively by considering the case in which the medium is infinite in both directions. In this case a transformation to a coordinate system moving with a velocity $E\mu$ gives the usual diffusion equation and immediately gives the exponential term. The additional terms in the above equation are caused by the asymmetry of a semi-infinite medium. The data for these three runs are shown in Table II. The charge transported by the diffusing barium was calculated with Einstein's relation:

$$\mu/D = q/kT.$$

The charge transported by the diffusing barium calculated from the average values was 1.7 electronic charges with an estimated probable error of 0.3 electronic charges. This was the charge transported by the slower or "near the surface" diffusion. As can be seen from Fig. 6, the slopes of the portions of the curves corresponding to the faster diffusion are the same, independent of the field, which indicates that the faster diffusion was not affected by the field.

V. SURFACE DIFFUSION

A measurement of the surface diffusion constant as a function of temperature was made, primarily to evaluate the possibility that the low temperature range internal diffusion was along cracks. All of these measurements were taken with low activity samples, which lead to a large random error in the measured distributions. Two types of initial distribution were used. For the three measurements in the middle of the temperature range investigated, the initial distribution was a band of radioactive Ba (as BaO) about $\frac{1}{4}$ mm wide across a crystal surface. For the two measurements at the extremes of the temperature range, one-half the surface of a crystal was coated with tracer BaO. The distribution for the lowest temperature case is shown in Fig. 7. The temperature dependence of the surface diffusion is shown in Fig. 8. The two points which were taken with the microtome were the results of two ionic mobility measurements in which the edge surfaces of the crystal were not removed before sectioning the crystal. These two crystals showed a distribution far from ($>10^{-2}$ cm) the front surface of the crystal, which was not present in another sample (cleaved from the same single crystal) which had been measured at about the same temperature and had had the edge surfaces removed before sectioning. This indicated that this portion of the distribution was probably on the surface and that the diffusion constant from this portion of the distribution was a surface diffusion constant. The values of D_0 and E for the surface diffusion are given in Table I.

The estimated errors quoted in Table I are probable errors. These estimates were made from an evaluation of the scatter in the data and from an estimate of the probable error in the temperature measurement. The method used to estimate the error from the scatter in the data was a test for the significance of the slope of a

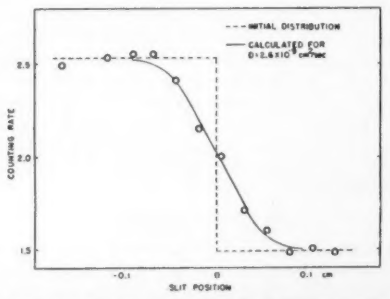

FIG. 7. Surface diffusion distribution of radioactive barium with a step function initial distribution.

regression line.[4] In making these estimates for the temperature dependence curves, the temperature was assumed to be correct, and the scatter was ascribed to the measurement of the diffusion constant. The random errors in the temperature measurement will affect the temperature dependence through their effect on the temperature range. This is the major source of error in the high temperature measurements. The probable error in the temperature measurement in the high temperature range was estimated from the heat transfer characteristics of the oven in the region around the crystal and thermocouple as $\pm 20°C$. The thermocouple could not be in contact with the crystal because platinum reacts with barium oxide at high temperatures and this contributed to the uncertainty in the temperature. The oven power was monitored and no variations from a smooth curve of oven temperature against oven power were noted which were larger than the ± 2 percent accuracy of the power measurement. With such an unexpectedly large temperature dependence, it might be suspected that the higher measured temperatures were too low. A calculation of the rate of evaporation of one of the nickel leads to the oven winding showed that, if the actual temperature were about 50°C higher than the measured temperature, an easily detectable change in diameter would have occurred during the course of the runs at the higher temperatures. No such change was observed. The crystal was shielded from this nickel vapor (see Fig. 1).

An estimate of the expected standard deviation for the temperature dependence curves was made for two runs (one from each temperature range). These estimates agreed within a few percent with the estimates from the temperature dependence data, which indicates that the estimate of the temperature error is probably conservative.

VI. DISCUSSION

Before these activation energies can be interpreted, some conclusions about the diffusion mechanism are necessary. The experimental observations indicate that two types of defects are required, one charge transporting and the other not. The numbers of both types of defects should vary reversibly with temperature in the high temperature range and it should be possible to "freeze in" both types of defects by quenching. The defect responsible for the non-charge-transporting diffusion process should be affected by impurities. The sharpness of the break in the typical high temperature curve shown in Fig. 2 indicates that the two diffusion mechanisms are substantially independent.

Four types of defects seem possible.[5] These are:

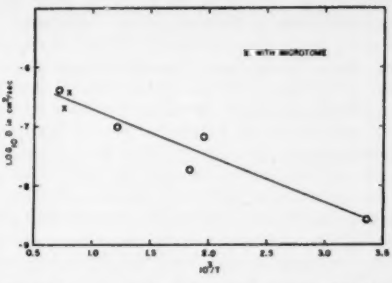

FIG. 8. Temperature dependence of the surface diffusion constant, $\log D$ *versus* $10^3/T$.

bound pairs of barium and oxygen vacancies, interstitial Ba ions, Ba vacancies, and interstitial Ba atoms. The bound pairs of vacancies would presumably be insensitive to impurities. Moreover, bound pairs of vacancies would be expected to have lower activation energy for motion than either Ba vacancies or interstitial Ba ions. Calculations[6] of the activation energies of pairs of vacancies compared to dissociated vacancies for other ionic crystals support this conclusion. Since the opposite of these conclusions was observed in the quenched crystals, the bound pairs of vacancies can be eliminated.

This gives the tentative identification of the non-charge-transporting defect as interstitial Ba atoms. If the two types of defects were identified as interstitial barium atoms and ions, it would be difficult to understand why (1) the two diffusion mechanisms appear to be independent, and (2) quenching gives both charged and non-charged defects, but impurities only non-charged. This gives the tentative identification of the charge-transporting defect as Ba vacancies.

These two defects, Ba vacancies and interstitial Ba atoms, satisfy the observed characteristics with the possible exception of the small coupling between the two diffusion mechanisms. This point will be discussed in terms of a solution of an approximate equation for diffusion by interstitial atoms, as measured by radioactive tracer techniques.

The radioactive Ba was evaporated onto the crystal as a thin layer ($\sim 10^{-4}$ cm thick) of BaO and thus did not introduce an appreciable or lasting gradient in the concentration of interstitial atoms. For an appreciable

[4] Harold Cramer, *Mathematical Methods of Statistics* (Princeton University Press, Princeton, 1946), p. 548 ff.

[5] This smaller coupling between the two mechanisms suggests some type of linear or laminar defect in which a portion of the crystal has a larger diffusion constant than the rest. If the diffusing barium is assumed to spend almost all of its time in such a defect, the different temperature dependences in the two temperature ranges would be difficult to understand. The stronger temperature dependence in the high temperature range could not be ascribed to an increase in the number of these defects as this should affect the percentage of material diffusing by these defects as strongly as the rate of diffusion, contrary to the observations. If the temperature dependence in the high temperature range is interpreted in terms of barium diffusion through the lattice from defect to defect, a non-charge-transporting diffusion mechanism is still required through the lattice; otherwise the high temperature non-charge-transporting diffusion would have been affected by the electric field in the ionic mobility measurements. Thus, at most, these extended defects play a nonessential role and will not be further considered.

[6] G. J. Dienes, J. Chem. Phys. **16**, 620 (1948).

amount of this radioactive Ba to diffuse away by the interstitial atom mechanism, some interchange between the lattice ions and the interstitial atoms must take place. Furthermore, this interchange must be possible throughout the bulk of the material as well as in the evaporated layer. If radioactive Ba in an interstitial position in the evaporated surface layer could not interchange with a lattice ion in the interior of the crystal, an equilibrium between the radioactive ions in the surface layer and in interstitial positions only would result. Because the number of interstitial atoms is small, this would give a negligible transport of radioactive material away from the surface. At high temperatures this interchange could take place during the spontaneous formation and destruction of interstitial atoms. At low temperatures in the "structure sensitive" region some other mechanism is required. Presumably this interchange could take place as the interstitial atom passes between two lattice ions at the saddle point as it jumps from one interstice to the next. This process is not described by the usual diffusion equation. An approximate solution for this type of diffusion is given in the Appendix.

This solution indicates that distributions at the observed type could be obtained with a probability of interstitial atom-lattice ion interchange as small as 10^{-10} per jump. The possibility of such a small probability of interchange is helpful in understanding the independence of the two diffusion mechanisms. For example, if this probability of interchange were 10^{-8}, an interstitial atom would, on the average, take about 10^8 jumps or diffuse 10^4 atom spacings before interchange.

Qualitatively, the difference in magnitude of the two diffusion constants can be ascribed to the difference in the vibrational frequency of an interstitial Ba atom and a Ba ion adjacent to a Ba vacancy. These frequencies would have to differ by more than an order of magnitude. From the temperature dependence of the width of the F-center optical absorption band,[7] Klick[8] calculated the vibrational frequency of a potassium ion next to an F center in KCl as 1.8×10^{12}/sec. Comparison with the Reststrahlen frequency of 4.8×10^{12} gives a factor of approximately 3. The frequency of the interstitial atom would be expected to be higher than the normal lattice ion by a similar amount. Thus one might expect a factor of about 10 in an alkali halide and an even larger factor in BaO where the distortion around a defect should be even larger because of the large (34) dielectric constant.[9]

On the basis of the preceding discussion, the temperature dependence in the high temperature range can be interpreted in terms of the energy of formation of an interstitial Ba atom and a Ba vacancy. If W is the energy required to form such a pair and U is the activation energy for motion, the diffusion constants in the high temperature range can be described by[10]

$$D=D_0\exp(-(\tfrac{1}{2}W+U)/kT).$$

Using the data in Table I, $W=23\pm5$ ev.

Both the temperature dependence and the D_0's for the high temperature range are unusually large. However, such large values are not unknown, since Seith[11] has found for the self-diffusion in bismuth perpendicular to the C axis a D_0 of 2.4×10^{16} and a temperature dependence of 6.1 ev. Both empirical[12] and theoretical[13] correlations between D_0 and the temperature dependence have been proposed. The large ($\sim10^{20}$)D_0's for the diffusion of Ba in BaO are consistent with these proposals.

VII. CONCLUSIONS

Diffusion of Ba in BaO takes place by two mechanisms and defects are responsible for both. These defects have the following characteristics:

(a) The number of defects responsible for both diffusion mechanisms vary reversibly with temperature above 1350°K.
(b) The defects responsible for both processes can be "frozen in" by quenching.
(c) The defects responsible for the neutral diffusion can be affected by impurities.

Of the five types of defects considered (barium vacancies, interstitial barium atoms, interstitial barium ions, bound pairs of barium, and oxygen vacancies, and a linear or laminar type defect), only the combination of the interstitial atom and the barium vacancy gave a phenomenologically correct account of the experimental observations. Furthermore, a simple theory of isotopic diffusion by interstitial atoms encounters no quantitative contradictions.

On the basis of this identification, the energy required to form an interstitial barium atom and a barium vacancy is 23 ± 5 ev. The activation energy for motion of the interstitial barium atom is 0.44 ± 0.03 ev, and for the motion of a barium vacancy 0.3 ± 0.05 ev.

The charge transported by the barium vacancy is 1.7 ± 0.3 electronic charges.

Although the temperature dependence of the surface diffusion (0.16 ± 0.03 ev) is not well established, the order of magnitude of the surface diffusion constant at temperatures around 1000°K is about 10^{-7} cm^2/sec. A comparison of this value with the internal diffusion constants in this temperature range indicates that, in agglomerations of particles (such as oxide cathodes) of less than 0.2 μ diameter, surface diffusion can be expected to be the predominate diffusion process.

The following qualitative conclusions can be drawn from a comparison of the ionic mobility measurements with the electronic conductivity measurements.[14]

[7] E. Burstein and J. J. Oberly, Phys. Rev. **78**, 349 (1950).
[8] C. C. Klick, J. Opt. Soc. Am. **41**, 816 (1951).
[9] R. S. Bever and R. L. Sproull, Phys. Rev. **83**, 801 (1951).
[10] N. F. Mott and R. W. Gurney, *Electronic Processes in Ionic Crystals* (Clarendon Press, Oxford, 1948), p. 34.
[11] W. Seith, Z. Electrochemie **39**, 538 (1933).
[12] G. J. Dienes, J. Appl. Phys. **21**, 1189 (1950).
[13] C. Zener, J. Appl. Phys. **22**, 372 (1951).
[14] R. L. Sproull and W. W. Tyler, *Semi-Conducting Materials* (Butterworths, London, 1951), pp. 112–131.

In the temperature range from 500 to 1350°K, the ionic conductivity in the untreated crystals is negligible compared with the electronic conductivity, but could easily be the order of a few percent in quenched crystals or in crystals with a different type of impurity.

Because the temperature dependence of the charge-transporting diffusion process in the low temperature range is about half that for the electronic conductivity, the ionic conductivity might dominate at room temperature and below.

Because of the very rapid increase with temperature above 1350°K, the ionic conductivity should be important at temperatures above this.

The author is greatly indebted to Professor R. L. Sproull for advice and assistance in this work and to Professor J. A. Krumhansl for many discussions.

APPENDIX

Let C be the concentration of barium, C_i be the concentration of barium in interstitial positions, and C_0 be the concentration of barium in lattice positions, and let an * indicate radioactive concentrations. Then,

$$C^*=C_0^*+C_i^*, \tag{1}$$

and

$$dC^*/dt=dC_0^*/dt+dC_i^*/dt. \tag{2}$$

Let the probability of an interstitial atom-lattice ion interchange per jump be p, and let q_i be the probability per second of jumping. There are two contributions to dC_0^*/dt: $pq_iC_i^*$, the number of radioactive interstitial atoms which become lattice ions per unit time; and $-pq_iC_iC_0^*/C_0$, the number of radioactive ions which become interstitial atoms per unit time. There is no contribution to dC_0^*/dt from the gradient of C_0^* in the simplest case in which no other diffusion mechanism is present.

There are three terms that contribute to dC_i^*/dt. The first two are the same as above, but with opposite sign. The third term is the contribution from the flow of radioactive interstitial atoms due to the isotopic gradient. This can be written as

$$\beta_iq_ia^2(1-p)d^2C_i^*/dx^2,$$

where β_i is a geometrical factor which gives the probability that an interstitial atom jumps in a particular direction, and a is the lattice spacing. The factor $(1-p)$ is the probability that it jumps without interchanging. Thus

$$dC^*/dt=\beta_iq_ia^2(1-p)d^2C_i^*/dx^2. \tag{3}$$

The equation

$$dC_0^*/dt=-pq_iC_iC_0^*/C_0+pq_iC_i^*$$

can be rewritten as

$$dC^*/dt+pq_iC_iC^*/C_0=pq_i(1+C_i/C_0)C_i^*+dC_i^*/dt.$$

Let $A=pq_iC_i/C_0$ and $B=pq_i(1+C_i/C_0)$. Then

$$C_i^*=\exp(-Bt)\int^t[dC^*(x,t')/dt'+AC^*(x,t')]\times\exp(Bt')dt', \tag{4}$$

$$=C^*-pq_i\exp(-Bt)\int^tC^*(x,t')\exp(Bt')dt'. \tag{5}$$

If $C^*(x,t')$ is assumed to be approximately constant for $t-t'\sim1/B$ and $C^*(x,t')$ is expanded by Taylor's series in terms of $t-t'$, the first two terms give

$$C_i^*=C^*-C^*/(1+C_i/C_0)+(dC^*/dt)/[pq_i(1+C_i/C_0)^2], \tag{6}$$
$$\doteq C_iC^*/C+(dC^*/dt)/pq_i.$$

The quantity B is approximately equal to the probability of interchange per second per interstitial atom. Thus this assumption restricts us to the case in which the concentration is varying slowly with respect to the rate of interchange, and the distribution of radioactive Ba between lattice sites and interstices is almost the equilibrium distribution. This condition will be satisfied if the probability of interchange is large enough. Inserting this in Eq. (3) gives

$$dC^*/dt=\beta_iq_ia^2(1-p)(C_i/C_0)(d^2/dx^2)\times[C^*+(C_0/pq_iC_i)dC^*/dt] \tag{7}$$

or

$$=\beta_iq_ia^2(1-p)(C_i/C_0)(d^2/dx^2)\times[C^*+\beta_ia^2\{(1-p)/p\}d^2C^*/dx^2].$$

The observed distributions can be described as

$$C^*=C_0\exp(-x^2/4DT), \tag{8}$$

which is a solution of the ordinary diffusion equation

$$dC^*/dt=Dd^2C^*/dx^2. \tag{9}$$

Thus $\beta_iq_ia^2(1-p)C_i/C_0$ can be identified as the diffusion constant if

$$\beta_ia^2[(1-p)/p]d^2C^*/dx^2\ll C^*.$$

From (9), $d^2C^*/dx^2=(x^2/4D^2t^2-1/2Dt)C^*$, and thus for the approximations to be valid,

$$\beta_ia^2[(1-p)/p](x^2/4D^2t^2-1/2Dt)\ll1.$$

With $\beta_i=1/6$, $a=2.8\times10^{-8}$ cm, $x\sim10^{-2}$ cm, and $Dt\sim10^{-5}$ for the last 9/10 of a run, the inequality is satisfied for $p>10^{-10}$ interchanges per jump. The order of magnitude of q_i, the jump frequency, can be estimated as 10^{10}, which, with $p\sim10^{-10}$, indicates that B, the probability of interchange, is greater than 1 per second. Thus, the approximate solution should be valid for the present case. Qualitatively, the effect of a smaller p on the distribution would be a curvature in the plot of the logarithm of the counting rate *versus* the square of the distance into the crystal. Within the experimental error, no such curvature was noticed.

The Resistivity of Cu_3Au during Neutron Irradiation

H. L. Glick, F. C. Brooks, W. F. Witzig, and W. E. Johnson
Westinghouse Electric Corporation, Pittsburgh, Pennsylvania
(Received May 6, 1952)

Samples of initially ordered and disordered Cu_3Au have been irradiated in a nuclear reactor at 80°C. Continuous in pile, electrical resistivity measurements suggest that pile irradiation has both ordering and disordering tendencies.

SPECIMENS of initially ordered and disordered copper-gold alloy (Cu_3Au) have been exposed to the neutron flux of a graphite moderated nuclear reactor. The two specimens were irradiated at the same time and at the same position in the reactor. Their temperature was controlled at 80°C±5C°, except during pile shut-down when the temperature dropped as low as 20°C. Electrical resistivity measurements were made on the specimens during the course of the irradiation. The results are plotted in Fig. 1 as a function of the integrated thermal neutron flux (*nvt*), which was chosen as a convenient measure of the radiation dose. The measurements extend up to a total $nvt=6.5\times10^{19}$ neutrons/cm^2.

The resistivity of the disordered specimen decreased continuously until *nvt* reached 4×10^{19} and remained essentially constant from then on at a value 7 percent below the initial value. The resistivity of the ordered specimen dropped rapidly at first, passing through a minimum 3 percent below the initial value at an integrated flux of 0.4×10^{19}. Thereafter, the resistivity climbed linearly with the flux, reaching a value 23 percent above the initial value.

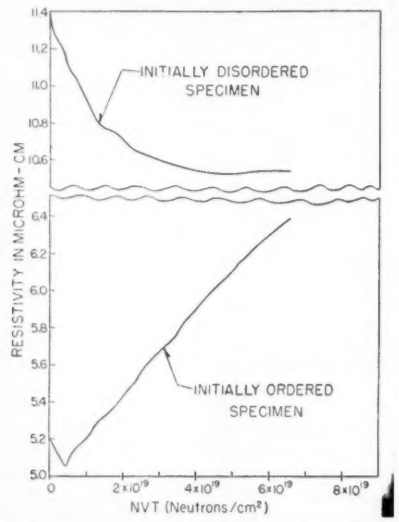

FIG. 1. The resistivity of initially ordered and disordered specimens of Cu_3Au during neutron irradiation at 80°C. The radiation dose is measured in terms of *nvt*, the integrated thermal neutron flux (neutrons/cm^2).

It is of interest to compare the present results with those of other investigators. Siegel[1] made before-and-after irradiation measurements on specimens exposed in a nuclear reactor at a temperature near 40°C. He found that the resistance of the initially disordered specimen remained substantially unchanged. The ordered specimen resistivity increased from the beginning, approaching that of the disordered after long times under irradiation. Because of the pre-post nature of this experiment, a minimum in the ordered resistivity at small *nvt* would not have been detected. Blewitt and Coltman[2] have found a decrease in the resistivity during irradiation of an initially disordered specimen maintained at 200°C, while Martin *et al.*[3] have observed little change in this resistivity using cyclotron irradiations at or below room temperature. Adam and Dugdale[4] report results similar to ours on an ordered sample.

Siegel's experiment suggested that the effect of neutron bombardment was purely a disordering one. Subsequent work indicated that this simple interpretation does not hold for all temperatures and fluxes. Assuming that the resistance of the alloy is a measure of its degree of order, our results suggest that reactor irradiation has both ordering and disordering tendencies.

During irradiation, mercury is produced by thermal neutron absorption in gold. At an integrated thermal neutron flux of 6×10^{19}, about one out of every 200 gold atoms has been converted to mercury. The possibility that mercury contributes to the disordering is being investigated.

[1] S. Siegel, Phys. Rev. **75**, 1823 (1949).
[2] T. H. Blewitt and R. R. Coltman, Oak Ridge National Laboratory (private communication, December 1951).
[3] A. B. Martin *et al.*, Phys. Rev. **81**, 664 (1951).
[4] J. Adam and R. A. Dugdale, Nature **168**, 582 (1951).

Vibrational and Centrifugal Effects on Nuclear Interactions and Rotational Moments in Molecules*

NORMAN F. RAMSEY
Harvard University, Cambridge, Massachusetts
(Received May 26, 1952)

The effects of zero point vibration and centrifugal stretching of molecules upon the spin-spin magnetic interaction, the spin-rotational magnetic interaction, the molecular rotational magnetic moment, the magnetic shielding of the nucleus, and the molecular diamagnetic susceptibility of the molecule are discussed. Expressions for these quantities with vibrational and centrifugal effects included are given in detail for diatomic molecules and numerical calculations for the cases of H_2 and D_2. It is shown that from measurements of the rotational magnetic moments of both H_2 and D_2 or of H_2 in two different rotational states, one can calculate the variation with internuclear separation of the high frequency terms of the molecular diamagnetic susceptibility. Measurements on the spin-rotational magnetic interactions in both H_2 and D_2 provide information on the variation of this interaction with internuclear spacing and thereby supply important corrections that are needed in calculating the nuclear magnetic shielding from the spin rotational magnetic interaction and in measuring the ratio of the proton magnetic moment to that of the deuteron. These calculations also supply a correction to the spin-spin magnetic interaction that must be used in determining the deuteron quadrupole moment from experiments with D_2.

I. INTRODUCTION

THE recent high precision experiments[1] on nuclear interactions in molecules make it necessary to include the effects of molecular zero point vibration and of centrifugal stretching in interpreting the results. Thus, the ratio of the rotational magnetic moment of D_2 to that of H_2 is not simply equal to the ratio of the mass of the proton to that of the deuteron as it would be if the two molecules were identical except for a difference in rotational angular velocity. Instead, allowance must be made for the fact that the suitably averaged mean internuclear spacing in the two molecules is different as a result of the difference in zero point vibration amplitude and centrifugal stretching. Similar considerations apply to the spin-spin magnetic interaction, the spin rotational magnetic interaction, the magnetic shielding of the nucleus, the electric quadrupole interaction, and the molecular diamagnetic susceptibility. Although Nordsieck,[2] Newell,[3] and Ramsey[1,4] have included these corrections for a few of the interactions, most of the cases have never been discussed previously and for the few that have been only specific numerical values were given with all detailed discussion being omitted. There has been no previous discussion of the inferences that can be drawn from the comparison of the above quantities in molecules that are similar except for differences in vibration amplitude and centrifugal stretching.

II. AVERAGE VALUES OF THE INTERACTIONS

In most past discussions of such quantities as molecular rotational magnetic moments, the effects of zero point vibration and centrifugal stretching have been neglected with the result that the formulas given are for a single discrete internuclear distance. However, averaging these formulas over the vibration, one can obtain suitably averaged expressions.

In the case of rotational magnetic moments, Wick[5,6] and Ramsey[7] have discussed molecular hydrogen. Their results are thereby particularly simplified since all the nuclear charges are unity, and the molecule possesses no electric dipole moment. However, their procedure can be extended to an arbitrary $^1\Sigma$ linear molecule and the results may be simplified for a particular choice of gauge as discussed in Ramsey's articles[8,9] on nuclear magnetic shielding. The most suitable choice is that which corresponds to the electron angular momenta being taken about an axis passing through the centroid of the electron distribution in the molecule (not in general the center of mass of the molecule). With this choice and with the expression averaged over zero point vibrations, one obtains

$$\begin{aligned}{}_v{}^z\langle(\mu_R/J\mu_{NM})\rangle_J = M_v{}^z\langle(1/I)\textstyle\sum_i Z_i(R_i-R_Z)^2\rangle_J \\ +M(\textstyle\sum_i Z_i)_v{}^z\langle(1/I)(D^2-d^2)\rangle_J \\ -8M(mc^2/e^2)_v{}^z\langle(1/I)\textstyle\sum_n{}'[1/(E_n-E_0)] \\ \times(0|\textstyle\sum_k m_{k\sigma}c^0|n)|^2\rangle_J. \quad (1)\end{aligned}$$

Most of the notation used here and in subsequent expressions is that used in previous related articles[7-9] except that R_Z is the coordinate of the centroid of the nuclear charge; the subscripts σ and C indicate, respectively, that the momenta are about an axis perpendicular to the internuclear line and passing through the centroid of the electron distribution; D is the distance from the

* This work was partially supported by the joint program of the ONR and the AEC.
[1] Kolsky, Phipps, Ramsey, and Silsbee, Phys. Rev. **81**, 1061 (1951); **87**, 395 (1952).
[2] A. Nordsieck, Phys. Rev. **58**, 310 (1940).
[3] G. F. Newell, Phys. Rev. **78**, 711 (1950); **80**, 476 (1950).
[4] N. F. Ramsey, Phys. Rev. **85**, 937 (1952).
[5] G. C. Wick, Z. Physik **85**, 25 (1933).
[6] G. C. Wick, Nuovo cimento **10**, 118 (1933).
[7] N. F. Ramsey, Phys. Rev. **58**, 226 (1940).
[8] N. F. Ramsey, Phys. Rev **78**, 699 (1950).
[9] N. F. Ramsey, Phys. Rev. **85**, 60 (1952).

center of mass to the centroid of the nuclear charge, d is the distance from the center of mass to the centroid of the electron distribution, and ${}_v{}^x\langle\ \ \rangle_J$ indicates the expectation value for the molecule x in vibrational state v and rotational state J. It can be seen from Eq. (1) that if the molecule has no permanent electric dipole moment so that d and D are equal, the second term in the brackets vanishes. In this case, in a comparison of molecules of different isotopic masses the rotational magnetic moments are approximately inversely proportional to the moments of inertia, I. Owing to the arbitrariness of the axis about which the electronic moments m^0 are taken, Eq. (1) is only one of many alternative expressions for the rotational magnetic moment, but in most respects it is the simplest, particularly in the absence of a permanent electric dipole moment. Although Eq. (1) is limited to linear molecules for simplicity, the methods of the present paper could be extended to polyatomic molecules by combining them with the procedures of Eshbach and Strandberg.[10]

Likewise, from the procedures of Van Vleck,[11] the mean molar diamagnetic susceptibility of a ${}^1\Sigma$ linear molecule is given by

$$ {}_v{}^x\langle\chi\rangle_J = = -(e^2L/6mc^2)\,{}_v{}^x\langle(0|\textstyle\sum_k r_{kc}{}^2|0)\rangle_J + (4/3)L\,{}_v{}^x\langle{\textstyle\sum_n}'[1/(E_n-E_0)]|\,(0|\textstyle\sum_k m_{k\sigma c}|n)|^2\rangle_J, \quad (2)$$

where the notation is as in previous related papers.[7-9] Although the origin about which the angular momenta can be calculated is arbitrary, the specific choice of the origin at C, the centroid of the electron distribution, has been made in order to facilitate subsequent comparisons between Eqs. (1) and (2). As pointed out by Ramsey,[7] if the effects of molecular vibration were negligible, one could use Eq. (1) to provide an experimental evaluation of the second or high frequency term in Eq. (2); as a result of the high frequency term in Eq. (1) being multiplied by $1/I$ in the averaging, this is not true when the vibration is considered. However, means for making this elimination even in the presence of vibration will be given below.

If c_N is the spin-rotational magnetic interaction constant[12] of nucleus N or if H' is the rotational magnetic field at the nucleus,[11] the discussions of Wick[13] and Ramsey[8,12] show that after suitable averaging for linear molecules

$$ {}_v{}^x\langle H'\rangle_J/J = 2\pi\,{}_v{}^x\langle c_N\rangle_J/\gamma_N = 2\mu_{NM}M\,{}_v{}^x\langle(1/I){\textstyle\sum_i} Z_i/R_i\rangle_J + h^2\,{}_v{}^x\langle{\textstyle\sum_{n\lambda'}}(1/I)[1/(E_n-E_0)] \times[H_{0\sigma n\lambda'}L_{n\lambda'0\sigma}+L_{0\sigma n\lambda'}H_{n\lambda'0\sigma}]\rangle_J, \quad (3)$$

where R_i is the distance of the i'th nucleus from the nucleus N that is being shielded, and the remaining quantities are as previously defined.[8,12]

For magnetic shielding, the theory of Ramsey[8,12] leads to

$$ {}_v{}^x\langle\sigma\rangle_J = (e^2/3mc^2)\,{}_v{}^x\langle(0|\textstyle\sum_k r_k{}^{-1}|0)\rangle_J + \tfrac{2}{3}\mu_0\,{}_v{}^x\langle{\textstyle\sum_{n\lambda'}}[1/(E_n-E_0)][H_{0\sigma n\lambda'}L_{n\lambda'0\sigma} - L_{0\sigma n\lambda'}H_{n\lambda'0\sigma}]\rangle_J. \quad (4)$$

It should be noted that if the effects of vibration are negligible, the last bracketed quantity in Eq. (4) can be eliminated with the aid of Eq. (3) but not when vibration effects are included. However, means for making this elimination even in the presence of vibration will be given subsequently.

Another intramolecular interaction for which zero point vibration corrections need to be made is the spin-spin magnetic interaction constant.[12,14] In the case of molecular hydrogen, for example, this constant is defined by

$$d_H = (4/5h)\mu_p{}^2\,{}_v{}^x\langle R^{-3}\rangle_J. \quad (5)$$

III. DIATOMIC MOLECULES

In each of the above relations except Eq. (5) at least one of the averages cannot readily be evaluated theoretically due to lack of knowledge as to its dependence on the internuclear spacings. However, for diatomic molecules the assumption introduced by Newell[3] can be made: that the high frequency terms vary with internuclear spacing, R as R^n, in which case the average can be carried out in terms of n. It should be noted, however, that this is an assumption for simplicity which is not necessarily valid. It will be shown that with this assumption the values of n in the different cases can then be evaluated experimentally by measurements on molecules in different rotational states or with different isotopic masses. In particular, if R_e is the equilibrium internuclear-spacing for a nonvibrating and nonrotating molecule, we assume that

$$ {\textstyle\sum_n}[1/(E_n-E_0)]|\,(0|\textstyle\sum_k m_{k\sigma c}{}^0|n)|^2 = F_e(R/R_e)^l, \quad (6)$$

$$ {\textstyle\sum_{n\lambda'}}'[1/(E_n-E_0)][H_{0\sigma n\lambda'}L_{n\lambda'0\sigma}+L_{0\sigma n\lambda'}H_{n\lambda'0\sigma}] = G_e(R/R_e)^m. \quad (7)$$

With these assumptions the previous relations reduce to

$$ {}_v{}^x\langle\mu_R/J\mu_{NM}\rangle_J = (M/2\mu')\{2Z_1Z_2/(Z_1+Z_2) + 2(Z_1+Z_2)\,{}_v{}^x\langle(D^2-\bar{d}^2)/R^2\rangle_J - 16(mc^2/e^2)R_e{}^{-2}F_e\,{}_v{}^x\langle(R/R_e)^{l-2}\rangle_J\}, \quad (8)$$

$$ {}_v{}^x\langle\chi\rangle_J = -(e^2L/6mc^2)\,{}_v{}^x\langle(0|\textstyle\sum_k r_{kc}{}^2|0)\rangle_J + (4/3)LF_e\,{}_v{}^x\langle(R/R_e)^l\rangle_J, \quad (9)$$

[10] J. R. Eshbach and M. W. P. Strandberg, Phys. Rev. **85**, 24 (1952).
[11] J. H. Van Vleck, *Electric and Magnetic Susceptibilities* (Oxford University Press, London, 1932).
[12] N. F. Ramsey, Phys. Rev. **85**, 60 (1952).
[13] G. C. Wick, Phys. Rev. **73**, 51 (1948).
[14] N. F. Ramsey, Phys. Rev. **85**, 938 (1952).

$$ {}_v{}^z\langle H'\rangle_J/J = 2\pi\ {}_v{}^z\langle c_N\rangle_J/\gamma_N $$
$$ = 2Z\mu_{NM}(M/\mu')R_e^{-3}\ {}_v{}^z\langle(R/R_e)^{-3}\rangle_J $$
$$ +(h^2/\mu')R_e^{-2}G_e\ {}_v{}^z\langle(R/R_e)^{m-3}\rangle_J, \quad (10) $$

$$ {}_v{}^z\langle\sigma\rangle_J = (e^2/3mc^2)\ {}_v{}^z\langle(0|\textstyle\sum_k r_k^{-1}|0)\rangle_J $$
$$ +\tfrac{2}{3}\mu_0 G_e\ {}_v{}^z\langle(R/R_e)^m\rangle_J, \quad (11) $$

$$ d_H = (4/5h)\mu_p{}^2R_e^{-3}\ {}_v{}^z\langle(R/R_e)^{-3}\rangle_J, \quad (12) $$

where μ' is the reduced mass of the diatomic molecule and Z is the charge of the nucleus that is not N. The quantity R_e for use in the above can be obtained empirically either from Eq. (12) in combination with an experimental value of d_H or from the molecular spectra determination of B_0, as by Herzberg,[15,16] together with the relation[16]

$$ R_e = \hbar^{\frac{1}{2}}/(8\pi^2 c\mu' {}^z B_{0J})^{\frac{1}{2}}\ {}_0{}^z\langle(R/R_e)^{-2}\rangle_J{}^{\frac{1}{2}}. \quad (13) $$

All quantities on the right side of the above equations that need to be averaged over the zero point vibration are of the form $(R/R_e)^n$ except for three of them. The analogous assumption to Eqs. (6) and (7) could also be made for these three in which case all the expressions to be averaged would be of the form $(R/R_e)^n$. However, since these quantities can sometimes be evaluated and averaged directly theoretically, as in the calculations of Newell,[3] they have been left in the form given above. For molecules with no resultant electrical moment, as H_2 and D_2, the quantity $(D^2-d^2)/R^2$ vanishes. In view of this, all the quantities that need to be averaged are either known or can be expressed in the form of ${}_v{}^z\langle(R/R_e)^n\rangle_J$. Hence, to make the averages for the quantities of interest, one need merely determine the averages of arbitrary powers of the internuclear spacing. Means for obtaining these averages will be discussed in the next section.

In Eq. (8) if all the quantities except F_e and l are known and if μ_R has been measured in two different rotational states of the same molecule or in two isotopically differing molecules, the values of both F_e and l can be obtained by the simultaneous solution of the two equations of the form (8) which result for the two states in which the measurements are made. An example of such a procedure is given in Sec. V below. These values for F_e and l can then be used in Eq. (8) to yield a predicted value of the rotational moment in any other state or in Eq. (9) to provide a definite determination of the high frequency term of the molecular susceptibility for any rotational or vibrational state. For example, if primes designate the state of the molecule in which the rotational moment was measured,

$$ {}_v{}^z\langle\chi\rangle_J = -(e^2L/6mc^2)\ {}_v{}^z\langle(0|\textstyle\sum_k r_k c^2|0)\rangle_J $$
$$ +(e^2/12mc^2)R_e{}^2L\ {}_v{}^z\langle(R/R_e)^l\rangle_J $$
$$ \times {}_{v'}{}^{z'}\langle(R/R_e)^{l-3}\rangle_{J'}{}^{-1}\{2Z_1Z_2/(Z_1+Z_2) $$
$$ +2(Z_1+Z_2)\ {}_{v'}{}^{z'}\langle(D^2-d^2)/R^2\rangle_{J'} $$
$$ -(2\mu'/M)\ {}_{v'}{}^{z'}\langle\mu_R/J\mu_{NM}\rangle_{J'}\}. \quad (14) $$

In a similar fashion, measurements of $\langle c_N\rangle$ in two different rotational states provide a determination of G_e and m as is discussed subsequently in greater detail. The value of G_e and m can then be used to predict the value of $\langle c_N\rangle$ in any other rotational state or to determine the high frequency term of the nuclear shielding $\langle\sigma\rangle$ for any rotational state. The latter determination, for example, gives

$$ {}_v{}^z\langle\sigma\rangle_J = (e^2/3mc^2)\ {}_v{}^z\langle(0|\textstyle\sum_k r_k^{-1}|0)\rangle_J $$
$$ -(e^2/6mc^2)R_e{}^2\mu_{NM}{}^{-1}\ {}_v{}^z\langle(R/R_e)^m\rangle_J $$
$$ \times {}_{v'}{}^{z'}\langle(R/R_e)^{m-3}\rangle_{J'}{}^{-1}\{2Z\mu_{NM}R_e{}^{-3}\ {}_{v'}{}^{z'}\langle(R/R_e)^{-3}\rangle_{J'} $$
$$ -(2\pi\mu'/M\gamma_N)\ {}_{v'}{}^{z'}\langle c_N\rangle_{J'}\}. \quad (15) $$

IV. AVERAGE VALUES

From the preceding equations it can be seen that the quantities to be evaluated in averaging over the molecular vibration are $\langle(R/R_e)^n\rangle$. This average can in turn be expressed in terms of the expectation values of $\langle(R-R_e)^q/R_e{}^q\rangle$ by the relation

$$ {}_v{}^z\langle(R/R_e)^n\rangle_J $$
$$ = \sum_{q=0}^{\infty}[n!/(n-q)!q!]\ {}_v{}^z\langle(R-R_e)^q/R_e{}^q\rangle_J. \quad (16) $$

A series expansion for the latter expectation values can be obtained if one assumes the nuclear vibrational potential to be approximately of the Morse potential[17] shape. In this case analytic values of the wave functions are known.[17] These can most conveniently be expressed in terms of the variable

$$ z = k\exp[-a(R-R_e)], \quad (17) $$

where[16,17] $1/k = (B_e/\omega_e)(aR_e)^2$ and a is the quantity which determines the asymmetry of the vibrational potential and is usually determined experimentally. In these variables Morse's wave function[17] is such that in the nonrotating and zeroth vibrational state

$$ {}_0{}^z\langle(R-R_e)^q/R_e{}^q\rangle_0 = \int_{-\infty}^{\infty}[(R-R_e)^q/R_e{}^q]\Re^2 dR $$
$$ = [1/\Gamma(k-1)]\int_0^{\infty}[-(1/aR_e) $$
$$ \times\ln(z/k)]^q e^{-z}z^{k-3}dz. \quad (18) $$

[15] G. Herzberg, Can. J. Research **A28**, 144 (1950).
[16] G. Herzberg, *Spectra of Diatomic Molecules* (D. Van Nostrand and Company, New York, 1950).
[17] P. M. Morse, Phys. Rev. **34**. 57 (1929); J. L. Dunham, ibid. **34**, 446 (1929).

If in Eq. (18) one uses the series expansion for $\ln(z/k)$ about $z/k=1$ and for any given number of terms in this expansion carries out the multiplications to the indicated q'th power, all terms except for constant factors are of the following integrable form

$$\int_0^\infty z^p e^{-z} dz = \Gamma(p+1).$$

If the series expansions are carried out to terms as high as z^6 and $(1/k)^3$, the resulting expectation values determined in the above manner are

$${}_0{}^v\langle(R-R_e)^q/R_e{}^q\rangle_0 = (1/aR_e)^q(\alpha/k+\beta/k^2+\gamma/k^3), \quad (19)$$

where α, β, and γ are given in Table I for different integral values of q.

The combination of Eq. (19) with Eq. (16) determines ${}_0{}^v\langle(R/R_e)^n\rangle_0$ for the zeroth rotational state only. However, it can be extended immediately to the J'th rotational state by the relation[16]

$${}_v{}^v\langle(R/R_e)^n\rangle_J = {}_v{}^v\langle(R/R_e)^n\rangle_0[1+4nJ(J+1)B_e{}^2/\omega_e{}^2]. \quad (20)$$

The combination of Eqs. (16), (19), and (20) and the omission of terms of higher order than $(B_e/\omega_e)^2$ yield

$$\begin{aligned}{}_0{}^v\langle(R/R_e)^n\rangle_J = 1&+(B_e/\omega_e)[(aR_e)C_1 3/2+C_2]\\&+(B_e/\omega_e)^2[(aR_e)^3C_1 13/12+(aR_e)^2C_2 15/4\\&+(aR_e)C_3 11/2+3C_4+4C_1J(J+1)], \quad (21)\end{aligned}$$

where $C_1=n$, $C_2=C_1(n-1)/2$, $C_3=C_2(n-2)/3$, and $C_4=C_3(n-3)/4$. From Eq. (21) the expectation values needed in Eqs. (8–13) can be calculated if n is known.

The determination of n in certain cases can be made by a measurement of a quantity such as the rotational magnetic moment in two different rotational or isotopic states. In this case, the ratio of the two experimental quantities experimentally determines the ratio of ${}_0{}^v\langle(R/R_e)^n\rangle_{J'}/{}_0{}^1\langle(R/R_e)^n\rangle_J$, and n is inferred by comparing the experimental value to the theoretical value. There is consequently need for a theoretical expression giving the ratio of the expectation values in two

TABLE I. Coefficients for

${}_0{}^v\langle(R-R_e)^q/R_e{}^q\rangle_0 = (1/aR_e)^q(\alpha/k+\beta/k^2+\gamma/k^3)$.

q	α	β	γ
1	3/2	13/12	1
2	1	15/4	65/12
3	0	11/2	131/8
4	0	3	61/2
5	0	0	65/2
6	0	0	15

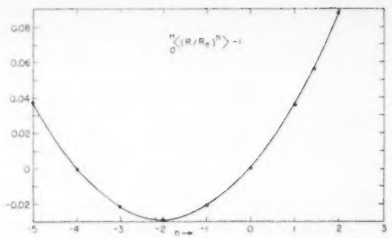

FIG. 1. ${}_0{}^H\langle(R/R_e)^n\rangle_1 - 1$ as a function of n.

different states. From Eq. (21) the ratio is given by

$$\begin{aligned}{}_0{}^2\langle(R/R_e)^n\rangle_{J'}/{}_0{}^1\langle(R/R_e)^n\rangle_J &= 1+[(B_e/\omega_e)_2-(B_e/\omega_e)_1][(aR_e)C_1 3/2+C_2]\\&+[(B_e/\omega_e)_2{}^2-(B_e/\omega_e)_1{}^2][(aR_e)^3C_1 13/12\\&+(aR_e)^2C_2 15/4+(aR_e)C_3 11/2+3C_4]+[(B_e/\omega_e)_1{}^2\\&-(B_e/\omega_e)_1(B_e/\omega_e)_2][(aR_e)C_1 3/2+C_2]^2\\&+(B_e/\omega_e)_2{}^2 4C_1J'(J'+1)\\&-(B_e/\omega_e)_1{}^2 4C_1J(J+1). \quad (22)\end{aligned}$$

V. SIGNIFICANCE OF MEASUREMENTS ON DIFFERENT STATES OF SIMILAR MOLECULES

It is sometimes possible to determine such quantities as μ_R or C_N in two similar molecules which differ only in rotational state or in isotopic mass. If one assumes that the differences are due only to changes of reduced mass, rotational quantum number, centrifugal stretching, and zero point vibration, and that these differences are in accordance with Eqs. (8) and (10), the values of l and m in such cases can be determined from the experimental measurements. Thus, from Eq. (8) in cases where $D^2=d^2$,

$$\begin{aligned}{}_0{}^2\langle(R/R_e)^{l-2}\rangle_{J'}/{}_0{}^1\langle(R/R_e)^{l-2}\rangle_J &= 1+\frac{{}_0{}^1\langle\mu_R/J\mu_{NM}\rangle_J-{}_0{}^2\langle\mu_R/J\mu_{NM}\rangle_{J'}(\mu_2'/\mu_1')}{(M/2\mu_1')2Z_1Z_2/(Z_1+Z_2)-{}_0{}^1\langle\mu_R/J\mu_{NM}\rangle_J}. \quad (23)\end{aligned}$$

A comparison of the experimental results obtained from Eq. (23) with the theoretical results given in Eq. (22) determines l. It should be noted that Eq. (23) does not include effects due to small changes of the electrons' reduced mass for different isotopes.

Similarly, if c_N is known in two different states,

$$\begin{aligned}{}_0{}^2\langle(R/R_e)^{m-2}\rangle_{J'}/{}_0{}^1\langle(R/R_e)^{m-2}\rangle_J &= 1-\frac{1-{}_0{}^2\langle(R/R_e)^{-3}\rangle_{J'}/{}_0{}^1\langle(R/R_e)^{-3}\rangle_J}{1-1/[2Z\mu_{NM}R_e{}^{-3}\,{}_0{}^1\langle(R/R_e)^{-3}\rangle_J\gamma_{N1}M/2\pi\mu_1'c_{N1}]}\\&+\frac{1-(\mu_2'c_{N2}\gamma_{N1}/\mu_1'c_{N1}\gamma_{N2})}{2Z\mu_{NM}R_e{}^{-3}\,{}_0{}^1\langle(R/R_e)^{-3}\rangle_J\gamma_{N1}M/2\pi\mu_1'c_{N1}-1}. \quad (24)\end{aligned}$$

If experimental values of c_{N2} and c_{N1} are inserted in Eq. (24) and if the resulting value for the expression is compared to Eq. (22), the value of m can be determined.

A quantity of particular importance in nuclear physics measurements is the ratio of the magnetic shielding in two molecules which differ only isotopically. The precision measurements[18,19] of the ratio of the proton magnetic moment to that of the deuteron depends upon such a quantity.[3,19,20] From Eq. (11), it can be seen that

$$
\begin{aligned}
{}_{v'}{}^{2}\langle\sigma\rangle_{J'}/{}_{v}{}^{1}\langle\sigma\rangle_{J}=1+(e^{2}/3mc^{2})[&{}_{v'}{}^{2}\langle(0|\textstyle\sum_{k} r_{k}^{-1}|0)\rangle_{J'}\\
&-{}_{v}{}^{1}\langle(0|\textstyle\sum_{k} r_{k}^{-1}|0)\rangle_{J}]\,{}_{v}{}^{1}\langle\sigma\rangle_{J}{}^{-1}+[{}_{v}{}^{1}\langle\sigma\rangle_{J}\\
&-(e^{2}/3mc^{2})\,{}_{v}{}^{2}\langle(0|\textstyle\sum_{k} r_{k}^{-1}|0)\rangle_{J}]\,{}_{v}{}^{1}\langle\sigma\rangle_{J}{}^{-1}\\
&\times[{}_{v'}{}^{2}\langle(R/R_{e})^{m}\rangle_{J'}/{}_{v}{}^{1}\langle(R/R_{e})^{m}\rangle_{J}-1]. \quad (25)
\end{aligned}
$$

VI. MOLECULAR HYDROGENS

Numerical values of the constants appearing in Eqs. (21) and (22) can be inserted for H_2 and D_2 and the quantities can be plotted as functions of n. Most of the necessary constants are given by Herzberg.[15] However, the parameter aR_e which determines the asymmetry of the Morse potential requires a slight discussion. This parameter is often determined from the molecular dissociation energy. However, the dissociation energy is chiefly affected by the shape of the potential at very large energies, whereas the zero point vibration is chiefly affected by the shape of the potential well at its bottom. Therefore, it is best to proceed as discussed by Newell[3] and determine (aR_e) by making the Morse potential agree with the leading terms of the Dunham[21] power series expansion of the potential. In this case,[3] aR_e is 1.608. With these values, Eqs. (21) and (22) yield the results shown in Figs. 1 and 2 for rotational state $J=1$. The superscripts H and D indicate H_2 and D_2, respectively. These curves are particularly valuable in determining the quantities l and m as discussed in the previous section. A determination of the actual values of l and m that can be inferred for hydrogen molecules will be given in a subsequent paper which describes the experiments.

VII. SPIN-SPIN MAGNETIC INTERACTION

Let the spin-spin magnetic interaction between the two nuclei of a diatomic molecule be called $K(R)$ so that

$${}_{v}{}^{z}K(R)_{J}=\mu_{1}\mu_{2}R_{e}^{-3}\,{}_{v}{}^{z}\langle(R/R_{e})^{-3}\rangle_{J}=5d_{\mathrm{H}}h/4, \quad (26)$$

where the last step applies only to molecular H_2. Then from Eq. (13),

$$
\begin{aligned}
{}_{v}{}^{z}K(R)_{J}=\mu_{1}\mu_{2}(8\pi^{2}c\mu_{1}'B_{0J'}/h)^{\frac{1}{2}}\,&{}_{v}{}^{z}\langle(R/R_{e})^{-3}\rangle_{J}\\
&\times{}_{0}{}^{1}\langle(R/R_{e})^{-3}\rangle_{J'}{}^{-\frac{1}{2}}. \quad (27)
\end{aligned}
$$

If Eq. (21) is used here and if the calculations are carried out,

$$
\begin{aligned}
{}_{0}{}^{z}K(R)_{J}=\mu_{1}\mu_{2}(8\pi^{2}c\mu_{x}'{}^{z}B_{00}/h)^{\frac{1}{2}}\{&1+(B_{e}/\omega_{e})3/2\\
&+(B_{e}/\omega_{e})^{2}[(aR_{e})^{2}9/4-(aR_{e})17/2\\
&+99/8-12J(J+1)]\}. \quad (28)
\end{aligned}
$$

Although this appears quite different from the equation recently published by the author,[4] it is actually very similar and slightly superior. The empirical quantity γ_e[4,15,16] does not appear here since it is more consistent to use the theoretical value for γ_e since the theoretical values must be used elsewhere in the same equation and by using theoretical values throughout there is a tendency for errors introduced thereby partially to cancel. If the numerical constants appropriate to H_2, as discussed in the previous section, are used,

$${}_{0}{}^{\mathrm{H}}K(R)_{1}=(4.7738\pm0.0030)\times10^{-22}\ \text{ergs}. \quad (29)$$

This result is in excellent agreement with the experimental results[1,4] for H_2:

$$5d_{\mathrm{H}}h/4=(4.7750\pm0.0010)\times10^{-22}\ \text{ergs}. \quad (30)$$

As recently pointed out in a brief note by Ramsey,[4] this close agreement indicates that any nonmagnetic tensor interaction between two protons at the internuclear distance of H_2 must be very small indeed (less than 10^{-19} Mev).

In the calculation[1] of the deuteron quadrupole moment from the measured interaction in molecular deuterium, it is necessary[1] to subtract off a spin-spin magnetic part of the measured interaction. This is usually done[1] by taking the measured spin-spin magnetic interaction in H_2 and multiplying it by the square of the ratio of the deuteron magnetic moment to that of the deuteron. However, obtaining the correction in this way is not completely accurate since the zero point vibration is different for H_2 and D_2. The added correction factor to be applied is then from Eq. (22) and the best constants

$${}_{0}{}^{\mathrm{D}}\langle(R/R_{e})^{-3}\rangle_{1}/{}_{0}{}^{\mathrm{H}}\langle(R/R_{e})^{-3}\rangle_{1}=1.0073. \quad (31)$$

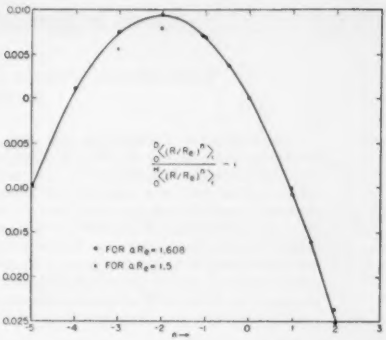

FIG. 2. ${}_{0}{}^{\mathrm{D}}\langle(R/R_e)^n\rangle_1/{}_{0}{}^{\mathrm{H}}\langle(R/R_e)^n\rangle_1-1$ as a function of n.

[18] G. Lindstrom, Phys. Rev. **78**, 817 (1950).
[19] B. Smaller, Phys. Rev. **83**, 812 (1951).
[20] N. F. Ramsey, Phys. Rev. **85**, 688 (1952).
[21] J. L. Dunham, Phys. Rev. **41**, 713, 721 (1932); **49**, 797 (1936).

Bursts in Material of Low Atomic Number*

F. E. Driggers†
Randall Laboratory of Physics, University of Michigan, Ann Arbor, Michigan
(Received April 24, 1952)

A large ionization chamber has been used to obtain an integral burst size-frequency distribution by amplifying and recording the electron pulses produced by bursts. A comparison of the integrated burst rate from the upper hemisphere with that produced by primaries with a small zenith angle permitted an estimate of the burst rate resulting from interactions of the N component. Calculations were made of the expected burst distributions arising from the electromagnetic interactions (bremsstrahlung, knock-on, and direct pair production) of spin 0 and spin $\frac{1}{2}$ μ-mesons. About $\frac{1}{4}$ of the bursts observed under 400 g cm^{-2} of sand-lime brick and concrete at sea level were attributed to interactions of the N component. The remaining burst rate agreed with the rate calculated for spin $\frac{1}{2}$ to within the estimated uncertainty of the comparison—about 20 percent. Lack of quantitative information concerning the nuclear interactions of μ-mesons prevents an estimation of the actual electromagnetic cross sections. The expected Z dependence of μ-meson bursts was roughly confirmed by a comparison with results obtained elsewhere under material of higher Z.

1. INTRODUCTION

ALTHOUGH many experiments on bursts have been performed under various conditions, only those of Schein and Gill[1] under lead and of Lapp[2] under iron have been suitable for comparison with the only available analysis of the burst rate to be expected from the bremsstrahlung and knock-on interactions of μ-mesons. This analysis was performed by Christy and Kusaka[3] for assumed values of the spin of 0, $\frac{1}{2}$, and 1. Comparison with experimental results is limited by the fact that this analysis was specifically designed for a spherical ionization chamber. A comparison between these experiments and the calculations have evidenced a definite disagreement with the expected burst rate for spin 1 μ-mesons but have failed to distinguish conclusively between the possibilities of spin 0 and spin $\frac{1}{2}$. Part of the reason for this failure is connected with the atomic number of the material surrounding the chamber.

The cross section for bremsstrahlung, which is the process making the largest contribution to the number of bursts of very large size, was derived by Heitler[4] using a Born approximation which was valid only if $2\pi Ze^2/\hbar v_0 \ll 1$, where Z is the atomic number of the material concerned and v_0 is the velocity of the incoming charged particle. Even for $v_0 \sim c$, this quantity has a value of 0.6 for lead, making the use of the approximation rather doubtful. For iron, this quantity is 0.2 and the approximation is considerably better.

Furthermore, cascade shower theory plays an important role in the analysis of this theoretical burst rate, and the approximations used are valid for high energy electrons and photons but are of doubtful validity for the low energy range. Since the critical energy β, which is roughly proportional to Z^{-1}, is in a sense a measure of the lowest energy an electron can have and still play a significant role in the further development of a shower, these approximations, which are very poor for lead, become better as the atomic number of the material around the chamber is decreased.

In order to permit a more valid theoretical calculation for comparison with experimental results, the present experiment A was designed to measure the burst rate under considerable thicknesses of material of low atomic number. In addition, the use of a material of low atomic number permits a more sensitive test of the Z dependence of these bursts than has been possible previously.

The burst rate observed in experiment A was somewhat larger than the calculated burst rate due to μ-meson interactions for this geometry. Experiment B was designed and performed to obtain information concerning the angular dependence and the absorption in lead of the primaries responsible for these excess bursts. The design was predicated on a tentative attribution of these excess bursts to interactions of the N component.

2. EXPERIMENTAL APPARATUS

Since the equipment was designed for the purpose of measuring the rate of bursts due to the high energy interactions of μ-mesons, provision had to be made to eliminate or identify, in some way, other types of bursts. A large amount of ionization may be produced in the ionization chamber by two distinct classes of events; that is, emission of an α-particle by an atom on or near the surface of the inner walls of the chamber plates or by one of several types of events associated with cosmic radiation. To minimize the useless recording of events of the first type, it was required that ionization in the chamber be accompanied by the discharge of one or more of the Geiger tubes in the coincidence tray.

The ionizing events associated with cosmic rays may be further divided into soft showers (mainly produced

* The research was aided by a grant to the cosmic-ray program of the University of Michigan from the joint program of the AEC and ONR and by a fellowship of 18 months duration administered by the AEC.
† Now with E. I. duPont de Nemours and Company, Argonne National Laboratory, Chicago, Illinois.
[1] M. Schein and P. S. Gill, Revs. Modern Phys. **11**, 267 (1939).
[2] R. E. Lapp, Phys. Rev. **69**, 312 (1946).
[3] R. F. Christy and S. Kusaka, Phys. Rev. **59**, 414 (1941).
[4] W. Heitler, *The Quantum Theory of Radiation* (Oxford University Press, London, 1936).

by μ-meson interactions in the material around the chamber) and nuclear events (produced by the few protons and π-mesons in the hard component at sea level). To some extent, it is possible to distinguish between these two types by the shape of the voltage pulse produced on the collecting wires. Some of the soft showers recorded may be expected to result when the core of an Auger shower strikes in the vicinity of the chamber. An auxiliary record was made of those soft-shower-like chamber pulses which were accompanied by the discharge of one or both of the Geiger tubes in the air-shower tray, which was located in the open a few feet from the chamber.

The equipment used in this experiment is displayed in symbolic form in the block diagram, Fig. 1, which is largely self-explanatory.

The chamber was constructed in the form of a rectangular parallelepiped. The top and bottom of the chamber are 1-inch thick Duralumin plates and the four sides are $\frac{5}{16}$-inch steel plates. The steel plates are 8.0 inches high and were welded together to form a rectangular area of dimension 24 inches by 92 inches. These plates were grounded and served as the cathode. As anodes, 6 wires were suspended halfway between the Duralumin plates and parallel to the long axis of the chamber. The volume controlled by each of the 4 collecting wires (the pulses induced on the two outer wires were not measured) was 4 inches wide, 8 inches high, and 86 inches long. These sensitive volumes were not bounded by the steel plates, protection being afforded either by dummy wires or by guard cylinders around the wires. The chamber was filled with argon at a pressure of 1.40 atmospheres. The argon contained 0.1 percent of unspecified impurities.

Polonium α-particle sources were used for the purpose of calibrating the chamber. The sources were made by plating polonium onto the end of a rod which could be inserted into and withdrawn from the chamber using an O-ring sealing device. For normal chamber operation, the source was withdrawn into a recess outside of the Duralumin plate. For calibration, the source could be moved from the inner surface of the Duralumin to a point 4 inches inside the plate.

The chamber was operated as an electron pulse chamber using a "delay line clipping" method of low frequency rejection.[5,6] The preamplifiers and amplifier *I* in the block diagram follow the wiring diagram identified in Elmore and Sands[7] as a Model 100 pulse amplifier, amplifier *I* being only the first of the two negative feedback loops in the main amplifier. The synchroscope follows the design of Fitch and Titterton.[8] These amplifiers are stable and linear and the distortion introduced in the pulse is small enough so that significant differences in pulse shapes are not destroyed.

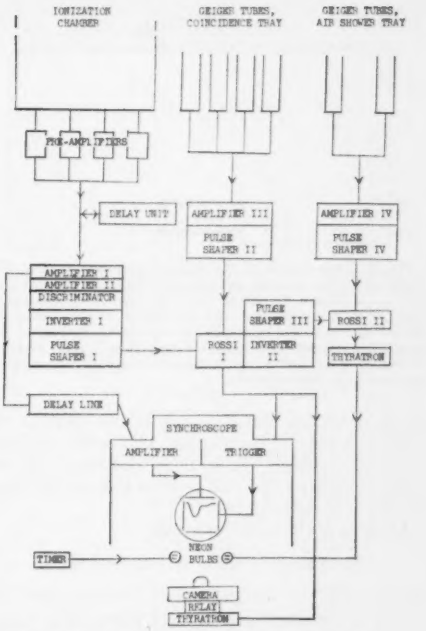

FIG. 1. Block diagram of equipment and electronics.

The advantage in using 4 preamplifiers lies in increasing the signal to noise ratio. Most of the input capacity C to the grid of a preamplifier is inside the chamber. For a charge Q induced on one wire, the voltage pulse is $\sim Q/C$. If the noise at the grid of the first tube is N, the signal to noise ratio out of the preamplifier is $\sim Q/CN$ and after combining the output of the four preamplifiers, it is $Q/4^{\frac{1}{2}}CN$, since the noise outputs are random and incoherent. On the other hand, if the four collecting wires are joined before the grid of the first tube, the capacity is nearly $4C$, the signal is $Q/4C$ and the signal to noise ratio out of the preamplifier is $Q/4CN$. A gain of two in this factor is thus obtained.

3. CHAMBER ENVIRONMENT

The experiments were performed in the second basement of Randall Laboratory. Surrounding the room, there is approximately 4 feet of brick, earth, and concrete. The chamber was placed several inches above the concrete floor, which had only sand underneath. The chamber itself was surrounded, except underneath, by a minimum of 116 cm of commercial sand-lime brick as illustrated in Fig. 2. The ends of the chamber were surrounded in a similar fashion with the exception of a

[5] B. Rossi and H. H. Staub, *Ionization Chamber and Counters* (McGraw-Hill Book Company, Inc., New York, 1949).
[6] Bridge, Hazen, Rossi, and Williams, Phys. Rev. **74**, 1083 (1948).
[7] W. C. Elmore and M. Sands, *Electronics* (McGraw-Hill Book Company, Inc., New York, 1949).
[8] V. L. Fitch and E. W. Titterton, Rev. Sci. Instr. **18**, 821 (1947).

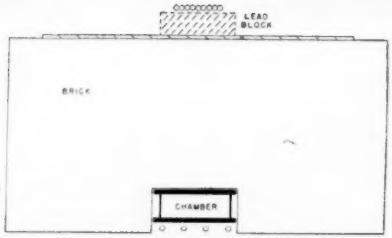

FIG. 2. Cross section of the chamber and environment. The circles under the chamber represent the Geiger tube coincidence tray in experiment A, during which the lead block was not in place. This tray was augmented and moved to the position indicated on top of the brick pile for experiment B. Part of this experiment was performed with the lead block in place and part without. The air-shower tray is represented by the two circles at the left outside the brick pile.

tunnel which led through the brick pile and was the height and width of the chamber. This permitted access to the preamplifiers, Geiger tubes, and the connecting leads. In addition, a 1-inch layer of lead covered most of the top of the brick pile.

In terms of the radiation length,

$$X_0=[4\alpha(N/A)r_0^2Z(Z+1)\ \log 183Z^{-\frac{1}{3}}]^{-1},$$

where $\alpha=1/137$, $r_0=2.82\times10^{-13}$, $N=6.02\times10^{23}$, and Z and A are the atomic number and weight, respectively, of the material, the chamber was shielded by ~9 radiation lengths in the building, 9.2 radiation lengths in the pile of brick, and, for some distance around the vertical, by 5 radiation lengths of lead. In terms of mass per unit area, a measure which is appropriate for the elimination of the N component, the building contained ~200 g-cm^{-2}, the lead contained 30 g-cm^{-2}, and the brick pile contributed 180 g-cm^{-2}.

The critical energy β for the material was obtained from the Bloch formula for collision energy loss[9] by setting $-(dE/dx)=\beta/X_0$ and by solving the resulting transcendental equation by successive approximations. I_0 in this equation was taken to have the value 11.5 ev in accordance with the measurements of Wilson.[10] The values of these shower theory parameters which are appropriate for the present arrangement will lie between those for brick (0.90 SiO_2, 0.10 CaO) and for Duralumin (0.96 Al, 0.04 Cu) but will be much closer to the values for brick since there is only $\frac{1}{4}$ radiation length of Duralumin between the brick and the sensitive volume of the chamber. For brick and Duralumin, X_0 in g cm^{-2} is 26.5 and 23.6, and β in Mev is 55.7 and 47.1, respectively. For the brick-Duralumin combination, values of $X_0=26$ g cm^{-2} and $\beta=54$ Mev were used.

In experiment A, the coincidence tray of Geiger tubes was placed immediately under the chamber. This arrangement insured that less than 0.1 percent of the bursts from any part of the upper hemisphere were missed because of the coincidence requirement. The smallest burst recorded contained about 35 particles capable of penetrating the bottom Duralumin plate. In experiment B, the coincidence tray was placed 7 inches above the top of the brick pile in such a position that the center of the tray was above the center of the ion chamber and the long axes of the tray and the chamber were parallel. The coincidence tray in the latter case consisted of 9 closely packed Geiger tubes giving a sensitive tray area of 18 inches by 88 inches. For bursts produced in the brick, the burst-producing particle triggered the coincidence tray. Part of the data in experiment B was gathered with air between the tray and the top of the brick pile and part with an additional 6 inches of lead filling this gap.

[9] F. Bloch, Z. Physik **81**, 363 (1933).
[10] R. R. Wilson, Phys. Rev. **60**, 749 (1941).

4. ELECTRON ATTACHMENT

An expression for the voltage pulse, V_p, produced on a central wire by the collection of the ions in a burst was developed in reference 5. This was

$$V_p=-(e/U_0C)\sum_1^N(U_0-U_i),$$

where U_0 is the potential of the central wire with respect to the grounded chamber shell, U_i is the potential at the point of formation of one of the N ion pairs in the burst, and e is the electronic charge. It was developed under the assumption of negligible electron attachment. Electron attachment is the process in which an electron collides with a neutral molecule and forms a negative ion (O_2 and H_2O are the two most common possibilities). Since the drift of ions is negligible during the collection time of an electron pulse chamber, the electron is essentially lost in this process and V_p is correspondingly smaller.

One customary criterion for freedom from electron attachment is the demonstration that, for a calibration source flush with the wall of the chamber, V_p does not continue to increase as U_0 is increased beyond a certain

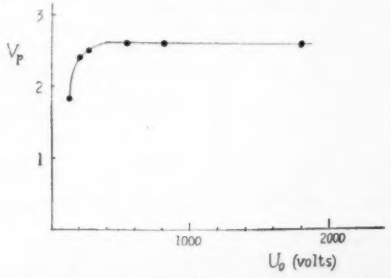

FIG. 3. Maximum voltage pulse V_p in arbitrary units, produced by an α-particle source flush with the chamber walls as a function of the potential difference across the chamber, U_0, in volts.

saturation voltage. The experimental values of V_p for a source flush with the chamber wall and directly under a collecting wire are plotted in Fig. 3 in arbitrary units as a function of the potential U_0 of the wire. An operating potential of $U_0=800$ volts was chosen on the basis of these results.

To check the basic criterion, a further series of measurements was made in which U_0 was maintained at 800 volts and the distance from the source to the collecting wire was varied from 4 inches to $\frac{1}{2}$ inch. An example of the results is plotted in Fig. 4. Since, in the absence of electron attachment, $\sum[U_0-U_i(r)]$, and thus V_p, is a constantly decreasing function of r, the experimental points (⊙) indicate that some attachment does exist. The saturation evidenced in Fig. 3 indicates either that w^-, the electron drift velocity, is almost independent of E^-, the field strength, or that the probability of attachment per collision rises for increasing w^- in such a way as to compensate for the decrease in the number of collisions due to the decrease in the collection time.

It is possible to make a rough estimate of the collection time by measuring the corresponding distance on the oscilloscope photograph. The initial slope of the calibration pulses is so small for $r=4$ inches that it is difficult to determine the point at which the pulse started. Within the limits set by this difficulty, the collection time for this value of r was found to be independent of U_0 for the range 400 volts$<U_0<$1800 volts. The field strengths at the Duralumin plate as well as throughout the chamber increased by a factor of 4.5 as U_0 was increased. We thus conclude that w^- is independent of E^- over this range. Another series of measurements was made in which r was varied holding U_0 fixed. This also had the effect of varying the average field strength for the electrons concerned, since the field strengths increase as the wire is approached. Measurements of this collection time are plotted in Fig. 5 for $U_0=800$ volts. A straight line through the point $r=0$, $t^-=0$ fits the data rather well, which again indicates

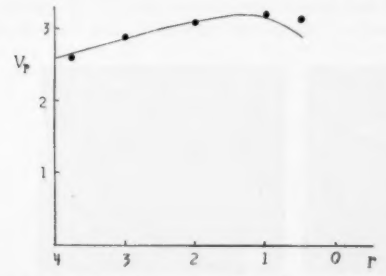

FIG. 4. The solid circles represent the maximum voltage pulse V_p in arbitrary units, produced by an α-particle source r inches from the collecting wire as a function of r for a chamber voltage of 800 volts. The curve is calculated on the basis of a simple model for electron attachment.

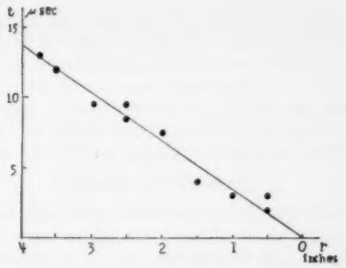

FIG. 5. The collection time t in μ-sec, for the electrons produced by an α-particle source r inches from the collecting wire as a function of r.

that w^- is independent of E^- over a considerable range of field strengths.

In view of this conclusion, a very simple treatment of the effect of electron attachment is possible. We have $dN=kNdr$ and, integrating, $\log N=c+kr$. Thus, if we have originally N_0 electrons produced at a distance r_0 from the wire, the number reaching the wire is $N_w=N_0e^{-kr_0}$. The contribution to the pulse height of those electrons which reach the wire is $V_p\sim N_0[U_0-U(r_0)]e^{-kr_0}$. An electron which is absorbed at a distance r from the wire after being produced at a distance r_0 also makes a contribution proportional to $[U(r)-U(r_0)]$, but since U behaves logarithmically in the neighborhood of the wire, the contribution is usually small and will be neglected.

Before the expression for V_p can be compared to the experimental points, one further consideration must be made. The source is located on a grounded metal rod which projects into the chamber and distorts the potential field. As a first approximation, it was assumed that the effect of the distortion was that the average potential in which the ions from an α-particle are produced is reduced by some constant fraction, b. Thus $V_p\sim N_0[U_0-bU(r_0)]e^{-kr_0}$. An attempt to match the experimental points in Fig. 4 by adjusting the parameters b and k in this expression results in a value of b slightly greater than one. In view of the existence of some uncertainty in the experimental results this is not surprising, but physically it is an impossibility. The value of b was therefore taken to be 1.0, and the best fit was then obtained for $k=0.215$ inch^{-1}. The curve plotted in Fig. 4 represents the above expression for V_p with these values of the parameters inserted. It should be mentioned that the value of k does not depend very critically on the value of b. If b had been assumed to be 0.8, k would have been 0.19 inch^{-1}. Several typical photographs on which the experimental points were measured are shown in Fig. 6.

A comparison may now be made between the two extreme cases of ionization distribution in the chamber involved in calibrating the chamber by integrating numerically the expression $[U_0-U(r_0)]e^{-kr_0}$ over the

appropriate volumes in the two cases and normalizing to N_0 original ions. If the same number of ions is distributed uniformly throughout the chamber or, on the other hand, is concentrated near one of the grounded plates of the chamber, the locally ionizing event (calibration type) will produce a pulse which is 4.9 percent lower than the generally ionizing event (burst type).

5. CHAMBER CALIBRATION

If, with the calibration source flush with the wall, the number $N(h)$ of α-particle pulses larger than a size h is plotted as a function of h, a curve similar to Fig. 7 in reference 6 is obtained. The maximum pulse size produced by an α-particle h_α may be taken as the h value obtained by extrapolating the nearly vertical, linear portion of this curve to zero frequency. About 75 percent of the pulses have a size which is not more than 3 percent smaller than h_α, and the number that have a size more than 3 percent larger than h_α is less than 1 percent of the total. It might be anticipated that, out of a group of about ten consecutive pulses, the largest would usually lie within 3 percent of h_α. This was demonstrated to be the case.

Thus the calibration procedure adopted during the experiment was to superimpose on the film, the synchroscope traces of a group of from five to twenty pulses from the calibration source flush with the chamber wall. Such a group is illustrated in Fig. 6, $U_0=800$, $r=4$. A record of five such groups was made in each calibration, and in general, the largest pulse in each of the five groups did not differ from any of the other largest pulses by more than the accuracy of measurement—that is, about 3 percent. Occasionally, one deviant in a group of five was eliminated before h_α was determined as the mean of the largest pulse in each of the groups.

Some of these deviants were recognizable as being the result of the superposition of two α-particle pulses. Other smaller deviations may have been due to noise fluctuations superimposed on some of the pulses.

This procedure was repeated for each of the four collecting wires and signal channels, the measurements were corrected for the results of electron attachment, and it was required that h_α for the four wires agree to within 5 percent before the related burst results were used. This requirement was imposed to insure that the gains of the four preamplifiers were the same within 5 percent. This was necessary because the outputs of the preamplifiers were mixed together and corrections for differences in gain could not be made. The correction for electron attachment was applied to the calibration pulses as described above, to make the corrected pulse height the same as that of a pulse produced by the same amount of ionization distributed generally.

6. EXPERIMENTAL RESULTS

Table I gives the results of experiment A. The column $n(J)$ is the number of events, with a pulse shape indicating general ionization, within the ionization limits listed in column 1 in the time t. J is expressed in units of 2.00×10^8 ion pairs, the ionization produced by a calibration α-particle. $N(J)$ is the number of events per hour with an ionization greater than the lower of the corresponding limits in column 1, and ΔN is approximately the statistical uncertainty $N^{\frac{1}{2}}/t$. Actually, it is somewhat larger than this because air-shower tray information was not available for all pulses and the application of a correction for air showers to that part of the burst rate for which air-shower bursts could not be directly eliminated increased the probable error slightly.

The number of events with a pulse shape indicating more or less local ionization was 0.13 per hour with a pulse size greater than 1.5 h_α. The corresponding frequencies of pulses of size greater than 2.0, 3.0, and 4.0 h_α were 0.05, 0.02, and 0.007 per hour, respectively.

The results of experiment B, both with and without the additional 6 inches of lead between the coincidence tray and the top of the pile, are presented in Table II in a similar manner.

7. THEORETICAL BURST-SIZE-FREQUENCY DISTRIBUTIONS

a. General Considerations

The differential energy spectrum gives the number of μ-mesons between the energies E_0 and E_0+dE_0 in a

(a) (b) (c)

FIG. 6. Photographs of synchroscope traces. (a) A group of α-particle pulses produced by a source 4 inches from the collecting wire. (b) Same as (a) with $r=1$ inch. (c) Cosmic-ray burst pulse involving 4.0×10^8 ion pairs. The light in the lower left corner indicates a coincidence with the air-shower tray.

TABLE I. Burst rates, experiment A.

J ionization units	$n(J)$ events	t hours	$N(J)$ per hour	ΔN per hour
1.2–1.49	514	447	3.54	0.08
1.5–1.99	539	589	2.38	0.07
2.0–2.49	311	611	1.49	0.05
2.5–2.99	171	611	0.985	0.044
3.0–3.99	208	611	0.707	0.039
4.0–4.99	95	611	0.366	0.031
5.0–5.99	48	611	0.211	0.026
6.0–	81	611	0.132	0.022

TABLE II. Burst rates, experiment B.

J ionization units	Without lead 312 hours $N(J)$ per hour	Without lead 312 hours ΔN per hour	With lead 308 hours $N(J)$ per hour	With lead 308 hours ΔN per hour
1.5	0.450	0.038	0.315	0.032
2.0	0.240	0.028	0.169	0.024
2.5	0.148	0.022	0.103	0.018
3.0	0.099	0.018	0.070	0.015
4.0	0.053	0.013	0.039	0.010
5.0	0.032	0.010	0.023	0.009

differential solid angle, $\sin\theta d\theta d\phi$. If this is multiplied by the probability $\sigma_i(E_0, \epsilon)d\epsilon dx$ of an interaction in a thickness of material, dx, resulting in the production of a soft secondary (knock-on electron or bremsstrahlung photon) of energy ϵE_0 and by the probability $P(\epsilon E_0, x, S)$ of a shower with a number of particles greater than S resulting from this secondary after traversing a thickness x of material, a differential expression is obtained for the number of bursts of this or greater size hitting the chamber. The ionization produced in the chamber by such a burst is related to the burst size by the average path length in the chamber of the electrons in the burst. If the expression resulting from this relation is integrated or summed over the variables θ, ϕ, x, ϵ, and E_0, and over the variables describing the position at which the shower hit the chamber, the number of events is obtained in which an ionization greater than a given amount is produced in the chamber.

As will be shown, the μ-meson spectrum at sea level is of the form

$$n(E_0, \theta) = ce^{-\alpha E_0}/(E_0 + k\sec\theta)^m.$$

The functions of θ and ϕ introduced by a consideration of the present geometry would make it necessary to integrate the integral over θ numerically and, consequently, the subsequent integrals over ϵ and E_0 would become prohibitively lengthy. It is more convenient to separate the integration over θ from the integrations over ϵ and E_0 by dividing the upper hemisphere into regions which will be specified by an index G, such that the denominator in the above expression does not change significantly within a particular region. This gives rise to a series of spectra,

$$n_G(E_0)dE_0d\Omega = ce^{-\alpha E_0}dE_0d\Omega/(E_0 + k_G)^m,$$

where $k_G = k\langle\sec\theta\rangle_{kv}$ and $\theta_{G\,\min} \leq \theta < \theta_{G\,\max}$.

The number of bursts with more than S electrons per square meter per hour per unit solid angle, $N_{iG}(S)$, arising from process i in region G may then be found by integrating $P(\epsilon E_0, S)$ over all possible ϵE_0 weighted by the appropriate number of secondaries of energy ϵE_0. This is expressed by the following integral:

$$N_{iG}(S)d\Omega = d\Omega\int_0^\infty dE_0 n_G(E_0)\int_0^{\epsilon_m} d\epsilon\sigma_i(E_0, \epsilon)P(\epsilon E_0, S).$$

The voltage pulse produced by a burst, which is proportional to the number of ion pairs J depends not only on S but also on the path length in the chamber of these S particles. If q is the number of ion pairs produced per unit path length by an electron of an energy equal to the average energy of electrons in a burst and $\bar{p}$ is the average path length of the electrons in the burst, then $J = q\bar{p}S$.

It is thus necessary to determine the differential spectrum of path lengths in the chamber in each of the regions G. This is most conveniently accomplished by determining the integral path spectrum and performing a numerical differentiation. The quantity $A(p, \theta, \phi)$, which is the area of the chamber over which a particle entering the chamber from the solid angle $d\Omega$ around (θ, ϕ) has a path length $\geq p$, will be integrated over $0 \leq \phi \leq 2\pi$ and $\theta_{G\,\min} \leq \theta \leq \theta_{G\,\max}$, giving the total aperture of the chamber for a path length $\geq p$ in region G,

$$A_G(p) = 4\int_{\theta_{G\,\min}}^{\theta_{G\,\max}} d\theta\sin\theta\int_0^{\pi/2} d\phi A(p, \theta, \phi).$$

$A_G(p)$ is then numerically differentiated to give $a_G(p)dp$, the aperture of the chamber in region G for path lengths between p and $p+dp$. If one particle were incident at random per unit area per unit time from region G, $a_G(p)$ would be the number per unit time which hit the chamber and had a subsequent path length in the chamber between p and $p+dp$.

The number of bursts $N_G(J)$ which produce an ionization in the chamber $>J$ is

$$N_{iG}(J) = \int_0^\infty dp a_G(p)N_{iG}\left(\frac{J}{q\bar{p}}\right);$$

that is, it is the number of bursts for which $q\bar{p}S > J$. In the final evaluation, this integral will be replaced by a summation over the apertures, $a_G(p)\Delta p$.

Finally, we sum $N_{iG}(J)$ over the subscripts i and G to obtain the total-ionization-frequency distribution $N(J)$ for the chamber:

$$N(J) = \sum_i\sum_G N_{iG}(J).$$

b. The μ-Meson Energy Spectrum

In the absence of any accurate direct determinations, the best estimate of the vertical μ-meson energy spec-

trum at sea level is obtained by transforming a depth-intensity relationship for cosmic rays (the measurements of Wilson[11] will be used) into an energy-intensity relationship using a range-energy correlation. Cosmic rays far underground consist of μ-mesons and associated soft secondaries. Randall's[12] estimate of the number of such soft secondaries included in Wilson's counting rates will be used to correct these underground data. This method is valid up to energies of the order of 2×10^{11} ev. Beyond this point, certain processes of a catastrophic nature become important (precisely those processes which result in the bursts under investigation).

Lyons[13] has investigated the effect of these catastrophic events and finds that they result in an exponential decrease superimposed on the power law in the depth spectrum. Wilson's data may be rather well represented by the analytical expression $N(h)\sim h^{-\gamma'}e^{-\alpha' h}$, where N is the frequency of mesons observed at a depth h in meters of water equivalent, and $\alpha'=1/(2000$ m.w.e.). It has been pointed out[14,15] that the knock-on and bremsstrahlung cross sections for spin $\frac{1}{2}$ μ-mesons are too small by about a factor of 10 to account for this observed value of α' and that the deviation results from a deviation in the μ-meson energy spectrum at sea level which may be explained on the basis of the competition between nuclear interactions and decay for π-mesons in the atmosphere.

The vertical differential μ-meson energy spectrum obtained from this transformation is

$$n(E_0,0)dE_0d\Omega=Ce^{-\alpha E_0}d\Omega dE_0/(E_0+1.8\times10^9)^\gamma,$$

with $\alpha=1/(5\times10^{11}$ ev) and $\gamma=2.9$ for $E<10^{11}$ ev and $\gamma=3.1$ for $E>10^{11}$ ev. 1.8×10^9 ev is the energy required for a μ-meson to reach sea level from an average point of production. C was taken to be $0.160\times10^{17.1}$ in order to normalize the integrated spectrum to Greisen's[16] experimental value at sea level.

The effect of increasing θ on this energy distribution is to increase the path length and thus the energy loss in reaching sea level. Since the relationship between range and energy is essentially linear for energies of the order of 1.8×10^9 ev, where only ionization is important, we finally have

$$n(E_0,\theta)dE_0d\Omega=Ce^{-\alpha E_0}d\Omega dE_0/(E_0+1.8\times10^9\sec\theta)^\gamma.$$

c. The Shower Function, $P(\epsilon E_0, S)$

$P(\epsilon E_0, x, S)$ was defined as the probability of occurrence of a shower containing more than S particles at a distance x from the position of a μ-meson interaction in which an energy ϵE_0 was transferred to a soft secondary. The function,

$$P(\epsilon E_0, S)=\int_0^\infty P(\epsilon E_0, x, S)dx,$$

is roughly a measure of the distance over which a shower of energy ϵE_0 contains more than S particles. This function depends not only on the average behavior of cascade showers, which is rather well known, but also upon the form and magnitude of the fluctuations in S from shower to shower, a subject which, at present, is in a considerably more unsettled state.

Christy and Kusaka[3] proposed an analytical approximation for the average behavior of a shower in the vicinity of the maximum of the shower development which agrees well with the recent calculations of Bernstein.[17] However, their expression for the average behavior was derived by considering only the longitudinal development of the shower, an approximation which is also used by Bernstein and which is valid for the high energy electrons in a shower but which breaks down completely for the lowest energies involved.

Roberg and Nordheim[18] have investigated the lateral development of cascade showers. They have calculated the fraction of electrons in a shower which have a root-mean-square scattering angle of one radian or more. This fraction, which to some extent measures the degree of failure of the longitudinal approximation, is one-sixth for material of low atomic number and increases to about four-fifths for lead. Wilson[19] has investigated the effect of scattering on the longitudinal development of a shower using a Monte Carlo method for lead and finds a reduction in the number of electrons at depths near the maximum of shower development by a factor of two compared to the results obtained neglecting scattering. We might expect a corresponding reduction in brick of the order of 15 or 20 percent. The effect of this reduction on the amount of ionization observed in an ion chamber is dependent on the chamber geometry and may result in a considerably smaller change in the ionization. Considerations of chamber geometry indicate that 95 percent of the bursts observed in the present experiment A have path lengths of less than 0.5 meter and that, for most of these, the effect of angular deviations from the shower is to increase the average path length in the chamber of the electrons in the burst as compared to the axis length. This increase in ionization compensates to some extent for the loss of electrons resulting from scattering.

Since the burst rate is a rapidly decreasing function of burst energy, the effect of fluctuations is to increase the burst rate. Christy and Kusaka[3] showed that the burst rate using the Furry expression for fluctuations was 2.2 times the burst rate R_0 which would be predicted on the basis of no fluctuations. Using the value

[11] V. C. Wilson, Phys. Rev. **53**, 377 (1938).
[12] C. A. Randall, unpublished thesis, University of Michigan (1950).
[13] D. Lyons, Physik. Z. **42**, 166 (1941).
[14] K. I. Greisen, Phys. Rev. **73**, 521 (1948).
[15] S. Hayakawa, Prog. Theoret. Phys. **3**, 199 (1948).
[16] K. I. Greisen, Phys. Rev. **61**, 212 (1942).
[17] I. B. Bernstein, Phys. Rev. **80**, 995 (1950).
[18] J. Roberg and L. W. Nordheim, Phys. Rev. **75**, 444 (1949).
[19] R. R. Wilson, Phys. Rev. **79**, 204 (1950).

obtained by Nordsieck, Lamb, and Uhlenbeck[20] for the second moment of the S distribution, $\sigma=\frac{1}{2}\bar{S}^2$ as compared to $\sigma=\bar{S}^2$ for the Furry model, they estimated a burst rate of $1.55R_0$. However, Scott and Uhlenbeck[21] recalculated this second moment and found a considerably lower value which, on the basis of one numerical calculation for the case of their cosmic-ray shower model is of the order of $\sigma=3\bar{S}$. It is estimated that the burst rate obtained using this figure, taking into account the reduced asymmetry of the distribution as compared to the Furry distribution, is $1.3R_0$. This figure, which is somewhat energy dependent, applies to the average energy involved in the present observations and should not be in error by more than 10 percent. An accurate calculation rather than an estimation is not in order since the information available on the fluctuations themselves is so meager.

d. Cross Sections for Spin ½ μ-Mesons

The cross section for bremsstrahlung was derived by Heitler.[4] If his nomenclature is modified by letting $\epsilon=k/E_0$ and $E=E_0-k$, and if the radius of the nucleus is introduced as the lower limit to his integration over the impact parameter, the cross section is

$$\sigma(E_0,\epsilon)d\epsilon=\frac{16}{3}d\epsilon\left[\frac{3\epsilon}{4}+\frac{1-\epsilon}{\epsilon}\right]\left[\ln\frac{12E_0(1-\epsilon)}{5\mu c^2\epsilon}-\frac{1}{2}\right],$$

where σ is measured in units of $(e^2/\mu c^2)^2\alpha Z^2$. Screening of the Coulomb field of the nucleus by the atomic electrons causes this cross section to become essentially independent of E_0 above an energy such that $(E_0/\mu^2c^3)\sim\hbar/me^2Z^{\frac{1}{3}}$ or $E_0\sim 9\times10^{11}$ ev for aluminum.

For the knock-on process, Bhabha[22] has derived a cross section which, for the case of $E_0\gg\mu c^2$, reduces to

$$\sigma(E_0,\epsilon)d\epsilon=\frac{2\pi e^4}{mc^2}\frac{1}{E_0}\frac{d\epsilon}{\epsilon^2}\left[1-\frac{\epsilon}{\epsilon_m}+\frac{\epsilon^2}{2}\right]$$

per electron. $\epsilon_m=[1+(\mu^2c^2/2mE_0)]^{-1}$ for large E_0, where ϵ_m is the maximum fractional energy transferable by a meson (energy E_0, mass μ) to an electron (mass m).

Bhabha[23,24] has derived a cross section for the direct production of an electron-positron pair by a relativistic particle of mass M in the field of a nucleus of charge Z. If we let $E=E_-+E_+$, where E_- and E_+ are the individual energies of the pair, this cross section is

$$dQ(\gamma,E,E_-)=(8/\pi)(\alpha Z)^2r_0^2m^2c^4\gamma^2E^{-4}\ln 2k\gamma dEdE_-,$$

which was derived under the condition that $mc^2\gamma\ll(E_-,E_+)\ll Mc^2\gamma$, where m is the electron rest mass, $\gamma=1/(1-v^2/c^2)^{\frac{1}{2}}$ for the incoming particle, and k is an indeterminant factor of the order of unity.

Integrating over E_- from γc^2m to $\gamma c^2(M-m)$, we obtain the total cross section for the production of a pair with energy between E and $E+dE$,

$$Q(\gamma,E)dE=(8/\pi)(\alpha Z)^2r_0^2m^2c^4\gamma^2E^{-4}(E-2\gamma mc^2)\ln 2k\gamma dE.$$

Screening becomes important when $E\lesssim 2\gamma^2mc^3/183Z^{\frac{1}{3}}$. For these small energies, $\ln 2k\gamma\rightarrow\ln 183Z^{-\frac{1}{3}}kE/\gamma mc^2$. This integrated cross section is only an approximation, since the limits of integration violated the conditions of derivation. This is not important since, as will be shown, the contribution of this process to the production of large bursts is negligible.

e. The Calculations

The function $N_{iG}(S)$ is obtained by inserting the functions $P(\epsilon E_0,S)$, $\sigma_i(E_0,\epsilon)$, and $n_G(E_0)$ in the symbolic expression for $N_{iG}(S)$ given previously and by evaluating the integral over ϵ exactly and that over E_0 graphically. This was done for each region G and for $S=35$, 180, and 800 electrons using the cross sections for the bremsstrahlung and knock-on processes.

Relative to bremsstrahlung, the largest contribution to the burst distribution by pair production will be for small shower energies and thus for small S, since $Q_{\text{pair}}\sim E^{-3}$ and $\sigma_{\text{brem}}\sim E^{-1}$ for large E, where E is the shower energy. Evaluating $N_{pp,G}$ (35) by inserting $Q(\gamma,E)dE$ into a differential expression for $N_{iG}(S)$ and integrating over E from 0 to E_0 and over E_0 from 0 to ∞ gives a figure, $N_{pp,G}(35)=0.06$ m^{-2} sterad^{-1} hour^{-1} independently of the region G, as compared to $N_{\text{ks},G}(35)+N_{\text{brem},G}(35)=2.55$ m^{-2} sterad^{-1} hour^{-1} for $G=$I. The pair production contribution will be relatively less for larger i values of S and will be neglected.

$N_G(S)=\sum_i N_{iG}(S)$ is plotted in Fig. 7 for the regions $G=$I, V, and VII, the regions being defined by the following θ-limits: I (0°–50°), II (50°–63.4°), III (63.4°–70°), IV (70°–75°), V (75°–80°), VI (80°–83°), VIII (83°–84.8°), and VIII (84.8°–90°).

To obtain the number of events causing an ionization greater than $J=\bar{p}qS$, the summation $N(J)=\sum_G\sum_p a_G\times(\bar{p})NJ/\bar{p}q$ is performed, where N_G is obtained from Fig. 7, q is evaluated in Appendix I, and $a_G(\bar{p})$ is discussed in Appendix II. $N(J)$ was evaluated for $J=2\times10^5$, 6×10^5, and 1.8×10^6 ion pairs and is plotted in Fig. 8 in comparison with the experimental points.

A fairly accurate estimate of the curve for spin 0 corresponding to that for spin ½ in Fig. 8 may be obtained from the tabulated values of burst frequencies in Christy and Kusaka, interpreting their data for the present material rather than for lead. Table III gives the value of $N(S)$ for the bremsstrahlung and knock-on processes together. Corrections have been made for a ratio of meson-to-electron mass of 210 rather than 177 and for the Z dependence of the knock-on contribution.

The major contributions to $N(J)$ for $J=2\times10^5$, 6×10^5, and 1.8×10^6 ion pairs come from bursts in the

[20] Nordsieck, Lamb, and Uhlenbeck, Physica **4**, 344 (1940).
[21] W. T. Scott and G. E. Uhlenbeck, Phys. Rev. **62**, 497 (1942). The author is indebted to Professor Uhlenbeck for calling his attention to this recalculation.
[22] H. J. Bhabha, Proc. Roy. Soc. (London) **A164**, 257 (1938).
[23] H. J. Bhabha, Proc. Cambridge Phil. Soc. **31**, 394 (1935).
[24] H. J. Bhabha, Proc. Roy. Soc. (London) **A152**, 257 (1935).

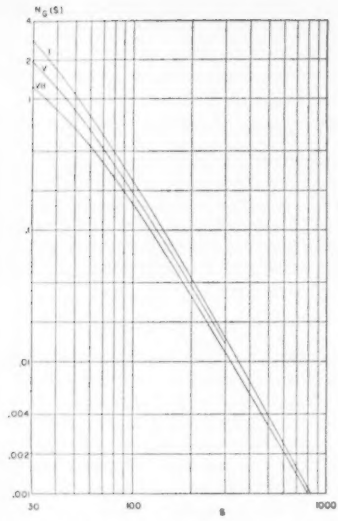

FIG. 7. The integral burst rate $N_G(S)$ per square meter per steradian in brick as a function of the number of particles S in the burst, for $G=I$ (top curve), $G=V$ (middle curve), and $G=VII$. The values for $G=II$, III, and IV lie between the top and middle curves while the values for $G=VI$ lie between the middle and bottom curves.

range $S=40$–80, 80–200, and 160–600, respectively. The ratio of $N(J)$ for spin 0 over that for spin $\frac{1}{2}$ will accordingly be taken as 0.65, 0.62, and 0.60, respectively, for these three values of J. These ratios are then used to plot the spin-0 curve in Fig. 8 relative to the curve for spin $\frac{1}{2}$.

8. DISCUSSION OF RESULTS

The uncertainties in the determination of the burst frequencies are not significantly greater than the statistical error $N^{\frac{1}{2}}/t$. The elimination of air showers, which amounts to a 3 percent correction for small bursts and to about 10 percent for large bursts, probably represents an overcorrection. Some of the eliminated bursts probably were caused by mesons associated with air showers, others being caused by similarly associated N component. The pulse sizes with which these frequencies are associated are uncertain by about 3 percent, which is equivalent to 6 percent in the frequency. The assumption concerning the equality in energy loss per ion pair for electrons and α-particles may be in error by 4 percent.

The energy spectrum of μ-mesons was estimated to have a probable error of 5 percent at 2×10^{11} ev and about 50 percent at 10^{12} ev which implies a 5 percent error in the calculated rate for small bursts and 15 percent for the largest bursts. The errors in the effect of fluctuations and of the average behavior of showers are both estimated to be about 10 percent.

The over-all probable error of the comparison between the experimental results and the calculations is thus about 18 percent for small bursts and increases to 23 percent for the largest bursts.

Assuming that the calculated μ-meson burst rate for experiment B is correct (the results to be derived are not very sensitive to the validity of this assumption), the ratio of the bursts observed in excess of this calculated rate with and without lead is 0.61 which corresponds to a mean free path of 340 g cm^{-2}. This mean free path is defined in terms of the observed burst production decrease and should be intermediate between the two extreme cases of mean free path for complete absorption and for interaction. Fahy[25] has obtained a similarly defined mean free path of 346 g cm^{-2} in lead for the bursts observed at high altitudes which are about 98 percent nuclear interactions. The agreement, which is fortuitously good, makes it reasonable to attribute the bursts observed in excess of the calculated rate to the N component primaries responsible for nuclear interactions.

The burst rate in experiment A resulting from nuclear interactions may be calculated if an assumption is made concerning the angular distribution of the N component. The ratio of the number of bursts due to nuclear interaction to be expected in experiment A compared to that observed in experiment B, assuming a $\cos^5\theta$ distribution for the N component, is

$$\frac{\int A_G(\theta,\phi,\exp A)\cos^5\theta d\Omega}{\int A_G(\theta,\phi,\exp B)\cos^5\theta d\Omega}=2.56.$$

The absolute rate of bursts in excess of that calculated for experiment B has been multiplied by this figure and subtracted from the rate observed in experiment A to give the corrected points in Fig. 8.

It should be noted that this result is not inconsistent with the results of the attempt to identify nuclear interactions by their pulse shape, which resulted in a negligible rate, since the triggering requirements are such as to almost completely eliminate the recording of events which produce an ionization of an entirely

TABLE III. Comparison of burst frequencies.

S	$N(S)$ (0)	$N(S)$ ($\frac{1}{2}$)	$N(0)/N$ ($\frac{1}{2}$)
20	5.7×10^{-7}	7.8×10^{-7}	0.73
40	1.35×10^{-7}	1.98×10^{-7}	0.68
80	3.0×10^{-8}	4.8×10^{-8}	0.63
160	6.5×10^{-9}	10.5×10^{-9}	0.62
320	1.31×10^{-9}	2.28×10^{-9}	0.58
640	2.5×10^{-10}	4.3×10^{-10}	0.58

[25] Edward F. Fahy, Phys. Rev. **83**, 413 (1951).

local character. The triggering probability is only increased by the presence of particles capable of penetrating the 1-inch Duralumin plate and recording on the bottom tray of Geiger tubes, and as this number increases, the discrimination according to pulse shape becomes more uncertain. It is also to be expected that a considerable fraction, if not the majority, of the recorded nuclear interaction bursts are produced by the soft showers initiated by the decay of π^0 mesons.

9. CONCLUSIONS

Lapp[26] has obtained burst data under 35 cm of iron using the Carnegie chamber for which Christie and Kusaka made their calculations. If we modify these calculations to the extent of changing the μ-meson mass to 210, renormalizing the μ-meson energy spectrum to the value used here and using 25.9 Mev for the critical energy in iron, we obtain a μ-meson burst rate, $N(S)=8.3\times10^{-9}$ cm^{-2} sec^{-1} sterad^{-1} for $S=300$ particles as compared to the value observed by Lapp of 12.9×10^{-9}. Bremsstrahlung accounts for 80 percent of the calculated rate and knock-on for the remainder. The bursts observed by Lapp in excess of the calculated rate, which amount to 55 percent of the μ-meson rate, may be translated into an expected excess for the present experiment A by assuming that the nuclear interaction bursts arise primarily from π^0 decay and that the N component is absorbed exponentially. It will be further assumed that the transparency of the nucleus is independent of Z for the types of interactions involved. The mean free paths in iron and brick corresponding to 340 g cm^{-2} in lead are, respectively, 225 g cm^{-2} and 175 g cm^{-2}. The cross section for knock-on, bremsstrahlung, and nuclear interactions will each have a different Z dependence, but the material dependence of the subsequent shower development will be the same in each case. Using a Z^{+1}, Z^{+2}, and Z^{+1} dependence for knock-on, bremsstrahlung, and nuclear interactions, and correcting for the additional 0.94 mean free path of absorber in the present experiment, Lapp's data indicate a ratio of nuclear interactions to μ-meson bursts of 0.47 which agrees very well with the values observed in experiment A for large bursts of 0.43. The assumed Z dependences are consistent with the results of this comparison although they are not thereby individually verified.

Although the agreement between the corrected results and the calculations for spin $\frac{1}{2}$ μ-mesons is well within the probable error, this does not constitute conclusive evidence that the spin of the μ-meson is $\frac{1}{2}$, since it is not at present possible to evaluate the contribution to the burst rate of possible specifically nuclear interactions of the spin 0 μ-meson. However, the present data might be used, given independent evidence concerning both the spin of the μ-meson and the magnitude of its nuclear interactions, to obtain an experimental estimate of the electromagnetic cross sections.

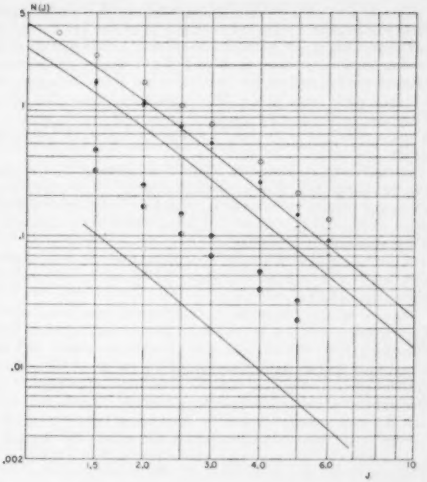

FIG. 8. The integral burst size-frequency distributions, $N(J)$, in bursts per hour for the present chamber and environment as a function of the number of ion pairs produced, J, in units of 2.00×10^8 ion pairs. The top and middle curves represent the calculated values for spin $\frac{1}{2}$ and spin 0 μ-mesons, respectively, in experiment A. The bottom curve is the calculated distribution for spin $\frac{1}{2}$ in experiment B. The experimental values are represented by the circles; (o) observed values in experiment A; (◓) observed values in experiment B without the lead block; (◐) values in experiment B with the lead block; (●) values in experiment A corrected for the estimated rate of nuclear interactions. The flags on these latter points represent the probable errors of the measurements.

The author is deeply indebted to Professor Wayne E. Hazen for his constant encouragement and advice during the course of this work. He is grateful to Mr. William P. Davis, Jr., for performing the tedious numerical integrations involved in evaluating the functions, $N_0(S)$, presented in Fig. 7.

APPENDIX 1

No reliable direct measurements of the average number of ion pairs produced by an electron per unit path length are available. This number (which is of course energy-dependent) may be estimated with some degree of accuracy, however, from the theoretical collision energy loss of an electron and from measurements of the average energy loss per ion pair produced.

It is not actually necessary to consider the total ionization produced by a burst in order to make comparisons with the theoretical predictions. We are interested essentially in the total energy expended in the chamber by a burst, and this may be derived directly from a comparison with the energy expended by a calibration α-particle if we know the ratio of the energy expended per ion pair formed by an α-particle (W_α) and by a high energy electron (W_β) in argon. Unfortunately, no measurements of these W are available using identical equipment and conditions, under which circumstance the effect of systematic errors in the measurements would tend to be negligible.

[26] R. E. Lapp, Phys. Rev. **69**, 312 (1946).

Curran, Cockroft, and Insch[27] have measured W_β with a proportional counter for electron energies of a few kev in various mixtures of argon and methane and arrive at an asymptotic value for low methane content of $W_\beta = 28.5$ ev. However, they state without further explanation that there are indications that W_β for very pure argon could differ appreciably from this value. They also quote a private communication from Nicodemus giving a value of $W_\beta = 26.9$ ev (experimental conditions, including gas purity, unknown).

Stetter[28] used an ionization chamber to measure W_α averaged over the complete path of a polonium α-particle in relatively pure argon and obtained a value of $W_\alpha = 28.4$ ev. Schmieder[29] found a value of $W_\alpha = 24.4$ ev under conditions which were, apparently, not fundamentally dissimilar.

A careful study of W for 340 Mev protons was made by Bakker and Segrè[30] and resulted in a figure for W_p of "a few percent" higher than 25.5 ev.

In view of the differences in experimental conditions and of the possible variations in systematic errors resulting from these differences, it is felt that these data are not inconsistent with the assumption that W is independent of the nature of the ionizing particle and, furthermore, that W is no more than slightly dependent on the energy of the ionizing particle. There is evidence[31] that W_β increases significantly for energies of the order of a few hundred ev compared to the value for high energy but it appears to be essentially constant for energies greater than a few kev. It will accordingly be assumed that $W_\alpha = W_\beta = 26.4$ ev.

Although the ion production occurs in argon, the energy distribution of the electrons in the burst is characteristic of the brick-duralumin combination since the amount of argon traversed is insufficient to produce an appreciable transition effect. Thus, the average energy near the maximum of the shower development is approximately the critical energy, that is, about 54 Mev. The Bloch[9] formula for energy loss by ionization gives the energy lost in collisions involving energy transfers up to some maximum value W_m,

$$-\frac{dE}{dx} = 2\pi\sigma Z r_0^2 \frac{mc^2}{\beta^2}\left[\ln\left(\frac{mc^2\beta^2 W_m}{(1-\beta^2)I^2}\right) + (1-\beta^2)\right],$$

where σZ is the electron density in the material; r_0 is the classical radius of the electron $= e^2/mc^2$; β is the fractional velocity of the incident electron; and I is the average ionization potential of the traversed material.

Bloch has demonstrated that $I \sim I_0 Z$ for any substance where I_0, if not quite constant, at least is a slowly varying function of Z. A value of I_0 of 11.5 rather than 13.5 will be used in accordance with the measurements of Wilson.[10]

In deciding what to use for W_m, the nature of the detection process must be considered. The Bloch formula represents an integration of a cross section for production of a secondary electron of energy W times W itself. For events in which somewhat more than the minimum amount of energy needed to ionize an atom is transferred, the energy will, in general, show up in the ionization chamber as tertiary, etc., ion formation unless the range of the secondary is sufficient to cause it to leave the chamber; in that case, some of the ions will be produced in the duralumin plate and will not be collected. The logarithmic dependence of dE/dx on W_m makes it relatively insensitive to the choice of W_m. A value of 2×10^5 ev will be used, corresponding to a range of 20 cm in argon at the present pressure of 1.4 atmospheres. The figure of 20 cm represents a rough compromise between a value of 12 cm, which would be appropriate for the most frequent bursts, with a path length of the order of 24 cm in the chamber and the value of 75 cm, which should be used for the very much less frequent bursts with a path length of the order of 1.5 meter.

The energy loss to secondaries of energy less than 2×10^5 ev is found to be 3770 ev cm^{-1}. The ionization produced in the chamber by those secondaries whose energy is greater than this corresponds to an additional energy loss of 160 ev cm^{-1}. This figure is obtained by calculation the number of such secondaries and assuming that the energy lost by each is only 2×10^5 ev.

A polonium α-particle source has been used to calibrate the chamber. Since the polonium α-particle energy is 5.30 Mev, the maximum number of ion pairs, n_α, produced in the chamber by the calibration source is

$$n_\alpha = 5.30\times10^6/26.4 = 2.00\times10^5 \text{ pairs}.$$

The number of ion pairs produced per cm by electrons is

$$n_p = 3930/26.4 = 149 \text{ pairs cm}^{-1}.$$

APPENDIX 2

The sensitive volume of the chamber is a rectangular parallelepiped of length a, width b, and height c. The projected area of the chamber over which a particle traveling in the direction (θ, ϕ) will have a path length in the sensitive volume $\geq p$ may be shown to be $A(p, \theta, \phi) = ab\cos\theta + bc\sin\theta\cos\phi + ac\sin\theta\sin\phi - 2pa\sin\theta \times\cos\theta\sin\phi - 2pb\sin\theta\cos\theta\cos\phi - 2pc\sin^2\theta\sin\phi\cos\phi + 3p^2\sin^2\theta \times\cos\theta\sin\phi\cos\phi$. This expression, multiplied by $\sin\theta$, is integrated to obtain the regional apertures $A_G(p)$. The integration limits for $p=0$ are from $0\leq\phi\leq2\pi$ and θ is restricted to the limits defining the region. In general, from any direction (θ, ϕ), any p may be found from $p=0$ to $p=p_{\max}(\theta, \phi)$. It is necessary to restrict the limits of integration for $A_G(p)$, $p>0$, to those angles for which $p<p_{\max}(\theta, \phi)$. The limits of the ϕ integration will then be functions of p and θ and the limits of θ will be functions of p.

The functions $A_G(p)$ are differentiated numerically to give the differential apertures $a_G(p)$. It was shown that the effect on $a_G(p)$ of the angular divergence of the showers (the previous calculations assumed a one-dimensional shower development) was small, and corrections were applied.

[27] Curran, Cockcroft, and Insch, Phil. Mag. **41**, 517 (1950).
[28] G. Stetter, Z. Physik **120**, 639 (1943).
[29] K. Schmieder, Ann. phys. **35**, 445 (1939).
[30] C. J. Bakker and E. Segrè, Phys. Rev. **81**, 489 (1951).
[31] L. H. Gray, Proc. Cambridge Phil. Soc. **40**, 72 (1944).

Investigation of the Beta-Spectra of Be^{10}, K^{40}, Tc^{99}, and Cl^{36}†

L. FELDMAN AND C. S. WU
Columbia University, New York, New York

(Received May 22, 1952)

The beta spectra of Be^{10}, K^{40}, Tc^{99}, and Cl^{36} were investigated with the Columbia University solenoidal spectrometer and it was found that each exhibited a forbidden shape. An analysis of the spectra yields the following results. The spectrum of Be^{10}, for which $\Delta J=3$, can be explained equally well by $2T$ or $2A$ for no parity change and by $3T$ or $3V$ if the parity does change. Similarly, the spectrum of K^{40}, for which $\Delta J=4$, can be accounted for by $3T$ or $3A$ if the parity changes and by $4T$ or $4V$ for no parity change. $\Delta J=2$ for the decays of both Tc^{99} and Cl^{36}. These spectra can be explained only by $2T$ or $2V$ with values for k^2 of 45 for Tc^{99} and 18 for Cl^{36} ($k^2=|A_{ij}|^2+|T_{ij}|^2$). If the true interaction prevailing in beta-decay is but a single one of the five linearly independent interactions, then it follows from these spectrum analyses that it must be the tensor interaction. A linear combination of tensor with one or more of the other interactions is possible. It seems, however, that more information than is provided by spectrum studies alone is necessary to determine the exact form of such a linear combination.

I. INTRODUCTION

THIS paper reports the results on the main portion of the investigation of forbidden beta-spectra begun in 1948 with the Columbia University solenoidal spectrometer. Preliminary results on the spectra of Be^{10},[1] K^{40},[2] Tc^{99},[3] and Cl^{36} [4] have been reported at several meetings of the American Physical Society and in various publications.[5] The measurements of the Cl^{36} spectrum presented in this paper were made with sources greatly improved in uniformity and thinness over those used in our earlier work,[4] thus extending the reliability of the data to much lower energies than was previously possible.

The momentum distribution of the electrons emitted in beta-decay is given by the Fermi theory as

$$P(p)dp=(G^2/2\pi^3)C_{nX}F(Z,W)p^2q^2dp, \qquad (1)$$

with $p^2=W^2-1$ and $q=W_0-W$. We will use the notation of Konopinski and Uhlenbeck[6] with the generalized expression for C_{nX} given by Greuling.[7] C_{nX} is the factor by which the allowed distribution must be multiplied to give a forbidden spectrum. It contains the matrix elements of the interaction between the nucleons and the beta-neutrino field in which appear factors dependent on the beta-energy, W and Z. n refers to the degree of forbiddenness and X to the interaction form. The essence of the Fermi theory is that the interaction giving rise to beta-decay is assumed to be proportional to the scalar product of relativistically invariant bilinear combinations of the wave functions of the neutrino and beta-particle and of the initial and final nuclei involved in the beta-process.[8] Fermi originally chose the form which transforms as a polar vector, but there are five possible linearly independent bilinear combinations which are relativistically invariant. These are classified according to their transformation properties and will be denoted by their usual abbreviations S, V, T, A, and P. The correct interaction may be none of these, but if it is to be Lorentz invariant and linear in the four wave functions involved, then it must be expressible as a linear combination of the five linearly independent forms. The properties of such a linear combination, except for interference effects, can be analyzed in terms of the properties of the individual forms.

For the allowed spectra, all the C_{0X} are constant, and therefore the energy dependence is completely given by the Coulomb factor, $F(Z, W)$, and the statistical factor p^2q^2dp describing the distribution of the decay energy between the beta-particle and the neutrino. Thus any theory which includes the neutrino concept and yields energy independent nuclear matrix elements to the first order could account for the experimentally observed shapes of the allowed spectra as well as the Fermi theory. Therefore, the investigation of the forbidden spectra will provide a decisive test of the theory and further select or limit the choice of the particular interaction form prevailing in beta-decay from the five linearly independent Lorentz invariant forms or linear combinations thereof.

The following is a condensation of the expressions given by Greuling[7] for C_{nX} and the appropriate selection rules:

† This work was made possible through partial support of the USAEC.

[1] C. S. Wu and L. Feldman, Phys. Rev. **76**, 698 (1949); L. Feldman and C. S. Wu, Phys. Rev. **78**, 318 (1950).

[2] L. Feldman and C. S. Wu, Phys. Rev. **81**, 298 (1951).

[3] C. S. Wu and L. Feldman, Phys. Rev. **82**, 332 (1951).

[4] C. S. Wu and L. Feldman, Phys. Rev. **76**, 693 (1949); **82**, 457 (1951).

[5] C. S. Wu, Revs. Modern Phys. **22**, 386 (1950); Proc. Intern. Conf. of Nuc. Phys., University of Chicago, 1951.

[6] E. J. Konopinski and G. E. Uhlenbeck, Phys. Rev. **60**, 308 (1941).

[7] E. Greuling, Phys. Rev. **61**, 568 (1942).

[8] A complete review of the theory of beta-decay is given by E. J. Konopinski, Revs. Modern Phys. **15**, 209 (1943).

$$
\begin{aligned}
C_{nS}&=S_{n,(n-1)'}(\beta\mathbf{r},\mathbf{r})\,|\,Q_n(\beta\mathbf{r},\mathbf{r})/n!\,|^2,\\
C_{nP}&=P_{n,(n-1)'}(\beta\gamma_5\mathbf{r},\mathbf{r})\,|\,Q_n(\beta\gamma_5\mathbf{r},\mathbf{r})/n!\,|^2,\\
C_{nV}&=V_{n,(n-1)'}(\mathbf{r},\mathbf{r})\,|\,Q_n(\mathbf{r},\mathbf{r})/n!\,|^2\\
&\quad+V_{n,(n-1)'}(\boldsymbol{\alpha},\mathbf{r})\,|\,Q_n(\boldsymbol{\alpha},\mathbf{r})/n!\,|^2\\
&\quad+iV_{n,(n-1)'}(\mathbf{r},\mathbf{r}:\boldsymbol{\alpha},\mathbf{r})[Q_n(\boldsymbol{\alpha},\mathbf{r})\cdot Q_n^*(\mathbf{r},\mathbf{r})\\
&\quad-\text{c.c.}]/(n!)^2+V_{n-1}([\boldsymbol{\alpha}\times\mathbf{r}],\mathbf{r})\\
&\qquad\times|\,Q_{n-1}([\boldsymbol{\alpha}\times\mathbf{r}],\mathbf{r})/(n-1)!\,|^2,\\
C_{nT}&=T_n(\beta[\boldsymbol{\sigma}\times\mathbf{r}],\mathbf{r})\,|\,Q_n(\beta[\boldsymbol{\sigma}\times\mathbf{r}],\mathbf{r}/n!\,|^2\\
&\quad+T_n(\beta\boldsymbol{\alpha},\mathbf{r})\,|\,Q_n(\beta\boldsymbol{\alpha},\mathbf{r})/n!\,|^2\\
&\quad-T_n(\beta\boldsymbol{\alpha},\mathbf{r}:\beta[\boldsymbol{\sigma}\times\mathbf{r}],\mathbf{r})[Q_n(\beta[\boldsymbol{\sigma}\times\mathbf{r}],\mathbf{r})\\
&\quad\cdot Q_n^*(\beta\boldsymbol{\alpha},\mathbf{r})+\text{c.c.}]/(n!)^2+T_{n',(n+1)}(\beta\boldsymbol{\sigma},\mathbf{r})\\
&\qquad\times|\,Q_{n+1}(\beta\boldsymbol{\sigma},\mathbf{r})/(n+1)!\,|^2,\\
C_{nA}&=A_n([\boldsymbol{\sigma}\times\mathbf{r}],\mathbf{r})\,|\,Q_n([\boldsymbol{\sigma}\times\mathbf{r}],\mathbf{r})/n!\,|^2\\
&\quad+A_{n',(n+1)}(\boldsymbol{\sigma},\mathbf{r})\,|\,Q_{n+1}(\boldsymbol{\sigma},\mathbf{r})/(n+1)!\,|^2.
\end{aligned}
\tag{2}
$$

The energy dependent factors as given by Greuling are represented here by the capital letters, $S_{n,(n-1)'}(\beta\mathbf{r},\mathbf{r})$, etc., denoting the particular interaction in which they occur. The expressions in parentheses identify the matrix elements, the Q_n's, with which each correction factor is associated. The subscripts n, $n-1$, and $n+1$ indicate the selection rules which apply for each matrix element. Thus the particular matrix element is nonvanishing in the nth forbidden approximation unless ΔJ is equal to one of the values in the subscript. A prime subscript signifies that the additional requirement $|J_i|+|J_f|>\Delta J$ must be satisfied. Thus, for example, a matrix element with the selection rule $\Delta J=n'$ does not appear in $n\to 0$ transitions. The selection rule for the change in parity is no for n even and yes for odd n in all cases except for C_{nP} in which the reverse is true. The expressions for C_{nX} as given by Greuling and above are complete except for certain matrix elements which appear in C_{1T}, C_{2T}, and C_{1A}, for which the selection rule is $\Delta J=0$, and do not apply to any of the forbidden spectra discussed in this paper. Also omitted are terms of $n+2$ order of magnitude which constitute negligible corrections to the nth forbidden approximation.

Certain general remarks can be made about the energy dependent factors. $S_n(\beta\mathbf{r},\mathbf{r})$ and $P_n(\beta\gamma_5\mathbf{r},\mathbf{r})$ are identical and also practically impossible to distinguish

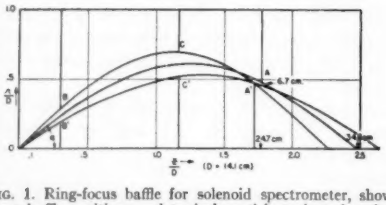

FIG. 1. Ring-focus baffle for solenoid spectrometer, showing various baffle positions and typical particle trajectories plotted in $r-Z$ plane.

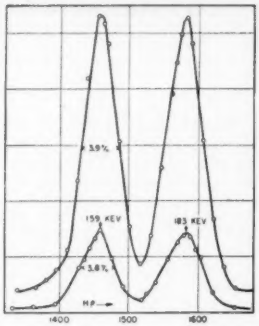

FIG. 2. Internal conversion line of In^{114} taken with ring-focus baffle and with Witcher-Haggstrom baffle. Ratio of peaks is 3.7.

experimentally from $V_n(\mathbf{r},\mathbf{r})$, $T_n(\beta[\boldsymbol{\sigma}\times\mathbf{r}],\mathbf{r})$, and $A_n([\boldsymbol{\sigma}\times\mathbf{r}],\mathbf{r})$. $V(\boldsymbol{\alpha},\mathbf{r})$ and $T(\beta\boldsymbol{\alpha},\mathbf{r})$ are identical for given n, as are $T(\beta\boldsymbol{\sigma},\mathbf{r})$ and $A(\boldsymbol{\sigma},\mathbf{r})$. $V(\boldsymbol{\alpha},\mathbf{r})$ and $T(\beta\boldsymbol{\alpha},\mathbf{r})$ for given degree of forbiddenness, n, are the same as $T(\beta\boldsymbol{\sigma},\mathbf{r})$ and $A(\boldsymbol{\sigma},\mathbf{r})$ for n one degree lower, i.e., if $n=m+1$, then

$$V_n(\boldsymbol{\alpha},\mathbf{r})=T_n(\beta\boldsymbol{\alpha},\mathbf{r})=T_{m+1}(\beta\boldsymbol{\sigma},\mathbf{r})=A_{m+1}(\boldsymbol{\sigma},\mathbf{r}).$$

Generally there is considerable arbitrariness in applying the C_{nX} to a particular spectrum because the magnitudes of the nuclear matrix elements are not known. The practice is to adjust the ratios of the matrix elements to give the best fit to the experimental data. This arbitrariness does not exist if $\Delta J=n+1$ in which case all the matrix elements vanish except the ones with the factors $T(\beta\boldsymbol{\sigma},\mathbf{r})$ and $A(\boldsymbol{\sigma},\mathbf{r})$. Thus only the T or A interactions can account for such a decay and the spectral shape predicted by the theory is unique since only one matrix element is involved with the well-defined energy factor, $A_{n+1}(\boldsymbol{\sigma},\mathbf{r})=T_{n+1}(\beta\boldsymbol{\sigma},\mathbf{r})$. A convenient method illustrating the selection rules is to regard the change in the total angular momenta of the parent and product nuclei, ΔJ, to be equal to the sum of the orbital plus spin angular momenta carried away by the neutrino and beta-particle. Thus $\Delta J=\Delta L+\Delta S$. ΔL determines the degree of forbiddenness and the change in parity, since $n=\Delta L$. The beta- and neutrino each have a spin of $\frac{1}{2}$, and thus $\Delta S=0$ or 1. For the case $\Delta J=n+1$, $\Delta S=1$ and only those matrix elements which contain the factors $A_{n+1}(\boldsymbol{\sigma},\mathbf{r})$ and $T_{n+1}(\beta\boldsymbol{\sigma},\mathbf{r})$ do not vanish. These are what are known as the G−T terms.

Beta-spectra are usually analyzed in terms of the Kurie plot. For magnetic spectrometers, this is the graph of $[N/p^2F(Z,W)]^{\frac{1}{2}}$ *vs* W, where $P(p)$ is taken to be proportional to N/p, N being the counting rate. For an allowed spectrum the Kurie plot is straight with an intercept equal to W_0. If the Kurie plot is not straight, the spectrum is forbidden, indicating that C_{nX} is not energy independent. The appropriate C_{nX} is then sought which will correct the Kurie plot to a straight line.

II. EXPERIMENTAL DESCRIPTION

The Columbia University spectrometer constructed in 1941 is of the solenoidal type, a complete description of its physical features having been given by Witcher,[9] and subsequent modifications by Haggstrom[10] and Wu and co-workers.[11] Essentially the solenoid consists of six layers of $\frac{1}{4}$-in. diameter copper tubing (0.035-in. wall thickness) wound on a brass tube 10.5-in. o.d., 10-in. i.d., and 66 in. long. The actual length of winding is 60 in. and there are 220 turns per layer. All six layers are connected in parallel, both electrically and hydraulically, by means of bus bars and manifolds. In addition correcting coils consisting of 90 turns of No. 12 wire were wound 12 in. from each end of the main winding to improve the homogeneity of the field inside the solenoid. Comparison measurements with a standard solenoid showed that the homogeneity of the field at all points between the source and counter is better than 1 percent. The defocusing effect of the earth's magnetic field for low energy electrons has been reduced to a negligible amount by aligning the spectrometer tube parallel to the horizontal component of the earth's field and neutralizing the vertical component by means of a pair of Thomson coils (42 in.×100 in.) placed above and below the spectrometer tube.

The long half-lives associated with the highly forbidden spectra implies unavoidable low specific activities and therefore prohibits the use of sources with activities greater than a few hundreths of a microcurie if the distortion of the spectrum shape due to excessive source thickness is to be avoided. To combat the problem of low intensity, a new baffle with improved resolution-transmission characteristics was constructed and several techniques were adopted for reducing the background of the G-M counter detection system. The new baffle was constructed using the design principles for ring-focusing as presented by Frankel[12] and Persico.[13] The existence of the ring-focus for a solenoid was first noted by Witcher, who did not, however, fully exploit its usefulness, since the original baffle was designed to transmit electrons with an average initial angle $\bar{\alpha}$ of 18°. The new baffle, whose physical dimensions are shown in Fig. 1, was designed for $\bar{\alpha}=38°$, $D=2p/eH=14.1$ cm, and $L=\pi D\cos\bar{\alpha}=34.8$ cm. The coordinates of disk A, $r_A=6.7$ cm, $Z_A=24.7$ cm, determine the calibration of the baffle, i.e., the energy of the electrons transmitted for a given magnetic field setting. The resolution and transmission can be varied without changing the baffle calibration by adjusting either or both the r and Z coordinates of disk A'. The factors determining the shape of the slit at AA' and the location of the beam defining diaphragm at either BB' or CC' have been discussed extensively in the literature.[14,15] The baffle was calibrated using the photoelectrons from a lead radiator by the annihilation radiation from the positrons of Cu^{64}, and it was found that $D=14.1$ cm. Subsequent checks with internal conversion lines of Cs^{137}, In^{114}, etc., have shown agreement well within experimental error.

The K and L lines from the internal conversion electrons of In^{114} as obtained with Witcher's baffle and with the new baffle adjusted to give the same resolution are shown in Fig. 2. The half-maximum width is 3.9 percent corresponding to a base width of about 9–10 percent. The increase in transmission achieved by the new baffle is 3.7 as obtained from the ratio of the line peaks. The value of four is predicted for a half-maximum width of 4 percent by Frankel for a point source and by Persico for the case of an extended source. A determination of the average solid angle transmitted by the baffle was obtained by integrating the momentum distribution of a Cl^{36} source whose total activity had been determined by absolute beta-counting. The half-maximum resolution for this source whose diameter is 0.8 cm is 5.8 percent and the average solid angle is 3.5 percent of 4π. The value reported by Witcher is 1 percent maximum solid angle for a source 2.0 cm in diameter with a half-maximum resolution of 5.8 percent.

The large spherical aberration of the solenoidal spectrometer for emission angles of the order of 40° enlarges the beam width to about 5 cm as it returns to the axis. An end-window G-M counter large enough to admit the beam has a prohibitively high background for use with low activity sources. Other type G-M counters or detectors suggest themselves to a solution of this problem, but it was deemed more feasible to attempt to reduce the background of an end-window G-M counter. This was accomplished by two methods. First, the sensitive volume for radiation entering perpendicular to the axis was considerably reduced by using a center wire of 0.006-in. tungsten, 4.0 cm in length, with a glass bead at one end and 0.040-in. Kovar wire butt soldered at the other end to serve as a lead-in (Fig. 3).[16] The sensitive volume of the counter is determined by the length of the 6-mil wire since the counting threshold for the 40-mil wire is above the entire plateau region of the 6-mil wire. The 6-mil wire was further reduced in length to 1.8 cm for spectrum

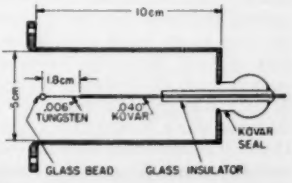

FIG. 3. Cross section of low background, end-window G-M counter.

[9] C. M. Witcher, Phys. Rev. **60**, 32 (1941).
[10] E. Haggstrom, Phys. Rev. **62**, 144 (1942).
[11] Wu, Havens, Albert, and Grimm, Phys. Rev. **73**, 1259 (1948).
[12] S. F. Frankel and E. C. Nelson, ONR Report NP-1120, June, 1948.
[13] E. Persico, Rev. Sci. Instr. **20**, 191 (1949).
[14] S. F. Frankel, Phys. Rev. **73**, 804 (1948).
[15] E. Persico and C. Geoffrion, Rev. Sci. Instr. **21**, 945 (1950).
[16] Good, Kip, and Brown, Rev. Sci. Instr. **17**, 262 (1946).

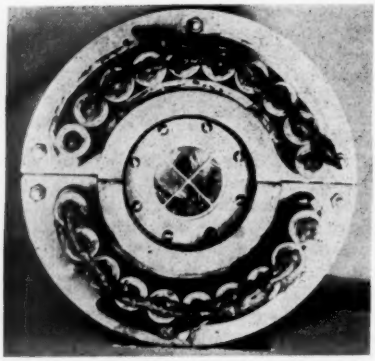

FIG. 4. Cutout showing G-M counter, lead shielding, anticoincidence counters and support.

measurements of K^{40}. Counters constructed in this way, 10 cm long and 5 cm in diameter, have a $1\frac{1}{2}$-in. lead shielded background of 44 c/min for the 4.0-cm wire and 30 c/min for the 1.8-cm wire. The background of these counters was further reduced to 28 c/min and 16 c/min by the use of an anticoincidence counting technique. The counter which serves as the beta-detector is completely surrounded by an array of cosmic-ray counters 1 in. in diameter and 12 in. long (Fig. 4). An anticoincidence circuit was constructed which records counts occurring only in the detector and rejects those detector counts which occur in coincidence with a count in any of the cosmic-ray counters. It was found that the number of counts rejected by this method is roughly independent of the amount of shielding used. This is readily explained by the fact that the components of the background capable of initiating ionizing events in both the cosmic-ray counters and the beta-counter are highly penetrating and unaffected by ordinary amounts of shielding. A gamma-ray, however, will not generally register counts in two counters and is not susceptible to rejection by the anticoincidence technique. The gamma-ray background can be minimized by using the maximum practical amount of shielding.

The thin windows used on the G-M counters are either Nylon or rubber hydrochloride, both of 0.6 mg/cm² thickness, and for measurements below 100 kev, five to six layers of collodion films each about 0.006 mg/cm² thick. The transmission of the electron beam is not at all affected by the Nylon windows above 90 kev and by collodion windows of about 0.03 mg/cm² thickness above 16 kev. The counters are filled with 15 mm of alcohol vapor when the collodion windows are used and with 8–10 cm of a 7:1 argon-alcohol mixture when Nylon windows are used in the investigation of the higher energy regions. Sufficient data are taken so that there is adequate overlap in the regions studied with Nylon and collodion windows. Measurements have shown that the G-M counters when used as described above have close to 100 percent efficiency for detection of beta-particles.[11]

Mechanical support is given to the counter windows by means of grids. If not properly designed, the grids can produce selective transmission effects. The solid parts of the grid should be completely opaque to the most energetic electrons in the beam. The importance of edge effects in the small circular apertures of the grids used to support collodion windows was investigated by comparing the transmission of several grids with varying ratios of aperture diameter to depth. It was found that a ratio of at least 2:1 was necessary to eliminate edge effects for all energies above 20 kev. The grid support for Nylon windows has a circular aperture of 5-cm diameter with two thin perpendicular strips of $\frac{1}{8}$-in. width forming a coordinate axis to support the window. A grid such as this has an open area of about 97 percent and negligible edge affects.

The recent history of beta-ray spectroscopy has stressed the importance of source uniformity as well as low surface density for reproducing accurate spectra. The best method seems to be the vacuum evaporation technique, which consists essentially of placing the source material in a vacuum on a heating strip or small oven. When heated in a high vacuum until its vapor pressure is about 10^{-2} mm of mercury or greater, the source material will volatilize and deposit on thin films placed a short distance away. Unfortunately, most of the substances exhibiting highly forbidden spectra are not available in sufficient quantities for use of the vacuum evaporation technique. The sources used for the Cl^{36} measurements were prepared by this method.[17] All the other sources were prepared in various ways which will be individually described and their limitations discussed.

III. SPECTRUM INVESTIGATIONS

A. Be^{10}

Be^{10} is an even-even nucleus and is assumed to have zero spin, whereas the spin of B^{10}, the product nucleus, has been found to be three.[18] Thus the spin change involved in the transition is three, and the interactions which can account for the decay are C_{2T}, C_{2A}, and C_{3P} if the parity does not change and C_{3S}, C_{3V}, C_{3T}, and C_{3A} if the parity does change. The matrix element $Q_3([\boldsymbol{\alpha}\times\mathbf{r}],\mathbf{r})$ for C_{4V} can also account for a $\Delta J=3$ transition, but this leads to a half-life much higher than the observed value. C_{2T} and C_{2A} are examples of the case $\Delta J=n+1$ and each contains a single matrix element with the same energy factor, $T_3(\beta\boldsymbol{\sigma},\mathbf{r})=A_3(\boldsymbol{\sigma},\mathbf{r})=(3p^4+10p^2q^2+3q^4)/90$. This factor, which has sometimes been called the D_2 factor, is also contained in matrix elements appearing in C_{3V} and C_{3T}, i.e., $V_3(\boldsymbol{\alpha},\mathbf{r})$

[17] We are indebted to L. Lidofsky and P. Macklin of this laboratory for use of the vacuum evaporator constructed by them.
[18] Gordy, Ring, and Berg, Phys. Rev. **74**, 1191 (1948).

and $T_3(\beta\alpha, \mathbf{r})$. There are two bases for predicting that the shape of the Be^{10} spectrum is that given by the D_2 factor. Marshak[19] has shown that only C_{2T}, C_{2A}, C_{3T}, and C_{3V} give minimum theoretical half-lives compatible with the observed value of 2.7×10^6 years. By using Greuling's method for estimating the magnitude of the matrix elements occurring in C_{3T} and C_{3V}, it was shown that in each case the term containing the D_2 factor, i.e., $T_3(\beta\alpha, \mathbf{r})$ and $V_3(\alpha, \mathbf{r})$ is much larger than all the others. Thus C_{3T} and C_{3V} as well as C_{2T} and C_{2A} all lead to the same spectrum shape, that determined by the D_2 factor. This result is obtained more directly from the shell model of the nucleus which predicts no parity change for the transition. Thus $\Delta J=3$ (no) and the possible interactions are restricted to C_{2T} and C_{2A}. Empirically the Be^{10} decay is classified as second forbidden by its f_0T value of 4.6×10^{14} (see Table I).

Experimental evidence that the spectrum shape of Be^{10} deviated from the allowed shape was first reported by Bell *et al.*[20] using a scintillation spectrometer. Wu and Feldman[1] first inferred the D_2 shape of the Be^{10} spectrum by comparing the spectrum shape of thick sources of radioactive BeO ($\sim$10 mg/cm^2) to that of the thick sources of inactive BeO containing activities of Cu^{64} and Cl^{36}. The availability of material of higher specific activity has made possible spectrum measurements with much thinner sources, of about 0.3–0.4 mg/cm^2. The source used in this work was obtained from the Y-12 Research Laboratory of the Carbide and Carbon Chemicals Corporation at Oak Ridge. It was prepared by activating Be metal in the pile and then was purified and isotopically enriched in Be^{10} by electromagnetic separation performed under the supervision of Dr. C. P. Keim. The source was mounted on a Formvar film 0.1 mg/cm^2 thick and consisted of 1.2 mg BeO spread over an area of about 4 cm^2. The activity of this source is about 0.01 microcurie and although fairly thin (0.3 mg/cm^2) is not particularly uniform and could not be expected to give reliable results below 100 kev. The ring-focus baffle has a resolution of 9 percent full width at half-maximum for a source of this diameter. The graph of the momentum distribution has the pronounced shift of the peak towards the high energy end, characteristic of a D_2 spectrum. Figure 5 contains graphs of the Kurie plot and the Kurie plot corrected by the D_2 factor. The uncorrected curve is concave towards the energy axis whereas the D_2 correction factor yields a straight line down to 120 kev and is seen to provide a good fit of the data. The deviation below 120 kev is attributed to source thickness effects. The extrapolated end point is 555±5 kev.

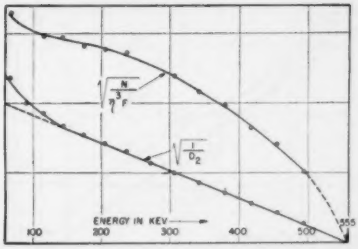

FIG. 5. Corrected and uncorrected Kurie plots Be^{10} spectrum.

TABLE I. Corrected and uncorrected fT values.

	ΔJ	π	$W_0(mc^2)$	T(sec)	f_0T	$f_\infty T$
Tc^{99}	2	2	1.57	0.97×10^{12}[a]	1.7×10^{12}	3.8×10^{11}
Cl^{36}	2	2	2.40	2.01×10^{13}[b]	4.1×10^{13}	1.2×10^{12}
Be^{10}	3	2	2.09	1.23×10^{16}[c]	4.6×10^{16}[e]	1.3×10^{12}[e]
K^{40}	4	3	3.60	5.79×10^{16}[d]	1.3×10^{18}	1.4×10^{15}

[a] Fried, Jaffey, Hall, and Glendenin, Phys. Rev. **81**, 741 (1951).
[b] D. J. Hughes and C. Eggler, Phys. Rev. **74**, 1239 (1948).
[c] Wu, Townes, and Feldman, Phys. Rev. **76**, 692 (1949).
[d] G. A. Sawyer and M. L. Wiedenbeck, Phys. Rev. **79**, 490 (1950).
[e] These values contain the factor $(2J_f+1)/(2J_i+1)=7$ because $J_f>J_i$.

[19] R. E. Marshak, Phys. Rev. **75**, 513 (1949).
[20] Bell, Ketelle, and Cassidy, Phys. Rev. **76**, 574 (1949).

Conclusion

The curves for the various correction factors applicable to the Be^{10} decay have been given by Marshak.[19] The experimental shape of the Be^{10} spectrum above 120 kev is in such close agreement with the D_2 shape that by inspection it is possible to exclude C_{3P}, C_{3S}, and C_{3A} as possible interactions. It can be further concluded that if the parity does change, requiring the transition to be third forbidden, then the terms in C_{3T} and C_{3V} other than the D_2 term ($T(\beta[\sigma\times\mathbf{r}], \mathbf{r})$, $V(\mathbf{r}, \mathbf{r})$ and the cross terms) must be negligibly small compared to the D_2 term. Thus it is seen that the Be^{10} spectrum provides a decisive confirmation of the Fermi theory exhibiting the unique shape predicted by Marshak's lifetime analysis for a spin change of three.

[21] Hughes, Eggler, and Alburger, Phys. Rev. **77**, 726 (1950).
[22] P. R. Bell and J. M. Cassidy, Phys. Rev. **77**, 301 (1950).
[23] B. H. Kettelle, Phys. Rev. **80**, 758 (1950).
[24] H. W. Fulbright and J. C. D. Milton, Phys. Rev. **76**, 1271 (1949).

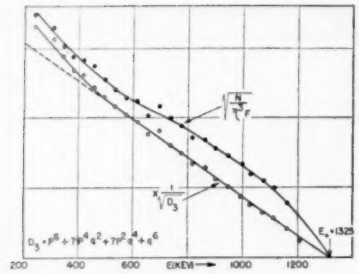

FIG. 6. Corrected and uncorrected Kurie plots of K^{40} spectrum for 2.5-mg/cm² source.

B. K^{40}

The measurement of the K^{40} beta-spectrum, a case of a highly forbidden transition for which the spin change is known, has long been anticipated as a sensitive test for the Fermi theory. The spin change is $\Delta J=4$, that of K^{40} having been found to be four,[25] while that of Ca^{40}, the product nucleus, is assumed to be zero because it is an even-even nucleus.

K^{40} occurs naturally with an abundance of 0.016 percent and since its half-life is 12.7×10^8 years, it has not been possible to prepare sources of sufficiently high specific activity necessary for a spectrum determination. Recently we obtained some KCl enriched to 7.13 percent in K^{40} by electromagnetic separation performed at Oak Ridge under the supervision of C. P. Keim. The source was prepared by precipitating the KCl out of a saturated water solution with a large volume of isopropyl alcohol to which a small amount of alcohol soluble Nylon was added as a binding agent. The uniform crystals formed in this way were allowed to settle from the alcohol over a circular area of 3.1 cm² on Nylon backing of 0.6 mg/cm² thickness The average source thickness is about 2.5 mg/cm². This technique for preparing thick sources was found to produce greater uniformity than several other methods that were tried. The ring-focus baffle for a source of this diameter has a resolution of 9 percent.

The uncorrected Kurie plot, shown in Fig. 6, is definitely forbidden, its shape being very similar to those of Cl^{36} and Be^{10}. The factor $D_3=p^6+7p^4q^2+7p^2q^4+q^6$, provides a good fit to the data from the end point, 1325 ± 15 kev down to 500 kev with the deviation increasing towards lower energies. This deviation is readily explained by the excessive thickness of the source. To determine the effect of 2.5 mg/cm² KCl on beta-spectra with end points in the neighborhood of 1.3 Mev, a source was prepared identical to the K^{40} source using inert KCl containing Y^{91} activity of negligible weight. The Kurie plot for this source corrected by the factor $a\sim p^2+q^2$ is shown in Fig. 7 together with the uncorrected Kurie plot. For a thin source the a factor corrected Kurie plot would be straight to below 50 kev. The effect of the 2.5 mg/cm² KCl on the Y^{91} spectrum is to produce a deviation which sets in at 500 kev similar to that observed for the K^{40} Kurie plot corrected by the D_3 factor. It can therefore be assumed that the data above 500 kev is unaffected by the source thickness of 2.5 mg/cm² and that with thin sources, the D_3 factor will provide a good fit to the Kurie plot to energies below 500 kev. These results are in general agreement with thick source ($\sim$2.5 mg/cm²) spectrum measurements of K^{40} reported by other laboratories. Alburger[26] using a thin lens with a resolution of about 17 percent found agreement with the D_3 corrected Kurie plot down to about 500 kev. Bell, Weaver, and Cassidy[27] using a scintillation spectrometer found the deviation to begin at about 700 kev.

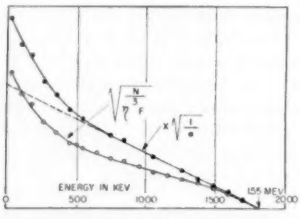

FIG. 7. Corrected and uncorrected Kurie plots of Y^{91} spectrum. Source consists of Y^{91} activity mixed with 2.5-mg/cm² KCl.

For $\Delta J=4$ the possible correction factors are C_{3T}, C_{3A}, and C_{4P} if the parity changes and C_{4S}, C_{4V}, C_{4T}, and C_{4A} for no parity change. The energy factors for these have been previously given by Marshak.[28] Of these C_{3T}, C_{3A}, C_{4P}, C_{4S}, and C_{4A} contain but one matrix element, and therefore the energy dependence for each is uniquely defined. C_{4P}, C_{4S}, and C_{4A} can be ruled out because their energy dependent factors are markedly different from the D_3 factor. The D_3 factor also occurs in C_{4T} and C_{4V} ($T_4(\beta\boldsymbol{\alpha},\mathbf{r})$ and $V_4(\boldsymbol{\alpha},\mathbf{r})$) and is the same unique energy factor in C_{3T} and C_{3A} ($T_4(\beta\boldsymbol{\sigma},\mathbf{r})$ and $A_4(\boldsymbol{\sigma},\mathbf{r})$). In a manner completely analogous to that used by Marshak in analyzing the case of Be^{10} it can be shown that the terms in C_{4V} and C_{4T} containing the D_3 factor are much larger than the other terms and therefore the energy dependence of C_{4T} is essentially that determined by the D_3 factor. By using Greuling's[7] method for estimating the magnitude of the matrix elements one obtains $|Q_4(\beta[\boldsymbol{\sigma}\times\mathbf{r}],\mathbf{r})/4!|^2\approx(2/7)R^8$ and $|Q_4(\beta\boldsymbol{\alpha},\mathbf{r})/4!|^2\approx(18/35)\alpha^2R^8$. If we use $R=0.004A^{\frac{1}{3}}$ for the nuclear radius and $\alpha^2=(v/c)^2=0.1-(W_0R)^2$, the ratio of the second term to the first in C_{4V} is $9\alpha^2T_4(\beta\boldsymbol{\alpha},\mathbf{r})/5R^2T_4(\beta\boldsymbol{\sigma}\times\mathbf{r},\mathbf{r})$, which is $\approx10^2T_4(\beta\boldsymbol{\alpha},\mathbf{r})/T_4(\beta\boldsymbol{\sigma}\times\mathbf{r},\mathbf{r})$. The variation in $T_4(\beta\boldsymbol{\alpha},\mathbf{r})/T_4(\beta\boldsymbol{\sigma}\times\mathbf{r},\mathbf{r})$ is negligible over the entire spectrum compared to 10^2. Thus the first term in C_{4T} and

[25] J. R. Zacharias, Phys. Rev. **60**, 168 (1941).

[26] D. E. Alburger, Phys. Rev. **78**, 629 (1950).
[27] Bell, Weaver, and Cassidy, Phys. Rev. **77**, 399 (1950).
[28] R. E. Marshak, Phys. Rev. **70**, 980 (1946).

also the cross term (since it can be taken as the geometric mean) are seen to be negligible compared to the term containing the $T_4(\beta\boldsymbol{\alpha}, \mathbf{r}) = D_3$ factor. The matrix element for the term in $T_{4'}(\beta\boldsymbol{\sigma}, \mathbf{r})$ doesn't apply for a $n \to 0$ transition. Therefore C_{4T} is essentially determined by one matrix element with its energy dependence given by the D_3 factor. The result for C_{4V} is exactly the same. Thus the spectrum of K^{40} can be explained equally well by C_{3A}, C_{3T}, C_{4V}, and C_{4T}. It is to be noted that these are the interactions which can account for the half-life of K^{40} as calculated by Greuling.[7] According to the shell model the parity should change in the beta-decay of K^{40}, in which case only C_{3T} and C_{3A} can account for the transition.

The reliability of the observed spectrum, because of excessive source thickness, is good only down to 500 kev. Therefore, these conclusions must be deferred until spectrum measurements can be made with thinner sources and the spectral shape below 500 kev can be determined.

C. Tc^{99}

Tc^{99}, a product of uranium fission, has a half-life of 2.12×10^5 years. Its comparative half-life is $f_0 T = 1.7 \times 10^{12}$ and the decay is thus empirically classified as second forbidden. The spin and magnetic moment of the ground state of Tc^{99} have been measured[29] confirming it to be a $g_{9/2}$ state as predicted by the nuclear shell model. Further, the shell model classifies the product Ru^{99} as either $d_{5/2}$ or $g_{7/2}$. In either case there is no change in parity, and since a $g_{9/2} \to g_{7/2}$ transition would be allowed and incompatible with the observed lifetime, the transition is believed to be $g_{9/2} \to d_{5/2}$. Thus it is second forbidden, with $\Delta J = 2$ (no) in agreement with the empirical classification of forbiddenness.

Tc^{99} of specific activity 1.7 μc/mg was obtained from the Isotope Division of the Atomic Energy Commission in the form of NH_4TcO_4. Several sources with average thickness varying from about 0.05 to 0.15 mg/cm² were prepared on collodion films of about 0.02 mg/cm² thickness by drying the aqueous solution under a heat lamp or in a vacuum desiccator. The source thickness was estimated from a measurement of the source activity and the specific activity of the material as given on the isotope packing slip. The NH_4TcO_4 is chemically purified at Oak Ridge but to ensure purity some of the sources were prepared from material which had gone through additional chemical purification and electroplating.

The resolution for the spectrum measurements of Tc^{99} was about 5 percent varying about ±1 percent with the diameter of the several sources used. The uncorrected Kurie plot exhibits a forbidden shape curving concave towards the energy axis. The curves of the energy factors which apply for a $\Delta J = 2$ (no) transition are shown in Fig. 8. None of these factors provides

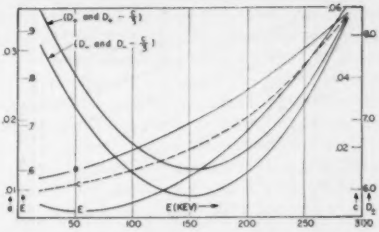

FIG. 8. Correction factors for the individual matrix elements of second forbidden transitions for Tc^{99} ($I = 9/2 \to I = 5/2$).

a satisfactory fit for the Kurie plot. The D_3 factor overcorrects the Kurie plot, resulting in a curvature in the opposite direction. The a factor gives agreement but only down to about 120 kev, with a deviation that increases towards lower energies setting in at this point. The high Z formulas were used to calculate the correction factors and Coulomb function. The low Z approximation formulas begin to introduce significant errors for $A \sim 100$. For Tc^{99}, the error for some of the factors was as much as 10–15 percent over the range where data were taken. A good fit for the Kurie plot is obtained with C_{2T} which for a $J = 9/2 \to J = 5/2$ transition is[30]

$$C_{2T} = T_2(\beta[\boldsymbol{\sigma}\times\mathbf{r}], \mathbf{r}) + k^2 T_2(\beta\boldsymbol{\alpha}, \mathbf{r}) - 2kT_2(\beta\boldsymbol{\alpha}, \mathbf{r}; \beta[\boldsymbol{\sigma}\times\mathbf{r}], \mathbf{r}) + m^2 T_2(\beta\boldsymbol{\sigma}, \mathbf{r}) \quad (3a)$$

or in the notation of Konopinski's review article[3]

$$C_{2T} = (D_+ - \tfrac{1}{3}c) + 12ak^2 - 4Ek + cm^2, \quad (3b)$$

where

$$k^2 = |Q_2(\beta\boldsymbol{\alpha}, \mathbf{r})|^2 \div |Q_2(\beta[\boldsymbol{\sigma}\times\mathbf{r}], \mathbf{r})|^2 = |A_{ij}|^2 \div |T_{ij}|^2$$

and

$$9m^2 = |Q_3(\beta\boldsymbol{\sigma}, \mathbf{r})|^2 \div |Q_2(\beta[\boldsymbol{\sigma}\times\mathbf{r}], \mathbf{r})|^2 = |S_{ijk}|^2 \div |T_{ij}|^2.$$

The corrected Kurie plots for the various sources used, shown in Fig. 9, are straight down to about 60 kev. Measurements below 50 kev were unreliable because of

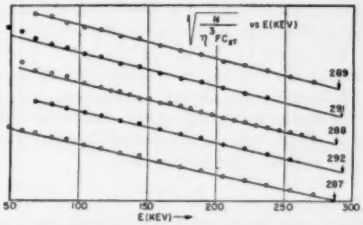

FIG. 9. Tc^{99} Kurie plots corrected by C_{2T} with $k^2 = |A_{ij}|^2/|T_{ij}|^2 = 45$.

[29] K. G. Kessler and W. F. Meggers, Phys. Rev. **80**, 901 (1950); **82**, 341 (1951).

[30] The requirement that $k = A_{ij}/T_{ij} = A_{ij}^*/T_{ij}^*$ is a consequence of the invariance of the nuclear Hamiltonian under time reversal. The proof is given by C. L. Longmire and A. M. L. Messiah, Phys. Rev. **83**, 464 (1951).

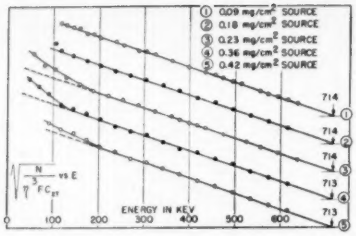

FIG. 10. Cl^{36} Kurie plots corrected by C_{2T} with $k^2=|A_{ij}|^2/|T_{ij}|^2=18$.

the low source activities. The extrapolated end point is 290±4 kev. The best fit was obtained with $k^2=45$ and $m^2=0$. The term in m^2, although permissible by the selection rules, is negligibly small since $c/(D_+-\frac{1}{3}c)$ $\approx 0.002-0.003$ over most of the spectrum and is at most 0.006 at the high energy end, while $m^2\approx 14/15$ according to Greuling's method for approximating the matrix elements.

Past experience in beta-spectroscopy has shown that very thin sources prepared by drying from aqueous solution do not always give reliable measurements at low energies because of inhomogeneities in surface density. Confirmation is required by measurements obtained with sources that are known to be very uniform as well as thin. A spectrum measurement of Tc^{99} was reported at the last American Physical Society meeting in New York[31] using a source prepared by the oven volatilization technique. It was found that a good fit to the spectrum down to 50 kev was provided by C_{2T} with $k^2=44$ in agreement with the results reported herein. The spectrum of Tc^{99} has also been investigated by Taimuty[32] and was fitted with C_{2T} by Nakamura *et al.*[33] The exact point of deviation caused by source scattering depends on the end point of the spectrum, on the atomic number of the nucleus responsible for the scattering, and on the thickness and uniformity of the source. Scattering effects for thin sources do not affect the spectrum shape for energies above the peak of the momentum distribution. The point of deviation always occurs at an energy somewhere to the left of the peak. Sixty kev occur to the left of the peak of the Tc^{99} momentum distribution at a momentum of about 0.4 that of the end point. On this basis it seems reasonable that no source scattering effects should be observed down to 60 kev with sources whose average thickness is as low as those used in this work.

D. Cl^{36}

We have previously published results on the spectrum of Cl^{36} [4] using sources of 0.3 to 1 mg/cm² average thickness prepared from aqueous solution by evaporation under a heat lamp or in a vacuum desiccator. The spin of Cl^{36} has been found to be two[34,35] while the product nucleus A^{36}, being even-even, is assumed to have zero spin. The possible interactions for a $\Delta J=2$ transition are C_{1A}, C_{1T}, C_{2P}, C_{3V} if the parity changes and C_{2S}, C_{2V}, C_{2T}, and C_{2A} if there is no parity change. As has been discussed previously,[4] all of these except C_{2T} and C_{2V} consist of but one matrix element and hence have a unique energy dependence (see reference 4 for the curves of the correction factors for Cl^{36}). However, only C_{2T} and C_{2V} with a suitable adjustment of the matrix elements can account for the Cl^{36} beta-spectrum.

We have reinvestigated the spectrum of Cl^{36} using sources of $NaCl^{36}$ of 0.08, 0.15, 0.19, 0.28, and 0.36 mg/cm² average thickness prepared by the vacuum evaporation technique. These sources are much thinner and considerably more uniform than those used in the earlier work. The source thickness was determined from the specific activity of the Cl^{36} given on the isotope invoice sheet together with a determination of the total activity of each source. The resolution of the ring-focus baffle for these sources which are 8 mm in diameter is 5.5 percent. The results are in complete agreement with our previously published results. We again find that C_{2T} (as well as C_{2V}) as given by Eq. (3) with $k^2=18$ and $m^2=0$ provides a good fit to the spectrum and with the improvement in the sources the corrected Kurie plot is now straight down to 100 kev. The extrapolated end point is 714±5 kev. The term in m^2 is prohibited by the selection rules in this case because the transition is of the $n\rightarrow 0$ type. The low activity of the sources made measurements below 100 kev impractical. The Kurie plots corrected by C_{2T} are shown in Fig. 10.

The Cl^{36} spectrum has been determined down to about 180 kev by Fulbright and Milton[36] using a proportional counter. They were able to fit the spectrum with C_{2T} for $k^2=25.73$. Our data cannot be fitted with a ratio this high in the region below 300 kev, corresponding to a relatively greater number of electrons at low energies than in the spectrum measurements of Fulbright and Milton.

IV. DISCUSSION

The half-life and fT values for the spectra investigated are given in Table I. Both f_0 and f_n were obtained by graphical integration of

$$f_n=\int_1^{W_0} C_{nX}F(Z,W)(W^2-1)^{\frac{1}{2}}(W_0-W)^2WdW.$$

Every term in this formula has been previously tabulated as a function of W in the interpretation of the

[31] F. Wagner, Jr., and M. S. Freedman, Phys. Rev. **86**, 631 (1952).
[32] S. I. Taimuty, Phys. Rev. **81**, 461 (1951).
[33] Nakamura, Umezawa, and Takebe, Phys. Rev. **83**, 1273 (1951).
[34] C. H. Townes and L. C. Aamodt, Phys. Rev. **76**, 695 (1949).
[35] Johnson, Gordy, and Livingston, Phys. Rev. **83**, 1249 (1951).
[36] H. W. Fulbright and J. C. D. Milton, Phys. Rev. **82**, 274 (1951).

spectrum shape, and therefore it is both simple and accurate to obtain f_0 and f_n by graphical integration. The values thus obtained for f_0 are in close agreement with those given in the f_0 charts of Feenberg and Trigg.[37] The f_0T correspond to $C_{0X}=1$, whereas the f_nT are calculated using the C_{nX} which is in best agreement with the spectrum. The factors $(n!)^2$ and $[(n+1)!]^2$ which appear in the denominators of the C_{nX} are 4, 4, 36, and 576, respectively, for Tc^{99}, Cl^{36}, Be^{10}, and K^{40}. It is these factors which are responsible for the greater reduction in the ratio of f_nT/f_0T for Be^{10} and K^{40} compared to Tc^{99} and Cl^{36}. The low end point of the Tc^{99} spectrum causes a relatively greater reduction in its f_nT value than in the case of Cl^{36}.

According to Greuling's method for approximating the matrix elements the value of k^2 should be $5(\gamma_5)^2/9R^2$. With γ_5^2 having a value probably between 0.01 and 0.1, k^2 is then between 30 and 300 for Cl^{36} and 18 to 180 for Tc^{99}. The values used for the best spectrum fit are 18 and 45, respectively. It might be noted that Greuling's method successfully accounts for the lifetimes of Be^{10} and K^{40} but yields values for Cl^{36} and Tc^{99} (assuming the interaction is $2T$) that are too low by a factor of the order of 100.

It is of interest to note that although the spin changes for the decays of Cl^{36}, Be^{10}, and K^{40} are 2, 3, and 4, respectively, and the spectrum shapes are explained by C_{2T} with $k^2=18$ for Cl^{36}, by the D_2 factor for Be^{10}, and by the D_3 factor for K^{40}, these three spectra have essentially the same energy dependence to within the accuracy of the measurements.

As a result of these spectrum investigations it is possible to arrive at the following analysis concerning the interaction prevailing in beta-decay. If the true interaction is just a single one of the five linearly independent interactions of Eqs. (2), then the tensor interaction is the only one which can satisfactorily account for spectra in which the change in angular momentum is equal to the degree of forbiddenness, i.e., $\Delta J=n$, as well as those spectra for which $\Delta J=n+1$. The polar vector interaction is exactly the same as the tensor for the case $\Delta J=n$ if one takes $A_{ij}/R_{ij}=2iA_{ij}/T_{ij}$, but is forbidden by the selection rules for the case $\Delta J=n+1$. The axial vector interaction is identical to the tensor interaction for the case $\Delta J=n+1$ but cannot explain the shape of forbidden spectra with $\Delta J=n$ (e.g., Cl^{36}, Tc^{99}). Although the tensor interaction seems to be able to explain the experimentally observed shapes of these forbidden spectra, there is so much flexibility available in the use of the parameter k^2 to fit the experimental data that no final conclusions should be drawn. Furthermore, a linear combination of the tensor interaction with an admixture of Fermi terms will serve as well as the tensor alone in the interpretation of the shapes of forbidden spectra. A linear combination of T and P has been used by Petschek and Marshak[38] to fit the shape of the RaE spectrum assuming the transition is $0\rightarrow0$ with change in parity. As was pointed out, the P interaction would give negligibly small contributions to the combination in all except $0\rightarrow0$ transitions because its terms would always be smaller in magnitude than those of the T interaction by two degrees of forbiddenness. The S and V interactions are prohibited by the selection rules for a $0\rightarrow0$ (yes) transition, and hence this type of transition cannot detect the presence of Fermi terms in the interaction prevailing in beta-decay. It has been shown by Tolhoek and de Groot[39] that the only linear combinations which can satisfy the condition of invariance of the beta-process to time reversal and possess complete symmetry of positron and negatron emission are either V and T only, or S, A, and P only. On the other hand, various authors have proposed a universal Fermi interaction between spin $\frac{1}{2}$ particles so that the interaction constant would be the same for the beta-decay of the neutron ($n\rightarrow p+e+\nu$), the spontaneous decay of the μ meson ($\mu^-\rightarrow e+2\nu$), and μ-meson absorption ($p+\mu^-\rightarrow n+\nu$). The only combinations consistent with this assumption are either V and A or S, T, and P. These combinations are incompatible with the symmetry principle of Tolhoek and de Groot.

If a linear combination of the invariant interactions does prevail in beta-decay then additional information will be required to determine its exact form. The sources which seem best able to provide the necessary data are the investigation of the shapes of parity unfavored spectra, i.e., $\Delta J=n$ or $\Delta J=n-1$ (especially $0\rightarrow0$ transitions) and various nuclear angular correlation measurements, particularly the electron-neutrino angular correlation. Further, any such linear combination should yield a consistent scheme of fT values.

[37] E. Feenberg and G. Trigg, Revs. Modern Phys. **22**, 399 (1950).

[38] A. G. Petschek and R. E. Marshak, Phys. Rev. **85**, 698 (1952).

[39] H. A. Tolhoek and S. R. de Groot, Phys. Rev. **84**, 150 (1951); L. C. Biedenharn and N. E. Rose, Phys. Rev. **83**, 459 (1951); S. R. de Groot and H. A. Tolhoek, Physica **16**, 456 (1950).

Structure of the Nucleon*

R. G. Sachs
University of Wisconsin, Madison, Wisconsin
(Received May 29, 1952)

An attempt is made to determine what restrictions are imposed on the nucleon wave functional by the known values of the nucleon moments and by the neutron-electron interaction. The nucleon is assumed to consist of a core particle (nucleore) of spin ½ surrounded by a pion field. No detailed reference is made to the interaction producing the field. Nucleore recoil is neglected. It is found that the neutron and proton moments satisfy a mirror condition

$$\mathfrak{M}_n+\mathfrak{M}_p=1-(4/3)P_1,$$

where P_1 is the probability that pions (any number or charge) occur in the field with total orbital angular momentum $L=1$. Insertion of the measured values of the moments in the equation yields $P_1=9$ percent. A model of the nucleon in which one pion plays the predominant role is not consistent with this result. This is probably the underlying reason for the failure of the weak coupling theory to give the correct ratio of neutron to proton moments. The neutron and proton moments can be accounted for if the field contains at least two pions with appreciable probability. A successful model consists of 91 percent bare nucleore, and 9 percent a pair of mesons, each in p states forming the state $L=1$.

The neutron electron interaction is shown to depend on the mean square radius of the charge distribution, $\langle r^2\rangle_{Av}$, in the nucleon. If only one or two pions with $L=1$ are contained in the proper field with appreciable probability, the observed interaction combined with the above value of P_1 leads to the very reasonable value of the mean square displacement of a pion, ≈ 0.5 times the square of the Compton wavelength of the pion.

The results suggest strongly that a weak nonlinear coupling would be capable of accounting for the data, but a linear coupling of intermediate strength cannot be excluded.

An analysis of the pseudoscalar field in terms of spherical waves is given in the Appendix. Consideration is also given there to the space and time inversion properties of the field functionals.

1. INTRODUCTION

THE original proposal of Yukawa that the nuclear forces are due to an emission and absorption of mesons by nucleons implies that the nucleon is a structured system, that it consists of a core (the *nucleore*) convoyed by a cloud of mesons, known as the meson proper field. Estimates of the coupling between the nucleore and the meson field lead to the conclusion that it is not weak, so the proper field may be presumed to be rather intense, from which it may be concluded that the structural features of the nucleon have a significant effect on its physical properties.

Attempts to describe the structure of the proper field have usually been based on a meson theory which is, at least in principle, complete. A specific form of the interaction between the meson and the nucleore is assumed and an attempt is made to solve the corresponding dynamical problem to obtain the wave functional of the nucleon. The physical properties of the nucleon, such as the magnetic moment, electron-neutron interaction, and so on, may then be obtained from this functional. These theories do not yield correct quantitative results in the approximations to which the calculations have been carried out. This failure may be due to the inadequacy of the approximations or it may be due to the use of an incorrect form of the nucleore-meson coupling.

Another approach to the problem, which may shed some light on the cause of failure of the theory, is to consider the structure of the nucleon much as we might consider the structure of a nucleus, namely, to seek a wave functional which fits the data.[1] This approach implies that we accept the spirit of the original Yukawa theory in that the nucleon is described by a functional of the meson field such that there is a finite probability for the occurrence of one, two, or possibly more mesons. But rather than attempt a derivation of the functional from a specific interaction, we make use of all the general principles and of all the quantitative properties of the nucleon that are at our disposal to fix the form of the wave functional in so far as that is possible. It could turn out that our information is so limited, and the parameterization of the functional so complicated that no very enlightening results are obtained in this way. However, we will find that this is not the case; on the contrary, rather specific limitations on the functional are indicated by the available data.

Although the proposed approach is somewhat less fundamental than the direct dynamical attack, it has the advantage that it offers a procedure for giving a physical interpretation of the data on the nucleon. Furthermore, it may turn out that the nucleon has so complex a structure as to require discussion in terms of its structure rather than in terms of the solution of a simple dynamical problem. Finally, there is a fair chance that a knowledge of the wave functional may make clear the source of difficulty in the present fundamental theories. In this connection it is to be noted that most attempts at the theory have been based on a linear coupling between nucleore and field which is treated either as small in magnitude (weak coupling) or as large in magnitude (strong coupling). It is possible that a calculation for intermediate coupling would be successful. On the other hand, the possibility that the correct coupling is nonlinear certainly cannot be excluded.[2] Of course, the field equations for free mesons

* This work was supported in part by the Wisconsin Alumni Research Foundation and in part by the AEC.

[1] A similar approach to the problem has recently been discussed by Umezawa, Takahashi, and Kamefuchi, Phys. Rev. 85, 505 (1952).

[2] See for example, L. I. Schiff, Phys. Rev. 84, 10 (1951) and R. J. Glauber, Phys. Rev. 84, 395 (1951).

may also be nonlinear as a consequence of meson-meson interactions.[8] Rather distinct differences between the wave functionals characteristic of these different possibilities are to be expected so direct information concerning the wave functional may suggest a choice between the alternative possible sources of difficulty.

It is characteristic of the presently conceived dynamical theories that they force consideration of mesons at relativistic energies and the consequent inclusion of nucleore recoil. On the grounds of simplicity, we argue that this is an undesirable feature of these theories and that, in view of the general failure of the theories, a feature which need not be included in our model of the nucleon. If we find a successful model involving only nonrelativistic mesons, we will then face the problem of constructing an interaction which is consistent with the model.

2. GENERAL RESTRICTIONS ON THE WAVE FUNCTIONAL

For the sake of definiteness we will base the discussion on the assumption that the only important structural element in the nucleon, other than the core, is the pion. The additional simplifying assumption is made that recoil of the nucleore can be neglected. Then the ground state of the system nucleore (at rest) plus pion field is that which is referred to as "the nucleon." The associated state vector is a functional of the pion field variables and a function of the spin variable of the nucleore. If an expansion of the wave functional in terms of appropriate free pion states (denoted by index s) is made, it is expected that it will have the form

$$\Psi=\Psi_0{}^{(\sigma)}+\sum_s\Psi_1{}^{(s,\sigma)}+\sum_{s,s'}\Psi_2{}^{(s,s',\sigma)}+\cdots, \quad (1)$$

where σ is the nucleore spin variable and $\Psi_N{}^{(s,s',\cdots,\sigma)}$ describes a state of N pions in states s, s', $\cdots s^{(N)}$. The usual weak coupling approximation amounts to the neglect of all terms beyond the first two in this expression.

The form (1) implies that the nucleore is taken to have spin $\frac{1}{2}$. The fact that the nucleon has spin $\frac{1}{2}$ means that the total angular momentum of the nucleore plus the pion field associated with any term in the series (1) must be $\frac{1}{2}$. If the states of a given number of pions are classified by the total (orbital) pion angular momentum L, the requirement that $\mathbf{J}=\mathbf{L}+\frac{1}{2}\boldsymbol{\sigma}$ have the characteristic value $\frac{1}{2}$, immediately leads to the restriction

$$L=0 \text{ or } 1 \quad (2)$$

on each term in Ψ, since we have chosen to ignore recoil of the nucleore. Furthermore, the parity of each term must be the same, so the pseudoscalar character of the pion field leads to the condition

$$(-1)^{\Sigma_j l_j}=(-1)^N \quad (3)$$

for each term in (1), if l_j is the orbital angular momentum quantum number of the jth pion.

It is worth remarking here that, whereas weak coupling implies the approximation

$$\Psi\approx\Psi_0+\sum_s\Psi_1{}^{(s)}, \quad (4)$$

linear coupling of the nucleore with the pion field implies that only terms with

$$l_j=1 \quad (5)$$

are important. This can be established by considering the process of creation of a nucleon from an initial state consisting of a bare nucleore. Linear coupling means that the pions are emitted one at a time so conservation of angular momentum and parity at every stage of the process limits the orbital angular momentum of each pion to the above value.

Additional restrictions on the functional are introduced by conservation of charge. The nucleore is assumed to have just two charge states, 0 and 1, (isotopic spin $\frac{1}{2}$) so the total charge, C, of the pion field for any term in (1) is limited to the values 0 and 1 for the proton or 0 and -1 for the neutron. We will make the assumption that Ψ has the mirror property, namely, that the wave functional for the neutron is obtained when positive and negative pions are interchanged in the proton wave functional and, at the same time, the charge on the nucleore in each term of (1) is reversed (i.e., 1 is replaced by 0 and 0 by 1). In the language of isotopic spin this mirroring can be accomplished by the transformation in charge space corresponding to a reflection in a plane containing the axis of quantization.

Since pions occur as positive, negative, and neutral particles, it is reasonable to assign to the pion an isotopic spin $t=1$ and to consider the consequences of the assumption that the interactions are charge invariant, i.e., that they are invariant under rotations in charge space. This is the condition that leads to charge independence of nuclear forces. It implies that the total isotopic spin

$$\mathbf{T}=\sum_j\mathbf{t}_j+\tfrac{1}{2}\boldsymbol{\tau} \quad (6)$$

is conserved. Here $\mathbf{t}_j$ is the isotopic spin vector of the jth pion and $\boldsymbol{\tau}$ is twice the isotopic spin operator of the nucleore. We take $\tau_j=\pm 1$ to correspond to nucleore charges 1 and 0, respectively. The value of T for the nucleon state Ψ is $T=\frac{1}{2}$. Therefore, if

$$\mathbf{Y}=\sum_j\mathbf{t}_j \quad (7)$$

is the total isotopic spin of the pions, its associated quantum numbers Y are restricted to the values

$$Y=0, 1. \quad (8)$$

In the state $Y=0$ the net pion charge (projection of Y on the axis of quantization) is always zero so the pions occur as neutrals or in positive-negative pairs. In the state $Y=1$, the relative amplitudes of the two possible charge states are determined by the condition that

[8] Compare L. I. Schiff, Phys. Rev. **84**, 1 (1951); B. J. Malenka, Phys. Rev. **85**, 686 (1952).

$T=\frac{1}{2}$. If $Z_Y{}^C$ is the isotopic spin wave function of the pions for charge $C=Y,\ Y-1,\ \cdots -Y$, and $x^\pm$ is the isotopic spin function of the nucleore, then the total isotopic spin function of a neutron, when the pions have $Y=1$, has the form

$$X_{\frac{1}{2}}{}^{-\frac{1}{2}}=-\sqrt{\tfrac{2}{3}}Z_1{}^{-1}x^+ +\sqrt{\tfrac{1}{3}}Z_1{}^0x^-. \tag{9}$$

Thus the probability, in the $Y=1$ state, for finding a net pion charge 0 is one-half the probability for finding a negative charge, -1.

More particular statements can be made concerning specific terms in Eq. (1). For one-pion states, Ψ_1, Eqs. (2) and (3) combine to impose the restriction

$$L=l=1, \quad \text{(one pion)}. \tag{10}$$

Also the total isotopic spin of the pions is just that of the single pion

$$Y=t=1, \quad \text{(one pion)}.$$

The charge in the one-pion state of the neutron is therefore distributed in accordance with Eq. (9), $\frac{2}{3}$ negative and $\frac{1}{3}$ neutral.

Simple statements concerning the two-pion states are also possible. If l_1 and l_2 are the orbital angular momenta of the two pions [not restricted by the linearity condition Eq. (5)], then $L=0$ can only be formed if $l_1=l_2$. For $L=1$ we might have $l_1=l_2$ or $l_1=l_2\pm 1$, but the parity condition, Eq. (3), eliminates all but the first possibility. Thus,

$$l_1=l_2 \quad \text{(two pions)}. \tag{11}$$

The fact that the pion satisfies Einstein-Bose statistics implies that the wave function of any system composed of a fixed number of particles must be symmetric for the interchange of all coordinates (including the isotopic spin variable) of any pair of pions. This condition restricts the structure of the functions Ψ_2, Ψ_3 and so on. In particular, the two-pion states have the property that $Y=0$ is a symmetric function and $Y=1$ is an antisymmetric function. Since $l_1=l_2$ the angular parts of the $L=0$ and $L=1$ functions are also symmetric and antisymmetric, respectively [see Eqs. (25) and (26)]. Therefore if the functions are classified by the symmetry of the radial functions, we find that the radially symmetric states are restricted to the combinations

$$\begin{aligned} &Y=0 \text{ for } L=0,\\ &Y=1 \text{ for } L=1, \end{aligned} \quad \text{(two pions—radial sym)} \tag{12a}$$

and the radially antisymmetric states to the combinations

$$\begin{aligned} &Y=1 \text{ for } L=0,\\ &Y=0 \text{ for } L=1. \end{aligned} \quad \text{(two pions—radial antisym)} \tag{12b}$$

It follows that, in the symmetric states, the net pion charge is zero for $L=0$, while for $L=1$ the distribution of pion charge in the neutron is $\frac{2}{3}$ negative, $\frac{1}{3}$ zero. In the radially antisymmetric states, the charge is zero for $L=1$, and is distributed in the 2 to 1 ratio for $L=0$.

If we denote by $P_L{}^C(N)$ the probability for the occurrence of N pions in the neutron with total orbital angular momentum L and total charge C, the results of our discussion may be summarized by the statements:

$$P_0{}^C(1)=0, \tag{13a}$$

$$P_1{}^\pm(1)=2P_1{}^0(1), \tag{13b}$$

$$P_0{}^\pm(2, \mathfrak{s})=0, \tag{13c}$$

$$P_1{}^\pm(2, \mathfrak{s})=2P_1{}^0(2, \mathfrak{s}), \tag{13d}$$

$$P_0{}^\pm(2, \mathfrak{a})=2P_0{}^0(2, \mathfrak{a}), \tag{13e}$$

$$P_1{}^\pm(2, \mathfrak{a})=0, \tag{13f}$$

where the symbols $\mathfrak{s}$ and $\mathfrak{a}$ classify the two-pion states according to their radial symmetry. Only one sign C is admissable for a given nucleon, $C=+$ for the proton, $C=-$ for the neutron.

3. DESCRIPTION OF THE PION FIELD

The analysis of the foregoing section proceeds on the assumption that individual pions are assigned to states of definite orbital angular momentum in contrast to the more usual assignment to states of given linear momentum. The description of the quantized field in terms of these spherical waves is quite similar to the description in terms of plane waves. Since this particular form of analysis is important for the treatment of the nucleon magnetic moment, its pertinent features are described in Appendix 1. The discussion is based on the assumption that the free pions are properly described by the linear Pauli-Weisskopf theory.[4] Nonlinear theories involving pion-pion interactions[3] are excluded for reasons of simplicity.

It is shown in the Appendix that the field can be described in terms of the number $N_{klm}{}^\gamma$ of pions with charge $\gamma(=1,\ 0,\ \text{or}\ -1)$ in a state of orbital angular momentum l with magnetic quantum number m. The energy of a neutral pion is $\hbar\omega_0$, with $\omega_0{}^2=c^2(k^2+\mu_0{}^2)$, and that of a charged pion is $\hbar\omega$, with $\omega^2=c^2(k^2+\mu^2)$, where $\hbar\mu_0/c$ and $\hbar\mu/c$ are the masses of neutral and charged pions. The quantum numbers (k, l, m) are collectively denoted by the symbol s, with the notation $-s\equiv(k, l, -m)$.

It is clear that in this representation the total angular momentum is not, in general, a good quantum number because each pion is assigned a magnetic quantum number. Since the pion field is to be assigned a total angular momentum L, it is of some interest to note the connection between the representation in terms of the $N_s{}^\gamma$ and that characterized by given L. The basic vectors in terms of which the functional of the field is

[4] For a discussion of the basic features of the theory in a corresponding notation see G. Wentzel, *Quantentheorie der Wellenfelder* (Franz Deuticke, Vienna, 1943); English translation (Interscience Publishers, Inc., New York, 1949).

described are the characteristic vectors $\Phi\{N_s{}^\gamma\}$ corresponding to fixed values of $N_s{}^\gamma$. For a state of a fixed number N^γ of pions of each charge, the functional $\Phi_L{}^{ML}$ of total angular momentum L is a linear combination of those $\Phi\{N_s{}^\gamma\}$ for which $\sum_s N_s{}^\gamma = N^\gamma$ and $\sum_{s,\gamma} m N_s{}^\gamma = M_L$. Since the functionals $\Phi\{N_s{}^\gamma\}$ are just the properly symmetrized products of one particle functions,[6] the relationship between $\Phi_L{}^{ML}$ and $\Phi\{N_s{}^\gamma\}$ is given by the unitary transformation

$$\langle l_1, m_1; l_2, m_2, \cdots l_N, m_N | l_1, l_2, \cdots l_N; L, M_L \rangle,$$

which can be obtained from standard sources.[6] Here, the number of (l_i, m_i) values equal to (l, m) is $\sum_{k,\gamma} N_s{}^\gamma$. Use is made of this transformation in calculating the two-pion contribution to the magnetic moment (Sec. 7). For more than two particles, the transformation is not, in general, uniquely determined.

Given the functionals $\Phi_L{}^{ML}(N^+, N^0, N^-)$ of fixed numbers of pions, they can be combined with the nucleore spin function to form functionals $\Psi^M(N^+, N^0, N^-; L)$ of total angular momentum $\frac{1}{2}$ and magnetic quantum number $M(=\pm\frac{1}{2})$. Then the nucleon functional indicated by Eq. (1) is a linear combination of these:

$$\Psi^M = \sum_{(N)} \sum_L B_L(N^+, N^0, N^-) \Psi^M(N^+, N^0, N^-, L). \quad (14)$$

Now we wish to show that the coefficients $B_L(N^+, N^0, N^-)$ can always be chosen to be real numbers. The importance of this statement is that it reduces, essentially by a factor of 2, the number of parameters required to describe the functional. The proof of the statement is based on a time reversal argument of the type suggested by Wigner.[7] He has pointed out that, if the time reversal operation is represented by an operator K, then for a state of given total angular momentum j the wave function $\psi_j{}^m$ can always be chosen in such a way that

$$K\psi_j{}^m = i^{2m}\psi_j{}^{-m}. \quad (15)$$

It is shown in Appendix 2 that the choice of representation of the pion field is consistent with Eq. (15):

$$K\Phi_L{}^{ML} = i^{2ML}\Phi_L{}^{-ML}. \quad (16)$$

Therefore, for an appropriate[8] choice of the coefficients used in combining the $\Phi_L{}^{ML}$ with the nucleore spin functions, this property carries over to the $\Psi^M(N^+, N^0, N^-; L)$:

$$K\Psi^M(N^+, N^0, N^-; L) = i^{2M}\Psi^{-M}(N^+, N^0, N^-; L).$$

Now K involves taking the conjugate complex, so in any linear combination of functions the coefficients are conjugated by K. Therefore,

$$K\Psi^M = i^{2M} \sum_{(N)} \sum_L B_L{}^*(N^+, N^0, N^-) \times \Psi^{-M}(N^+, N^0, N^-; L).$$

But, unless there is an accidental degeneracy,

$$K\Psi^M = i^{2M}\Psi^{-M} = i^{2M} \sum_{(N)} \sum_L B_L(N^+, N^0, N^-) \times \Psi^{-M}(N^+, N^0, N^-; L),$$

whence it follows that the coefficients B_L are real. The possibility that the ground state of the nucleon is accidentally degenerate does not appear to warrant serious consideration.

The probability $P_L(N^+, N^0, N^-)$ for the occurrence in the nucleon of a state of N^γ pions of charge γ having total orbital angular momentum L is given by

$$P_L(N^+, N^0, N^-) = |B_L(N^+, N^0, N^-)|^2.$$

Since the B_L are real,

$$B_L(N^+, N^0, N^-) = \pm[P_L(N^+, N^0, N^-)]^{\frac{1}{2}}, \quad (17)$$

a result which will be used in Sec. 7.

4. MAGNETIC MOMENT OF THE NUCLEON

The contribution $\mathfrak{M}_0$ of the pion field to the magnetic moment operator is obtained in Appendix 1 by considering the change in energy of the pions caused by the introduction of a uniform magnetic field. There is some ambiguity about $\mathfrak{M}_0$ because it may receive a contribution from the pion-nucleore interaction term. It is well known that the electromagnetic field induces emission of pions in the pseudoscalar theory. However, any such "interaction moment" is ignored here, the justification being that for a point interaction between pion and nucleore, the static interaction moment vanishes in the approximation that nucleore recoil is negligible.

The pion moment operator may be expressed in terms of the creation and annihilation operators, $a_s{}^*$, a_s, for positive pions in states of given energy and angular momentum, and in terms of similar operators for negatives, $b_s{}^*$, b_s:

$$\mathfrak{M}_0 = \tfrac{1}{2}ec \sum_{s,s'} \delta_{kk'}\delta_{ll'}\omega^{-1}(a_s{}^* a_{s'} - b_s{}^* b_{s'} + (-1)^{m'} a_s{}^* b_{-s'}{}^* + (-1)^m b_{-s} a_{s'})(l, m|\mathbf{L}|l, m'), \quad (18)$$

where $(l, m|\mathbf{L}|l, m')$ is the matrix element of the one particle angular momentum operator, $\mathbf{L} = -i\mathbf{r}\times\text{grad}$.

In a state for which the number of pions is prescribed, only the first two terms contribute to the expectation value of the magnetic moment. Aside from the relativistic correction factor $(\mu c/\omega)$, the magnetic

[5] See, for example, H. Weyl, *The Theory of Groups and Quantum Mechanics* (Methuen & Company, Ltd., London, 1931), p. 246 ff.

[6] E. Condon and G. Shortley, *The Theory of Atomic Spectra* (Cambridge University Press, Cambridge, 1951), p. 76.

[7] E. P. Wigner, Nachr. Akad. Wiss. Göttinger, Math.-physik Kl., p. 546 (1932).

[8] Since we have chosen the functionals $\Phi_L{}^{ML}$ in such a way that they satisfy the condition Eq. (16), it follows from Wigner's general statement that one can always choose the basis in accordance with Eq. (15). The usual transformation coefficients $(J, M, L, S|L, M_L, S, M_S)$ satisfy the condition

$$(J, -M, L, S|L, -M_L, S, -M_S) = (-1)^{L+S-J}(J, M, L, S|L, M_L, S, M_S),$$

from which it follows that they are to be modified by multiplication by i^{L+S-J} in order that Eq. (15) be satisfied. This point was called to the author's attention by Dr. E. N. Adams, II.

moment contribution in such a state is just what would be expected for a system of particles with given l values, $\pm(e/2\mu)\mathbf{l}$ for each pion, the sign being positive for positive pions, negative for negative pions. But in the nucleon state, Eq. (14), the number of pions is not specified, so the pair terms $a_s^* b_{-s'}^*$ and $a_s b_{-s'}$ in Eq. (18) may play a role in determining the nucleon moment. Since they can contribute only to matrix elements between states $\Psi(N^+, N^0, N^-)$ and $\Psi(N^+-1, N^0, N^--1)$, these terms are only of importance if at least two pions occur with appreciable probability in the nucleon proper field.

$\mathfrak{M}_0$ is just the pion orbital part of the magnetic moment operator. Presumably the charged nucleore has a moment of about[9] one nuclear magneton associated with its spin, $\boldsymbol{\sigma}$. The total moment operator is therefore

$$\mathfrak{M}=(e/2\mathfrak{M})\tfrac{1}{2}(1+\tau_3)\boldsymbol{\sigma}+\mathfrak{M}_0,$$

where $\hbar\mathfrak{M}/c$ is the mass of the nucleore. The magnetic moment of the nucleon is the expectation value

$$\mathfrak{M}=\langle\Psi^{\frac{1}{2}}, \mathfrak{M}_z\Psi^{\frac{1}{2}}\rangle \tag{19}$$

in the state $\Psi^{\frac{1}{2}}$ for which the z component of the total angular momentum is $\frac{1}{2}$.

5. THE MIRROR THEOREM

It seems very reasonable to assume that the mirror property described in Sec. 2 applies to the nucleon functional Ψ in good approximation. This assumption is less restrictive than the requirement of charge invariance (conservation of total isotopic spin) although it is contained implicitly in that property.

According to the mirror property, the same functional can be used to describe neutron and proton if we understand that a given variable appearing in Ψ refers to oppositely charged pions for the two different nucleons. The isotopic spin of the nucleore also has the opposite value. Then, if the operators a_s, b_s refer to positive and negative pions respectively for the neutron, they refer to negative and positive pions for the proton; so the operators describing an observable characteristic of the proton differ from those characteristic of a neutron by the interchange of the quantities a_s and b_s and by changing the sign of τ_3. In particular, if the neutron moment is obtained by taking the expectation value of (we now use units of nuclear magnetons)

$$\mathfrak{M}_n=\tfrac{1}{2}(1+\tau_3)\boldsymbol{\sigma}+\sum_{s,s'}(\mathfrak{M}c/\omega)\delta_{kk'}\delta_{ll'}(l, m|\mathbf{L}|l, m') \times(a_s^* a_{s'}-b_s^* b_{s'}+(-1)^{m'}a_s^* b_{-s'}^*+(-1)^m b_{-s}a_{s'}), \tag{20}$$

then the proton moment is to be obtained by taking the expectation value for the identical state of

$$\mathfrak{M}_p=\tfrac{1}{2}(1-\tau_3)\boldsymbol{\sigma}+\sum_{s,s'}(\mathfrak{M}c/\omega)\delta_{kk'}\delta_{ll'}(l, m|\mathbf{L}|l, m') \times(b_s^* b_{s'}-a_s^* a_{s'}+(-1)^{m'}b_s^* a_{-s'}^* +(-1)^m a_{-s}b_{s'})\epsilon_m\epsilon_{m'}.$$

A quantity of particular significance is then seen to be the sum of neutron and proton moments, which is to be found by taking the expectation value in the given state of

$$\mathfrak{M}_n+\mathfrak{M}_p=\boldsymbol{\sigma}+\sum_{s,s'}(\mathfrak{M}c/\omega)\delta_{kk'}\delta_{ll'}(l, m|\mathbf{L}|l, m') \times((-1)^{m'}a_s^* b_{-s'}^*+(-1)^m b_{-s}a_{s'} +(-1)^{m'}b_s^* a_{-s'}^*+(-1)^m a_{-s}b_{s'}).$$

Diligent application of Eq. (A-5) leads immediately to the vanishing of the second term[10] so the sum of neutron and proton moments is, according to Eq. (19),

$$\mathfrak{M}_n+\mathfrak{M}_p=\langle\Psi^{\frac{1}{2}}, \sigma_z\Psi^{\frac{1}{2}}\rangle. \tag{21}$$

Now we have seen in Sec. 2 that $\Psi^{\frac{1}{2}}$ consists of a mixture of a state containing no pions with states containing one or more pions whose total orbital angular momentum is either $L=0$ or $L=1$. The total angular momentum for each state is $J=\frac{1}{2}$. Equation (21) clearly contains no cross terms between the states with differing numbers of pions or different L values. In the no-pion state

$$\langle\Psi_0^{\frac{1}{2}}, \sigma_z\Psi_0^{\frac{1}{2}}\rangle=1$$

and in a state of given L, the expectation value may be calculated by the usual vector rule:

$$\langle\Psi^{\frac{1}{2}}(L=0), \sigma_z\Psi^{\frac{1}{2}}(L=0)\rangle=1,$$
$$\langle\Psi^{\frac{1}{2}}(L=1), \sigma_z\Psi^{\frac{1}{2}}(L=1)\rangle=-\tfrac{1}{3}.$$

If we introduce the probability P_L for the occurrence of any number of pions of any energy but having a fixed total orbital angular momentum L, each of these expectation values contributes to the moment with a weight given by the appropriate P_L. The probability of the no-pion state is $1-P_0-P_1$ so the sum of the moments is found to be

$$\mathfrak{M}_n+\mathfrak{M}_p=1-(4/3)P_1. \tag{22}$$

Thus the sum of the measured neutron and proton moments yields direct information on the probability for the occurrence of pion states with $L=1$ in the nucleon. Insertion of the experimental value $\mathfrak{M}_n+\mathfrak{M}_p=0.880$ leads to the result

$$P_1=0.090. \tag{23}$$

6. THE NEUTRON MOMENT—ONE-PION MODEL

It is now of some interest to consider the restrictions imposed on the magnetic moment of a single nucleon by the condition Eq. (23). The moment depends in a detailed way on the structure of the nucleon wave functional so rather detailed assumptions concerning the functional must be made in order to arrive at definite conclusions. The simplest assumption is that suggested by the weak coupling theory, that no more than one pion occurs with an appreciable probability.

[9] The nucleore magneton rather than the nucleon magneton should be used here, but, in the absence of knowledge concerning the nucleore mass, we assume that the difference is small.

[10] The fact that the pion contributions cancel has been observed by Y. Takahashi, Prog. Theoret. Phys. **6**, 624 (1951); see also reference 1.

This will be called the one-pion model of the nucleon. For the sake of definiteness we treat the neutron.

In the one-pion model of the neutron,

$$P_1 = P_1^0(1) + P_1^-(1).$$

According to Eq. (13b), the two probabilities are then

$$P_1^0(1) = \tfrac{1}{3}P_1,$$

and

$$P_1^-(1) = \tfrac{2}{3}P_1.$$

Furthermore,

$$P_0 = P_0^0(1) = P_0^-(1) = 0.$$

The pair terms in the magnetic moment operator Eq. (20) play no role in determining the static moment in this model, so the moment is to be obtained by the usual vector rule. There is no magnetic moment contribution from the no-pion and neutral pion states, while in the negative pion state which occurs with probability $\frac{2}{3}P_1$, the contribution of the nucleore is $-\frac{1}{2}$ while that of the pion is $-\frac{2}{3}\langle \mathfrak{M}c/\omega \rangle$. Here, the angular brackets denote the average over the energy (ω) distribution of the pions. The neutron moment is therefore

$$\mathfrak{M}_n = -(2/9)[1 + 2\langle \mathfrak{M}c/\omega \rangle]P_1. \tag{24}$$

Now $\langle \mathfrak{M}c/\omega \rangle$ is clearly less than $\mathfrak{M}/\mu$, so

$$|\mathfrak{M}_n| < (2/9)(1 + 2\mathfrak{M}/\mu)P_1.$$

If we insert the nucleon to pion mass ratio, $\mathfrak{M}/\mu = 6.64$, and the value $P_1 = 0.09$, the result is

$$|\mathfrak{M}_n| < 0.29.$$

This is in direct contradiction to the experimental fact that $\mathfrak{M}_n = -1.91$. Thus we can say that, although Eq. (24) could give agreement with the neutron moment alone, agreement is not possible if we take cognizance of the condition imposed on P_1 by the sum of neutron and proton moments. The neutron and proton moments together are not in accord with the one-pion model. This conclusion is quite independent of the assumption of charge invariance which is required to obtain the particularly simple form of Eq. (24).

Since the one-pion model is substantially equivalent to weak coupling theory, our result is probably the underlying reason for the failure of that theory to give the correct ratio of neutron to proton moment. However, the usual dynamical meson theories are such that relativistic pions play a dominant role, so nucleon recoil is an important factor in the calculation of the moments.[11] Therefore, too close a correspondence between the results of the dynamical theories and our no-recoil theory is not to be made.

7. THE NEUTRON MOMENT—TWO-PION MODEL

Relatively simple results are obtained if we extend the treatment of the neutron moment to include two-pion states. The contribution of one-pion states is still given by Eq. (24). Three different kinds of contributions arise from the two-pion states: the orbital moment of the two pions in state $L=1$,

$$\langle N=2,\ L=1\,|\mathfrak{M}_n|\,N=2,\ L=1\rangle,$$

the cross term of the orbital moment between $L=0$ and $L=1$, $\langle N=2,\ L=1\,|\mathfrak{M}_n|\,N=2,\ L=0\rangle$, and the cross term between the 2-pion and 0-pion states introduced by the pair creation operators appearing in Eq. (20), $\langle N=2,\ L\,|\mathfrak{M}_n|\,N=0\rangle$. In calculating the cross terms explicit use must be made of the (real) radial functions $F_{L,\,\mathcal{S},\,l}(r_1, r_2)$ of the two-pion state with given l of each pion and with given L and S. S is the symmetry parameter which distinguishes a function symmetric for interchange of r_1 and r_2, $S=\mathcal{S}$, from an antisymmetric function, $S=\mathcal{A}$. The operator $\mathfrak{M}_n$ is independent of the distances r_1 and r_2, so the matrix elements involve simple overlap integrals of the radial functions and no cross terms arise between states of opposite symmetry. In calculating the matrix elements we will assume, for the sake of simplicity, that pions of relativistic energies do not play an important role so the factor $\mathfrak{M}c/\omega$ appearing in Eq. (20) can be replaced by $\mathfrak{M}/\mu$.

The $L=1$ to $L=1$ matrix element may be obtained by direct application of the vector rule. From Eq. (11) we see that the two pions share equally in the orbital angular momentum, hence pion pairs of opposite charge make no contribution and the pion contribution in the state containing one negative and one neutral pion ($C=-1$) is one-half of that due to a single pion with $l=1$. Since the nucleore has positive charge in the latter state, its intrinsic moment must be included. Thus

$$\langle N=2,\ C=0,\ L=1\,|\mathfrak{M}_n|\,N=2,\ C=0,\ L=1\rangle = 0,$$

$$\langle N=2,\ C=-1,\ L=1\,|\mathfrak{M}_n|\,N=2,\ C=-1,\ L=1\rangle = -\tfrac{1}{2}(1+\mathfrak{M}/\mu).$$

Determination of the $L=1$, $L=0$ cross term can also be made on the basis of simple two-particle wave functions. The $L=0$ state has no net charge in the $\mathcal{S}$ states [see Eq. (13c)] and the $L=1$ has none in the $\mathcal{A}$ states [see Eq. (13f)] so the moment must arise from positive-negative pairs. The angular part, $\Phi_L{}^{M_L}$, of the $L=0$ wave function has the form

$$\Phi_0{}^0(1,2) = (-1)^l \textstyle\sum_m (-1)^m Y_l{}^m(1) Y_l{}^{-m}(2)/(2l+1)^{\frac{1}{2}}, \tag{25}$$

while that of the $L=1$ function for $M_L=0$ (the only contributing function) is

$$\Phi_1{}^0(1,2) = (-1)^l \textstyle\sum_m (-1)^m m Y_l{}^m(1) Y_l{}^{-m}(2)/(\sum_m m^2)^{\frac{1}{2}}. \tag{26}$$

If $\mathbf{l}_1$ and $\mathbf{l}_2$ are the orbital angular momentum operators of the positive and negative pions, respectively, the magnetic moment operator is $\mathbf{l}_1 - \mathbf{l}_2$ and the matrix

[11] J. M. Luttinger, Helv. Phys. Acta **21**, 483 (1948); M. Slotnick and W. Heitler, Phys. Rev. **75**, 1645 (1949); K. M. Case, Phys. Rev. **76**, 1 (1949).

element of the z component is

$$\langle \Phi_1{}^0, (\mathbf{I}_1-\mathbf{I}_2)_z\Phi_0{}^0\rangle = 2(\textstyle\sum_m m^2)/[(2l+1)\sum_m m^2]^{\frac{1}{2}} = 2[l(l+1)/3]^{\frac{1}{2}}.$$

The $L=1$ function is combined with the spin function of the nucleore to form total angular momentum $J=\frac{1}{2}$. The coefficient of the $M_L=0$ function is therefore $-1/\sqrt{3}$. Furthermore, in the $Y=0$ isotopic spin function the charged pair term occurs with a probability $\frac{2}{3}$. This introduces a factor $\sqrt{\frac{2}{3}}$ into the matrix element. The net result is then

$$\langle N=2, C=0, L=1\,|\mathfrak{M}_n|\,N=2, C=0, L=0\rangle = (2/3)^{\frac{1}{2}}(\mathfrak{M}/\mu)\textstyle\sum_l[l(l+1)]^{\frac{1}{2}}I_{01}(S,l),$$

where $I_{LL'}(S,l)$ is the overlap integral

$$I_{LL'}(S,l)=\int_0^\infty\int_0^\infty F_{LSl}(r,r')F_{L'Sl}(r,r')r^2r'^2drdr'.$$

After the pair creation and annihilation operators in Eq. (20) have been applied, the calculation of the (two-pion)$-$(no-pion) cross term is very similar to the treatment of the $L=0$, $L=1$ cross term. There is no contribution from the two-pion term with $L=0$. For $L=1$ the matrix element is

$$\begin{aligned}&\langle N=2, C=0, L=1\,|\mathfrak{M}_n|\,N=0\rangle\\ &=\sqrt{\tfrac{1}{3}}(\mathfrak{M}/\mu)\textstyle\sum_l(-1)^l[\sum_m m^2]I_1(S,l)/(\sum_m m^2)^{\frac{1}{2}}\\ &=(\mathfrak{M}/\mu)\textstyle\sum_l\frac{1}{3}[l(l+1)(2l+1)]^{\frac{1}{2}}I_1(S,l),\end{aligned}$$

where $I_L(S,l)$ is the radial integral,

$$I_L(S,l)=(-1)^l\int_0^\infty F_{LSl}(r,r)r^2dr,$$

which vanishes for $S=\mathfrak{a}$.

If we introduce the (real) probability amplitudes and add all contributions to the moment in the two-pion model, the result is, according to Eq. (17),

$$\begin{aligned}\mathfrak{M}_n=&-\tfrac{1}{3}(1+2\mathfrak{M}/\mu)P_1{}^-(1)-\tfrac{1}{3}(1+\mathfrak{M}/\mu)P_1{}^-(2)\\ &\pm2(2/3)^{\frac{1}{2}}(\mathfrak{M}/\mu)\textstyle\sum_S[P_1{}^0(2,S)P_0{}^0(2,S)]^{\frac{1}{2}}\\ &\times\textstyle\sum_l[l(l+1)]^{\frac{1}{2}}I_{01}(S,l)\\ &\pm2(\mathfrak{M}/\mu)[(1-P_0-P_1)P_1{}^0(2,\mathfrak{s})]^{\frac{1}{2}}\\ &\times\tfrac{1}{3}\textstyle\sum_l[l(l+1)(2l+1)]^{\frac{1}{2}}I_1(\mathfrak{s},l),\end{aligned}$$

which can be reduced by means of the charge-invariance conditions Eqs. (13) to

$$\begin{aligned}\mathfrak{M}_n=&-(2/9)(1+2\mathfrak{M}/\mu)P_1(1)-(2/9)(1+\mathfrak{M}/\mu)P_1(2,\mathfrak{s})\\ &\pm(4/9)\sqrt{2}(\mathfrak{M}/\mu)\textstyle\sum_S[P_1(2,S)P_0(2,S)]^{\frac{1}{2}}\\ &\times\textstyle\sum_l[l(l+1)]^{\frac{1}{2}}I_{01}(S,l)\pm(2/\sqrt{3})(\mathfrak{M}/\mu)\\ &\times[(1-P_0-P_1)P_1(2,\mathfrak{s})]^{\frac{1}{2}}\\ &\times\tfrac{1}{3}\textstyle\sum_l[l(l+1)(2l+1)]^{\frac{1}{2}}I_1(\mathfrak{s},l).\end{aligned}\quad(27)$$

Here P_L is the total probability for finding either one or two pions in state L, while $P_0(2,S)$ and $P_1(2,S)$ are the probabilities for finding two pions (any allowed charge) of given S in the states $L=0$ and $L=1$, respectively.

The linear coupling condition, Eq. (5), suggests that consideration be limited to $l=1$, in which case we drop the index l. Then

$$\begin{aligned}\mathfrak{M}_n=&-(2/9)(\mathfrak{M}/\mu)\{(2+\mu/\mathfrak{M})P_1(1)\\ &+(1+\mu/\mathfrak{M})P_1(2,\mathfrak{s})\\ &\pm4\textstyle\sum_S[P_1(2,S)P_0(2,S)]^{\frac{1}{2}}I_{01}(S)\\ &\pm3\sqrt{2}[(1-P_0-P_1)P_1(2,\mathfrak{s})]^{\frac{1}{2}}I_1(\mathfrak{s})\}.\end{aligned}\quad(28)$$

Clearly for the nucleon to pion mass ratio $\mathfrak{M}/\mu=6.64$, this equation is capable of yielding the known value of the neutron moment, $\mathfrak{M}_n=-1.91$, even within the restrictions imposed by Eq. (23), $P_1=0.09$, because no conditions have been set on P_0. However, it is of particular interest that the values

$$P_1(1)=P_1(2,\mathfrak{a})=P_0=0,\quad P_1(2,\mathfrak{s})=P_1=0.090,\quad(29)$$

along with the relationship

$$I_1(\mathfrak{s})=\int_0^\infty F_{1\mathfrak{s}}(r,r)r^2dr=1,\quad(30)$$

and an appropriate choice of sign of the square root, gives

$$\mathfrak{M}_n=-1.93,$$

in rather remarkable (but probably fortuitous) agreement with the observed moment. This result, that the magnetic moments of both nucleons can be accounted for if the proper field contains only a pair of pions, and that with the small probability of 9 percent, is very suggestive. However, many other selections of the coefficients in Eq. (28) will give the correct moment. An even greater variety of possibilities is offered by l values different from $l=1$ or by numbers of pions greater than two.

It should be remarked that Eq. (30) is quite consistent with the normalization condition

$$\int\int F_{1\mathfrak{s}}{}^2(r,r')r^2r'^2drdr'=1.$$

A square radial distribution, i.e., a sharp cutoff at some fixed value of r and r' would lead to just such a relationship.

8. THE NEUTRON-ELECTRON INTERACTION

Another source of information concerning the structure of the nucleon is the neutron-electron interaction. To calculate the interaction on the basis of our model, we note that the interaction with any external electrostatic field $V(\mathbf{r})$ is

$$W=\int[\rho(\mathbf{r})+\tfrac{1}{2}e(1+\tau_3)\delta(\mathbf{r})]V(\mathbf{r})d^3r,$$

where $\rho(\mathbf{r})$ is the charge density operator for the pion

field,

$$\rho(\mathbf{r})=-(ie/\hbar)[\pi(\mathbf{r})\psi(\mathbf{r})-\pi^*(\mathbf{r})\psi^*(\mathbf{r})].$$

From Eqs. (A-3) and (A-4) we find

$$W=\tfrac{1}{2}e\{(1+\tau_3)V(0)+\sum_{s,s'}\times[(\omega/\omega')^{\frac{1}{2}}((-1)^m a_s^*-b_{-s})(a_{s'}+(-1)^{m'}b_{-s'}^*)(-1)^m+(\omega'/\omega)^{\frac{1}{2}}((-1)^{m'}a_{s'}-b_{-s'}^*)(a_s^*+(-1)^m b_{-s})(-1)^{m'}](s|V|s')\},$$

where

$$(s|V|s^*)=\int\phi_s^*V\phi_{s'}d^3r.$$

Note that, since $V(r)$ is a real function,

$$(-s'|V|-s)=(-1)^{m+m'}(s|V|s').$$

The factors $(\omega/\omega')^{\frac{1}{2}}$ can be dropped if relativistic pions are assumed to be unimportant. Then

$$W=e\{\tfrac{1}{2}(1+\tau_3)V(0)\sum_{s,s'}(a_s^*a_{s'}-b_s^*b_{s'})(s|V|s')\}.$$

There are no pair creation or annihilation terms remaining in this approximation to the operator W, so the interaction is made up of terms arising from states of a given number of pions, and the contribution of each such state can be calculated by use of the properly symmetrized product of Schrödinger wave functions. Since the neutron has no net charge, $\frac{1}{2}(1+\tau_3)=-(N^+-N^-)$, and the expectation value of W is

$$\overline{W}=\int\bar{\rho}(\mathbf{r})V(\mathbf{r})d^3r-V(0)\sum_{(N)}\times P(N^+,N^0,N^-)(N^+-N^-),$$

where $\bar{\rho}(\mathbf{r})$ is the mean pion charge density in the nucleon proper field.

If $V(r)$ is a slowly varying function it may be expanded about $r=0$:

$$V(\mathbf{r})=V(0)+\mathbf{r}\cdot(\mathrm{grad}V)_{r=0}+\sum_{ij}x_ix_j(\partial^2V/\partial x_i\partial x_j)_{r=0}+\cdots.$$

Now

$$\int\bar{\rho}(\mathbf{r})V(0)d^3r=V(0)\sum_{(N)}P(N^+,N^0,N^-)(N^+-N^-).$$

Furthermore, $\bar{\rho}$ has even parity since all pion states have the same parity, so

$$\int\bar{\rho}(\mathbf{r})\mathbf{r}\cdot(\mathrm{grad}V)_0d^3r=0.$$

Finally, each pion state has $J=\frac{1}{2}$ so only the part of $x_ix_j(\partial^2V/\partial x_i\partial x_j)_{r=0}$ with the angular dependence of an S function can contribute to the integral. Therefore,

$$\overline{W}=-\tfrac{1}{6}e(\nabla^2V)_{r=0}\langle r^2\rangle_{\mathrm{av}},$$

where $\langle r^2\rangle_{\mathrm{av}}$ is the mean square radius of charge in the proper field,

$$e\langle r^2\rangle_{\mathrm{av}}=-\int r^2\bar{\rho}(\mathbf{r})d^3r,$$

the sign having been chosen in accordance with the fact that the net charge of the proper field is negative.

When the external field is produced by an electron at the point $\mathbf{R}$, we have

$$(\nabla^2V)_{r=0}=4\pi e\delta(\mathbf{R}),$$

so the neutron-electron interaction is simply[12]

$$\overline{W}=-(4\pi/3)e^2\langle r^2\rangle_{\mathrm{av}}\delta(\mathbf{R}).$$

It is customary to describe the measured values of the interaction in terms of the effective depth

$$W_0=\int\overline{W}(\mathbf{R})d^3R/(4\pi/3)(e^2/mc^2)^3,$$

which is now found to be

$$W_0=-[\langle r^2\rangle_{\mathrm{av}}/(e^2/mc^2)^2]mc^2.$$

The experimental value[13] $|W_0|\approx 4$ kev requires that

$$\langle r^2\rangle_{\mathrm{av}}/(e^2/mc^2)^2\approx 8\times 10^{-3},$$

or

$$\mu^2\langle r^2\rangle_{\mathrm{av}}\approx 3.2\times 10^{-2}, \tag{31}$$

where μ^{-1} is the Compton wavelength of the pion.

The order of magnitude of the displacement of a pion in the proper field of a nucleon would be expected to be μ^{-1}, so Eq. (31) may be interpreted as a measure of the probability of occurrence of charged pions. This probability, 3.2 percent, is in rough agreement with the results of our discussion of the magnetic moment. A more specific statement can be made on the basis of either the one-pion or two-pion model. The only contribution to $\langle r^2\rangle_{\mathrm{av}}$ in the former comes from the negative pion so we have

$$\langle r^2\rangle_{\mathrm{av}}=\langle N=1|r^2|N=1\rangle P_1^-(1),$$

or, by Eq. (13b)

$$\langle r^2\rangle_{\mathrm{av}}=(2/3)\langle N=1|r^2|N=1\rangle P_1(1),$$

where $\mathbf{r}$ is a pion coordinate. Since only one pion occurs in this model, $P_1(1)=P_1=0.09$ so Eq. (31) yields the very reasonable value for the mean square displacement of a pion:

$$\langle N=1|r^2|N=1\rangle\approx 0.5\mu^{-2}.$$

The failure of the one-pion model to account for the magnetic moments suggests that we carry the argument to the two-pion model; then the contributions to $\langle r^2\rangle_{\mathrm{av}}$ include a term produced by states of net negative

[12] Compare L. L. Foldy, unpublished Case Inst. of Technology Technical Report No. 15 (1952); Phys. Rev. **87**, 688 (1952). The separation of the term associated with the nuclear magnetic moments, enlightening though it be, is quite artificial for slow neutrons. See B. D. Fried, Phys. Rev. **86**, 434 (1952).

[13] Harvey, Hughes, and Goldberg, Phys. Rev. **87**, 220 (1952).

charge (one negative, one neutral pion) and a cross term between $\mathcal{S}$ and $\mathfrak{A}$ states of net charge 0 (one negative, one positive pion). The charged pairs do not contribute within states of given symmetry because in them there is an equal chance for pions of opposite charge to be at a given distance from the nucleore. The expression for $\langle r^2\rangle_M$ is found to be (note again that charged pairs occur with amplitude $\sqrt{\frac{2}{3}}$ in the $Y=0$ state),

$$\begin{aligned}\langle r^2\rangle_M=\tfrac{2}{3}\{&P_1(1)\langle N=1|r^2|N=1\rangle\\&\pm 2\sqrt{2}\textstyle\sum_L[P_L(2,\mathcal{S})P_L(2,\mathfrak{A})]^{\frac{1}{2}}\\&\times\langle N=2,\mathcal{S},L|r^2|N=2,\mathfrak{A},L\rangle\\&+P_1(2,\mathcal{S})\langle N=2,\mathcal{S},L=1|r^2|N=2,\mathcal{S},L=1\rangle\\&+P_0(2,\mathfrak{A})\langle N=2,\mathfrak{A},L=0|r^2|N=2,\\&\qquad\mathfrak{A},L=0\rangle\}.\end{aligned}\tag{32}$$

This result is so ambiguous that the condition $P_1=0.09$ does not lead to any clear cut conclusion. However, we can again turn to the very simple conditions, Eq. (29), which are consistent with the observed nucleon moments. Then Eq. (32) becomes

$$\langle r^2\rangle_M=0.06\langle 2\mathcal{S}1|r^2|2\mathcal{S}1\rangle,$$

where $\langle 2\mathcal{S}1|r^2|2\mathcal{S}1\rangle$ is the mean square displacement of the pion in the prescribed state,

$$\langle 2\mathcal{S}1|r^2|2\mathcal{S}1\rangle\equiv\langle N=2,\mathcal{S},L=1|r^2|N=2,\mathcal{S},L=1\rangle.$$

Again a very reasonable value is obtained for the pion displacement from the condition, Eq. (31), imposed by the observed neutron-electron interaction:

$$\mu^2\langle 2\mathcal{S}1|r^2|2\mathcal{S}1\rangle\approx 0.5.\tag{33}$$

The principal significance of these results abides in the support they lend to the view that the pion proper field occurs with a relatively small probability.

9. CONCLUSION

It is not surprising that just three experimental data, the two moments and the electron-neutron interaction, can be fitted by considering a sufficiently complex model of the nucleon. What is surprising is the strong indication that the model must involve more than one pion, but that otherwise a rather weak and simple pion field is adequate to account for the data. The limitation on the number of pions might be somewhat softened by the inclusion of nucleore recoil, but the failure of dynamical theories along those lines would seem to lend support to the present model. Further support is provided by the fact that the neutron-electron interaction, as expressed by Eq. (33), seems to fit so well with our estimate of P_1 based on the mirror theorem.

The simplest model which accounts for the data consists of a bare nucleore (core of nucleon) with a 91 percent probability and a nucleore plus two pions with a 9 percent probability. Each of the pions is in a p state and the two together are in a radially symmetric state and have total orbital angular momentum $L=1$. This suggests that a rather weak nonlinear coupling warrants serious consideration as the source of the pion field.

A further test of the model is available in the form of data on the cross sections for photoproduction of pions and data on the nucleon pion scattering. However, these data involve excited states of the nucleon so they may not provide very direct information.

Interesting discussions of these matters with his colleagues, Professors J. M. Luttinger and J. L. Powell, have contributed much to the author's understanding of the subject.

APPENDIX I

Analysis of the Field in Spherical Waves

We use, as a basis for discussion, the Pauli-Weisskopf theory of a charged plus a neutral field.[4] If $\psi_0(\mathbf{r})$, $\pi_0(\mathbf{r})$ are the (real) field variables of the neutral field and $\psi(\mathbf{r})$, $\pi(\mathbf{r})$ those of the charged field, the field Hamiltonian in the absence of the nucleore is taken to be

$$\begin{aligned}H_0=\int d^3r\{&\tfrac{1}{2}[\pi_0^2+c^2(\mathrm{grad}\psi_0)^2+c^2\mu_0^2\psi_0^2]+\pi^*\pi\\&+c^2(\mathrm{grad}\psi^*\cdot\mathrm{grad}\psi)+c^2\mu^2\psi^*\psi\},\end{aligned}$$

where $\hbar\mu_0/c$ and $\hbar\mu/c$ are the masses of neutral and charged pions, respectively. The momentum density of the field is

$$\begin{aligned}\mathbf{G}=-\tfrac{1}{2}&[\pi_0\,\mathrm{grad}\psi_0+(\mathrm{grad}\psi_0)\pi_0]\\&-[\pi\,\mathrm{grad}\psi+(\mathrm{grad}\psi^*)\pi^*].\end{aligned}\tag{A1}$$

The field commutation relations are

$$[\pi_0(\mathbf{r}),\psi_0(\mathbf{r}')]=[\pi(\mathbf{r}),\psi(\mathbf{r}')]=(\hbar/i)\delta(\mathbf{r}-\mathbf{r}'),$$

and all other pairs commute.

The functions ψ_0, π_0, ψ, π are expanded in terms of the spherical solutions ϕ_s of the equation

$$\nabla^2\phi_s+k^2\phi_s=0.$$

These solutions take the form

$$\phi_s=f_l(kr)Y_l^m,\quad s\equiv(k,l,m),$$

where the Y_l^m are spherical harmonics and $f_l(kr)$ are the spherical Bessel functions which are regular at the origin. The ϕ_s are assumed to vanish on the surface of a sphere of very large radius, a condition which leads to discrete values for k, and the $f_l(kr)$ are taken to be normalized within this volume. The definition of the Y_l^m is such that[6]

$$Y_l^{m*}=(-1)^mY_l^{-m}.\tag{A2}$$

The field operators are expanded in terms of the ϕ_s as

$$\begin{aligned}\psi_0=\textstyle\sum_s q_s\phi_s,\quad \pi_0=\sum_s p_s\phi_{-s},\\ \psi=\textstyle\sum_s Q_s\phi_s,\quad \pi=\sum_s P_s\phi_{-s},\end{aligned}\tag{A3}$$

where the notation $-s\equiv(k,l,-m)$ has been used. Then

the nonvanishing commutators of the operators q_s, p_s, Q_s, P_s are

$$[p_s, q_{s'}]=[P_s, Q_{s'}]=(-1)^m(\hbar/i)\delta_{ss'}.$$

The reality conditions on ψ_0 and π_0 become

$$q_s^*=(-1)^m q_{-s}, \quad p_s^*=(-1)^m p_{-s}.$$

The Hamiltonian H_0 is now

$$H_0=\sum_s \{\tfrac{1}{2}(p_s^* p_s+\omega_0^2 q_s^* q_s)+P_s^* P_s+\omega^2 Q_s^* Q_s\},$$

where

$$\omega_0^2=c^2(k^2+\mu_0^2), \quad \omega^2=c^2(k^2+\mu^2).$$

Diagonalization of H_0 is accomplished in the usual way by the introduction of the creation and annihilation operators, c_s^*, c_s for neutral, a_s^*, a_s for positive and b_s^*, b_s for negative pions:

$$\begin{aligned} q_s&=(\hbar/2\omega_0)^{\frac{1}{2}}(c_s+(-1)^m c_{-s}^*),\\ p_s&=i(\hbar\omega_0/2)^{\frac{1}{2}}((-1)^m c_s^*-c_{-s}),\\ Q_s&=(\hbar/2\omega)^{\frac{1}{2}}(a_s+(-1)^m b_{-s}^*),\\ P_s&=i(\hbar\omega/2)^{\frac{1}{2}}((-1)^m a_s^*-b_{-s}). \end{aligned} \tag{A4}$$

The energy is, of course, given by

$$H_0=\sum_s[N_s^0\hbar\omega_0+(N_s^+ +N_s^-)\hbar\omega],$$

where N_s^γ is the number of pions of charge γ in state s if the zero-point energy is ignored.

The angular momentum (in units of $\hbar$) of the pion field is $\mathbf{M}=\hbar^{-1}\int \mathbf{r}\times\mathbf{G}d^3r$, where $\mathbf{G}$ is the momentum density, Eq. (A1). Thus

$$\mathbf{M}=(i\hbar)^{-1}\int\{\tfrac{1}{2}[\pi_0\mathbf{L}\psi_0+(\mathbf{L}\psi_0)\pi_0]+\pi\mathbf{L}\psi+(\mathbf{L}\psi^*)\pi^*\}d^3r,$$

where $\mathbf{L}=-i\mathbf{r}\times\text{grad}$ is the usual one-particle orbital angular momentum operator. When $\mathbf{M}$ is expressed in terms of the p_s, q_s, P_s, Q_s, the coefficients are just the matrix elements

$$(l, m|\mathbf{L}|l, m')=\int Y_l^{m*}\mathbf{L}Y_l^{m'}d\Omega,$$

which have, via Eq. (A2), the important property

$$(l, -m'|\mathbf{L}|l, -m)=-(-1)^{m+m'}(l, m|\mathbf{L}|l, m'). \tag{A5}$$

By making use of this property the angular momentum can be expressed in terms of the creation and annihilation operators as

$$\begin{aligned}\mathbf{M}=&\sum_{s,s'}\delta_{kk'}\delta_{ll'}(l, m|\mathbf{L}|l, m')\\ &\times(a_s^* a_{s'}+b_s^* b_{s'}+c_s^* c_{s'}).\end{aligned} \tag{A6}$$

It is clear that M_z is diagonal (if z is the axis of quantization of the Y_l^m) and has the characteristic values

$$M_z=\sum_s m(N_s^0+N_s^+ +N_s^-).$$

Thus N_s^γ is the number of charge γ-pions with z component of angular momentum m. Since the magnetic quantum number of each pion is specified, it is clear that the total angular momentum of the pion system cannot be diagonal. However, the special state of one pion, $N_s=0$, $s\neq\sigma$, and $N_\sigma=1$, where $\sigma\equiv(\kappa, \lambda, \mu)$ is easily shown to be a characteristic state of the operator $\mathbf{M}^2$ with characteristic value $\lambda(\lambda+1)$.

In order to determine the magnetic moment, we consider the change in energy of the nucleon produced by the introduction of a weak, uniform magnetic field $\mathbf{H}$. Care must be taken to include the interaction of the pion field with the nucleore in the discussion since for a pseudoscalar field an external field may induce pion emission. For this purpose we make the assumption that the pion-nucleore interaction is a point interaction of the form $\int H'\{\psi_0, \psi\}\delta(\mathbf{r})d^3r$, if the origin is taken to be at the nucleore. Then the introduction of an external field characterized by vector potential $\mathbf{A}(\mathbf{r})$ leads to a pion plus nucleore Hamiltonian of the form

$$\begin{aligned} H=\int d^3r\{&\tfrac{1}{2}[\pi_0^2+c^2(\text{grad}\psi_0)^2+c^2\mu_0^2\psi_0^2]+\pi^*\pi\\ &+c^2([\text{grad}+(ie/\hbar c)\mathbf{A}(\mathbf{r})]\psi^*\\ &\cdot[\text{grad}-(ie/\hbar c)\mathbf{A}(\mathbf{r})]\psi\\ &+c^2\mu^2\psi^*\psi+H'\{\mathbf{A}, \psi_0, \psi\}\delta(\mathbf{r})\}, \end{aligned} \tag{A7}$$

where $H'\{\mathbf{A}, \psi_0, \psi\}$ includes any modification of the interaction produced by $\mathbf{A}$. Only the linear terms in $\mathbf{A}$ of Eq. (A7) are of interest for our purpose and these are

$$\begin{aligned} H_1=\int d^3r\{&(iec/\hbar)[\psi^*(\mathbf{A}\cdot\text{grad}\psi)-(\text{grad}\psi^*\cdot\mathbf{A})\psi]\\ &+(\mathbf{A}(\mathbf{r})\cdot\mathbf{h}'\{\psi_0, \psi\})\delta(\mathbf{r})\}, \end{aligned} \tag{A8}$$

if $\mathbf{h}'$ is a vector which provides the coefficients of the linear term in $\mathbf{A}$ when $H'\{\mathbf{A}, \psi_0, \psi\}$ is expanded in powers of $\mathbf{A}$. For the uniform field, $A=-\frac{1}{2}\mathbf{r}\times\mathbf{H}$ so the pion-nucleore interaction term in Eq. (A8) makes no contribution to the magnetic moment in consequence of our assumption of a point interaction. The pion magnetic moment operator, $\mathfrak{M}_0$, is obtained by setting $H_1=-(\mathfrak{M}_0\cdot\mathbf{H})$ for the uniform field. Hence

$$\mathfrak{M}_0=(ec/2\hbar)\int d^3r\{\psi^*\mathbf{L}\psi-(\mathbf{L}\psi^*)\psi\}.$$

Substitution for $\psi(\mathbf{r})$ in terms of a_s, b_s, etc., by means of Eqs. (A3) and (A4) leads, after application of Eq. (A5), to the result Eq. (18).

APPENDIX 2

Space and Time Inversion Properties of the Functional

An amusing feature of the spherical wave expansion is the simple formulation it provides for the space-inversion transformation. The inversion is to be accom-

plished by means of a unitary transformation U_i of the field variables, and U_i satisfies the conditions

$$U_i\psi(\mathbf{r})U_i^{-1}=\psi(-\mathbf{r}), \quad U_i\pi(\mathbf{r})U_i^{-1}=\pi(-\mathbf{r}),$$

etc., which are easily seen, on the basis of Eqs. (A3) and (A4) and the fact that the field functions have an intrinsic odd parity, to be equivalent to

$$U_i a_s U_i^{-1}=(-1)^{l+1}a_s, \tag{A9}$$

and similar equations for the operators b_s and c_s. A transformation U satisfying the condition Eq. (A9) is

$$U_i(a)=\exp\{i\pi\textstyle\sum_s(l+1)a_s^*a_s\},$$

as can be established by means of the commutation relations for the operators a_s and a_s^*. The complete U_i is to be obtained by supplementing $U_i(a)$ with corresponding factors $U_i(b)$ and $U_i(c)$. The associated transformation of the wave functional $\Psi\{N_s{}^\gamma\}$ for a characteristic state associated with the integers $N_s{}^\gamma$, is

$$\Psi'\{N_s{}^\gamma\}=U_i\Psi\{N_s{}^\gamma\}=(-1)^{\Sigma_{s,\gamma}(l+1)N_s{}^\gamma}\Psi\{N_s{}^\gamma\},$$

which agrees with the parity assignment of Eq. (3).

It is also of interest to construct the time reversal transformation for the pion field. We consider time reversal in Wigner's sense[7] so the operation on the functional is expected to be of the form

$$K=UK_0,$$

where K_0 means simple complex conjugation and U is a unitary transformation. The form of U can be determined from the condition that the angular momentum must change sign on time reversal:

$$K\mathbf{M}K^{-1}=-\mathbf{M}. \tag{A10}$$

When this transformation is applied to Eq. (A6), it is to be noted that the creation and annihilation operators a_s, a_s^*, etc., are taken to have real matrix elements so they are not affected by K_0. Then if use is made of Eq. (A5), we find that the condition Eq. (A10) is equivalent to

$$U(a_{-s}{}^*a_{-s'}+b_{-s}{}^*b_{-s'}+c_{-s}{}^*c_{-s'})U^{-1}=(-1)^{m+m'}(a_s^*a_{s'}+b_s^*b_{s'}+c_s^*c_{s'}),$$

so a sufficient condition on U is

$$Ua_sU^{-1}=(-1)^m a_{-s}, \text{ etc.} \tag{A11}$$

It is to be noted that this condition is sufficient to establish the change in sign of the magnetic moment $\mathfrak{M}_0$ (Eq. (18)) under time reversal, as is required. Furthermore, it is evident that the energy and total charge are invariant under the transformation.

A transformation which accomplishes our purpose is

$$U=U_aU_bU_c,$$

if

$$U_a=\exp\{-\tfrac{1}{2}i\pi\textstyle\sum_s(2|m|+1)a_s^*a_{-s}\}\times\exp\{\tfrac{1}{2}i\pi\textstyle\sum_s a_s^*a_s\}, \tag{A12}$$

and U_b, U_c are given by similar expressions in b_s and c_s, respectively. That (A12) satisfies Eq. (A11) can easily be established by means of the commutation relations for the a_s, a_s^*.

It must now be established that our transformation yields Eq. (16). For the sake of simplicity we consider a wave functional Φ_a of just the positive pions (no nucleore), and we will temporarily drop the superscript on $N_s{}^+$ for the sake of the printer. The action of the annihilation operator a_s on the state $\Phi_a{}^{(0)}$ of no pions is to produce 0, so

$$U_a\Phi_a{}^{(0)}=\Phi_a{}^{(0)}. \tag{A13}$$

Now we wish to show by induction that

$$U_a\Phi_a\{N_s\}=(-1)^{\Sigma_s mN_s}\Phi_a\{N_{-s}\}, \tag{A14}$$

where the change of sign $N_s\rightarrow N_{-s}$ is meant to indicate that the number of pions with quantum number m in the one state is equal to the number with quantum number $(-m)$ in the other state. If Eq. (A14) is valid for N pions, we can show that it is valid for the state $\Phi_a\{N_s'\}$ of $N+1$ pions. Here $N_s'=N_s$ except for $s=\sigma\equiv(\kappa,\lambda,\mu)$ and $N_\sigma'=N_\sigma+1$. The proof is as follows: We have

$$\Phi_a\{N_s'\}=(N_\sigma+1)^{-\frac{1}{2}}a_\sigma{}^*\Phi_a\{N_s\},$$

whence

$$U_a\Phi_a\{N_s'\}=(N_\sigma+1)^{-\frac{1}{2}}U_aa_\sigma{}^*U_a{}^{-1}U_a\Phi_a\{N_s\}=(N_\sigma+1)^{-\frac{1}{2}}(-1)^\mu(-1)^{\Sigma_s mN_s}a_{-\sigma}{}^*\Phi_a\{N_{-s}\},$$

according to Eqs. (A11) and (A14). But $a_{-\sigma}{}^*\Phi_a\{N_{-s}\}=(N_\sigma+1)^{\frac{1}{2}}\Phi_a\{N_{-s}'\}$, so

$$U_a\Phi_a\{N_s'\}=(-1)^{\Sigma_s mN_s'}\Phi_a\{N_{-s}'\}.$$

Since Eq. (A13) shows that Eq. (A14) is valid for $N=0$, it is valid for all N. The generalization to include negative and neutral pions is evident.

The magnetic quantum number of the pions is $M_L=\sum_{s,\gamma}mN_s{}^\gamma$, and hence for a pion functional $\Phi_L{}^{ML}$ of a fixed number of pions with total orbital angular momentum L

$$U\Phi_L{}^{ML}=i^{2ML}\Phi_L{}^{-ML}.$$

Our representation is such that the functionals Φ are the basic vectors, so they are real functions of the numbers $mN_s{}^\gamma$ and are therefore not affected by the operation K_0. Thus

$$K\Phi_L{}^{ML}=i^{2ML}\Phi_L{}^{-ML},$$

in accord with Eq. (16).

Interaction Moment Contributions to Magnetic Moments of Nuclei*,†

ARNOLD RUSSEK AND LARRY SPRUCH
New York University, Washington Square, New York, New York
(Received April 14, 1952)

A model of a heavy odd A nucleus is used in which the outer nucleon is in the state predicted by the Mayer scheme, and the core is in a state of zero angular momentum. It is found that the general trend of the deviations of the experimentally determined magnetic moments from the Schmidt curves is describable in terms of a linear combination of the three phenomenological interaction moment operators which can arise from a charge exchange potential in a second order meson calculation. The final expression for the interaction moment, matched to the data, is, by and large, independent of any detailed properties of the radial functions associated with these operators, of the radial function of the outer nucleon, and, except for a dependence on the relative number of neutrons and protons in the core, of the core structure. The consequent predictions that, for given l and j, the interaction moments of heavy odd neutron nuclei should be smaller in magnitude than those of heavy odd proton nuclei and that the addition of two protons to an odd proton nucleus or of two neutrons to an odd neutron nucleus should push the moments toward the Schmidt curves are in general accord with the data. Odd-odd nuclei are also considered.

I. INTRODUCTION

THE independent particle model of the nucleus advanced by Mayer[1] and by Haxel, Jensen, and Suess[2] has been extremely useful in correlating large bodies of data. In particular, the experimental values of the total angular momentum J of odd A nuclei are in definite disagreement with the strict one-particle interpretation of this model in only three cases, and the magnetic moments of almost all nuclei lie reasonably close to the Schmidt values predicted by this model. The deviations from the Schmidt values are not random; with the exception of a few very light nuclei, the experimental values lie between the Schmidt curves.

Attempts have been made to explain these deviations by modifying the model,[3] and by dropping the strict one-particle interpretation to allow for cases in which three or more particles outside of closed shells are effective in determining the spin and magnetic moment of the nucleus.[4] Other attempts have been made using the strict one-particle interpretation and modifying the magnetic moment operator instead. If the cases in which the spin predictions of the one-particle interpretation are at variance with the experimental values are excluded, it is of interest to see how closely the data can be matched on the basis of such an approach.

Siegert[5] pointed out that charge exchange forces imply the existence of currents which must modify the magnetic moment operator. While meson theoretical calculations to determine this interaction moment operator[6] suffer from the usual difficulties, it is significant that Villars[7] was able to show that the H^3-He^3 anomaly could be explained using pseudoscalar meson theory. Sachs,[8] however, showed that the longitudinal part of this interaction moment could be expressed in terms of the space exchange potential, the result being independent of meson theory. The longitudinal moment was thus given a firm basis, but calculations carried out by Sachs for H^3 and by Spruch[9] for a number of light nuclei showed that this operator alone could not account for the deviations from the Schmidt values.

Bloch and de Shalit independently pointed out[10] that the data could be qualitatively understood by assuming that the anomalous magnetic moment of the odd nucleon is quenched somewhat in the presence of other nucleons. This quenching could also be considered as an interaction contribution.[11]

Miyazawa[11] carried through the calculation of the interaction moment contribution for heavy nuclei, the core of the nucleus being approximated by a Fermi gas. The longitudinal part of the moment was treated phenomenologically, while the rest was calculated meson-theoretically. Miyazawa was able to match the general trend of the deviations by a small but arbitrary readjustment of the numerical constants in his final expression.

It is possible to proceed entirely phenomenologically. Thus, by invariance and symmetry considerations, Osborn and Foldy[12] derived the most general operators which can arise from a charge exchange potential; other than for the longitudinal operator, however, these can

* Reported at the Washington Meeting of the American Physical Society, 1952.

† Submitted by one of the authors (A.R.) in partial fulfillment of the requirements for the degree of Doctor of Philosophy at New York University.

[1] M. G. Mayer, Phys. Rev. **78**, 16 (1950).

[2] Haxel, Jensen, and Suess, Phys. Rev. **75**, 1766 (1949).

[3] J. Rainwater, Phys. Rev. **79**, 432 (1950); L. L. Foldy and E. J. Milford, Phys. Rev. **80**, 751 (1950); Y. A. Romanov, J. Exptl. Theor. Phys. (U.S.S.R.) **20**, 577 (1950); A. Bohr, Phys. Rev. **81**, 134 (1951); S. Gallone and G. Salveti, Phys. Rev. **84**, 1064 (1951); J. P. Davison, Phys. Rev. **85**, 432 (1952).

[4] M. Mizushima and M. Umezawa, Phys. Rev. **85**, 37 (1952).

[5] A. F. Siegert, Phys. Rev. **52**, 787 (1937).

[6] S. T. Ma and C. F. Yu, Phys. Rev. **62**, 118 (1942); C. Møller and L. Rosenfeld, Kgl. Danske Videnskab. Selskab. Math.-fys. Medd. **20**, No. 12 (1943); W. Pauli and S. Kusaka, Phys. Rev. **63**, 400 (1943).

[7] F. Villars, Helv. Phys. Acta **20**, 476 (1947).

[8] R. G. Sachs, Phys. Rev. **74**, 433 (1948).

[9] L. Spruch, Phys. Rev. **80**, 372 (1950).

[10] F. Bloch, Phys. Rev. **83**, 839 (1951); A. de Shalit, Helv. Phys. Acta **24**, 296 (1951).

[11] H. Miyazawa, Prog. Theoret. Phys. **6**, 801 (1951).

[12] R. K. Osborn and L. Foldy, Phys. Rev. **79**, 795 (1950).

be determined only to within arbitrary functions of the interparticle distances. Under the requirement that these operators behave properly under time reversal[13] and with the arbitrary restriction that they can arise from a second-order meson calculation, only three operators remain.

An investigation has been undertaken to determine the contributions of these three operators and to seek a combination which leads to agreement with the data. The calculation differs from that of Miyazawa in that it is completely phenomenological and in that the shell model is used to represent the core rather than a Fermi gas. The Fermi gas approach as used by Miyazawa has the mathematical advantage that the interaction contributions are independent of any details of the core of the particular nucleus under consideration. The shell model has the physical advantage that it is a closer representation of the actual situation and should give a more faithful picture of the trends and of the details of the variations from the Schmidt lines. Further, since the interaction contributions do depend upon some of the details of the core, calculations based on the shell model should ultimately be useful in the analysis of the details of the shell model, e.g., the order in which the shells fill and whether or not nucleons of high angular momentum "hide."[1]

The operators $\mathbf{M}_\alpha$ are encountered in the calculation of isomeric half-lives[14] and radiative capture and photomagnetic disintegration cross sections,[15,16] as well as magnetic moments. These other effects have not been considered.

II. MATRIX ELEMENTS

Only those interaction moment operators are considered which can arise from a charge exchange potential, in a second-order meson theory. In particular, operators which can arise from velocity dependent forces or from many-body forces are not considered. There are three operators listed in Osborn and Foldy[17] which satisfy the above conditions and which behave properly under time reversal. After the isotopic spin dependence has been removed and use has been made of the operator identity $\boldsymbol{\sigma}_\tau \times \boldsymbol{\sigma}_\nu Q_{\tau\nu} = i(\boldsymbol{\sigma}_\tau - \boldsymbol{\sigma}_\nu)$, these operators can be written in the form[18]

$$\begin{aligned}
\mathbf{M}_1 &= \mathbf{M}_{\text{long}} = (ie/2\hbar c)\textstyle\sum_\nu \sum_\tau \mathbf{r}_\tau \times \mathbf{r}_\nu V(\mathbf{r}_{\tau\nu}, \boldsymbol{\sigma}_\tau, \boldsymbol{\sigma}_\nu) P_{\tau\nu}, \\
\mathbf{M}_2 &= (e/2\hbar c)\textstyle\sum_\nu \sum_\tau r_{\tau\nu}^2 f_2(r_{\tau\nu})(\boldsymbol{\sigma}_\tau - \boldsymbol{\sigma}_\nu) P_{\tau\nu}, \\
\mathbf{M}_3 &= (e/2\hbar c)\textstyle\sum_\nu \sum_\tau f_3(r_{\tau\nu})(\mathbf{r}_{\tau\nu} \cdot (\boldsymbol{\sigma}_\tau - \boldsymbol{\sigma}_\nu))\mathbf{r}_{\tau\nu} P_{\tau\nu},
\end{aligned} \tag{1}$$

where $V(\mathbf{r}_{\tau\nu}, \boldsymbol{\sigma}_\tau, \boldsymbol{\sigma}_\nu)P_{\tau\nu}$ represents the charge exchange potential and $f_2(r_{\tau\nu})$ and $f_3(r_{\tau\nu})$ are undetermined functions of the interparticle distances, which are expected, however, to have ranges comparable with the range of nuclear forces. $P_{\tau\nu}$ and $Q_{\tau\nu}$ are the space and spin interchange operators, and it is understood that the operators (1) are to act on wave functions which have been antisymmetrized separately in neutrons and protons.

It will specifically be assumed throughout the article that

(a) an odd A nucleus consists of an odd nucleon in the state with radial, orbital angular momentum, and total angular momentum quantum numbers n, l, and j, respectively, and a core of zero total angular momentum.[19]

The contribution of the outer particle then gives the Schmidt values and the interaction magnetic moment [i.e., the sum of the expectation values of the operators (1)] is found to arise only from the interaction of the outer particle with the core. It also follows that antisymmetrization between the outer particle and the core is unnecessary, although the core wave function Φ must still be antisymmetrized in neutrons and protons separately. For the sake of notational convenience in what follows, the outer particle is taken to be a proton and is designated by the subscript π^0. The protons and neutrons in the core are designated by π' and ν', respectively.

The potential function $V(\mathbf{r}_{\pi^0\nu'}, \boldsymbol{\sigma}_{\pi^0}, \boldsymbol{\sigma}_{\nu'})$ is given as the sum of a function $f_1(r_{\pi^0\nu'})$ plus a term in $\boldsymbol{\sigma}_{\pi^0} \cdot \boldsymbol{\sigma}_{\nu'}$ plus a tensor term. If, in addition to the assumption (a) that the core has total angular momentum zero, the further assumption is made that

(b) the spin of the neutrons in the core is zero and/or the total spin of the core is zero,

then the contributions to $\mathbf{M}_1$ of the $\boldsymbol{\sigma}_{\pi^0} \cdot \boldsymbol{\sigma}_{\nu'}$ term and of the tensor term vanish and only the first term contributes. It is then found (see Appendix) that

$$\langle M_1^z \rangle = b\langle l_{\pi^0}^z \rangle I_1(n, l), \tag{2}$$

where the various quantities will be defined shortly.

Under the same assumptions (a) and (b), the contribution of $\mathbf{M}_2$ is given by

$$\langle M_2^z \rangle = -b\langle \sigma_{\pi^0}^z \rangle K_2(n, l). \tag{3}$$

If, in addition to (a) and (b), the further assumption is made that

(c) the orbital angular momentum of the neutrons in the core is zero,

then it is found, setting $j_z = j$, that

$$\langle M_3^z \rangle = -b(2j_{\pi^0}+2)^{-1}[K_3(n, l) + 2\langle \boldsymbol{\sigma}_{\pi^0} \cdot \mathbf{l}_{\pi^0} \rangle I_3(n, l)]. \tag{4}$$

[13] G. J. Kynch, Phys. Rev. **81**, 1060 (1951).
[14] R. G. Sachs and M. Ross, Phys. Rev. **84**, 379 (1951).
[15] N. Austern and R. G. Sachs, Phys. Rev. **81**, 710 (1951).
[16] N. Austern, Phys. Rev. **83**, 672 (1951).
[17] See reference 12. The longitudinal moment operator, sometimes called the space exchange operator, derived there has the wrong sign.
[18] There are certain formal advantages to using a linear combination of these as the basic operators. See the Appendix.
[19] The statement that the core has a certain angular momentum equal to zero will always mean that the core is in an eigenstate of that particularly angular momentum operator with eigenvalue zero, and not merely that the expectation value of that angular momentum operator is zero.

All magnetic moments are given in nuclear Bohr magnetons, $b=J_0a_1^2M/\hbar^2$, D_1J_0 and a_1 are the effective strength and range of the space exchange part of the nuclear potential, and M is the proton mass. D_1 gives the fraction of the total potential which is of the space exchange type. $\langle l_{\tau^0}{}^z\rangle$ and $\langle\sigma_{\tau^0}{}^z\rangle$ refer to the odd proton state. The factors $I_\alpha(n,l)$ and $K_\alpha(n,l)$, where $\alpha=1,2,3$, are given by the integrals

$$I_\alpha(n,l)=\sum_{\tau'}\int d\tau F_\alpha(n,l)U(\mathbf{r}_{\tau^0},\mathbf{r}_{\tau'}),$$
$$K_\alpha(n,l)=\sum_{\tau'}\int d\tau F_\alpha(n,l)W(\mathbf{r}_{\tau^0},\mathbf{r}_{\tau'}), \tag{5a}$$

where

$$F_\alpha(n,l)=f_\alpha(r_{\tau^0\tau'})R_{nl}(r_{\tau^0})R_{nl}(r_{\tau'})(\Phi,P_{\tau^0\tau'}\Phi),$$
$$U(\mathbf{r}_{\tau^0},\mathbf{r}_{\tau'})=(-4\pi l(l+1)a_1{}^2J_0)^{-1}r_{\tau^0\tau'}(1-\mu^2)P_{l'}(\mu),$$
$$W(\mathbf{r}_{\tau^0},\mathbf{r}_{\tau'})=(-4\pi a_1{}^2J_0)^{-1}r_{\tau^0\tau'}{}^2P_l(\mu). \tag{5b}$$

Here, $\sum_{\tau'}$ is extended over all neutrons in the core and integration is indicated over the coordinates of all nucleons. The inner product symbol refers only to the core spin coordinates, $\mu=\cos\theta_{\tau^0\tau'}$, P_l and P_l' are the ordinary Legendre polynomial of order l and its derivative with respect to the argument, respectively, and R_{nl} is the normalized radial function associated with the odd proton wave function. The presence of the factor $1/a_1{}^2J_0$ in the integrals is purely formal; it appears also in the definition of b and was introduced to make the integrals dimensionless. The radial function f_1 is that associated with the space exchange part of the nuclear potential V.

With the restriction noted above as to the operators to be considered, and under the assumptions (*a*), (*b*), and (*c*)

$$\langle M_{\text{int}}{}^z\rangle=\sum_{\alpha=1}^{3}\langle M_\alpha{}^z\rangle=b\{\langle l_{\tau^0}{}^z\rangle I_1(n,l)-\langle\sigma_{\tau^0}{}^z\rangle K_2(n,l)$$
$$-(2j_{\tau^0}+2)^{-1}[K_2(n,l)+2\langle\boldsymbol{\sigma}_{\tau^0}\cdot\mathbf{l}_{\tau^0}\rangle I_3(n,l)]\}. \tag{6}$$

III. SHELL MODEL CALCULATIONS

According to the shell model, the core of a heavy nucleus consists mainly of complete orbital angular momentum shells plus or minus a few nucleons. With the wave function for the core obtained on the basis of the shell model, the interaction moment breaks up into the sum of contributions due to each neutron shell interacting separately with the outer proton, and for each of these shells, all of the assumptions made in the previous section are valid. The contribution to the moment of the complete orbital angular momentum shells is therefore given by (6), where the integrals now reduce to

$$I_\alpha(n,l)=(1/4\pi)\sum_{n'l'}N(n',l')\int d\tau_1\int d\tau_2\bar{F}_\alpha U(\mathbf{r}_1,\mathbf{r}_2),$$
$$K_\alpha(n,l)=(1/4\pi)\sum_{n'l'}N(n',l')\int d\tau_1\int d\tau_2\bar{F}_\alpha W(\mathbf{r}_1,\mathbf{r}_2), \tag{7}$$

where

$$\bar{F}_\alpha=f_\alpha(r_{12})R_{nl}(r_1)R_{nl}(r_2)R_{n'l'}(r_1)R_{n'l'}(r_2)P_{l'}(\mu)$$

and where $N(n',l')$ represents the number of neutrons in the $n'l'$ shell, namely, $2(2l'+1)$. Equation (6) is not applicable to any incomplete shells, for while these have a total angular momentum of zero, assumptions (*b*) and (*c*) are not satisfied. However, estimates made indicate that the use of Eqs. (6) and (7) with $N(n',l')$ taken to be the number of neutrons actually present in the incomplete shell is sufficiently accurate for the determination of the contribution of the incomplete shell, especially when it is considered that this is only a small part of the total contribution.

In order to obtain numerical results, it remains only to assume particular radial functions for the f_α, R_{nl}, and $R_{n'l'}$. The range and maximum depth of f_1, the radial function associated with the space exchange part of the exchange potential, are known with reasonable accuracy. For convenience of integration,[9] it is here approximated by a Gaussian well. The range is taken to be 1.5×10^{-13} cm. f_2 and f_3 are also assumed to be Gaussian wells of the same range, so that the three radial functions differ only in their respective strengths which are taken to be in the ratios $D_1:D_2:D_3$. Thus

$$f_\alpha(r_{\tau\tau'})=-D_\alpha J_0\exp(-r_{\tau\tau'}{}^2/a_1{}^2), \tag{8}$$

where J_0 is taken to be 55 Mev and D_1, which is certainly positive, must be of the order of unity if the neutron-proton potential is assumed to be primarily space exchange in nature. D_2 and D_3 may be positive or negative but are expected to be roughly of the same order of magnitude as D_1. The radial wave functions are chosen to be oscillator functions, also for convenience of integration.[9]

Subject to these assumptions, $K_\alpha(n,l)$ and $I_\alpha(n,l)$ are found to be roughly independent of n, l, and A. For heavy odd proton nuclei,

$$K_\alpha\approx0.25D_\alpha,\quad I_\alpha\approx0.10D_\alpha,\quad K_\alpha/I_\alpha\approx2.5, \tag{9}$$

where the ratio K_α/I_α is much more reliable than the values of either of the two integrals separately. With the values taken for a_1 and J_0, $b=3.0$ and the interaction moment contributions for odd proton nuclei are given by

$$\langle M_{\text{int}}(\text{odd }Z)\rangle=0.3\{D_1\langle l_{\tau^0}{}^z\rangle-2.5D_2\langle\sigma_{\tau^0}{}^z\rangle$$
$$-D_3(2j_{\tau^0}+2)^{-1}[2.5+2\langle\boldsymbol{\sigma}_{\tau^0}\cdot\mathbf{l}_{\tau^0}\rangle]\}. \tag{10}$$

For odd neutron nuclei the magnitudes of the integrals are somewhat diminished (owing to the preponderance

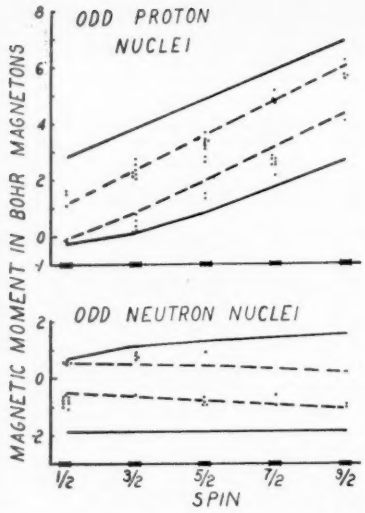

FIG. 1. The solid lines are the Schmidt curves for the magnetic moment in nuclear Bohr magnetons; the broken lines are the corrected curves taking into consideration interaction moments. The dots represent the experimental values for the magnetic moments of nuclei with A greater than 30.

of neutrons in heavy nuclei), although the ratio of the two integrals remains essentially unchanged, and

$$\langle M_{\text{int}}(\text{odd } N)\rangle = -0.25\{D_1\langle l_{s^0}{}^z\rangle - 2.5D_2\langle\sigma_{s^0}{}^z\rangle - D_3(2j_{s^0}+2)^{-1}[2.5+2\langle\boldsymbol{\sigma}_{s^0}\cdot\mathbf{l}_{s^0}\rangle]\}. \quad (11)$$

The minus sign is a consequence of the antisymmetry of the operators (1) in neutrons and protons. The multiplicative constant 0.25 is not expected to be accurate to two decimal places but merely indicates that the magnitude of the interaction moment of a heavy odd neutron nucleus has been found to be somewhat smaller than that of a corresponding odd proton nucleus.

The expressions (10) and (11) differ from the corresponding expressions of Miyazawa in two respects. Firstly, since he assumed the same density for neutrons as for protons, his expression for odd Z and odd N nuclei differs in sign but not in magnitude. Secondly, his expression is slightly different from the expression contained within the curly brackets of Eqs. (10) and (11). Since the nuclear model used here is the more realistic one, the results obtained here are probably somewhat better.

Reasonable agreement with the data is obtained with $D_1=0.4$, $D_2=4.6$, and $D_3=-7.0$. It is to be noted that D_1, which is a measure of the fraction of the potential which is of an exchange nature, lies between 0 and 1, as is to be expected. While the above values are not very precisely determined, it would be difficult to match the data with D_1 outside of the range 0 to 0.8, but because of the uncertainties in the numerical values of the I_a and of the K_a, and because of the scatter of the experimental data, the value of D_1 cannot be very much more restricted. The interaction moments are plotted with the above values of the D_a as corrections to the Schmidt curves in Fig. 1.

IV. MORE DETAILED BEHAVIOR OF THE INTERACTION MOMENTS

It was found, in the previous section, that the interaction moments of odd neutron nuclei are less than the interaction moments of odd proton nuclei of comparable A and with the same l and j. This prediction that odd neutron nuclei should deviate less from the Schmidt curves than do odd proton nuclei is in general agreement with the data.

In the analysis of the general trend of the deviations, it was found that the $I_a(n, l)$ and the $K_a(n, l)$ are roughly independent of A. This is due to the compensation of two effects; as one goes to heavier nuclei, the number of interactions is increased but the average interaction moment per pair is decreased. The decrease will be referred to as a size effect. However, on the addition of two nucleons of the odd type, i.e., two protons to an odd proton nucleus or two neutrons to an odd neutron nucleus, provided that there is no change in l or j, there is only a size effect, so that the magnitude of the interaction moment should decrease. Thus the addition of two nucleons of the odd type should push the moment toward the Schmidt values.[20]

Table I lists all pairs of nuclei which are in the same l and j state and which differ by two nucleons of the odd type. $\delta(\Delta M)$ is the difference in the magnitudes of the deviations from the Schmidt curves between the lighter and heavier nucleus, respectively, and is so defined as to be positive if the heavier nucleus lies closer to the Schmidt value. The decrease $\delta(\Delta M)$ in the magnitude of the interaction moment is estimated to be of the order of a few hundredths of a nuclear Bohr magneton, and if the observed shift is much greater than this, it is probably due primarily to other effects, making the above predictions invalid. As is seen in Table I, the predicted behavior is followed in nearly all known cases. As for the two exceptions, the magnitude of the difference in the moments of Nd^{143} and Nd^{145} indicates that it is due to other effects, while the Mayer level scheme requires the coupling of three or more nucleons to explain the angular momentum of Sm^{147} and Sm^{149}.

It is to be noted that the above prediction is valid even if the nuclear state is not of the pure Mayer type but involves some small admixture of other states,[21] provided that the percentage of the admixed state is not altered by the addition of the two odd type nucleons.

[20] de Shalit arrived at a similar conclusion for two nucleons of the odd or even type by an examination of the data. R. K. Wangness, Phys. Rev. **78**, 620 (1950); A. de Shalit, Phys. Rev. **80**, 103 (1950).

[21] See, e.g., J. P. Davidson, reference 3.

On the other hand, any theory which correlates some relevant nuclear property, such as the percentage of admixed states, to the nuclear size may also be able to explain the above effect.

Nothing can reliably be predicted regarding the effect of the addition of two neutrons to an odd proton nucleus or of the addition of two protons to an odd neutron nucleus, for in this case both effects, namely, the size effect and the increase in the number of interactions, are present, and it has already been seen that these two effects are in opposite directions. There is the further complication that the extra particles will not, in general, enter in such a way that the assumptions required for the applicability of Eqs. (10) and (11) to calculate the additional interaction moment are satisfied. Thus, for example, in computing the additional interaction moment, the tensor term contribution to $\langle M_1{}^z\rangle$ will not in general vanish.

It should be mentioned here that none of the effects obtained in this section depend on the values of the D_a.

V. GENERALIZATION OF THE MODEL

The results derived thus far presuppose not only the the validity of the general features of the one-particle interpretation of the shell model, but even depend upon the details of that model. Thus, a particular order of energy levels has been assumed and specific radial functions have been chosen for the nucleons within the core and for the outer nucleon. While the possibility exists that levels which are full for lighter nuclei may be empty for heavier nuclei (owing to level crossings), the fair degree of constancy of the $I_a(n, l)$ and $K_a(n, l)$ as the levels are filled indicates that the results obtained are not too dependent upon the particular order used, but the question remains as to how sensitive the results are to the specific radial functions chosen for the nucleons within the core and for the outer nucleon, and indeed to the very assumption that the core need be thought of as consisting of shells.[22]

A more serious question that must be considered is the sensitivity of the results to the assumptions made concerning the radial functions f_2 and f_3 about which nothing is known *a priori* other than that their ranges must be comparable with that of f_1.

It will be assumed, in what follows, that most of the nucleons in the core are in a state in which the spin angular momenta and orbital angular momenta of the neutrons and protons separately are all equal to zero. It will also be assumed that the particle density is roughly uniform throughout the core. (Both of these assumptions are, for heavy nuclei, certainly satisfied by the shell model.) Finally, it will be assumed that the ranges a_a of the functions f_a are small compared to the dimensions of the nucleus under consideration. Very light nuclei are thus specifically excluded.

It follows from the last assumption that the only appreciable contributions to the integrals $I_a(n, l)$ and $K_a(n, l)$ come from the regions in which $\mathbf{r}_{\pi^0}\approx\mathbf{r}_{\nu^0}$. Under these conditions,

$$r_{\pi^0}r_{\nu^0}(1-\mu^2)\approx r_{\pi^0\nu^0}{}^2\approx r_{\pi^0}{}^2\theta_{\pi^0\nu^0}{}^2. \tag{12}$$

The integrands are thus vanishingly small for $r_{\pi^0\nu^0}>a_a$, or $\theta_{\pi^0\nu^0}>a_a/r_{\pi^0}$. Taking typical values for a_a and r_{π^0} and considering the the maximum values of l found in the nucleus, it is, then, a good approximation to let

$$[l(l+1)]^{-1}P_l{}'(\mu)\approx\tfrac{1}{2}P_l(\mu). \tag{13}$$

Using Eqs. (12) and (13), it is found that $K_a(n, l)/I_a(n, l)\approx 2$. This is to be compared with the value of 2.5 obtained for this ratio in Sec. III on the basis of the shell model. Since the proton interacts with only those neutrons in a volume of radius a_a, it follows, since we can take $P_l(\mu)\approx 1$, that

$$\tfrac{1}{2}K_a(n, l)\approx I_a(n, l)\approx CD_a{}'(N/A), \tag{14}$$

where

$$D_a{}'=(1/8\pi)(a_a/a_1)^2(a_a/r_0)^3,$$

$(4/3)\pi r_0{}^3A$ is the nuclear volume, and C is a constant between 0 and 1. Equation (6) now gives

$$\begin{aligned}\langle M_{\rm int}{}^z(\text{odd } Z)\rangle&=bC(N/A)\{D_1{}'\langle l_{\pi^0}{}^z\rangle-2D_2{}'\langle\sigma_{\pi^0}{}^z\rangle\\&\quad-D_3{}'(2j_{\pi^0}+2)^{-1}[2+2\langle\boldsymbol{\sigma}_{\pi^0}\cdot\mathbf{l}_{\pi^0}\rangle]\},\\\langle M_{\rm int}{}^z(\text{odd } N)\rangle&=-bC(Z/A)\{D_1{}'\langle l_{\pi^0}{}^z\rangle-2D_2{}'\langle\sigma_{\pi^0}{}^z\rangle\\&\quad-D_3{}'(2j_{\pi^0}+2)^{-1}[2+2\langle\boldsymbol{\sigma}_{\pi^0}\cdot\mathbf{l}_{\pi^0}\rangle]\},\end{aligned} \tag{15}$$

where the (N/A) (which is proportional to the neutron density) of the odd proton case is replaced by $(-Z/A)$ (which is proportional to the proton density) for the

TABLE I. Variations in the deviations of the magnetic moments from the Schmidt curves for nuclei of the same l and j differing by two nucleons of the odd nucleon type.

		State	$\delta(\Delta M)_{\rm exp}$
Odd Z			
	Cl^{37}		
	K^{39}	$d_{3/2}$	+0.29
	Cs^{137}		
	La^{139}	$g_{7/2}$	+0.06
Odd N			
	Mo^{95}		
	Mo^{97}	$d_{5/2}$	+0.02
	Cd^{111}		
	Cd^{113}	$s_{1/2}$	+0.02
	Sn^{115}		
	Sn^{117}	$s_{1/2}$	+0.08
	Sn^{117}		
	Sn^{119}	$s_{1/2}$	+0.05
	Te^{123}		
	Te^{125}	$s_{1/2}$	+0.15
	Ba^{135}		
	Ba^{137}	$d_{3/2}$	+0.10
	Nd^{143}		
	Nd^{145}	$f_{7/2}$	−0.38
	Sm^{147}		
	Sm^{149}	$?_{5/2}$	−0.05

$\delta(\Delta M)=|\Delta M_L|-|\Delta M_H|$ where ΔM_L and ΔM_H are the deviations from the Schmidt curves of the moments of the lighter nucleus and heavier nucleus, respectively.

[22] One of the authors (L.S.) would like to thank Dr. R. G. Sachs for a very helpful comment on the possibility of generalizing the model.

TABLE II. Magnetic moments of odd-odd nuclei. $\Delta M = M_{\text{exp}} - M_{\text{Schmidt}}$. ΔM_{calc} is the deviation from the Schmidt value calculated from the data on odd-A nuclei.

	Proton orbital	Neutron orbital	J	M_{exp}	ΔM	ΔM_{calc}
K^{40}	$d_{3/2}$	$f_{7/2}$	4	−1.29	0.39	1
K^{40}	$s_{1/2}$	$f_{7/2}$	4	−1.29	2.17	−0.5
Co^{60}	$f_{7/2}$	$p_{3/2}$	5	3.2[a]	−0.7	0.3[b]
Rb^{86}	$f_{5/2}$	$g_{9/2}$	2	−1.68	0.46	0.3

[a] C. J. Gorter *et al.*, Physica **18**, 135 (1952); B. Bleany *et al.*, Phys. Rev. **85**, 688 (1952).
[b] Gorter *et al.* quote a value of −0.37.

odd neutron case. The only differences between Eqs. (15) and the Eqs. (10) and (11) derived using the shell model is the value 2 rather than 2.5 for the ratio K_α/I_α appearing within the curly brackets and the appearance of the factors (N/A) and $(-Z/A)$. The presence of the D_α' rather than the D_α is, except for the interest in D_1, of no significance since these quantities are chosen to match the data.

It is seen from Eqs. (15), derived under fairly broad assumptions, that any small variations in the ranges and shapes of the wells cannot critically affect the results of the previous sections, since the errors introduced in assuming them to be of the same form are by and large taken into account when the coefficients are matched to the data. It is further seen that the conclusions reached in those sections, except those concerning the magnitudes of D_2 and D_3 and, to a much lesser extent, of D_1, are essentially independent of the assumption of the shell model for the core.

The conclusions of Sec. IV concerning the moments of odd neutron *vs* odd proton nuclei and concerning nuclei differing by two nucleons of the odd type are now immediate consequences of the "density factors"‡ (N/A) and (Z/A) of Eqs. (15). Taken literally, the Eqs. (15) also predict that for given l and j, the interaction moments of odd proton nuclei should increase with increasing A, while those of odd neutron nuclei should decrease with increasing A. That this last prediction does not give good agreement with the data is not surprising, for its validity requires that the I_α and K_α remain fairly constant over a wide range of A and for those cases in which the odd nucleon is in different radial quantum number states. The former predictions, however, require only the relative constancy of the I_α and K_α for small variations of A.

VI. ODD-ODD NUCLEI

For self-conjugate nuclei, the operator given in Eq. (1) will give no contribution to the magnetic moment, to the extent of the equality of neutron-neutron and proton-proton forces. There will be contributions due to operators which are symmetric in neutrons and protons but these operators arise only in higher order meson calculations, and their contributions can therefore be expected to be small. It is then satisfying that the magnetic moments of self-conjugate nuclei can all be reasonably well accounted for by the orbital and spin contributions of the individual nucleons.[23]

For odd-odd nuclei which are not too light, for which the odd proton and odd neutron are in states l_{π^0}, j_{π^0} and l_{ν^0}, j_{ν^0}, respectively, and for which the core has zero angular momentum, it is found, neglecting the contribution due to the interaction of the odd proton with the odd neutron, that[24]

$$\Delta M(l_{\pi^0}, j_{\pi^0}, l_{\nu^0}, j_{\nu^0}, j) = (\langle j_{\pi^0 z}\rangle/j_{\pi^0})\Delta M(l_{\pi^0}, j_{\pi^0}) + (\langle j_{\nu^0 z}\rangle/j_{\nu^0})\Delta M(l_{\nu^0}, j_{\nu^0}). \quad (16)$$

Here ΔM represents the difference between the experimental value and the calculated spin and orbital contributions. Thus, $\Delta M(l_{\pi^0}, j_{\pi^0})$ and $\Delta M(l_{\nu^0}, j_{\nu^0})$ can be taken from the experimental data for odd A-nuclei. (The data should, however, be weighted in favor of nuclei with comparable A.) Equation (16) is valid for any two-particle interaction moment operator; there is no restriction to the operators listed in Eq. (1).

Table II lists the experimental and calculated deviations from the Schmidt values of the measured odd-odd nuclei which are not self-conjugate. The only case in which the contributions of the odd proton and odd neutron to the calculated deviation are of the same sign is that of K^{40} with the odd proton in the $d_{\frac{3}{2}}$ state, and in this case the sign of the calculated deviation is in the right direction,[24] although the magnitude is too large. The other calculated values are therefore more questionable; in particular, ΔM of Co^{60} could be slightly negative. On the other hand, the possibility that the odd proton in K^{40} is in the $s_{\frac{1}{2}}$ state (which would eliminate the contradiction of the Nordheim spin composition rule[25]) is ruled out, for ΔM in this case cannot reasonably be taken to be greater than about zero.

VII. CONCLUSIONS

Making very few assumptions about the nature of the core of the nucleus, the radial function of the outer nucleon, or the radial functions associated with the interaction operators, it is found that the general trend of the deviations of the experimentally determined magnetic moments from the Schmidt curves is describable in terms of a linear combination of three interaction moment operators that can arise from a second order meson theoretical calculation. As is to be expected on physical grounds, the interaction moments of odd proton nuclei and of odd neutron nuclei turn out to be proportional to the neutron and proton densities, respectively. Interaction moment contributions are thus one possible explanation of the fact that the addi-

‡ *Note added in proof:*—The larger deviation of odd proton nuclei can also be explained by the assumption of a strong spin-orbit coupling term in the Hamiltonian; J. H. D. Jensen and M. G. Mayer, Phys. Rev. **85**, 1040 (1952).

[23] E. Feenberg, Phys. Rev. **76**, 1275 (1949).
[24] This result was indicated by I. Talmi, Phys. Rev. **83**, 1248 (1951), who did not, however, discuss its scope or range of validity.
[25] L. W. Nordheim, Revs. Modern Phys. **23**, 322 (1951).

tion of two neutrons to an odd neutron nucleus or of two protons to an odd proton nucleus pushes the moments towards the Schmidt curves, provided that l and j are unchanged, and of the fact that odd neutron nuclei tend to deviate less from the Schmidt curves than do odd proton nuclei with the same l and j and with comparable A.

The authors would like to thank Joy Russek for her invaluable aid in performing the numerical calculations.

APPENDIX

The evaluation of the matrix elements of M_1^{ε} and M_3^{ε} is greatly facilitated by the use of the well-known theorem that in the diagonal matrix element of any vector $\mathbf{A}$ whose components satisfy certain commutation rules, $\mathbf{A}$ can be replaced by $[j(j+1)]^{-1}(\mathbf{A}\cdot\mathbf{J})\mathbf{J}$. In the case of $\mathbf{M}_3$, the theorem should be applied immediately. In the case of $\mathbf{M}_1$, the theorem should be applied after the spin of the outer particle has been eliminated, with j now replaced by l. The matrix element then involves a scalar operator and, as such, is independent of the projection of l. Equation (2) follows, finally, upon the use of the relation

$$\mathbf{r}_1\times\mathbf{r}_2\cdot\mathbf{L}_1P_l(\mu)=-i\hbar r_1r_2(1-\mu^2)P_l'(\mu).$$

Specialization to the shell model is then trivial. The shell model evaluation of $\langle M_1^{\varepsilon}\rangle$ also follows from Appendix I of reference 9 by setting

$$I_{nln'l'}=\Big(\sum_{m=-l}^{l}m^2K_{nlmn'l'}\Big)\Big/\sum_{m=-l}^{l}m^2.$$

The derivation there is more general in that it includes cases in which there are three or more particles outside of the core.

There are certain formal advantages to replacing the factor $[\mathbf{r}_{\pi\nu}\cdot(\boldsymbol{\sigma}_\pi-\boldsymbol{\sigma}_\nu)]\mathbf{r}_{\pi\nu}$ of $\mathbf{M}_3$ by $[\mathbf{r}_{\pi\nu}\cdot(\boldsymbol{\sigma}_\pi-\boldsymbol{\sigma}_\nu)]\mathbf{r}_{\pi\nu}-\frac{1}{3}(\boldsymbol{\sigma}_\pi-\boldsymbol{\sigma}_\nu)r_{\pi\nu}^2$, which corresponds to a linear combination of $\mathbf{M}_2$ and $\mathbf{M}_3$, since this has simpler transformation properties under space rotation and Eq. (4) assumes a simpler form.

PHYSICAL REVIEW VOLUME 87, NUMBER 6 SEPTEMBER 15, 1952

Surface Production of Charged Mesons by Photons on Nuclei*

S. T. BUTLER
Laboratory of Nuclear Studies, Cornell University, Ithaca, New York

(Received May 8, 1952)

An estimate has been made of the photoproduction cross section of charged mesons from nuclei, and in particular from "surface-nucleons," i.e., the weakly interacting nucleons which make up the less dense nucleon atmosphere surrounding the main body of a nucleus. Comparison with experiment indicates that the production of mesons from the core of a nucleus is appreciably suppressed, apart from the effects of the initial momentum distribution of the nucleus, and of meson absorption. It is found, for example, that apart from having the correct $A^{\frac{1}{3}}$ dependence for the $\pi^++\pi^-$ cross section, the surface production alone can account for large fractions of the observed yields, and because of differences in average binding between neutrons and protons in nuclei, gives π^-/π^+ ratios which have the same trends as a function of A as the observed ratios. A possible explanation of these results is that there occurs a large competing photodisintegration process as a result of meson exchange effects between strongly coupled nucleons in the interior of a nucleus.

1. INTRODUCTION

THE main features of the experimental observations on the production of charged π-mesons from nuclei are the following:

(1) The yields are considerably less than from appropriate equal numbers of free nucleons,[1,2] and

(2) the sum of the π^+ and π^- cross sections exhibits very accurately an $A^{\frac{1}{3}}$ dependence.[1,3]

There are two well-known effects that are in the right direction for explaining these results. Firstly, because of the momentum distribution of nucleons in a nucleus, it is not energetically possible for all the protons or all the neutrons to participate in the production.[4] Secondly, some of the mesons which are produced will be absorbed before they escape from the nucleus. Each of these effects in general reduces the meson yields, and since the absorption of a meson produced in the interior of a nucleus is more probable than for one produced at the surface, the second tends to produce the observed $A^{\frac{1}{3}}$ dependence.[5]

However, on the basis of estimates[6] of the absorption mean free path for mesons in nuclear matter, obtained from the results of meson scattering experiments, the very good experimental $A^{\frac{1}{3}}$ dependence is difficult to understand as due merely to absorption of the mesons. This result might be taken to indicate, therefore, that there is in some way a further suppression of the meson

* This work was supported in part by contract with the ONR.

[1] R. M. Littauer and D. Walker, Phys. Rev. **83**, 206 (1951); **86**, 838 (1952).
[2] J. Steinberger and A. Bishop, Phys. Rev. **78**, 494 (1950).
[3] R. F. Mozley, Phys. Rev. **80**, 493 (1950).
[4] M. Lax and H. Feshbach, Phys. Rev. **81**, 189 (1951).
[5] Brueckner, Serber, and Watson **84**, 258 (1951).
[6] J. Steinberger (private communication).

production in the interior of a nucleus, and that the actual production from surface nucleons is predominant in the first place. For such a conclusion to be justified, however, it must also be shown that the above two effects are not by themselves sufficient to explain the observed yields, and in particular that the observed cross sections, as well as characteristic features such as the π^- to π^+ ratios, also are compatible with predominant surface production.

In the present paper, the cross sections for charged meson production from surface nucleons is estimated, surface nucleons being defined as those nucleons which the photon catches outside the main core of a nucleus, i.e., with radial coordinates greater than the nuclear "radius" r_0, and which are subject to weak nuclear interaction. It is found that, apart from having the correct $A^{\frac{1}{3}}$ dependence, this effect can account also for large fractions (60–70 percent) of the observed cross sections Moreover, the average ratio of neutron and proton numbers outside a nuclear core is dependent on the average binding of neutrons as compared with protons in the nucleus, and this introduces a variation with A in the ratio of the yields of negative and positive mesons which has the same trends as the experimental variation.

These results support the view, therefore, that meson production from surface nucleons is predominant, and that production from the interior of a nucleus is largely suppressed. This conclusion is also consistent with what is considered to be a lower estimate of the total production in the event of no such interior suppression (allowance being made for meson absorption by the final nucleus), this estimate being considerably greater than the observed yields. The results indicate, in fact, that the production from the core of a nucleus is suppressed in general by a factor $\gtrsim 3$ (assuming the suppression to occur only in the nuclear core), apart from the effects of the initial momentum distribution of the nucleons and of meson absorption.

Such suppression can, perhaps, be understood as the result of a large competing photodisintegration process due to meson exchange effects between strongly interacting nucleons within the nucleus. When a high energy photon interacts with a nucleon which is itself interacting with one or more neighbors in a nucleus and capable of exchanging energy with them, there exists the possibility that there will occur a direct photodisintegration of this interacting nucleon group via meson exchange.[7] This process would then compete with meson production, some of the mesons which would have escaped the influence of the parent nucleon had it been free being retained by one member of the interacting nucleon group, the excess energy being taken up in the form of a disintegration of the group. Of course, once a meson does escape from the influence of the parent nucleon and any strongly interacting neighbors, there is also the possibility of it being absorbed in other parts of the nucleus before it finally escapes altogether. This also produces a photodisintegration of the nucleus, but is just the absorption allowed for by use of the mean free path obtained from scattering experiments. The process mentioned above is best thought of as causing a damping of the actual meson production in the first place.

The probability of such a competing process will depend, among other things, on the extent to which nucleons in a nucleus are coupled by their interaction. In particular, for photons incident on nuclei, the process will be much more important on the average for nucleons in the core of a nucleus than for surface nucleons, and should therefore enhance the surface production of mesons relative to production from the interior. This is essentially the process recently proposed by Wilson,[8] and if assumed to account for the entire suppression mentioned above, must have a cross section comparable with that of the actual meson production.

In the particular case of the deuteron, the anomalously large cross sections observed for high energy photodisintegration[9–11] seem consistent with the above picture.[12,13] In this case the nucleons are interacting strongly for a small fraction of the time only, and any suppression of meson production will be quite small. Only a relatively small probability for the above competing process is, however, sufficient to explain the high photodisintegration cross section.

2. PHOTOMESON PRODUCTION FROM NUCLEI

We wish to calculate the cross section for production of charged mesons by photons on nuclei, in such a way that we can estimate the production from those nucleons which the photon catches beyond the boundary defined by the radius r_0 of the nucleus. By r_0 we will mean the radius of the central core of a nucleus, inside of which the density of nucleons is roughly constant, but outside of which the density falls off rapidly, any one nucleon being here subject to weak interaction with other members of the nucleus. We shall, in fact, consider a nucleon outside this boundary to be free, and to have an energy (in general negative) depending on the particular state of the nucleus it leaves behind.

In the following calculations we shall, for definiteness,

[7] This effect can be described by particular models, e.g., in terms of the role played by the nucleon isobaric state in photomeson production (see reference 11). In the case of a free nucleon, an intermediate excited state produced by a photon has but two modes of decay—either by re-emission of the photon, or by emission of a meson. For a nucleon interacting with one or more neighbors, however, an intermediate excited state has a third possible mode of decay, *viz.* that in which a meson in the excited state of the first nucleon transfers to the ground state of a second nucleon, the excess energy going into kinetic energy of separation of the nucleon group.

[8] R. R. Wilson, Phys. Rev. **86**, 125 (1952).
[9] T. Benedict and W. Woodward, Phys. Rev. **86**, 629 (1952).
[10] S. Kikuchi, Phys. Rev. **85**, 753 (1952).
[11] W. Gilbert and J. Rose, Phys. Rev. **85**, 766 (1952).
[12] N. Austern, Bull. Am. Phys. Soc. **27**, No. 3, 32 (1952).
[13] R. H. Huddlestone and T. V. Lepore, Bull. Amer. Phys. Soc. **27**, No. 3, 31 (1952).

consider the production of π^+ mesons, that of π^- mesons being completely analogous.

(a) Free Particle Production

We first write the free particle cross section in the form required later for comparison (using throughout the notation employed by Lax and Feshbach[4]).

The matrix element for this process can always be written

$$\langle n|T|p\rangle, \tag{1}$$

$|n\rangle$ representing the final neutron state, $|p\rangle$ the initial proton state, and T being an operator which has the form

$$T=e^{i\mathbf{q}\cdot\mathbf{r}}\tau^+(\mathbf{K}\cdot\boldsymbol{\sigma}+L).$$

Here $\mathbf{r}$ is the space coordinate of the nucleon, $\mathbf{q}$ the difference $(\boldsymbol{\nu}-\boldsymbol{\mu})$ between the photon momentum $\boldsymbol{\nu}$ and meson momentum $\boldsymbol{\mu}$, τ^+ the isotopic spin operator which converts the proton into a neutron, and $\boldsymbol{\sigma}$ the spin operator, while $\mathbf{K}$ and L are matrices that depend, in general, on the photon and meson momenta and polarizations as well as the nucleon momenta. Thus the free proton cross section, in units $\hbar=c=$ meson mass $=$ unity, and for a particular meson momentum (interval $d\boldsymbol{\mu}$) becomes

$$\sigma_f=(2\pi)^{-2}d\boldsymbol{\mu}\int d\mathbf{n}(K^2+L^2)\delta(\mathbf{n}+\mathbf{q})\delta(n_0+\mu_0-\nu_0), \tag{2}$$

where $\mathbf{n}$ is the neutron momentum, n_0 the neutron kinetic energy, $\mu_0=(1+\mu^2)^{\frac{1}{2}}$ the meson energy, and $\nu_0=\nu$ the photon energy. Here we have considered the initial proton to be at rest, and are writing the nucleon energies nonrelativistically.

We will later be making comparisons with experimental results obtained with a bremsstrahlung spectrum, say $f(\nu_0)d\nu_0$. On multiplying (2) by this distribution, therefore, and carrying out the integration over $\mathbf{n}$ and ν_0, we obtain

$$\sigma_f=(2\pi)^{-2}d\boldsymbol{\mu}[(K^2+L^2)f]_{\mathbf{n}=-\mathbf{q},\nu_0=n_0+\mu_0}. \tag{3}$$

The solution of the simultaneous equations $\mathbf{n}=-\mathbf{q}$, and $\nu_0=n_0+\mu_0$ for a given μ tell us, of course, the recoil momentum and energy of the neutron and the particular photon energy responsible for the production.

(b) Nuclear Production Cross Section

The cross section for a nuclear target is

$$\sigma=(2\pi)^{-2}d\boldsymbol{\mu}\int f(\nu_0)d\nu_0|\sum_f\psi_f,\sum_\lambda T_\lambda\psi_i|^2\delta(E_f-E_i), \tag{4}$$

where ψ_i and ψ_f are the initial and final nuclear states, E_i and E_f the initial and final energies of the complete system, and T_λ operates on the coordinates of particle λ. The sum over λ goes over all particles in the nucleus.

To compute the matrix-element $(\psi_f,\sum_\lambda T_\lambda\psi_i)$ we expand the antisymmetrical wave function ψ_i of the initial nucleus with respect to states of the remaining nucleus when one proton (say the αth) has been extracted, and certain single-particle wave functions for the αth proton, i.e.,

$$\psi_i=\sum_{stm_sm_\alpha}a^\alpha_{st,j_sm_sm_\alpha}v_{s,j_sm_s}(\xi_\alpha)g_t(\mathbf{r}_\alpha)\chi(\mu_\alpha), \tag{5}$$

where ξ_α represents all coordinates of the initial nucleus apart from those of the αth proton, and the $v_{s,j_sm_s}(\xi_\alpha)$ are the antisymmetrical wave functions of the states s of the nucleus with the αth proton absent. These states have total spins designated by j_s and orientations m_s. The spatial coordinates of the αth proton are given by $\mathbf{r}_\alpha$, and its spin orientation is μ_α, χ_α being the spin function.

The $g_t(\mathbf{r}_\alpha)$ are wave functions of states t of the proton in some potential field $V(\mathbf{r}_\alpha)$, and the expansion (5) is valid for any $V(\mathbf{r}_\alpha)$ for which the solutions of the corresponding wave equation (the $g_t(\mathbf{r}_\alpha)$) form a complete and orthogonal set. Eventually we will like to think of $V(\mathbf{r}_\alpha)$ as being a good average of the interaction by a proton in the nucleus, and to assume that $V\to 0$ for $r_\alpha\geqslant r_0$ where we identify r_0 with the radius of the nucleus. We assume all the functions in (5) are normalized to unity so that

$$\sum_{stm_sm_\alpha}|a^\alpha_{st,j_sm_sm_\alpha}|^2=1.$$

Such an expansion as (5) is always possible, the antisymmetrization of ψ_i exhibiting itself in certain properties of the a's. It is, of course, equally possible to perform the expansion in terms of wave functions $v_s(\xi_{\alpha'})$ and $g_t(\mathbf{r}_{\alpha'})$ in which the coordinates of a different proton (the α'th) have been chosen for the single particle wave functions. And because of the asymmetry of ψ_i, we will have that

$$a^{\alpha'}_{st,j_sm_s\mu}=\pm a^\alpha_{st,j_sm_s\mu},$$

the sign being determined by the number of pairs of particle coordinates which must be interchanged in the new expansion in order to put it in a form identical with (5). We may, therefore, choose whichever of the Z such expansions is most convenient; in computing the matrix element $(\psi_f,\sum_\lambda T_\lambda\psi_i)$ we will use the expansion involving a^α with the term T_α acting on proton α, paying attention to the appropriate sign when later converting one a^α into another.

We intend calculating the meson production from the "outside" region of a nucleus; and when the incident photon catches a nucleon outside the nucleus, producing a meson, this nucleon which is essentially free will recoil with a certain momentum $\mathbf{n}$, its final wave function being given by a plane wave $\exp(i\mathbf{n}\cdot\mathbf{r}_\alpha)$. The final wave function ψ_f (f designating a state s of the remaining nucleus with spin orientation m_s, and a spin orientation μ_f of the recoil particle, as well as a particular momentum $\mathbf{n}$) we will take therefore to be the

normalized function

$$\psi_f=(2\pi)^{-\frac{1}{2}}Z^{-\frac{1}{2}}[v_{s,j_s m_s}(\xi_\alpha)\exp(i\mathbf{n}\cdot\mathbf{r}_\alpha)\chi(\mu_\alpha)]^{(A)}, \quad (6)$$

the notation $[\ \ ]^{(A)}$ meaning the product within the bracket is to be made antisymmetrical. The normalization factor $Z^{-\frac{1}{2}}$ is not exact; however, we will find that, for cases to which we apply the results, the recoil momentum ($\mathbf{n}$) is much higher than the momentum of a nucleon in any of the states s of importance of the remaining nucleus. The nondiagonal overlap integrals will therefore be very small.

Substituting Eqs. (5) and (6) for the wave functions ψ_i and ψ_f, respectively, and neglecting nondiagonal overlap integrals (the "two-particle" contributions of Lax and Feshbach[4]) the matrix element becomes

$$(\psi_f,\sum_\lambda T_\lambda\psi_i)=(2\pi)^{-\frac{1}{2}}Z^{-\frac{1}{2}}\sum_{\mu_i t}\chi(\mu_f)(\mathbf{K}\cdot\boldsymbol{\sigma}+L)\chi(\mu_i)\sum_{\alpha=1}^{Z}$$

$$\pm a^\alpha{}_{st,j_s m_{s\mu_i}}\int\exp[i\mathbf{r}_\alpha\cdot(\mathbf{q}+\mathbf{n})]g_t(\mathbf{r}_\alpha)d\mathbf{r}_\alpha. \quad (7)$$

The signs of the a^α's are, however, such as to give all terms under the summation the same sign. Equation (6) becomes therefore

$$(\psi_f,\sum_\lambda T_\lambda\psi_i)=\pm(2\pi)^{-\frac{1}{2}}Z^{\frac{1}{2}}\sum_{\mu_i t}\chi(\mu_f)(\mathbf{K}\cdot\boldsymbol{\sigma}+L)\chi(\mu_i)$$

$$\times a_{st,j_s m_{s\mu_i}}\int\exp[i\mathbf{r}\cdot(\mathbf{q}+\mathbf{n})]g_t(\mathbf{r})d\mathbf{r}, \quad (8)$$

where the superscript α can now be dropped.

On substituting (8) in (4) and performing the summation over final states and integrating over ν_0, we obtain

$$\sigma=(2\pi)^{-5}Zd\boldsymbol{\mu}\sum_{s m_s\mu}\int d\mathbf{n}[(K^2+L^2)f]_{\nu_0=n_0+\mu_0+\epsilon_s}$$

$$\times\left|\sum_t a_{st,j_s m_{s\mu}}\int\exp[i\mathbf{r}\cdot(\mathbf{q}+\mathbf{n})]g_t(\mathbf{r})d\mathbf{r}\right|^2, \quad (9)$$

where ϵ_s is the binding energy of a proton in the initial nucleus when the remaining nucleons are in the state s.

It is of interest to note that if the integration over $\mathbf{r}$ in (9) is taken over all space, then (9) would give the complete production cross section under the approximation of neglecting the interaction of the emerging neutron, as well as the meson, with the residual nucleus (if there were no damping factor of the type discussed in the introduction). This is the procedure of Lax and Feshbach,[4] who further assume that the most important of the residual states s have a small energy spread. Under these circumstances Eq. (9) becomes immediately

$$\sigma=Z(2\pi)^{-5}d\boldsymbol{\mu}\int d\mathbf{n}[(K^2+L^2)f]_{\nu_0=n_0+\mu_0+\epsilon}\rho(\mathbf{n}+\mathbf{q}), \quad (10)$$

where $\rho(\mathbf{k})$ is the normalized distribution of momenta $\mathbf{k}$ in the initial nucleus, and where ϵ is the average value of ϵ_s, i.e., is the average binding energy of a proton in the initial nucleus. This is precisely the result given by Lax and Feshbach, but actually derived by them only on the basis of the Hartree model of nuclear structure.

The integrand of (10) has a maximum when $\mathbf{n}\simeq-\mathbf{q}$, i.e., at or near the Compton line for free production, and if the factor $[(K^2+L^2)f]_{\nu_0=n_0+\mu_0+\epsilon}$ is substantially constant over the region where $\rho(\mathbf{n}+\mathbf{q})$ is large, the cross section becomes of course merely $Z\sigma_f$. However, because of the large spread in the momenta available to nucleons in a nucleus, the width of $\rho(\mathbf{n}+\mathbf{q})$ is quite large and the cross section is usually reduced due to the product $[(K^2+L^2)f]$ becoming zero over part of the significant range of integration of $\mathbf{n}$ (corresponding ν_0 above the cutoff of the bremsstrahlung spectrum). An exception to this, which will be important in the case to which we apply the results, will be discussed shortly.

For computing the surface effect we take the integral over $\mathbf{r}$ in (9) only over the region $r>r_0$ (the nuclear radius). In this event Eq. (9) becomes

$$\sigma=Z(2\pi)^{-5}\tau d\boldsymbol{\mu}$$

$$\times\int d\mathbf{n}[(K^2+L^2)f]_{\nu_0=n_0+\mu_0+\epsilon}\rho'(\mathbf{n}+\mathbf{q},r_0), \quad (11)$$

where $\rho'(\mathbf{k},r_0)$ is the normalized distribution of momenta for protons outside the core of the initial nucleus, and where we have again represented the shift in the energy equation from that for free production by the average value ϵ. In (11) also, τ is the fraction of the time which a proton in the initial nucleus spends outside the core of radius r_0, i.e.,

$$\tau=\sum_{s m_s\mu}\int_{r\geqslant r_0}d\mathbf{r}\left|\sum_t a_{st,j_s m_{s\mu}}g_t(\mathbf{r})\right|^2$$

$$=\int_{r\geqslant r_0}d\mathbf{r}\left|\sum_t A_t g_t(\mathbf{r})\right|^2=\int_{r\geqslant r_0}D(\mathbf{r})d\mathbf{r}, \quad (12)$$

where $D(\mathbf{r})$ is the normalized density distribution of protons in the initial nucleus.

The integrand of (11) also has a maximum when $\mathbf{n}\simeq-\mathbf{q}$, but here the spread about this point is appreciably less than in (10), due to the fact that a nucleon beyond the range of interaction with other nucleons in general has a low momentum, and the entire spread of momenta given in (10) by $\rho(\mathbf{n}+\mathbf{q})$ is not available to these nucleons. This may be seen from the fact that, provided our potential $V(r)=0$ for $r\geqslant r_0$, we can write

$$g_l(r)=\sum_{lm}b_{l,lm}\frac{K_{l+\frac{1}{2}}(\kappa_f r)}{r^{\frac{1}{2}}}Y_{lm}(\theta\varphi)$$

$$=\sum_{lm}b_{l,lm}'\frac{e^{-\kappa_f r}}{r}Y_{lm}(\theta\varphi)\sum_{n=0}^{l}\frac{(l+n)!}{n!(l-n)!(2\kappa_f r)^n}, \quad (13)$$

where $K_{l+\frac{1}{2}}$ is a Bessel function of imaginary argument. The spread in ρ' is determined essentially by something like the average value of κ_l (i.e., $\sum_l |A_l|^2 \kappa_l$), corresponding to an energy equal to the average binding energy ϵ of a proton in the initial nucleus ($\simeq$8 Mev) rather than approximately 20 Mev as for the general distribution in (10).

In cases where the product $[(K^2+L^2)f]_{\nu_0=\pi_0+\mu_0+\epsilon}$ is substantially constant over the significant spread of ρ', (11) becomes, as in the similar case for Eq. (10), merely

$$\sigma = \sigma_f Z \tau. \tag{14}$$

Also, for the same reason as in the case of Eq. (10), the surface cross section will usually be somewhat lower than this, although the reduction is less than for Eq. (10) because of the smaller spread in momenta in this case. However, for the conditions appropriate for a comparison, as will be made in the next section, with the experimental results of Littauer and Walker,[1] Eq. (14) should be a quite good approximation to the surface cross section, and may even slightly underestimate it. These experimental results were obtained by observing mesons with energies in the interval 50–80 Mev at an angle of 135° to the photon direction, and which were produced by a 310-Mev maximum energy bremsstrahlung spectrum from the Cornell synchrotron. In Fig. 1 is plotted the product $(K^2+L^2)_{\mathbf{n}=-\mathbf{q},\nu_0=\pi_0+\mu_0}$ against ν_0 and the corresponding meson kinetic energy at this angle, making use of the (corrected) cross section for meson production from hydrogen as obtained by Bishop, Steinberger, and Cook,[14] as well as the known bremsstrahlung spectrum. It is seen that free-particle production of mesons in the range 50–80 Mev utilizes photons in the energy range 265 to 330 Mev. (The corresponding recoil energies lie between 75 and 110 Mev.) In particular, the meson energy 65 Mev corresponds to a photon energy of 298 Mev, which is in the region where the $[(K^2+L^2)f]$ curve is dropping rapidly to zero. Hence the free-particle yield of Littauer and Walker, to which all their other results are referred, contains contributions from mesons essentially in the energy region 50–65 Mev only.

For production from a nucleus there is, as just discussed, no such unique photon energy corresponding to a given meson energy. For each meson energy there is a spread in photon energies about (approximately) the free-particle value which, in the case of surface production for these energies, has a width $\sim$50 Mev. Thus the probability per nucleon of producing a meson with energy between 50–65 Mev from a nuclear surface is less than the corresponding free particle probability, since the photon energy spread will continue above the cutoff of the $[(K^2+L^2)f]$ curve. On the other hand, such loss of yield for mesons in the lower half of the accepted energy region will be largely counterbalanced by the corresponding increase in yield for mesons in the upper half of this region, particularly since the cross section carries a weighting factor μ^2 from the volume element in the meson momentum space.

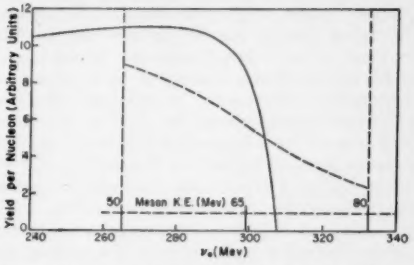

FIG. 1. Energy dependences for the yields of charged mesons produced from nucleons by photons from a bremsstrahlung spectrum. The full curve is for free-particle production as a function of the photon energy and the corresponding meson kinetic energy. The dotted curve gives the corresponding yield per nucleon from surface nucleons as a function of meson kinetic energy only. The ordinates at 50- and 80-Mev meson kinetic energy are the energy limits of the mesons observed in the experiments of Littauer and Walker (see reference 1).

As an example, suppose we take ρ' of the form

$$\rho' = \kappa_{k_0}/[\pi^2(\kappa_{k_0}{}^2+k^2)],$$

where κ_{k_0} corresponds to an energy of 8 Mev. Then from Eq. (11) we find (taking also ϵ=8 Mev in the energy equation) that the surface yield per nucleon as a function of meson energy is as given by the dotted curve in Fig. 1. The total area under this curve between the limits 50<meson K.E.<80 Mev is very similar to that under the free-particle curve. Thus Eq. (14) should be a good approximation to the surface cross section for the interval of meson energies considered.

Arguments similar to the above also indicate that Eq. (10), which gives the total production cross section in the event of there being no interior suppression, should give $\sigma \simeq Z\sigma_f$ for the above experimental conditions (although there is some small reduction in this case due to the larger spread of momenta available). Equation (10), however, does not take into account the interaction of the recoil particle or of the meson with the final nucleus, and although small for surface production, the effects of these may well be important for interior production. Indeed, if the average interaction of the recoil nucleon with the final nucleus is represented by an attractive well of depth 30 Mev, the effect of this is to lower the most probable photon energy corresponding to a given meson energy by about 50 Mev from the free-particle value (see appendix). This will greatly enhance the production, since more of the required photon energies are now available in the bremsstrahlung spectrum, and moreover the magnitude of the product $(K^2+L^2)f$ at the appropriate energies will be appreciably greater. The latter effect is due to the fact that the beginning of the rise of the (K^2+L^2) function[14] (threshold) occurs for lower photon energies,

[14] Bishop, Steinberger, and Cook, Phys. Rev. **80**, 291 (1950).

i.e., larger f values, so that the above product attains higher values than in the free-particle case. On the other hand, if the average interaction of the meson with the final nucleus is represented by an attractive well of depth 30 Mev (see Sec. 3), this raises the above most probable photon energy by about 30 Mev. The over-all effect of these interactions is, however, to lower the photon energies utilized (on the above model by 20 Mev), and hence to produce a corresponding increase in the cross section over that given by Eq. (10).

It is estimated, in fact, that if there is no suppression of meson production in the interior of a nucleus, the total yields under the conditions of the above experiments, before allowing for meson absorption, should certainly satisfy

$$\sigma \gtrsim Z\sigma_f, \tag{15}$$

and this inequality will be sufficient for any later discussion. The above lower limit would actually be higher if the well depth to be taken for the meson attractive interaction were appreciably less than 30 Mev, and very much so if this interaction were in part repulsive.[15]

It is also worth noting that, although the average interaction experienced by a nucleon or meson in the nuclear surface is expected to be much smaller than in the interior, the effect of any such interaction should be to increase the surface yield over the value given by (14).

To estimate τ in (14) we first note from (12) and (13) that, for most of the orbital angular momentum states and binding energies of importance in nuclei,

$$\int_{r_0}^{\infty} D(\mathbf{r})dr \simeq \sum_{ll'} \frac{A_l A_{l'}{}^* [g_l(\mathbf{r}) g_{l'}{}^*(\mathbf{r})]_{r=r_0}}{\kappa_l + \kappa_{l'}}. \tag{16}$$

Now when we choose our generating function $V(r)$ to be the best possible such potential to represent the average interaction experienced by a proton in the initial nucleus (and therefore $\to 0$ at $r=r_0$) we expect the important coefficients A_l to have corresponding values of κ_l which represent energies congregating in the region of the actual binding energies for protons in the nucleus, i.e., with an average value ~ 8 Mev.[16] If we replace $\kappa_l + \kappa_{l'}$ approximately by $2\kappa_{h\nu} = 2(2m\epsilon)^{\frac{1}{2}}$ therefore, we obtain

$$\int_{r_0}^{\infty} D(\mathbf{r})dr = \frac{\rho(r)_{r_0}}{2\kappa_{h\nu}}. \tag{17}$$

To obtain τ from (17) we must assume something about the density within the central core; if, for example, for a given orientation of $\mathbf{r}$, $D(\mathbf{r})$ is taken to be constant for $0 \lesssim r \lesssim r_0$, we obtain

$$\tau = 1/(1+\tfrac{3}{2}\kappa_{h\nu} r_0), \tag{18}$$

and this is the estimate we use.

In the case of π^- production the same formulas are obtained, of course, with Z replaced by N, the $\kappa_{h\nu}$ of (18) being now given by the average binding energy of a neutron in the initial nucleus rather than a proton.

3. COMPARISON WITH EXPERIMENT AND DISCUSSION

Since $\kappa_{h\nu} r_0$ is in general substantially greater than unity, it is seen, as was to be expected of course, that the sum of the π^- and π^+ surface cross sections has an $A/r_0 = A^{\frac{2}{3}}$ proportionality.

The magnitude of the $\pi^+ + \pi^-$ surface yield for different elements, obtained from (14) and (18), is plotted in Fig. 2 and compared with the experimental results of Littauer and Walker.[1] The $\kappa_{h\nu}$ used was obtained directly from the average binding energy of a proton or a neutron in the appropriate initial nucleus, allowance being made for the Coulomb differences between the two cases. The radius r_0 was taken to be $1.2\times 10^{-13} A^{\frac{1}{3}}$ cm. On the nuclear model which assumes constant density out to a certain radius r_0, and zero beyond, the more usual value of r_0 is $1.45\times 10^{-13} A^{\frac{1}{3}}$ cm. However, when the diffuse surface region in which the density falls off in a distance $\sim \frac{1}{2}\kappa_{h\nu}$ is considered, the experimental results on neutron scattering indicate a radius of the core appreciably less than this,[17] and also the mass differences between mirror nuclei (interpreted as due mainly to differences in Coulomb energy) give approximately the value 1.2 for the coefficient.

The results in Fig. 2 have all been normalized to unity for the production of π^+ mesons from hydrogen (for the theoretical values the free-particle π^-/π^+ ratio being taken as 1.2).[1] Also, the theoretical values have already been reduced from those given directly by Eq. (14), on the average by $\sim$40–50 percent, to allow for the absorption of some of the surface meaons as they pass through the nucleus before escaping. For estimating this the mean free path for absorption of charged mesons in a nuclear core was taken to be 9.5×10^{-13} cm, and the interaction of a meson with the nucleus represented by an attractive well whose shape is that of the density distribution of nucleons in the nucleus (approximated by a well of trapezoidal shape), and whose central depth is approximately 30 Mev. This is the model employed by Steinberger,[6] and the above mean free path and well depth are the results obtained by him, in interpreting experimental results of Byfield, Kessler and Lederman,[18] and of Sachs and Steinberger[19] concerning the inelastic cross section and elastic scattering of 60-Mev mesons. [This is about the average

[15] R. LeLevier, Bull. Am. Phys. Soc. **27**, No. 3, 41 (1952).

[16] In the case of the independent particle model of nuclear structure, the sum over l has Z terms, and the number of different values of κ_l is equal to the number of proton subshells filled or partially filled in the nucleus. The limits of the spread in κ_l are given by the binding energy of a proton in the lowest subshell and that in the highest, the average value $\kappa_{h\nu}$ being given by the average of the κ_l's, each one being weighted by the number of protons in the appropriate subshell.

[17] R. Jastrow and J. E. Roberts, Phys. Rev. **85**, 757 (1952).

[18] Byfield, Kessler, and Lederman, Phys. Rev. **86**, 17 (1952).

[19] A. Sachs and J. Steinberger, Phys. Rev. **82**, 958 (1951).

energy of the mesons observed by Littauer and Walker (see Fig. 1).]

It is seen that quite large fractions of the observed yields can be accounted for by surface production. Moreover, it is of interest to note that, because of differences in the average binding energies of neutrons as compared to protons in a nucleus, and thus in the number of neutrons as compared to protons in the nuclear surfaces [Eq. (18)], there is a variation in the ratio of the individual π^- to π^+ surface yields which has the same trends as the experimental ratios. In the case of Be^9, for example, if the small binding energy difference between this nucleus and Be^8 be attributed to the additional neutron, the effect of such a lightly bound neutron which spends a large amount of its time on the outside of the nucleus is to increase the π^- surface yield relative to the π^+ by more than just the ratio N/Z of the total neutron and proton numbers. For symmetrical light nuclei such as C^{12}, the average binding energies and therefore the π^- and π^+ surface yields are about equal, but for heavier such nuclei the Coulomb interaction causes the protons to be less bound than the neutrons. There is, therefore, for symmetrical nuclei, a gradual decrease of the surface π^-/π^+ ratio as A is increased up to Ca^{40}, the last stable such nucleus. For nuclei in this range which have an additional odd neutron, the ratio will be above the general trend just mentioned. For heavy elements in which the neutrons appreciably exceed the protons in number, the average binding energies of the two again become about equal, and the π^-/π^+ surface ratios become merely the ratio of total neutron and proton numbers in the nucleus.

These trends are all in agreement with the experimental observations, although the magnitudes of the variations are not as large as the experimental ones. To take the two extremes, for example, one would expect on the above basis a π^-/π^+ ratio of something like 1.6—1.7 for Be^9 compared with the observed value 2.2, and for Ca^{40} something like 0.8 compared with the observed value of 0.6. However with much of the variation thus accounted for, there are some further effects which, although in themselves probably quite small, should bring the magnitudes of the variations more closely into line with experiment when added to the above. These may be summarized as follows:

(a) The average binding of a neutron or proton enters not only into the expression for τ [Eq. (18)] but also in the energy equation $\nu_0=n_0+\mu_0+\epsilon$ of (11). The larger ϵ the higher the photon energies necessary to produce mesons of a given energy, and the differences between neutron and proton binding energies will in this way, therefore, result in slightly different π^- and π^+ yields. The resultant deviations from unity of the π^-/π^+ ratios will certainly be in the right direction, but will be quite small.

(b) There are essentially different lower limits on the recoil nucleon energies for π^- and π^+ production, due to differences in binding energies of the ground states of the two final nuclei.[20] The fact, however, that the most probable recoil energies are $\sim$100 Mev leads to a very small probability of forming the final nuclei in low-lying states (the reason for being able to neglect "two-particle" contributions when obtaining the cross section). Any deviations from unity of the π^-/π^+ ratio resulting from the foregoing must therefore be quite small, although again they will be in the right direction (see the correlation between the binding energy differences and the π^-/π^+ ratios given by Littauer and Walker[1]). Estimates by Bethe and Hayakawa[21] indicate, in fact, that for production from the whole nucleus, these deviations will amount to less than 10–20 percent, and this will be less for surface production.

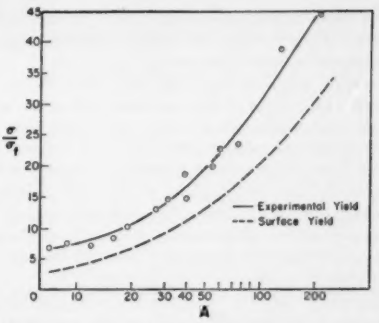

FIG. 2. The yields of charged mesons, produced by photons incident on nuclei, as a function of A. The full curve is drawn through the experimental points of Littauer and Walker (see reference 1) and the dotted curve gives the yields to be expected for surface production.

(c) Although in deriving (11) we assumed no interaction for nucleons outside the nuclear radius, there will in general be some weak interaction which has the effect of lowering the photon energies utilized. Any difference in this average interaction for neutrons and protons may therefore cause differences in the π^- and π^+ yields in the same way as do differences in the binding energies (a). Similarly, differences in the average interactions of π^- and π^+ mesons with surface nucleons may produce differences in the yields, and in particular the Coulomb interaction will tend to increase the π^+ yield relative to the π^-. We again expect these to be rather small effects for the energies under consideration,[22] except perhaps for the different Coulomb interactions just mentioned which might be expected to

[20] G. F. Chew and J. Steinberger, Phys. Rev. **78**, 497 (1950).
[21] H. A. Bethe and S. Hayakawa (private communication).
[22] Of course if the upper limit of the photon spectrum were appreciably lower than 310 Mev (say 250 Mev), then for production of the same energy mesons (about 65 Mev) the deviations from unity in the π^-/π^+ ratios by effects (a) and (c) would be much greater than for the energies we are considering. Here the total yields would be very much smaller in the first place, and the differences in the π^- and π^+ yields produced by these effects would be relatively much more important.

play a more important role for heavy elements. The observed π^-/π^+ ratios for heavy elements appear, however, to be little influenced by this.

It seems therefore that the main features of the experimental results of Littauer and Walker are compatible with surface production alone, and that the interior production must contribute to a small extent only in these results and must therefore be quite heavily damped. In fact, on referring to (15) and estimating the absorption of mesons produced in the interior of a nucleus by means of the model previously mentioned, we conclude that the production from the interior of a nucleus must be suppressed by a factor $\gtrsim 3$.

Obviously the view that no nucleons outside the boundary r_0 interact with other nucleons and that the above suppression of meson production must occur only for nucleons within a certain core, is an idealization. It is true, nevertheless, that nucleons near the outside of a nucleus are subject, on the average, to much weaker interaction than those well within a nucleus. Thus the above results indicate that there is a suppression of meson production, and that this suppression occurs mainly in the case of production from nucleons which are subject to relatively strong nuclear interaction. This is compatible with the idea that the damping is due to the competing process discussed in the Introduction, of a photodisintegration via meson exchange between strongly coupled nucleons. This process should, if this be the case, have a cross section comparable with that of the actual meson production.

In conclusion I would like to thank Professors H. A. Bethe and R. R. Wilson, and Dr. N. Austern and Dr. E. E. Salpeter for interesting and informative discussions, and also Dr. R. M. Littauer for details of experimental results prior to their publication.

APPENDIX

1. For free-particle production, the conservation of energy and momentum equations are

$$\nu_0 = n_0 + \mu_0, \quad \mathbf{v} = \mathbf{n} + \boldsymbol{\mu}.$$

The solution for ν_0 from these equations is

$$\nu_0 = \tfrac{1}{2}(2mc^2 + \cos\vartheta\mu_0 v/c) \times\left[1 - \left\{1 - \frac{4(2mc^2\mu_0 + \mu_0^2 v^2/c^2)}{(2mc^2 + \cos\vartheta\mu_0 v/c)^2}\right\}^{\frac{1}{2}}\right],$$

where mc^2 is the rest energy of a nucleon, v the velocity of the meson, and ϑ the angle between the meson and photon directions. For $\mu_0 = 215$ Mev (K.E. $= 65$ Mev) and $\vartheta = 135°$, for example, this yields $\nu_0 = 298$ Mev.

2. Production from a nucleus

We consider production from a nucleon which leaves the rest of the (A-1) nucleus in a state s. The energy of this nucleus is $-\epsilon_s$, whatever its kinetic energy, and for the high recoil energies pertaining to the cases of interest to us, the energy of the rest of the nucleus remains unchanged by the production process. Using the average value $-\epsilon$ for the energy of the initial nucleon, the conservation of energy condition is therefore

$$\nu_0 - \epsilon = n_0' + \mu_0',$$

where n_0' and μ_0' are the energies of the recoil nucleon and meson after they escape from the nucleus.

The average or most probable momentum of the initial nucleon is $\mathbf{k} \simeq 0$ and the most probable photon energy can therefore be obtained from the additional equation

$$\mathbf{v} = \mathbf{n} + \boldsymbol{\mu}$$

as in the free-particle case. Here $\mathbf{n}$ and $\boldsymbol{\mu}$ are the recoil nucleon and meson momenta inside the final nucleus (corresponding energies n_0 and μ_0). If there is no interaction of these particles with the final nucleus, n_0' and $\mu_0' = n_0$ and μ_0. If, however, the interaction of the recoil nucleon be represented by an attractive well of depth V_n, and that of the meson by an attractive well of depth V_μ, the energy equation becomes

$$\nu_0 = n_0 + \mu_0 + \epsilon - V_n - V_\mu.$$

The solution giving the most probable photon energy is now

$$\nu_0 = \tfrac{1}{2}(2mc^2 + \cos\vartheta\mu_0 v/c) \times\left[1 - \left\{1 - \frac{4(2mc^2(\mu_0 + \epsilon - V_n - V_\mu) + \mu_0^2 v^2/c^2)}{(2mc^2 + \cos\vartheta\mu_0 v/c)^2}\right\}^{\frac{1}{2}}\right].$$

For comparison with the free-particle case, we take, for example, $\mu_0' = \mu_0 - V_0 = 215$ (external K.E. $= 65$ Mev) and $\vartheta = 135°$ (and put $\epsilon = 0$). Then

(a) for $V_n = 30$ Mev and $V_\mu = 0$, $\nu_0 \simeq 248$ Mev;
(b) for $V_n = 0$, $V_\mu = 30$ Mev, $\nu_0 \simeq 328$ Mev;
(c) for $V_n = 30$ Mev, $V_\mu = 30$ Mev, $\nu_0 \simeq 278$ Mev.

Thus the over-all effect of the nucleon and meson interactions with the final nucleus is to lower the photon energies utilized.

Letters to the Editor

PUBLICATION of brief reports of important discoveries in physics may be secured by addressing them to this department. The closing date for this department is five weeks prior to the date of issue. No proof will be sent to the authors. The Board of Editors does not hold itself responsible for the opinions expressed by the correspondents. Communications should not exceed 600 words in length and should be submitted in duplicate.

Field Dependent Fluorescence of Vitreous Zn_2SiO_4 Phosphor

ARTHUR BRAMLEY AND JENNY E. ROSENTHAL
Bramley Consultants, Long Branch, New Jersey
(Received July 31, 1952)

AT the March, 1952, Massachusetts Institute of Technology Conference on Physical Electronics we reported on the behavior of field dependent fluorescence of zinc silicate phosphor. Fluorescence could be obtained only when the electric field had an ac component. The fluorescence observed in our samples was interpreted as being due to field emission, either cold emission or Zener tunneling at regions of high field intensity. The need for the presence of an ac component was ascribed to the existence of space charge associated with traps in the semiconducting vitreous phosphor. These assumptions also explained the anomalous behavior of the radiation as the temperature of the semiconductor was increased above 200°C.

Additional experimental results have now been obtained. The samples consist of a thin strip of glass, 0.01 cm wide and about 2 cm long placed between two conducting electrodes so that the electric field is applied across the width of the strip. The glass has a low softening point, and the Zn_2SiO_4:Mn phosphor is imbedded in it. The radiation is observed from a cross section in a plane perpendicular to the plane of the strip. Aluminum, silver, and graphite were used for the electrodes, the graphite giving the best performing sample as far as the efficiency of fluorescence is concerned. The vitreous mixture is a semiconductor with a resistance between 5 and 100 megohms/cm² at room temperature. However, the resistance is a function of the temperature and depends on the frequency of the applied potential.

Observation with a low power microscope shows that the radiation is emitted from the interface between the electrode and the vitreous phosphor.

The lowest potential for which radiation is observed varies between 100 v and 500 v depending on the thickness and other parameters of the sample. At a fixed potential the light output varies slightly with the frequency. For a frequency variation of the applied field from 120 cps to 16 kc/sec the light output varies by a factor less than 5. At 60 cps the light output varies roughly as the square of the potential in the range from 100 v above the low voltage cutoff to the crystal breakdown potential. The low voltage cutoff is defined arbitrarily as the potential at which radiation is first observed. Possibly a more sensitive photocell arrangement, such as a photomultiplier, would detect radiation at a potential lower than the presently observed cutoff.

These observations further substantiate the hypothesis that field emission is responsible for the phenomena. The transport of charge from deep-lying energy levels across the interface barriers excites the phosphor component of the glass matrix near the potential barrier at the interface. The value of this electric field across the interface will depend, of course, on the dielectric constant of the glass matrix and on the rate of conduction of the charge through the semiconducting glass matrix to the opposite electrode.

It is interesting to note that Piper and Williams[1] in their recent studies on the electroluminescence of single crystals of ZnS:Cu have arrived at a similar conclusion.

[1] W. W. Piper and F. E. Williams, Phys. Rev. **87**, 151 (1952).

Paramagnetic Resonance Absorption in Additively Colored Crystals of Alkali Halides*

CLYDE A. HUTCHISON, JR., AND GORDON A. NOBLE†
Institute for Nuclear Studies and Department of Chemistry, University of Chicago, Chicago, Illinois
(Received August 4, 1952)

SOME time ago one of us[1] observed paramagnetic resonance absorption in crystals of alkali halides colored by irradiation with neutrons. Subsequently, techniques were developed for studying simultaneously the optical and magnetic absorptions in such crystals as a function of time of irradiation or of time of thermal bleaching. No satisfactory correlation between the two types of absorption could be established, presumably due to the presence of a very great variety of color centers and paramagnetic species and the consequent complexity of both types of absorption. We have undertaken the study of additively colored crystals, in which case the situation may be made much simpler. Under optimum conditions the color centers and paramagnetic species present in such crystals may be predominantly of one type, the *F*-center.[2]

Tinkham and Kip[3] have also observed paramagnetic resonance absorption in crystals of KBr colored electrolytically and with x-rays.

We have observed paramagnetic resonance absorption at room temperature and at 9.0×10^9 cycles sec^{-1} in KCl which contained excess K and in KBr which contained excess K. The paramagnetism of such crystals in static fields has been studied by Jensen[4] and by Scott, Hrostowski, and Bupp.[5] The KCl with excess K was prepared by heating a single crystal in the presence of redistilled K in a glass capsule with a stainless steel liner.[6-8] The crystal was maintained at 965°K for about 4 hr and then cooled very rapidly in air to room temperature. Subsequent chemical analysis showed that it contained 4.4×10^{-4} mole of excess K per g of crystal (5.3×10^{18} atoms of K per cm³). A piece of this crystal weighing 1.28 g was placed with a cubic axis parallel to the static magnetic field at the midpoint of a rectangular box cavity operated in the TE_{102} mode at a frequency of approximately 9.0×10^9 cycles sec^{-1}. The reflection from the cavity was measured using a magic tee bridge. The magnetic field was modulated at 40 cycles sec^{-1} and phase sensitive detection was employed. The static field strength was measured by means of the proton resonance.

The variation with field strength of energy absorbed by the sample, as determined by numerical integration of the output of the phase sensitive detector, was a Gaussian within the error of the measurement. The area under this absorption curve was found to be only about one tenth that under the curve for an amount of $CuCl_2\cdot2H_2O$ equal in number of moles to the excess K in the colored crystal. This may be indicative of colloidal aggregation of a large fraction of the K. The full width between points of maximum slope was found to be 49.3 ± 0.8 gauss as a result of five measurements. However, the Van Vleck theory of dipole-dipole broadening applied to a face-centered cubic crystal assuming Gaussian line shape, random location of single electrons at Cl^- sites, and a concentration of electrons equal to the excess K concentration gives a full width between points of maximum slope of only 23 gauss. (If the electron concentration is as much lower than this as is indicated by the intensity measurements, the width would be only 7.3 gauss.) This difference is probably in agreement with the fact that at the concentrations concerned relatively very large amounts of higher aggregates of *F*-centers are present.[7]

The spectroscopic splitting factor was found to be 1.995 ± 0.001. This is considerably lower than the value, 2.0023, of the *g*-factor for a free electron.

Further studies of this resonance as a function of temperature and of concentration of excess K are in progress. We are also planning an investigation of the effect on the resonance of illumination of the crystal in the *F*-band to produce the *F'*-centers which would be expected to be diamagnetic. The method of paramagnetic resonance absorption offers advantages over the measurement of static susceptibilities for the study of magnetic color centers in

crystals. The paramagnetic resonance phenomenon is peculiar to the unpaired spins, and the magnetic centers result in the primary effect observed, not in a small change in the effect of the large amount of diamagnetic material present.[6,9] Paramagnetic resonance absorption will probably permit counting color centers in regions of concentration inaccessible to the optical methods.

We thank Clarence Arnow for the development and construction of part of the electronic equipment and Edward A. Bartal for construction of some of the apparatus employed in these experiments.

* This work was supported by the ONR.
† AEC Predoctoral Fellow 1951–1952.
[1] C. A. Hutchison, Jr., Phys. Rev. **75**, 1769 (1949).
[2] F. Seitz, Revs. Modern Phys. **18**, 384 (1946).
[3] M. Tinkham and A. F. Kip, Phys. Rev. **83**, 657 (1951).
[4] Jensen, Ann. phys. **34**, 161 (1939).
[5] Scott, Hrostowski, and Bupp, Phys. Rev. **79**, 346 (1950).
[6] Rogener, Ann. phys. **29**, 386 (1937).
[7] Scott and Bupp, Phys. Rev. **79**, 341 (1950).
[8] J. P. Molnar, thesis (unpublished).
[9] Hutchison, Kowalsky, Pastor, and Wheland, J. Chem. Phys. (to be published).

Disintegration of Cr^{51}†

W. S. Lyon
Analytical Chemistry Division, Oak Ridge National Laboratory, Oak Ridge, Tennessee
(Received August 4, 1952)

SPECTROMETER studies made by previous investigators have established that Cr^{51} decays entirely by orbital electron capture partially accompanied by gamma-radiation. Kern *et al.*[1] list the γ-ray energies as 0.32 Mev and 0.267 Mev. Bradt *et al.*[2] find the gamma-energies to be 0.320 and 0.237 Mev, and in addition suggest that the decay proceeds 97 percent directly to the ground state, 3 percent through the 0.32-Mev excited state, and ~1 percent through the 0.237-Mev level. By use of Cr^{51} supplied by the Operations Division of the Oak Ridge National Laboratory, the branching ratio of this nuclide has been investigated with the aid of coincidence counting, x-ray counting, and NaI crystal spectrometry.

Very little β^- or ϵ^- was found associated with the decay, in agreement with the data of Bradt.[2] By use of a helium filled tube as a negatron detector 3.0×10^{-4} ϵ^-/x-ray disintegration was found. The x-rays observed, therefore, are essentially all from orbital capture, and no interference from a conversion process is encountered. A measured aliquot of Cr^{51} was coincidence counted using a krypton-methane filled, thin end window, β-proportional counter as an x-ray detector and an anthracene crystal counter as a γ-detector. X-ray γ-coincidence data were taken as a function of Be absorber placed before the x-ray counter. The disintegration rate of the source so measured was calculated and found to be constant and independent of Be absorber.

A source of Mn^{54}, the disintegration rate of which was known through coincidence counting and ion chamber measurements, was used to determine the efficiency of a Kr-methane counter for Cr K x-rays. (2.29A). A measured aliquot of Cr^{51} (V x-rays, 2.50A) was then counted on this counter, and using the previously determined efficiency, the disintegration rate of the Cr^{51} was obtained. Agreement between this value and that obtained by coincidence counting was within 3 percent. A source of Cr^{51} of known disintegration rate was then placed on a previously calibrated NaI crystal scintillation spectrometer and the gamma-spectrum of this nuclide was obtained. The presence of only one gamma-ray of energy 0.32 Mev was observed. The area beneath this gamma-peak was obtained and multiplied by an appropriate efficiency factor. This total corrected area in disintegrations per minute was then compared to the known decay rate of the sample and the branching ratio obtained. Eight percent of the Cr^{51} disintegrations were found to proceed through the 0.32-Mev excited state. Sunyar[3] has recently stated that the lower energy γ-ray reported by workers can be ascribed to impurities. A preliminary figure ~10 percent branching has been given by him. Decay of a Cr^{51} source has been followed for five half-lives on both a GM counter and an ion chamber. A value for the half-life of 27.75 ± 0.3 days is indicated.

Acknowledgment is made to A. R. Brosi and B. H. Ketelle for advice and assistance in this work and to E. I. Wyatt who aided in the decay measurements.

† Based on work performed for the AEC.
[1] Kern, Mitchell, and Zaffarano, Phys. Rev. **76**, 94 (1949).
[2] H. Bradt *et al.*, Helv. Phys. Acta **18**, 259 (1945).
[3] A. W. Sunyar (private communication); National Bureau of Standards Seminar on Assay of Electron Capturing Nuclides (April 30, 1952) (unpublished).

Similarity Properties of the Two-Fluid Model of Superconductivity

E. Maxwell
Cryogenics Section, National Bureau of Standards, Washington, D. C.
(Received July 23, 1952)

RECENT measurements[1–3] on superconducting tin isotopes have shown that the threshold curves for the different isotopes are all of the form, $H_c=H_0(T/T_c)$, where H_0 is the critical field at absolute zero of temperature and T_c is the zero-field transition temperature. These form a family of geometrically similar curves, that is, a uniform expansion or contraction of scale transforms one into another. As a consequence of this fact, it can be shown[3] that the corresponding electronic entropies of the superconducting state, $S_{s(el)}(T)$, are also geometrically similar functions of the form

$$S_{s(el)}=\gamma T f(T/T_c), \tag{1}$$

where γ is a parameter and $f(T/T_c)$ a function, both of which are invariant with respect to the isotopic mass. The function is represented within experimental error by either a polynomial in T/T_c or by a single term of the type $(T/T_c)^n$, where n is a positive but not necessarily integral number. This result is significant because it is consistent with features of the two-fluid model of a superconductor not previously subjected to experimental test.

In the two-fluid model proposed by Gorter and Casimir,[4] the electron assembly is visualized as consisting of two phases, a "gaseous" phase of normal electrons having the properties of a Sommerfeld electron gas and a "crystallized" phase of superconducting electrons in a lower energy state. It is assumed that the normal fraction alone contributes entropy and that the superconducting fraction has zero entropy. The fractional concentration of normal electrons x varies continuously from zero to unity as the temperature goes from zero to T_c. The free energies and entropies of the two electron "phases" are given by

$$F_g=\tfrac{1}{2}\gamma T^2x^\alpha; \quad F_c=-\beta(1-x); \tag{2}$$

$$S_g=\gamma Tx^\alpha; \quad S_c=0. \tag{3}$$

The subscripts g and c refer to the "gaseous" and "crystalline" phases, respectively, and $\beta=(H_0^2/8\pi)V_m$, the molar free energy difference between the normal and superconducting states at the absolute zero, (V_m is the molar volume) and γ has the usual significance as the coefficient of T in the electronic entropy of a Sommerfeld electron gas. α is a parameter, characteristic of the metal but not given by the theory. (Empirically it is found that $\alpha\sim\frac{1}{4}$.) The condition that the total free energy of the electron assembly be a minimum determines the temperature dependence of x as

$$x=(H_0^2V_m/4\pi)^{1/(\alpha-1)}T^{-2/(\alpha-1)}. \tag{4}$$

This two-fluid model was originally proposed to explain some of the thermodynamic properties which had been observed in real superconductors. These are the facts: that the free energy difference between the normal and superconducting states vanishes at T_c, and that the electronic entropy of the superconducting state varies as (approximately) the third power of temperature and contains no term linear in the temperature. In addition to these, however, it may be shown that the model also implies the simi-

larity property recently observed in the isotope measurements. Of course the two-fluid model has nothing to say, directly, about an isotope effect, but it does predict how $S_{s(el)}$ should behave if we vary β (or, what amounts to the same thing, the transition temperature, T_c), while keeping the parameters α and γ constant. The isotope measurements are just such an experiment.

Making use of Eqs. (3) and (4) and of the fact that $x=1$ when $T=T_c$, we can write for the total electronic entropy of the superconducting state:

$$S_{s(el)}=\gamma T(T/T_c)^{2\alpha/(1-\alpha)}=\gamma Tt^{2\alpha/(1-\alpha)}, \tag{5}$$

where $t=T/T_c$ is the reduced temperature. Equation (5) immediately sets forth the geometrical similarity property and is of the form of Eq. (1). The similarity feature is inherent in the two-fluid formulation which says that the entropy is that due to a gas of normal electrons, γT, multiplied by a concentration function involving only the reduced temperature t.

Equation (1) is derived in the following way. Starting from the well-known thermodynamic relation,

$$\Delta S=S_n-S_s=S_{n(el)}-S_{s(el)}=-\frac{V_m}{4\pi}H_c\frac{dH_c}{dT}, \tag{6}$$

and expressing the critical field relation in normalized polynomial form,[3]

$$H_c(T)/H_0=h=1-at^2+bt^3+\cdots, \tag{7}$$

we obtain

$$\Delta S=-\frac{H_0^2}{T_c}\frac{V_m}{4\pi}h\frac{dh}{dt}=\frac{H_0^2}{T_c}\frac{V_m}{4\pi}2at+\frac{H_0^2}{T_c}\frac{V_m}{4\pi}\times(-3bt^2-2a^2t^3+5abt^4-3b^2t^5+\cdots). \tag{8}$$

Since $S_{s(el)}$ contains no linear term in T, the first term of Eq. (8) must be identical with $S_{n(el)}$, the electronic entropy of the normal state. This leads to the Kok relation[5] $\gamma/V_m=(H_0^2/T_c^2)(a/2\pi)$, if we set $S_{n(el)}=\gamma T$. Subtracting $S_{n(el)}$ from Eq. (8) then gives for $S_{s(el)}$

$$S_{s(el)}=\gamma T\cdot(3bt+2a^2t^2-5abt^3+3b^2t^4+\cdots)/2a. \tag{9}$$

The geometrical similarity property of the critical field curves insures that γ, a, $b\cdots$ are all invariant with isotopic mass. Consequently Eq. (9) is of the form of Eq. (1) and also possesses the similarity property.

The two-fluid model characterizes the superconductor in terms of three parameters, α, β, and γ. In the experimental work on tin[3] referred to above, it was found that the critical field curves could, within experimental error, also be represented by a three-parameter equation, and the parameters could be directly correlated with the three parameters of the model. In the isotope experiments one of these parameters, β, is changed by varying the atomic mass. The other two quantities, α and γ, remain constant and the similitude properties are accurately described by the two-fluid model without the necessity of introducing any new parameters. This gives good support to the two-fluid theory.

[1] Lock, Pippard, and Shoenberg, Proc. Cambridge Phil. Soc. **47**, 811 (1951); Nature **166**, 1071 (1950).
[2] Serin, Reynolds, and Lohman, Phys. Rev. **86**, 162 (1952).
[3] E. Maxwell, Phys. Rev. **86**, 235 (1952).
[4] C. J. Gorter and H. Casimir, Physik. Z. **35**, 963 (1934).
[5] J. A. Kok, Leiden Comm. **77a** (1934).

Remarks on "Stability of the Laminar Parabolic Flow"

TOMOMASA TATSUMI
Physical Institute, Faculty of Science, University of Kyoto, Kyoto, Japan
(Received July 18, 1952)

PEKERIS' paper on the above subject[1] gives a remarkable result that the laminar parabolic flow is stable for any value of Reynolds number R, in contradiction to earlier results.[2-4] As is shown below, this contradiction is to be attributed to the incompleteness of approximation on Pekeris' part.[5]

Using nondimensional variables, the main flow U and the superposed disturbance ψ are represented, respectively, by

$$U=1-y^2, \tag{1}$$

$$\psi=f(y)\exp[i\alpha(ct-x)], \tag{2}$$

where α is the wave number, $c=c_r+ic_i$, where c_r is the phase velocity and αc_i the logarithmic decrement of the disturbance. Then, from the assumption of small disturbance, $f(y)$ must satisfy the equation

$$f^{iv}-2\alpha^2f''+\alpha^4f+i\alpha R[(1-y^2-c)(f''-\alpha^2f)+2f]=0, \tag{3}$$

subject to the boundary conditions (for even solution):

$$f(1)=f'(1)=f'(0)=f'''(0)=0. \tag{4}$$

If we confine ourselves to the case of small α^2, Eq. (3) can be written as

$$f^{iv}+i\alpha R[(1-y^2-c)f''+2f]=\alpha^2[2f''+i\alpha R(1-y^2-c)f]+O(\alpha^4). \tag{3a}$$

Now we attempt to find the solutions of Eq. (3a) by successive substitutions:

$$f_0^{iv}+i\alpha R[(1-y^2-c_0)f_0+2f_0]=0, \tag{5}$$

$$f_1^{iv}+i\alpha R[(1-y^2-c_1)f_1+2f_1]=\alpha^2(2f_0''+i\alpha R(1-y^2-c_0)f_0]. \tag{6}$$

The general even solutions f_0 and f_1 are given, respectively, by

$$f_0=(1-y^2-c_0)+B_0\varphi(\eta), \tag{7}$$

$$f_1=(1-y^2-c_1)[1+\alpha^2k(y)]+B_1\varphi(\eta), \tag{8}$$

with

$$k(y)=\int(1-y^2-c_1)^{-2}dy\int(1-y^2-c_0)f_0dy,$$

where B_0 and B_1 denote arbitrary constants, and φ is the solution of the equation

$$d^6\varphi/d\eta^6+\eta\cdot d^3\varphi/d\eta^3=0. \tag{9}$$

Therefore,

$$\varphi=\int d\eta\int\eta^{\frac{1}{2}}H_{\frac{1}{3}}^{(2)}[\tfrac{2}{3}\eta^{\frac{3}{2}}]d\eta, \tag{10}$$

with

$$y-y_c=\epsilon\eta, \qquad y_c=(1-c_0)^{\frac{1}{2}}, \quad \epsilon=(2y_c\alpha R)^{-\frac{1}{3}}e^{-i\pi/6}. \tag{11}$$

Imposing the condition (4) upon f_0, we obtain

$$\eta_{10}=\tau_me^{2\pi i/3}, \quad (m=1,2,\cdots), \qquad \tau_1=1.019, \quad \tau_2=3.248,\cdots, \tag{12}$$

where η_{10} denotes the zeroth approximation value of η_1, and $\eta_1=(1-y_c)/\epsilon$ (corresponding to $y=1$). Thus, for the first root, we have

$$c_0=2\tau_1e^{i\pi/6}(2\alpha R)^{-\frac{1}{3}}+O(\epsilon^2)=1.617e^{i\pi/6}(\alpha R)^{-\frac{1}{3}}+O(\epsilon^2). \tag{13}$$

Turning next to the first approximation f_1, the condition (4) imposed on the solution (8) gives, through similar analysis, a secular equation:

$$\left(\frac{d^3\varphi/d\eta^3}{d\varphi/d\eta}\right)_{\eta=\eta_c}=-\frac{\alpha^2}{2y_c\epsilon}\frac{(8/15)-(4/3)c_0+c_0^2}{2-\alpha^2k'(1)}. \tag{14}$$

For the real values of c_1, the asymptotic behavior of the left-hand side of Eq. (14) as $\alpha R\to\infty$ is readily found from Lin's calculation,[3] which leads to the existence of two asymptotic branches of the "neutral curve":

$$R=601\alpha^{-11}, \quad c_1=(4/15)\alpha^2, \quad \text{(the first branch)} \tag{15}$$

$$R=212\alpha^{-7}, \quad c_1=0.611\alpha^2, \quad \text{(the second branch)}$$

On the other hand, if we develop the left-hand side of Eq. (14) near the point $\eta_1=\eta_{10}$, we have

$$\left(\frac{d^3\varphi/d\eta^3}{d\varphi/d\eta}\right)_{\eta=\eta_c}=-\frac{1}{N}(\eta_1-\eta_{10}), \tag{16}$$

where $N=1.483$, the computation of which is given by Pekeris.[1] Further, introducing the expansion

$$c_1=c_0+\alpha^2c_1+\cdots, \tag{17}$$

we have

$$\eta_1-\eta_{10}=\frac{1}{2y_{c\epsilon}}(c_1-c_0)=\frac{\alpha^2}{2y_{c\epsilon}}c_1+O(\alpha^4). \tag{18}$$

Inserting (16) and (18) into Eq. (14) and retaining only the lowest terms in respect to α^2, we have

$$c_1=[(4/15)-\tfrac{1}{2}c_0+\tfrac{1}{2}c_0^2]N. \tag{19}$$

Results (13) and (19) are identical with Pekeris' results P(6) and P(7), so far as the principal terms are concerned, and indicate stability for the disturbance. This approximation $c_0+\alpha^2c_1$ is, however, quite inadequate for evaluating the real eigenvalue c_1, since it leads to the neglect, on both sides of Eq. (14), of the rapid variation of φ and of the imaginary part in k' which usually plays an important role for instability. Thus, it may be concluded that if Pekeris' procedure, that is, the adoption of the expansion (17), is carried out up to further stages of approximation, it would inevitably lead to the earlier conclusion of the existence of the "neutral curve."

Concerning his second result, the prediction of the "second class" of perturbation, Pekeris has reached erroneous results by using an inadequate asymptotic expansion formula for $\alpha R\to\infty$:

$${}_1F_1(a,3/2,x_1)\sim\frac{\Gamma(3/2)}{\Gamma(a)}e^{x_1}x_1^{a-1}(1+O(x_1^{-1})), \tag{20}$$

with

$$a=[5-(1-c_0)(i\alpha R)^{\frac{1}{2}}]/4,\ x_1=(i\alpha R)^{\frac{1}{2}}.$$

Equation (20) represents the asymptotic behavior of ${}_1F_1$ for $x_1\to\infty$ but for finite a, while in our problem both a and x_1 tend to ∞ as $\alpha R\to\infty$. On closer examinations it appears that the "second class" of perturbation is nothing but an alternative expression of the ordinary class of perturbation.

A more detailed account will be published elsewhere.

[1] C. L. Pekeris, Phys. Rev. **74**, 191 (1948).
[2] W. Heisenberg, Ann. Physik **74**, 577 (1924).
[3] C. C. Lin, Quart. Appl. Math. **3**, 117, 218, 277 (1945–46).
[4] D. Meksyn, Proc. Roy. Soc. (London) **A186**, 391 (1946).
[5] See also L. H. Thomas, Phys. Rev. **86**, 812 (1952).

The Interference of Amplitudes in Cascade Processes

O. Halpern
University of Southern California, Los Angeles, California
and
B. A. Lippmann
Nuclear Development Associates, White Plains, New York
(Received July 22, 1952)

THE rate of a two-step cascade emission process leading from a definite initial state 0 through $2j+1$ degenerate intermediate states i to a final state f is proportional to

$$|\Sigma_i H_{0i}H_{if}|^2. \tag{1}$$

Generally, the appearance of the characteristic cross terms in (1) offers difficulties in evaluation. These interference terms were first[1] eliminated analytically by assuming the direction of the emission of the first or second particle to coincide with the axis of the emission of the angular momentum; this procedure is feasible as long as the initial state is unpolarized. Later, more general analytical proofs[2–5] permitted one to include the case of initial polarization, reducing (1) to the expression

$$\Sigma_i|H_{0i}|^2|H_{if}|^2. \tag{2}$$

Still earlier,[6] it had been remarked that the interference terms can be eliminated without calculation by direct appeal to quantum mechanical principles. If the intermediate state can be determined by a measurement compatible with the data assumed for the emitted quantum, all consecutive emissions are independent and the sum (2) reduces to a single term. Such compatible measurements were shown to be possible in the absence of polarization of the initial state if the angular momentum was resolved as described before.

The treatment is here extended for the twofold purpose of eliminating certain complications[7] arising in the case of a polarized initial state and of proving that in the most general cascade process a description can always be introduced according to which each step of the cascade leads to one and only one "causal" intermediate state.

The matrix elements H_{0i} obviously transform like the eigenfunctions ψ_i of the intermediate states; a unitary transformation $\psi_k'=\Sigma_iC_{ki}\psi_i$ will now be chosen so that all $H_{0k}'=\Sigma_iC_{ki}H_{0i}$ become zero except, shall we say, H_{01}'. This is always possible. The array of coefficients C_{ik}, being complex, contains $2(2j+1)^2$ numbers. We have to satisfy $4j+2j+1+2j(2j+1)+2j+1=4j^2+10j+2$ conditions, leaving $2j(2j-1)$ degrees of freedom. The conditions to be satisfied are the following: (a) vanishing of H_{0k}' $(k>1)$ $(4j$ conditions); (b) $(2j+1)$ normalization conditions; (c) $2j(2j+1)$ orthogonality conditions; (d) $(2j+1)$ arbitrary factors $\exp(i\varphi_k)$, one for every ψ_k'.

The remaining $2j(2j-1)$ degrees of freedom can easily be understood as the number of unitary transformations of the eigenfunctions $\psi_k'(k>1)$ among themselves.

In this representation, the summation over i in (2) obviously reduces to a single term; namely, the causal state of the step considered.[8] The extension to cascades of arbitrary length is obvious.

Our description requires, of course, a different unitary transformation (defined by the scheme C_{ik}) for every direction of emission of the quantum (particle). This was already necessary in the simple case discussed before. In the absence of polarization, the axis of resolution of the angular momentum is given by the direction of the emitted quantum; in the presence of polarization, a more involved analytical description leading to the causal state is necessary.

[1] D. R. Hamilton, Phys. Rev. **58**, 122 (1940).
[2] D. L. Falkoff and G. E. Uhlenbeck, Phys. Rev. **79**, 323 (1950).
[3] S. P. Lloyd, Phys. Rev. **80**, 118 (1950).
[4] J. A. Spiers, Phys. Rev. **80**, 491 (1950).
[5] H. A. Tolhoek and S. R. de Groot, Phys. Rev. **83**, 189 (1951).
[6] B. A. Lippmann, Phys. Rev. **81**, 165 (1951).
[7] O. Halpern, Phys. Rev. **82**, 753 (1951).
[8] The connection of our presentation with that given, for example, in reference 5 is established by the remark that the matrix $D_{ii'}=H_{0i}{}^*H_{0i'}$, which Tolhoek and de Groot choose to call a density matrix, is highly singular and reduces to a single term when diagonalized. This fact, not mentioned in reference 5, corresponds to the appearance of our causal state. The elimination of the cross terms automatically removes the summation over intermediate states in (2).

The K/L Ratio for the 90-kev Line of Nd^{147}†

Alan B. Smith and Allan C. G. Mitchell
Indiana University, Bloomington, Indiana
(Received July 9, 1952)

VARIOUS measurements of the spectrum of the 11-day Nd^{147} have been made by several authors. The most recent measurements have been made with the help of magnetic spectrometers using counter recording or photographic plate recording.[1–3] Emmerich and Kurbatov,[1] and Kondaiah[2] used spectrometers with counter recording while Rutledge *et al.*[3] used photographic recording only. The main features of the disintegration scheme, as given by Kondaiah, are three beta-ray groups whose end-point energies are 0.350, 0.470, and 0.223 Mev, and gamma-rays of energies 0.522, 0.392, 0.310, and 0.091 Mev. Many weak internal conversion lines have been observed by Rutledge *et al.* The 0.091-Mev line is highly internally converted. Widely divergent values for the ratio K/L for this line have been obtained by the above-mentioned authors. In view of the wide divergence in the reported values of K/L we undertook an experiment to redetermine this ratio.

The previous authors reported trouble with source thickness since they used Nd^{147} produced by neutron capture. The present measurements were made on a source of Nd^{147} produced as a

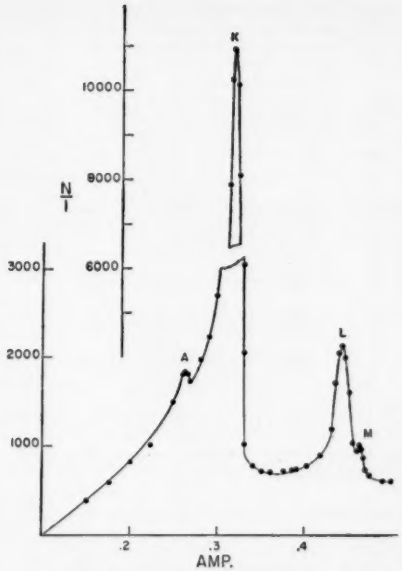

FIG. 1. Internal conversion electrons emitted by Nd^{147}.

fission product in the Oak Ridge pile. Hence it was essentially carrier-free. The measurements were made with a magnetic lens spectrograph using a zapon window, supported on a grid, which would transmit electrons having energies greater than 3.5 kev.

Figure 1 shows the spectrum of the electrons in the region of the internal conversion lines due to the 91-kev gamma-ray. It will be noted that the K, L, and M lines are resolved. In addition an Auger line is also observed. From an $N/H\rho$ plot, the areas under the K, L, and M lines were determined giving the ratios shown in Table I. The only cases in which the L and M lines have been

TABLE I. Ratios of intensities of K, L, and M lines.

	K/L	$K/(L+M)$
Present work	7.55	6.88
Kondaiah	...	6.5
Emmerich and Kurbatov	...	2.5[a]
Rutledge *et al.*	4.9	3.9[b]

[a] Corrected for window absorption.
[b] $K/(L+M+N)$.

resolved are the present work and that of Rutledge *et al.* The present experiment leads to a considerably higher value for K/L than observed by Rutledge *et al.* Most of the experiments on which the empirical curves of Goldhaber and Sunyar[4] are based failed to resolve the M line from the L-line. What they plot as K/L should be, of course, $K/(L+M+N)$. The value of $K/(L+M)$ determined in the present experiment is in excellent agreement with the value of Kondaiah. From the curves presented by Goldhaber and Sunyar for $E2$, $M1$, and $M2$ radiations, the best agreement for the 91-kev line, from its $K/(L+M)$ ratio, is with an $M1$ transition.

† Assisted by the joint program of the ONR and AEC.
[1] W. S. Emmerich and J. D. Kurbatov, Phys. Rev. **83**, 40 (1951); **81**, 1062 (1951).
[2] E. Kondaiah, *Manne Siegbahn Anniversary Volume* (Uppsala, Sweden, 1951); Arkiv Fysik **4**, 84 (1951); Phys. Rev. **81**, 1056 (1951).
[3] Rutledge, Cork, and Burson, Phys. Rev. **86**, 775 (1952).
[4] M. Goldhaber and A. Sunyar, Phys. Rev. **83**, 906 (1951).

Calculation of Range-Energy Relations for Alpha-Particles in Photographic Emulsions

M. BOGAARDT
Joint Establishment for Nuclear Energy Research, Kjeller, Norway
AND
B. KOUDIJS
Physical Laboratory, The University, Utrecht, Netherlands
(Received July 28, 1952)

THE rate of energy loss, dE/dx, by charged particles traversing composite media such as nuclear emulsions, may be calculated by assuming the stopping power of the different constituents of the emulsion to be additive. On this assumption, Bogaardt and Vigneron[1,2] obtained range-energy relations for charged particles in Ilford photographic emulsions that fit very well to experimental data.

The rates of energy loss for the different elements present in the emulsion were calculated on the basis of Bethe's[3] well-known formula, into which Mano's[4] values of the average excitation potentials, I, had been introduced.

The present authors reconsidered Mano's and many other authors' work, aiming to derive more accurate information about average excitation potentials of several elements. The results of this re-evaluation for some of the light elements have been reported recently.[5]

When dealing with heavier elements at low energies of the incident particles, one has to introduce into Bethe's formula correction terms C_K as well as C_L in order to account for the inefficiency in stopping of the K- and the L-electrons, respectively.

The correction term C_L not being known at present, Bethe's formula is not rigorous under these circumstances. One may, however, use the Bethe formula as an empirical formula while not applying the correction term C_L. It can be shown[6] that this procedure provides very satisfactory rates of energy loss in the energy region under discussion. To emphasize this modified use of the formula, the present authors replaced the average excitation potential I by a purely empirical quantity J, and fitted its value such as to make the calculated rate of energy loss agree as closely as possible with the empirical values. Integration of the quantities dx/dE, calculated in this way, supplies range-energy relations which fit the empirical points within the limits of experimental determination. This calculation has been performed for copper, krypton, silver, xenon, and gold in the region of alpha-particle energy from 2 up to 10 Mev.

For carbon, sulfur, bromine, and iodine enough experimental data were not available, so an evaluation of J could not be made. For these elements the values of these quantities were found by interpolation.

The total rate of energy loss suffered by alpha-particles traversing a dry Ilford C2 emulsion has then been computed according to the chemical composition of the plates as indicated by Ilford[7] and using the values gathered in Table I.

TABLE I. Constants used in Bethe's formula (see reference 3) for the rate of energy loss, according to reference 6.

Element	I in ev	J in ev	Element	I in ev	J in ev
H	17½	...	S	197	...
C	75	...	Br	...	425
N	76	...	Ag	...	556
O	96	...	I	...	600

The range-energy relation for alpha-particles in this type of emulsion may then be obtained by integration of the total dx/dE in the energy region between 2 and 10 Mev. The integration constant was determined such as to make the experimental points of Rotblat[8] and the calculated curve coincide as well as possible. Rotblat only published his final range-energy relation, but stated that the departure of any point from the curves was never greater than 2 percent. From Fig. 1 one can see how good the agreement is be-

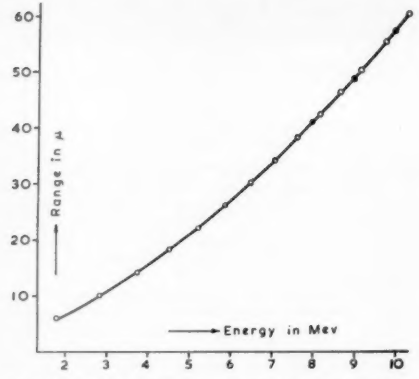

FIG. 1. Calculated range-energy curve for alpha-particles in dry Ilford C2 emulsions. The circles represent readings taken from Rotblat's (see reference 8) and the dots those taken from Catala's (see reference 9) experimental results.

tween the experimental points and the semi-empirical curve. In this figure some readings taken from the curve obtained by Catala and Gibson,[9] are also represented. These points also show very good agreement with the calculated values. Hence one may expect that range-energy relations in other types of emulsions are calculable with rather good accuracy.

[1] M. Bogaardt and L. Vigneron, J. phys. et radium **11**, 652 (1950).
[2] L. Vigneron and M. Bogaardt, Compt. rend. **233**, 940 (1951).
[3] M. S. Livingston and M. A. Bethe, Revs. Modern Phys. **9**, 245 (1937).
[4] G. Mano, Ann. phys. **1**, 407 (1934).
[5] M. Bogaardt and B. Koudijs, Physica **18**, 249 (1952).
[6] M. Bogaardt, thesis, Utrecht (to be published).
[7] Leaflet of Ilford Ltd.
[8] J. Rotblat, Nature **167**, 550 (1951).
[9] J. Catala and W. M. Gibson, Nature **167**, 551 (1951).

New Infrared Absorption Bands in *p*-Type Germanium

H. B. BRIGGS AND R. C. FLETCHER
Bell Telephone Laboratories, Murray Hill, New Jersey
(Received July 31, 1952)

TWO absorption bands have been discovered in the normally transparent region of the infrared in samples of germanium to which *p*-type impurities have been added. The extinction coefficient of a series of such samples of varying conductivity is shown in Fig. 1 as a function of wavelength. The absorption bands at 3.4 and 4.7 microns are clearly evident in all samples, the absorption at each wavelength being approximately proportional to the conductivity. The absorption bands at 15.5 and 19 microns have previously been reported.[1] These latter bands are clearly not due to the presence of the added impurities, as can be seen by comparison with the high purity sample also plotted in Fig. 1. They are probably associated with lattice vibrations.

A further experiment was performed to determine whether the new absorption bands were proportional to the number of acceptor centers present or to the number of free carriers. These were approximately equal to each other for the samples of Fig. 1. Several single crystals were grown which were scheduled to have a fairly uniform distribution of acceptor centers, but part way through the growth process donor impurity was added to the melt. The results from two such samples are shown in Fig. 2. Sample *A* was only partially compensated so that it remained *p*-type, while sample *B* was converted to an even lower resistivity *n*-type. The absorption bands are still present, although much reduced, in the partially

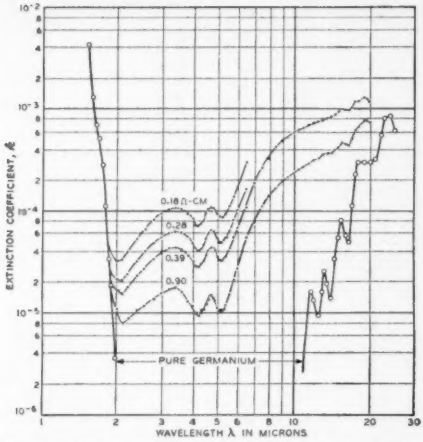

FIG. 1. Extinction coefficients of *p*-type germanium of various resistivities as a function of wavelength. These are compared with pure germanium (circled points).

compensated sample *A*, but entirely disappear in the sample converted to *n*-type. This leads us to conclude that the absorption is proportional to the concentration of free holes and not proportional to the concentration of the acceptor impurities.

Two possible mechanisms are conceived as consistent with the observations. First, the absorption bands may be caused by the presence of unknown impurities or lattice defects. These must be present in the different samples in approximately equal concentrations and must give energy levels which are within 0.1 ev of the filled band in order that the observed absorption be proportional to the number of free holes over the range of resistivities measured (0.1 ev is the approximate location of the Fermi level for the lowest resistivity *p*-type sample used). A second possible mechanism is absorption by the free holes themselves. This latter does not require constancy of the uncontrolled impurity concentration and thus seems more likely. In either event, the fact that we obtain absorption bands rather than continuous absorption suggests that the valence band of germanium has fine structure in the vicinity of 0.3 ev of its upper edge.

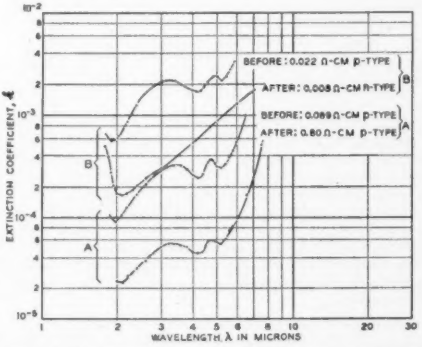

FIG. 2. Extinction coefficients for two germanium crystals containing acceptor centers both before and after donor centers have been added. Crystal *A* was partially compensated to give a higher resistivity *p*-type, while crystal *B* was converted to *n*-type.

If we assume the absorption is by the free holes, then by dividing the absorption coefficient ($4\pi k/\lambda$) by the number of free carriers we can compute a cross section for capture of photons. At 3.4 microns this cross section for holes is 1.5A², while for electrons it is only 0.13A². These are both much larger than the cross section calculated from classical theory, which is of the order of 10^{-3}A² for mobilities of the order of 1500 cm²/volt sec such as are found in these samples. Similar discrepancies with classical theory have previously been pointed out for *n*-type germanium[2] and *p*-type silicon.[2,3]

[1] R. C. Lord, Phys. Rev. **85**, 140 (1952).
[2] H. Y. Fan and M. Becker, *Proceedings of Reading Conference* (Butterworth Scientific Publications, London, 1951), pp. 132–147.
[3] H. B. Briggs, Phys. Rev. **77**, 727 (1950); M. Becker and H. Y. Fan, **76**, 1531 (1949).

The Double Compton Effect

PATRICK E. CAVANAGH
Atomic Energy Research Establishment, Harwell, Didcot, Berkshire, England
(Received July 21, 1952)

AN effect was predicted by Heitler and Nordheim[1] in which, in addition to the normal scattered quantum in the Compton process, one or more further quanta were produced, with decreasing order of probability. For two scattered quanta having comparable energies, and for incident quantum energies $\gg m_0c^2$, the ratio of the cross section to that of the normal Compton process $\sim 1/137$.

Co^{60} γ-rays from a 200-mC source were defined by a horizontal collimator designed to minimize scattering, secondary electrons being removed by a magnetic field. Effects due to coincident γ-rays from the source were negligible. The γ-rays fell on a foil placed perpendicular to the beam, scattered quanta being detected by two NaI(Tl) crystals 2¼ in. in diameter and just under 1 in. thick placed symmetrically in a plane just below, so that they were not struck by the incident beam. They accepted quanta with scattering angles between 45° and 145°, subtended a solid angle at the scatterer of ~4 percent sphere, and were shielded from each other by 20 g/cm² lead to eliminate cross-scattering.

From a preliminary experiment, in which the scatterer was a 170-mg/cm² naphthalene-anthracene crystal, it was found that all coincidences between the quantum counters due to the source were accompanied by the ejection of an electron from the scatterer.

The ratio of the quantum-quantum coincidence rate to the sum of the single quantum rates should be constant and independent of scatterer thickness for coincidences produced by a primary process. In addition to those from the double Compton effect, coincidences may also be produced by a normal Compton process in which the scattered electron suffers an inelastic nuclear collision in the material of the scatterer, resulting in a bremsstrahlung. The coincidence rate due to this secondary process is proportional to the square of the scatterer thickness, if this is fairly small compared with the electron range, and gives rise to a component in the coincidence rate per recorded quantum which varies linearly with scatterer thickness. The magnitude of the component depends on the atomic number of the scatterer.

Scatterers of thickness varying from 40–400 mg/cm² of Be, Al, Cu, and Ag were used. In each case, below ~200 mg/cm², the variation of coincidence rate per recorded quantum with thickness can be represented by the sum of a constant term, and a term varying linearly with thickness, as shown in Fig. 1. The magnitude of the constant term is independent of the atomic number of the scatterer, as it should be for an effect depending only on scattering from free electrons. The coefficient of the linear term $\propto Z^{2.34}$; the increase in the value of the exponent over that appropriate to bremsstrahlung production, $\propto Z^2$, being due possibly to the increased path length of electrons brought about by scattering.

To obtain a rough estimate of the relative cross sections for double and single Compton scattering, it will be assumed that one quantum has the normal distribution and the other is isotropically emitted and detected with 100 percent efficiency. This gives the double Compton cross section, integrated over the energy range 80–530 kev, to be 3×10^{-3} of the single Compton cross section. Mandl and Skyrme[2] have used the Feynman method to calculate the differential cross section where the two quanta are scattered at right angles to each other and to an incident quantum of energy 1 Mev, a case which approximates to the experimental one. Integrating over the energy range accepted by the discriminators and assuming 100 percent detection efficiency, a value for the coincidence rate per recorded quantum of 0.4×10^{-4} results. This is to be compared with the experimental value of 1.0×10^{-4}.

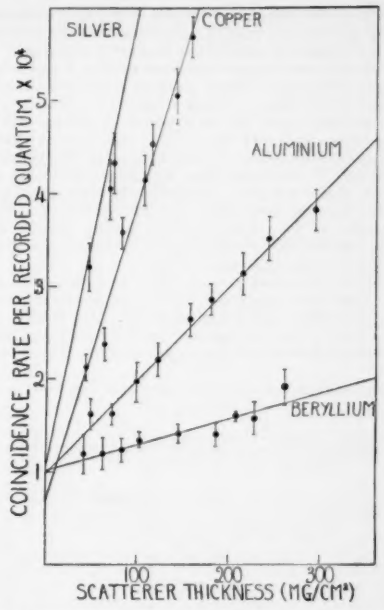

FIG. 1. Coincidence rate per recorded quantum *versus* scatterer thickness.

Thanks are due to Mr. W. H. Taylor and especially to Mr. G. A. Gard for able assistance in performing this experiment. Acknowledgment is made to the Director, Atomic Energy Research Establishment, England, for permission to publish this letter.

[1] W. Heitler and L. Nordheim, Physica **1**, 1059 (1934).
[2] F. Mandl and T. H. R. Skyrme (to be published).

Mobility of Electrons in Germanium

P. P. DEBYE AND E. M. CONWELL*
Bell Telephone Laboratories, Murray Hill, New Jersey
(Received August 4, 1952)

IN the past, measurements of the Hall coefficient and conductivity of *n*-type germanium have yielded mobility values which, although increasing with time and presumably better crystals, were consistently lower than the drift mobility.[1] Measurements have now been made, at room temperature, on a number of new samples in various conductivity ranges which have yielded higher mobilities than any previously found. In the range of resistivity for which drift mobility values are available, these new values substantially agree with the drift mobility values measured

by Haynes.[2] The variation of mobility with impurity content observed in these new samples agrees quantitatively with the theoretically predicted variation due to impurity scattering.

The samples were prepared from single crystals of germanium that had previously undergone extensive purification.[3] Special precautions were taken to obtain a high degree of uniformity within the single crystal. The lower resistivities were obtained by adding arsenic. Slices were cut from these crystals and a suitable sample shape[4] was obtained by using a die driven by a magnetostrictive rod. The measured values of electron Hall mobility are plotted *vs* resistivity in Fig. 1. For the samples which are not near intrinsic, this is just the product of the Hall coefficient R and the conductivity σ. For the near intrinsic samples, electron Hall mobility was obtained by measuring $R\sigma$ over a range of temperatures and extrapolating along a $T^{-\frac{3}{2}}$ line.

The theoretical values shown in Fig. 1 were obtained from a theory based on the assumption that the surfaces of constant energy in the Brillouin zone are spherical. The lattice mobility, μ_L, which, of course, does not depend on impurity content, was taken as 3600, the best value from Haynes' measurements. The impurity

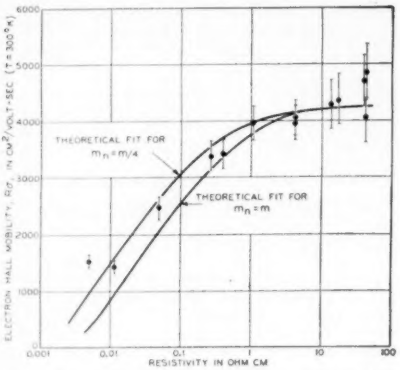

FIG. 1. Electron hole mobility in Ge as a function of resistivity.

mobility was computed from the theoretical formula[5]

$$\mu_I = \frac{8(2)^{\frac{1}{2}}\kappa^2(kT)^{\frac{3}{2}}}{\pi^{\frac{1}{2}}N_I e^3 m_n^{\frac{1}{2}} \ln[1+(3\kappa kT/e^2N_I^{\frac{1}{3}})^2]},$$

where κ is the dielectric constant, taken as 16.1, k Boltzmann's constant, T the absolute temperature, N_I the density of ionized impurities, e and m_n the charge and effective mass of the electron, respectively. N_I was taken equal to the density of conduction electrons. The calculations were done for m_n equal to the mass of a free electron, and one-quarter this value. The two mobilities were combined according to the exact formula,[6] the resulting integral being evaluated numerically.

If the bottom of the conduction band is not degenerate, theory indicates that the ratio of Hall mobility to drift mobility should vary from 1.18, for very pure samples, to 1.93, for very impure ones. Using the published values of this ratio,[7] one can convert the mobility values calculated as described to Hall mobility. The results are shown in Fig. 1. For the very pure samples, 1.18×3600 lies within the range of experimental Hall mobilities, as expected if the energy surfaces are spherical. The excellence of the fit for $m_n = m/4$ would seem to be definite evidence for an effective mass of this order of magnitude. A more precise calculation of the impurity scattering might, however, modify the theoretical impurity mobility sufficiently to affect this estimate of the effective mass considerably. Other evidence for such a value of effective mass comes from data on density of conduction electrons *vs* temperature in germanium, which are best fitted by an effective mass of about this size. Beyond an impurity density of 10^{18}/cm³ a good fit cannot be expected, because the assumptions on which (1) is based are not well justified.

* On leave from Brooklyn College, Brooklyn, New York.

[1] For discussion and references, see W. Shockley, *Electrons and Holes in Semiconductors*, (D. Van Nostrand Company, Inc., New York, 1950). Also G. L. Pearson (private communication).

[2] J. R. Haynes and W. Shockley, Phys. Rev. **81**, 835 (1951).

[3] These crystals were supplied by W. W. Bradley and K. M. Olsen of Bell Laboratories.

[4] G. L. Pearson and H. Suhl, Phys. Rev. **83**, 768 (1951). A similar sample is shown in Fig. 2 of this paper.

[5] E. M. Conwell and V. F. Weisskopf, Phys. Rev. **77**, 388 (1950).

[6] See, for example, reference 1, p. 276.

[7] V. A. Johnson and K. Lark-Horovitz, Phys. Rev. **82**, 977 (1951) and H. Jones, Phys. Rev. **81**, 149 (1951).

K-Shell Conversion Coefficient of Ce^{141}

R. L. HEATH*
Oak Ridge National Laboratory, Oak Ridge, Tennessee
(Received June 18, 1952)

THE K-shell internal conversion coefficient of the 141-kev transition in Pr^{141} has been measured with a NaI scintillation spectrometer. It has also been possible to assign a classification to this transition.

Ce^{141} is known[1] to decay by β^- emission to Pr^{141}. The β^- spectrum of 442-kev end point is followed by a 141-kev gamma-ray.

The response of a 1½-in. diameter by 1-in. NaI crystal to the K x-ray and 141-kev gamma-ray is shown in Fig. 1. The pulse-height

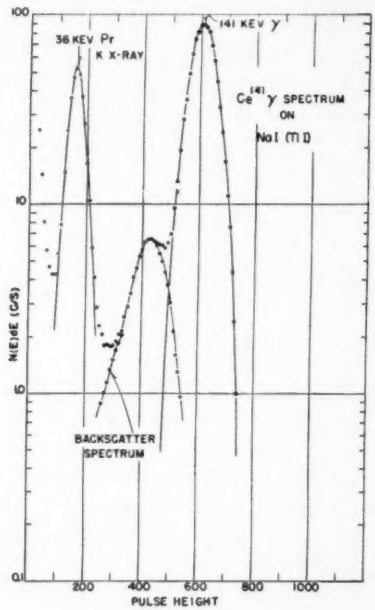

FIG. 1. Spectrum of the γ-radiation of Ce^{141}.

spectrum has been resolved into the gamma-ray, x-ray, and Compton backscatter from a graded shield surrounding the detector. The response of the crystal to scattered radiation was obtained through the use of a "shadow shield" which cut off the

direct radiation. The approximate Compton response of the crystal for the 141-kev gamma-ray was obtained by critically absorbing the x-ray with Sn and Cu.

The intensity of the x-ray has been corrected for the escape of iodine K x-rays from the surface of the crystal. This correction was obtained from computations made for a collimated beam of gamma-radiation entering normal to the surface of a semi-infinite crystal of NaI. A further correction was applied to the intensity of the x-ray for fluorescent yield in the K-shell.[2]

The intrinsic efficiency of the crystal for the γ-ray was based on measurements of the total broad beam absorption cross section of NaI with a scintillation spectrometer. Edge effects have been accounted for by integration over the crystal for a given geometrical arrangement. The ratio of the K x-ray intensity to the gamma-ray yields the experimental value: $\alpha_K = 0.46 \pm 0.02$.

Theoretical K-shell conversion coefficients were obtained by extrapolation of the values of Rose *et al.*[3] For magnetic dipole radiation $\beta_1{}^K = 0.457$ and for electric quadrupole radiation $\alpha_2{}^K = 0.428$. Since these values do not make an assignment conclusive, a measurement of the K/L conversion ratio was made by measuring the intensity of the conversion electrons in coincidence with β^- rays between 250–350 kev on anthracene. A tentative value of 5 ± 1 was obtained. Theoretical values for the K/L conversion ratio were obtained by using the K-shell values of Reitz[4] and L-shell values of Gellman *et al.*[5] From a plot against Z^3/E, for $E2$ radiation $N_K/N_L = 2.7$ for $Z = 49$, and 1.3 for $Z = 84$. For $M1$, the values are 6.8 and 6.0, respectively. Comparison of the experimental value for the K/L conversion ratio, together with the value for α_K, would seem to indicate that this transition is a mixture of $M1$ and $E2$ radiation, $M1$ predominating.

* On loan from American Cyanamid Company, National Reactor Testing Station.

[1] Way, Fano, Scott, and Thew, *Nuclear Data*, National Bureau of Standards Circular 499 (1950).
[2] H. Tellez-Plasencia, J. phys. et radium **10**, 16 (1949).
[3] Rose, Goertzel, Spinrad, Harr, and Strong, Phys. Rev. **83**, 79 (1951).
[4] J. R. Reitz, Phys. Rev. **77**, 10 (1950).
[5] Gellman, Griffith, and Stanley, Phys. Rev. **85**, 944 (1952).

The Anomalous Paramagnetism of Copper Sulfate Pentahydrate

WARREN E. HENRY
Naval Research Laboratory, Washington, D.C.
(Received August 1, 1952)

THE low temperature and high field investigations of paramagnetic ions increase understanding of their quantum behavior (such as adherence to or departure from Brillouin functions), and provides information for the practical problem of producing extremely low temperatures by paramagnetic cooling and determining these temperatures through a knowledge of magnetization behavior.

The Brillouin function for free spins has been shown to be applicable (with almost negligible deviation) up to saturation[1] for iron ($^6S_{5/2}$ state for free ion) ammonium alum[1] and chromium ($^4F_{3/2}$ state for free ion) potassium alum in which specific case the orbital moment is quenched by the crystalline electric field.

However, for copper sulfate pentahydrate, ballistic measurements[1] indicate a pronounced departure of the moment (reproducible to 0.5 percent) of a solid sphere from any Brillouin or other unique function of H/T, Fig. 1. H/T is known to better than 1.5 percent. It is seen that the four magnetic moment isotherms do not superimpose and show a systematic dispersion. These results are in qualitative agreement with the dispersion of calculated magnetic moment isentropes of Geballe,[2] since isothermal and isentropic moments approach each other in the limit of zero field.

The magnetic moment can be calculated[3] from a partition function, provided that the energy levels are known. Thus, a limitation of temperature independent energy levels to a first power dependence on the magnetic field is a necessary condition for the applicability of Brillouin functions. A departure from any Brillouin function can therefore be expected if there are sufficiently large terms in which H occurs in any power besides the first in the energy levels or if the energy levels are sufficiently temperature dependent. Such conditions can arise from various types of interaction as has been shown by several authors.[4] They used Hamiltonians containing terms for the contribution of the crystalline field, spin-orbit interaction, nuclear spin-electron spin interaction, and the like, from which energy levels were calculated.

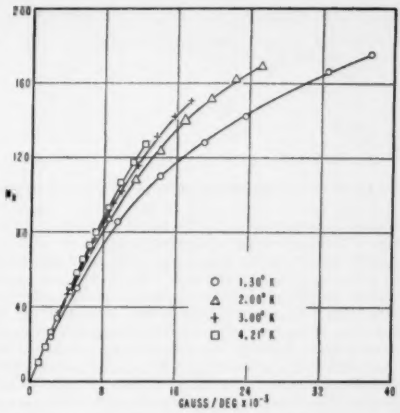

FIG. 1. Plot of relative magnetic moment for a sphere of copper sulfate pentahydrate against the ratio of applied magnetic field to absolute temperature. The four isotherms are for 4.21°, 3.00°, 2.00°, and 1.30°K.

We are unable to account theoretically for the observed variation from the Brillouin function. However, interionic interaction (such as may give rise to antiferromagnetism) and the action of the crystalline electric field through appropriate coupling mechanisms may prove sufficient to account for the observed deviations. Further study of this salt is being carried out to approach nearer to saturation and to make more precise comparisons of experiment and theory.

[1] W. E. Henry, Phys. Rev. **87**, 229 (1952); Phys. Rev. **85**, 487 (1952).
[2] T. H. Geballe, Ph.D. dissertation, University of California (1950) (unpublished).
[3] J. H. Van Vleck, *Electric and Magnetic Susceptibilities* (Oxford University Press, London, 1932), p. 356.
[4] E. F. Carr and C. Kikuchi, Phys. Rev. **80**, 1107 (1950); O. M. Jordahl, Phys. Rev. **45**, 87 (1934).

Angular Correlation of Gamma-Rays in Ti^{48}†

P. S. JASTRAM AND C. E. WHITTLE
Washington University, St. Louis, Missouri
(Received July 28, 1952)

THE angular correlation function has been determined for the cascaded gamma-rays of 1.32 and 0.99 Mev in Ti^{48}. The source used was a sample of V^{48} prepared by deuteron bombardment of titanium dioxide. A careful chemical separation[1] performed after bombardment effectively removed the considerable quantity of impurities formed; in addition, the correlated gamma-rays were identified by verifying that they followed the 16-day half-life of V^{48}. The arrangement of the scintillation counters used is shown schematically in Fig. 1. The coincidence circuit comprised a fast component to provide a time resolution of 8×10^{-9} second and a slow (0.2 microsecond rise-time) amplifier and integral discriminator for energy selection.

The V^{48} nuclide decays by positron emission, so that in addition to the two nuclear gamma-rays from Ti^{48} there are two 0.5-Mev

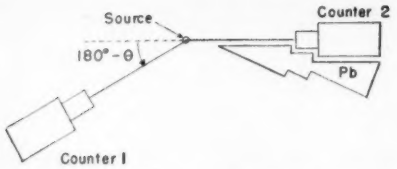

FIG. 1. Arrangement of counters for angular correlation measurements.

annihilation quanta produced in the source container in a large fraction of the decay events. These quanta are uncorrelated in angle with the subsequent gamma-rays, with the result that if care is not taken to discriminate against them, they wash out the correlation. The points marked with triangles in Fig. 2 show the resulting essentially isotropic distribution. Adjusting the discriminators to reject most of the annihilation photons reveals the angular correlation between the two nuclear gamma-rays (circles in Fig. 2). The 180° annihilation peak persists, but is considerably reduced. The experimental points are in good agreement with the distribution $1+(1/8)\cos^2\theta+(1/24)\cos^4\theta$, which holds for spin assignments 0–2–4 for the ground state and first two excited states of Ti^{48}. Ticho *et al.*,[2] using a scintillation spectrometer, have set an upper limit on the number of 2.31-Mev cross-over gamma-rays of 0.5 percent of the 1.32-Mev quanta; of the possible parity assignments for the first and second excited states, this value excludes only odd-even. Hence, while the angular correlation requires that both gamma-transitions must be quadrupole, the low intensity of the cross-over ray excludes only the possibility that they be both magnetic. Present information on the decay scheme of V^{48} is shown in Fig. 3. The K-capture-to-positron ratio[3] (0.72) for the decay of the V^{48} ground state, together with the value 6.1 of $\log(f_{total}t)$ indicates[4] that the transition to the second excited state of Ti^{48} is allowed, so that the spin change involved cannot be greater than ±1; but a spin of 3 for V^{48} is ruled out by the lack of transitions to the first excited state of Ti^{48}: hence, the spin of the ground state of V^{48} must be either 4 or 5.

The value[4] 5.4 of $\log ft$ for the beta-decay of Sc^{48} to the 2.31-Mev state of Ti^{48} precludes a spin change of more than 1 unit. The values 2 and 4 for the spins of the two excited states of Ti^{48}, and the absence of beta-transitions to either the ground state or first excited state[5] establishes that the ground-state spin of Sc^{48} cannot be less than 4 nor more than 5. On the basis of negative results in a search[6] for beta-decay of Ca^{48} to the ground state of Sc^{48}, Jones and Kohman set a lower limit to the partial half-life for single beta-decay of Ca^{48} at 2×10^{16} years; the corresponding $\log ft$ has a minimum value of about 25 (where f is computed from the expression for allowed transitions), appropriate to a Sc^{48} ground-state spin of about 5. It is entirely possible, however, that a small transition matrix element could permit a spin of 4 for the ground state of Sc^{48} to be consistent with the observed minimum half-life for single beta-decay of Ca^{48}.

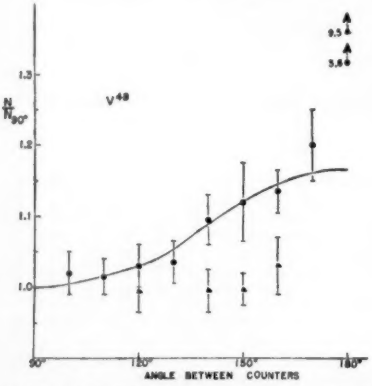

FIG. 2. Angular correlation of Ti^{48} gamma-rays. The points marked with triangles show the uniform distribution due to annihilation radiation background.

Shell model considerations indicate that the Sc^{48} ground state should have even parity. If, as seems likely, the Sc^{48} beta-decay is allowed, then the second excited state of Ti^{48} will also have even

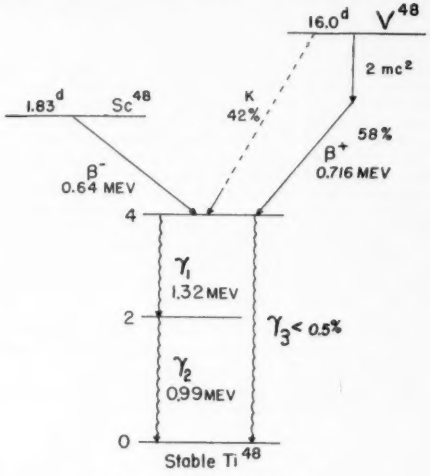

FIG. 3. Decay schemes of Sc^{48} and V^{48}.

parity, with the consequence as remarked earlier that the intermediate state in Ti^{48} can have only even parity. The same parity assignment will hold for the ground state of V^{48}.

To summarize: the results that follow directly from experimental evidence are that the spins of the ground state and first two excited states of Ti^{48} are, respectively, 0, 2, 4; the parities of the two excited states may be anything except the combination odd, even, respectively; for both Sc^{48} and V^{48}, the spin of the ground state is either 4 or 5. Of a more speculative nature are proposed assignments that are at least consistent with all the evidence at hand: even parity for the two excited states of Ti^{48} and the ground states of V^{48} and Sc^{48}, and a spin of 5 for the latter.

† Supported jointly by the ONR and AEC.
‡ The separation was carried out by Mr. Ulrich Merten of the Washington University Chemistry Department.
[2] Ticho, Green, and Richardson, Phys. Rev. **86**, 422 (1952).
[3] Good, Peaslee, and Deutsch, Phys. Rev. **69**, 313 (1946).
[4] E. Feenberg and G. Trigg, Revs. Modern Phys. **22**, 406 (1950).
[5] G. P. Smith, Phys. Rev. **61**, 578 (1942).
[6] J. W. Jones and T. P. Kohman, Phys. Rev. **85**, 941 (1952).

Radioactive Decay of Indium 114

M. W. JOHNS, C. D. COX, R. J. DONNELLY, AND C. C. MCMULLEN
Department of Physics, McMaster University, Hamilton, Canada
(Received August 4, 1952)

IN the decay of In^{114} a 50-day isomeric transition from the 0.192-Mev level to the ground state is followed by a 72-second beta-transition to the ground state of Sn^{114}. In addition to this dominant mode of decay, K-capture occurs in a few percent of the disintegra-

tions. The K-capture transition goes to the 1.28-Mev excited level of Cd^{114}, which is followed by cascade gammas of energy 0.722 and 0.556 Mev.[1,2] On the basis of our angular correlation measurements[3,4] the spins of the three states of Cd^{114} are 2−2−0. These measurements are in agreement with those of Steffen,[5] who has also shown that the transitions to the K-capture branch originate in the ground state of In^{114} and that hence the alternative 4−2−0 interpretation of the angular correlation data is untenable.[6] Boehm and Preiswerk[1] have estimated the number of positrons per disintegration as 10^{-4} and suggest that the end point of the positron spectrum is about 0.650 Mev.

Using the Siegbahn type beta-spectrometer of radius 50 cm built in this laboratory, we have examined the beta- and gamma-spectra of this nuclide. In addition a number of coincidence experiments have been carried out using anthracene detectors in conjunction with a coincidence circuit of resolving time 5×10^{-9} sec.[7] The source consisted of 150 mg of indium metal with an initial specific activity of 1 mC/mg. On the basis of these studies and previous work on this isotope we believe that the decay

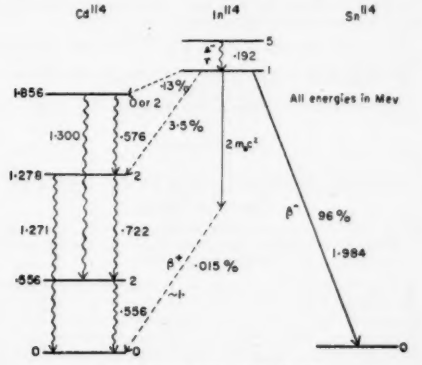

FIG. 1. Proposed decay scheme for In^{114}.

scheme is as shown in Fig. 1. Our evidence for this scheme is presented below.

(a) Using the 50-cm spectrometer, the energies of the gamma-rays were measured by observing the photoelectrons ejected from an 18-mg/cm² Pb radiator of dimensions 2.5×0.5 cm and an instrumental resolution of 0.6 percent. With this resolution a weak photoelectron peak corresponding to a gamma-energy of 0.576 Mev appears between the K and L photoelectron peaks of the 0.556-Mev radiation. In addition the 1.30-Mev peak shows a partially resolved peak on its low energy side corresponding to an energy of 1.27 Mev. The energies of the 0.576- and the 1.300-Mev gamma-rays establish a third excited level in Cd^{114} at 1.856 Mev. A search for the direct transition from this level to the ground state of Cd^{114} gave negative results. If a 1.85-Mev gamma-ray exists, its intensity is less than 0.25 of that of the 1.300-Mev radiation. The relative intensities of the gamma-rays and the number of quanta of each per disintegration were obtained by comparing their intensities with the strongly converted 0.192-Mev radiation. The results of these measurements are summarized in Table I.

(b) With a source of thickness 1 mg/cm², the beta-spectrum has been examined with an instrument resolution of 0.5 percent. The end point of the beta-spectrum was found to be at 1.984 ±0.004 Mev. The strong beta-spectrum made it impossible to detect the internal conversion of the weak gamma-rays listed in Table I.

(c) A coincidence absorption experiment in lead using the circuit and source mentioned above showed that the 1.300-Mev gamma-ray is in cascade with the 0.556-Mev radiation. In this experiment one counter was unshielded while the other was shielded with from 0 to 10 cm of Pb. For thicknesses greater than 5 cm the absorption curve followed the correct slope for a 1.3-Mev gamma-ray as determined by a repetition of the experiment with a Co^{60} source.

TABLE I. Energies and intensities of the gamma-rays of In^{114}.

Energy Mev	Relative intensities	Quanta per 100 disintegrations of In^{114}
0.192	5.4	19.3
0.556±0.001	1.02	3.6
0.576±0.003	0.03	0.1
0.722±0.001	1.00	3.5
1.271±0.006	0.008	0.02
1.300±0.003	0.043	0.12

(d) Since the two 0.511-Mev quanta produced upon annihilation of a positron are emitted in opposite directions, positron absorption in the source will affect the $\gamma-\gamma$ coincidence rate only when the angle formed by the counters at the source is 180°. By measuring the positron contribution to the $\gamma-\gamma$ rate with a small source enclosed in sufficient matter to stop all the positrons, we have determined that $1.5\pm0.5\times10^{-4}$ positron occur per disintegration. (The previous value reported[4] is in error.)

(e) By using an indium foil (100 mg/cm²) as source and aluminum absorbers we have been able to measure the number of positrons stopped as a function of the thickness of aluminum placed around it. The experimental data is consistent with that expected for a beta-spectrum whose end point lies in the range 1.0 to 1.4 Mev. This result supports the value of the $In^{114}-Cd^{114}$ mass difference of 2.07±0.2 Mev as obtained by McGinnis[8] from $p-n$ threshold measurements.

Using the 2.07-Mev energy difference and the intensities in Table I, the logft values for the transitions from the ground state of In^{114} to the 0, 0.556-, 1.28-, and 1.85-Mev levels of Cd^{114} are 5.0, >5.3, 3.5, and 3.7, respectively, while that of the β^- branch is 4.4.

One might surmise that the spin of the 1.85-Mev level is either 0 or 2. It is known from the angular correlation measurements that the experimental data does not give a good fit to the theoretical 2−2−0 curve even with a dipole-quadrupole mixture for the 2−2 transition. This discrepancy may be due to the 1.300−0.556 Mev cascade which would be expected to distort the observed correlation. If this cascade were either 0−2−0 or 2−2−0 its effect would be of the correct magnitude to remove the discrepancy between theory and experiment in the strong 0.722 −0.556 Mev cascade.

The financial support received from the Research Council of Ontario and the National Research Council of Canada is gratefully acknowledged.

[1] F. Boehm and P. Preiswerk, Helv. Phys. Acta **22**, 331 (1949).
[2] Mei, Mitchell, and Zaffarano, Phys. Rev. **76**, 1883 (1949).
[3] Johns, Cox, and Petch, Trans. Roy. Soc. Canada III, **45**, 174 (1951).
[4] Johns, Cox, and McMullen, Phys. Rev. **86**, 632 (1952).
[5] R. M. Steffen, Phys. Rev. **83**, 166 (1951).
[6] R. M. Steffen and W. Zobel, Bull. Am. Phys. Soc. **27**, No. 4, 19 (1952).
[7] H. E. Petch and M. W. Johns, Phys. Rev. **80**, 478 (1950).
[8] C. L. McGinnis, Phys. Rev. **81**, 734 (1951).

Helium Film Transport over Copper below 1°K*

L. LESENSKY AND H. A. BOORSE†
Pupin Physics Laboratories, Columbia University, New York, New York
(Received August 4, 1952)

RECENTLY Ambler and Kurti[1] have measured the transport rate of the He II film over glass down to 0.15°K. The results show the very interesting feature of an increased rate beginning at about 0.9°K and rising thereafter down to the lowest temperatures. The purpose of this letter is to report the result of some film measurements over a copper surface carried out with

an electronic technique[2] over the temperature range from the λ-point to 0.75°K.

Earlier results[2] from this laboratory showed that the transport rate over machined copper is reasonably reproducible and for this reason, as well as for convenience, a copper surface was used in the present experiments. Temperatures below 1°K were obtained by adiabatic demagnetization of iron ammonium alum (Fig. 1, curve A) and of gadolinium sulfate octahydrate (Fig. 1,

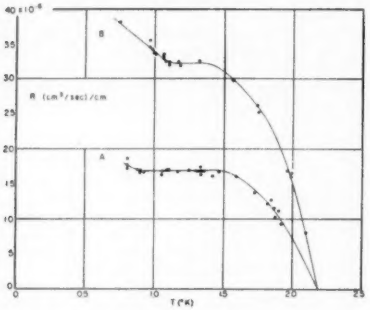

FIG. 1. Transport rate of the He II film as a function of temperature. (A) clean machined copper; (B) contaminated machine copper.

curve B) and were measured by means of the changes in self-inductance of a single layer coil which currounded the salt. The self-inductance was determined by the use of an Anderson bridge operated at 1000 cps. The sensitivity of balance was made independent of the temperature of the coil by placing a variable resistance in the inductive arm. It was possible at all temperatures to determine variations of 0.2 μh in a self-inductance of approximately 2.5 mh. The self-inductance was plotted against the reciprocal of the Kelvin temperature determined from equilibrium vapor pressure readings. The resultant straight line had a slope of approximately 180 μh per reciprocal degree for gadolinium sulfate and 85 μh per reciprocal degree for iron alum.

The electronic technique previously described[2] required a calibration based on visual observation of the helium level in the apparatus. In the present measurements this procedure was no longer necessary since convenient markers of the helium level were provided by grooves or shoulders (Fig. 2) which had been

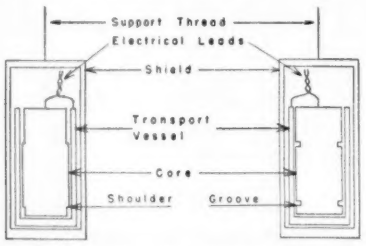

FIG. 2. Simplified sectional views of transport vessel and shield.

cut into the core of the cylindrical capacitor. This modification enabled the rate measurement to be made by noting the elapsed time required to empty the known annular volume of liquid helium from the region between the markers.

In all the experiments the salt and liquid helium were contained in a completely silvered glass vessel in which the temperature could be reduced to about 1°K by pumping on the liquid helium. The capacitor type transfer vessel was suspended in the helium-and-salt chamber by a thread attached at its upper end to a winch so that the vessel could be raised or lowered. Considerable difficulty was experienced in maintaining sufficient thermal isolation. Although temperatures as low as 0.4°K were obtained with the small magnet at our disposal, the initial rates of heating were too large to obtain reliable measurements below 0.75°K. It was expected that various modifications which were made from time to time would improve the isolation but this has not proved to be the case. Since the experiments are being temporarily discontinued, we are reporting the data thus far obtained.

The results are shown in Fig. 1. The data shown on curve A represent three experimental runs, the part below 1°K consisting mostly of results obtained in one of the runs (8/2/51). It is to be noted that these rates are approximately in agreement with those of Dash and Boorse for an uncontaminated machined copper surface. Curve B, on the other hand (data of 11/12/51), shows much higher rates than curve A. The high rates are believed to have been due to contamination.[3] Attention is directed to the fact that curve B shows a much more pronounced rise at the lower temperatures whereas curve A is essentially constant down to at least 0.9°K with perhaps the start of a rise at 0.8°K.

* Assisted by the ONR, Linde Air Products Company, and Research Corporation.
† Barnard College, Columbia University, New York, New York.
[1] E. Ambler and N. Kurti, Phil. Mag. **43**, 260 (1952).
[2] J. G. Dash and H. A. Boorse, Phys. Rev. **82**, 851 (1951).
[3] R. Bowers and K. Mendelsohn, Proc. Phys. Soc. (London) **A,63**, 1318 (1950).

α-Energy Systematics and Proton Shells for Heavier Nuclei

S. SENGUPTA
Physics Laboratory, Krishnagar College, Krishnagar, Calcutta, India
(Received July 7, 1952)

THE variation of α-energies of different isotopes of a nuclei has been studied by a number of authors.[1–4] They have shown that E_α for different isotopes of an element decreases almost linearly with increasing neutron number. However, at certain points the relation is reversed and there is a very sudden increase in the α-energy. These reversals are associated with particularly stable neutron shells and consequent sudden drops in the binding energy of the neutrons. From the point of reversal we can easily determine the magic neutron number for which a completed shell exists.

Recent extension of the table of known α-active nuclei[5] makes possible a similar study of the α-energies of different isotones. Great regularities are noticed if the α-energies for nuclei with the same number of neutrons are plotted against Z. In Fig. 1 such a plot is given for several neutron numbers. The data are all taken from Seaborg *et al.*[5] and Perlman *et al.*[4] E_α in the figure denotes the total decay energy. It is seen from the figure that the general trend here is an increase of E_α with Z. The curves are fairly well represented by approximately parallel straight lines. It is also clearly seen that at certain proton numbers there is a very sudden increase in E_α. These jumps are quite well marked and cannot be confused with the regular trend.

If $B_p(N, Z)$ be the binding energy of the last proton in the nucleus (N, Z), then it can easily be shown that

$$E_\alpha(N, Z) - E_\alpha(N, Z-1) = B_p(N-2, Z-2) - B_p(N, Z).$$

If we are proceeding from higher to lower Z, then a sudden drop in the value of $E_\alpha(N, Z-1)$ must be due to either a sudden increase of $B_p(N-2, Z-2)$ or a sudden decrease of $B_p(N, Z)$. The latter cannot be true since B_p values always increase with decreasing Z (see Fuchs[6]). Thus we conclude that, for decreasing Z, a sudden drop in E_α at (N, Z) is associated with a sudden increase in the proton binding energy at $(N-2, Z-2)$. Thus the proton number $Z-2$ must be regarded as a magic number giving rise to a closed proton shell.

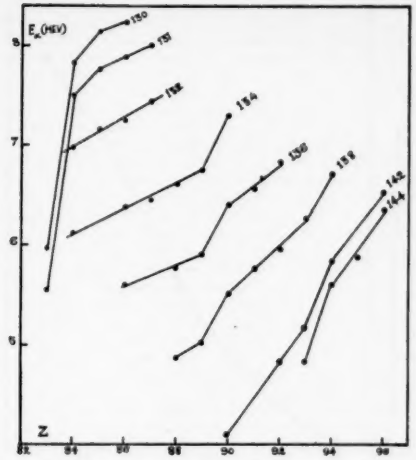

FIG. 1. Variation of E_α with Z. Constant neutron number is shown at the end of each curve.

In Fig. 1 we get a very sharp fall of E_α of about 2 Mev at $Z=84$, which obviously is due to the well-known proton shell at $Z=82$. In addition to this, however, we get two other less marked falls of about 0.7 and 0.5 Mev at $Z=94$ and 90, respectively. These probably correspond to proton subshells at $Z=92$ and 88. It may be noted that Stahelin and Preiswerk's[7] analysis of the energy of the first excited states of even-even nuclei has also revealed a magic number at $Z=92$.

According to Mayer's scheme[8] there ought to be a proton subshell at 92 due to the completion of the $1h_{9/2}$ level. However, this is not corroborated by the spin data, as has been shown by Dube and Jha.[9] According to the above scheme both $_{89}Ac^{227}$ and $_{91}Pa^{231}$ should have spin 9/2. Actually both are found to have a spin 3/2. These experimental values clearly indicate that from $Z=89$ to 92 the four protons must be filled in the $3p_{3/2}$ level. This at once gives us two subshells at $Z=88$ and 92, in agreement with what is found from our present investigation. The level order after $Z=82$ seems to be $2f_{5/2}$, $3p_{3/2}$, rather than $1h_{9/2}$, $2f_{7/2}$, as is given by the square well potential. But then the spin 9/2 of $_{83}Bi^{209}$ turns out to be anomalous.

A more detailed discussion of these and other related points will soon be published in a separate paper.

[1] G. Fournier, Compt. rend. **184**, 878 (1927).
[2] W. Elsasser, J. phys. et radium **4**, 635 (1934).
[3] A. Berthelot, J. phys. et radium **3**, 17 (1942).
[4] I. Perlman *et al.*, Phys. Rev. **77**, 26 (1950).
[5] G. T. Seaborg *et al.*, Revs. Modern Phys. **20**, 585 (1948).
[6] K. Fuchs, Proc. Cambridge Phil. Soc. **35**, 242 (1939).
[7] P. Stahelin and P. Preiswerk, Helv. Phys. Acta **24**, 623 (1951).
[8] M. G. Mayer, Phys. Rev. **78**, 16 (1950).
[9] G. P. Dube and S. Jha, Phys. Rev. **85**, 1042 (1952).

Superconductivity below 1°K

M. C. STEELE
Naval Research Laboratory, Washington, D. C.
(Received July 24, 1952)

IN their study of superconductivity below 1°K, Daunt and Heer[1] observed an excess "paramagnetism" as the specimen of paramagnetic salt and superconducting metal warmed up in the presence of a finite applied magnetic field (Fig. 1).

The extrapolated dashed curve in Fig. 1 represents the paramagnetism of the salt alone. That portion (from C to B) of the full curve which lies below the dashed curve represents the situation when the metal has a diamagnetic susceptibility (in the superconducting state). From B to A the system exhibits a paramagnetic susceptibility in excess of that due to the salt alone.

It is the purpose of this note to suggest an explanation for the shape of this warm-up curve which is not restricted to multiply-connected superconductors.[1] Figure 2 shows typical isothermal (dashed lines, with $T_1<T_2<T_3\cdots$) and isentropic (solid lines, with $S_1<S_2<S_3\cdots$) magnetization curves for a large ideal super-

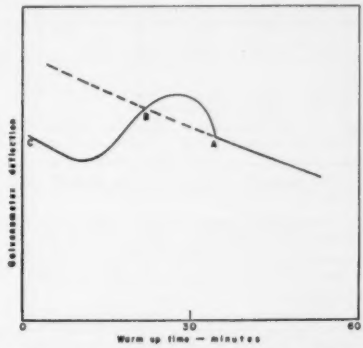

FIG. 1. Typical curve showing change of susceptibility with warm-up time in the presence of a small applied magnet field.

conducting sphere. The isentropic lines were obtained from the critical field and entropy data for tin. The other superconductors should give similar curves. The curves are plotted on a dimensionless basis with H_0, the critical field at $T=0$°K, as the normalizing factor. The vertical line in Fig. 2 represents the field h_1 in which the warm-up curve was observed. We seek the derivative $\partial\mu/\partial h$ (the differential susceptibility) of the magnetization curves at $h=h_1$. At this point we must distinguish between the isothermal and isentropic situations. In experiments such as carried out by Daunt

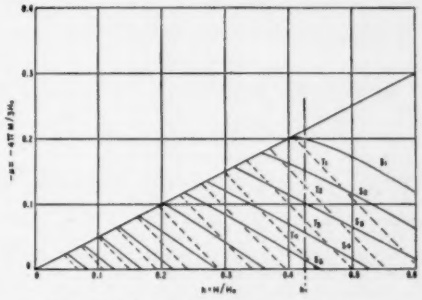

FIG. 2. Typical magnetization curves for an ideal large superconducting sphere.

and Heer[1] the process would be more nearly isentropic than isothermal. Hence, a plot of $(\partial\mu/\partial h)_S$ as a function of reduced temperature ($t=T/T_c$, T_c is the zero field transition temperature) is shown as the solid line in Fig. 3. For a real sphere the discontinuities shown in Fig. 3 would be replaced by smoothed curves.

Since increasing time in Fig. 1 corresponds to increasing temperature, it is clear that the essential features of the observed full curve can be obtained from a superposition of the dashed curve in Fig. 1 and a curve having the general shape shown in Fig. 3. If the

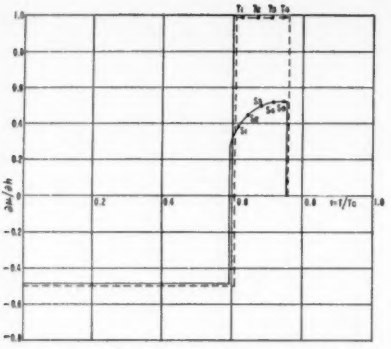

FIG. 3. Differential susceptibility as a function of temperature.

process were isothermal one would get a differential susceptibility given by the dashed line in Fig. 3. It is noted that the shape of the solid curve in Fig. 3 is a function of the applied field h. This should reflect itself in a change in the warm-up curves (Fig. 1) as the fields are varied.

Preliminary experiments performed at this laboratory in studying the critical magnetic field curves for ruthenium and cadmium have revealed warm-up curves which are considerably different from that shown in Fig. 1. Since the metal particles used for these experiments were much smaller than those of previous workers, the difference in warm-up curves may be associated with size effects in the superconductors. This supposition is made plausible in terms of the suggested explanation given above when one examines the isothermal magnetization curves of small superconducting spheres.[2] In fact one can utilize the warm-up curves obtained for small particles to construct the magnetization curves. Such data would be useful in the study of penetration depths for those elements having transition points below 1°K. Such a program is now in progress at this laboratory.

The author wishes to thank M. F. M. Osborne for profitable discussions relating to this problem.

[1] J. G. Daunt and C. V. Heer, Phys. Rev. **76**, 1324 (1949).
[2] D. Shoenberg, Proc. Roy. Soc. (London) **A175**, 49 (1940).

Cross Section for the Reaction $Br^{81}(\gamma,\alpha)As^{77}$

J. G. V. TAYLOR AND R. N. H. HASLAM
Department of Physics, University of Saskatchewan, Saskatoon, Saskatchewan, Canada
(Received July 30, 1952)

THE cross section for the (γ,α) reaction in Br^{81} has been found by counting forty-hour As^{77}. Arsenic was separated from sodium bromide which had been irradiated with the University of Saskatchewan betatron. Ten ninety-gram samples of reagent NaBr were irradiated at betatron energies from 16.0 to 25.4 Mev. Arsenic was precipitated from solutions 3N in HCl and obtained for counting as As_2S_3. The usual counting corrections were applied. The chemical yield determined gravimetrically was 100 percent. It was assumed that exchange of active and carrier ions was complete.

X-ray doses were recorded by tantalum monitors mounted at the front of each sample, appropriate corrections being made for inverse square attenuation and x-ray absorption in the sample.

The yield curve is shown in Fig. 1. No attempt was made to determine yields at energies lower than 16 Mev on account of the very long irradiations that would have been necessary. From the yield curve the cross section, Fig. 2, was computed by the photon difference method.[1] This cross section has a peak value of 270 microbarns at 21.5 Mev. The integrated cross section is about

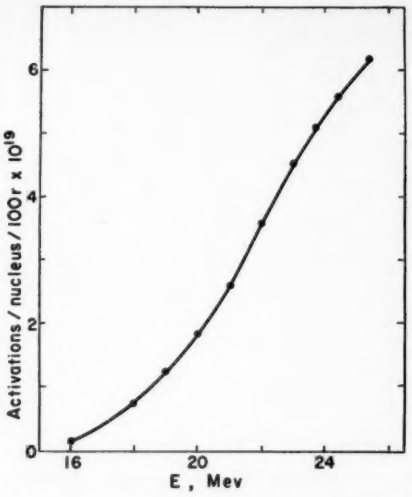

FIG. 1. Yield curve for $Br^{81}(\gamma,\alpha)As^{77}$. The number of activations/Br^{81} nucleus/100 roentgens is plotted against the maximum betatron energy in Mev.

1.5 Mev-millibarns. In shape this cross section is quite similar to those found for $Cu^{65}(\gamma,\alpha)Co^{61}$,[2] and $Rb^{87}(\gamma,\alpha)Br^{83}$,[3] while in magnitude it lies between them, the cross sections declining with increasing atomic number. This trend is similar to that observed for photoproton yields from middle-weight nuclei.[4]

It is of interest to compare our result with measurements of alpha-tracks arising from the photodisintegration of bromine and silver in nuclear emulsions.[5–7]

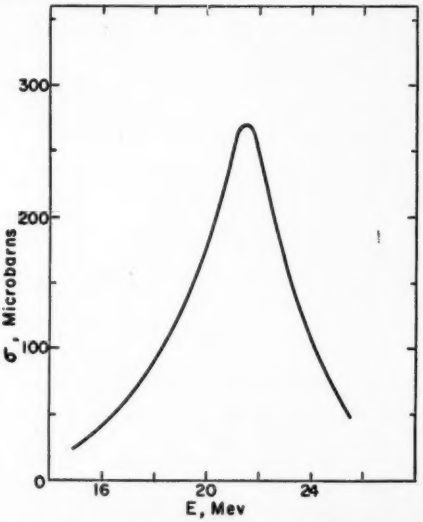

FIG. 2. Cross section for $Br^{81}(\gamma,\alpha)As^{77}$. The cross section in microbarns is plotted against photon energy.

Nabholz, Stoll, and Wäffler[5] have investigated the energy distribution of α-particles ejected from heavy nuclei in photographic emulsions by lithium γ-rays. They estimate that the contribution of silver to the spectrum at its peak is negligible but find close agreement between the observed spectrum and that calculated from statistical theory for bromine. Accordingly they calculate the average $Br^{79,81}(\gamma,\alpha)$ cross section at 17.6 Mev to be $(1.2\pm0.5)\times10^{-28}$ cm². For Br^{81} at this energy we find the cross section to be 0.80×10^{-2} cm². Making the same assumptions as Nabholz *et al.* regarding the cross-section ratios for the two isotopes we obtain 1.3×10^{-28} cm² as the average cross section for bromine at 17.6 Mev, in agreement with the above value.

It might be noted that the small number of α-particles with energies higher than the theoretical spectrum for bromine in Fig. 1 of reference 5 might arise from silver and would in no way affect the good agreement noted above.

Haslam, Cameron, Cooke, and Crosby[6] made no attempt to separate the effects of silver and bromine since their observed α-spectrum did not agree closely with theoretical distributions for either element. The methods described in their paper, while suitable for investigation of the general features of photo-alpha processes, are not well adapted to accurate determination of cross sections at a particular energy. Statistics in photographic emulsion work are poor, and the effect is aggravated by the use of a continuous rather than a discrete photon spectrum. If silver is assumed to make a negligible contribution at 17.6-Mev excitation, a cross section of 3×10^{-28} cm² for an average bromine nucleus is obtained, but this value is open to considerable doubt due to the steepness of the cross-section curve in this energy region.

We wish to thank Dr. K. J. McCallum of the Department of Chemistry for helpful advice and Mr. L. H. Greenberg for valuable discussions. This work was supported by the National Research Council of Canada.

[1] L. Katz and A. G. W. Cameron, Can. J. Phys. **29**, 518 (1951).
[2] Haslam, Smith, and Taylor, Phys. Rev. **84**, 840 (1951).
[3] R. N. H. Haslam and H. M. Skarsgard, Phys. Rev. **81**, 479 (1951).
[4] A. K. Mann and J. Halpern, Phys. Rev. **82**, 733 (1951).
[5] Nabholz, Stoll, and Wäffler, Phys. Rev. **86**, 1043 (1952).
[6] Haslam, Cameron, Cooke, and Crosby, Can. J. Phys. (to be published).
[7] C. H. Millar and A. G. W. Cameron, Can. J. Phys. (to be published).

The Angular Distribution of Fission Fragments in the Photofission of Thorium*

E. J. Winhold, P. T. Demos, and I. Halpern
Physics Department and Laboratory for Nuclear Science, Massachusetts Institute of Technology, Cambridge, Massachusetts
(Received July 28, 1952)

MEASUREMENTS of the angular distribution of photofission fragments from thorium have been made using the x-ray beam of the MIT linear accelerator. They were performed by counting the β-activities of the fragments which were emitted from a thorium foil and caught at various angles to the x-ray beam. The observed angular distribution has a maximum at right angles to the beam and the amount of the anisotropy decreases with increasing photon energy.

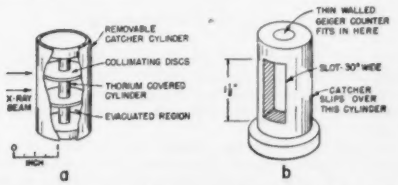

FIG. 1. The arrangements for exposure and counting of the cylindrical fragment catcher. After exposure the catcher is slipped over the cylinder in *b* and rotated so as to expose (to the counter inside) the activities caught at various angles to the x-ray beam.

With the accelerator running at about 16 Mev, the set-up shown in Fig. 1(a) was exposed at 6 inches from the x-ray target. It consists essentially of two concentric cylinders; the inner one is covered with thorium foil which is thick to fission fragments and the outer one serves as the fragment catcher. The activities of 30°-wide strips of this catcher cylinder (each strip corresponding to a different angle of fragment emission with respect to the beam) are measured after the exposure by means of the arrangement of Fig. 1(b).

A number of runs have been made at 16 Mev with this arrangement, and the results are given in the following table normalized

#	0°	45°	90°	135°	180°	270°
Measured activity for slot 30° wide	1.00	1.14 ±0.05	1.34 ±0.03	1.22 ±0.07	1.00 ±0.06	1.31 ±0.07

to the activity at 0° with respect to the x-ray beam. It is seen that the distribution is peaked at 90° and is symmetrical from front to back. These facts and the amount of activity measured at 45° and 135° suggest that the angular distribution can be written in the form $a+b\sin^2\theta$. When the data in the table is corrected for the

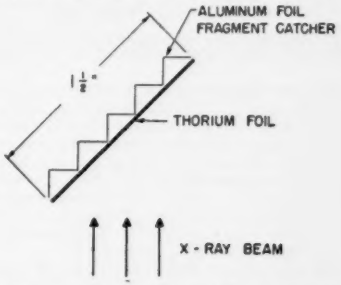

FIG. 2. The exposure geometry used in the energy-dependence runs.

finite angular resolution of the exposure and counting arrangements,[1] the ratio b/a is 0.41 ± 0.09. Some small corrections have been made for x-ray flux variations over the target, and it was established that a negligible fraction of the observed fissions are caused by fast neutrons.

It is conceivable that the measured asymmetry might involve not only different numbers of fragments at 90° and 0°, but also different types of fragments. To check this possibility, the exposure time in the experiment was varied. No dependence of the angular asymmetry on exposure times (from 6 minutes to 3 hours) or on the counting time was found. This would seem to imply that the same fragments are emitted in all directions. The question of a possible connection between the angular distribution and the fragment mass distribution is being investigated more carefully at the present time by means of a technique involving chemical separations.

In order to examine the energy dependence of the angular distribution it was necessary to use the arrangement of Fig. 2. This arrangement sacrifices angular resolution in order to keep the intensity up at the lower energies, where the photofission yield is small. A sheet of one-mil aluminum foil folded into a step-like shape serves as the fragment catcher; it is exposed next to a thorium foil set at 45° to the x-ray beam. Thus alternate faces receive fragments emitted mainly at 90° and 0° to the beam. After exposure the foil is flattened out and counted under a brass mask covering either set of faces. Checks were made to show that flux non-uniformities and the counting geometry introduced no serious errors in the results.

The geometrical corrections for angular resolution are necessarily rather large in this arrangement. At 16 Mev the measured activity ratio was 1.09 ± 0.03 for the 90° faces to the 0° faces. This

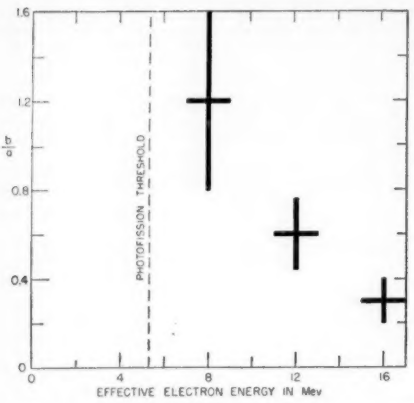

FIG. 3. The dependence of the asymmetry b/a as a function of effective electron energy for an angular distribution of the form $a+b\sin^2\theta$.

corresponds to a value for b/a of 0.30 ± 0.10, agreeing with the cylinder results within the errors of the two experiments.

A number of runs using the step-like geometry were made at energies from about 8 to 16 Mev. The asymmetry was found to increase rapidly as the accelerator energy was decreased (Fig. 3). Unfortunately the electron spectrum is about 3 Mev wide and it has not been possible to determine the "effective energy" of the electrons to better than about 1 Mev. This energy uncertainty and the use of a thick x-ray target prevent us at present from being able to give b/a as a function of photon energy.

No really convincing explanation of the observed angular distribution has so far been developed. The form of the distribution suggests an electric dipole transition, but the ratio of e/m values for the fission end products does not indicate a process involving a particularly large dipole moment. The energy dependence shows, moreover, that the effect is not largest at the dipole resonance peak in thorium (~15 Mev). This may, however, not be particularly significant because most fissions caused by 15-Mev photons may come from (γ,nf) reactions rather than (γ,f) reactions and the former would perhaps be expected to give a more isotropic fragment distribution. If very strong selection rules obtain for the allowed spins of the fragments at the moment of fission, the angular momentum brought in by the photon might on the average go mostly to the orbital momentum between the fragments. Although this would "explain" an angular distribution, it involves a rather arbitrary assumption. In order to investigate any dependence of the angular distribution on spins, we are preparing to repeat the experiment with a number of other fissionable materials having various ground-state spins.

* This research has been supported by the joint program of the ONR and AEC. A preliminary report appears in Phys. Rev. **85**, 728 (1952).

[1] In this geometrical correction, it is assumed that fragments emitted isotropically would emerge from a thick foil in a cosine distribution with respect to the foil normal. This has been checked experimentally to about 10 percent.

The Beta-Spectrum of He^6†

C. S. WU, B. M. RUSTAD, V. PEREZ-MENDEZ, AND L. LIDOFSKY
Columbia University, New York, New York
(Received August 5, 1952)

THE beta-spectrum of He^6 is of great theoretical interest. Not only can its linear Kurie plot serve to exclude one of the Fierz interference terms (A, T), but its end point together with its half-life determines an ft value which helps to estimate the relative contributions of the Fermi (S or V) and Gamow-Teller (A or T) interactions in the process of beta-decay.

The only reported measurement of the He^6 beta-spectrum was made on a semicircular focusing magnetic spectrometer and gave an end point of 3.215 Mev.[1] This end point together with $t_{\frac{1}{2}}=0.823\pm0.013$ sec[2] yields an ft value of 584 sec.

Because of its theoretical interest we have recently remeasured the beta-spectrum of He^6 using the Columbia magnetic solenoidal spectrometer whose characteristics have been well investigated.

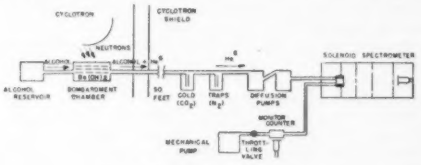

FIG. 1. Block diagram of apparatus.

The spectrometer was placed about 50 feet from the cyclotron to minimize the effects of stray fields from the cyclotron magnet. The spectrometer axis was oriented parallel to the small horizontal component of the nearly vertical stray field, while the vertical component was compensated by a pair of Thomson coils.

The He^6, produced by the reaction $Be^9(n,\alpha)He^6$, was swept from the target chamber with ethyl alcohol vapor. Before reaching the spectrometer source chamber, the alcohol vapor was frozen out in CO_2 and N_2 cold traps and the He^6 concentrated by two successive oil diffusion pumps as shown in Fig. 1.

The source chamber was an aluminum cylinder 1.5 cm diameter by 1 cm depth with a 2-mg/cm² mica front window and a 3-mg/cm² mica back window. After passing through the source chamber, the He^6 entered a monitor counter chamber and was finally evacuated by a mechanical pump.

Data were taken in the following manner to reduce background from the cyclotron. The cyclotron was turned on for 5 sec. A half-

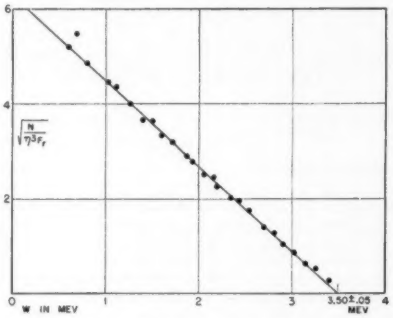

FIG. 2. Kurie plot of He^6 beta-spectrum.

second later, the spectrometer and monitor GM counters were turned on for 5 sec. This cycle was controlled by a system of relays actuated by a cam shaft driven by a synchronous motor. Under these conditions the radioactive purity of the source was >98 percent.

The baffle slit in the spectrometer together with the source volume used gave 5–6 percent resolution. The Kurie plot shown in Fig. 2 is linear from its end point of 3.50 ± 0.05 Mev to about 0.6 Mev, below which counting statistics became very poor. The end point together with $t_{\frac{1}{2}}=0.823$ yields the ft value of He^6 of 815 ± 70 sec.[3] Moszkowski[4] estimated the relative contribution of

F and $G-T$ interactions by equating $ft|M|^2$ for the H^3-He^3 and He^6-Li^6 transitions. Using the old He^6 "ft" value he obtained $K=C_F^2/C_G^2=0.11\pm0.45$, which leads to the conclusion of the insignificant role of the F interaction in beta-decay. Similarly, Trigg[6] obtained a value of $K\approx0.5$ by considering all the mirror and the isobaric triad nuclei, but still relying primarily on the old He^6 "ft" value. If one repeats the calculation of Moszkowski using the new ft values for He^6 one obtains $K\leq1.4\pm0.7$ which completely alters the picture. The recent finding of the $C^{10}-B^{10*}$ and $O^{14}-N^{14*}$ transitions which should be allowed and favored $0-0$ transitions, demonstrates that the presence of the Fermi interaction in the β-process is definitely necessary.

A more general comparison of the He^6 ft value can be made with those of the odd A mirror nuclei in the manner of Kofoed-Hansen.[6] The linear plot $B=ft[(1-x)|\int1|^2+x|\int\boldsymbol{\sigma}|^2]$ for the He^6-Li^6 transition passes through the region defined by the least squares fit for the odd A mirror nuclei ($B=2600\pm85$ and $x=0.50\pm0.05$).[6] Thus the ft value for He^6 is compatible with those of the mirror nuclei.[7,8]

Recently Dewan and his co-workers calculated the energy equivalent of the He^6-Li^6 mass difference by using Q-values of nuclear reactions. They gave a value 3.55 ± 0.03 Mev, which is in fair agreement with the direct spectroscopic determination.[9]

The authors wish to express their thanks to Miss M. Levin and Mr. R. W. Siegel for their valuable assistance in this experiment.

† This work is supported by the research program of the AEC.

[1] V. Perez-Mendez and H. Brown, Phys. Rev. **77**, 404 (1950).
[2] Holmes, Proc. Phys. Soc. (London) **62**, 293 (1949).
[3] The f valtbe was calculated using a formula according to E. Feenberg and G. Trigg, Revs. Modern Phys. **22**, 399 (1950).
[4] S. Moszkowski, Phys. Rev. **82**, 118 (1951).
[5] G. L. Trigg, Phys. Rev. **86**, 506 (1952).
[6] O. Kofoed-Hansen, and A. Winther, Phys. Rev. **86**, 428 (1952).
[7] The latest value $ft=1019$ for H^3 [L. Langer (private communication)] seems low when compared with those of the mirror nuclei and so was not used in computing K.
[8] The value $|\int\boldsymbol{\sigma}|^2\leq5.4$ should be used for He^6-Li^6 to fit the observed magnetic and quadrupole moments of Li^6. This change does not alter the fit of He^6 with the mirror nuclei (D. C. Peaslee, private communication).
[9] J. T. Dewan *et al.*, Phys. Rev. **86**, 416 (1952).

Interpretation of the Low Temperature Hall Curve of a Degenerate Germanium Sample*

D. M. FINLAYSON, V. A. JOHNSON, AND F. M. SHIPLEY
Purdue University, Lafayette, Indiana
(Received August 5, 1952)

GERMANIUM samples which have room temperature resistivities less than 0.01 ohm-cm show practically constant Hall coefficients from 300°K down to 1°K.[1] This implies a practically constant carrier density n of the order 10^{18} to 10^{19} per cm³. However, careful measurements made on an n-type antimony-doped sample, with $\rho(300°K)=0.0051$ ohm-cm show that the Hall coefficient R exhibits a maximum near 120°K (Fig. 1) and drops by 20 percent as the temperature decreases from 116°K to 1.3°K. Application of the common relation, $n=3\pi/(8Re)$, suggests that n *increases* by 20 percent as temperature drops, a behavior which would be opposite to that predicted by the concept that conduction electrons are due to thermal activation of donor impurity atoms.

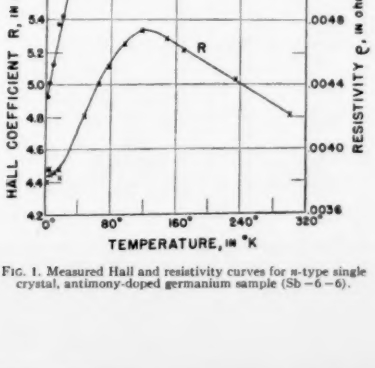

FIG. 1. Measured Hall and resistivity curves for n-type single crystal, antimony-doped germanium sample (Sb−6−6).

The Fermi level,[2] which is several kT below the bottom of the conduction band at 300°K, rises with decreasing temperature, crosses into the conduction band around 70°K and approaches a value of about 0.0048 ev above the bottom of the conduction band. Such a sample is termed degenerate, and Fermi-Dirac statistics are required in its analysis. With n as high as 10^{18} per cm³, scattering by impurity ions[2] is comparable with scattering by the lattice even at room temperature. At temperatures as low as 120°K, impurity scattering completely dominates, so that the use of a mean-free-path proportional to the square of the electron kinetic energy is justified. Consideration of these points shows that the low temperature drop in Hall coefficient is consistent with a *decrease* in carrier density.

Insertion of the Fermi-Dirac distribution function and a mean free path $l=Ke^2$ into the usual weak magnetic field expression for the Hall coefficient leads to the expression

$$|R|=\frac{3}{16\pi e}\left(\frac{h^2}{2mkT}\right)^{\frac{1}{2}}\frac{J_{1/2}(\zeta^*)}{\{J_3(\zeta^*)\}^2}, \tag{1}$$

where ζ^* represents the ratio of the Fermi level ζ to kT, and $J_k(\zeta^*)$ represents the Fermi-Dirac integral[4]

$$J_k(\zeta^*)=\int_0^\infty x^k(1+e^{x-\zeta^*})^{-1}dx. \tag{2}$$

Apart from uncertainty in the effective mass m, the measurable quantity $|R|T^{\frac{1}{2}}$ uniquely determines ζ^* as a function of temperature. The carrier density is uniquely determined by ζ^* through the relation

$$n=4\pi h^{-3}(2mkT)^{\frac{1}{2}}J_{1/2}(\zeta^*). \tag{3}$$

One can find n directly from $|R|$ by numerically eliminating ζ^* between Eqs. (1) and (3) and making a plot of $|R|T^{\frac{1}{2}}$ *vs* $nT^{-\frac{1}{2}}$. Alternately, one may define a ratio

$$r=\frac{|R|}{(1/ne)}=\frac{3}{4}\frac{J_{1/2}(\zeta^*)J_{1/2}(\zeta^*)}{\{J_3(\zeta^*)\}^2}; \tag{4}$$

then n may be found from $r/(e|R|)$. Table I gives the general relations among ζ^*, $|R|T^{\frac{1}{2}}$, and r applicable to any degenerate semiconductor.

TABLE I. Dependence of r, $|R|T^{1/2}$, and $nT^{-3/2}$ upon ζ^* for a degenerate semiconductor.

ζ^*[a]	r[b]	$\lvert R\rvert T^{1/2}$ °K$^{1/2}$ −cm^3/coulomb	$nT^{-3/2}$ cm^{-3} °K$^{-3/2}$
−2.0	1.897	19.0×10^{18}	0.06245×10^{16}
−1.5	1.877	11.7	0.100
−1.0	1.846	7.28	0.158
−0.5	1.804	4.60	0.272
0.0	1.750	3.00	0.370
1.0	1.60	1.31	0.761
2.0	1.45	0.663	1.36
3.0	1.34	0.386	2.17
4.0	1.261	0.250	3.15
5.0	1.196	0.173	4.27
6.0	1.151	0.130	5.53
7.0	1.119	0.101	6.90
8.0	1.096	0.0816	8.38
9.0	1.079	0.0676	9.96
10.0	1.065	0.0572	11.6
11.0	1.055	0.0492	13.4
12.0	1.047	0.0429	15.2

[a] ζ^* is the ratio of the Fermi level to kT.
[b] r is defined as $|R|ne$, where R is the Hall coefficient and n the number of carriers per cm³.

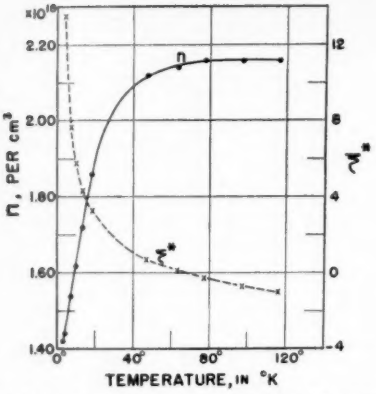

FIG. 2. Temperature dependence of carrier density and ζ^* for germanium sample Sb−6−6, as calculated from the measured Hall curve by use of Fermi-Dirac statistics and a mean-free-path characteristic of scattering by impurity ions. The quantity ζ^* is defined as the ratio of the Fermi level to kT; the zero of ζ^* is the bottom of the conduction band and negative values lie below the conduction band.

For the sample considered, r decreases from 1.84 at 116°K to 1.00 at 1.3°K; this decrease is sufficient to produce a drop in n in spite of the decrease in $|R|$ (Fig. 2). Analysis of the data shows that, as the temperature of this sample decreases, carrier density remains constant to quite low temperatures, then drops somewhat, but probably does not reach zero at 0°K. The impurity activation energy is calculated as about −0.005 ev, i.e., the donor levels lie just above the bottom of the conduction band.

* Work assisted by Signal Corps contract.
[1] C. S. Hung and J. R. Gliessman, Phys. Rev. **79**, 726 (1950).
[2] Hutner, Rittner, and DuPré, Philips Res. Rep. **5**, 188 (1950).
[3] E. Conwell and V. F. Weisskopf, Phys. Rev. **77**, 388 (1950).
[4] J. McDougall and E. C. Stoner, Trans. Roy. Soc. (London) **A237**, 67 (1938).

Theoretical and Experimental Heat Capacities of Superconducting Metals*

R. D. WORLEY, M. W. ZEMANSKY,† AND H. A. BOORSE‡
Pupin Physics Laboratories, Columbia University, New York, New York
(Received July 31, 1952)

A THEORY of the heat capacity of superconducing metals, based on Heisenberg's theory of superconductivity,[1] was given in 1947 by Koppe.[2] This theory predicts that the ratio $C_{el}^s/(C_{el}^n)_{T=T_0}$ is the same function of the reduced temperature T/T_0 for all superconductors. Here C_{el}^s and C_{el}^n refer to the electronic contributions to the heat capacity of the superconducting and normal phases, respectively, and T_0 to the zero field transition temperature.

A comparison between theory and experiment was given by Koppe using the experimental results on tin[3] and tantalum.[4] More recently Bender and Gorter[5] have made the comparison using the data on tin[3] and niobium.[6] The existence of experimental data on other superconductors, notably indium,[7] and lanthanum,[8] and vanadium,[9] prompted us to make a more thorough comparison than has been made heretofore.

In carrying out this comparison, the molar heat capacity data for each of the metals were plotted using the coordinates C/T *versus* T^2, since this plot gives directly the coefficient γ of the electronic term in the normal heat capacity and also presents the lattice heat capacity in a convenient form. No attempt was made to fit any portion of the superconducting heat capacity curve to a particular kind of dependence, instead the best smooth curve was drawn through the existing data. Subtracting the normal lattice heat capacity from the total superconducting heat capacity at any temperature, one obtains C_{el}^s, and dividing this by $(C_{el}^n)_{T=T_0}$

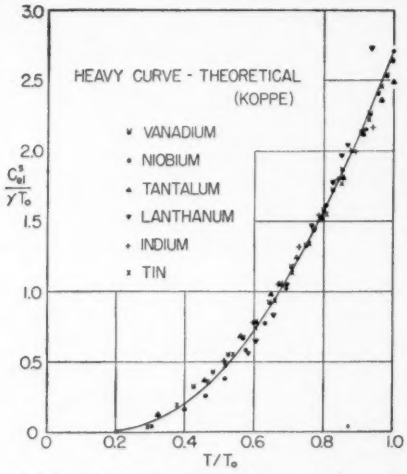

FIG. 1. Reduced electronic specific heat of superconducting metals.

$=\gamma T_0$, one obtains the individual points plotted in Fig. 1. The heavy curve is a graph of Eq. (21.1) in Koppe's paper, constructed from a recalculation of his Table I and extended to lower reduced temperatures. Bender and Gorter did not make the comparison as in Fig. 1 but plotted $(C_{el}^s/\gamma T_0)/(T/T_0)^3$ against the reduced temperature T/T_0. While their method has the advantage of emphasizing departures from Koppe's relation and from a T^3 law, especially at the lower temperatures, it must be noted that the experimental errors are likely to be largest in this region.

Koppe's relation predicts that $(C_{el}^s)_{T=T_0}/\gamma T_0=2.71$. To test this, a graph of $(C_{el}^s)_{T=T_0}$ *versus* γT_0 was drawn and is shown in Fig. 2. At the transition temperature T_0, data for two more metals,

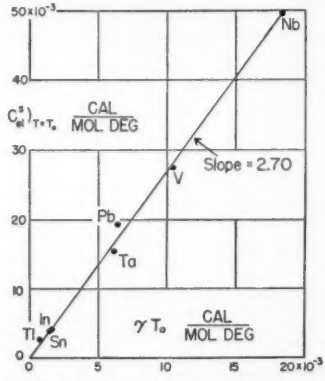

FIG. 2. Test of Koppe's relation at the transition temperature.

lead[10] and thallium,[11] are available. However, the data for lanthanum at this temperature are incomplete, and it is omitted. The points are seen to determine a line whose slope is 2.70.

The agreement between experiment and the calculation of Koppe, as shown in Figs. 1 and 2, is on the whole striking, although the departure from the curve in Fig. 1 of the low temperature points for niobium and vanadium is beyond the limit of experimental error. Nevertheless, the general fit of Koppe's curve suggests a real regularity displayed by all superconductors, a regularity which may be regarded as an approximate "law of corresponding states."

* Assisted by the ONR and Linde Air Products Company.
† City College of New York, New York, New York.
‡ Barnard College, Columbia University, New York, New York.
[1] W. Heisenberg, Z. Naturforsch. **IIa**, 185 (1937).
[2] H. Koppe, Ann. phys. **1**, 405 (1947).
[3] W. H. Keesom and P. H. van Laer, Physica **5**, 193 (1938).
[4] W. H. Keesom and M. Désirant, Physica **8**, 273 (1941).
[5] P. L. Bender and C. J. Gorter, Physica **18**, 1 (1952). We are indebted to Professor Gorter for a copy of their paper in advance of publication.
[6] Brown, Zemansky, and Boorse, Phys. Rev. **86**, 134 (1952).
[7] J. R. Clement and E. H. Quinnell, Phys. Rev. **79**, 1028 (1950).
[8] Parkinson, Simon, and Spedding, Proc. Roy. Soc. (London) **A207**, 137 (1951).
[9] Worley, Zemansky, and Boorse, Phys. Rev. (to be published). See also the Report of the Low Temperature Conference of the ONR, General Electric Research Laboratories, Schenectady, New York, October 1952.
[10] J. R. Clement and E. H. Quinnell, Phys. Rev. **85**, 502 (1952). (γ was calculated from magnetic data and taken to be 8.92×10^{-4} cal/mole-deg^2.)
[11] W. H. Keesom and J. A. Kok, Physica **1**, 175, 595 (1934).

Evidence for Domain Structure in Antiferromagnetic CoO from Elasticity Measurements

M. E. Fine
Bell Telephone Laboratories, Murray Hill, New Jersey
(Received July 15, 1952)

YOUNG'S modulus in CoO on cooling undergoes a large decrease near the Néel point.[1] Street and Lewis[1] suggest that this is due to the influence of an applied stress on the preferred orientation of the spin vectors in antiferromagnetic domains. A more detailed study and explanation of the elasticity of CoO is herein reported.

A rod of CoO was prepared by pressing powdered CoO and sintering at 1130°C in N_2. X-rays revealed only the CoO structure; the apparent density after sintering was 86 percent of the density of CoO.

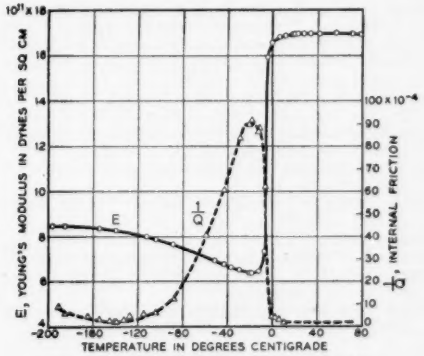

FIG. 1. Young's modulus and internal friction of CoO.

Young's modulus (E) and the internal friction ($1/Q$) were measured from 80 to −196°C in the pressed and sintered rod, employing both electromagnetic and piezoelectric excitation and detection of longitudinal vibrations (35 to 60 kc sec^{-1}). On cooling from 20 to −20°C, as shown in Fig. 1, E drops from 17 to 6.3×10^{11} dynes cm^{-2}, the region of maximum change being 0 to −8°C. (The Néel temperature, determined from paramagnetic susceptibilities, is −2°C.[2]) The effect persists to low temperature, for at −196°C E is 8.5×10^{11} dynes cm^{-2}. The internal friction ($1/Q$) for a constant maximum strain amplitude of 10^{-7}, also shown in Fig. 1, rises on cooling from 2×10^{-4} (the background) to a peak value of 91×10^{-4} at −20°C, then decreases to a minimum at −150°C and rises again to 8.5×10^{-4} at 190°C. At room temperature and −20°C, increasing the maximum strain amplitude from 10^{-8} to 10^{-5} has little effect on E or $1/Q$, but at −190°C E decreases 1 percent and $1/Q$ increases from 5 to 25×10^{-4}.

The general course of our modulus-temperature curve and that reported by Street and Lewis[1] are in substantial agreement; however, our modulus values are larger by approximately a factor of 5, and the Néel temperature appears to be −2°C in our sample rather than 16°C. The discrepancy among modulus values and Néel points may be due to composition and porosity variations.

In considering possible explanations the following properties of CoO seem important: The formation of antiferromagnetism causes an increase in volume; the coefficient of linear expansion is high in the temperature range 5 to −75°C, with a peak of 22×10^{-6} deg C^{-1} at −2°C. Antiferromagnetism distorts CoO from cubic (NaCl structure) to tetragonal;[3,4] c/a becomes increasingly less than one as the temperature is decreased, being 0.9884 at −180°C.[3] The antiferromagnetically aligned atomic magnetic moments are parallel to (100).[5] Presumably it is this direction that becomes shortened.

The large decrease in E implies that an applied stress produces strains in addition to, and in some cases even larger than, the normal elastic strain. In antiferromagnets an effect analogous to the stress-induced change in domain structure in ferromagnets is suggested.[6] Neighboring domains within a crystal are postulated differing as to which of the three possible orientations of the c axis is present. Then, for example, tension would increase the area of those domains whose c axes are nearly perpendicular to the stress axis, thereby increasing the sample length. The amount of strain from a given amount of domain boundary movement would increase on cooling since c/a decreases, but domain boundary movement becomes more difficult owing to the lattice strain produced. Thus, E from this effect would not continuously decrease on cooling. Stress-induced antiferromagnetic domain boundary movement, like domain movement in ferromagnets, is expected to be hysteretic; consequently, the proposed mechanism seems especially reasonable for low temperatures where $1/E$ and $1/Q$ increase with strain amplitude and, furthermore, well-defined domains are expected.

Near the Néel temperature, where the magnetic moments are loosely coupled, another mechanism which may yield a strain and internal friction is a stress-induced change in the degree of antiferromagnetic order. The strain would come from the resulting change in volume and tetragonality. E and $1/Q$ are more conceivably independent of strain amplitude by this mechanism.

This investigation has benefited from the assistance of Miss N. T. Kenney and helpful suggestions from and discussion with Mr. P. W. Anderson, Mr. W. C. Ellis, Mr. J. K. Galt, Mr. H J. McSkimin, Mr. F. J. Schnettler, and Mr. E. E. Schumacher.

[1] R. Street and B. Lewis, Nature **168**, 1036 (1951).
[2] H. Bizette, Ann. phys. **1**, 295 (1946).
[3] N. C. Tombs and H. P. Rooksby, Nature **165**, 442 (1950).
[4] S. Greenwald and J. S. Smart, Nature **166**, 523 (1950).
[5] Shull, Strauser, and Wollan, Phys. Rev. **83**, 333 (1951).
[6] R. M. Bozorth, *Ferromagnetism* (D. Van Nostrand, Inc., New York, 1951), pp. 472, 595.

Errata

The Symmetrical Pseudoscalar Meson Theory of Nuclear Forces, MAURICE M. LÉVY [Phys. Rev. **86**, 806 (1952)]. In the last portion of Eq. (3), replace $[(2/\pi)K_0(\mu r)]^2$ with $(\mu/2M)[(2/\pi)K_1(\mu r)]^2$.

Angular Distribution of Shower Particles as a Function of Depth, L. EYGES AND S. FERNBACH [Phys. Rev. **82**, 287 (1951)]. Equation (1) should read: $\pi(E_0, E, \theta, t)2\pi\theta d\theta dE = \pi_{\text{ions}}(E_0, E, t)dE\cdot P(x, s)\theta d\theta\cdot(E/E_s)^2$. The present addresses

of the authors are as follows: L. Eyges, American Embassy, Paris, France; S. Fernbach, Stanford University, Palo Alto, California.

Soft Radiations from Am^{241}, J. K. BELING, J. O. NEWTON, AND B. ROSE [Phys. Rev. **86**, 797 (1952)]. Because of a computational error, the values in Table I are incorrect. The correct values are as follows:

Radiation energy (kev)	59.7	26.3	20.9	17.3	13.5
Relative intensity	1	0.069 ± 0.007	0.155 ± 0.016	0.56 ± 0.04	0.32 ± 0.04

Helium II Transfer Rates on Lucite and Perspex Surfaces, B. S. CHANDRASEKHAR [Phys. Rev. **86**, 414 (1952)]. The units along the y axis of the graph should be 10^{-5} cm³/cm sec.

Nuclear Matrix Elements in the Theory of Beta-Decay, HENRY BRYSK [Phys. Rev. **86**, 996 (1952)]. The fifth sentence of the first paragraph on p. 1000, reading "These matrix elements correspond to the spin-orbit coupling implicit in the Dirac equation; for the larger empirical spin-orbit coupling (from shell breaks), they would presumably be considerably larger," was misplaced. It refers to the l-forbidden transitions, and should be in the next paragraph.

Low Energy γ-Transitions in Some Rare Earth Isotopes, J. W. MIHELICH AND E. L. CHURCH [Phys. Rev. **85**, 690 (1952)]. In Table I, the $(K/L)_{exp}$ value for $_{68}Er_{98}^{166}(Ho^{166}\ 27\ hr)$ should be $0.07^{+0.2}_{-0.02}$.

PHYSICAL REVIEW VOLUME 87, NUMBER 6 SEPTEMBER 15, 1952

Author Index to Volume 87

References with (A) are to abstracts of papers presented at meetings of the American Physical Society, and those with (T) designate title only. References with (L) are to Letters to the Editor.

Abe, Hidetarô (see Kumagai, Hiroo)—385(L)
Abelson, P. H. (see Aldrich, L. T.)—186(A)
Adair, Robert K. Conservation of isotopic spin in nuclear reactions—1041
—— (see Argo, H. V.)—205(A)
—— (see Walt, M.)—238(A)
Adams, Edward N., II. Weak potential model for electrons in metal—211(A)
Aeppli, H., H. Frauenfelder, E. Heer, and R. Rüetschi. Directional correlation of Ni^{60} γ-γ cascade—379(L)
Agnew, H. M. (see Argo, H. V.)—205(A); 612
Ahrens, T., E. Feenberg, and H. Primakoff. Pseudoscalar interaction in theory of β-decay—663(L)
Ajzenberg, Fay. Energy levels of Be^7 and B^{10}—205(A)
Alberts, Henry C., George A. Coulter, and Charles M. Warden. Motion of elliptical vortices—911(A)
Alburger, David E. Pair measurement of γ-rays with lens spectrometer—194(A)
—— **and J. J. Kraushaar.** Decay scheme and angular correlation of Pr^{144}—448
Aldrich, L. T., L. F. Herzog, P. H. Abelson, and E. T. Bolton. Separation of trace elements in minerals with resin ion exchange columns—186(A)
Alford, W. L. (see Wanlass, S. D.)—183(A)
Allen, A. J. (see Arthur, J. S.)—237(A)
—— (see Hausman, H. J.)—238(A)
Allen, H. C., Jr. Pure quadrupole spectra of solid chloroacetic acids and substituted chloroacetic acids—227(A)
Allen, William A. Transient high amplitude waves through steel—910(A)
Allis, W. P., and Sanborn C. Brown. High frequency electrical breakdown of gases—419
Allred, J. C. (see Armstrong, A. H.)—238(A)
Alperin, H. A. (see Siegel, K. M.)—234(A)
Altshuler, Saul. Excitation cross section for He atoms—992
Anderegg, J. W., W. W. Beeman, and S. Shulman. Small-angle x-ray scattering from serum albumin solutions—186(A)
—— (see Kaesberg, Paul)—186(A)
Anderson, C. D., R. B. Leighton, F. H. Shelton, and S. D. Wanlass. General properties of V^0-particle decay—183(A)
—— (see Wanlass, S. D.)—183(A)
Anderson, C. E., G. W. Wheeler, and W. W. Watson. Mass of Cl^{39} and A^{39}—897(L)
——, **G. W. Wheeler, and W. W. Watson.** Radiative K-capture in A^{37}—668(L)
——, **G. W. Wheeler, and W. W. Watson.** Radioactivity of A^{39}—195(A)
Anderson, Roy S., William V. Smith, and Walter Gordy. Line-breadths of the microwave spectrum of O—561
Angell, C. E. (see Barnes, S. W.)—669(L)
Annis, M. (see Clark, G. W.)—182(A)
Antonoff, George. Equilibria in liquid systems—242(A)
—— Equilibria in liquids. II. Liquid-vapor systems—185(A)
Argo, H. V., R. K. Adair, H. M. Agnew, A. Hemmendinger, W. T. Leland, and R. F. Taschek. Cross section of $D(T,n)He^4$ reaction for 80- to 1200-kev tritons—205(A)
——, **R. F. Taschek, H. M. Agnew, A. Hemmendinger, and W. T. Leland**—612
Armstrong, A. H., J. C. Allred, A. M. Hudson, R. M. Potter, E. S. Robinson, L. Rosen, and E. J. Stovall, Jr. Scattering of 10-Mev deuterons by H^3 and He^3—238(A)
Arthur, J. S., A. J. Allen, R. S. Bender, H. J. Hausman, C. J. McDole, L. M. Diana, K. B. Rhodes, and R. A. Barjon. Energy levels resulting from 8-Mev protons on Be^9, C^{12}, N^{14}, S^{32}—237(A)
—— (see Hausman, H. J.)—238(A)
Artman, J. O. and J. P. Gordon. Pressure broadening of $(O^{16})_2$ lines in mm wavelength region—227(A)
Asaro, Frank and I. Perlman. First excited states of even-even nuclides in the heavy element region—393(L)
——, **F. L. Reynolds, and I. Perlman.** Complex α-spectra of Am^{241} and Cm^{242}—277
Ashkin, Arthur and W. M. Woodward. Positron-electron scattering—236(A)
Atkinson, William R. (see Fowler, Richard G.)—966(L)
Austern, N. "Nucleon isobar" as intermediate state—208(A)
Avery, C. J., K. C. Kaericher, and M. L. Pool. Nuclear reactions in Co and As—216(A)
Auxier, John and Guy Forman. Characteristics of x-ray excited phosphorescence of calcite—170(A)

Bailey, Jep H. (see Mockler, Richard)—172(A)
Bair, J. K. (see Willard, H. B.)—206(A)
Bajwa, G. S. (see Bhowmik, B.)—530(L)
Baker, P., B. L. Jones, and A. W. Waltner. Low energy yield of $H^3(d,n)He^3$—176(A)
Baldock, Russell (see Sites, John R.)—171(A)
Ballard, Stanley, S. (see Combes, Lewis S.)—201(A)
Bandtel, Kenneth C., (see Madey, Richard)—204(A)
Bardeen, J. Change in superconducting penetration depth with field—192(A)

—— (see Leurgans, Paul)—200(A)
Barjon, R. A. (see Arthur, J. S.)—237(A)
—— (see Hausman, H. J.)—238(A)
Barkas, Walter H. and J. Kent Bowker. Products of C disintegration by 330-Mev protons—207(A)
Barnes, R. G. and P. J. Bray. Rf spectroscopy of D—229(A)
—— (see Bray, P. J.)—229(A)
Barnes, S. W., D. L. Clark, J. P. Perry, and C. E. Angell. Total cross sections of positive pions in H—669(L)
Barnett, S. J. and G. S. Kenny. Gyromagnetic ratios of Fe, Co, and binary alloys of Fe, Co, and Ni—723
—— (see Brown, Sheldon)—601
Barr, E. Scott. Infrared absorption spectrum of liquid stearic acid—170(A)
Barr, Thomas A., Jr. Anomalous osmotic pressures of polymer solutions as measured in metal membrane osmometer—171(A)
Barrett, L. C. and C. J. Thorne. Oscillations of gas bubble produced by underwater explosion—913(A)
Bashkin, S. (see Yonts, O.)—175(A)
Basri, Saul A. Absorption of π^- meson from K-shell of H^2—866
Bass, A. M. and W. S. Benedict. Infrared emission spectrum of FeO—214(A)
Battat, M. E. (see Bondelid, R. O.)—699
Bay, Z. Determination of resolving time of coincidences—194(A)
——, **M. R. Cleland, and F. McLernon.** Fast coincidences with Čerenkov counters—901(L)
Beach, E. H. (see Parkinson, W. C.)—387(L)
Beams, J. W., W. E. Walker, and H. S. Morton, Jr. Mechanical properties of thin films of Ag—524(L)
—— (see Robeson, A.)—186(A)
Beck, C. K. North Carolina state reactor—168(T)
Becker, E. W. and O. Stehl. Difference in viscosity of ortho- and para-hydrogen at low temperatures—525(L)
Becker, R. A. (see Bendel, W. L.)—195(A)
—— (see Shore, F. J.)—202(A)
Bederson, B. and V. Jaccarino. Precision measurements of hfs of Rb^{85} and Rb^{87}—228(A)
—— (see Jaccarino, V.)—676(L)
Beeman, W. W. (see Anderegg, J. W.)—186(A)
—— (see Kaesberg, Paul)—186(A)
Béique, René A. (see Lorrain, Paul)—183(A)
Belinfante, Frederik J. Are direct nucleon-lepton interactions charge-independent—521(L)
—— Matter-matter interaction through retarded fields—224(A)
Beling, J. K., J. O. Newton, and B. Rose. Decay of Am^{241}—670(L)
——, **J. O. Newton, and B. Rose.** Soft radiations from Am^{241}, erratum—1143(L)
Bell, P. R. (see Heath, R. L.)—176(A)
—— (see Kelley, G. G.)—174(A)
Bell, R. E. and R. L. Graham. Complex time decay of positrons annihilated in condensed materials—236(A)
Belser, Richard B. High temperature, economical, infrared oven—172(A)
Bendel, W. L., F. J. Shore, H. N. Brown, and R. A. Becker. Internal conversion electron ratios in Ba^{137m}, Y^{89m}, and Zr^{89m}—195(A)
—— (see Shore, F. J.)—202(A)
Bender, R. S. (see Arthur, J. S.)—237(A)
—— (see Hausman, H. J.)—238(A)
Benedict, W. S., B. W. Bullock, Shirleigh Silverman, and A. V. Grosse. Infrared emission of H-F flame—213(A)
—— (see Bass, A. M.)—214(A)
Benenson, R. E. Levels of N^{14} observed from $C^{13}(d,n)N^{14}$—207(A)
Bennett, F. D. and G. D. Kahl. Theory of Mach-Zehnder interferometer—234(A)
Berger, J. M., L. L. Foldy, and R. K. Osborn. Equivalence theorems for pseudoscalar coupling—1061
Berger, Martin J. Multiple scattering of high energy protons in photographic plates—238(A)
Bergmann, Peter G. and Ralph Schiller. Structure of canonical coordinate transformation group—198(A)
—— (see Goldberg, Joshua)—198(A)
—— (see Schiller, Ralph)—198(A)
Beringer, R. and E. B. Rawson. Electron spin gyromagnetic ratio in atomic H—228(A)
Bernardini, G. (see Lindenbaum, S. J.)—207(A)
Bernstein, S., L. B. Borst, C. P. Stanford, T. E. Stephenson, and J. B. Dial. Slow neutron crystal spectrometry: Total cross sections of Co, Er, Hf, Ni^{58}, Ni^{60}, Ho, and fission Sm—487
—— (see Stephenson, T. E.)—174(A)
Bershader, D. and D. C. Pack. Structure of two-dimensional supersonic jet.—909(T)
Bersohn, R. Nuclear resonance spectrum of system of four nuclei—226(A)
Bethe, H. A. (see Davies, Handel)—156(L)
—— (see Maximon, L. C.)—156(L)
Bhowmik, B. and G. S. Bajwa. Azimuthal variation of cosmic radiation for Zenith angle at 40° at λ = 19N—530(L)
Billig, Ernst. Effect of minority carriers on breakdown of point contact rectifiers—1060
Bilpuch, E. G. and A. V. Masket. Star production by heavy ion component of cosmic rays—168(A)
Biondi, Manfred A. Processes involving thermal electrons and ions in mercury afterglow—232(A)
Bird, R. B. Quantum corrections to transport properties of gases at low temperatures—212(T)
Bittman, Loran, Milton Furst, and Hartmut Kallmann. Decay times, fluorescent efficiencies, and energy storage properties for various substances with γ-ray or α-particle excitation—83
Black, Clayton F. Angular distributions of (d,ϕ) reactions—205(A)
Blau, M. and A. R. Oliver. Stars induced by high energy neutrons in light elements of photographic emulsion—182(A)
Bleuler, E. and D. J. Tendam. (α,n) and (α,an) cross sections with Ag^{109}—216(A)
Block, M. M., S. Passman, and W. W. Havens, Jr. Production of charged pions by protons on C and other nuclei—168(A)
Bloembergen, N. and Shyh Wang. Influence of anisotropy on ferromagnetic relaxation—392(L)
Bloom, Stewart D. Internal pair creation in Mg^{24}—236(A)
Bockelman, C. K. (see Buechner, W. W.)—237(A)
Bogaardt, M. and B. Koudijs. Calculation of range-energy relations for α-particles in photographic emulsions—1129(L)
Bohlman, P. (see Bondelid, R. O.)—699
Bohm, David. Reply to criticism of causal re-interpretation of quantum theory—389(L)
Bollinger, L. M., S. P. Harris, and R. W. Schumann. New equipment and methods used with Argonne fast neutron chopper—184(A)
—— (see Harris, S. P.)—222(A)
Bolton, E. T. (see Aldrich, L. T.)—186(A)
Bondelid, R. O., C. H. Braden, M. E. Battat, and P. Bohlman. Proton-proton scattering at 5 Mev by a coincidence method—699
Bonfiglioli, G. Fusion as hydrodynamic instability in thermal wave propagation—897(L)
Bonner, T. W., R. A. Ferrell, and M. C. Rinehart. Study of spectrum of neutrons of low energy from fission of U^{235}—1032
Boorse, H. A. (see Lesensky, L.)—1135(L)
—— (see Worley, R. D.)—192(A); 1142(L)
Borie, B. (see Roberts, L. D.)—192(A)
Borst, L. B. (see Bernstein, S.)—487
—— (see Sailor, V. L.)—161(L)

Bostick, Winston H. and Morton A. Levine. Experimental demonstration in the laboratory of existence of magneto-hydrodynamic waves in ionized He—671(L)
Bouchez, R. (see Nataf, R.)—155(L)
Bowers, W. A. Lattice vibrations and resistivity—173(A)
Bowker, J. Kent (see Barkas, Walter H.)—207(A)
Boyd, G. A. (see Joran, J. R.)—177(A)
Bozorth, R. M. and R. W. Hamming. Measurement of magnetostriction in single crystals.—209(A)
Brace, P. H. (see Okress, E. C.)—209(A)
Braden, C. H. (see Bondelid, R. O.)—699
Bradley, Lee C., III (see Wilets, Lawrence)—1018
Bradner, Hugh and Bayard Rankin. Fast meson interactions in nuclear emulsions. I. π^- mesons—547
—— (see Rankin, Bayard)—553
Bragg, J. K. Relation of Monte Carlo and variational calculation method in quantum mechanics—199(A)
—— (see Sharbaugh, A. H.)—232(A)
Bramley, Arthur and Jenny E. Rosenthal. Field dependent fluorescence of vitreous Zn_2SiO_4 phosphor—1125(L)
Brattain, W. H. Surface properties of Ge—221(T)
Bray, P. J., R. G. Barnes, and N. J. Harrick. Magnetic moment ratios in hydrogen-like molecules—229(A)
—— (see Barnes, R. G.)—229(A)
Breidenbach, H. I., Jr. (see Dewey, J. N.)—909(A)
Breit, G. Tentative hypothesis of proton isomers—208(A)
—— Theory of elementary-particle scattering—222(T)
——, **M. H. Hull, Jr., and R. L. Gluckstern.** Possibilities of heavy ion bombardment in nuclear studies—74
Bridge, H. S. (see Clark, G. W.)—182(A)
Briggs, H. B. and R. C. Fletcher. New infrared absorption bands in p-type Ge—1130(L)
Brillouin, L. Negentropy principle of information—221(T)
Brimberg, S. A. S. Internal conversion of γ-rays with pair production—150(L)
Brinkley, S. R., Jr., and John M. Richardson. Application of cell method in grand canonical ensemble to equation of state of liquid mixture—199(A)
—— (see Richardson, John M.)—199(A)
Brittin, Wesley E. Conformal invariance in special relativity—197(A)
Brockhouse, B. N. and D. G. Hurst. Energy distribution of slow neutrons scattered from solids—239(A)
Brolley, J. E., Jr., J. L. Fowler, and L. K. Schlacks. $(n,2n)$ reactions in C^{12}, Cu^{63}, and Mo^{92}—206(A)
Brooks, F. C. (see Glick, H. L.)—1074
Brown, B. M. Nuclear quadrupole moment of Ta^{181}—228(A)
Brown, F. B., Jr., and A. V. Masket. Statistical study of star formation in photographic emulsions—168(A)
Brown, H. N. (see Bendel, W. L.)—195(A)
—— (see Shore, F. J.)—202(A)
Brown, Robert R. Mean free path of high energy N-component of cosmic radiation—999
Brown, Sanborn C. (see Allis, W. P.)—419
Brown, Sheldon and S. J. Barnett. Carriers of electricity in metals exhibiting positive Hall effects—601
Browne, C. P. (see Buechner, W. W.)—237(A)
Broyles, C. D. and S. K. Haynes. K-Auger yield of Hg—174(A)
Brueckner, Keith A. Application of theory of effective range to meson-nucleon scattering—1026
—— **and R. W. Thompson.** Decay scheme of V^0-particle—390(L)
—— **and Kenneth M. Watson.** Possibility of obtaining experimental information concerning the meson-meson interaction—621
Brysk, Henry. Nuclear matrix elements in theory of β-decay, erratum—1144(L)
Buck, W. L. and R. K. Swank. Plastic phosphors for scintillation counters—191(A)
Buechner, W. W., C. P. Browne, M. M. Elkind, A. Sperduto, H. A. Enge, and C. K. Bockelman. Inelastic proton scattering from B^{10}—237(A)
—— (see Endt, P. M.)—27
—— (see Van Patter, D. M.)—51
Buehler, E. (see Teal, G. K.)—190(A)
Bullock, B. W. (see Benedict, W. S.)—213(A)
Burke, W. H. and J. R. Risser. Angular correlation between protons and gammas in the $Li^6(d,p\gamma)Li^7$ reaction—294
Busch, G. Magnetism due to current carriers and to impurities in semiconductors—221(T)
Bushkovitch, A. V. (see Jones, L. C.)—227(A)
Butler, S. T. Surface production of charged mesons—1117; 217(A)

Caird, Robert S. (see Mitchell, Allan, C. G.)—388(L)
—— (see Smith, Alan B.)—454
Callen, (see Love, W. F.)—844
Cameron, A. G. W. (see Haslam, R. N. H.)—196(A)
Cameron, J. R. (see Jackson, H. L.)—237(A)
Campbell, Edward C. XYZ method of coincidence correlation spectrometry—175(A)
Canavan, Frederick L., S.J. Angular distribution and excitation function of the long-range protons from the $Be^9(d,p)Be^{10}$ reactions—136
Carr, H. E. (see Donnally, B. L.)—170(A)
Carter, R. S. and W. L. Whittemore. Relative specific ionization of fast mesons—494
Casson, Harvey. γ-rays from Na, Mg, and Al under bombardment by 200–420 kev protons—215(A)
Cathey, LeConte. Decay of μ^- mesons in SiC—169(A)
Caulk, H. M. (see Davis, L. R.)—239(A)
Cavanagh, Patrick E. Double Compton effect—1131(L)
Chamberlain, Owen and Emilio Segrè. Proton-proton collisions within Li nuclei—81
Chandrasekhar, B. S. He II transfer rates on Lucite and Perspex surfaces, erratum—1144(L)
Chang, C. S. Wang (see Uhlenbeck, G. E.)—195(T)
Chartres, B. A. and H. Messel. Moments of angular distribution for high energy nuclear collisions—748
Chew, Geoffrey F. and M. L. Goldberger. Scattering of elementary particles by complex nuclei—generalization of impulse approximation—778
Chou, C. N. Internal absorption of fluorescent light in large plastic scintillators—376(L)
—— Nature of saturation effect of fluorescent scintillators—904(L)
—— Saturation effect of plastic scintillators—903(L)
——, **W. F. Fry, and J. J. Lord.** Acceleration of Be and C ions in a synchrocyclotron—671(L)
Christensen, S. H. Compressible laminar boundary layers—911(A)
Church, E. L. (see Mihelich, J. W.)—1144(L)
Cladis, J. B., W. N. Hess, and B. J. Moyer. Nucleon momentum distributions in D and C inferred from proton scattering—425
Clark, Donald L. Production of 40-Mev π^+ and π^- mesons in seven elements by 240-Mev protons—157(L)
—— (see Barnes, S. W.)—669(L)
Clark, G. W., M. Annis, H. S. Bridge, H. W. Courant, and B. Rossi. Two examples of V^0-decay observed in multiple plate cloud chamber—182(A)
Clark, K. C. Ionospheric absorption by N_2 and O_2 of certain extreme ultraviolet solar wavelengths—271
Clark, Malcolm A. Hard component of cosmic rays in upper atmosphere—87
Class, C. M. and S. S. Hanna. Angular correlations in $Li^6(d,p)Li^{7*}(\gamma)Li^7$ reaction—247
—— (see Cohen, L.)—206(A)
Cleland, M. R. (see Bay, Z.)—901(L)

Clement, J. R. and E. H. Quinnell. Atomic heat of Pb in neighborhood of transition to superconductivity—192(A)
Cochran, L. W., J. L. Ryan, H. H. Givin, B. D. Kern, and T. M. Hahn. γ-ray yield from the proton bombardment of B—672(L)
—— (see Ryan, J. L.)—177(A)
Cohen, L., S. M. Shafroth, C. M. Class, and S. S. Hanna. Angular correlation in $Be^{9}(d,p)Be^{10*}(\gamma)Be^{10}$ reaction—206(A)
Cohn, H. O. (see Thompson, R. W.)—182(A)
Colgate, Stirling A. γ-ray absorption measurements—592
Collins, Thomas L., Alfred O. Nier, and Walter H. Johnson, Jr. Atomic masses and nuclear shell structure at 20 and 28 neutrons and protons—236(A)
Colvin, T. H. (see Prestwich, G. D.)—1030
Combes, Lewis S., Stanley S. Ballard, and Kathryn A. McCarthy. Comparative elastic studies of single crystals of CaF_2 and CsCl types—201(A)
Comenetz, G. (see Okress, E. C.)—209(A)
Conklin, G. L. (see Mendenhall, R. I.)—203(A)
Conrad, G. and J. J. Dropkin. Temperature dependence of infrared photocond ctivity in standard VII phosphor——192(A)
Conwell, E. M. and E. J. Ryder. High field mobility in Ge with impurity scattering dominant—190(A)
—— (see Debye, P. P.)—1131(L)
Cook, C. Sharp (see Porter, Fred T.)—464
Cook, M. A. Detonation equation of state—909(T)
Cool, R. L. and O. Piccioni. Interaction of pions originating in penetrating showers—531(L)
—— (see Piccioni, O.)—216(T)
Cooper, C. D. and F. W. Noegel. Near uv absorption spectra of 1,4 $C_6H_4(CF_3)_2$ and 1,3,5 $C_6H_3(CF_3)_3$—169(A)
—— **and H. Sponer.** Absorption system of light and heavy naphthalene vapor at 2900–2500A—213(A)
Cork, J. M., J. M. LeBlanc, F. B. Stumpf, and W. H. Nester. γ-radiation from Pt—203(A)
—— (see LeBlanc, J. M.)—202(A)
Corson, Dale R. Radiation loss by electrons in large orbits——233(A)
Coryell, Charles D. (see Fairhall, Arthur W.)—215(A)
Cotter, T. P. Measurement of reaction time in detonating liquid—909(A)
Coulter, George A. (see Alberts, Henry C.)—911(A)
Courant, E. D. Meson production by nucleons in Coulomb fields—217(A)
Courant, H. W. (see Clark, G. W.)—182(A)
Cowie, Dean B., N. P. Heydenburg, and G. C. Phillips. Inelastic scattering of protons from light nuclei—304
Cox, C. D. (see Johns, M. W.)—1134(L)
Cox, E. F. Damaging air shocks at large distances from explosions—909(T)
Craig, D. S., D. J. Donahue, and K. W. Jones. B^{10} and O^{18} reaction energies—206(A)
Cronemeyer, D. C. Electrical and optical properties of rutile single crystals—876
Cross, William G. Angular distribution of n-p scattering——223(A)
Crowe, R. W. (see Sharbaugh, A. H.)—232(A)
Culler, Vaughn and R. W. Waniek. Total cross sections for high energy neutrons—221(A)
Curtis, C. W., R. J. Emrich, and J. E. Mack. Measurement of transient flow variables as function of time—913(A)

Daitch, P. B. and J. B. French. Born approximation theory of (d,p) and (d,n) reactions—900(L)
Darling, B. T. and P. R. Zilsel. Uniqueness in theory of fundamental length—198(A)
Dauphinee, T. M. Isolated potential-difference comparator——230(A)
Davies, E. B. (see Stoner, R. G.)—913(A)
Davies, Handel and H. A. Bethe. Integral cross section for bremsstrahlung and pair production—156(L)
Davies, L. R., H. M. Caulk, C. Y. Johnson, G. J. Perlow, and C. A. Schroeder. Proportional counter measurement of primary protons and α-particles—239(A)
Davis, Luther, Jr., G. A. deMars, L. G. Rubin, and J. H. Saunders. Effect of 11-Mev electron bombardment on electrical properties of Ge—190(A)
——, **and Lawrence G. Rubin.** Dielectric properties of Ba-Sr titanate ceramics—201(A)
Deal, W. E. and R. G. Shreffler. Free surface properties of explosive-driven metal plates—910(A)
De Benedetti, S. (see Siegel, R.)—235(A)
Debs, R. J., J. T. Eisinger, A. W. Fairhall, I. Halpern, and H. G. Richter. Photonuclear yields from Cu through As——196(A)
Debye, P. P. and E. M. Conwell. Mobility of electrons in Ge—1131(L)
—— (see Rubin, R. J.)—214(A)
Dedrick, K. G. Influence of multiple scattering on angular width of Čerenkov radiation—891
de Haas, N. (see Elder, F. K., Jr.)—911(A)
de Klerk, Dirk. Paramagnetism below 1°K—187(T)
deMars, G. A. (see Davis, Luther, Jr.)—190(A)
Demos, P. T. (see Winhold, E. J.)—1139(L)
der Mateosian, E. and A. Smith. "Impregnated" scintillating crystal as tool for study of radioactive decay—193(A)
de-Shalit, A. Cosine interaction between nucleons—843
Detwiler, D. P. Low temperature thermal conductivity of Sn and Sn-Bi alloys—192(A)
Deutsch, Martin. New results on positronium—168(T)
—— Physics of positronium—212(T)
—— (see Kluyver, Jan C.)—203(A)
Dewey, J. N., H. I. Breidenbach, Jr., and J. W. Gehring, Jr. Determination of detonation pressures from flash radiographs—909(A)
DeWitt, Bryce Seligman and Cecile Morette DeWitt. Quantum theory of interacting gravitational and spinor fields——116
DeWitt, Cecile Morette (see DeWitt, Bryce Seligman)—116
Dexter, D. L. Scattering of electrons from point singularities in metals—768
—— (see Seitz, F.)—189(A)
Dharmatti, S. S. and H. E. Weaver, Jr. Nuclear magnetic reasonance lines of Sb in antimony hexafluoride ion—675(L)
Dial, J. B. (see Bernstein, S.)—487
Diana, L. M. (see Arthur, J. S.)—237(A)
—— (see Hausman, H. J.)—238(A)
Dibeler, Vernon H., Robert M. Reese, and Fred L. Mohler. Dissociation energies of C—C and C—F bonds in several fluorocarbons by electron impact—213(A)
Dickinson, R. W. (see Greenfield, M. A.)—184(A)
Dieke, G. H. and C. S. Rainwater. Continuous spectrum of H_2—212(A)
Dienes, G. J. Effect of radiation on elastic constants—666(L)
Diesendruck, L. (see True, W. W.)—381(L)
Dimond, A. E. (see Pollard, E. C.)—186(A)
Doggett, W. O. Electrical analog for radioactivity of primary fission products with intermittent reactor operation—171(A)
Donahue, D. J. (see Craig, D. S.)—206(A)
Donnally, B. L., J. B. Dozier, and H. E. Carr. Negative metastable ions—170(A)
Donnelly, R. J. (see Johns, M. W.)—1134(L)
Downes, K. W. (see Sher, R.)—523(L)
Doyle, William T. and Donald H. Jacobs. Ultra-compact magnetic storage system—231(A)
Dozier, J. B. (see Donnally, B. L.)—170(A)
Draper, James E. and Boyce D. McDaniel. Fast neutron scintillation spectrometer—185(A)

Drell, S. D. Recoil correction to bremsstrahlung cross section—753
Dresden, M. Nonlinear interaction of scalar fields—224(A)
Driggers, F. E. Bursts in material of low atomic number—1080
Dropkin, J. J. (see Conrad, G.)—192(A)
Duff, Russell E. Interaction of plane shock waves and rough surfaces—912(A)
—— (see Knight, Herbert T.)—909(A)
Dumond, J. W. M. Recent and prospective improvements in measurement of nuclear energy-levels—216(T)
Dunlap, W. C., Jr. Lattice defects in Ge—190(A)
Dunlavey, Dean C. and Glenn T. Seaborg. Investigations of complex structure in α-emission with nuclear emulsions—165(L)
Dutton, David. Release of trapped charge in alkali halide crystals—191(A)

Easter, D. P. (see Foner, S. N.)—204(T)
Eckerman, J. and R. N. Schwartz. Observations on luminescence accompanying cone-cylindrical and spherical missiles traveling at high speeds—912(A)
Edmonson, R. B. (see Olsen, H. L.)—232(A)
Edwards, Donald A. (See Tongiorgi, V. Cocconi)—220(A)
Edwards, L. S. and F. A. MacMillan. Relative yields of photonuclear reactions—377(L)
Eisenstein, Julian. Paramagnetic relaxation in CsTi alum—522(L)
Eisinger, J. T. (see Debs, R. J.)—196(A)
Ekstein, H. Scattering by many-body systems in terms of two-body collision parameters—31
Elder, F. K., Jr., and N. de Haas. Experimental study of formation of vortex ring—911(A)
Elkind, M. M. First-order theory for ion optics of Van de Graaff accelerators—184(A)
—— (see Buechner, W. W.)—237(A)
Ellis, S. G. Plural electron scattering and its influence on electron diffraction patterns—970
Elsasser, W. M. Magnetohydrodynamics—909(T)
Emmerich, W. S., Y. Nogami, L. A. Kiley, and J. D. Kurbatov. Electron paths in magnetic lens spectrometer—194(A)
Emrich, R. J. (see Curtis, C. W.)—913(A)
Endt, P. M., H. A. Enge, J. Haffner, and W. W. Buechner. Excited states of Mg^{28} from $Al^{27}(d,\alpha)Mg^{25}$ and $Mg^{24}(d,p)Mg^{25}$—27
Enge, H. A. (see Buechner, W. W.)—237(A)
—— (see Endt, P. M.)—27
Eppling, F. J. (see Jackson, H. L.)—237(A)
Estermann, I., S. A. Friedberg, and J. E. Goldman. Specific heats of several metals between 1.8° and 4.2°K—582
Etzel, H. W. Enhancement of *F*- and *V*-bands in NaCl containing Ca—906(L)
Everhart, Edgar (see Lorrain, Paul)—183(A)
Eyges, L. and S. Fernbach. Angular distribution of shower particles as function of depth, erratum—1143(L)
Eyring, H., A. L. Wahrhaftig, and H. M. Rosenstock. Interpretation of mass-spectra in terms of molecular structure—204(T)

Fafarman, A. and M. H. Shamos. γ-radiation associated with stopping of μ^--mesons in Pb—219(A)
Fainberg, Joseph (see Lord, J. J.)—538(L)
Fairhall, Arthur W. and Charles D. Coryell. Relative yields of Br^{80} isomers in nuclear reactions—215(A)
—— (see Debs, R. J.)—196(A)
Fan, Chang-Yun. β-spectra and internal conversion coefficients for Co^{60}, Nb^{95}, Au^{198}, and Hf^{181}—252
Feenberg, E. (see Ahrens, T.)—663(L)
—— (see Hammack, K. C.)—218(A)
—— (see King, R.)—218(A)
Feldman, D. (see Goldfarb, L. J. B.)—208(A)
Feldman, L. and C. S. Wu. Investigation of β-spectra of Be^{10}, K^{40}, Tc^{99}, and Cl^{36}—1091
Ferentz, Melvin and David Pines. Collective description of nucleon interactions—188(A)
Ferguson, A. J. and J. H. Montague. Neutron activation of Ne^{22} and N^{15}, and attempt to detect dineutrons in a pile—215(A)
Fernbach, S. (see Eyges, L.)—1143(L)
Ferrell, R. A. (see Bonner, T. W.)—1032
Feshbach, Herman, C. Porter, and V. F. Weisskopf. Theory of nuclear reactions—188(A)
—— (see Hauser, Walter)—366
Findley, D. E. (see McGruer, J. N.)—223(A)
—— (see Worthington, H. R.)—223(A)
Fine, M. E. Evidence for domain structure in antiferromagnetic CoO from elasticity measurements—1143(L)
Finlayson, D. M., V. A. Johnson, and F. M. Shipley. Interpretation of low temperature Hall curve of degenerate Ge sample—1141(L)
Fisher, John C., Edward W. Hart, and Robert H. Pry. Theory of slip-band formation—210(A); 958
—— (see Hart, Edward W.)—211(A)
Fletcher, C. H. and A. H. Taub. Effects of curved shock waves in pseudo-stationary flows—912(A)
—— (see Taub, A. H.)—912(A)
Fletcher, R. C. (see Briggs, H. B.)—1130(L)
Flowers, J. W. (see Jones, Mark W.)—175(A)
Foldy, L. L. Electromagnetic properties of Dirac particles—688
—— Electron-neutron interaction—693
—— Nucleon recoil and the electron-neutron interaction—675(L)
—— (see Berger, J. M.)—1061
Folger, R. L. (see Rudstam, G.)—358
Foner, Simon and Emerson M. Pugh. Hall effect in Co above magnetic saturation—210(A)
—— (see Pugh, Emerson M.)—210(A)
Foner, S. N. and R. L. Hudson. Flame studies with rapid sampling mass spectrometer—204(T)
——, **F. T. McClure, A. Kostiakoff, and D. P. Easter.** Detailed study of appearance-potential curves—204(T)
Fonger, W. (see Simpson, J. A.)—240(A)
Foote, R. S. and G. Kamm. Pair spectrometer using four scintillation crystals—193(A)
Forbush, S. E. (see Neher, H. V.)—889
Forman, Guy (see Auxier, John)—170(A)
Fowler, J. L. (see Brolley, J. E., Jr.)—206(A)
—— (see Jones, W. H.)—174(A)
Fowler, Richard G. Shock waves in spark discharges in gases—909(T)
——, **William R. Atkinson, and Luther W. Marks.** Ion concentrations and recombination in expanding low pressure sparks—966
Fox, R. E., W. M. Hickam, T. Kgeldaas, Jr., and D. J. Grove. Appearance-potentials and ionization probability studies by electron-impact—204(T)
Foy, P. W. (see Pearson, G. L.)—190(A)
Frank, Wilson J. (see Madey, Richard)—204(A)
Franzen, W. and J. G. Likely. Excited states of Li isotopes—205(A); 667(L)
—— (see Likely, J. G.)—666(L)
—— (see Rhodes, J.)—141
Fraser, P. A. Pair-production cross section for high energies—523(L)
Frauenfelder, H. (see Aeppli, H.)—379(L)
Freeman, B. E. (see McIntosh, J. S.)—237(A)
Freistadt, Hans. Darling's theory of elementary particles and Born's reciprocity hypothesis—198(A)
French, J. B. and M. L. Goldberger. Coulomb scattering of deuterons—899(L)
—— (see Daitch, P. B.)—900(L)

Fretter, W. B. *V*-particles—199(T)
Fried, H. M. (see Zilsel, P. R.)—193(A)
Friedberg, S. A. (see Estermann, I.)—582
Friedman, F. L. and W. Tobocman. Wave-mechanical description of deuteron stripping process—208(A)
Froehlich, Fritz E., Erich M. Harth, and Kurt Sitte. High energy nuclear interactions in Pb—504
Fry, W. F. Unusual $\pi-\mu$ decays in photographic emulsions—219(A)
—— **and J. J. Lord.** Unusual meson induced star—533(L)
—— (see Chou, C. N.)—671(L)
—— (see Morinaga, H.)—182(A)
—— (see White, George R.)—219(A)
Fulbright, H. W., J. A. McCarthy, and C. W. McCutchen. Thirty-channel pulse-height discriminator based on cathode-ray tube—184(A)
Fuller, C. S. and J. D. Struthers. Cu as acceptor element in Ge—526(L)
Fung, Si-Chang and I. Perlman. Momentum transfer in nuclear excitation by high energy particles—622
Furst, Milton (see Bittman, Loran)—83
Fuson, Nelson, Marie-Louise Josien, and Thomas M. Gregory, Jr. Infrared spectroscopic studies of carbonyl vibration in polycyclic quinones. I. Influence of substituents—170(A)
—— (see Josien, Marie-Louise)—170(A); 170(A); 212(A)

Galonsky, A. I. (see Jackson, H. L.)—237(A)
Gamba, A., R. Malvano, and L. A. Radicati. Selection rules in nuclear reactions—440
Garfunkel, M. P. Effect of surface energy on superconducting phase transition—108
Garstang, R. H. Charge transfer for protons in He—529(L)
Garstens, M. A. and S. H. Liebson. Paramagnetic resonance in concentrated liquid solutions—230(A)
Garth, R. C., D. J. Hughes, and J. S. Levin. Level densities from fast neutron capture—222(A)
Gayhart, E. L. (see Olsen, H. L.)—232(A)
Gehring, J. W., Jr. (see Dewey, J. N.)—909(A)
Gell-Mann, Murray and Marvin L. Goldberger. Strong coupling in relativistic meson theory—218(A)
George, E. P. Report on recent work at Bristol University, England—199(T)
Ghiorso, A., G. H. Higgins, A. E. Larsh, G. T. Seaborg, and S. G. Thompson. Spontaneous fission of U^{234}, Pu^{238}, Cm^{240}, and Cm^{244}—163(L)
Ghosh, S. N., Walter Gordy, and D. G. Hill. Paramagnetic resonance in U salts—229(A)
——, **R. Trambarulo, and Walter Gordy.** Dipole moments of several molecules from their microwave spectra—172(A)
Gibson, R. E. Research, development and guided missiles.—909(T)
Givin, H. H. (see Cochran, L. W.)—672(L)
—— (see Ryan, J. L.)—177(A)
Glaser, Donald A. Effects of ionizing radiation on formation of bubbles in liquids—665(L)
Glaser, H. and A. J. F. Siegert. Electron distribution in irradiated *N*-type semiconductors—191(A)
Glauber, Roy J. Scattering of neutrons by systems of nuclei—189(A)
Glaubman, Michael J. and Franz R. Metzger. Properties of Nuclear levels associated with decay of Sb^{122}—203(A)
Glick, H. L., F. C. Brooks, W. F. Witzig, and W. E. Johnson. Resistivity of Cu_3Au during neutron irradiation—1074
Gluckstern, R. L. (see Breit, G.)—74
—— (see McIntosh, J. S.)—237(A)
Godfrey, T. N. K. (see Keuffel, J. W.)—942
Goldberg, E. (see Jackson, H. L.)—237(A)
Goldberg, Joshua and Peter G. Bergmann. New approximation for gravitational field equations—198(A)
Goldberg, M. D. (see Harvey, J. A.)—220(A)
Goldberger, M. L. (see Chew, Geoffrey F.)—778
—— (see French, J. B.)—899(L)
—— (see Gell-Mann, Murray)—218(A)
Goldfarb, L. J. B. and D. Feldman. Polarization effects in p-p scattering at high energies—208(A)
Goldhaber, Gerson. Elastic scattering of pions from H and D—220(A)
—— (see Goldhaber, S.)—185(A)
Goldhaber, S. and G. Goldhaber. Loading of photographic emulsions with light elements—185(A)
Goldman, J. E. (see Estermann, I.)—582
—— (see Urquhart, H. M. A.)—210(A)
Goldstein, J. H. (see Morgan, H. W.)—172(A)
—— (see Wilcox, W. S.)—172(A)
Goodenough, John B. Mechanism causing variations of axial ratio in noncubic metallic crystals—200(A)
Goodman, Leonard (see Hamermesh, Bernard)—528(L)
Goodrich, Max (see Stirling, W. L.)—176(A)
Gordon, J. P. (see Artman, J. O.)—227(A)
Gordy, Walter (see Anderson, Roy S.)—561
—— (see Ghosh, S. N.)—172(A); 229(A)
—— (see Luck, Clarence F.)—172(A)
—— (see Mockler, Richard)—172(A)
Goss, C. G. (see Kelley, G. G.)—174(A)
Gove, H. E. and H. F. Stoddart. Angular distributions of $C^{12}(p,p')C^{12*}$ $Q=-4.45$ Mev and the $Mg^{24}(p,p')Mg^{24*}$ $Q=-1.38$ Mev reactions using a NaI scintillation counter—237(A)
—— (see Stoddart, H. F.)—238(A); 262
Graham, R. L. (see Bell, R. E.)—236(A)
Graves, E. R. and L. Rosen. Energy spectrum of neutrons from interaction of 14-Mev neutrons with C, Al, Fe, Cu, Zn, Ag, Cd, Sn, Au, Pb, and Bi—239(A)
Green, David, Harold K. Ticho, and J. Reginald Richardson. γ-radiations from V^{48} and Nb^{92}—195(A)
Green, H. S. (see Messel, H.)—378(L); 738
Greenberg, J. Mayo. Scattering by high potential barriers and by potentials with shell structure—209(A)
Greenfield, M. A., L. B. Silverman, and R. W. Dickinson. Irradiation chamber for 100-curie Co^{60}—184(A)
Gregg, E. C. (see Tucker, B. L.)—907(L)
Gregory, Thomas M., Jr. (see Fuson, Nelson)—170(A)
Greifinger, P., J. Levinger, and F. Rohrlich. Elastic scattering of gammas by bound electrons—663(L)
Greuling, E. Modified Fermi theory of neutron moderation—177(A)
Griffin, P. M., R. A. Loring, G. K. Werner, and J. R. McNally, Jr. Preliminary design and performance of fast high resolution Echelle spectrograph—171(A)
Griffing, V. and D. Sette. Luminescence produced as result of intense ultrasonic waves—234(A)
Griffith, Wayland. Vibrational energy lag in shock waves—234(A)
Groetzinger, Gerhart and Fred L. Ribe. Cloud chamber studies of production of light "positive particles" near β^--ray emitters—1003
—— (see Hacskaylo, Michael)—789
Grosse, A. V. (see Benedict, W. S.)—213(A)
—— (see Javan, A.)—227(A)
Grove, D. J. (see Fox, R. E.)—204(T)
Groven, L. (see Roy, R. R.)—619
Gugelot, P. C. Data on elastic scattering of 18.3-Mev protons—525(L)
Gursky, Herbert (see Pomeroy, David)—179(A)
Guth, E. (see Thie, Joseph A.)—962
Gutowsky, H. S. and B. R. McGarvey. Broadening of magnetic resonance lines in metals by spin-lattice interactions—226(A)
Gyorgy, E. M. and G. G. Harvey. Spectroscopy of the solid state: Cu and Cr—861

Hacskaylo, Michael and Gerhart Groetzinger. Generation of color center precursors in alkali halides by electrolysis—789
Haffner, J. (see Endt, P. M.)—27
Hagstrum, H. D. Ionization and dissociation of diatomic molecules by electron impact—195(T)
Hahn, T. M. (see Cochran, L. W.)—672(L)
—— (see Ryan, J. L.)—177(A)
Haisley, W. E., Jr. Decoherence curve investigation of "narrow air showers" in cosmic rays—169(A)
Haldar, B. C. Radioactivity produced in Pt by slow neutron capture—158(L)
Hall, H. H. and J. L. Powell. Scattering of protons by protons. IV—223(A)
—— (see Powell, J. L.)—223(A)
Hall, R. N. Electron-hole recombination in Ge—387(L)
Halliday, D. (see Wheatley, J.)—235(A)
Halpern, I. (see Debs, R. J.)—196(A)
—— (see Winhold, E. J.)—1139(L)
Halpern, J., A. K. Mann, and M. Rothman. Angular distribution of photoprotons from C—164(L)
—— (see Mann, A. K.)—146
Halpern, Otto. Condensation phenomenon of ideal Einstein-Bose Gas. II—520(L)
—— Proposed re-interpretation of quantum mechanics—389(L)
—— **and C. P. Hsu.** Evaluation of neutron-electron scattering experiments—519(L)
—— **and B. A. Lippmann.** Interference of amplitudes in cascade processes—1128(L)
Hamermesh, Bernard, Virginia Hummel, Leonard Goodman, and Donald Engelkemeir. γ-rays from Sc^{48}—528(L)
Hamlin, D. (see Schulz, A. G.)—219(A)
Hammack, K. C. and E. Feenberg. Surface energy in free-particle nuclear model—218(A)
Hammel, E. F. and Adam F. Schuch. Anomalous type of He^3 flow—154(L)
Hammerle, W. G. (see Montgomery, D. J.)—202(A)
Hamming, R. W. (see Bozorth, R. M.)—209(A)
Hanna, S. S. (see Class, C. M.)—247
—— (see Cohen, L.)—206(A)
—— (see Pruitt, J. S.)—534(L)
Hardy, W. A. (see Silvey, G.)—236(A)
Harrick, N. J. (see Bray, P. J.)—229(A)
Harris, S. P., and L. M. Bollinger. Neutron resonances in Hf isotopes and in As—222(A)
—— (see Bollinger, L. M.)—184(A)
Harrison, F. B. (see Keuffel, J. W.)—942
Harrison, Mark and Alan O. Sykes. Reciprocity calibration of accelerometers—231(A)
Hart, Edward W., John C. Fisher, and Robert H. Pry. Strain hardening of metal crystals—211(A)
—— (see Fisher, John C.)—210(A); 958
Hart, H. E. and R. D. Hatcher. Regular meson potentials in low energy proton-proton scattering—375(L)
Harth, Erich M. (see Frochlich, Fritz E.)—504
Hartman, P. L. and D. H. Tomboulian. Uv radiation from Cornell synchrotron—233(A)
Harvey, G. G. (Gyorgy, E. M.)—861
Harvey, J. A., D. J. Hughes, and M. D. Goldberg. Neutron-electron interaction—220(A)
Haskin, D. M. (see Lord, J. J.)—538(L)
Haslam, R. N. H., L. Katz, R. J. Horsley, A. G. W. Cameron, and R. Montalbetti. Fine structure in $O^{16}(\gamma,n)O^{15}$ activation curve—196(A)
—— (see Horsley, R. J.)—756
—— (see Taylor, J. G. V.)—1138(L)
Hatcher, R. D. (see Hart, H. E.)—375(L)
Hauser, Walter and Herman Feshbach. Inelastic scattering of neutrons—366
Hausman, H. J., A. J. Allen, J. S. Arthur, R. S. Bender, C. J. McDole, L. M. Diana, K. B. Rhodes, and R. A. Barjon. Excited states of Mg^{24}, Cr^{52}, and Mn^{55}—238(A)
—— (see Arthur, J. S.)—237(A)
Havas, Peter. Classical equations of motion of point particles. I—309
—— Conservation laws for fields of zero rest mass. II—898(L)
—— (see McLennan, James A., Jr.)—898(L)
Havens, W. W., Jr. (see Block, M. M.)—168(A)
—— (see Sheer, C.)—239(A)
Hayashi, Izuo (see Kumagai, Hiroo)—374(L)
Hayden, R. J. (see Karraker, D. G.)—901(L)
Haynes, S. K. (see Broyles, C. D.)—174(A)
—— (see Holladay, W. G.)—175(A)
Hayward, R. W. Decay of Cd^{115} isomer—202(A)
Heath, R. L. K-shell conversion coefficient of Ce^{141}—1132(L)
—— **and P. R. Bell.** Determination of K-shell conversion coefficients using NaI single crystal scintillation spectrometer—176(A)
Heckrotte, W., L. R. Henrich, and J. V. Lepore. Photoproduction of π^0-mesons from deuterium—219(A)
Heer, E. (see Aeppli, H.)—379(L)
Hegenberger, R. F. and A. W. Waltner. Low energy yield of $H^2(d,p)H^3$—176(A)
Hein, R. A. (see Steele, M. C.)—908(L)
Heineman, R. E. Multiple-wire ionization chamber for study of large air showers—240(A)
Heller, Jack. Possible convergent solution of interaction state equation—225(A)
Helmholz, A. C. Photodisintegration of deuteron at high energies—195(T)
Hemmendinger, A. (see Argo, H. V.)—612
Hemstreet, H. W. and J. M. Reynolds. Electrical resistivity of graphite at low temperatures—178(A)
Henley, E. M. Nonlinear pseudoscalar meson theory—42
Hennig, G. and L. Meyer. Search for low temperature superconductivity in graphite compounds—439
Henrich, L. R. (see Heckrotte, W.)—219(A)
Henry, Warren E. Anomalous paramagnetism of $CuSO_4 \cdot 5H_2O$—1133(L)
—— Paramagnetic saturation of Fe ammonium alum—229(A)
Herlin, Melvin A. (see Rorschach, H. E., Jr.)—193(A)
Herring, Conyers. Energy of Bloch wall on band picture. II. Perturbation approach—60
Hershberger, W. D. and H. N. Leifer. Paramagnetic resonance in phosphors—229(A)
Hershey, A. V. Six-dimensional representation of stress and strain in face-centered cubic crystal—200(A)
Hershkowitz, J., H. P. Kallmann, and W. A. Schneider. Coincidence method for investigation of cosmic rays using scintillations in liquids—241(A)
Herzfeld, K. F. Relaxation phenomena in polyatomic gases—212(T)
Herzog, L. F. (see Aldrich, L. T.)—186(A)
Hess, W. N. (see Cladis, J. B.)—425
Heydenburg, N. P. (see Cowie, Dean B.)—304
—— (see Rose, William B.)—382(L)
Hibdon, Carl T. and C. O. Muehlhause. Internal conversion of neutron capture γ-rays—222(A)
Hibi, Tadatosi and Kazuo Ishikawa. Spectral dependence of thermionic emission with activation from (Ba-Sr)O cathodes over the visible region—673(L)
Hickam, W. M. (see Fox, R. E.)—204(T)
Higgins, G. H. (see Ghiorso, A.)—163(L)
Hill, D. G. (see Ghosh, S. N.)—229(A)
Hill, David L. Distributions-in-energy for α-particles and protons from U^{238} fission—1049
—— Neutron energy spectrum from U^{235} thermal fission—1034
Hill, R. W. (see Jackson, H. L.)—237(A)

Hine, G. J. (see Prestwich, G. D.)—1030
Hirschberg, J. G., Jr. Lamb shift in ionized He—228(A)
Hirschfelder, J. O. Flames and detonations—909(T)
Hitchcock, A. Spin and magnetic moment of V^{50}—664(L)
Hittmair, O. Inelastic scattering resulting in short-lived isomers—375(L)
Hoesterey, Donald C. Proton groups from deuteron bombardment of Co^{59} and Cu^{63}—216(A)
Hoffmann, Banesh. Dirac's new classical theory of electrons 703
Hofstadter, R. (see Van Sciver, W.)—522(L)
Hoke, G. Robert. Positron-electron scattering in He—285; ——, **and Paul E. Shearin**—176(A)
Holladay, W. G. and S. K. Haynes. Empirical determination of trajectories in thick, non-uniform field magnetic lens spectrometer—175(A)
Hollyer, R. N., Jr., A. C. Hunting, Otto Laporte, E. H. Schwarcz, and E. B. Turner. Luminous effects in shock tube—911(A)
Holmes, D. K. Application of the cellular method to Si—782
Holt, R. B., R. N. Thorn, and R. W. Waniek. Measurement of short β-decay lifetimes—378(L)
Holtzman, Richard B. and Nathan Sugarman. Identification and yields of $((\gamma,xn)$ reactions—632
Hopkins, J. I. and C. N. Wright. Scintillation counter studies of slow α-particles—174(A)
Horan, J. R. and G. A. Boyd. Autoradiographic analysis of Murray, Kentucky meteorite—177(A)
Horsley, R. J., R. N. H. Haslam, and H. E. Johns. γ-neutron reactions in F—756
—— (see Haslam, R. N. H.)—196(A)
Howard, J. N. and J. H. Shaw. Absorption by telluric CO in 2.34μ region—679(L)
—— (see Shaw, J. H.)—380(L)
Hsu, C. P. (see Halpern, Otto)—519(L)
Hubbard, J. C. and D. Sette. Ultrasonic dispersion and absorption in vapors of *cis*- and *trans*-$C_2H_2Cl_2$—233(A)
Hubbard, Thomas P., Jr., Edward B. Nelson, and James A. Jacobs. Angular correlation in the reaction $B^{11}(p;\gamma_1,\gamma_2)C^{12}$—378(L)
Hubbell, Harry H., Jr. Thermal neutron flux distribution in Oak Ridge uranium-graphite reactor—184(A)
Huddlestone, R. H. and J. V. Lepore. Meson exchange contributions to high energy deuteron photoeffect—207(A)
Hudson, A. M. (see Armstrong, A. H.)—238(A)
Hudson, R. L. (see Foner, S. N.)—204(T)
Hudspeth, Emmett L. (see Rose, William B.)—382(L)
Hughes, D. J. (see Garth, R. C.)—222(A)
—— (see Harvey, J. A.)—220(A)
—— (see Palevsky, H.)—221(A)
Hughes, V. (see Weinreich, G.)—229(A)
Hull, M. H., Jr. (see Breit, G.)—74
Hulm, J. K. (see Matthias, B. T.)—799
Hulthén, L. and S. Skavlem. $n-p$ scattering in the region 0-5 Mev—297
Hummel, Virginia (see Hamermesh, Bernard)—528(L)
Hunt, S. E. Absolute resonant energies for radiative capture of protons by Be below 520 kev—902(L)
Hunt, Warren A. (see Zaffarano, D. J.)—194(A)
Hunting, A. C. (see Hollyer, R. N., Jr.)—911(A)
Huntington, H. B., G. A. Shirn, and E. S. Wajda. Self-diffusion in Zn—211(A)
Hurst, D. G. (see Brockhouse, B. N.)—239(A)
Hutchison, Clyde A., Jr., and Gordon A. Noble. Paramagnetic resonance absorption in additively colored crystals of alkali halides—1125(L)
Huxford, W. S. (see Olsen, H. N.)—233(A); 922

Inghram, M. G. (see Karraker, D. G.)—901(L)
Inghram, M. H. Ion-molecule collisions as tool in chemical physics—204(T)
Inglis, D. R. Intermediate coupling as encountered in p-shell nuclei—915
Irving, John. Binding energy of α-particle—519(L)
Ishikawa, Kazuo (see Hibi, Tadatosi)—673(L)

Jaccarino, V., B. Bederson, and H. H. Stroke. Nuclear spin and magnetic moment of $_{55}Cs^{134}$—676(L)
—— (see Bederson, B.)—228(A)
—— (see King, J. G.)—228(A)
Jackson, H. L., A. I. Galonsky, F. J. Eppling, R. W. Hill, E. Goldberg, and J. R. Cameron. Determination of angular distribution and absolute differential cross section of $C^{12}(p,p)C^{12}$ reaction—237(A)
Jackson, Julius L. Irreversibility and generalized noise—471
Jacobs, Donald H. and Seymour Scholnick. Addition of general-purpose program to JAINCOMP-B electronic digital computer—231(A)
—— (see Doyle, William T.)—231(A)
—— (see Martin, Marcel)—231(A)
Jacobs, James A. (see Hubbard, Thomas P., Jr.)—378(L)
Jakobson, M. J. (see Schulz, A. G.)—219(A)
Jastram, Philip S. and C. E. Whittle. Angular correlation of γ-rays in Ti^{48}—1133(L)
—— (see Whittle, Charles E.)—203(A)
Jastrow, Robert. Low energy properties of pseudoscalar interaction with hard core—209(A)
Javan, A. and A. V. Grosse. Microwave spectrum of MnO_3F—227(A)
—— (see Nethercot, A. H.)—226(A)
Jaynes, E. T. Internal fields in crystals—200(A)
Johns, H. E. (see Horsley, R. J.)—756
Johns, M. W., C. D. Cox, R. J. Donnelly, and C. C. McMullen. Radioactive decay of In^{114}—1134(L)
Johnson, C. Y. (see Davis, L. R.)—239(A)
Johnson, Charles M. and Donald M. Slager. Line breadth of OCS as a function of rotational transition and temperature—677(L)
Johnson, Peter D. and Ferd E. Williams. Electron traps in KCl:Tl phosphor—192(A)
Johnson, V. A. (see Finlayson, D. M.)—1141(L)
Johnson, W. E. (see Glick, H. L.)—1074
Johnson, Walter H., Jr. Mass of V^{50}—166(L)
—— (see Collins, Thomas L.)—236(A)
Jones, B. L. (see Baker, P.)—176(A)
Jones, Ernest A. (see Josien, Marie-Louise)—170(A)
—— (see Stephenson, Charles V.)—169(A)
Jones, June G. and David Pomeroy. Effects of delaying of germination of seeds subjected to radiation—179(A)
Jones, K. W. (see Craig, D. S.)—206(A)
Jones, L. C., A. V. Bushkovitch, C. A. Potter, and A. G. Rouse. Variation of collision diameters with mix ratio in binary mixtures in microwave pressure broadening—227(A)
Jones, L. W. (see Terwilliger, K. M.)—196(A)
Jones, Mark W., J. W. Flowers, and David Pomeroy. Improved vibrating probe electrometer for use in biophysical research—175(A)
Jones, W. H., J. L. Fowler, and J. H. Paehler. Mo^{99}, Ag^{111}, and Ba^{140} yields from proton induced fission—174(A)
Josien, Marie-Louise and Nelson Fuson. Influence of molecular structure upon infrared carbonyl band in polycyclic quinones—212(A)
——, **Nelson Fuson, Ernest Jones, and James R. Lawson.** Infrared and Raman spectroscopic study of CF_3COOH 170(A)
——, **Nelson Fuson, and Jeanne-Marie Lebas.** Infrared spectroscopic studies of carbonyl vibration in polycyclic quinones. II. Influence of fused benzene rings—170(A)
—— (see Fuson, Nelson)—170(A)
Jost, Res and Walter Kohn. Construction of potential from phase shift—977
—— (see Pais, A.)—871

Kaericher, K. C. (see Avery, C. J.)—216(A)
Kaesberg, Paul, J. A. Anderegg, B. R. Leonard, and W. W. Beeman. Size, shape, and hydration of tomato bushy stunt virus—186(A)
Kahl, G. D. (see Bennett, F. D.)—234(A)
Kahn, Bernd. Determination of counting efficiency of gas-flow proportional counter—175(A)
Kaiser, H. F. Electron cyclotron (microtron) for 3-cm rf operation—183(A)
Kallmann, H. P. (see Hershkowitz, J.)—241(A)
Kallmann, Hartmut and Bernard Kramer. Induced conductivity and light emission in different luminescent type powders—91
—— (see Bittman, Loran)—83
Kambe, Kenjirô (see Kumagai, Hiroo)—374(L)
Kamm, G. (see Foote, R. S.)—193(A)
Kammer, E. W. Velocity determination for microseisms in coral formations—177(A)
Kantrowitz, A. (see Resle, E. L., Jr.)—909(T)
Känzig, W. Wall energy of ferroelectric domains—385(L)
Kaplan, Louis, G. R. Ringo, and K. E. Wilzbach. Thermal neutron absorption cross section of D—785
Kaplon, M. F. and D. M. Ritson. ζ^0-meson—664(L)
Karplus, Robert and Abraham Klein. Electrodynamic displacement of atomic energy levels. III. Hfs of positronium—848
—— (see Klein, A.)—235(A)
Karraker, D. G., R. J. Hayden, and M. G. Inghram. Half-lives of Eu^{152}, Eu^{154}, and Sm^{151}—901(L)
Karzmark, C. J. (see Thompson, R. W.)—182(A)
Katcoff, Seymour. Thermal neutron capture cross section of A^{40} and observation of A^{42}—886
Katz, L., L. Pease, and H. Moody. Photoneutron cross sections for reactions $Br^{81}(\gamma,n)Br^{80}$ and $Br^{81}(\gamma,n)Br^{80*}$ and analysis of ratio between these cross sections—196(A)
—— (see Haslam, R. N. H.)—196(A)
Kebler, R. W., W. W. McCormick, and R. A. Sawyer. Excitation characteristics of spectra of highly ionized Al in low pressure spark—212(A)
Keck, James (see Littauer, Raphael)—195(A)
Keenan, Thomas K., Robert A. Penneman, and B. B. McInteer. Determination of half-life of Am^{242m} for negative electron emission—204(A)
Keffer, Frederic. Anisotropy in antiferromagnetic MnF_2—608
Kelley, G. G., P. R. Bell, and C. G. Goss. ORNL 20-channel analyzer—174(A)
Kelley, J. C. R. (see Okress, E. C.)—209(A)
Kelly, F. M. and D. K. C. MacDonald. θ-values in metals—210(A)
Kendall, James M. Compressible flow of viscous fluid in small diameter tube closed at one end—913(A)
—— Precision micromanometer—230(A)
Kennedy, James M. μ-meson capture and nuclear shell structure—953
Kenny, G. S. (see Barnett, S. J.)—723
Kern, B. D. (see Cochran, L. W.)—672(L)
—— (see Ryan, J. L.)—177(A)
Kerst, D. W., L. J. Koester, A. S. Penfold, and J. H. Smith. Angular distribution of neutrons exceeding 50 Mev ejected by 320-Mev bremsstrahlung—197(A)
Keuffel, J. W., F. B. Harrison, T. N. K. Godfrey, and George T. Reynolds. Capture of μ-mesons in heavy elements—942
Keywell, Frank. Mechanism for sputtering in high vacuum based upon theory of neutron cooling—160(L)
Kgeldaas, T., Jr. (see Fox, R. E.)—204(T)
Kienberger, C. A. Specific α-activity of U^{234}—520(L)
Kiger, E. O. (see McManaway, G. W.)—176(A)
Kiley, L. A. (see Emmerich, W. S.)—194(A)
Kinard, Frank E. Thin wall Geiger counters for research on soft component—168(A)
King, J. G. and V. Jaccarino. Anomalous spin gyromagnetic ratio of electron—228(A)
King, J. S. (see Parkinson, W. C.)—387(L)
King, Jean I. Generation of convection in planetery atmosphere—911(A)
King, R. and E. Feenberg. Nuclear structure and interpretation of β-decay—218(A)
Kington, J. D. (see Willard, H. B.)—206(A)
Kirkwood, J. G. Statistical mechanics of transport properties—212(T)
Kistiakowsky, Vera. Pm isotopes—859
Kittel, C. (see Yafet, Y.)—290
Kivelson, D. and E. Bright Wilson, Jr. Centrifugal distortion in asymmetric rotor molecules—214(A)
Klein, Abraham and R. Karplus. Electrodynamic corrections to fine structure of positronium—235(A)
—— (see Karplus, Robert)—848
Klein, Martin J. Ergodic theorem in quantum statistical mechanics—111
Klema, E. D. and F. K. McGowan. γ-γ angular correlation in Cd^{114}—524(L)
—— **and R. H. Ritchie.** Thermal neutron flux measurements in graphite using Au and In foils—167(L)
Kluyver, Jan C. and Martin Deutsch. Effect of electron shell on angular correlations—203(A)
Knight, Herbert T. and Russell E. Duff. Experimental investigation of spinning detonation—909(A)
Knox, William J. Multiple ionization by electron impact—232(A)
Koehler, W. C. and E. O. Wollan. Neutron diffraction studies of lighter rare earth oxides—238(A)
Koenig, J. Frank. Transient response of linear systems—231(A)
Koester, L. J. (see Kerst, D. W.)—197(A)
Kohman, Truman P. (see Mulholland, George I.)—681(L)
Kohn, Walter. Validity of Born expansions—539(L)
—— Variational methods in periodic lattices—472
—— (see Jost, Res)—977
Kolb, E. D. (see Slichter, W. P.)—527(L)
Kolsky, H. G., T. E. Phipps, Jr., N. F. Ramsey, and H. B. Silsbee. Nuclear rf spectra of H_2 and D_2 in high and low magnetic fields—595
Koffi, S. A. Further experiments on cosmic-ray neutrons—204(T)
Kostiakoff, A. (see Foner, S. N.)—204(T)
Kothari, L. S. Mass of a photon—536(L)
Koudijs, B. (see Bogaardt, M.)—1129(L)
Kouts, H. J. (see Sher, R.)—523(L)
Kramer, Bernard (see Kallmann, Hartmut)—91
Kraushaar, J. J. (see Alburger, D. E.)—448
Kriessman, C. J., Jr. Magnetic susceptibility of Cb, Ta, V, Mo, and W at high temperatures—209(A)
Krishnan, K. S. and S. K. Roy. Evjen's method of evaluating Madelung constant—581
Krohn, V. E., Jr., and E. F. Shrader. $Cu^{63}(\gamma,n)Cu^{62}$ cross section—685
Krotkov, R. V. (see Scheidegger, A. E.)—197
Kubo, Ryogo. Spin wave theory of antiferromagnetics—568
—— Theory of optical and thermal transitions in solids—201(A)
Kuhlthau, A. R. Application of high rotational speed techniques to low density gas dynamics—171(A)
Kumagai, Hiroo, Hidetarô Abe, and Junji Shimada. Anomalous magnetic resonance absorption of Cu^{++}—385(L)
——, **Kazuo Ôno, Izuo Hayashi, and Kenjirô Kambe.** Fine structure of resonance absorption of Mn^{++} in a rhombic crystalline field—374(L)
Kundu, D. N., J. D. Service, and M. L. Pool. Erbium 165—203(A)

Kuperian, J. E., Jr., and E. D. Palmatier. Ionization losses of fast μ-mesons in gases—169(A)
Kurath, Dieter. Decay scheme of $_{21}Sc^{48}$—528(L)
—— Ground-state spins and energy differences from *jj*-coupling model—218(A)
Kurbatov, J. D. (see Emmerich, W. S.)—194(A)

Ladenburg, R. Survey of neutron-density and neutron-production in atmosphere—204(T)
Lal, D., Yash Pal, B. Peters, and M. S. Swami. Production and interaction of mesons at very high energies—545(L)
Landé, Alfred. Thermodynamic continuity and quantum principles—267
Laporte, Otto (see Hollyer, R. N., Jr.)—911(A)
Larsh, A. E. (see Ghiorso, A.)—163(L)
Lawson, James R. (see Josien, Marie-Louise)—170(A)
Leachman, R. B. Velocities of fragments from fission of U^{233}, U^{235}, and Pu^{239}—444
Lebas, Jeanne-Marie (see Josien, Marie-Louise)—170(A)
LeBlanc, J. M., F. B. Stumpf, W. H. Nester, and J. M. Cork. Radioactivity in Ru^{103}—202(A)
—— (see Cork, J. M.)—203(A)
Ledley, R. S. Relation of tooth surfaces to stability of artificial dentures—187
Lee, T. D. and C. N. Yang. Statistical theory of equations of state and phase transitions. II. Lattice gas and Ising model—410
—— (see Yang, C. N.)—404
Leifer, H. N. (see Hershberger, W. D.)—229(A)
Leighton, R. B. Some recent studies of *V*-particles—199(T)
—— (see Anderson, C. D.)—183(A)
—— (see Shelton, F. H.)—183(A)
—— (see Wanlass, S. D.)—183(A)
Leinhardt, T. E. and J. M. Reynolds. Superconductivity in dendritic deposition of pure Sn—178(A)
Leland, W. T. (see Argo, H. V.)—205(A); 612
LeLevier, Robert E. Phenomenological potentials in meson scattering—217(A)
—— **and David S. Saxon.** Optical model for nucleon-nuclei scattering—40
Leonard, B. R. (see Kaesberg, Paul)—186(A)
Lepore, Joseph V. Nuclear forces yielded by symmetrical pseudoscalar meson theory with pseudoscalar coupling—209(A)
—— (see Heckrotte, W.)—219(A)
—— (see Huddlestone, R. H.)—207(A)
Lesensky, L. and H. A. Boorse. He film transport over Cu below 1K°—1135(L)
Lessen, Martin. Hydrodynamic stability of laminar flame fronts—913(A)
Leurgans, Paul and J. Bardeen. Interaction of excitons and phonons—200(A)
Levin, J. S. (see Garth, R. C.)—222(A)
Levine, Harold and Julian Schwinger. Radiation force and torque—224(A)
Levine, Morton A. (see Bostick, Winston H.)—671(L)
Levinger, J. S. Small angle coherent scattering of gammas by bound electrons—656
—— (see Greifinger, P.)—663(L)
Levinson, John. Detection of nuclear magnetic octopole interaction—188(A)
Levy, Henri A. (see Peterson, S. W.)—462
Lévy, Maurice M. Symmetrical pseudoscalar meson theory of nuclear forces, erratum—1143(L)
Libby, W. F. Natural radio carbon and radio-carbon dating—204(T)
Lide, D. R., Jr. Microwave spectrum of CH_2F_2—227(A)
Lidofsky, L., P. Macklin, and C. S. Wu. Radiations of Tl^{204}—204(A); 391(L)
—— (see Macklin, P.)—391(L)
—— (see Wu, C. S.)—1140(L)
Liebson, S. H. (see Garstens, M. A.)—230(A)
Likely, J. G. and W. Franzen. Response of NaI crystals to high energy protons—666(L)
—— (see Franzen, W.)—205(A); 667(L)
Lillie, Alan B. Disintegration of O and N by 14.1-Mev neutrons—716
Lin, S. C. (see Resle, E. L., Jr.)—909(T)
Lindenbaum, S. J. and G. Bernardini. Interactions of 150-Mev protons with nucleus $A=100$—207(A)
Lindsay, John C. and A. V. Masket. Electronic method of measuring forces resisting armor penetration—175(A)
Lindström, Gunnar. Absolute determination of the X-line from ThC″—678(L)
Linz, Arthur, Jr., and A. V. Masket. Short base length range for air-drag studies—175(A)
Lippmann, B. A. (see Halpern, O.)—1128(L)
Littauer, Raphael and James Keck. Photo disintegration of D at 180–260 Mev—195(A)
Livingston, Ralph. Nuclear quadrupole resonance in solids—168(T)
Loferski, J. J. Optical polarization in single crystals of Te—905(L)
Long, Earl A. and Lothar Meyer. Heat conduction by unsaturated He II film—153(L)
—— (see Weaver, A. B.)—531(L)
Lord, J. J., Joseph Fainberg, D. M. Haskin, and Marcel Schein. Narrow angle pairs of particles from nuclear interactions—538(L)
—— (see Chou, C. N.)—671(L)
—— (see Fry, W. F.)—533(L)
Loring, R. A. (see Griffin, P. M.)—171(A)
Lorrain, Paul, Edgar Everhart, and René A. Béique. Theoretical study of modified Cockroft-Walton high tension generator—183(A)
Love, W. F., E. Callen, and F. C. Nix. Magnetic properties of superconducting alloys of In and Tl—844
Luck, Clarence F. and Walter Gordy. Molecular-beam modulation microwave spectrograph—172(A)
—— (see Trambarulo, R. F.)—172(A)
Lyon, W. S. Disintegration of Cr^{51}—1126(L)

Ma, S. T. Bound states and interaction representation—652
MacDonald, D. K. C. Experiments on electrical conductivity—210(A)
—— (see Kelly, F. M.)—210(A)
Mack, J. E. Outer electron structure and *Z*-dependence of x-ray *K*-level values for heavy atoms—225(A)
—— (see Curtis, C. W.)—913(A)
Macklin, P., L. Lidofsky, and C. S. Wu. Evaluation of ratio F_n/F_0 in theory of forbidden β-transitions—391(L)
—— (see Lidofsky, L.)—204(A); 391(L)
MacMillan, F. A. (see Edwards, L. S.)—377(L)
Madey, Richard, Kenneth C. Bandtel, Wilson J. Frank, and Burton J. Moyer. Identification of reaction $p+d\rightarrow\pi^++t$—204(A)
Maeder, D. and V. Winterstelger. Line shape of monochromatic γ-rays in scintillation spectrometer—537(L)
Magnuson, D. W. (see Smith, D. F.)—226(A)
Malvano, R. (see Gamba, A.)—440
Mandeville, C. E. (see Mendenhall, R. I.)—203(A)
—— (see Swann, C. P.)—215(A)
Mann, A. K., J. Halpern, and M. Rothman. Angular distributions of photoprotons—146
—— (see Halpern, J.)—164(L)
Mann, L. G. and W. E. Meyerhof. γ-rays in decay of Ga^{68}—202(A)
Marks, Luther W. (see Fowler, Richard G.)—966
Marshall, J., L. Marshall, V. A. Nedzel, and S. Warshaw. π^0-meson production by 430-Mev protons on H—220(A)
—— (see Marshall, L.)—220(A)

Marshall, L., J. Marshall, V. A. Nedzel, and S. Warshaw. π^0-meson production by 430-Mev protons on Be—220(A)
—— (see Marshall, J.)—220(A)
Martin, Marcel, Donald H. Jacobs, and Seymour Scholnick. Supersensitive differential altimeter—231(A)
Martin, Ronald L. Nuclear cross sections for negative pions of energy 113 and 137 Mev—1052
Marton, L. Electron scattering experiments at low and middle energies—200(A)
Masket, A. V. (see Bilpuch, E. G.)—168(A)
—— (see Brown, F. B., Jr.)—168(A)
—— (see Lindsay, John C.)—175(A)
—— (see Linz, Arthur, Jr.)—175(A)
Matossi, Frank. Modification of Silberstein model of optical anisotropy—214(A)
Matthias, B. T. Superconductivity in Co-Si system—380(L)
—— **and J. K. Hulm.** Search for new superconducting compounds—799
—— (see Wood, Elizabeth A.)—544(L)
Maximon, L. C. and H. A. Bethe. Differential cross section for bremsstrahlung and pair production—156(L)
Maxwell, E. Isotope effect in supraconductivity—187(T)
—— Similarity properties of two-fluid model of superconductivity—1126(L)
Mayfield, Earle B. Time-resolved spectroscopy of incandescence associated with ultra-speed pellets—912(A)
McAfee, K. B. and G. L. Pearson. Electrical properties of Si p-n junctions grown from the melt—190(A)
McCarthy, J. A. Experimental effort to detect double β-decay in Sn^{124} and Zr^{96}—194(A)
—— (see Fulbright, H. W.)—184(A)
McCarthy, Kathryn A. (see Combes, Lewis S.)—201(A)
McClure, F. T. (see Foner, S. N.)—204(T)
McClure, G. W. Ionization by cosmic-ray mesons in A—680(L)
—— (see Pomerantz, M. A.)—240(A)
McCormick, W. W. (see Kebler, R. W.)—212(A)
—— (see Kebler, R. W.)—212(A)
McCutchen, C. W. (see Fulbright, H. W.)—184(A)
McDaniel, Boyce D. (see Draper, James E.)—185(A)
McDole, C. J. (see Arthur, J. S.)—237(A)
—— (see Hausman, H. J.)—238(A)
McFarland, C. E. (see Shull, F. B.)—216(A)
McGarvey, B. R. (see Gutowsky, H. S.)—226(A)
McGinnis, Carl L. Radioactivity of Pd^{111}—202(A)
McGowan, F. K. Lifetime of excited state of Hf^{178}—542(L)
—— (see Klema, E. D.)—524(L)
McGruer, J. N., D. E. Findley, and H. R. Worthington. Scattering of protons by protons. I—223(A)
—— (see Worthington, H. R.)—223(A)
McInteer, B. B. (see Keenan, Thomas K.)—204(A)
McIntosh, J. S., R. L. Gluckstern, S. Sack, and B. E. Freeman. Analysis of p-T scattering—237(A)
McLennan, James A., Jr., and Peter Havas. Conservation laws for fields of zero rest mass. I—898(L)
McLernon, F. (see Bay, Z.)—901(L)
McManaway, G. W., E. O. Kiger, and A. W. Waltner. Low energy portion of C^{14} β-spectrum—176(A)
McManus, H. and W. T. Sharp. Direct interaction and compound nucleus for 14-Mev neutrons—188(A)
McMillan, B. Entropy and information—221(T)
McMullen, C. C. (see Johns, M. W.)—1134(L)
McNally, J. R., Jr. (see Griffin, P. M.)—171(A)
Mendelssohn, K., C. Squire, and Tom S. Teasdale. Measurements on temperature, current, magnetic field phase diagram of superconductivity—589
Mendenhall, R. I., C. E. Mandeville, E. Shapiro, E. R. Zucker, and G. L. Conklin. Radiations from Sn^{125}—203(A)
Menius, A. C., Jr. (see Poulson, J. A.)—174(A)
—— (see Robinson, Esther Davis)—177(A)
Menzel, D. H. Electrodynamics of magnetic storms—212(T)
Merritt, J. (see Schulz, A. G.)—219(A)
Merz, Walter J. (see Wood, Elizabeth A.)—544(L)
Merzbacher, Eugen. Spin-orbit coupling and nuclear shell model—173(A)
Messel, H. and H. S. Green. Angular and lateral distribution functions for nucleon component of cosmic radiation—738
—— **and H. S. Green.** High energy nuclear collisions and Fermi model—378(L)
—— **and R. B. Potts.** Cascade theories with ionization loss—759
—— (see Chartres, B. A.)—748
Messiah, A. M. L. Absorption of slow π^- mesons by He^3—639
Metzger, Franz R. (see Glaubman, Michael J.)—203(A)
Meyer, L. (see Hennig, G.)—439
Meyer, Lothar (see Long, Earl)—153(L)
Meyerhof, W. E. (see Mann, L. G.)—202(A)
Michener, J. W. (see Prebus, A. F.)—201(A)
Mihelich, J. W. Internal conversion of γ-ray transitions in L sub-shells—646
—— **and E. L. Church.** Low energy γ-transitions in some rare earth isotopes, erratum—1144(L)
Milone, Carmelo. Energy spectrum of electrons in extensive cosmic-ray showers—680(L)
Miskel, John A. and Morris L. Perlman. Average charge produced by electron capture in A^{37}—543(L)
Mitchell, Allan C. G. and Robert S. Caird. Electron capture in Tl^{204}—388(L)
—— (see Smith, Alan B.)—454; 1128(L)
Mockler, Richard, Jep H. Bailey, and Walter Gordy. Microwave investigations of $HSiCl_3$ and CH_3SiCl_3—172(A)
Mohler, Fred L. (see Dibeler, Vernon H.)—213(A)
Monahan, James E. Neutron inelastic cross sections for excitation of single levels of middle-weight nuclei—188(A)
Montague, J. H. (see Ferguson, A. J.)—215(A)
Montalbetti, R. (see Haslam, R. N. H.)—196(A)
Montgomery, D. J. and W. G. Hammerle. Dynamic behavior of Nylon filaments—202(A)
Moody, H. (see Katz, L.)—196(A)
Moore, J. (see Sheer, C.)—239(A)
Moore, Mildred D. (see Rusk, Rogers D.)—239(A)
Morewitz, H. A. and M. H. Shamos. Variation of positive-negative ratio of cosmic-ray mesons with momentum and altitude—241(A)
Morgan, H. W. and J. H. Goldstein. Microwave spectrum of vinyl iodide—172(A)
—— (see Walchli, H. E.)—541(L)
Morgan, K. Z. and C. P. Straub. Calculation of maximum permissible concentration of radioactive contamination in air and water following atomic explosion—178(A)
Morinaga, H. and W. F. Fry. Stars induced by μ-mesons in photographic emulsions—182(A)
Morowitz, Harold J. Energy requirements for bacterial motility—186(A)
Morton, H. S., Jr. (see Beams, J. W.)—524(L)
Moses, H. E. and Ta-You Wu. Self-consistent calculation of dissociation of O_2 in upper atmosphere—627
Motz, Lloyd. Gauge invariance and classical electrodynamics—224(A)
Moyer, Burton J. Characteristics of neutral meson production in nucleon collisions—220(A)
—— (see Cladis, J. B.)—425
—— (see Madey, Richard)—204(A)
Muehlhause, C. O. (see Hibdon, Carl T.)—222(A)
Mulholland, George I. and Truman P. Kohman. Natural radioactivity of La^{138}—681(L)
Mullin, Charles J. (see Thie, Joseph A.)—962
Murakawa, Kiyoshi and Shigeki Suwa. Hfs in spectra of Ir and Os—1048
Murray, Raymond L. Generation and storage of radioactive gases from intermittent reactor operation—171(A)
Myers, Vernon. Forces between acetone molecules—185(A)

Nabarro, F. R. N. Effect of radiation on elastic constants—665(L)
Nataf, R. and R. Bouchez. Nucleon-lepton interaction in β-decay—155(L)
Nedzel, V. A. (see Marshall, J.)—220(A)
—— (see Marshall, L.)—220(A)
Neher, H. V. Correlation of cosmic-ray intensities at high altitudes with neutron intensities—240(A)
—— **and S. E. Forbush.** Correlation of cosmic-ray ionization measurements at high altitudes, at sea level, and neutron intensities at mountain tops—889
—— (see Peterson, V. Z.)—240(A)
Nelson, Edward B. (see Hubbard, Thomas P. Jr.)—378(L)
Nereson, N. Measurement of total neutron cross sections at energies between 3 and 12 Mev—221(A)
Nester, W. H. (see Cork, J. M.)—203(A)
—— (see LeBlanc, J. M.)—202(A)
Nethercot, A. H., A. Javan, and C. H. Townes. Microwave spectrum of $C_5H_{11}Br$—226(A)
Newcomb, W. A. (see Salpeter, E. E.)—150(L)
Newman, J. B. Some static axially symmetric gravitational fields—173(A)
Newson, Henry W. and Robert H. Rohrer. Level spacings and magic numbers—177(A)
Newton, J. O. (see Beling, J. K.)—670(L); 1143(L)
Newton, T. D. Process of binary fission—187(A)
Nier, Alfred O. (see Collins, Thomas L.)—236(A)
Nierenberg, W. A. Octupole moment interaction—225(A)
Nix, F. C. (see Love, W. F.)—844
Noble, Gordon A. (see Hutchison, Clyde A., Jr.)—1125(L)
Noegel, F. W. (see Cooper, C. D.)—169(A)
Nogami, Y. (see Emmerich, W. S.)—194(A)
Noyes, H. P. Decay of neutral scalar heavy meson—344

Odgers, G. J. (see Stewart, R. W.)—909(T)
Okazaki, A. (see Walt, M.)—238(A)
Okress, E. C., D. M. Wroughton, G. Comenetz, P. H. Brace, and J. C. R. Kelly. Electromagnetic levitation of solid and molten metals—209(A)
Olbert, Stanislaw. Application of multiple scattering theory to cloud-chamber measurements. I—319
Oldenberg, O. Resonance in collision processes—786
Oliver, A. R. (see Blau, M.)—182(A)
Olsen, H. L., R. B. Edmonson, and E. L. Gayhart. Observations in phenomena initiated in gases by electric spark—232(A)
Olsen, H. N. and W. S. Huxford. Dynamic characteristics of plasma in discharges through rare gases—922
—— **and W. S. Huxford.** Ion concentrations in intense discharges from Stark effect broadening—233(A)
Ôno, Kazuo (see Kumagai, Hiroo)—374(L)
O'Rourke, R. C. Multiple Compton scattering of low energy γ-radiation—225(A)
Osborn, R. K. (see Berger, J. M.)—1061
Osterbrock, Donald E. Electrical conductivity in solar atmosphere—468
Oxley, C. L. Proton scattering experiments with Rochester 130-inch cyclotron—222(T)

Pack, D. C. (see Bershader, D.)—909(T)
Paehler, J. H. (see Jones, W. H.)—174(A)
Pais, A. and R. Jost. Selection rules imposed by charge conjugation and charge symmetry—871
Pal, Yash (see Lal, D.)—545(L)
Palevsky, H., D. J. Hughes, and R. R. Smith. Cross section of Fe for cold neutrons—221(A)
Palmatier, E. D. (see Kuperian, J. E., Jr.)—169(A)
Panofsky, Wolfgang K. H. and Daryl Reagan. Reaction $N^{14}(\gamma,2n)N^{12}$—543(L)
Pappas, Alexis C. Isomers in Te^{132}—162(L)
Pardue, Turner E. Yield strength of mild steel under impulsive loading—172(A)
Parker, Eugene N. Turbulent heat transfer for flow in channel—911(A)
Parker, James P. Zenith angle dependence of extensive air showers—169(A)
Parkinson, W. C., E. H. Beach, and J. S. King. Experimental test of shell model—387(L)
Parlin, R. B., C. J. Thorne, D. W. Roninson. Effect of charge radius on detonation velocity—910(A)
Paskin, Arthur. Analysis of some photoneutron and photoproton experiments—197(A)
Passman, S. (see Block, M. M.)—168(A)
Pawlicki, G. S. and E. C. Smith. Preliminary investigations of neutron total cross sections with Oak Ridge National Laboratory fast chopper—221(A)
Peaslee, D. C. Elastic π-C scattering—862
Pearson, G. L. and P. W. Foy. Si p-n junction diodes prepared by alloying process—190(A)
—— (see McAfee, K. B.)—190(A)
Pearson, John and John S. Rinehart. Surface motion associated with obliquely incident elastic waves—910(A)
Pease, L. (see Katz, L.)—196(A)
Peaslee, D. C. Angular distribution of π-C scattering—217(A)
Peierls, R. E., K. S. Singwi, and D. Wroe. Polyneutron theory of origin of elements—46
Pell, E. M. Hall effect in single crystals of BaO—457
Penfold, A. S. (see Kerst, D. W.)—197(A)
Penneman, Robert A. (see Keenan, Thomas K.)—204(A)
Perez-Mendez, V. (see Wu, C. S.)—1140(L)
Perlman, I. (see Asaro, Frank)—277; 393(L)
—— (see Fung, Si-Chang)—622
Perlman, Morris L. (see Miskel, John A.)—543(L)
Perls, Thomas A. Magnetostriction magnetometer—230(A)
Perlow, G. J. (see Davis, L. R.)—239(A)
Perry, J. P. (see Barnes, S. W.)—669(L)
Peshkin, Murray and A. J. F. Siegert. 7.4-Mev state of Li^7—735
Peters, B. (see Lal, D.)—545(L)
Peterson, S. W. and Henri A. Levy. Coherent neutron scattering cross sections of N and V—462
Peterson, V. Z., H. V. Neher, and E. A. Stern. Further results on cosmic-ray latitude effect between Bismarck and Thule, Greenland—240(A)
Petrie, W. Forbidden line of NII in the aurora—1002
Petritz, Richard L. Diffusion theory of noise in rectifiers and transistors—189(A)
—— Theory of contact noise—535(L)
Petschek, H. (see Resle, E. L., Jr.)—909(T)
Phillips, G. C. (see Cowie, Dean B.)—304
Phipps, T. E., Jr. (see Kolsky, H. G.)—395
Piccioni, O. and R. L. Cool. Cosmic-ray experiment on inelastic cross sections of H and other nuclei for pions—216(T)
—— (see Cool, R. L.)—531(L)
Pieper, G. F. Energy levels of Ti^{49}—215(A)
Pines, David (see Ferentz, Melvin)—188(A)
Piper, William W. and Ferd E. Williams. Electroluminescence of single crystals of ZnS:Cu—151(L)
Pipkin, F. M. (see Ridgway, S. L.)—202(A)
Pirani, F. A. E., A. Schild, and R. Skinner. Quantization of Einstein's gravitational field equations. II—452
Plass, Gilbert N. Radiation loss from atmosphere—187(A)
Pollard, E. C. and A. E. Dimond. Inactivation of southern beam mosaic virus by deuterons—186(A)
Pomerantz, M. A. and G. W. McClure. Enhanced primary cosmic-ray intensity associated with solar disturbances—240(A)
Pomeroy, David and Herbert Gursky. Effect of x-radiation on bioelectric potentials of rats—179(A)
—— (see Jones, June G.)—179(A)

—— (see Jones, Mark W.)—175(A)
Pool, M. L. (see Avery, C. J.)—216(A)
—— (see Kundu, D. N.)—203(A)
Porter, C. (see Feshbach, H.)—188(A)
Porter, Fred T. and C. Sharp Cook. Disintegration of Ce^{144} and Pr^{144}—464
Porter, W. C. and W. E. Ramsey. Limitation of discharge in GM counters—194(A)
Poss, H. L., E. O. Salant, G. A. Snow, and Luke C. L. Yuan. Total cross sections for 14-Mev neutrons—11
Potter, C. A. (see Jones, L. C.)—227(A)
Potter, R. M. (see Armstrong, A. H.)—238(A)
Potter, Roy F. Charge transfer cross sections between atoms and slow ions in A, Ne, and He—232(A)
Potts, R. B. (see Messel, H.)—759
Poulson, J. A. and A. C. Menius, Jr. Negative H ion wave functions—174(A)
Powell, J. L. and H. H. Hall. Scattering of protons by protons. III—223(A)
—— (see Hall, H. H.)—223(A)
Prebus, A. F. and J. W. Michener. Micellar structure in silicate glass—201(A)
Prener, J. S. (see Roberts, S.)—191(A)
Preston-Thomas, H. Electrical resistance of Ta—210(A)
Prestwich, G. D., T. H. Colvin, and G. J. Hine. Average energy of secondary electrons in anthracene due to γ-irradiation—1030
Price, P. J. Energy quantization for colliding molecules; application to liquid He—173(A)
—— Second sound in He^3—He^4 mixtures—381(L)
Primakoff, H. (see Ahrens, T.)—663(L)
Pringle, R. W., H. W. Taylor, and K. I. Roulston. Radiative capture of thermal neutrons by Cd^{113}—1016
——, **H. W. Taylor, and S. Standil.** Some observations on γ-radiation from Po—384(L)
—— (see Roulston, K. I.)—930
Pruitt, J. S., S. S. Hanna, and C. D. Swartz. Angular distributions of Be^9+D neutrons—534(L)
Pry, Robert H. (see Fisher, John C.)—210(A); 958
—— (see Hart, Edward W.)—211(A)
Pugh, Emerson M. and Simon Foner. Ordinary Hall effect in Co-Ni alloys—210(A)
—— (see Foner, Simon)—210(A)
Putnam, T. M. Differential cross section for scattering of 9.48-Mev protons by He—932

Quinnell, E. H. (see Clement, J. R.)—192(A)

Rabi, I. I. Atomic beam resonance method for excited states—379(L)
Radicati, L. A. Influence of charge independence of nuclear forces on electromagnetic transitions—521(L)
—— (see Gamba, A.)—440
Rainwater, C. S. (see Dieke, G. H.)—212(A)
Rainwater, L. J. (see Sheer, C.)—239(A)
Ramsey, Norman F. Vibrational and centrifugal effects on nuclear interactions and rotational moments in molecules—1075
—— (see Kolsky, H. G.)—395
—— (see Porter, W. C.)—194(A)
Ramsey, W. E. (see Porter, W. C.)—194(A)
Randall, C. A. Absorption of cosmic rays under 120 MWE of earth—241(A)
Rankin, Bayard and Hugh Bradner. Fast meson interactions in nuclear emulsions. II. π^+ mesons—553
—— (see Bradner, Hugh)—547
Rao, V. Ramakrishna and H. Sponer. Near uv absorption spectrum of meta difluorobenzene—213(A)
Ravenhall, G. D. (see Wolfenstein, L.)—217(A)
Rawson, E. B. (see Beringer, R.)—228(A)
Rayburn, L. A. and E. O. Wollan. Total neutron scattering cross sections at 1.44 ev—174(A)
Read, W. T., Jr. (see Shockley, W.)—835
Reagan, Daryl (see Panofsky, Wolfgang K. H.)—543(L)
Redington, R. W. Diffusion of Ba in BaO—1066
Reese, Robert M. (see Dibeler, Vernon H.)—213(A)
Reff, Israel. High energy nuclear photoeffect—207(A)
Resle, E. L., Jr., H. Petschek, S. C. Lin, and A. Kantrowitz. Strong shock waves—909(T)
Reynolds, F. L. (see Asaro, Frank)—277
Reynolds, George T. Energy response of organic liquid scintillation counters—193(A)
—— (see Keuffel, J. W.)—942
Reynolds, J. M. (see Hemstreet, H. W.)—178(A)
—— (see Leinhardt, T. E.)—178(A)
Rhodes, J. and W. E. Stephens. Ionization measurement of $B^{10}(n,\alpha)Li^7$—206(A)
——, **W. Franzen, and W. E. Stephens.** Ionization measurement of $B^{10}(n,\alpha)Li^7$—141
Rhodes, J. E., Jr. (see Woodward, L. A.)—178(A)
Rhodes, K. B. (see Arthur, J. S.)—237(A)
—— (see Hausman, H. J.)—238(A)
Ribe, Fred L. Disintegration of Li^8 by fast neutrons—205(A)
—— (see Groetzinger, Gerhart)—1003
Rich, Stanley R. and Wilfred Roth. Ultrasonic automatic viscosity measurement—235(A)
Richardson, J. Reginald (see Green, David)—195(A)
Richardson, John M. and S. R. Brinkley, Jr. Cell method in grand canonical ensemble—199(A)
—— (see Brinkley, S. R., Jr.)—199(A)
Richter, H. G. (see Debs, R. J.)—196(A)
Riddell, R. J., Jr. Fermi-Thomas model of the nucleus—189(A)
Ridgway, S. L. and F. M. Pipkin. β-γ angular correlation in As^{76}—202(A)
Rinehart, John S. Fracturing under impulsive loading—909(T)
—— (see Pearson, John)—910(A)
Rinehart, M. C. (see Bonner, T. W.)—1032
Ringo, G. R. (see Kaplan, Louis)—785
Risser, J. R. (see Burke, W. H.)—294
Ritchie, R. H. (see Klema, E. D.)—167(L)
Ritson, D. M. (see Kaplon, M. F.)—664(L)
Roberts, A. Neutron scattering experiments with Rochester 130-inch cyclotron—222(T)
Roberts, L. D., C. C. Sartain, and B. Borie. Nuclear and electronic contributions to specific heat of $Nd(EtSO_4)_3$ near 1°K—192(A)
Roberts, S. and J. S. Prener. Field strength and temperature dependence of electroluminescence in powders—191(A)
Robeson, A., N. Snidow, and J. W. Beams. Interferometer method of recording sedimentation in the ultracentrifuge—186(A)
Robinson, E. S. (see Armstrong, A. H.)—238(A)
Robinson, Esther Davis and A. C. Menius, Jr. Investigation of homocharge of electrets—177(A)
Rogosa, George L. and Guenter Schwarz. Transmission of x-rays through calcite near Bragg angle—995
—— (see Schwarz, Guenter)—201(A)
Rohrer, Robert H. Neutron capture resonances in Cs, La, Pr, Rb, Tl, and Y—177(A)
—— (see Newson, Henry W.)—177(A)
Rohrlich, F. (see Greifinger, P.)—663(L)
Rollosson, George W. Study of penetrating cosmic-ray showers in water—71
Roninson, D. W. (see Parlin, R. B.)—910(A)
Rorschach, H. E., Jr., and Melvin A. Herlin. Resistance minimum in Mg at low temperatures—193(A)
Rose, B. (see Beling, J. K.)—670(L); 1143(L)

Rose, William B., Emmett L. Hudspeth, and N. P. Heydenberg. Neutrons from deuteron bombardment of N^{14}—382(L)
Rosen, L. (see Armstrong, A. H.)—238(A)
—— (see Graves, E. R.)—239(A)
Rosen, Nathan. Electron in one-dimensional field—173(A)
—— Interaction between electron and one-dimensional electromagnetic field—940
Rosenstock, H. M. (see Eyring, H.)—204(T)
Rosenthal, Jenny E. (see Bramley, Arthur—1125(L)
Rosenzweig, N. Configuration interaction in Fe group elements—225(A)
Rossi, B. (see Clark, G. W.)—182(A)
Roth, Wilfred (see Rich, Stanley R.)—235(A)
Rothman, M. (see Halpern, J.)—164(L)
—— (see Mann, A. K.)—146
Roulston, K. I. and R. W. Pringle. Decay scheme of Ir^{192}—930
—— (see Pringle, R. W.)—1016
Rouse, A. G. (see Jones, L. C.)—227(A)
Roy, R. R. and L. Groven. Single elastic scattering of positrons by N nuclei—619
Roy, S. K. (see Krishnan, K. S.)—581
Rubin, L. G. (see Davis, Luther, Jr.)—190(A); 201(A)
Rubin, R. J. and P. Debye. Phenomenological model for excluded volume problem—214(A)
Ruderman, M. Multiple meson production—217(A)
—— Reactions $p+d \rightarrow \pi^+ + H^3$ and $p+d \rightarrow \pi^0 + He^3$—383(L)
Rudstam, G., P. C. Stevenson, and R. L. Folger. Nuclear reactions of Fe with 340-Mev protons—358
Rüetschi, R. (see Aeppli, H.)—379(L)
Rusk, Rogers D. and Mildred D. Moore. Mean life of neutral penetrating ray—239(A)
Russek, Arnold and Larry Spruch. Interaction moment contributions to magnetic moments of nuclei—1111
—— (see Spruch, L.)—189(A)
Rustad, B. M. (see Wu, C. S.)—1140(L)
Ryan, J. L., H. H. Givin, L. W. Cochran, B. D. Kern, and T. M. Hahn. Yield of γ-rays from proton bombardment of B—177(A)
—— (see Cochran, L. W.)—672(L)
Ryder, E. J. (see Conwell, E. M.)—190(A)

Sachs, R. G. Structure of nucleon—1100
Sack, S. (see McIntosh, J. S.)—237(A)
Sailor, V. L. Slow neutron resonances in In^{113} and In^{115}—222(A); —— **and L. B Borst**—161(L)
Salant, E. O. (see Poss, H. L.)—11
Salpeter, E. E. Mass corrections to fine structure of hydrogen-like atoms—328
—— **and W. A. Newcomb.** Mass corrections to hfs—150(L)
Sanders, Aaron P. Monitor for low intensity β-radiations—184(A)
Sartain, C. C. (see Roberts, L. D.)—192
Saunders, J. H. (see Davis, Luther, Jr.)—190(A)
Savitt, J. and R. H. Stresau. Recent air shock velocity measurements near detonating explosives—234(A)
Sawyer, R. A. (see Kebler, R. W.)—212(A)
Saxon, David S. (see LeLevier, Robert E.)—40
Schaeffer, O. A. Effect of mass on dissociation-probability and study of dissociation-processes with conditioned isotopes—204(T)
Scharff-Goldhaber, Gertrude. Excited states of even-even nuclei—218(A)
Scheidegger, A. E. and R. V. Krotkov. Relativistic statistical thermodynamics—197(A)
Schein, Marcel, (see Lord, J. J.)—538(L)
—— (see Weaver, A. B.)—531(L)
Schiff, L. L. Radiative correction to angular distribution of nuclear recoils from electron scattering—750
Schild, A. (see Pirani, F. A. E.)—452
—— (see Skinner, R.)—224(A)
Schiller, Ralph and Peter G. Bergmann. Canonical coordinate transformations and constraints in nonlinear theories—198(A)
—— (see Bergmann, Peter G.)—198(A)
Schlacks, L. K. (see Brolley, J. E., Jr.)—206(A)
Schneider, W. A. (see Hershkowitz, J.)—241(A)
Schlegel, Richard. Possible solution of clock paradox—198(A)
Scholnick, Seymour (see Jacobs, Donald H.)—231(A)
—— (see Martin, Marcel)—231(A)
Schroeder, C. A. (see Davis, L. R.)—239(A)
Schuch, Adam F. (see Hammel, E. F.)—154(L)
Schulz, A. G., D. Hamlin, M. J. Jakobson, and J. Merritt. Excitation function for π^+ mesons produced in p-p collisions—219(A)
Schumann, R. W. (see Bollinger, L. M.)—184(A)
Schwarcz, E. H. (see Hollyer, R. N., Jr.)—911(A)
Schwartz, R. N. (see Eckerman, J.)—912(A)
Schwarz, Guenter and George L. Rogosa. X-ray absorption in calcite crystal—201(A)
—— (see Rogosa, George L.)—995
Schweinler, H. C. Ferroelectricity in the Ilmenite structure—5
Schwinger, Julian (see Levine, Harold)—224(A)
Scott, G. G. Gyromagnetic ratios of ferromagnetic elements—697
Seaborg, Glenn T. (see Dunlavey, Dean C.)—165(L)
—— (see Ghiorso, A.)—163(L)
Seed, Richard G. Stars induced in nuclear emulsions by 100-Mev protons—182(A)
Seeger, R. J. Shock wave phenomena; Aerothermodynamic interaction—909(T)
Segrè, Emilio (see Chamberlain, Owen)—81
Seitz, F. and D. L. Dexter. Effects of dislocations on mobilities in semiconductors—189(A)
Sengupta, S. α-energy systematics and proton shells for heavier nuclei—1136(L)
Serber, R. and H. S. Snyder. Effect of atomic binding on nuclear reaction energies—152(L)
Service, J. D. (see Kundu, D. N.)—203(A)
Sette, D. (see Griffing, V.)—234(A)
—— (see Hubbard, J. C.)—233(A)
Shafroth, S. M. (see Choen, L.)—206(A)
Shamos, M. H. (see Fafarman, A.)—219(A)
—— (see Morewitz, H. A.)—241(A)
Shapiro, E. (see Mendenhall, R. I.)—203(A)
Shapiro, Maurice M. and Bertram Stiller. Ionization loss at relativistic velocities in nuclear emulsions—682(L)
Sharbaugh, A. H., R. W. Crowe, and J. K. Bragg. Aqueous electrolyte cathode in dielectric breakdown studies of liquids—232(A)
Sharma, J. Thermoluminescence and changes of color centers in LiF—535(L)
Sharp, D. Gordon. Electron microscopy of viruses in crude animal fluids—178(A)
Sharp, W. T. (see McManus, H.)—188(A)
Shaw, J. H. and J. N. Howard. Quantitative determination of abundance of telluric CO above Columbus, Ohio—380(L)
—— (see Howard, J. N.)—679(L)
Shearin, Paul E. (see Hoke, G. Robert)—176(A)
Sheer, C., J. Moore, W. W. Havens, Jr., and L. J. Rainwater. Measurement of neutron scattering cross sections in resonance region—239(A)
Sheline, Raymond K. Search for betatron induced, low Z, activities of short half life—557
—— **and Raymond W. Stoughton.** Nuclide Ni^{66}—1
Shelton, F. H., S. D. Wanlass, and R. B. Leighton. Production of V^6-particles—183(A)
—— (see Anderson, C. D.)—183(A)
—— (see Wanlass, S. D.)—183(A)
Sher, R., H. J. Kouts, and K. W. Downes. Half-life of 139-min Dy^{165}—523(L)
Shimada, Junji (see Kumagai, Hiroo)—385(L)

Shipley, F. M. (see Finlayson, D. M.)—1141(L)
Shirn, G. A. (see Huntington, H. B.)—211(A)
Shockley, W. and W. T. Read, Jr. Statistics of recombinations of holes and electrons—835
Shore, F. J., H. N. Brown, W. L. Bendel, and R. A. Becker. Additional branch in decay scheme of Zr^{89m}—202(A)
—— (see Bendel, W. L.)—195(A)
Shrader, E. F. (see Krohn, V. E., Jr.)—685
Shreffler, R. G. Boundary disturbances in high explosive shock tubes—909(T)
—— (see Deal, W. E.)—910(A)
—— (see Walsh, J. M.)—910 (A)
—— (see Willig, F. J.)—910(A)
Shull, F. B. and C. E. McFarland. Reactions $Sr^{88}(d,p)Sr^{89}$, $Zr^{90}(d,p)Zr^{91}$, and $Mo^{92}(d,p)Mo^{93}$—216(A)
Shulman, S. (see Anderegg, J. W.)—186(A)
Shutt, R. P. High pressure diffusion cloud chambers and their applications, with results of scattering of pions by light nuclei—216(T)
—— (see Whittemore, W. L.)—241(A)
Siegel, K. M. and H. A. Alperin. Scattering by semi-infinite cone—234(A)
Siegel, R. and S. De Benedetti. Conservation of energy in three-quantum annihilation—235(A)
Siegert, A. J. F. (see Glaser, H.)—191(A)
—— (see Peshkin, Murray)—735
Silsbee, H. B. (see Kolsky, H. G.)—395
Silverman, L. B. (see Greenfield, M. A.)—184(A)
Silverman, Shirleigh. Energy distribution of CO molecules in CO-O_2 flames—214(A)
—— (see Benedict, W. S.)—213(A)
Silvey, G., W. A. Hardy, and C. H. Townes. Masses of stable Te isotopes from microwave spectrum of TeCS—236(A)
Simmons, James W. (see Wilcox, W. S.)—172(A)
Simpson, J. A. Latitude and time variations of cosmic-ray neutrons—204(T)
——, **W. Fonger, and L. Wilcox.** Temporal changes of nucleonic component intensity—240(A)
Singwi, K. S. Electron-lattice interaction and super conductivity—1044
—— Entropy and specific heat of liquid He^3—540(L)
—— (see Peierls, R. E.)—46
Sites, John R. and Russell Baldock. Mass spectrometer studies of high vacuum materials—171(A)
Sitte, Kurt. Ratio of soft and hard particles in air showers—351
—— (see Froehlich, Fritz E.)—504
Skavlem, S. (see Hulthén, L.)—297
Skinner, R. and A. Schild. Quantization of interacting gravitational, electromagnetic and electron fields—224(A)
—— (see Pirani, F. A. E.)—452
Slager, Donald M. (see Johnson, Charles M.)—677(L)
Slater, J. C. Soluble problem in energy bands—807
Slichter, W. P. and E. D. Kolb. Impurity effects in thermal conversion of Ge—527(L)
Smith, A. (see der Mateosian, E.)—193(A)
Smith, Alan B. and Allan C. G. Mitchell. K/L ratio for 90-kev line of Nd^{147}—1128(L)
——, **Allan C. G. Mitchell, and Robert S. Caird.** Disintegration of Cs^{130}—454
Smith, Alan W. and John Turkevich. Electron traps in ZnS phosphor—306
Smith, D. F. and D. W. Magnuson. Microwave spectrum of NO_2F—226(A)
Smith, E. C. (see Pawlicki, G. S.)—221(A)
Smith, J. H. (see Kerst, D. W.)—197(A)
Smith, R. R. (see Palevsky, H.)—221(A)
Smith, William V. (see Anderson, Roy S.)—561
Smoluchowski, R. Theory of grain boundary diffusion—482
Snyder, Hartland S. Gauge invariance problem—164(L)
—— (see Serber, R.)—152(L)
Snidow, N. (see Robeson, A.)—186(A)
Snow, George. Analysis of 14-Mev n-p scattering—21
—— (see Poss, H. L.)—11
Snowdon, S. C. Neutrons from disintegration of P by deuterons—1022
Spencer, L. V. Method for determining cross sections from photonuclear yield curves—196(A)
Sperduto, A. (see Buechner, W. W.)—237(A)
Sponer, H. Wavelength shift in spectra of aromatics containing F—213(A)
—— (see Cooper, C. D.)—213(A)
—— (see Rao, V. Ramakrishna)—213(A)
Spruch, Larry and A. Russek. Interaction contributions to magnetic moments of nuclei—189(A)
—— (see Russek, Arnold)—1111
Squire, C. (see Mendelssohn, K.)—589
Staehelin, P. Lowest excitation level of Hg^{198}—374(L)
Standil, S. (see Pringle, R. W.)—384(L)
Stanford, C. P. (see Bernstein, S.)—487
—— (see Stephenson, T. E.)—174(A)
Stearns, Mary Beth. Nuclear scattering of 17-Mev γ-rays—706
Steele, M. C. Superconductivity below 1°K—1137(L)
—— **and R. A. Hein.** Size effects in superconductivity of Cd—908(L)
Stehl, O. (see Becker, E. W.)—525(L)
Stein, F. S. Mass spectra of isotopic CO_2 molecules—236(A)
Steinberg, M. S. Magneto-hydrodynamic waves—173(A)
Stephens, W. E. (see Rhodes, J.)—141; 206(A)
Stephenson, Charles V. and Ernest A. Jones. Raman spectrum, structure, force constants, and calculated thermodynamic properties of BrF_5—169(A)
Stephenson, Harold P. Near uv absorption spectra of halogenated pyridines in liquid solution—169(A)
—— Near uv absorption spectra of 2- and 3-fluoropyridine in vapor state—213(A)
Stephenson, T. E., C. P. Stanford, and S. Bernstein. Total cross section of Ho *vs* energy for slow neutrons—174(A)
—— (see Bernstein, S.)—487
Stern, Alexander W. Aether of Dirac in light of contemporary field theory—199(A)
Stern, E. A. (see Peterson, V. Z.)—240(A)
Stevenson, D. P. Contributions of electron-impact studies to knowledge of molecular energies—195(T)
Stevenson, P. C. (see Rudstam, G.)—358
Stewart, John Q. List of physical dimensions—197(A)
Stewart, R. W. and G. J. Odgers. Hydrodynamical theory of origin of multiple star systems—909(T)
Stiller, Bertram (see Shapiro, Maurice M.)—682(L)
Stirling, W. L. and Max Goodrich. Decay of Ba^{131} and Cs^{131}—176(A)
Stoddart, H. F. and H. E. Gove. Energy levels in C^{13}, Al^{27}, and Na^{23} using a scintillation spectrometer for heavy particles—238(A); 262
—— (see Gove, H. E.)—237(A)
Stone, Richard S. Investigation of three-photon annihilation of positron—235(A)
Stoner, R. G., E. B. Davies, and C. L. Woodbridge. Experimental study of shock refraction—913(A)
Stoughton, Raymond W. (see Sheline, Raymond K.)—1
Stovall, E. J., Jr. (see Armstrong, A. H.)—238(A)
Straub, C. P. (see Morgan, K. Z.)—178(A)
Stresau, R. H. Low velocity detonation of certain primary explosives—234(A)
—— (see Savitt, J.)—234(A)
Stroke, H. H. (see Jaccarino, V.)—676(L)
Struthers, J. D. (see Fuller, C. S.)—526(L)
Studer, W. F. and A. W. Waltner. Build-up of deuterium on metal targets—176(A)
Stuhlman, Otto, Jr. Refractions of spherical laminated lens—178(A)

Stumpf, F. B. (see Cork, J. M.)—203(A)
—— (see LeBlanc, J. M.)—202(A)
Sugarman, Nathan (see Holtzman, Richard B.)—632
Suwa, Shigeki (see Murakawa, Kiyoshi)—1048
Swami, M. S. (see Lal, D.)—545(L)
Swank, R. K. (see Buck, W. L.)—191(A)
Swann, C. P. and C. E. Mandeville. Neutrons from deuterons on Ne^{20}—215(A)
—— (see Swingle, J. S., Jr.)—184(A)
Swanson, Don R. Interpretation of high energy p-p scattering—208(A)
Swartz, C. D. (see Pruitt, J. S.)—534(L)
Swingle, J. S., Jr., and C. P. Swann. Rf ion source with transverse magnetic field—184(A)
Sykes, Alan O. (see Harrison, Mark)—231(A)

Tannenwald, P. Disintegration of He by 90-Mev neutrons—205(A)
Taschek, R. F. (see Argo, H. V.)—205(A); 612
Tatsumi, Tomomasa. Stability of laminar parabolic flow—1127(L)
Taub, A. H. and C. H. Fletcher. Reflection of shock waves as pseudo-stationary phenomenon—912(A)
—— (see Fletcher, C. H.)—912(A)
Taylor, A. E. and E. Wood. Neutron total cross section for Pb between 37 and 156 Mev—907(L)
Taylor, H. W. (see Pringle, R. W.)—384(L); 1016
Taylor, J. G. V. and R. N. H. Haslam. Cross section for reaction $Br^{81}(\gamma,\alpha)As^{77}$—1138(L)
Taylor, William J. Density matrix formulation of LCAO molecular orbital theory—214(A)
Teal, G. K. Ge and Si single crystals—221(T)
—— **and E. Buehler.** Growth of Si single crystals and single crystal Si p-n junctions—190(A)
Teasdale, Tom S. (see Mendelssohn, K.)—589
Teichmann, T. and E. P. Wigner. Field expansions in loss-free microwave junctions—228(A)
—— **and E. P. Wigner.** Sum rules in the dispersion theory of nuclear reactions—123
Telegdi, V. L. Investigation of reaction $C^{12}+h\nu=3He^4$ with γ-rays up to 48 Mev—196(A)
Tendam, D. J. (see Bleuler, E.)—216(A)
Terwilliger, K. M. and L. W. Jones. Neutron production by high energy quanta—195(A)
Thie, Joseph A., Charles J. Mullin, and E. Guth. Electron excitation of nuclei—962
Thomas, Richard N. and William C. White. Semi-quantitative interpretation of Al fast-particle spectrum—912(A)
—— (see White, William C.)—912(A)
Thompson, R. W., C. J. Karzmark, and H. O. Cohn. Analysis of V^{49}-disintegration in flight—182(A)
—— (see Brueckner, K. A.)—390(L)
Thompson, S. G. (see Ghiorso, A.)—163(A)
Thompson, Sanford P. Effective use of reciprocity in vibrometer calibrations—230(A)
Thorn, R. N. (see Holt, R. B.)—378(L)
Thorne, C. J. (see Barrett, L. C.)—913(A)
—— (see Parlin, R. B.)—(910A)
Thulin, Sigvard. Decay of Kr^{87}—684(L)
Ticho, Harold K. Collision cross section of high energy primary cosmic rays—241(A)
—— (see Green, David)—195
Tipton, Isabel H. Spectrographic analysis of trace elements in human tissues—179(A)
Tobocman, W. (see Friedman, F. L.)—208(A)
Tomboulian, D. H. (see Hartman, P. L.)—233(A)
Tongiorgi, V. Cocconi and Donald A. Edwards. Neutrons from capture of slow π^--mesons—220(A)
Toulon, Pierre. Applications of electrostatic control of electric charges furnished by glow discharge—232(A)
Townes, C. H. (see Nethercot, A. H.)—226(A)
—— (see Silvey, G.)—236(A)
Trambarulo, R. F. and C. F. Luck. Simple Stark-modulation microwave spectrograph—172(A)
—— (see Ghosh, S. N.)—172(A)
Treiman, S. B. Effect of equatorial ring currents on cosmic radiation—240(A)
True, W. W. and L. Diesendruck. Interpretation of long range protons from deuteron bombardment of Be^9—381(L)
Truitt, Robert Wesley. Approximate solution for pressure distribution over flat plate airfoil at free stream Mach number one—171(A)
Tucker, B. L. and E. C. Gregg. Threshold for (γ,p) reaction in Be^9—907(L)
Tucker, G. (see Weinreich, G.)—229(A)
Tucker, Maurice. Effects of damping screens and stream contraction on turbulence—911(A)
Turkevich, John (see Smith, Alan W.)—306
Turner, E. B. (see Hollyer, R. N., Jr.)—911(A)

Uhlenbeck, G. E. and C. S. Wang Chang. Theory of transport phenomena in polyatomic gases—195(T)
Urquhart, H. M. A. and J. E. Goldman. Single crystal magnetostriction constants of Fe-Co alloy—210(A)

Van Nostrand, Robert. Theoretical study of geoelectrical prospecting over dome structure—177(A)
Van Patter, D. M. and W. W. Buechner. Investigation of (d,p) and (d,α) reactions of Si isotopes—51
Van Sciver, W. and R. Hofstadter. γ- and α-produced scintillations in CsF—522(L)
van Trier, A. A. Th. M. Anomalous wavetypes in waveguides containing ferromagnetics—227(A)
von Hippel, A. Piezoelectricity, ferroelectricity, and crystal structure—200(A)

Wada, W. W. Crystalline Stark effect and Zeeman effect in vanadous Tutton salts—229(A)
Wahrhaftig, A. L. (see Eyring, H.)—204(T)
Wajda, E. S. (see Huntington, H. B.)—211(A)
Walchli, H. E. and H. W. Morgan. Magnetic shielding effects in compounds of V—541(L)
Walker, W. E. (see Beams, J. W.)—524(L)
Walnut, Thomas H. Theory of shape and width of bands in vibrational spectra of crystals—201(A)
Walsh, J. M., R. G. Shreffler, and F. J. Willig. Limiting conditions for jet formation in high velocity collisions—910(A)
—— (see Willig, F. J.)—910(A)
Walt, M., A. Okazaki, and R. K. Adair. Scattering of fast neutrons by deuterons—238(A)
Waltner, A. W. (see Baker, P.)—176(A)
—— (see Hegenberger, R. F.)—176(A)
—— (see McManaway, G. W.)—176(A)
—— (see Studer, W. F.)—176(A)
Walton, T. S. Numerical solution of equations for discrete model of spherical blast—910(A)
Waniek, R. W. (see Culler, Vaughn)—221(A)
—— (see Holt, R. B.)—378(L)
Wanlass, S. D., R. B. Leighton, W. L. Alford, C. D. Anderson, and F. H. Shelton. Energy release in V^{49}-decay—183(A)
—— (see Anderson, C. D.)—183(A)
—— (see Shelton, F. H.)—183(A)
Wang, Shyh (see Bloembergen, N.)—392(L)
Wannier, Gregory H. Motion of gaseous ions in a strong electric field. II—795
Warden, Charles M. (see Alberts, Henry C.)—911(A)
Warshaw, S. (see Marshall, L.)—220(A)
—— (see Marshall, J.)—220(A)
Watson, H. A. Excited states of F^{20} and O^{17}—215(A)
Watson, Kenneth M. (see Brueckner, Keith A.)—621

Watson, W. W. (see Anderson, C. E.)—195(A); 668(L); 897(L)
Watt, B. E. Energy spectrum of neutrons from thermal fission of U^{235}—1037
Weatherly, Thomas L. and Dudley Williams. *l*-type doubling transitions in HCN and DCN—517
Weaver, A. B., Earl A. Long, and Marcel Schein. Narrow angle pair of particles produced in H—531(L)
Weaver, H. E., Jr. (see Dharmatti, S. S.)—675(L)
Weinreich, G., G. Tucker, and V. Hughes. Zeeman effect of Ne in metastable $^3P_2$ state; evidence for zero spin of $_{10}Ne^{20}$—229(A)
Weiss, P. Relation between phase-shifts and energy levels—226(A)
Weisskopf, V. F. (see Feshbach, H.)—188(A)
Welber, Benjamin. Measurement of internal energy in Cu introduced by cold work—211(A)
Welton, T. A. Rational relativistic single particle theory—225(A)
Wenzel, Anneliese. Existence of hidden transition in biphenyl and anthracene—169(A)
Wenzel, W. A. and Ward Whaling. Stopping cross section of D_2O ice—499
Werle, J. Influence of relativistic corrections upon singular nuclear potentials—159(L)
Werner, G. K. (see Griffin, P. M.)—171(A)
Whaling, Ward (see Wenzel, W. A.)—499
Wheatley, J. and D. Halliday. Quenching of three-quantum annihilation from positronium by magnetic field—235(A)
Wheeler, G. W. (see Anderson, C. E.)—195(A); 668(L); 897(L)
White, George R. and W. F. Fry. Range distribution of μ-mesons from π-meson decays in photographic emulsions—219(A)
White, M. G. (see Yntema, J. L.)—223(A)
White, William C. and Richard N. Thomas. Qualitative comparison of meteor and fast-particle spectra—912(A)
—— (see Thomas, Richard N.)—912(A)
Whittemore, W. L. and R. P. Shutt. Electric and non-electric scattering of cosmic-ray mesons and protons—241(A)
—— (see Carter, R. S.)—494
Whittle, Charles E., and Philip S. Jastram. Angular correlation of γ-rays in Pt^{194}—203(A)
—— (see Jastram, P. S.)—1133(L)
Wiener, N. Quantal and non-quantal uncertainties—221(T)
Wigner, E. P. (see Teichman, T.)—123; 228(A)
Wilcox, L. (see Simpson, J. A.)—240(A)
Wilcox, W. S., J. H. Goldstein, and James W. Simmons. Microwave spectrum of vinyl cyanide—172(A)
Wilets, Lawrence and Lee C. Bradley, III. Isotope shifts in Er—1018
Willard, H. B., J. K. Bair, and J. D. Kington. $B^{11}(p,n)C^{11}$ angular distribution—206(A)
Williams, Dudley (see Weatherly, Thomas L.)—517
Williams, Ferd E. (see Johnson, Peter D.)—192(A)
—— (see Piper, William W.)—151(L)
Willig, F. J. Fast metal jets—910(A)
——, **R. G. Shreffler, and J. M. Walsh.** Jetless and jet forming collisions of explosive driven metal plates—910(A)
—— (see Walsh, J. M.)—910(A)
Wilson, E. Bright, Jr. Significance of results of microwave spectroscopy for chemical valence theory—195(T)
—— (see Kivelson, D.)—214(A)
Wilzbach, K. E. (see Kaplan, Louis)—785
Winckler, John. Čerenkov radiation from cosmic-ray particles—241(A)
Winhold, E. J., P. T. Demos, and I. Halpern. Angular distribution of fission fragments in photofission of Th—1139(L)
Wintersteiger, V. (see Maeder, D.)—537(L)
Witmer, Enos E. Nature of nuclei and elementary particles—242(A)
—— Nuclear masses and electron mass—237(A)
Witzig, Warren F. Creep of Cu under deuteron bombardment—211(A)
—— (see Glick, H. L.)—1074
Wolfenstein, L. and G. D. Ravenhall. Decay of scalar particle into three photons—217(A)
Wolff, Peter A. Scattering of protons from C—434
Wollan, E. O. (see Koehler, W. C.)—238(A)
—— (see Rayburn, L. A.)—174(A)
Wood, Elizabeth A., Walter J. Merz, and Bernd T. Matthias. Polymorphism of $ND_4D_2PO_4$—544(L)
—— (see Taylor, A. E.)—907(L)
Woodbridge, C. L. (see Stoner, R. G.)—913(A)
Woodward, L. A. Heating of samples in electron microscope—178(A)
—— **and J. E. Rhodes, Jr.** Test and demonstration object for phase microscopy—178(A)
Woodward, W. M. (see Ashkin, Arthur)—236(A)
Workman, E. J. Properties of F-contaminated ice as crystal rectifier—212(T)
Worley, R. D., M. W. Zemansky, and H. A. Boorse. Low temperature heat capacity of V—192(A)
——, **M. W. Zemansky, and H. A. Boorse.** Theoretical and experimental heat capacities of superconducting metals—1142(L)
Worthington, H. R., D. E. Findley, and J. N. McGruer. Scattering of protons by protons. II—223(A)
—— (see McGruer, J. N.)—223(A)
Worthington, W. J., Jr. Nickel 56—158(L)
Wright, C. N. (see Hopkins, J. I.)—174(A)
Wroe, D. (see Peierls, R. E.)—46
Wroughton, D. M. (see Okress, E. C.)—209(A)
Wu, C. S., B. M. Rustad, V. Perez-Mendez, and L. Lidofsky. β-spectrum of He^6—1140(L)
—— (see Feldman, L.)—1091
—— (see Lidofsky, L.)—204(A); 391(L)
—— (see Macklin, P.)—391(L)
Wu, Ta-You. Exchange scattering of electrons by an atom and inverse Auger effect—1012
—— (see Moses, H. E.)—627
Wyard, S. J. Absorption coefficients of γ-rays—165(L)
Wyckoff, James M. Construction and operation of high pressure diffusion cloud chamber—185(A)

Yadoff, Oleg. Whirling movements of conductor as result of interaction between electric and magnetic fields—233(A)
Yafet, Y. and C. Kittel. Antiferromagnetic arrangements in ferrites—290
Yang, C. N. and T. D. Lee. Statistical theory of equations of state and phase transitions. I. Theory of condensation—404
—— (see Lee, T. D.)—410
Yennie, D. R. Quantum corrections to classical nonlinear meson theory—224(A)
Yevick, George J. Theory of pick-up process—208(A)
Yntema, J. L. and M. G. White. p-p scattering at 18.3 Mev—223(A)
Yonts, O. and S. Bashkin. 100-kev positive ion accelerator—175(A)
Yuan, Luke C. L. (see Poss, H. L.)—11

Zaffarano, D. J. and Warren A. Hunt. Automatic scanner for multichannel pulse-height analysis of 35-mm film record—194(A)
Zemansky, M. W. (see Worley, R. D.)—192(A); 1142(L)
Zilsel, P. R. and H. M. Fried. Nonlinear stationary flow in liquid He II—193(A)
—— (see Darling, B. T.)—198(A)
Zucker, E. R. (see Mendenhall, R. I.)—203(A)
Zweifel, Paul. Modification of potential in Dirac equation—173(A)

Analytic Subject Index to Volume 87

References with (A) are to abstracts of papers presented at meetings of the American Physical Society. References with (L) are to Letters to the Editor.

Absorption of radiation (see **Radiation**)

Acoustics
- Luminescence produced as result of intense ultrasonic waves, V. Griffing and D. Sette—234(A)
- Ultrasonic automatic viscosity measurement, Stanley R. Rich and Wilfred Roth—235(A)
- Ultrasonic dispersion and absorption in vapors of *cis-* and *trans-* $C_2H_2Cl_2$, J. C. Hubbard and D. Sette—233(A)

Aerodynamics (see also **Hydrodynamics**)
- Approximate solution for pressure distribution over flat plate airfoil at free stream Mach number one, Robert Wesley Truitt—171(A)
- Short base length range for air-drag studies, Arthur Linz, Jr., and A. V. Masket—175(A)

Afterglow (see **Discharge of electricity in gases**)

Alloys (see **Crystalline state**)

Annihilation (see **Pair production and annihilation**)

Antiferromagnetism (see **Magnetic properties**)

Arcs (see **Discharge of electricity in gases**)

Astrophysics
- Electrical conductivity in solar atmosphere, Donald E. Osterbrock—468
- Generation of convection in planetary atmosphere, Jean I. King—911(A)

Atmosphere (see also **Meteorology**)
- Absorption by telluric CO in 2.3μ region, J. N. Howard and J. H. Shaw—679(L)
- Abundance of telluric CO above Columbus, Ohio, J. H. Shaw and J. N. Howard—679(L)
- Dissociation of O_2 in upper atmosphere, H. E. Moses and Ta-You Wu—627
- Radiation loss from atmosphere, Gilbert N. Plass—187(A)

Atomic and molecular beams
- Atomic beam resonance method for excited states, I. I. Rabi—379(L)
- Charge transfer for protons in He, R. H. Garstang—529(L)
- Magnetic moment ratios in hydrogen-like molecules, P. J. Bray, R. G. Barnes, and N. J. Harrick—229(A)
- Nuclear rf spectra of H_2 and D_2 in high and low magnetic fields, H. F. Kolsky, T. E. Phipps, Jr., N. F. Ramsey, and H. F. Silsbee—395
- Rf spectroscopy of D_2, R. G. Barnes and P. J. Bray—229(A)

Atomic and molecular radii (see also **Scattering of electrons**)
- Variation of collision diameters with mix ratio in binary mixtures in microwave pressure broadening, L. C. Jones, A. V. Bushkovitch, C. A. Potter, and A. G. Rouse—227(A)

Atomic mass (see **Isotopes and atomic mass; Mass spectroscopy**)

Atomic structure (see **Spectra, atomic**)

Aurora
- Forbidden line of N II, W. Petrie—1002

Biophysics
- Effect of x-radiation on bioelectric potentials of rats, David Pomeroy and Herbert Gursky—179(A)
- Effects of delaying of germination of seeds subjected to radiation, June G. Jones and David Pomeroy—179(A)
- Electron microscopy of viruses in crude animal fluids, D. Gordon Sharp—178(A)
- Energy requirements for bacterial motility, Harold J. Morowitz—186(A)
- Inactivation of southern beam mosaic virus by deuterons, E. C. Pollard and A. E. Dimond—186(A)
- Interferometer method of recording sedimentation in ultracentrifuge, A. Robeson, N. Snidow, and J. W. Beams—186(A)
- Refractions of spherical laminated lens, Otto Stuhlman, Jr.—178(A)
- Relation of tooth surfaces to stability of artificial dentures, R. S. Ledley—187(A)
- Size, shape, and hydration of tomato bushy stunt virus, Paus Kaesberg, J. A. Anderegg, B. R. Leonard, and W. W. Beeman—186(A)
- Small-angle x-ray scattering from serum albumin solutions, J. W. Anderegg, W. W. Beeman, and S. Shulman—186(A)
- Spectrographic analysis of trace elements in human tissues, Isabel H. Tipton—179(A)

Boson theory (see **Field theory**)

Bremsstrahlung (see **Radiation**)

Broadening of spectral lines
- Ion concentrations in intense discharges from Stark effect broadening, H. N. Olsen and W. S. Huxford—233(A)
- Pressure broadening of O_2^{16} lines in mm wavelength region, J. O. Artman and J. P. Gordon—227(A)
- Variation of collision diameters with mix ratio in binary mixtures in microwave pressure broadening, L. C. Jones, A. V. Bushkovitch, C. A. Potter and A. G. Rouse—227(A)

Chemical reactions
- Separation of trace elements in minerals with resin ion exchange columns, L. T. Aldrich, L. F. Herzog, P. H. Abelson, and E. T. Bolton—186(A)

Collision diameter (see **Atomic and molecular radii**)

Collisions of second kind
- Resonance in collision processes, O. Oldenberg—786

Compton effect (see **Scattering of radiation**)

Conductivity, electrical (see **Electrical conductivity; Discharge of electricity in gases; Semiconductors; Superconductivity**)

Conductivity, thermal (see **Thermal conductivity**)

Constants, physical standards
- List of physical dimensions, John Q. Stewart—197(A)
- Nature of nuclei and elementary particles, Enos E. Witmer—242(A)
- Nuclear masses and electron mass, Enos E. Witmer—237(A)

Cosmic radiation
- Absorption of cosmic rays under 120 MWE of earth, C. A. Randall—241(A)
- Angular and lateral distribution functions for nucleon component of cosmic radiation, H. Messel and H. S. Green—738
- Angular distribution of shower particles as function of depth, erratum, L. Eyges and S. Fernbach—1143(L)
- Azimuthal variation, B. Bhowmik and G. S. Bajwa—530(L)
- Bursts in material of low atomic number, F. E. Driggers—1080
- Cascade theories with ionization loss, H. Messel and R. B. Potts—759
- Čerenkov radiation from cosmic-ray particles, John Winckler—241(A)
- Coincidence method for investigation of cosmic rays using scintillations in liquids, J. Hershkowitz, H. P. Kallmann, and W. A. Schneider—241(A)
- Collision cross section of high energy primaries, Harold K. Ticho—241(A)
- Correlation of cosmic-ray intensities at high altitudes with neutron intensities, H. V. Neher—240(A)

Cosmic radiation (continued)
Correlation of cosmic-ray ionization measurements at high altitudes, at sea level, and neutron intensities at mountain tops, H. V. Neher and S. E. Forbush—889
Decoherence curve investigation of "narrow air showers," W. E. Haisley, Jr.—169(A)
Effect of equatorial ring currents, S. B. Treiman—240(A)
Electric and non-electric scattering of cosmic-ray mesons and protons, W. L. Whittemore and R. P. Shutt—241(A)
Energy spectrum of the electrons in extensive showers, Carmelo Milone—680(L)
Enhanced primary cosmic-ray intensity associated with solar disturbances, M. A. Pomerantz and G. W. McClure—240(A)
Hard component in upper atmosphere, Malcolm A. Clark—87
High energy nuclear collisions and Fermi model, H. Messel and H. S. Green—378(L)
High energy nuclear interactions in Pb, Fritz E. Froehlich, Erich M. Harth, and Kurt Sitte—504
Interaction of pions, R. L. Cool and O. Piccioni—531(L)
Ionization by cosmic-ray mesons in A, G. W. McClure—680(L)
Latitude effect between Bismarck and Thule, Greenland, V. Z. Peterson, H. V. Neher, and E. A. Stern—240(A)
Mean free path of high energy *N*-component, Robert R. Brown—999
Mean life of neutral penetrating ray, Rogers D. Rusk and Mildred D. Moore—239(A)
Multiple-wire ionization chamber for study of large air showers, R. E. Heineman—240(A)
Narrow angle pair of particles produced in H, A. B. Weaver, Earl A. Long, and Marcel Schein—531(A)
Narrow angle pairs of particles from nuclear interactions, J. J. Lord, Joseph Fainberg, D. M. Haskin, and Marcel Schein—538(L)
Penetrating showers in water, George W. Rollosson—71
Production and interaction of mesons at very high energies, D. Lal, Yash Pal, B. Peters, and M. S. Swami—545(L)
Proportional counter measurement of primary protons and α-particles, L. R. Davis, H. M. Caulk, C. Y. Johnson, G. J. Perlow, and C. A. Schroeder—239(A)
Ratio of soft and hard particles in air showers, Kurt Sitte—351
Star production by heavy ion component, E. G. Bilpuch and A. V. Masket—168(A)
Statistical study of star formation in photographic emulsions, F. B. Brown, Jr., and A. V. Masket—168(A)
Temporal changes of nucleonic component intensity, J. A. Simpson, W. Fonger, and L. Wilcox—240(A)
Unusual meson induced star, W. F. Fry and J. J. Lord—533(L)
Variation of positive-negative ratio of cosmic-ray mesons with momentum and altitude, H. A. Morewitz and M. H. Shamos—241(A)
Zenith angle dependence of extensive air showers, James P. Parker—169(A)

Cosmology
Polyneutron theory of origin of elements, R. E. Peierls, K. S. Singwi, and D. Wroe—46

Cross section, measurements, theory (see also **Scattering of electrons**)
Collision cross section of high energy primary cosmic rays, Harold K. Ticho—241(A)
Of Fe for cold neutrons, H. Palevsky, D. J. Hughes, and R. R. Smith—221(A)
Neutron total cross section for Pb between 37 and 156 Mev, A. E. Taylor and E. Wood—907(L)
Neutron total cross sections with Oak Ridge National Laboratory fast chopper, G. S. Pawlicki and E. C. Smith—221(A)
Nuclear cross sections for negative pions of energy 113 and 137 Mev, Ronald L. Martin—1052
For scattering of 9.84-Mev protons by He, T. M. Putnam—932
Stopping cross section of D_2O ice, W. A. Wenzel and Ward Whaling—499
Thermal neutron absorption cross section of D, Louis Kaplan, G. R. Ringo, and K. E. Wilzbach—785
Thermal neutron capture cross section of A^{40} and observation of A^{42}, Seymour Katcoff—886
Total cross section of Ho *vs* energy for slow neutrons, T. E. Stephenson, C. P. Stanford, and S. Bernstein—174(A)
Total cross sections for 14-Mev neutrons, H. L. Poss, E. O. Salant, G. A. Snow, and Luke C. L. Yuan—11
Total cross sections for high energy neutrons, Vaughn Culler and R. W. Waniek—221(A)
Total cross sections of Co, Er, Hf, Ni^{58}, Ni^{60}, Ho, and fission Sm for slow neutrons, S. Bernstein, L. B. Borst, C. P. Stanford, T. E. Stephenson, and J. B. Dial—487
Total cross sections of positive pions in H, S. W. Barnes, D. L. Clark, J. P. Perry, and C. E. Angell—669(L)
Total neutron cross sections at energies between 3 and 12 Mev, N. Nereson—221(A)
Total neutron scattering cross sections at 1.44 ev, L. A. Rayburn and E. O. Wollan—174(A)

Crystal counters (see **Methods and instruments**)

Crystal structure
Piezoelectricity, ferroelectricity, and crystal structure, A. von Hippel—200(A)

Crystalline state
Antiferromagnetic arrangements in ferrites, Y. Yafet and C. Kittel—290
Comparative elastic studies of single crystals of CaF_2 and CsCl types, Lewis S. Combes, Stanley S. Ballard, and Kathryn A. McCarthy—201(A)
Cu as acceptor element in Ge, C. S. Fuller and J. D. Struthers—526(L)
Creep of Cu under deuteron bombardment, Warren F. Witzig—211(A)
Crystalline Stark effect and Zeeman effect in vanadous Tutton salts, W. W. Wada—229(A)
Diffusion of Ba in BaO, R. W. Redington—1066
Effect of minority carriers on breakdown of point contact rectifiers, Ernst Billig—1060
Effect of radiation on elastic constants, G. J. Dienes—666(L); F. R. N. Nabarro—665(L)
Electrical and optical properties of rutile single crystals, D. C. Cronemeyer—876
Electroluminescence of single crystals of ZnS:Cu, William W. Piper and Ferd W. Williams—151(L)
Electron-lattice interaction and superconductivity, K. S. Singwi—1044
Electron traps in KCl:Tl phosphor, Peter D. Johnson and Ferd E. Williams—192(A); in ZnS phosphor, Alan W. Smith and John Turkevich—306
Enhancement of *F*- and *V*-bands in NaCl containing Ca, H. W. Etzel—906(L)
Evjen's method of evaluating Madelung constant, K. S. Krishnan and S. K. Roy—581
Fusion as hydrodynamic instability in thermal wave propagation, G. Bonfiglioli—897(L)
Generation of color center precursors in alkali halides by electrolysis, Michael Hacskaylo and Gerhart Groetzinger—789
Growth of Si single crystals and single crystal Si *p-n* junctions, G. K. Teal and E. Buehler—190(A)
Hall effect in single crystals of BaO, E. M. Pell—457
Impurity effects in thermal conversion of Ge, W. P. Slichter and E. D. Kolb—527(L)

Induced conductivity and light emission in different luminescent type powders, Hartmut Kallmann and Bernard Kramer—91
Interaction of excitons and phonons, Paul Leurgans and J. Bardeen—200(A)
Internal fields in crystals, E. T. Jaynes—200(A)
Lattice defects in Ge, W. C. Dunlap, Jr.—190(A)
Lattice vibrations and resistivity, W. A. Bowers—173(A)
Magnetic properties of superconducting alloys of In and Tl, W. F. Love, E. Callen, and F. C. Nix—844
Measurement of internal energy in Cu introduced by cold work, Benjamin Welber—211(A)
Mechanism causing variations of axial ratio in noncubic metallic crystals, John B. Goodenough—200(A)
Micellar structure in silicate glass, A. F. Prebus and J. W. Michener—201(A)
Optical polarization in single crystals of Te, J. J. Loferski—905(L)
Paramagnetic resonance absorption in additively colored crystals of alkali halides, Clyde A. Hutchison, Jr., and Gordon A. Noble—1125(L)
Polymorphism of $ND_4D_2PO_4$, Elizabeth A. Wood, Walter J. Merz, and Bernd T. Matthias—544(L)
Release of trapped charge in alkali halide crystals, David Dutton—191(A)
Resistivity of Cu_3Au during neutron irradiation, H. L. Glick, F. C. Brooks, W. F. Witzig, and W. E. Johnson—1074
Scattering of electrons from point singularities in metals, D. L. Dexter—768
Self-diffusion in Zn, H. B. Huntington, G. A. Shirn, and E. S. Wajda—211(A)
Six-dimensional representation of stress and strain in face-centered cubic crystal, A. V. Hershey—200(A)
Slip-band formation, John C. Fisher, Edward W. Hart, and Robert H. Pry—210(A); 958
Spectroscopy of solid state: Cu and Cr, E. M. Gyorgy and G. G. Harvey—861
Strain hardening of metal crystals, Edward W. Hart, John C. Fisher, and Robert H. Pry—211(A)
Theory of grain boundary diffusion, R. Smoluchowski—482
Theory of optical and thermal transitions in solids, Ryogo Kubo—201(A)
Theory of shape and width of bands in vibrational spectra of crystals, Thomas H. Walnut—201(A)
θ-values in metals, F. M. Kelly and D. K. C. MacDonald—210(A)
Transmission of x-rays through calcite, George L. Rogosa and Guenter Schwarz—995
Weak potential model for electrons in metal, Edward N. Adams, II—211(A)
X-ray absorption in calcite crystal, Guenter Schwarz and George L. Rogosa—201(A)

Dielectrics and dielectric properties
Aqueous electrolyte cathode in dielectric breakdown studies of liquids, A. H. Sharbaugh, R. W. Crowe, and J. K. Bragg—232(A)
Of Ba-Sr titanate ceramics, Luther Davis, Jr., and Lawrence G. Rubin—201(A)
Of rutile single crystals, D. C. Cronemeyer—876
Diffraction of electrons (see **Electron diffraction**)
Diffraction of neutrons (see **Neutron diffraction**)
Diffusion (see also **Thermal diffusion**)
Diffusion theory of noise in rectifiers and transistors, Richard L. Petritz—189(A)
Of Ba in BaO, R. W. Redington—1066
Self-diffusion in Zn, H. B. Huntington, G. A. Shirn, and E. S. Wajda—211(A)
Theory of grain boundary diffusion, R. Smoluchowski—482

Discharge of electricity in gases
Dynamic characteristics of plasma, H. N. Olsen and W. S. Huxford—922
Electrostatic control of electric charges furnished by glow discharge, Pierre Toulon—232(A)
High frequency electrical breakdown of gases, W. P. Allis and Sanborn C. Brown—419
Ion concentrations and recombination in expanding low pressure sparks, Richard G. Fowler, William R. Atkinson, and Luther W. Marks—966
Ion concentrations in intense discharges from Stark effect broadening, H. N. Olsen and W. S. Huxford—233(A)
Magneto-hydrodynamic waves in ionized He, Winston H. Bostick and Morton A. Levine—671(L)
Phenomena initiated in gases by electric spark, H. L. Olsen, R. B. Edmonson, and E. L. Gayhart—232(A)
Processes involving thermal electrons and ions in Hg afterglow, Manfred A. Biondi—232(A)
Disintegration and excitation of nucleus (see also **Nuclear spectra; Radioactivity; Photodisintegration**)
Absolute resonant energies for radiative capture of protons by Be below 520 kev, S. E. Hunt—902(L)
Acceleration of Be and C ions in synchrocyclotron, C. N. Chou, W. F. Fry, and J. J. Lord—671(L)
(α,n) and $(\alpha,2n)$ cross sections with Ag^{109}, E. Bleuler and D. J. Tendam—216(A)
Angular correlation between protons and gammas in $Li^6(d,p\gamma)Li^7$, W. H. Burke and J. R. Risser—294
Angular correlation in $Be^9(d,p)Be^{10*}(\gamma)Be^{10}$, L. Cohen, S. M. Shafroth, C. M. Class, and S. S. Hanna—206(A)
Angular correlation in $B^{11}(p;\gamma_1,\gamma_2)C^{12}$, Thomas P. Hubbard, Jr., Edward B. Nelson, and James A. Jacobs—378(L)
Angular correlations in $Li^6(d,p)Li^{7*}(\gamma)Li^7$, C. M. Class and S. S. Hanna—247
Angular distribution and excitation function of long-range protons from $Be^9(d,p)Be^{10}$, Frederick L. Canavan, S. J.—136
Angular distributions of Be^9+D neutrons, J. S. Pruitt, S. S. Hanna, and C. D. Swartz—534(L)
Angular distributions of $C^{12}(p,p')C^{12*}$, $Q=-4.45$ Mev, and $Mg^{24}(p,p')Mg^{24*}$, $Q=-1.38$ Mev, using NaI scintillation counter, H. E. Gove and H. F. Stoddart—237(A)
Angular distributions of (d,p) reactions, Clayton F. Black—205(A)
Be^7 and B^{10} energy levels, Fay Ajzenberg—205(A)
$Be^9(\gamma,p)$ threshold, B. L. Tucker and E. C. Gregg—907(L)
Born approximation theory of (d,p) and (d,n) reactions, P. B. Daitch and J. B. French—900(L)
B^{10} and O^{16} reaction energies, D. S. Craig, D. J. Donahue, and K. W. Jones—206(A)
$B^{10}(n,\alpha)Li^7$, ionization measurement, J. Rhodes and W. E. Stephens—206(A)
$B^{11}(p;\gamma_1,\gamma_2)C^{12}$, angular correlation, Thomas P. Hubbard, Jr., Edward B. Nelson, and James A. Jacobs—378(L)
$B^{11}(p,n)C^{11}$ angular distribution, H. B. Willard, J. K. Bair, and J. D. Kington—206(A)
Conservation of isotopic spin, Robert K. Adair—1042
Determination of angular distribution and absolute differential cross section of $C^{12}(p,p)C^{12}$, H. L. Jackson, A. I. Galonsky, F. J. Eppling, R. W. Hill, E. Goldberg, and J. R. Cameron—237(A)
$D(t,n)He^4$ cross section for 80- to 1200-kev tritons, H. V. Argo, R. K. Adair, H. M. Agnew, A. Hemmendinger, W. T. Leland, and R. F. Taschek—205(A); H. V. Argo, R. F. Taschek, H. M. Agnew, A. Hemmendinger, and W. T. Leland—612
Direct interaction and compound nucleus for 14-Mev neutrons, H. McManus and W. T. Sharp—188(A)
Disintegration of He by 90-Mev neutrons, P. Tannenwald 205(A)

Disintegration and excitation of nucleus (continued)
Disintegration of O and N by 14.1-Mev neutrons, Alan B. Lillie—716
Effect of atomic binding on nuclear reaction energies, R. Serber and H. S. Snyder—152(L)
Electron excitation of nuclei, Joseph A. Thie, Charles J. Mullin, and E. Guth—962
Energy levels in C^{12}, Al^{27}, and Na^{23} using a scintillation spectrometer for heavy particles, H. F. Stoddart and H. E. Gove—238(A); 262
Energy levels of Ti^{49}, G. F. Pieper—215(A)
Energy levels resulting from 8-Mev protons on Be^9, C^{12}, N^{14}, S^{32}, J. S. Arthur, A. J. Allen, R. S. Bender, H. J. Hausman, C. J. McDole, L. M. Diana, K. B. Rhodes, and R. A. Barjon—237(A)
Energy spectrum of neutrons from interaction of 14-Mev neutrons with C, Al, Fe, Cu, Zn, Ag, Cd, Sn, Au, Pb, and Bi, E. R. Graves and L. Rosen—239(A)
Excited states of F^{20} and O^{17}, H. A. Watson—215(A)
Excited states of Li isotopes, W. Franzen and J. G. Likely—205(A); 667(L)
Excited states of Mg^{24}, Cr^{52}, and Mn^{55}, H. J. Hausman, A. J. Allen, J. S. Arthur, R. S. Bender, C. J. McDole, L. M. Diana, K. B. Rhodes, and R. A. Barjon—238(A)
Excited states of Mg^{25} from $Al^{27}(d,\alpha)Mg^{25}$ and $Mg^{24}(d,p)Mg^{25}$, P. M. Endt, H. A. Enge, J. Haffner, and W. W. Buechner—27
Experimental test of shell model, W. C. Parkinson, E. H. Beach, and J. S. King—387(L)
γ-ray yield from proton bombardment of B, L. W. Cochran, J. L. Ryan, H. H. Givin, B. D. Kern, and T. M. Hahn—672(L)
γ-rays from Na, Mg, and Al under bombardment by 200–420 kev protons, Harvey Casson—215(A)
High energy nuclear interactions in Pb, Fritz E. Froehlich, Erich M. Harth, and Kurt Sitte—504
$H^2(d,n)He^3$, low energy yield, P. Baker, B. L. Jones, and A. W. Waltner—176(A)
$H^2(d,p)H^3$, low energy yield, R. F. Hegenberger and A. W. Waltner—176(A)
Inelastic proton scattering from B^{10}, W. W. Buechner, C. P. Browne, M. M. Elking, A. Sperduto, H. A. Enge, and C. K. Bockelman—237(A)
Inelastic scattering of neutrons, Walter Hauser and Herman Feshbach—366
Inelastic scattering resulting in short-lived isomers, O. Hittmair—375(L)
Interactions of 150-Mev protons with nucleus $A=100$, S. J. Lindenbaum and G. Bernardini—207(A)
Interpretation of long-range protons from deuteron bombardment of Be^9, W. W. True and L. Diesendruck—381(L)
Ionization measurement of $B^{10}(n,\alpha)Li^7$, J. Rhodes, W. Franzen, and W. E. Stephens—141
Levels of N^{14} observed from $C^{13}(d,n)N^{14}$, R. E. Benenson—207(A)
Li^8 disintegration by fast neutrons, F. L. Ribe—205(A)
Momentum transfer in nuclear excitation by high energy particles, Si-Chang Fung and I. Perlman—622
Neutron activation of Ne^{22} and N^{15}, and attempt to detect dineutrons in a pile, A. J. Ferguson and J. H. Montague—215(A)
Neutron capture resonances in Cs, La, Pr, Rb, Tl, and Y, Robert H. Rohrer—177(A)
Neutron inelastic cross sections for excitation of single levels of middle-weight nuclei, James E. Monahan—188(A)
$(n,2n)$ reactions in C^{12}, Cu^{63}, and Mo^{92}, J. E. Brolley, Jr., J. L. Fowler, and L. K. Schlacks—206(A)
Neutrons from deuteron bombardment of N^{14}, William B. Rose, Emmett L. Hudspeth, and N. P. Heydenburg—382(L)
Neutrons from deuterons on Ne^{20}, C. P. Swann and C. E. Mandeville—215(A)
Neutrons from disintegration of P by deuterons, S. C. Snowdon—1023
Nuclear reactions in Co and As, C. J. Avery, K. C. Kaericher, and M. L. Pool—216(A)
Nuclear reactions of Fe with 340-Mev protons, G. Rudstam, P. C. Stevenson, and R. L. Folger—358
Possibilities of heavy ion bombardment in nuclear studies, G. Breit, M. H. Hull, Jr., and R. L. Gluckstern—74
Production of 40-Mev π^+- and π^--mesons in 7 elements by 240-Mev protons, Donald L. Clark—157(L)
Products of C disintegration by 330-Mev protons, Walter H. Barkas and J. Kent Bowker—207(A)
Proton groups from deuteron bombardment of Co^{59} and Cu^{63}, Donald C. Hoesterey—216(A)
$p+d\rightarrow\pi^++t$ reaction, Richard Madey, Kenneth C. Bandtel, Wilson J. Frank, and Burton J. Moyer—204(A)
Proton-proton collisions within Li nuclei, Owen Chamberlain and Emilio Segrè—81
Radiative capture of thermal neutrons by Cd^{113}, R. W. Pringle, H. W. Taylor, and K. I. Roulston—1017
Reactions $p+d\rightarrow\pi^++H^3$ and $p+d\rightarrow\pi^0+He^3$, M. Ruderman—383(L)
Relative yields of Br^{80} isomers in nuclear reactions, Arthur W. Fairhall and Charles D. Coryell—215(A)
Selection rules in nuclear reactions, A. Gamba, R. Malvano, and L. A. Radicati—440
$Si(d,p)$ and (d,α) reactions, D. M. Van Patter and W. W. Buechner—51
Slow neutron resonances in In^{112} and In^{115}, V. L. Sailor—222(A); V. L. Sailor and L. B. Borst—161(L)
Stars induced by high energy neutrons in light elements of photographic emulsion, M. Blau and A. R. Oliver—182(A)
Stars induced by μ-mesons in photographic emulsions, H. Morinaga and W. F. Fry—182(A)
Stars induced in nuclear emulsions by 100-Mev protons, Richard G. Seed—182(A)
$Sr^{88}(d,p)Sr^{89}$, $Zr^{90}(d,p)Zr^{91}$, and $Mo^{92}(d,p)Mo^{93}$ reactions, F. B. Shull and C. E. McFarland—216(A)
Sum rules in dispersion theory of nuclear reactions, T. Teichman and E. P. Wigner—123
Theory of nuclear reactions, H. Feshbach, C. Porter, and V. F. Weisskopf—188(A)
Yield of γ-rays from proton bombardment of B, J. L. Ryan, H. H. Givin, L. W. Cochran, B. D. Kern, and T. M. Hahn—177(A)

Dissociation
Dissociation energies of C−C and C−F bonds in several fluorocarbons by electron impact, Vernon H. Dibeler, Robert M. Reese, and Fred L. Mohler—213(A)
Of O_2 in upper atmosphere, H. E. Moses and Ta-You Wu 627

Dynamics
Canonical coordinate transformations and constraints in nonlinear theories, Ralph Schiller and Peter G. Bergmann—198(A)
Structure of canonical coordinate transformation group, Peter G. Bergmann and Ralph Schiller—198(A)

Elasticity
Comparative elastic studies of single crystals of CaF_2 and CsCl types, Lewis S. Combes, Stanley S. Ballard, and Kathryn A. McCarthy—201(A)
Dynamic behavior of Nylon filaments, D. J. Montgomery and W. G. Hammerle—202(A)

Effect of radiation on elastic constants, G. J. Dienes—666(L); F. R. N. Nabarro—665(L)
Mechanical properties of thin films of Ag, J. W. Beams, W. E. Walker, and H. S. Morton, Jr.—524(L)
Six-dimensional representation of stress and strain in face-centered cubic crystal, A. V. Hershey—200(A)
Strain hardening of metal crystals, Edward W. Hart, John C. Fisher, and Robert H. Pry—211(A)
Yield strength of mild steel under impulsive loading, Turner E. Pardue—172(A)

Electrets
Homocharge of electrets, Esther Davis Robinson and A. C. Menius, Jr.—177(A)

Electrical circuits (see **Methods and instruments**)

Electrical conductivity and resistance (see also **Semiconductors; Superconductivity**)
Carriers of electricity in metals exhibiting positive Hall effects, Sheldon Brown and S. J. Barnett—601
Effect of minority carriers on breakdown of point contact rectifiers, Ernst Billig—1060
Experiments on electrical conductivity, D. K. C. MacDonald—210(A)
Of graphite at low temperatures, H. W. Hemstreet and J. M. Reynolds—178(A)
Lattice vibrations and resistivity, W. A. Bowers—173(A)
Resistance minimum in Mg at low temperatures, H. E. Rorschach, Jr., and Melvin A. Herlin—193(A)
Resistivity of Cu_3Au during neutron irradiation, H. L. Glick, F. C. Brooks, W. F. Witzig, and W. E. Johnson—1074
In solar atmosphere, Donald E. Osterbrock—468
Of Ta, H. Preston-Thomas—210(A)
Whirling movements of conductor as result of interaction between electric and magnetic fields, Oleg Yadoff—233(A)

Electrodynamics (see **Electromagnetic theory and electrodynamics**)

Electromagnetic theory and electrodynamics
Dirac's new classical theory of electrons, Banesh Hoffmann—703
Electromagnetic levitation of solid and molten metals, E. C. Okress, D. M. Wroughton, G. Comenetz, P. H. Brace, and J. C. R. Kelly—209(A)
Electron paths in magnetic lens spectrometer, W. S. Emmerich, Y. Nogami, L. A. Kiley, and J. D. Kurbatov—194(A)
Gauge invariance and classical electrodynamics, Lloyd Motz—224(A)
Interaction between electron and one-dimensional electromagnetic field, Nathan Rosen—940
Mass of photon, L. S. Kothari—536(L)
Radiation loss by electrons in large orbits, Dale R. Corson—233(A)

Electron diffraction
Plural electron scattering and influence on electron diffraction patterns, S. G. Ellis—970

Electron optics
Electron paths in magnetic lens spectrometer, W. S. Emmerich, Y. Nogami, L. A. Kiley, and J. D. Kurbatov—194(A)
Heating of samples in electron microscope, L. A. Woodward—178(A)

Electrons (see also **Positrons; E/m; Electromagnetic theory and electrodynamics**)
Anomalous spin gyromagnetic ratio of electron, J. G. King and V. Jaccarino—228(A)
Cloud-chamber studies of production of light "positive particles" near β^- ray emitters, Gerhart Groetzinger and Fred L. Ribe—1003
Dirac's new classical theory of electrons, Banesh Hoffmann—703
Electron-neutron interaction, L. L. Foldy—693
Electron spin gyromagnetic ratio in atomic H, R. Beringer and E. B. Rawson—228(A)
Interaction between electron and one-dimensional electromagnetic field, Nathan Rosen—940
Neutron-electron interaction, J. A. Harvey, D. J. Hughes, and M. D. Goldberg—220(A)
Nuclear masses and electron mass, Enos E. Witmer—237(A)
Radiation loss by electrons in large orbits, Dale R. Corson—233(A)

Electrons in metals
Carriers of electricity in metals exhibiting positive Hall effects, Sheldon Brown and S. J. Barnett—601
Scattering of electrons from point singularities in metals, D. L. Dexter—768
Weak potential model for electrons in metal, Edward N. Adams, II—211(A)

Electrons, positive (see **Positrons**)

Electrons, scattering of
Electron scattering experiments at low and middle energies, L. Marton—200(A)
Exchange scattering of electrons, Ta-You Wu—1012
Plural electron scattering and its influence on electron diffraction patterns, S. G. Ellis—970
From point singularities in metals, D. L. Dexter—768

Electrons, thermionic (see **Thermionic emission**)

Electro-optical effects (see also **Photoelectric effect and properties**)
Electroluminescence of single crystals of ZnS:Cu, William W. Piper and Ferd E. Williams—151(L)
Field strength and temperature dependence of electroluminescence in powders, S. Roberts and J. S. Prener—191(A)

Elements (see **Isotopes**)

Energy loss of particles (see **Range and energy loss of particles**)

Energy states of atoms (see **Spectra, atomic**)

Energy states of molecules (see **Molecular structure and constants; Spectra, molecular**)

Energy states of nucleus (see **Disintegration and excitation of nucleus; Nuclear spectra; Nuclear structure**)

Errata
Angular distribution of shower particles as a function of depth, L. Eyges and S. Fernbach—1143(L)
He II transfer rates on Lucite and Perspex surfaces, B. S. Chandrasekhar—1144(L)
Low energy γ-transitions in rare earth isotopes, J. W. Mihelich and E. L. Church—1144(L)
Nuclear matrix elements in theory of β-decay, Henry Brysk 1144(L)
Soft radiations from Am^{241}, J. K. Beling, J. O. Newton, and B. Rose—1143(L)
Symmetrical pseudoscalar meson theory of nuclear forces, Maurice M. Levy—1143(L)

Evaporation
Effects of ionizing radiation on formation of bubbles in liquids, Donald A. Glaser—665(L)

Excitation of atoms and molecules
Cross section for He atoms, Saul Altshuler—992
Resonance in collision processes, O. Oldenberg—786

Excitation of nuclei (see **Disintegration and excitation of nucleus; Nuclear spectra; Nuclear structure**)

Explosion phenomena (see also **Shock waves**)
Detonation pressures from flash radiographs, J. N. Dewey, H. I. Breidenbach, Jr., and J. W. Gehring, Jr.—909(A)
Effect of charge radius on detonation velocity, R. B. Parlin, C. J. Thorne, and D. W. Roninson—910(A)
Fast metal jets, F. J. Willig—910(A)
Free surface properties of explosive-driven metal plates, W. E. Deal and R. G. Shreffler—910(A)
Jetless and jet forming collisions of explosive driven metal plates, F. J. Willig, R. G. Shreffler, and J. M. Walsh—910(A)

Explosion phenomena (continued)
Limiting conditions for jet formation in high velocity collisions, J. M. Walsh, R. G. Shreffler, and F. J. Willig—910(A)
Low velocity detonation of certain primary explosives, R. H. Stresau—234(A)
Luminescence accompanying cone-cylindrical and spherical missiles traveling at high speeds, J. Eckerman and R. N. Schwartz—912(A)
Luminous effects in shock tube, R. N. Hollyer, Jr., A. C. Hunting, Otto Laporte, E. H. Schwarcz, and E. B. Turner—911(A)
Numerical solution of equations for discrete model of spherical blast, T. S. Walton—910(A)
Oscillations of gas bubble produced by underwater explosion, L. C. Barrett and C. J. Thorne—913(A)
Qualitative comparison of meteor and fast-particle spectra, William C. White and Richard N. Thomas—912(A)
Reaction time in detonating liquid, T. P. Cotter—909(A)
Recent air shock velocity measurements near detonating explosives, J. Svitt and R. H. Stresau—234(A)
Semiquantitative interpretation of Al fast-particle spectrum, Richard N. Thomas and William C. White—912(A)
Spinning detonation, Herbert T. Knight and Russell E. Duff—909(A)
Time-resolved spectroscopy of incandescence associated with ultra-speed pellets, Earle B. Mayfield—912(A)

Ferroelectric and antiferroelectric phenomena
Dielectric properties of Ba-Sr titanate ceramics, Luther Davis, Jr., and Lawrence G. Rubin—201(A)
Ferroelectricity in Ilmenite structure, H. C. Schweinler—5
Piezoelectricity, ferroelectricity, and crystal structure, A. von Hippel—200(A)
Wall energy of ferroelectric domains, W. Känzig—385(L)
Ferromagnetism (see **Magnetic properties**)
Field theory (see also **Quantum electrodynamics**)
Absorption of π^- meson from K-shell of H^3, Saul A. Basri—866
Aether of Dirac in light of contemporary field theory, Alexander W. Stern—199(A)
Canonical coordinate transformations and constraints in nonlinear theories, Ralph Schiller and Peter G. Bergmann—198(A)
Classical equations of motion of point particles. I, Peter Havas—309
Conservation laws for fields of zero rest mass. I, James A. McLennan, Jr., and Peter Havas—898(L); II, Peter Havas—898(L)
Decay of neutral scalar heavy meson, H. P. Noyes—344
Decay of scalar particle into three photons, L. Wolfenstein and G. D. Ravenhall—217(A)
Equivalence theorems for pseudoscalar coupling, J. M. Berger, L. L. Foldy, and R. K. Osborn—1061
Influence of relativistic corrections upon singular nuclear potentials, J. Werle—159(L)
Low energy properties of pseudoscalar interaction with hard core, Robert Jastrow—209(A)
Matter-matter interaction through retarded fields, Frederik J. Belinfante—224(A)
Meson production by nucleons in Coulomb fields, E. D. Courant—217(A)
Multiple meson production, M. Ruderman—217(A)
Nonlinear interaction of scalar fields, M. Dresden—224(A)
Nonlinear pseudoscalar meson theory, E. M. Henley—42
Nuclear forces yielded by symmetrical pseudoscalar meson theory with pseudoscalar coupling, Joseph V. Lepore—209(A)
Nucleon recoil and the electron-neutron interaction, L. L. Foldy—675(L)
Pseudoscalar interaction in β-decay theory, T. Ahrens, E. Feenberg, and H. Primakoff—663(L)
Quantization of interacting gravitational, electromagnetic and electron fields, R. Skinner and A. Schild—224(A)
Quantum corrections to classical nonlinear meson theory, D. R. Yennie—224(A)
Quantum theory of interacting gravitational spinor fields, Bryce Seligman DeWitt and Cecile Morette DeWitt—116
Regular meson potentials in low energy proton-proton scattering, H. E. Hart and R. D. Hatcher—375(L)
Selection rules imposed by charge conjugation and charge symmetry, A. Pais and R. Jost—871
Strong coupling in relativistic meson theory, Murray Gell-Mann and Marvin L. Goldberger—218(A)
Symmetrical pseudoscalar meson theory of nuclear forces, erratum, Maurice M. Lévy—1143(L)
Films, properties of
Mechanical properties of thin films of Ag, J. W. Beams, W. E. Walker, and H. S. Morton, Jr.—524(L)
Fine structure (see **Spectra; Hyperfine structure**)
Fission of nucleus (see also **Disintegration and excitation of nucleus**)
Angular distribution of fission fragments in photofission of Th, E. J. Winhold, P. T. Demos, and I. Halpern—1139(L)
Binary fission, T. D. Newton—187(A)
Distributions-in-energy for α-particles and protons, David L. Hill—1049
Electrical analog for radioactivity of primary fission products with intermittent reactor operation, W. O. Doggett—171(A)
Energy spectrum of neutrons, B. E. Watt—1038
Generation and storage of radioactive gases from intermittent reactor operation, Raymond L. Murray—171(A)
Mo^{99}, Ag^{111}, and Ba^{140} yields from proton induced fission, W. H. Jones, J. L. Fowler, and J. H. Paehler—174(A)
Neutron energy spectrum, David L. Hill—1035
Spectrum of neutrons of low energy, T. W. Bonner, R. A. Ferrell, and M. C. Rinehart—1033
Spontaneous fission of U^{234}, Pu^{238}, Cm^{240}, and Cm^{244}, A. Ghiorso, G. H. Higgins, A. E. Larsh, G. T. Seaborg, and S. G. Thompson—163(L)
Velocities of fragments from fission of U^{233}, U^{235}, and Pu^{239}, R. B. Leachman—444
Fluctuation phenomena
Application of multiple scattering theory to cloud-chamber measurements. I, Stanislaw Olbert—319
Diffusion theory of noise in rectifiers and transistors, Richard L. Petritz—189(A)
Irreversibility and generalized noise, Julius L. Jackson—471
Theory of contact noise, Richard L. Petritz—535(L)
Fluid dynamics (see also **Hydrodynamics; Aerodynamics**)
Compressible flow of viscous fluid in small diameter tube closed at one end, J. M. Kendall—913(A)
Compressible laminar boundary layers, S. H. Christensen—911(A)
Effects of damping screens and stream contraction on turbulence, Maurice Tucker—911(A)
Hydrodynamic stability of laminar flame fronts, Martin Lessen—913(A)
Limiting conditions for jet formation in high velocity collisions, J. M. Walsh, R. G. Shreffler, and F. J. Willig—910(A)
Magneto-hydrodynamic waves, M. S. Steinberg—173(A)
Oscillations of gas bubble produced by underwater explosion, L. C. Barrett and C. J. Thorne—913(A)
Stability of laminar parabolic flow, Tomomasa Tatsumi—1127(L)
Turbulent heat transfer for flow in channel, Eugene N. Parker—911(A)

Fluorescence (see also **Luminescence**)
Decay times, fluorescent efficiencies, and energy storage properties for various substances with γ-ray or α-particle excitation, Loran Bittman, Milton Furst, and Hartmut Kallmann—83
Energy response of organic liquid scintillation counters, George T. Reynolds—193(A)
Field dependent fluorescence of vitreous Zn_2SiO_4 phosphor, Arthur Bramley and Jenny E. Rosenthal—1125(L)
Internal absorption of fluorescent light in large plastic scintillators, C. N. Chou—376(L)
Nature of saturation effect of fluorescent scintillators, C. N. Chou—904(L)
Saturation effect of plastic scintillators, C. N. Chou—903(L)
Scintillation counter studies of slow α-particles, J. I. Hopkins and C. N. Wright—174(A)

Gamma-rays (see also **Disintegration and excitation of nucleus; Nuclear spectra; Radioactivity**)
Absorption coefficients of γ-rays, S. J. Wyard—165(L)
Average energy of electrons in anthracene due to γ-irradiation, G. D. Prestwich, T. H. Colvin, and G. T. Hine—1031
Elastic scattering of gammas by bound electrons, P. Greifinger, J. Levinger, and F. Rohrlich—663(L)
γ-γ angular correlation in Cd^{114}, E. D. Klema and F. K. McGowan—524(L)
γ-radiation associated with stopping of μ^- mesons in Pb, A. Fafarman and M. H. Shamos—219(A)
γ-ray absorption measurements, Stirling A. Colgate—592
Line shape of monochromatic γ-rays, D. Maeder and V. Wintersteiger—537(L)
Nuclear scattering of 17-Mev γ-rays, Mary Beth Stearns—706
Pair measurement of γ-rays with lens spectrometer, David E. Alburger—194(A)
From Sc^{48}, Bernard Hamermesh, Virginia Hummel, Leonard Goodman, and Donald Engelkemeir—528(L)

Gases (see also **Kinetic theory**)
Application of high rotational speed techniques to low density gas dynamics, A. R. Kuhlthau—171(A)
Condensation phenomenon of ideal Einstein-Bose gas. II, Otto Halpern—520(L)

Geophysics
Absorption by telluric CO in 2.3μ region, J. N. Howard and J. H. Shaw—679(L)
Abundance of telluric CO above Columbus, Ohio, J. H. Shaw and J. N. Howard—380(L)
Autoradiographic analysis of Murray, Kentucky meteorite, J. R. Horan and G. A. Boyd—117(A)
Forbidden line of N II in the aurora, W. Petrie—1002
Geoelectrical prospecting over dome structure, theory, Robert Van Nostrand—177(A)
Velocity determination for microseisms in coral formations, E. W. Kammer—177(A)

Gravitation
New approximation for gravitational field equations, Joshua Goldberg and Peter G. Bergmann—198(A)
Quantization of Einstein's gravitational field equations. II, F. A. E. Pirani, A. Schild, and R. Skinner—452
Quantum theory of interacting gravitational and spinor fields, Bryce Seligman DeWitt and Cecile Morette DeWitt—116
Some static axially symmetric gravitational fields, J. B. Newman—173(A)

Gyromagnetization (see **Magnetic properties**)

Hall effect
Carriers of electricity in metals exhibiting positive Hall effects, Sheldon Brown and S. J. Barnett—601
In Co above magnetic saturation, Simon Foner and Emerson M. Pugh—210(A)
In Co-Ni alloys, Emerson M. Pugh and Simon Foner—210(A)
Of degenerate Ge sample, D. M. Finlayson, V. A. Johnson, and F. M. Shipley—1141(L)
In single crystals of BaO, E. M. Pell—457

Heat capacity (see **Specific heat**)

Helium, liquid
Anomalous type of He^3 flow, E. F. Hammel and Adam F. Schuch—154(L)
Condensation phenomenon of ideal Einstein-Bose Gas. II. Otto Halpern—520(L)
Energy quantization for colliding molecules; application to liquid He, P. J. Price—173(A)
Entropy and specific heat of liquid He^3, K. S. Singwi—540(L)
Heat conduction by unsaturated He II film, Earl Long and Lothar Meyer—153(L)
He film transport over Cu below 1°K, L. Lesensky and H. A. Boorse—1135(L)
He II transfer rates on Lucite and Perspex surfaces, erratum, B. S. Chandrasekhar—1144(L)
Nonlinear stationary flow in liquid He II, P. R. Zilsel and H. M. Fried—193(A)
Second sound in He^3–He^4 mixtures, P. J. Price—381(L)

High voltage tubes and machines (see **Methods and instruments**)

Hydrodynamics
Magneto-hydrodynamic waves, M. S. Steinberg—173(A)

Hyperfine structure (see also **Nuclear moments and spin**)
Of Ir and Os, Kiyoshi Murakawa and Shigeki Suwa—1048
Isotope shifts in Er, Lawrence Wilets and Lee C. Bradley, III—1019
Mass corrections to hfs, E. E. Salpeter and W. A. Newcomb—150(L)
Of positronium, Robert Karplus and Abraham Klein—848
Precision measurements of hfs of Rb^{85} and Rb^{87}, B. Bederson and V. Jaccarino—228(A)

Instruments (see **Methods and instruments**)

Internal conversion (see **Nuclear spectra**)

Ionization
Charge transfer for protons in He, R. H. Garstang—529(L)
Effects of ionizing radiation on formation of bubbles in liquids, Donald A. Glaser—665(L)
Ionization loss at relativistic velocities in nuclear emulsions, Maurice M. Shapiro and Bertram Stiller—682(L)
Ionization losses of fast μ-mesons in gases, J. E. Kuperian, Jr., and E. D. Palmatier—169(A)
Ionization measurement of $B^{10}(\pi,\alpha)Li^7$, J. Rhodes, W. Franzen, and W. E. Stephens—141
Multiple ionization by electron impact, William J. Knox—232(A)
Relative specific ionization of fast mesons, R. S. Carter and W. L. Whittemore—494

Ionosphere
Ionospheric absorption by N_2 and O_2 of certain extreme uv solar wavelengths, K. C. Clark—271

Ions
Acceleration of Be and C ions in synchrocyclotron, C. N. Chou, W. F. Fry, and J. J. Lord—671(L)
Charge transfer cross sections between atoms and slow ions in A, Ne, and He, Roy F. Potter—232(A)
Mechanism for sputtering in high vacuum based upon theory of neutron cooling, Frank Keywell—160(L)
Motion of gaseous ions in strong electric field. II, Gregory H. Wannier—795
Negative metastable ions, B. L. Donnally, J. B. Dozier, and H. E. Carr—170(A)

Ions and electrons, mobility (see also **Semiconductors**)
Mobility of electrons in Ge, P. P. Debye and E. M. Conwell—1131(L)
Motion of gaseous ions in strong electric field. II, Gregory H. Wannier—795

Isomers, nuclear (see also **Nuclear spectra; Radioactivity**)
Additional branch in decay scheme of Zr^{89m}, F. J. Shore, H. N. Brown, W. L. Bendel, and R. A. Becker—202(A)
Am^{242m} half-life for negative electron emission, Thomas K. Keenan, Robert A. Penneman, and B. B. McInteer—204(A)
Cd^{115} isomer decay, R. W. Hayward—202(A)
Inelastic scattering resulting in short-lived isomers, O. Hittmair—375(L)
Relative yields of Br^{80} isomers in nuclear reactions, Arthur W. Fairhall and Charles D. Coryell—215(A)
In Te^{122}, Alexis C. Pappas—162(L)
Tentative hypothesis of proton isomers, G. Breit—208(A)

Isotopes and atomic mass
Atomic masses and nuclear shell structure at 20 and 28 neutrons and protons, Thomas L. Collins, Alfred O. Nier, and Walter H. Johnson, Jr.—236(A)
Cl^{39} and A^{39} masses, C. E. Anderson, G. W. Wheeler, and W. W. Watson—897(L)
Masses of stable Te isotopes from microwave spectrum of TeCS, G. Silvey, W. A. Hardy, and C. H. Townes—236(A)
Nuclear masses and electron mass, Enos E. Witmer—237(A)
Pm isotopes, Vera Kistiakowsky—859
V^{50} mass, Walter H. Johnson, Jr.—166(L)

Liquids (see also **Hydrodynamics**)
Aqueous electrolyte cathode in dielectric breakdown studies of liquids, A. H. Sharbaugh, R. W. Crowe, and J. K. Bragg—232(A)
Effects of ionizing radiation on formation of bubbles in liquids, Donald A. Glaser—665(L)
Equilibria in liquid systems, George Antonoff—242(A)
Equilibria in liquids. II. Liquid-vapor systems, George Antonoff—185(A)
Forces between acetone molecules, Vernon Myers—185(A

Low temperature phenomena (see also **Helium, liquid**)
Electrical resistivity of graphite at low temperatures, H. W. Hemstreet and J. M. Reynolds—178(A)
Low temperature heat capacity of V, R. D. Worley, M. W. Zemansky, and H. A. Boorse—192(A)
Low temperature thermal conductivity of Sn and Sn-Bi alloys, D. P. Detwiler—192(A)
Nuclear and electronic contributions to specific heat of $Nd(EtSO_4)_3$ near 1°K, L. D. Roberts, C. C. Sartain, and B. Borie—192(A)
Resistance minimum in Mg at low temperatures, H. E. Rorschach, Jr., and Melvin A. Herlin—193(A)
Specific heats of several metals between 1.8° and 4.2°K, I. Estermann, S. A. Friedberg, and J. E. Goldman—582
Viscosity of ortho- and para-hydrogen, E. W. Becker and O. Stehl—325(L)

Luminescence (see also **Fluorescence, Phosphorescence**)
Accompanying cone-cylindrical and spherical missiles traveling at high speeds, J. Eckerman and R. N. Schwartz—912(A)
Electroluminescence of single crystals of ZnS:Cu, William W. Piper and Ferd E. Williams—151(L)
Field strength and temperature dependence of electroluminescence in powders, S. Roberts and J. S. Prener—191(A)
Induced conductivity and light emission in different luminescent type powders, Hartmut Kallmann and Bernard Kramer—91
Luminous effects in shock tube, R. N. Hollyer, Jr., A. C. Hunting, Otto Laporte, E. H. Schwartz, and E. B. Turner—911(A)
Produced as result of intense ultrasonic waves, V. Griffing and D. Sette—234(A)
Thermoluminescence and changes of color centers in LiF, J. Sharma—535(L)

Magnetic properties (see also **Nuclear moments and spin; Crystal line state; Magnetic resonance absorption**)
Anisotropy in antiferromagnetic MnF_2, Frederic Keffer—608
Anomalous paramagnetism of $CuSO_4 \cdot 5H_2O$, Warren E. Henry—1133(L)
Anomalous spin gyromagnetic ratio of electron, J. G. King and V. Jaccarino—228(A)
Antiferromagnetic arrangements in ferrites, Y. Yafet and C. Kittel—290
Electron spin gyromagnetic ratio in atomic H, R. Beringer and E. B. Rawson—228(A)
Energy of Bloch wall on band picture. II. Perturbation approach, Conyers Herring—60
Gyromagnetic ratios of ferromagnetic elements, G. G. Scott—697
Gyromagnetic ratios of Fe, Co, and binary alloys of Fe, Co, and Ni, S. J. Barnett and G. S. Kenny—723
Magnetic shielding effects in compounds of V, H. E. Walchli and H. W. Morgan—541(L)
Magnetic susceptibility of Cb, Ta, V, Mo, and W at high temperatures, C. J. Kriessman, Jr.—209(A)
Magnetostriction in single crystals, R. M. Bozorth and R. W. Hamming—209(A)
Paramagnetic relaxation in CsTi alum, Julian Eisenstein—522(L)
Single crystal magnetostriction constants of Fe-Co alloy, H. M. A. Urquhart and J. E. Goldman—210(A)
Spin wave theory of antiferromagnetics, Ryogo Kubo—568
Of superconducting alloys of In and Tl, W. F. Love, E. Callen, and F. C. Nix—844

Magnetic resonance absorption (see also **Nuclear moments and spin**)
Anomalous wave types in wave guides containing ferromagnetics, A. A. Th. M. van Trier—227(A)
Broadening of magnetic resonance lines in metals by spin-lattice interactions, H. S. Gutowsky and B. R. McGarvey—226(A)
Cu^{++}, anomalous magnetic resonance absorption, Hiroo Kumagai, Hidetarô Abe, and Junji Shimada—385(L)
Electron spin gyromagnetic ratio in atomic H, R. Beringer and E. B. Rawson—228(A)
Fine structure of resonance absorption of Mn^{++} in rhombic crystalline field, Hiroo Kumagai, Kazuo Ôno, Izuo Hayashi, and Kenjirô Kambe—374(L)
Influence of anisotropy on ferromagnetic relaxation, N. Bloembergen and Shyh Wang—392(L)
Nuclear magnetic octopole interaction, John Levinson—188(A)
Nuclear magnetic resonance lines of Sb in antimony hexafluoride ion, S. S. Dharmatti and H. E. Weaver, Jr.—675(L)
Nuclear rf spectra of H_2 and D_2 in high and low magnetic fields, H. G. Kolsky, T. E. Phipps, Jr., N. F. Ramsey, and H. B. Silsbee—395
Nuclear resonance spectrum of system of four nuclei, R. Bersohn—226(A)
Paramagnetic resonance absorption in additively colored crystals of alkali halides, Clyde A. Hutchison, Jr., and Gordon A. Noble—1125(L)
Paramagnetic resonance in concentrated liquid solutions, M. A. Garstens and S. H. Liebson—230(A)

Paramagnetic resonance in phosphors, W. D. Hershberger and H. N. Leifer—229(A)
Paramagnetic resonance in U salts, S. N. Ghosh, Walter Gordy, and D. G. Hill—229(A)
Paramagnetic saturation of Fe ammonium alum, W. E. Henry—229(A)
Magnetostriction (see **Magnetic properties**)
Mass spectroscopy
Mass spectra of isotopic CO_2 molecules, F. S. Stein—236(A)
Mass spectrometer studies of high vacuum materials, John R. Sites and Russell Baldock—171(A)
Measurements (see **Methods and instruments**)
Mechanics (see **Dynamics**)
Mechanics, quantum—atomic structure and spectra
Configuration interaction in Fe group elements, N. Rosenzweig—225(A)
Negative H ion wave functions, J. A. Poulson and A. C. Menius, Jr.—174(A)
Mechanics, quantum—general
Bound states and interaction representation, S. T. Ma—652
Darling's theory of elementary particles and Born's reciprocity hypothesis, Hans Freistadt—198(A)
Electromagnetic properties of Dirac particles, L. L. Foldy—688
Energy quantization for colliding molecules; application to liquid He, P. J. Price—173(A)
Ergodic theorem in quantum statistical mechanics, Martin J. Klein—111
Interaction between electron and one-dimensional electromagnetic field, Nathan Rosen—940
Modification of potential in Dirac equation, Paul Zweifel—173(A)
Octupole moment interaction, W. A. Nierenberg—225(A)
Possible convergent solution of interaction state equation, Jack Heller—225(A)
Proposed re-interpretation of quantum mechanics, Otto Halpern—389(L)
Quantum theory of interacting gravitational and spinor fields, Bryce Seligman DeWitt and Cecile Morette DeWitt—116
Relation of Monte Carlo and variational calculation method in quantum mechanics, J. Kr Bragg—199(A)
Reply to criticism of causal re-interpretation of quantum theory, David Bohm—389(L)
Thermodynamic continuity and quantum principles, Alfred Lande—267
Uniqueness in theory of fundamental length, B. T. Darling and P. R. Zilsel—198(A)
Validity of Born expansions, Walter Kohn—539(L)
Mechanics, quantum—molecular structure and spectra
Centrifugal distortion in asymmetric rotor molecules, D. Kivelson and E. Bright Wilson, Jr.—214(A)
Density matrix formulation of LCAO molecular orbital theory, William J. Taylor—214(A)
Vibrational and centrifugal effects on nuclear interactions and rotational moments in molecules, Norman F. Ramsey—1075
Mechanics, quantum—nuclear
Absorption of slow π^- mesons by He^3, A. M. L. Messiah—639
Analysis of 14-Mev $n-p$ scattering, George Snow—21
Binding energy of α-particle, John Irving—519(L)
Born approximation theory of (d,p) and (d,n) reactions, P. B. Daitch and J. B. French—900(L)
Charge independence of nuclear forces, L. A. Radicati—521(L)
Collective description of nucleon interactions, Melvin Ferentz and David Pines—188(A)
Construction of a potential from phase shift, Res Jost and Walter Kohn—977
Cosine interaction between nucleons, A. de-Shalit—843
Direct interaction and compound nucleus for 14-Mev neutrons, H. McManus and W. T. Sharp—188(A)
Electron excitation of nuclei, Joseph A. Thie, Charles J. Mullin, and E. Guth—962
Fermi-Thomas model of the nucleus, R. J. Riddell, Jr.—189(A)
Ground-state spins and energy differences from jj-coupling model, D. Kurath—218(A)
Inelastic scattering of neutrons, Walter Hauser and Herman Feshbach—366
Influence of relativistic corrections upon singular nuclear potentials, J. Werle—159(L)
Interaction moment contributions to magnetic moments of nuclei, L. Spruch and A. Russek—189(A); 1111
Interference of amplitudes in cascade processes, O. Halpern and B. A. Lippmann—1128(L)
Internal conversion of γ-rays with pair production, S. A. S. Brimberg—150(L)
$n-p$ scattering in 0–5 Mev region, L. Hulthén and S. Skavlem—297
Nuclear structure and interpretation of β-decay, R. King and E. Feenberg—218(A)
Nuclear matrix elements in theory of β-decay, erratum, Henry Brysk—1144(L)
"Nucleon isobar" as intermediate state, N. Austern—208(A)
Nucleon-lepton interaction in β-decay, R. Nataf and R. Bouchez—155(L)
Nucleon-lepton interactions, Frederik J. Belinfante—521(L)
Optical model for nucleon-nuclei scattering, Robert E. LeLevier and David S. Saxon—40
Pseudoscalar interaction in theory of β-decay, T. Ahrens, E. Feenberg, and H. Primakoff—663(L)
Ratio F_a/F_v in theory of forbidden β-transitions, P. Macklin, L. Lidofsky, and C. S. Wu—391(L)
Reactions $p+d\rightarrow\pi^++H^3$ and $p+d\rightarrow\pi^0+He^3$, M. Ruderman—383(L)
Relation between phase-shifts and energy levels, P. Weiss—226(A)
Scattering by high potential barriers and by potentials with shell structure, J. Mayo Greenberg—209(A)
Scattering of protons from C, Peter A. Wolff—434
Selection rules in nuclear reactions, A. Gamba, R. Malvano, and L. A. Radicati—440
7.4-Mev state of Li^7, Murray Peshkin and A. J. F. Siegert—735
Spin-orbit coupling and nuclear shell model, Eugen Merzbacher—173(A)
Sum rules in dispersion theory of nuclear reactions, T. Teichman and E. P. Wigner—123
Surface production of charged mesons by photons on nuclei, S. T. Butler—217(A)
Tentative hypothesis of proton isomers, G. Breit—208(A)
Theory of nuclear reactions, H. Feshbach, C. Porter, and V. F. Weisskopf—188(A)
Theory of pick-up process, George J. Yevick—208(A)
Wave-mechanical description of deuteron stripping process, F. L. Friedman and W. Tobocman—208(A)
Mechanics, quantum—of solid bodies
Application of cellular method to Si, D. K. Holmes—782
Interaction of excitons and phonons, Paul Leurgans and J. Bardeen—200(A)
Scattering of electrons from point singularities in metals, D. L. Dexter—768
Soluble problem in energy bands, J. C. Slater—807
Theory of optical and thermal transitions in solids, Ryogo Kubo—201(A)
Variational methods in periodic lattices, W. Kohn—472
Weak potential model for electrons in metal, Edward N. Adams, II—211(A)

Mechanics, statistical
Application of cell method in grand canonical ensemble to equation of state of liquid mixture, S. R. Brinkley, Jr., and John M. Richardson—199(A)
Cell method in grand canonical ensemble, John M. Richardson and S. R. Brinkley, Jr.—199(A)
Condensation phenomenon of ideal Einstein-Bose gas. II, Otto Halpern—520(L)
Ergodic theorem in quantum statistical mechanics, Martin J. Klein—111
Relativistic statistical thermodynamics, A. E. Scheidegger and R. V. Krotkov—197(A)
Statistical theory of equations of state and phase transitions. I. Theory of condensation—404; II. Lattice gas and Ising model, T. D. Lee and C. N. Yang—410
Meson field theory (see **Field theory**)
Mesons (see also **Cosmic radiation**)
Absorption of π^- meson from K-shell of H^3, Saul A. Basri—866
Absorption of slow π^- mesons by He^4, A. M. L. Messiah—639
Angular distribution of π-C scattering, D. C. Peaslee—217
Application of theory of effective range to meson-nucleon scattering, Keith A. Brueckner—1027
Capture of μ-mesons, J. W. Keuffel, F. B. Harrison, T. N. K. Godfrey, and George T. Reynolds—942
Decay of μ^- mesons in SiC, LeConte Cathey—169(A)
Decay of neutral scalar heavy meson, H. P. Noyes—344
Decay scheme of V^0-particle, K. A. Brueckner and R. W. Thompson—390(L)
Elastic π-C scattering, D. C. Peaslee—862
Elastic scattering of pions from H and D, Gerson Goldhaber—220(A)
Electric and non-electric scattering of cosmic-ray mesons and protons, W. L. Whittemore and R. P. Shutt—241(A)
Excitation function for π^+ mesons produced in $p-p$ collisions, A. G. Schulz, D. Hamlin, M. J. Jakobson, and J. Merritt—219(A)
Fast π-mesons interactions in nuclear emulsions, Hugh Bradner and Bayard Rankin—547; Bayard Rankin and Hugh Bradner—553
γ-radiation associated with stopping of μ^--mesons in Pb, A. Fafarman and M. H. Shamos—219(A)
Interaction of pions originating in penetrating showers, R. L. Cool and O. Piccioni—531(L)
Ionization by cosmic-ray mesons in A, G. W. McClure—680(L)
Ionization losses of fast μ-mesons in gases, J. E. Kuperian, Jr., and E. D. Palmatier—169(A)
Mean life of neutral penetrating ray, Rogers D. Rusk and Mildred D. Moore—239(A)
Meson-meson interaction, Keith A. Brueckner and Kenneth M. Watson—621
Meson production by nucleons in Coulomb fields, E. D. Courant—217(A)
μ-meson capture, James M. Kennedy—953
Multiple meson production, M. Ruderman—217(A)
Narrow angle pair of particles produced in H, A. B. Weaver, Earl A. Long, and Marcel Schein—531(L)
Narrow angle pairs of particles from nuclear interactions, J. J. Lord, Joseph Fainberg, D. M. Haskin, and Marcel Schein—538(L)
Neutral meson production in nucleon collisions, B. J. Moyer—220(A)
Neutrons from capture of slow π^- mesons, V. Cocconi Tongiorgi and Donald A. Edwards—220(A)
Nuclear cross sections for negative pions of energy 113 and 137 Mev, Ronald L. Martin—1052
Phenomenological potentials in meson scattering, R. LeLevier—217(A)
Photoproduction of π^0 mesons from deuterium, W. Heckrotte, L. R. Henrich, and J. V. Lepore—219(A)
π^0 meson production by 430-Mev protons on Be, L. Marshall, J. Marshall, V. A. Nedzel, and S. Warshaw—220(A); on H—220(A)
Production and interaction at very high energies, D. Lal, Yash Pal, B. Peters, and M. S. Swami—545(L)
Production of charged pions by protons on C and other nuclei, M. M. Block, S. Passman, and W. W. Havens, Jr.—168(A)
Production of 40-Mev π^+ and π^- mesons in 7 elements by 240-Mev protons, Donald L. Clark—157(L)
$p+d \rightarrow \pi^+ + t$ reaction, Richard Madey, Kenneth C. Bandtel, Wilson J. Frank, and Burton J. Moyer—204(A)
Range distribution of μ-mesons from π-meson decays in photographic emulsions, George R. White and W. F. Fry—219(A)
Reactions $p+d \rightarrow \pi^+ + H^3$ and $p+d \rightarrow \pi^0 + He^3$, M. Ruderman—383(L)
Relative specific ionization of fast mesons, R. S. Carter and W. L. Whittemore—494
Stars induced by μ-mesons in photographic emulsions, H. Morinaga and W. F. Fry—182(A)
Surface production of charged mesons, S. T. Butler—1117; 217(A)
Thin wall Geiger counters for research on soft component, Frank E. Kinard—168(A)
Total cross sections of positive pions in H, S. W. Barnes, D. L. Clark, J. P. Perry, and C. E. Angell—669(L)
Unusual $\pi-\mu$ decays in photographic emulsions, W. F. Fry—219(A)
Unusual star, W. F. Fry and J. J. Lord—533(L)
Variation of positive-negative ratio of cosmic-ray mesons with momentum and altitude, H. A. Morewitz and M. H. Shamos—241(A)
V^0-decay, energy release, S. D. Wanlass, R. B. Leighton, W. L. Alford, C. D. Anderson, and F. H. Shelton—183(A)
V^0-decay, general properties, C. D. Anderson, R. B. Leighton, F. H. Shelton, and S. D. Wanlass—183(A)
V^0-decay in multiple plate cloud chamber, G. W. Clark, M. Annis, H. S. Bridge, H. W. Courant, and B. Rossi—182(A)
V^0-disintegration in flight, R. W. Thompson, C. J. Karzmark, and H. O. Cohn—182(A)
V^0-particles, production, F. H. Shelton, S. D. Wanlass, and R. B. Leighton—183(A)
ζ^0-meson, M. F. Kaplon and D. M. Ritson—664(L)
Metals (see **Crystalline state**)
Metastable atoms and molecules
Negative metastable ions, B. L. Donnally, J. B. Dozier, and H. E. Carr—170(A)
Methods and instruments
Acceleration of Be and C ions in a synchrocyclotron, C. N. Chou, W. F. Fry, and J. J. Lord—671(L)
Addition of general-purpose program to JAINCOMP-B electronic digital computer, Donald H. Jacobs and Seymour Scholnick—231(A)
Application of high rotational speed techniques to low density gas dynamics, A. R. Kuhlthau—171(A)
Application of multiple scattering theory to cloud-chamber measurements. I, Stanislaw Olbert—319
Argonne fast neutron chopper, L. M. Bollinger, S. P. Harris, and R. W. Schumann—184(A)
Atomic beam resonance method for excited states, I. I. Rabi—379(L)
Automatic scanner for multichannel pulse-height analysis of 35-mm film record, D. J. Zaffarano and Warren A. Hunt—194(A)
Build-up of D on metal targets, W. F. Studer and A. W. Waltner—176(A)

Coincidence method for investigation of cosmic rays using scintillations in liquids, J. Hershkowitz, H. P. Kallmann, and W. A. Schneider—241(A)
Counting efficiency of gas-flow proportional counter, Bernd Kahn—175(A)
Determination of resolving time of coincidences, Z. Bay—194(A)
Effective use of reciprocity in vibrometer calibrations, Sanford P. Thompson—230(A)
Effects of ionizing radiation on formation of bubbles in liquids, Donald A. Glaser—665(L)
Electromagnetic levitation of solid and molten metals, E. C. Okress, D. M. Wroughton, G. Comenetz, P. H. Brace, and J. C. R. Kelly—209(A)
Electron cyclotron (microtron) for 3-cm rf operation, H. F. Kaiser—183(A)
Electron paths in magnetic lens spectrometer, W. Emmerich, Y. Nogami, L. A. Kiley, and J. D. Kurbatov—194(A)
Electronic method of measuring forces resisting armor penetration, John C. Lindsay and A. V. Masket—175(A)
Electrostatic control of electric charges furnished by glow discharge, Pierre Toulon—232(A)
Energy of secondary electrons in anthracene due to γ-irradiation, G. D. Prestwich, T. H. Colvin, and G. J. Hine—1031
Energy response of organic liquid scintillation counters, George T. Reynolds—193(A)
Fast coincidences with Čerenkov counters, Z. Bay, M. R. Cleland, and F. McLernon—901(L)
Fast high resolution Echelle spectrograph, P. M. Griffin, R. A. Loring, G. K. Werner, and J. R. McNally, Jr.—171(A)
Fast neutron scintillation spectrometer, James E. Draper and Boyce D. McDaniel—185(A)
γ- and α-produced scintillations in CsF, W. Van Sciver and R. Hofstadter—522(L)
Heating of samples in electron microscope, L. A. Woodward—178(A)
High pressure diffusion cloud chamber, James M. Wyckoff—185(A)
High temperature, economical, infrared oven, Richard B. Belser—172(A)
"Impregnated" scintillating crystal as tool for study of radioactive decay, E. der Mateosian and A. Smith—193(A)
Internal absorption of fluorescent light in large plastic scintillators, C. N. Chou—376(L)
Ion optics of Van de Graaff accelerators, M. M. Elkind—184(A)
Irradiation chamber for 100-curie Co^{60}, M. A. Greenfield, L. B. Silverman, and R. W. Dickinson—184(A)
Isolated potential-difference comparator, T. M. Dauphinee—230(A)
Limitation of discharge in GM counters, W. C. Porter and W. E. Ramsey—194(A)
Line shape of monochromatic γ-rays, D. Maeder and V. Wintersteiger—537(L)
Loading of photographic emulsions with light elements, S. Goldhaber and G. Goldhaber—185(A)
Mach-Zehnder interferometer theory, F. D. Bennett and G. D. Kahl—234(A)
Magnetostriction magnetometer, Thomas A. Perls—230(A)
Measurement of short β-decay lifetimes, R. B. Holt, R. N. Thorn, and R. W. Waniek—378(L)
Mechanism for sputtering in high vacuum based upon theory of neutron cooling, Frank Keywell—160(L)
Modified Cockroft-Walton high tension generator, theory, Paul Lorrain, Edgar Everhart, and René A. Béique—183(A)
Molecular-beam modulation microwave spectrograph, Clarence F. Luck and Walter Gordy—172(A)
Monitor for low intensity β-radiations, Aaron P. Sanders—184(A)
Multiple-wire ionization chamber for study of large air showers, R. E. Heineman—240(A)
ORNL 20-channel analyzer, G. G. Kelley, P. R. Bell, and C. G. Goss—174(A)
100-kev positive ion accelerator, O. Yonts and S. Bashkin—175(A)
Pair measurement of γ-rays with lens spectrometer, David E. Alburger—194(A)
Pair spectrometer using four scintillation crystals, R. S. Foote and G. Kamm—193(A)
Plastic phosphors for scintillation counters, W. L. Buck and R. K. Swank—191(A)
Possibilities of heavy ion bombardment in nuclear studies, G. Breit, M. H. Hull, Jr., and R. L. Gluckstern—74
Precision micromanometer, James M. Kendall—230(A)
Rf ion source with transverse magnetic field, J. S. Swingle, Jr., and C. P. Swann—184(A)
Reciprocity calibration of accelerometers, Mark Harrison and Alan O. Sykes—231(A)
Refractions of spherical laminated lens, Otto Stuhlman, Jr.—178(A)
Response of NaI crystals to high energy protons, J. G. Likely and W. Franzen—666(L)
Separation of trace elements in minerals with resin ion exchange columns, L. T. Aldrich, L. F. Herzog, P. H. Abelson, and E. T. Bolton—186(A)
Simple stark-modulation microwave spectrograph, R. F. Trambarulo and C. F. Luck—172(A)
Supersensitive differential altimeter, Marcel Martin, Donald H. Jacobs, and Seymour Scholnick—231(A)
Test and demonstration object for phase microscopy, L. A. Woodward and J. E. Rhodes, Jr.—178(A)
Thermal neutron flux distribution in Oak Ridge uranium-graphite reactor, Harry H. Hubbell, Jr.—184(A)
Thin wall Geiger counters for research on soft component, Frank E. Kinard—168(A)
Thirty-channel pulse-height discriminator based on cathode-ray tube, H. W. Fulbright, J. A. McCarthy, and C. W. McCutchen—184(A)
Trajectories in thick, non-uniform field magnetic lens spectrometer, W. G. Holladay and S. K. Haynes—175(A)
Transient response of linear systems, Frank J. Koenig—231(A)
Ultra-compact magnetic storage system, William T. Doyle and Donald H. Jacobs—231(A)
Vibrating probe electrometer for biophysical research, Mark W. Jones, J. W. Flowers, and David Pomeroy—175(A)

Microwaves (see also **Electromagnetic theory; Electronic tubes; Spectra, microwave**)
Anomalous wavetypes in waveguides containing ferromagnetics, A. A. Th. M. van Trier—227(A)
Field expansions in loss-free microwave junctions, T. Teichmann and E. P. Wigner—228(A)

Mobility of ions and electrons (see **Ions and electrons, mobility**)

Molecular beams (see **Atomic and molecular beams**)

Molecular structure and constants (see also **Spectra microwave; Spectra, molecular; Raman spectra**)
Centrifugal distortion in asymmetric rotor molecules, D. Kivelson and E. Bright Wilson, Jr.—214(A)
Dipole moments of several molecules from their microwave spectra, S. N. Ghosh, R. Trambarulo, and Walter Gordy—172(A)
Dissociation energies of C—C and C—F bonds in several fluorocarbons by electron impact, Vernon H. Dibeler, Robert M. Reese, and Fred L. Mohler—213(A)
Forces between acetone molecules, Vernon Myers—185(A)

Molecular structure and constants (continued)
Influence of molecular structure upon infrared carbonyl band in polycyclic quinones, Marie-Louise Josien and Nelson Fuson—212(A)
Microwave investigations of $HSiCl_3$ and CH_3SiCl_3, Richard Mockler, Jep H. Bailey, and Walter Gordy—172(A)
Modification of Silberstein model of optical anisotropy, Frank Matossi—214(A)
Phenomenological model for excluded volume problem, R. J. Rubin and P. Debye—214(A)
Raman spectrum, structure, force constants, and calculated thermodynamic properties of BrF_5, Charles V. Stephenson and Ernest A. Jones—169(A)
Magnetic moment ratios in hydrogen-like molecules, P. J. Bray, R. G. Barnes, and N. J. Harrick—229(A)
Vibrational and centrifugal effects on nuclear interactions and rotational moments in molecules, Norman F. Ramsey—1075
Moments, nuclear (see **Nuclear moments and spin**)

Neutrons
Angular distributions of Be^9+D neutrons, J. S. Pruitt, S. S. Hanna, and C. D. Swartz—534(L)
Coherent neutron scattering cross sections of N and V, S. W. Peterson and Henri A. Levy—462
Correlation of cosmic-ray intensities at high altitudes with neutron intensities, H. V. Neher—240(A)
Cross section of Fe for cold neutrons, H. Palevsky, D. J. Hughes, and R. R. Smith—221(A)
Electron-neutron interaction, L. L. Foldy—693
Energy spectrum of neutrons from interaction of 14-Mev neutrons with C, Al, Fe, Cu, Zn, Ag, Cd, Sn, Au, Pb, and Bi, E. R. Graves and L. Rosen—239(A)
Level densities from fast neutron capture, R. C. Garth, D. J. Hughes, and J. S. Levin—222(A)
Modified Fermi theory of neutron moderation, E. Grueling—177(A)
Neutron capture resonances in Cs, La, Pr, Rb, Tl, and Y, Robert H. Rohrer—177(A)
Neutron-electron interaction, J. A. Harvey, D. J. Hughes, and M. D. Goldberg—220(A)
Neutron-electron scattering, Otto Halpern and C. P. Hsu—519(L)
Neutron energy spectrum from U^{235} thermal fission, David L. Hill—1035; B. E. Watt—1038
Neutron inelastic cross sections for excitation of single levels of middle-weight nuclei, James E. Monahan—188(A)
Neutron resonances in Hf isotopes and in As, S. P. Harris and L. M. Bollinger—222(A)
Neutron total cross section for Pb between 37 and 156 Mev, A. E. Taylor and E. Wood—907(L)
Neutrons of low energy from fission of U^{235}, T. W. Bonner, R. A. Ferrell, and M. C. Rinehart—1033
Nucleon recoil and electron-neutron interaction, L. L. Foldy—675(L)
Preliminary investigations of neutron total cross sections with Oak Ridge National Laboratory fast chopper, G. S. Pawlicki and E. C. Smith—221(A)
Radiative capture by Cd^{113}, R. W. Pringle, H. W. Taylor, and K. I. Roulston—1017
Resistivity of Cu_3Au during neutron irradiation, H. L. Glick, F. C. Brooks, W. F. Witzig, and W. E. Johnson—1074
Slow neutron resonances in In^{113} and In^{115}, V. L. Sailor—222(A); V. L. Sailor and L. B. Borst—161(L)
Studies of lighter rare earth oxides, W. C. Koehler and E. O. Wollan—238(A)
Thermal neutron absorption cross section of D, Louis Kaplan, G. R. Ringo, and K. E. Wilzbach—785
Thermal neutron capture cross section of A^{40} and observation of A^{43}, Seymour Katcoff—886
Thermal neutron flux distribution in Oak Ridge uranium-graphite reactor, Harry H. Hubbell, Jr.—184(A)
Thermal neutron flux measurements in graphite using Au and In foils, E. D. Klema and R. H. Ritchie—167(L)
Total cross section of Ho *vs* energy for slow neutrons, T. E. Stephenson, C. P. Stanford, and S. Bernstein—174(A)
Total cross sections for high energy neutrons, Vaughn Culler and R. W. Waniek—221(A)
Total cross sections of Co, Er, Hf, Ni^{58}, Ni^{60}, Ho, and fission Sm, for slow neutrons, S. Bernstein, L. B. Borst, C. P. Stanford, T. E. Stephenson, and J. B. Dial—487
Total neutron cross sections at energies between 3 and 12 Mev, N. Nereson—221(A)
Total neutron scattering cross sections at 1.44 ev, L. A. Rayburn and E. O. Wollan—174(A)
Noise (see **Fluctuation phenomena**)
Nuclear induction (see **Magnetic resonance absorption; Nuclear moments and spin**)
Nuclear moments and spin (see also **Hyperfine structure**)
Of $_{55}Cs^{134}$, V. Jaccarino, B. Bederson, and H. H. Stroke—676(L)
Interaction moment contributions to magnetic moments of nuclei, L. Spruch and A. Russek—189(A); Arnold Russek and Larry Spruch—1111
Magnetic shielding effects in compounds of V, H. E. Walchli and H. W. Morgan—541(L)
Nuclear magnetic octopole interaction, John Levinson—188(A)
Nuclear quadrupole moment of Ta^{181}, B. M. Brown—228(A)
Of V^{50}, A. Hitchcock—664(L)
Zeeman effect of Ne in metastable $^3P_2$ state; evidence for zero spin of $_{10}Ne^{20}$, G. Weinreich, G. Tucker, and V. Hughes—229(A)
Nuclear reactions (see **Disintegration and excitation of nucleus**)
Nuclear spectra (see also **Disintegration and excitation of nucleus**)
Absolute determination of the *X*-line from ThC″, Gunnar Lindström—678(L)
Additional branch in decay scheme of Zr^{89m}, F. J. Shore, H. N. Brown, W. L. Bendel, and R. A. Becker—202(A)
Of Am^{241}, J. K. Beling, J. O. Newton, and B. Rose—670(L)
Am^{243} and Cm^{242}, complex α-spectra, Frank Asaro, F. L. Reynolds, and I. Perlman—277
Am^{241} soft radiations, erratum, J. K. Beling, J. O. Newton, and B. Rose—1143(L)
Angular correlation between protons and gammas in $Li^6(d,p\gamma)Li^7$, W. H. Burke and J. R. Risser—294
Angular correlation in $Be^9(d,p)Be^{10*}(\gamma)Be^{10}$, L. Cohen, S. M. Shafroth, C. M. Class, and S. S. Hanna—206(A)
Angular correlation of γ-rays in Pt^{194}, Charles E. Whittle and Philip S. Jastram—203(A)
Angular correlation of γ-rays in Ti^{48}, P. S. Jastram and C. E. Whittle—1133(L)
Angular correlations in $Li^6(d,p)Li^{7*}(\gamma)Li^7$, C. M. Class and S. S. Hanna—247
Angular distributions of Be^9+D neutrons, J. S. Pruitt, S. S. Hanna, and C. D. Swartz—534(L)
Of Ba^{131} and Cs^{131}, W. L. Stirling and Max Goodrich—176(A)
Be^7 and B^{10} energy levels, Fay Ajzenberg—205(A)
β-γ angular correlation in As^{76}, S. L. Ridgway and F. M. Pipkin—202(A)
β-spectra and internal conversion coefficients for Co^{60}, Nb^{95}, Au^{198}, and Hf^{181}, Chang-Yun Fan—252
β-spectra of Be^{10}, K^{40}, Tc^{99}, and Cl^{36}, L. Feldman and C. S. Wu—1091
$B^{11}(p;\gamma_1,\gamma_2)C^{12}$, angular correlation, Thomas P. Hubbard, Jr., Edward B. Nelson, and James A. Jacobs—378(L)
Cd^{113} isomer decay, R. W. Hayward—202(A)

C^{14} β-spectrum, low energy proton G. W. McManaway, E. O. Kiger, and A. W. Waltner—176(A)
Ce^{141} K-shell conversion coefficient, R. L. Heath—1132(L)
Of Ce^{144} and Pr^{144}, Fred T. Porter and C. Sharp Cook—464
Of Cs^{130}, Alan B. Smith, Allan C. G. Mitchell, and Robert S. Caird—454
Of Cr^{51}, W. S. Lyon—1126(L)
Decay scheme of Ir^{192}, K. I. Roulston and R. W. Pringle—930
Decay scheme of $_{21}Sc^{46}$, Dieter Kurath—528(L)
Directional correlation of Ni^{60} $\gamma-\gamma$ cascade, H. Aeppli, H. Frauenfelder, E. Heer, and R. Rüetschi—379(L)
Effect of electron shell on angular correlations, Jan C. Kluyver—203(A)
Energy levels from 8-Mev protons on Be^{9}, C^{12}, N^{14}, S^{32}, J. S. Arthur, A. J. Allen, R. S. Bender, H. J. Hausman, C. J. McDole, L. M. Diana, K. B. Rhodes, and R. A. Barjon—237(A)
Energy levels in C^{12}, Al^{27}, and Na^{23} using scintillation spectrometer for heavy particles, H. F. Stoddart and H. E. Gove—238(A); 262
Energy levels of Ti^{49}, G. F. Pieper—215(A)
Energy spectrum of neutrons from interaction of 14-Mev neutrons with C, Al, Fe, Cu, Zn, Ag, Cd, Sn, Au, Pb, and Bi, E. R. Graves and L. Rosen—239(A)
Er^{168}, D. N. Kundu, J. D. Service, and M. L. Pool—203(A)
Excited states of even-even nuclei, Gertrude Scharff-Goldhaber—218(A)
Excited states of F^{20} and O^{17}, H. A. Watson—215(A)
Excited states of Mg^{24}, Cr^{52}, and Mn^{55}, H. J. Hausman, A. J. Allen, J. S. Arthur, R. S. Bender, C. J. McDole, L. M. Diana, K. B. Rhodes, and R. A. Barjon—238(A)
Excited states of Mg^{25} from $Al^{27}(d,\alpha)Mg^{25}$ and $Mg^{24}(d,p)Mg^{25}$, P. M. Endt, H. A. Enge, J. Haffner, and W. W. Buechner—27
First excited states of even-even nuclides in heavy element region, Frank Asaro and I. Perlman—393(L)
$\gamma-\gamma$ angular correlation in Cd^{114}, E. D. Klema and F. K. McGowan—524(L)
γ-radiation from Pt, J. M. Cork, J. M. LeBlanc, F. B. Stumpf, and W. H. Nester—203(A)
γ-radiations from V^{48} and Nb^{92}, David Green, Harold K. Ticho, and J. Reginald Richardson—195(A)
γ-ray yield from the proton bombardment of B, L. W. Cochran, J. L. Ryan, H. H. Givin, B. D. Kern, and T. M. Hahn—672(L)
γ-rays from Sc^{46}, Bernard Hamermesh, Virginia Hummel, and Leonard Goodman—528(L)
γ-rays in decay of Ga^{66}, L. G. Mann and W. E. Meyerhof—202(A)
Ground-state spins and energy differences from jj-coupling model, D. Kurath—218(A)
He^{6} β-spectrum, C. S. Wu, B. M. Rustad, V. Perez-Mendez, and L. Lidofsky—1140(L)
Of In^{114}, M. W. Johns, C. D. Cox, R. J. Donnelly, and C. C. McMullen—1134(L)
Inelastic scattering resulting in short-lived isomers, O. Hittmair—375(L)
Interference of amplitudes in cascade processes, O. Halpern and B. A. Lippmann—1128(L)
Internal conversion electron ratios in Ba^{137m}, Y^{89m}, and Zr^{89m}, W. L. Bendel, F. J. Shore, H. N. Brown, and R. A. Becker—195(A)
Internal conversion of γ-ray transitions in L sub-shells, J. W. Mihelich—646
Internal conversion of γ-rays with pair production, S. A. S. Brimberg—150(L)
Internal conversion of neutron capture γ-rays, Carl T. Hibdon and C. O. Muehlhause—222(A)
Internal pair creation in Mg^{24}, Stewart D. Bloom—236(A)
K-Auger yield of Hg, C. D. Broyles and S. K. Haynes—174(A)
K/L ratio for 90-kev line of Nd^{147}, Alan B. Smith and Allan C. G. Mitchell—1128(L)
K-shell conversion coefficients using NaI single crystal scintillation spectrometer, R. L. Heath and P. R. Bell—176(A)
Of Kr^{87}, Sigvard Thulin—684(L)
Level densities from fast neutron capture, R. C. Garth, D. J. Hughes, and J. S. Levin—222(A)
Levels of N^{14} observed from $C^{13}(d,n)N^{14}$, R. E. Benenson—207(A)
Lifetime of excited state of Hf^{176}, F. K. McGowan—542(L)
Low energy γ-transitions in rare earth isotopes, erratum, J. W. Mihelich and E. L. Church—1144(L)
Lowest excitation level of Hg^{198}, P. Staehelin—374(L)
Neutron resonances in Hf isotopes and in As, S. P. Harris and L. M. Bollinger—222(A)
Of Ni^{66}, Raymond K. Sheline and Raymond W. Stoughton—1
Nuclear levels associated with decay of Sb^{122}, Michael J. Glaubman and Franz R. Metzger—203(A)
Nuclear structure and interpretation of β-decay, R. King and E. Feenberg—218(A)
Of Pd^{111}, Carl L. McGinnis—202(A)
Po γ-radiation, R. W. Pringle, H. W. Taylor, and S. Standil—384(L)
Pr^{144} decay scheme and angular correlation, D. E. Alburger and J. J. Kraushaar—448
Radiative capture of thermal neutrons by Cd^{113}, R. W. Pringle, H. W. Taylor, and K. I. Roulston—1017
Radiative K-capture in A^{37}, C. E. Anderson, G. W. Wheeler, and W. W. Watson—668(L)
Radioactivity of A^{39}, C. E. Anderson, G. W. Wheeler, and W. W. Watson—195(A)
Ratio F_A/F_B in the theory of forbidden β-transitions, P. Macklin, L. Lidofsky, and C. S. Wu—391(L)
In Ru^{103}, J. M. LeBlanc, F. B. Stumpf, W. H. Nester, and J. M. Cork—202(A)
Slow neutron resonances in In^{113} and In^{115}, V. L. Sailor—222(A); V. L. Sailor and L. B. Borst—161(L)
Te^{125} isomers, Alexis C. Pappas—162(L)
Of Tl^{204}, L. Lidofsky, P. Macklin, and C. S. Wu—204(A); 391(L)
Tl^{204} electron capture, Allan C. G. Mitchell and Robert S. Caird—388(L)
Sn^{126} radiations, R. I. Mendenhall, C. E. Mandeville, E. Shapiro, E. R. Zucker, and G. L. Conklin—203(A)
Nuclear structure (see also **Disintegration and excitation of nucleus; Nuclear spectra; Radioactivity**)
α-energy systematics and proton shells for heavier nuclei, S. Sengupta—1136(L)
Binding energy of α-particle, John Irving—519(L)
Collective description of nucleon interactions, Melvin Ferentz and David Pines—188(A)
Conservation of isotopic spin in nuclear reactions, Robert K. Adair—1042
Cosine interaction between nucleons, A. de-Shalit—843
Experimental test of shell model, W. C. Parkinson, E. H. Beach, and J. S. King—387(L)
Fermi-Thomas model of the nucleus, R. J. Riddell, Jr.—189(A)
Ground-state spins and energy differences from jj-coupling model, D. Kurath—218(A)
High energy nuclear collisions and the Fermi model, H. Messel and H. S. Green—378(L)
Interaction moment contributions to magnetic moments of nuclei, L. Spruch and A. Russek—189(A); Arnold Russek and Larry Spruch—1111
Intermediate coupling as encountered in some p-shell nuclei, D. R. Inglis—915

Nuclear structure (continued)
Level spacings and magic numbers, Henry W. Newson and Robert H. Rohrer—177(A)
μ-meson capture and shell structure, James M. Kennedy—953
Nuclear structure and interpretation of β-decay, R. King and E. Feenberg—218(A)
Nucleon momentum distributions in deuterium and carbon inferred from proton scattering, J. B. Cladis, W. N. Hess, and B. J. Moyer—425
Optical model for nucleon-nuclei scattering, Robert E. LeLevier and David S. Saxon—40
Scattering of protons from C, Peter A. Wolff—434
7.4-Mev state of Li^7, Murray Peshkin and A. J. F. Siegert—735
Spin-orbit coupling and nuclear shell model, Eugen Merzbacher—173(A)
Surface energy in free-particle nuclear model, K. C. Hammack and E. Feenberg—218(A)

Nucleons
"Nucleon isobar" as intermediate state, N. Austern—208(A)
Structure of nucleon, R. G. Sachs—1100

Optical constants and properties
Modification of Silberstein model of optical anisotropy, Frank Matossi—214(A)
Of rutile single crystals, D. C. Cronemeyer—876

Optical instruments (see **Methods and instruments**)

Pair production and annihilation
Complex time decay of positrons annihilated in condensed materials, R. E. Bell and R. L. Graham—236(A)
Conservation of energy in three-quantum annihilation, R. Siegel and S. De Benedetti—235(A)
Differential cross section for bremsstrahlung and pair production, L. C. Maximon and H. A. Bethe—156(L)
Integral cross section for bremsstrahlung and pair production, Handel Davies and H. A. Bethe—156(L)
Internal conversion of γ-rays with pair production, S. A. S. Brimberg—150(L)
Internal pair creation in Mg^{24}, Stewart D. Bloom—236(A)
Pair production cross section for high energies, P. A. Fraser—523(L)
Quenching of three-quantum annihilation from positronium by magnetic field, J. Wheatley and D. Halliday—235(A)
Three-photon annihilation of positron, Richard S. Stone—235(A)

Phosphors and phosphorescence (see also **Luminescence; Fluorescence**)
Electron traps in KCl:Tl phosphor, Peter D. Johnson and Ferd E. Williams—192(A); in ZnS phosphor, Alan W. Smith and John Turkevich—306
Plastic phosphors for scintillation counters, W. L. Buck and R. K. Swank—191(A)
Temperature dependence of infrared photoconductivity in standard VII phosphor, G. Conrad and J. J. Dropkin—192(A)
X-ray excited phosphorescence of calcite, John Auxier and Guy Forman—170(A)

Photoconductivity
Induced conductivity and light emission in different luminescent type powders, Hartmut Kallmann and Bernard Kramer—91
Temperature dependence of infrared photoconductivity in standard VII phosphor, G. Conrad and J. J. Dropkin—192(A)

Photodisintegration
Analysis of some photoneutron and photoproton experiments, Arthur Paskin—197(A)
Angular distribution of fission fragments in photofission of Th, E. J. Winhold, P. T. Demos, and I. Halpern—1139(L)
Angular distribution of neutrons exceeding 50 Mev ejected by 320-Mev bremsstrahlung, D. W. Kerst, L. J. Koester, A. S. Penfold, and J. H. Smith—197(A)
Angular distributions of photoprotons, A. K. Mann, J. Halpern, and M. Rothman—146; J. Halpern, A. K. Mann, and M. Rothman—164(L)
$Br^{81}(\gamma,\alpha)As^{77}$ cross section, J. G. V. Taylor and R. N. H. Haslam—1138(L)
$C^{12}+h\nu=3He^4$, using γ-rays up to 48 Mev, V. L. Telegdi—196(A)
$Cu^{63}(\gamma,n)Cu^{62}$ cross section, V. E. Krohn, Jr., and E. F. Shrader—685
Of D at 180–260 Mev, Raphael Littauer and James Keck—195(A)
Fine structure in $O^{16}(\gamma,n)O^{15}$ activation curve, R. N. H. Haslam, L. Katz, R. J. Horsley, A. G. W. Cameron, and R. Montalbetti—196(A)
$(\gamma,\alpha n)$ reactions, Richard B. Holtzman and Nathan Sugarman—632
(γ,n) reactions in F, R. J. Horsley, R. N. H. Haslam, and H. E. Johns—756
High energy nuclear photoeffect, Israel Reff—207(A)
Meson exchange contributions to high energy deuteron photoeffect, R. H. Huddlestone and J. V. Lepore—207(A)
Method for determining cross sections from photonuclear yield curves, L. V. Spencer—196(A)
Neutron production by high energy quanta, K. M. Terwilliger and L. W. Jones—196(A)
$N^{14}(\gamma,2n)N^{12}$ reaction, Wolfgang K. H. Panofsky and Daryl Reagan—543(L)
"Nucleon isobar" as intermediate state, N. Austern—208(A)
Photoneutron cross sections for reactions $Br^{81}(\gamma,n)Br^{80}$ and $Br^{81}(\gamma,n)Br^{80*}$, L. Katz, P. Pease, and H. Moody—196(A)
Photonuclear yields from Cu through As, R. J. Debs, J. T. Eisinger, A. W. Fairhall, I. Halpern, and H. G. Richter—196(A)
Relative yields of photonuclear reactions, L. S. Edwards and F. A. MacMillan—377(L)

Photons (see also **Gamma-Rays; Radiation**)
Mass of a photon, L. S. Kothari—536(L)

Piezoelectric effect
Piezoelectricity, ferroelectricity, and crystal structure, A. von Hippel—200(A)

Plasmoidal discharges (see **Discharge of electricity in gases**)

Plasticity
Creep of Cu under deuteron bombardment, Warren F. Witzig—211(A)
Dynamic behavior of Nylon filaments, D. J. Montgomery and W. G. Hammerle—202(A)
Measurement of internal energy in Cu introduced by cold work, Benjamin Welber—211(A)
Slip-band formation, John C. Fisher, Edward W. Hart, and Robert H. Pry—210(A); 958
Strain hardening of metal crystals, Edward W. Hart, John C. Fisher, and Robert H. Pry—211(A)

Polarization of radiation
Optical polarization in single crystals of Te, J. J. Loferski—905(L)

Polymerization, properties of polymers
Anomalous osmotic pressures of polymer solutions as measured in metal membrane osmometer, Thomas A. Barr, Jr.—171(A)

Positrons
Complex time decay of positrons annihilated in condensed materials, R. E. Bell and R. L. Graham—236(A)
Electrodynamic corrections to fine structure of positronium, A. Klein and R. Karplus—235(A)
Hfs of positronium, Robert Karplus and Abraham Klein—848

Positron-electron scattering, Arthur Ashkin and W. M. Woodward—236(A)
Positron-electron scattering in He, G. Robert Hoke and Paul E. Shearin—176(A); G. Robert Hoke—285
Quenching of three-quantum annihilation from positronium by magnetic field, J. Wheatley and D. Halliday—235(A)
Single elastic scattering of positrons by N nuclei, R. R. Roy and L. Groven—619
Three-photon annihilation of positron, Richard S. Stone—235(A)

Proceedings of the American Physical Society
Southeastern Section Meeting at Raleigh, North Carolina, April 10–12, 1952—168
Washington Meeting, May 1–3, 1952 [Bull. Am. Phys. Soc. **27**, No. 3 (1952)]—179
Division of Fluid Dynamics, Salt Lake City, Utah, June 25–27, 1952—909

Quantum electrodynamics (see also **Field theory**)
Differential cross section for bremsstrahlung and pair production, L. C. Maximon and H. A. Bethe—156(L)
Elastic scattering of gammas by bound electrons, P. Greifinger, J. Levinger, and F. Rohrlich—663(L)
Electrodynamic corrections to fine structure of positronium, A. Klein and R. Karplus—235(A)
Electromagnetic properties of Dirac particles, L. L. Foldy—688
Electron in one-dimensional field, Nathan Rosen—173(A)
Gauge invariance problem, Hartland S. Snyder—164(L)
Hfs of positronium, Robert Karplus and Abraham Klein—848
Integral cross section for bremsstrahlung and pair production, Handel Davies and H. A. Bethe—156(L)
Mass corrections to fine structure of hydrogen-like atoms, E. E. Salpeter—328
Mass corrections to hfs, E. E. Salpeter and W. A. Newcomb—150(L)
Radiative correction to angular distribution of nuclear recoils from electron scattering, L. L. Schiff—750
Rational relativistic single particle theory, T. A. Welton—225(A)
Recoil correction to bremsstrahlung cross section, S. D. Drell—753
Selection rules imposed by charge conjugation and charge symmetry, A. Pais and R. Jost—871
Small angle coherent scattering of gammas by bound electrons, J. S. Levinger—656

Quantum mechanics (see **Mechanics, quantum**)

Radiation (see also **Scattering of radiation; Thermal radiation**)
Absorption coefficients of γ-rays, S. J. Wyard—165(L)
Angular distribution of neutrons exceeding 50 Mev ejected by 320-Mev bremsstrahlung, D. W. Kerst, L. J. Koester, A. S. Penfold, and J. H. Smith—197(A)
Čerenkov radiation from cosmic-ray particles, John Winckler—241(A)
Differential cross section for bremsstrahlung and pair production, L. C. Maximon and H. A. Bethe—156(L)
Fast coincidences with Čerenkov counters, Z. Bay, M. R. Cleland, and F. McLernon—901(L)
Influence of multiple scattering on the angular width of Čerenkov radiation, K. G. Dedrick—891
Integral cross section for bremsstrahlung and pair production, Handel Davies and H. A. Bethe—156(L)
Radiation loss by electrons in large orbits, Dale R. Corson—233(A)
Radiation loss from atmosphere, Gilbert N. Plass—187(A)
Recoil correction to bremsstrahlung cross section, S. D. Drell—753
Uv radiation from Cornell synchrotron, P. L. Hartman and D. H. Tomboulian—233(A)

Radioactivity (see also **Disintegration and excitation of nucleus; Nuclear spectra**)
α-energy systematics and proton shells for heavier nuclei, S. Sengupta—1136(L)
Of Am^{243}, J. K. Beling, J. O. Newton, and B. Rose—670(L)
Am^{241} and Cm^{242}, complex α-spectra, Frank Asaro, F. L. Reynolds, and I. Perlman—277
Am^{241} soft radiations, erratum, J. K. Beling, J. O. Newton, and B. Rose—1143(L)
Am^{242m} half-life for negative electron emission, Thomas K. Keenan, Robert A. Penneman, and B. B. McInteer—204(A)
Of A^{39}, C. E. Anderson, G. W. Wheeler, and W. W. Watson—195(A)
Autoradiographic analysis of Murray, Kentucky meteorite, J. R. Horan and G. A. Boyd—177(A)
Average charge produced by electron capture in A^{37}, John A. Miskel and Morris L. Perlman—543(L)
Of Ba^{131} and Cs^{131}, W. L. Stirling and Max Goodrich—176(A)
β-spectra and internal conversion coefficients for Co^{60}, Nb^{95}, Au^{198}, and Hf^{181}, Chang-Yun Fan—252
Of Ce^{144} and Pr^{144}, Fred T. Porter and C. Sharp Cook—464
Of Cs^{130}, Alan B. Smith, Allan C. G. Mitchell, and Robert S. Caird—454
Of Cr^{51}, W. S. Lyon—1126(L)
Complex structure in α-emission, Dean C. Dunlavey and Glenn T. Seaborg—165(L)
Double β-decay in Sn^{124} and Zr^{96}, J. A. McCarthy—194(A)
Effect of atomic binding on nuclear reaction energies, R. Serber and H. S. Snyder—152(L)
Electrical analog for radioactivity of primary fission products with intermittent reactor operation, W. O. Doggett—171(A)
Eu^{152}, Eu^{154}, and Sm^{151} half-lives, D. G. Karraker, R. J. Hayden, and M. G. Inghram—901(L)
Generation and storage of radioactive gases from intermittent reactor operation, Raymond L. Murray—171(A)
Half-life of 139-min Dy^{165}, R. Sher, H. J. Kouts, and K. W. Downes—523(L)
He^6 β-spectrum, C. S. Wu, B. M. Rustad, V. Perez-Mendez, and L. Lidofsky—1140(L)
Of In^{114}, M. W. Johns, C. D. Cox, R. J. Donnelly, and C. C. McMullen—1134(L)
Of Kr^{87}, Sigvard Thulin—684(L)
La^{138} natural radioactivity, George I. Mulholland and Truman P. Kohman—681(L)
Lifetime of excited state of Hf^{178}, F. K. McGowan—542(L)
Maximum permissible concentration of radioactive contamination in air and water following atomic explosion, K. Z. Morgan and C. P. Straub—178(A)
Measurement of short β-decay lifetimes, R. B. Holt, R. N. Thorn, and R. W. Waniek—378(L)
Ni^{66}, W. J. Worthington, Jr.—158(L); Raymond K. Sheline and Raymond W. Stoughton—1
Nuclear matrix elements in theory of β-decay, erratum, Henry Brysk—1144(L)
Nucleon-lepton interaction in β-decay, R. Nataf and R. Bouchez—155(L)
Of Pd^{111}, Carl L. McGinnis—202(A)
In Pt produced by slow neutron capture, B. C. Haldar—158(L)
Pr^{144} decay scheme and angular correlation, D. E. Alburger and J. J. Kraushaar—448
Production of light "positive particles" near β^- ray emitters, Gerhart Groetzinger and Fred L. Ribe—1003
Pm isotopes, Vera Kistiakowsky—859
Ratio F_0/F_0 in theory of forbidden β-transitions, P. Macklin, L. Lidofsky, and C. S. Wu—391(L)
In Ru^{103}, J. M. LeBlanc, F. B. Stumpf, W. H. Nester, and J. M. Cork—202(A)

Radioactivity (continued)
Search for betatron induced, low Z, activities of short half-life, Raymond K. Sheline—557
Specific α-activity of U^{233}, C. A. Kienberger—520(L)
Thermal neutron capture cross section of A^{40} and observation of A^{42}, Seymour Katcoff—886
Raman spectra
Of BrF_5, Charles V. Stephenson and Ernest A. Jones—169(A)
Of CF_3COOH, Marie-Louise Josien, Nelson Fuson, Ernest Jones, and James R. Lawson—170(A)
Range and energy loss of particles
Calculation of range energy relations for α-particles in photographic emulsions, M. Bogaardt and B. Koudijs—1129(L)
Ionization by cosmic-ray mesons in A, G. W. McClure—680(L)
Ionization loss at relativistic velocities in nuclear emulsions, Maurice M. Shapiro and Bertram Stiller—682(L)
Ionization losses of fast μ-mesons in gases, J. E. Kuperian, Jr., and E. D. Palmatier—169(A)
Relative specific ionization of fast mesons, R. S. Carter and W. L. Whittemore—494
Stopping cross section of D_2O ice, W. A. Wenzel and Ward Whaling—499
Rectifier (see **Electrical conductivity and resistance; Semiconductors**)
Relativity
Conformal invariance in special relativity, Wesley E. Brittin—197(A)
New approximation for gravitational field equations, Joshua Goldberg and Peter G. Bergmann—198(A)
Possible solution of clock paradox, Richard Schlegel—198(A)
Some static axially symmetric gravitational fields, J. B. Newman—173(A)
Resistance, electrical (see **Electrical conductivity and resistance**)

Scattering of electrons, mesons, neutrons, protons, deuterons, and ions (see also **Electron diffraction; Cross section, measurements, theory**)
Analysis of 14-Mev $n-p$ scattering, George Snow—21
Analysis of $p-T$ scattering, J. S. McIntosh, R. L. Gluckstern, S. Sack, and B. E. Freeman—237(A)
Angular distribution of $n-p$ scattering, William G. Cross—223(A)
Angular distribution of π-C scattering, D. C. Peaslee—217(A)
Angular distributions of $C^{12}(p,p')C^{12*}$, $Q=-4.45$ Mev, and $Mg^{24}(p,p')Mg^{24*}$, $Q=-1.38$ Mev, using a NaI scintillation counter, H. E. Gove and H. F. Stoddart—237(A)
Application of multiple scattering theory to cloud-chamber measurements. I. Stanislaw Olbert—319
Application of theory of effective range to meson-nucleon scattering, Keith A. Brueckner—1027
Coherent neutron scattering cross sections of N and V, S. W. Peterson and Henri A. Levy—462
Construction of potential from phase shift, Res Jost and Walter Kohn—977
Coulomb scattering of deuterons, J. B. French and M. L. Goldberger—899(L)
Cross section of Fe for cold neutrons, H. Palevsky, D. J. Hughes, and R. R. Smith—221(A)
Determination of angular distribution and absolute differential cross section of $C^{12}(p,p)C^{12}$ reaction, H. L. Jackson, A. I. Galonsky, F. J. Eppling, R. W. Hill, E. Goldberg, and J. R. Cameron—237(A)
Elastic π-C scattering, D. C. Peaslee—862
Elastic Scattering of 18.3-Mev protons, P. C. Gugelot—525(L)
Elastic scattering of pions from H and D, Gerson Goldhaber—220(A)
Electric and non-electric scattering of cosmic-ray mesons and protons, W. L. Whittemore and R. P. Shutt—241(A)
Electron scattering experiments at low and middle energies, L. Marton—200(A)
Energy distribution of slow neutrons scattered from solids, B. N. Brockhouse and D. G. Hurst—239(A)
Energy spectrum of neutrons from interaction of 14-Mev neutrons with C, Al, Fe, Cu, Zn, Ag, Cd, Sn, Au, Pb, and Bi, E. R. Graves and L. Rosen—239(A)
Exchange scattering of electrons, Ta-You Wu—1012
Excitation cross section for He atoms, Saul Altshuler—992
Excited states of Mg^{24}, Cr^{52}, and Mn^{55}, H. J. Hausman, A. J. Allen, J. S. Arthur, R. S. Bender, C. J. McDole, L. M. Diana, K. B. Rhodes, and R. S. Barjon—238(A)
Inelastic proton scattering from B^{10}, W. W. Buechner, C. P. Browne, M. M. Elkind, A. Sperduto, H. A. Enge, and C. K. Bockelman—237(A)
Inelastic scattering of neutrons, Walter Hauser and Herman Feshbach—366
Inelastic scattering of protons from light nuclei, Dean B. Cowie, N. P. Heydenburg, and G. C. Phillips—304
Inelastic scattering resulting in short-lived isomers, O. Hittmair—375(L)
Influence of multiple scattering on the angular width of Čerenkov radiation, K. G. Dedrick—891
Interpretation of high energy $p-p$ scattering, Don R. Swanson—208(A)
Modified Fermi theory of neutron moderation, E. Greuling—177(A)
Moments of the angular distribution for high energy nuclear collisions, B. A. Chartres and H. Messel—748
Multiple scattering of high energy protons in photographic plates, Martin J. Berger—238(A)
Neutron-electron scattering, Otto Halpern and C. P. Hsu—519(L)
$n-p$ scattering in 0–5 Mev region, L. Hultheń and S. Skavlem—297
Neutron scattering cross sections in resonance region, C. Sheer, J. Moore, W. W. Havens, Jr., and L. J. Rainwater—239(A)
Neutron total cross section for Pb between 37 and 156 Mev, A. E. Taylor and E. Wood—907(L)
Neutron total cross sections with Oak Ridge National Laboratory fast chopper, G. S. Pawlicki and E. C. Smith—221(A)
Of 9.48-Mev protons by He, T. M. Putnam—932
Nucleon momentum distributions in deuterium and carbon inferred from proton scattering, J. B. Cladis, W. N. Hess, and B. J. Moyer—425
Phenomenological potentials in meson scattering, R. LeLevier—217(A)
Plural electron scattering and its influence on electron diffraction patterns, S. G. Ellis—970
Polarization effects in $p-p$ scattering at high energies, L. J. B. Goldfarb and D. Feldman—208(A)
Positron-electron scattering, Arthur Ashkin and W. M. Woodward—236(A)
Positron-electron scattering in He, G. Robert Hoke and Paul E. Shearin,—176(A); G. Robert Hoke—285
Proton-proton collisions within Li nuclei, Owen Chamberlain and Emilio Segrè—81
$p-p$ scattering at 5 Mev by coincidence method, R. O. Bondelid, C. H. Braden, M. E. Battat, and P. Bohlman—699
$p-p$ scattering at 18.3 Mev, J. L. Yntema and M. G. White—223(A)

Radiative correction to angular distribution of nuclear recoils from electron scattering, L. I. Schiff—750
Regular meson potentials in low energy proton-proton scattering, H. E. Hart and R. D. Hatcher—375(L)
Scattering by high potential barriers and by potentials with shell structure, J. Mayo Greenberg—209(A)
Scattering by many-body systems in terms of two-body collision parameters, H. Ekstein—31
Scattering of electrons from point singularities in metals, D. L. Dexter—768
Scattering of elementary particles by complex nuclei, Geoffrey F. Chew and M. L. Goldberger—778
Scattering of fast neutrons by deuterons, M. Walt, A. Okazaki, and R. K. Adair—238(A)
Scattering of neutrons by systems of nuclei, Roy J. Glauber—189(A)
Scattering of protons by protons. I, J. N. McGruer, D. E. Findley, and H. R. Worthington—223(A); II, H. R. Worthington, D. E. Findley, and J. N. McGruer—223(A); III, J. L. Powell and H. H. Hall—223(A); IV, H. H. Hall and J. L. Powell—223(A)
Scattering of protons from C, Peter A. Wolff—434
Scattering of 10-Mev deuterons by H^2 and He^3, A. H. Armstrong, J. C. Allred, A. M. Hudson, R. M. Potter, E. S. Robinson, L. Rosen, and E. J. Stovall, Jr.—238(A)
Single elastic scattering of positrons by N nuclei, R. R. Roy and L. Groven—619
Slow neutron resonances in In^{113} and In^{115}, V. L. Sailor and L. B. Borst—161(L)
Theory of pick-up process, George J. Yevick—208(A)
Total cross sections for 14-Mev neutrons, H. L. Poss, E. O. Salant, G. A. Snow, and Luke C. L. Yuan—11
Total cross sections for high energy neutrons, Vaughn Culler and R. W. Waniek—221(A)
Total cross sections of Co, Er, Hf, Ni^{58}, Ni^{60}, Ho, and fission Sm for slow neutrons, S. Bernstein, L. B. Borst, C. P. Stanford, T. E. Stephenson, and J. B. Dial—487
Total cross sections of positive pions in H, S. W. Barnes, D. L. Clark, J. P. Perry, and C. E. Angell—669(L)
Total neutron cross sections at energies between 3 and 12 Mev, N. Nereson—221(A)
Total neutron scattering cross sections at 1.44 ev, L. A. Rayburn and E. O. Wollan—174(A)
Validity of Born expansions, Walter Kohn—539(L)
Wave-mechanical description of deuteron stripping process, F. L. Friedman and W. Tobocman—208(A)

Scattering of radiation (see also **Raman spectra; X-rays**)
Double Compton effect, Patrick E. Cavanagh—1131(L)
Elastic scattering of gammas by bound electrons, P. Greifinger, J. Levinger, and F. Rohrlich—663(L)
Multiple Compton scattering of low energy γ-radiation, R. C. O'Rourke—225(A)
Nuclear scattering of 17-Mev γ-rays, Mary Beth Stearns—706
Radiation force and torque, Harold Levine and Julian Schwinger—224(A)
Scattering by semi-infinite cone, K. M. Siegel and H. A. Alperin—234(A)
Small angle coherent scattering of gammas by bound electrons, J. S. Levinger—656

Scintillation counters (see **Methods and instruments**)

Selection rules (see **Mechanics, quantum; Spectra**)

Semiconductors (see also **Electrical conductivity and resistance**)
Application of cellular method to Si, D. K. Holmes—782
Cu as acceptor element in Ge, C. S. Fuller and J. D. Struthers—526(L)
Diffusion theory of noise in rectifiers and transistors, Richard L. Petritz—189(A)
Effect of 11-Mev electron bombardment on electrical properties of Ge, Luther Davis, Jr., G. A. DeMars, L. G. Rubin, and J. H. Saunders—190(A)
Effects of dislocations on mobilities in semiconductors, F. Seitz and D. L. Dexter—189(A)
Electrical properties of Si $p-n$ junctions grown from the melt, K. B. McAfee and G. L. Pearson—190(A)
Electron distribution in irradiated N-type semiconductors, H. Glaser and A. J. F. Siegert—191(A)
Electron-hole recombination in Ge, R. N. Hall—387(L)
Growth of Si single crystals and single crystal Si $p-n$ junctions, G. K. Teal and E. Buehler—190(A)
High field mobility in Ge with impurity scattering dominant, E. M. Conwell and E. J. Ryder—190(A)
Interpretation of low temperature Hall curve of degenerate Ge sample, D. M. Finlayson, V. A. Johnson, and F. M. Shipley—1141(L)
Lattice defects in Ge, W. C. Dunlap, Jr.—190(A)
Mobility of electrons in Ge, P. P. Debye and E. M. Conwell—1131(L)
New infrared absorption bands in p-type Ge, H. B. Briggs and R. C. Fletcher—1130(L)
Si $p-n$ junction diodes prepared by alloying process, G. L. Pearson and P. W. Foy—190(A)
Statistics of the recombinations of holes and electrons, W. Shockley and W. T. Read, Jr.—835

Shock waves (see also **Explosion phenomena; Supersonics**)
Effects of curved shock waves in pseudo-stationary flows, C. H. Fletcher and A. H. Taub—912(A)
Formation of vortex ring, F. K. Elder, Jr., and N. de Haas—911(A)
Interaction of plane shock waves and rough surfaces, Russell E. Duff—912(A)
Luminous effects in shock tube, R. N. Hollyer, Jr., A. C. Hunting, Otto Laporte, E. H. Schwarcz, and E. B. Turner—911(A)
Motion of elliptical vortices, Henry C. Alberts, George A. Coulter, and Charles M. Warden—911(A)
Reflection of shock waves as pseudo-stationary phenomenon, A. H. Taub and C. H. Fletcher—912(A)
Shock refraction, R. G. Stoner, E. B. Davies, and C. L. Woodbridge—913(A)
Surface motion associated with obliquely incident elastic waves, John Pearson and John S. Rinehart—910(A)
Transient flow variables as function of time, C. W. Curtis, R. J. Emrich, and J. E. Mack—913(A)
Transient high amplitude waves through steel, William A. Allen—910(A)
Vibrational energy lag in shock waves, Wayland Griffith—234(A)

Solid state (see **Crystalline state; Mechanics, quantum—of solid bodies**)

Sound (see **Acoustics**)

Spark discharge (see **Discharge of electricity in gases**)

Specific heat
Atomic heat of Pb in neighborhood of transition to superconductivity, J. R. Clement and E. H. Quinnell—192(A)
Heat capacities of superconducting metals, R. D. Worley, M. W. Zemansky, and H. A. Boorse—1142(L)
Low temperature heat capacity of V, R. D. Worley, M. W. Zemansky, and H. A. Boorse—192(A)
Nuclear and electronic contributions to specific heat of $Nd(EtSO_4)_3$ near 1°K, L. D. Roberts, C. C. Sartain, and B. Borie—192(A)
Of several metals between 1.8° and 4.2°K, I. Estermann, S. A. Friedberg, and J. E. Goldman—582

Spectra, absorption (see also **Absorption of radiation; Spectra, general; Spectra, microwave; Spectra, molecular**)
Absorption by telluric CO in 2.3μ region, J. N. Howard and J. H. Shaw—679(L)

Spectra, absorption (continued)
Absorption system of light and heavy naphthalene vapor at 2900–2500A, C. D. Cooper and H. Sponer—213(A)
Infrared absorption spectrum of liquid stearic acid, E. Scott Barr—170(A)
Infrared and Raman spectroscopic study of CF_3COOH, Marie-Louise Josien, Nelson Fuson, Ernest Jones, and James R. Lawson—170(A)
Infrared spectroscopic studies of carbonyl vibration in polycyclic quinones. I. Influence of substituents, Nelson Fuson, Marie-Louise Josien, and Thomas M. Gregory, Jr.—170(A); II. Influence of fused benzene rings, Marie-Louise Josien, Nelson Fuson, and Jeanne-Marie Lebas—170(A)
Near uv absorption spectra of halogenated pyridines in liquid solution, Harold P. Stephenson—169(A)
Near uv absorption spectra of 1,4 $C_6H_4(CF_3)_2$ and 1,3,5 $C_6H_3(CF_3)_3$, C. D. Cooper and F. W. Noegel—169(A)
Near uv absorption spectra of 2- and 3-fluoropyridine in vapor state, H. P. Stephenson—213(A)
Near uv absorption spectrum of meta difluorobenzene, V. Ramakrishna Rao and H. Sponer—213(A)
New infrared absorption bands in *p*-type Ge, H. B. Briggs and R. C. Fletcher—1130(L)
Spectra, atomic
Electrodynamic corrections to fine structure of positronium, A. Klein and R. Karplus—235(A)
Excitation characteristics of spectra of highly ionized Al in low pressure spark, R. W. Kebler, W. W. McCormick, and R. A. Sawyer—212(A)
Forbidden line of N II, W. Petrie—1002
Isotope shifts in Er, Lawrence Wilets and Lee C. Bradley, III—1019
Lamb shift in ionized He, J. G. Hirschberg, Jr.—228(A)
Mass corrections to fine structure of hydrogen-like atoms, E. E. Salpeter—328
Spectra, general
Energy distribution of CO molecules in CO–O_2 flames, Shirleigh Silverman—214(A)
Infrared emission of H-F flame, W. S. Benedict, B. W. Bullock, Shirleigh Silverman, and A. V. Grosse—213(A)
Infrared emission spectrum of FeO, A. M. Bass and W. S. Benedict—214(A)
Nuclear rf spectra of H_2 and D_2 in high and low magnetic fields, H. G. Kolsky, T. E. Phipps, Jr., N. F. Ramsey, and H. B. Silsbee—395
Qualitative comparison of meteor and fast-particle spectra, William C. White and Richard N. Thomas—912(A)
Radiation loss from atmosphere, Gilbert N. Plass—187(A)
Rf spectroscopy of D_2, R. G. Barnes and P. J. Bray—229(A)
Semiquantitative interpretation of Alfast-particle spectrum, Richard N. Thomas and William C. White—912(A)
Theory of shape and width of bands in vibrational spectra of crystals, Thomas H. Walnut—201(A)
Time-resolved spectroscopy of incandescence associated with ultra-speed pellets, Earle B. Mayfield—912(A)
XYZ method of coincidence correlation spectrometry, Edward C. Campbell—175(A)
Spectra, microwave
Of CH_3F_2, D. R. Lide, Jr.—227(A)
Of $C_3H_{11}Br$, A. H. Nethercot, A. Javan, and C. H. Townes—226(A)
Dipole moments of several molecules from their microwave spectra, S. N. Ghosh, R. Trambarulo, and Walter Gordy—172(A)
Of $HSiCl_3$ and CH_3SiCl_3, Richard Mockler, Jep H. Bailey, and Walter Gordy—172(A)
l-type doubling transitions in HCN and DCN, Thomas L. Weatherly and Dudley Williams—517
Line breadth of OCS as a function of rotational transition and temperature, Charles M. Johnson and Donald M. Slager—677(L)
Line-breadths of the microwave spectrum of oxygen, Roy S. Anderson, William V. Smith, and Walter Gordy—561
Of MnO_3F, A. Javan and A. V. Grosse—227(A)
Masses of stable Te isotopes from microwave spectrum of TeCS, G. Silvey, W. A. Hardy, and C. H. Townes—236(A)
Molecular-beam modulation microwave spectrograph, Clarence F. Luck and Walter Gordy—172(A)
Of NO_2F, D. F. Smith and D. W. Magnuson—226(A)
Pressure broadening of O_2^{16} lines in mm wavelength region, J. O. Artman and J. P. Gordon—227(A)
Pure quadrupole spectra of solid chloroacetic acids and substituted chloroacetic acids, H. C. Allen, Jr.—227(A)
Simple Stark-modulation microwave spectrograph, R. F. Trambarulo and C. F. Luck—172(A)
Variation of collision diameters with mix ratio in binary mixtures in microwave pressure broadening, L. C. Jones, A. V. Bushkovitch, C. A. Potter, and A. G. Rouse—227(A)
Of vinyl cyanide, W. S. Wilcox, J. H. Goldstein, and James W. Simmons—172(A)
Of vinyl iodide, H. W. Morgan and J. H. Goldstein—172(A)
Spectra, molecular (see also **Molecular structure and constants**)
Absorption by telluric CO in 2.3μ region, J. N. Howard and J. H. Shaw—679(L)
Abundance of telluric CO above Columbus, Ohio, J. H. Shaw and J. N. Howard—380(L)
Continuous spectrum of H_2, G. H. Dieke and C. S. Rainwater—212(A)
Hidden transition in biphenyl and anthracene, Anneliese Wenzel—169(A)
Influence of molecular structure upon infrared carbonyl band in polycyclic quinones, Marie-Louise Josien and Nelson Fuson—212(A)
Line breadth of OCS as a function of rotational transition and temperature, Charles M. Johnson and Donald M. Slager—677(L)
Vibrational and centrifugal effects on nuclear interactions and rotational moments in molecules, Norman F. Ramsey—1075
Wavelength shift in spectra of aromatics containing F, H. Sponer—213(A)
Spectra, nuclear (see **Nuclear spectra**)
Spectra, X-ray (see **X-rays, spectra**)
Spectroscopy, technique (see **Methods and instruments**)
Spinor fields (see **Field theory**)
Standards (see **Constants, physical standards**)
Stark effect
Crystalline Stark effect and Zeeman effect in vanadous Tutton salts, W. W. Wada—229(A)
Ion concentrations in intense discharges from Stark effect broadening, H. N. Olsen and W. S. Huxford—233(A)
Statistical mechanics (see **Mechanics, statistical**)
Superconductivity (see also **Electrical conductivity and resistance; Low temperature phenomena**)
Atomic heat of Pb in neighborhood of transition to superconductivity, J. R. Clement and E. H. Quinnell—192(A)
Change in superconducting penetration depth with field, J. Bardeen—192(A)
In Co-Si system, B. T. Matthias—380(L)
In dendritic deposition of pure Sn, T. E. Leinhardt and J. M. Reynolds—178(A)
Effect of surface energy on superconducting phase transition, M. P. Garfunkel—108
Electron-lattice interaction and superconductivity, K. S. Singwi—1044
In graphite compounds, G. Hennig and L. Meyer—439

Heat capacities of superconducting metals, R. D. Worley, M. W. Zemansky, and H. A. Boorse—1142(L)
Low temperature thermal conductivity of Sn and Sn–Bi alloys, D. P. Detwiler—192(A)
Below 1°K, M. C. Steele—1137(L)
Search for new superconducting compounds, B. T. Matthias and J. K. Hulm—799
Similarity properties of two-fluid model of superconductivity, E. Maxwell—1126(L)
Size effects in superconductivity of Cd, M. C. Steele and R. A. Hein—908(L)
Of superconducting alloys of In and Tl, W. F. Love, E. Callen, and F. C. Nix—844
Temperature, current, magnetic field phase diagram of superconductivity, K. Mendelssohn, C. Squire, and Tom S. Teasdale—589

Thermal conductivity
Low temperature thermal conductivity of Sn and Sn–Bi alloys, D. P. Detwiler—192(A)
By unsaturated He II film, Earl Long and Lothar Meyer—153(L)

Thermionic emission, emitting surfaces
Spectral dependence of thermionic emission with activation from (Ba-Sr)O cathodes over visible region, Tadatosi Hibi and Kazuo Ishikawa—673(L)

Thermodynamics
Entropy and specific heat of liquid He^3, K. S. Singwi—540(L)
Irreversibility and generalized noise, Julius L. Jackson—471
Relativistic statistical thermodynamics, A. E. Scheidegger and R. V. Krotkov—197(A)
Thermodynamic continuity and quantum principles, Alfred Landé—267

Thermoluminescence
Electron traps in KCl:Tl phosphor, Peter D. Johnson and Ferd E. Williams—192(A); in ZnS phosphor, Alan W. Smith and John Turkevich—306.

Ultrasonics (see Acoustics)

Vacuum tubes (see **Electronic tubes**)
Vaporization (see **Evaporation**)

Viscosity
Application of high rotational speed techniques to low density gas dynamics, A. R. Kuhlthau—171(A)
Of ortho- and para-hydrogen at low temperatures, E. W. Becker and O. Stehl—325(L)
Ultrasonic automatic viscosity measurement, Stanley R. Rich and Wilfred Roth—235(A)

Wave guide (see **Electromagnetic theory; Electrical circuits**)
Wave mechanics (see **Mechanics, quantum**)

Wave motion
Surface motion associated with obliquely incident elastic waves, John Pearson and John S. Rinehart—910(A)
Transient high amplitude waves through steel, William A. Allen—910(A)

X-rays, absorption, diffraction, scattering, reflection, refraction, and polarization
Small-angle x-ray scattering from serum albumin solutions, J. W. Anderegg, W. W. Beeman, and S. Shulman—186(A)
Transmission through calcite near Bragg angle, George L. Rogosa and Guenter Schwarz—995
X-ray absorption in calcite crystal, Guenter Schwarz and George L. Rogosa—201(A)

X-rays, spectra and spectroscopy, wavelength measurements (see also **X-rays, emission**)
Outer electron structure and Z-dependence of x-ray K-level values for heavy atoms, J. E. Mack—225(A)
Spectroscopy of solid state: Cu and Cr, E. M. Gyorgy and G. G. Harvey—861

Zeeman effect
Crystalline Stark effect and Zeeman effect in vanadous Tutton salts, W. W. Wada—229(A)
Of Ne in metastable $^3P_2$ state, G. Weinreich, G. Tucker, and V. Hughes—229(A)

Notice

The Volume Table of Contents will be omitted in this and succeeding index issues by action of the Publication Board of the American Institute of Physics.

THE AMERICAN INSTITUTE OF PHYSICS

INCORPORATED

57 East 55 Street — [illegible] 22, N.Y.

MEMBER SOCIETIES:

American Physical Society
Karl K. Darrow, Secretary, Columbia University, New York 27, New York

Optical Society of America
Arthur C. Hardy, Secretary, Massachusetts Institute of Technology, Cambridge 39, Massachusetts

Acoustical Society of America
Wallace Waterfall, Secretary, 57 East 55th Street, New York 22, New York

Society of Rheology
G. J. Dienes, Secretary, Brookhaven National Laboratory, Upton, Long Island, New York

American Association of Physics Teachers
R. F. Paton, Secretary, University of Illinois, Urbana, Illinois

AFFILIATED SOCIETIES:

American Crystallographic Association
American Society for Metals
Western Metallurgical Society of America
Physical Society of Philadelphia
Physics Club of Chicago
Physics Club of Pittsburgh
Cleveland Physics Society
Physics Club of the Lehigh Valley
Sigma Pi Sigma

ASSOCIATES:

Over seventy-five leading industrial enterprises and other institutions which contribute to the support of the Institute.

JOURNALS:

The Physical Review
S. A. Goudsmit, Editor, Brookhaven National Laboratory, Upton, Long Island, New York

Reviews of Modern Physics
J. W. Buchta, Editor, University of Minnesota, Minneapolis, Minnesota

Journal of the Optical Society of America
Wallace R. Brode, Editor, National Bureau of Standards, Washington 25, D. C.

The Journal of the Acoustical Society of America
Floyd A. Firestone, Editor, 57 East 55th Street, New York 22, New York

American Journal of Physics
Thomas H. Osgood, Editor, Michigan State College, East Lansing, Michigan

The Review of Scientific Instruments
Gaylord P. Harnwell, Editor, Randal Morgan Laboratory of Physics, University of Pennsylvania, Philadelphia, Pennsylvania

The Journal of Chemical Physics
Joseph E. Mayer, Editor, Institute for Nuclear Studies, University of Chicago, Chicago 37, Illinois

Journal of Applied Physics
Elmer Hutchisson, Editor, Case Institute of Technology, Cleveland 6, Ohio

Physics Today
Gaylord P. Harnwell, Editorial Director; Beatrice Scharf, Managing Editor; American Institute of Physics, 57 East 55th Street, New York 22, New York

OFFICERS

George B. Pegram, Chairman
Columbia University

Gaylord P. Harnwell, Director
Columbia University

GOVERNING BOARD

Karl K. Darrow
G. J. Dienes
S. A. Goudsmit
G. P. Harnwell
George R. Harrison
F. V. Hunt
Rudolph Kingslake
Hugh S. Knowles
C. C. Lauritsen
F. W. Loomis
William F. Meggers
George B. Pegram
I. I. Rabi
Duane Roller
Frederick Seitz
Francis G. Slack
John C. Slater
Richard M. Sutton
Mark W. Zemansky

Consultant on Printing
Melvin Loos

ADMINISTRATIVE STAFF

Henry A. Barton, *Director*
Wallace Waterfall, *Executive Secretary*
Theresa Vaccaro, *Advertising Manager*
Ruth P. Bryan, *Publication Manager*
Betty H. Goodwin, *Assistant Secretary*
Esther B. Newman, *Circulation Manager*
Katherine Smith, *Assistant Treasurer*

THE American Institute of Physics was founded in 1931 as a federation of leading societies in the field of Physics. It combines into one operating unit those functions common to all which can best be done by the societies jointly. Its purpose is the advancement and diffusion of physics and its applications to human welfare. To this end it publishes for itself or the Societies the journals listed on this page; promotes unity and effectiveness of effort among all who are engaged in physics; renders information and direct services to physicists and to the public; and cooperates with governmental agencies, educational institutions, technical industries, and other organizations in such manner as to promote the interests of physics and fulfill the responsibilities of physics as an international and constructive human activity.